RÉPUBLIQUE FRANÇAISE
Liberté Égalité Fraternité

Université de Toulouse

Doctorat de l'Université de Toulouse

préparé à l'Université Toulouse III - Paul Sabatier

Etude pétrophysique, pétrologique et géochimique de l'interface croûte-manteau en Amérique du Sud centrale et méridionale

---

Thèse présentée et soutenue, le 14 décembre 2023 par

Noé MUCKENSTURM

École doctorale
SDU2E - Sciences de l'Univers, de l'Environnement et de l'Espace

Spécialité
Sciences de la Terre et des Planètes Solides

Unité de recherche
GET - Geosciences Environnement Toulouse

Thèse dirigée par
Michel GREGOIRE et Mary-Alix KACZMAREK

Composition du jury
Mme Stéphanie DUCHÊNE, Présidente, Université Toulouse III - Paul Sabatier
Mme Véronique GARDIEN, Rapporteure, Université Lyon1
M. Morales LUIZ, Rapporteur, ETH Zürich
Mme Benita PUTLITZ, Examinatrice, Institut des sciences de la Terre, Faculté des Géosciences et de l'environnement, Université de Lausanne
M. Michel GREGOIRE, Directeur de thèse, CNRS - GET
Mme Mary-Alix KACZMAREK, Co-directrice de thèse, Université Toulouse III - Paul Sabatier

Membres invités
M. Frédéric Mouthereau, University Paul Sabatier Toulouse III

REMERCIEMENTS

Il y a trois ans et demi, j'écrivais dans les remerciements de mon Mémoire de Master que j'étais enfin devenu un Grand. Ce que j'ignorais en écrivant ces lignes, c'est que j'étais encore très con. Cependant, aujourd'hui, à défaut de revendiquer d'être parmi les Grands, je peux me targuer d'être un peu moins petit et d'être un meilleur scientifique qu'au début de cette aventure. Ce n'est pas à moi-même que je dois ça, mais aux autres. D'abord, parce que chaque ligne rédigée, chaque idée transmise dans ce manuscrit, est le reflet de l'influence d'une personne tierce. Ensuite, parce que le bon déroulement d'une thèse nécessite toute une structure solide, incluant techniciens, ingénieurs, gestionnaires… Enfin parce qu'on m'a grassement diverti quand j'explorais ce bac à sable, puis, quand ce dernier s'est transformé en piscine olympique, qu'on m'a généreusement soutenu lorsque je naviguais sans voiles. Donc, à tout ce que les autres m'ont transmis ou offert. A mes directeurs d'abord, Mary-Alix et Michel, pour l'opportunité tendue, leur bienveillance, leur science, et pour m'avoir sans cesse répété que j'avais ma place parmi les Grands. A Fred, pour avoir aussi construit le projet, pour son ambition et sa science que j'ai toujours appréciées. A Theo Ntaflos, Ernesto Bjerg, Friedrich Lucassen pour m'avoir partagé leur collection de xénolithes, sur lesquelles est basé une énorme partie de ce travail, et à Jacqueline Vander Auwera pour ses échantillons du volcan Calbuco. A Stéphanie, pour m'avoir fait venir au Chili en dessinant un plan parfait d'abord et pour ses immenses qualités humaines ensuite, pour la franchise, la communication, le soutien et les coups de cravache (j'ai aimé ça). A Rodrigo, le Fernando Alonso de l'Atacama, pour son accueil, son extrême gentillesse et sa patience. A Alexandre et Gaëlle de Valdivia, pour leur exceptionnel accueil. A Hector, pour son tour du Chili en 24h. A Audrey et sa fille Anaïs de Santiago, pour leur très bonne compagnie. A Julie et Marie, pour avoir fait 28h d'avion pour venir manger des chips à la framboise. Aux gens du labo. A Hadrien, pour toute l'aide, pour m'avoir fait comprendre ce que je faisais, pour la caféine, les blagues, pour Lé Tongé !!! Julien et Oscar, pour les pseudosex (ne cherchez pas la définition sur internet). Oscar toujours et Cali, pour avoir donné vie à mes zircons. A Neil, pour m'avoir appris à tolérer l'étude des microstructures. A Arnaud, Philippe, Fabienne, Françoise, Thierry, et les personnes du service ICP, pour leur Aide pendant mes analyses et le traitement des données, pour leur bienveillance générale. A Murielle et Sonia, et les gens de TIL (les gensTIL lol), pour leurs précieux conseils. Et merci à Véronique, Jérome et Luis d'avoir accepté la lourde tâche d'être les rapporteurs de ma thèse, à Stéphanie pour sa présidence de Jury et également à Benita et à ses généreuses et précieuses remarques sur mon travail. A tous les thésards, postdoc et stagiaires, ceux partis trop tôt, quoicoubébou Neil, Anissa, Rémi, Clément, Léo…ceux toujours très près, ceux que je n'ai pas eu le temps de mieux connaître, tous ceux que j'oublie. A Louise, merci pour ton fromage, merci à Marie et ses gâteaux, Louise et ses crêpes, Mickaël et son empathie hors norme, Louise et le col d'Agnes, Mathilde et son calme, Malissa qui l'est moins, Marine qui court aussi vite que M'Bappé même si personne ne l'a vu faire, Anne et ses histoires, Hugo et son skate, Félix et son rhum goût framboise ou jsais pas jsuis pas fruitier, Paul qui ferait bien d'arrêter de mettre les mêmes sneakers que moi, Kévin ce clubbeur. A Cali, Matthieu, Isah, Théo, Salia, Félix, Isalyne, Laudine, Gwen, Loren, Théo, et Zoé. Pour toutes les blagues, les goûters, les pauses courtes et celles qui l'étaient un peu moins, pour leur chaleur humaine et les soirées coinches. A Aurignac, qui rassemble plus qu'on ne peut l'imaginer. A Montmaurin, et tous les clubbeurs qui en découlent. A mes collocs et ceux qui l'ont été, Sylvain, Enzo, Quentin, Camille, Pos, Emma et Simone, pour leur soutien et leur divertissement. A Vénice, pour la résilience, la confiance, le soutien et pour toutes les autres choses. A ma famille, à mes parents qui croient en moi, à Niels qui grandit bien et vite. A mon papi. A l'Alsace. s'gelt !



Mary-Alix, Fred, moi, Rodrigo, Stéphanie, et le volcan Socompa en arrière-plan.



Deux géologues préparant le déjeuner au pied du volcan Láscar, l'un des plus actifs des Andes.



Le volcan Villarica, qui n'est pas porteur de xénolithes. De fait, son inutilité n'a d'égal que sa forme pyramidale parfaite.

RÉSUMÉ

L'interface croûte-manteau, aussi appelé Moho, est une zone clé de transfert de matière, de chaleur et mécanique pour la compréhension notamment de la croissance, de l'évolution et de la déformation de la croûte. Cependant, en domaine continental, la rareté des affleurements de cette zone de la lithosphère fait que sa compréhension reste encore limitée. Cette étude caractérise les microstructures et les processus pétrologiques en jeu en base de croûte et dans le manteau supérieur dans le domaine continental de l'Amérique du Sud centrale et méridionale. Pour ce faire, des xénolithes de granulites, de pyroxénites et de péridotites remontées par des laves de trois régions ont été sélectionnées: celles des basaltes Oligo-Miocène et Pléistocène du Massif Nord Patagonien (MNP; 41-43°S, Argentine), et celles des basaltes crétacés supérieurs de la région de Salta (26°S, Argentine), deux zones situés en domaine arrière-arc de la convergence Nazca/Amérique du Sud, ainsi que celles des andésites récentes du volcan Calbuco (41°S, Chili), situé au niveau de l'arc de cette convergence. Des analyses microstructurales par *Electron Backscattered Diffraction* ont été effectuées sur ces xénolithes, et couplées avec des analyses pétrologiques, géochimiques et géochronologiques. Les résultats de cette approche multidisciplinaire révèlent que la croûte inférieure du MNP est homogène, peu déformée et affectée par le magmatisme intense qui caratérise le massif depuis le Dévonien. En revanche, la croûte inférieure à Salta est d'origine métasédimentaire et présente un métamorphisme UHT et une déformation en lien avec l'événement thermique associé au rift intracontinental crétacé observé dans cette région. Le manteau lithosphérique de ces deux régions à l'héritage contrasté ont néanmoins subi des événements de déformation similaires, certainement en lien avec des phases extensives en domaine arrière-arc. Enfin, la croûte inférieure sous le volcan Calbuco présente des zones mylonitisées associées à des cumulats magmatiques, montrant le lien étroit dans cette zone entre magmatisme et déformation active. Cette étude révèle l'influence de l'héritage chimique et structural de la lithosphère et de la géodynamique sur la déformation au niveau de l'interface croûte inférieur-manteau subcontinental et des zones avoisinantes.

ABSTRACT

The crust-mantle interface, also known as the Moho, is a key zone of material heat and mechanical transfer, particularly important to better understand the growth, evolution and deformation processes of the crust. However, in the continental domain, the scarcity of outcrops means that our understanding of this zone of the lithosphere remains limited. The present study characterises the microstructures and petrological processes occurring at the base of the crust and within the upper mantle from the continental domain of central and southern South America. Granulite, pyroxenite and peridotite xenoliths sampled by lavas from three regions were selected: those from the Oligo-Miocene and Pleistocene basalts from the Northern Patagonian Massif (MNP; 41-43°S, Argentina), and from the Upper Cretaceous basalts from the Salta region (26°S, Argentina), both located in the back-arc domain of the Nazca/South America convergence, as well as xenoliths from recent andesites from the Calbuco volcano (41°S, Chile), located in the arc of this convergence. Electron Backscattered Diffraction microstructural analyses were carried out on these xenoliths, coupled with petrological, geochemical and geochronological analyses. The results of this multidisciplinary approach reveal that the lower crust of the MNP is homogeneous, only slightly deformed and affected by the intense magmatism that characterises the massif since the Devonian. In contrast, the lower crust from Salta is of metasedimentary origin, showing UHT metamorphism and deformation related to the thermal event associated with the Cretaceous intracontinental rift observed in this region. The lithospheric mantle of these two regions of contrasting heritage has nevertheless undergone similar deformation events, certainly linked to extensive phases in the back-arc domain. Finally, the lower crust beneath the Calbuco volcano shows mylonitised zones associated with magmatic cumulates, demonstrating the close link in this area between magmatism and active deformation. This study reveals the influence of the petrological, chemical and structural heritage of the lithosphere and geodynamics on deformation at the lower crust-subcontinental mantle interface and in neighbouring areas.

Table of Contents

ABSTRACT **5**
Table of Contents **6**
INTRODUCTION **1**
1 DEFINITIONS: GEOPHYSICAL MOHO VS. PETROLOGICAL MOHO **1**
2 KEY GEOLOGICAL PROCESSES ACROSS THE MOHO **2**
3 HOW THE PETROLOGICAL MOHO IS STUDIED? **3**
3.1 Accessing the Moho through direct exposures 3
3.2 Accessing the Moho through xenoliths 4
3.3 The recent petrophysical characterisation of the Moho and its link with the petrogenetic approach 5
4 THE KNOWLEDGE UPON THE CENTRAL AND SOUTHERN SOUTH AMERICAN MOHO **6**
5 AIMS AND PLAN OF THIS STUDY **10**

CHAPTER I: Geological setting **13**
ABSTRACT **13**
RÉSUMÉ **13**
I. 1 CENTRAL AND SOUTHERN SOUTH AMERICA **15**
I. 1.1 Cratons and Terranes formation 16
I. 1.2 Rodinia dislocation 18
I. 1.3 Early Paleozoic sutures 19
I. 1.4 Middle to Late Paleozoic active margin 19
I. 1.5 Late Paleozoic-Early Mesozoic Choiyoi magmatic province 20
I. 1.6 Mesozoic arcs and rifting events 20
I. 1.7 Cretaceous-Paleogene inversion 23
I. 1.8 Cenozoic crustal shortening and Patagonian magmatism 23
I. 2 XENOLITH OCCURRENCES IN CENTRAL AND SOUTHERN SOUTH AMERICA **24**
I. 2.1 Mesozoic-Cretaceous rift-related xenoliths, including Salta xenoliths 26
I. 2.2 Cenozoic Patagonian xenoliths, including North Patagonian Massif xenoliths 26
I. 2.3 Recent arc crustal xenoliths, including Calbuco xenoliths: Crustal contamination magmas and related xenoliths 28
I. 3 STRUCTURE AND COMPOSITION OF THE LITHOSPHERE FROM THE STUDIED ZONES **32**
I. 3.1 North Patagonian Massif 32
I. 3.2 Calbuco 35
I. 3.3 Salta 36

CHAPTER II: Petrology and microstructures of deep crustal rocks from the North Patagonian Massif, given by meta-igneous granulite xenoliths. **38**
ABSTRACT **38**
RÉSUMÉ **39**
II. 1. INTRODUCTION **41**
II. 2. GEOLOGICAL SETTING **42**
II. 3. SAMPLE COLLECTION AND ANALYTICAL METHODS **45**
II. 3.1. Samples collection **45**
II. 3.2. Bulk-rock analyses 46
II. 3.3. Backscatter images and minerals major elements compositions 46
II. 3.4. Clinopyroxene trace elements 47

II. 3.5. Thermobarometry 47
II. 3.6. Crystallographic orientations of minerals 47
II. 4. RESULTS 48
II. 4.1. Sample description and petrography 48
II. 4.1.1. Mafic granulites 48
II. 4.1.2. Websterites 51
II. 4.2. Bulk-rock chemistry 51
II. 4.2.1. Major elements 51
II. 4.2.2. Trace elements 53
II. 4.3. Minerals major elements composition 54
II. 4.3.1. Clinopyroxene 54
II. 4.3.2. Orthopyroxene 55
II. 4.3.3. Plagioclase 56
II. 4.3.4. Spinel-group 56
II. 4.3.5. Accessory minerals (olivine, ilmenite) 58
II. 4.4. Clinopyroxene trace elements 59
II. 4.4.1. Rare Earth Elements 59
II. 4.4.2. Trace Elements 59
II. 4.5. Thermobarometry 61
II. 4.6. Microstructures 63
II. 4.6.1. Crystallographic Preferential Orientation (CPO) 63
II. 4.6.2. Intragranular deformation 66
II. 5. DISCUSSION 69
II. 5.1. Protolith of mafic granulite and websterite xenoliths 69
II. 5.2. Magmatic and deformation processes recorded by the xenolith suite 72
II. 5.2.1. Mafic Granulites 72
II. 5.2.2. Websterites 75
II. 5.3. Pressure, temperature conditions and stability of the lower crust 76
II. 5.4. New constraints on the lower crust and the petrological Moho below the NPM 78
II. 6. CONCLUSIONS 78
FUNDING 79
ACKNOWLEDGEMENTS 79
REFERENCES 80

CHAPTER III: The deformation of the deep crust from the southern Cordillera of the Andes: Calbuco xenoliths 94
ABSTRACT 94
RÉSUMÉ 95
III. 1 INTRODUCTION 96
III. 2 GEOLOGICAL SETTING 98
III. 3 SAMPLE COLLECTION AND ANALYTICAL METHODS 99
III. 3.1 Sample collection 99
III. 3.2 Minerals major and minor elements compositions 100
III. 3.3 Phase equilibrium modelling 100
III. 3.4 Crystallographic orientations of minerals 101
III. 4 RESULTS 101
III. 4.1 Sample description and petrography 101
III. 4.1.1 Mylonites and ultra-mylonites 102

III. 4.1.2 Magmatic porphyric rocks 104
III. 4.2 Minerals major elements chemistry 108
III. 4.2.1 Clinopyroxene 108
III. 4.2.2 Orthopyroxene 110
III. 4.2.3 Plagioclase 111
III. 4.2.4 Amphibole 112
III. 4.2.5 Olivine 113
III. 4.2.6 Titanomagnetite 113
III. 4.3 Thermometry and phase equilibrium modelling 115
III. 4.3.1 Thermometry 115
III. 4.3.2 Phase equilibrium modelling 115
III. 4.4 Microstructures 119
III. 4.4.1 Mylonite crystal preferred orientation (CPO) 119
III. 4.4.2 Igneous rocks CPO 121
III. 4.4.3 Intragranular deformation 124
III. 5 DISCUSSION 127
III. 5.1 Pressure-temperature estimations 127
III. 5.2 Crystallisation sequence 130
III. 5.3 Deformation recorded by the lower crust 131
III. 5.3.1 Mylonites and ultramylonites 131
III. 5.3.2 Magmatic porphyric xenolith fabrics 133
III. 5.4 A temporal model of crystallisation and deformation of Calbuco xenoliths 134
III. 6 CONCLUSION 136

CHAPTER IV: The lower crust beneath Salta intracontinental rift: zircon petrochronology and microstructural analysis of granulite xenoliths 138
ABSTRACT 138
RÉSUMÉ 139
IV. 1 INTRODUCTION 140
IV. 2 GEOLOGICAL SETTING 143
IV. 3 SAMPLE COLLECTION AND ANALYTICAL METHODS 144
IV. 3.1 Sample collection 144
IV. 3.2 Phase equilibrium modelling 144
IV. 3.3 Backscatter images and minerals major elements compositions 145
IV. 3.4 Zircon U-Pb datation and trace elements analyses 145
IV. 3.5 Crystallographic orientations of minerals 146
IV. 4 RESULTS 147
IV. 4.1 Sample description and petrography 147
IV. 4.2 Zircon dating and trace element compositions 149
IV. 4.3 Phase equilibrium modelling and thermometry 152
IV. 4.4 Microstructures 152
IV. 4.4.1 Crystallographic Preferential Orientation (CPO) 152
IV. 4.4.2 Intragranular deformation 154
IV. 5 DISCUSSION 156
IV. 5.1 Petrochronology of the zircon from the Salta granulites 156
IV. 5.2 P-T conditions of the felsic granulites 157
IV. 5.3 Deformation events recorded by the xenolith suite 158
IV. 5.4 Structure of the lower crust during the Salta rift event 159

IV. 6 CONCLUSIONS **161**

CHAPTER V: The microstructural state of the lithospheric mantle near the Moho in the North Patagonian Massif and Salta rift **163**
ABSTRACT **163**
RÉSUMÉ **164**
V. 1 INTRODUCTION **165**
V. 2 GEOLOGICAL SETTING **167**
V. 3 SAMPLE COLLECTION AND ANALYTICAL METHODS **170**
V. 3.1 Sample collection **170**
V. 3.2 Crystallographic orientations of minerals 170
V. 4 RESULTS **172**
V. 4.1 Sample description and petrography 172
V. 4.1.1 North Patagonian Massif peridotite xenoliths 172
V. 4.1.2 Las Conchas Valley ultramafic xenoliths 174
V. 4.2 Minerals major and trace element compositions 177
V. 4.2.1 Chemical compositions of minerals from the North Patagonian Massif 177
V. 4.2.2 Chemical compositions of minerals from Las Conchas Valley 182
V. 4.3 Thermometry 183
V. 4.4 Microstructures 183
V. 4.4.1 North Patagonian Massif peridotites 183
V. 4.4.2 Las Conchas Valley peridotites 190
V. 4.4.3 Las Conchas Valley clinopyroxenites 195
V. 5 DISCUSSION **196**
V. 5.1 Plastic deformation recorded by North Patagonian Massif xenoliths 196
V. 5.1.1 Plastic deformation 196
V. 5.1.2 Thermal and magmatic state of the mantle in the NPM 198
V. 5.1.3 Deformation and chemistry relationships 201
V. 5.1.4 Timing of deformational processes 202
V. 5.2 Plastic deformation recorded by Salta rift xenoliths 203
V. 5.2.1 Plastic deformation 203
V. 5.2.2 Deformation and chemistry relationships 204
V. 6 CONCLUSION **204**

BIBLIOGRAPHY **211**

APPENDICES **241**
Supplementary Material from the Chapter II : Petrology and microstructures of deep crustal rocks from the North Patagonian Massif, given by meta-igneous granulite xenoliths. **241**
APPENDICE SIII **252**
APPENDICES SIV. **253**
APPENDICE SV. **261**

INTRODUCTION

1 DEFINITIONS: GEOPHYSICAL MOHO VS. PETROLOGICAL MOHO

The Mohorovičić discontinuity, abbreviated Moho, was first described in 1909 by Mohorovičić as a seismic boundary defined by a velocity increase of compressional P waves (Mohorovičić, 1909). During the ’60s, this geophysical Moho was more precisely defined by a P-wave velocity increase from 7.6 to 8.6 km/s (Steinhart, 1967). In the ‘80s petrologists introduced the term “Petrological Moho” to indicate that the geophysical Moho reflects a compositional change from crustal felsic rocks to mantle ultramafic peridotites (Griffin & O’Reilly, 1987; Mengel & Kern, 1992; Peron-Pinvidic, 2022). Many years of research led to propose that in numerous cases the Petrological Moho represents a transitional zone consisting of a succession of ultramafic and mafic layers, rather than a sharp boundary (Grégoire *et al.*, 2001; O’Reilly & Griffin, 2013; Cawood *et al.*, 2022; Fig. 1). The transition zone is estimated to have a thickness varying from 5 to 15 kilometres in non-cratonic settings (O’Reilly & Griffin, 2013), but seems to be sharper below cratonic regions (Abbott *et al.*, 2013; Levin *et al.*, 2016). In order to assess a finite petrologic threshold between the crust and the mantle, O’Reilly & Griffin (2013) defined the base of the crust “as the depth at which ultramafic rocks become a significant (>10-20%) component of the section”. The depth of the Petrological Moho is settled at around 30-40 kilometres for a stable continental lithosphere, either cratonic or modern, and reaches 80 kilometres for orogens. It finally decreases for ocean-continent transitions down to 10 kilometres for a mean oceanic crust (Hacker *et al.*, 2015; Pearson *et al.*, 2021; Wang *et al.*, 2021; Cawood *et al.*, 2022).

According to O’Reilly & Griffin (2013), the “Petrological Moho” terminology was unpopular among geophysicists, who preferred the term “crust-mantle boundary” (CMB). However, major limitations to the geophysical observation of the Moho have since been pointed out. First, the geophysical approach is dependent on the method leading to various results for the same studied region (Peron-Pinvidic, 2022). Second, the CMB often represents a sharp boundary, contrasting in many cases with the progressive Petrological Moho model. Complex lithologies occurring near the CMB may distort its depth estimate. For instance, eclogites formed as a result of metamorphism of thickened cold orogenic or cratonic zones

have the same density and P-waves velocity as mantle peridotites and can create a bias for seismic interpretations (Mengel & Kern, 1992; Wang *et al.*, 2013). In the same line of exception, O'Reilly & Griffin (1985) evidenced that the CMB beneath south-eastern Australia coincides with the depth of the spinel- to garnet-lherzolite upper mantle transition zone (Austrheim, 2013). Apart from theses biases, O'Reilly & Griffin (2013) outlined that the Petrological Moho is located in this generally at a much shallower depth than the CMB (Fig. 1), and therefore that the CMB does not always coincide with the boundary between the felsic crust and the ultramafic upper mantle.

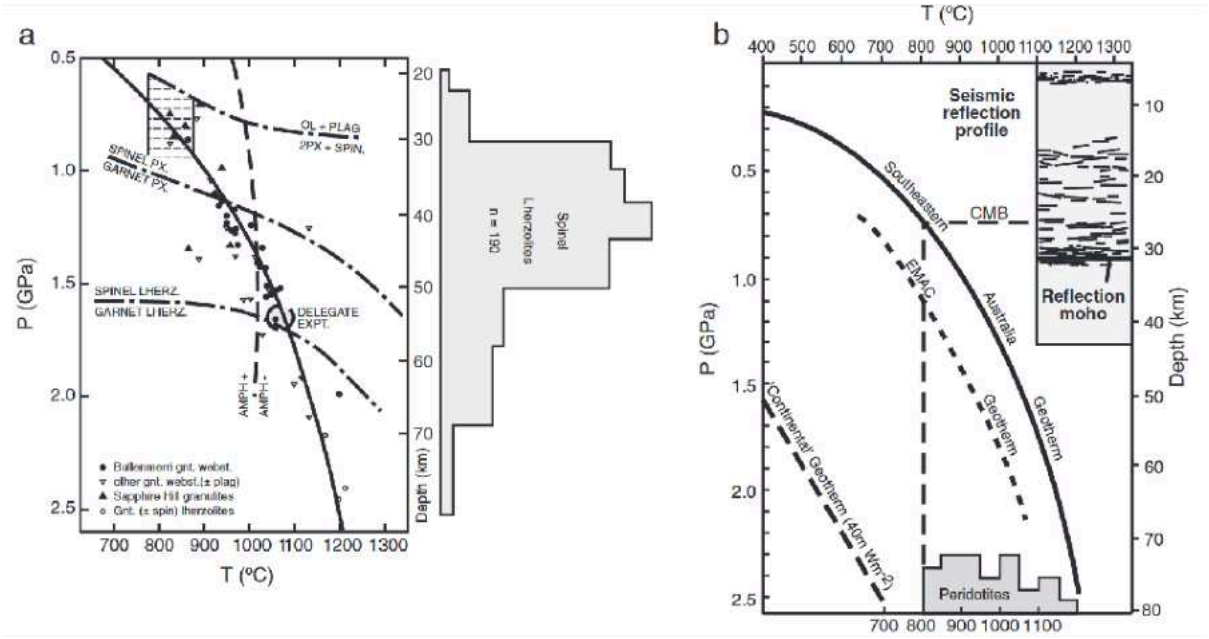


Fig. 1. Geotherm calculated from two-pyroxene and garnet xenolith data from alkaline basalts in East Autralia (figure from O'Reilly & Griffin, 2013). (a) Thermobarometric data from peridotites and pyroxenites, defining the geotherm of the region. The "Delegate Expt." field includes experimental conditions that reproduce the mineralogical assemblages of garnet pyroxenite xenoliths from the Delegate volcanic vent. The histogram shows the distribution of T estimates of spinel lherzolites from volcanoes in eastern Australia. (b) Distribution of T estimates of peridotites from Bullenmerri, compared with the seismic reflection profile of the region (Finlayson *et al.*, 1993); the crust-mantle boundary (CMB) - whose depth corresponds to the lowest P-T estimates where peridotite xenoliths are found - lies above the reflector package corresponding to the geophysical CMB.

2 KEY GEOLOGICAL PROCESSES ACROSS THE MOHO

Magmatic and mechanical processes are involved across the crust-mantle transition. They can be summarized as follows: (i) magma underplating below the crust (e.g. Embey-Isztin *et al.*, 1990; Bryant *et al.*, 2007; Li *et al.*, 2018; Valera *et al.*, 2019) associated with magma

fractionation - with potential crustal assimilation - before the ascent of mantle-derived magmas through the crust (e.g. (López De Luchi *et al.*, 2017; Burns *et al.*, 2020; Vander Auwera *et al.*, 2021; Oriolo *et al.*, 2023), (ii) mantle-derived magmatism at the base of the crust during continental delamination (Navarrete *et al.*, 2019; Gianni & Navarrete, 2022) and subduction processes (Lamb & Davis, 2003; Stern, 2020), (iii) the degree of mechanical decoupling between the crust and the lithospheric mantle during mountain building or continents rifting, that is controlled by age-dependent compositional and physical properties of the continental lithosphere (e.g. Mouthereau *et al.*, 2013, 2021). In addition, the continental crust-mantle boundary can be very heterogeneous including variations in lithologies, thermal gradients, rock anisotropies and the occurrence and nature of fluid(s). These inherited heterogeneities are potential mechanically weak zones that impact decoupling and therefore the styles of deformation. Positive feedback between mechanical and mass transfers is also a very important process. For instance, melt or fluid circulation may concentrate in deformation zones, which favours additional mechanical weakening of the deformation zone (e.g. Contreras-Reyes *et al.*, 2021).

Those parameters may vary from metre to kilometre scale and thus are not always constrained by geophysical observations (seismicity, gravity, magnetism). However, few recent studies start to improve the models by including natural sample studies (e.g. Gomez Dacal *et al.*, 2021; Wang *et al.*, 2021). In summary, because the Moho can be more complex in terms of composition and mechanical properties than viewed by the geophysical approaches, studying it from the petrological point of view provides an independent approach and become necessary to refine geophysical models and improve our understanding of lithosphere-scale dynamic processes, which in turn impact mitigation of natural risks such as earthquakes and volcanism.

3 HOW THE PETROLOGICAL MOHO IS STUDIED?

3.1 Accessing the Moho through direct exposures

The petrology of the Moho has been intensely studied at oceanic ridges where the Moho is shallower than in continental settings, using deep drilling campaigns such as those conducted under the International Ocean Discovery Program and International continental drilling program (IODP and ICDP, e.g. Godard *et al.*, 2009; Pistone *et al.*, 2017; Lambart *et al.*, 2019; Kourim *et al.*, 2022). Ocean-continent transition or advanced back-arc regions constitute

other favourable contexts, where hyper-extended continental margins could exhume pieces of subcontinental upper mantle and associated crustal domains and yet, provide directly at (or near) the surface of the Earth some outcrops of the Moho, reached by drilling programs or accessible in ophiolite occurrences (e.g. Boillot *et al.*, 1988; Beslier *et al.*, 1993; Manatschal & Müntener, 2009; Péron-Pinvidic & Manatschal, 2010; Pistone *et al.*, 2017; Rospabé *et al.*, 2018; Kourim *et al.*, 2022). Thus, the mantle-crust transition zone in such types of divergence settings is relatively well-constrained (e.g. Péron-Pinvidic & Manatschal, 2010; Duretz *et al.*, 2016; Jolivet *et al.*, 2018, 2021; Ganade *et al.*, 2023).

There are scarce known exposures of the continental Moho onland. In some localities, continental collision has thrust up deep granulite-facies terrains, which may be contiguous with large ultramafic bodies, like in the Ivrea-Verbano Zone (Italy; Rivalenti *et al.*, 1981; Zingg *et al.*, 1990; Siegesmund *et al.*, 2008), the Betic Cordillera (S. Spain and N. Africa; Tubía *et al.*, 2013), the Musgrave Ranges (central Australia; O'Reilly & Griffin, 2013), and Platta and Err nappes in the Alps (Manatschal, 2004). Those contacts have been suggested as examples of the crust-mantle boundary. However, if their exhumation is slow, it may erase granulite metamorphic assemblages which challenge their lower crust origin, as well as the fact that ultramafic bodies belong to the upper mantle near the Moho, as it could be tectonic lenses within the upthrust granulites (Rudnick & Fountain, 1995; O'Reilly & Griffin, 2013). In this case, many of these sections may represent mid-crustal levels, rather than the true lower crust and CMB. Hacker *et al.* (2015) suggest that only the Ivrea zone represents the lowermost crust.

3.2 Accessing the Moho through xenoliths

Mantle and deep crustal xenoliths brought to the surface in basaltic flows allow us to have direct access to the Petrological Moho and adjacent rocks. Even if the xenolith occurrence remains punctual through the Earth's surface, it provides crucial information on the structure of the Moho and on diverse petrogenetic processes occurring between the lower crust and the upper mantle (Downes, 1993, 2001; Kempton *et al.*, 1995; Villaseca *et al.*, 1999 and references therein). Among them, magma crystallisation and differentiation in continental arc (e.g. the Andean Southern Volcanic Zone; Hickey-Vargas *et al.*, 1995) and oceanic arc settings (e.g. the Luzon arc; Valera *et al.*, 2019) have been highlighted, as well as the underplating of large mafic crustal component and remobilisation of inherited lower crust in non-cratonic (e.g. in Europe; Embey-Isztin *et al.*, 1990; Kempton *et al.*, 1997; Laurent *et al.*,

2023) and cratonic lithosphere (Markwick & Downes, 2000; Kempton *et al.*, 2001; Markwick *et al.*, 2001; Yu *et al.*, 2003; Li *et al.*, 2018; Shatsky *et al.*, 2019; Su *et al.*, 2020; Volkova *et al.*, 2022). More rarely, some studies highlight that lower crust partial melting is linked to the metamorphic contact related to mafic intrusions (Dorfler *et al.*, 2015). In some cases, both crustal and mantle-derived xenoliths could be sampled, for instance in the Betic Cordillera (Bianchini *et al.*, 2013), Scotland (Upton *et al.*, 2011), the Kamchatka subduction arc (Bryant *et al.*, 2007) or the Kerguelen archipelago (Grégoire *et al.*, 1994, 1998, 2001). Those studies have established the layered character of the Petrological Moho made of the accumulation of ultramafic or mafic magmatic rocks within or below the lower crust, as well as the depleted character of the lithospheric mantle which may be refertilised through melt percolation (e.g. Mundl *et al*., 2016).

3.3 The recent petrophysical characterisation of the Moho and its link with the petrogenetic approach

Recent technological advances in the study of microstructures, such those made using Electron backscattered diffraction (EBSD), have intensified the attention paid to deformation processes occurring at the crust-mantle boundary, as it enhanced seismic properties knowledge of the Moho (Almqvist & Mainprice, 2017; Wang *et al.*, 2013). Studies using EBSD have focused mainly on the lithospheric mantle in various geodynamic settings, including extensive domains in continental rift (Kaczmarek & Reddy, 2013; Baptiste *et al.*, 2015; Fernández-Roig *et al.*, 2018), oceanic detachment (Kaczmarek & Tommasi, 2011), oceanic or continental strike-slip fault (Vauchez *et al.*, 2012; Kourim *et al.*, 2015; Hidas *et al.*, 2019; Bickert *et al.*, 2023) and back-arc settings (Zaffarana *et al.*, 2014), or in compressive domain in subduction setting (Xu *et al.*, 2006; Soustelle *et al.*, 2010; Liu *et al.*, 2019).

The number of studies focusing on the deformation of the continental lower crust is much limited. We may cite for example one on lower crustal cumulates formation (Ji *et al.*, 2014), and one on fluid-melt interaction (Degli Alessandrini *et al.*, 2017). Finally, crustal and mantle xenoliths from the California and Baja California shear zones allowed the study of both sides of the Moho at a strike-slip plate boundary (Bernard & Behr, 2017; van der Werf *et al.*, 2017).

Even more recent studies tend to pay particular attention to linking both petrogenetic and deformation processes using petrology, geochemistry and microstructural analysis (e.g.

Kaczmarek & Tommasi, 2011; Kaczmarek *et al.*, 2016; Puziewicz *et al.*, 2020, 2023; Vieira Duarte *et al.*, 2020; Tedonkenfack *et al.*, 2021; Heckel *et al.*, 2022). The interest of this type of project is to characterise the rock in detail to determine their conditions of formation and evolution (e.g. temperature, magmatism, plastic deformation, mineralogic reactions). Nevertheless, to our knowledge, only two studies have looked at both the lower crust and the upper mantle using microstructure and petrology (Bernard & Behr, 2017; van der Werf *et al.*, 2017). The purely microstructural study by Bernard & Behr (2017) targets the shear zone in California, and shows that the lower crust has a magmatic texture while the mantle has recorded more deformation related to the geodynamic context. The study by van der Werf *et al.* (2017), in a rifting context, shows that the upper mantle and lower crust have similar rheology, which is a major result for characterising the Moho. However, since 2017, there have been no similar studies, even though the continental Moho need to be characterised to understand the relationships between petrological evolution (e.g. magma production and circulation), metamorphism and plastic deformation, which remain poorly defined.

4 THE KNOWLEDGE UPON THE CENTRAL AND SOUTHERN SOUTH AMERICAN MOHO

In central and southern South America, the absence of direct outcrops of recent (i.e. Mesozoic or younger) continental lower crust complicates our understanding of its composition and structure. Indeed, high-pressure metamorphic rocks from Limón Verde in N-Chile (Lucassen *et al.*, 1999a; Soto Verdugo, 2013) and the Guarguaraz Complex in W-Argentina (Willner *et al.*, 2011) are at a minimum Permian in age. Moreover, they represent subducted metamorphic rocks rather than stable continental lower crust. Nevertheless, those rocks are good evidence of continental block sutures and assembling in South America (e.g. Ramos *et al.*, 2000).

The knowledge of the central and southern South America lower crust was mainly built from indirect information obtained on middle to upper crust rock. For example, old outcropping rocks, such as Paleozoic metamorphic rocks located along the Chilean coast have been considered as part of the nearby basement, extending possibly to the Petrological Moho (Hervé *et al.*, 2007).The nature of the lower crust in South America has been characterised in part by provenance studies and statistical analysis of detrital zircon

populations, suggesting a potential inherited basement now covered by younger rocks (see section I.1.1-3). Sm-Nd and Hf isotope analysis applied to magmatic rocks can be used to highlight potential interactions between the lower crust and mantle-derived magmas and crustal anatexis events, and allow to estimate an age - often Mesoproterozoic - of the lower crust (e.g. Pankhurst *et al.*, 2014). Today, there are only two petrological and geochemical studies focusing on xenoliths in the lower crust, one concerning the Salta province in northwest Argentina and the other the Calbuco volcano in southern Chile (Hickey-Vargas *et al.*, 1995; Lucassen *et al.*, 1999b). The first demonstrated the predominance of anhydrous felsic garnet granulites in the lower crust below the Sub-Andean ranges(Lucassen *et al.*, 1999b). The second linked the presence of mafic granulite xenoliths from the lower crust to outcrops of Carboniferous metabasalts present on the Coastal Cordillera and in the North Patagonian Andes, and thus suggested the predominance of Upper Paleozoic rocks in the crustal basement of the North Patagonian Andes (Hickey-Vargas *et al.*, 1995). Authors also described cumulates formed in the lower crust by magmas from the Calbuco volcano.

Geophysical data and models, including gravity, seismic tomography and seismic data are employed to confirm the continuity, homogeneity and depth of this supposed basement or to detect different lithologies and structures (Assumpção *et al.*, 2013; Chulick *et al.*, 2013; Yáñez Carrizo & Herrera, 2019; Contreras-Reyes *et al.*, 2021 and references therein). For example, these models have highlighted the current partial melting of a large volume of middle and lower crust beneath the Altiplano plateau (i.e. the Altiplano-Puna magma body; Chmielowski *et al.*, 1999; Zandt *et al.*, 2003; Prezzi *et al.*, 2009). Similarly, the plunge angle of the Nazca plate beneath the South American lithosphere has been calculated by seismic studies, which have highlighted the flat subduction zone in the central Andes between 28 and 34°S latitude (e.g. Gutscher *et al.*, 2000). High-resolution geophysical studies are often focused on the seismically and volcanically active regions, such as the Andean Cordillera and Chile (Wigger *et al.*, 1994; Chmielowski *et al.*, 1999; Oncken *et al.*, 2003; Zandt *et al.*, 2003; Prezzi *et al.*, 2009; Dzierma *et al.*, 2012; Tassara & Echaurren, 2012; Sielfeld *et al.*, 2019), or on sedimentary basins rich in valuable resources (e.g. Zeller *et al.*, 2015). Consequently, small-scale and high-resolution geophysics models for regions such as the back-arc region of the Pacific-South America convergence, encompassing most of Argentina, are limited.

On the other side of the Moho, studies of mantle xenoliths at various locations in Argentina, particularly in Patagonia, have provided insights into the petrological and

geochemical characteristics of the subcontinental lithospheric mantle (SCLM; Stern *et al.*, 1999; Dantas, 2007; Bjerg *et al.*, 2009; Mundl *et al.*, 2016; Melchiorre *et al.*, 2020). However, the petrophysical characteristics of the SCLM have only been studied in detail in a study of Gobernador Gregores and Pali Aike xenoliths in southern Patagonia (Zaffarana *et al.*, 2014).

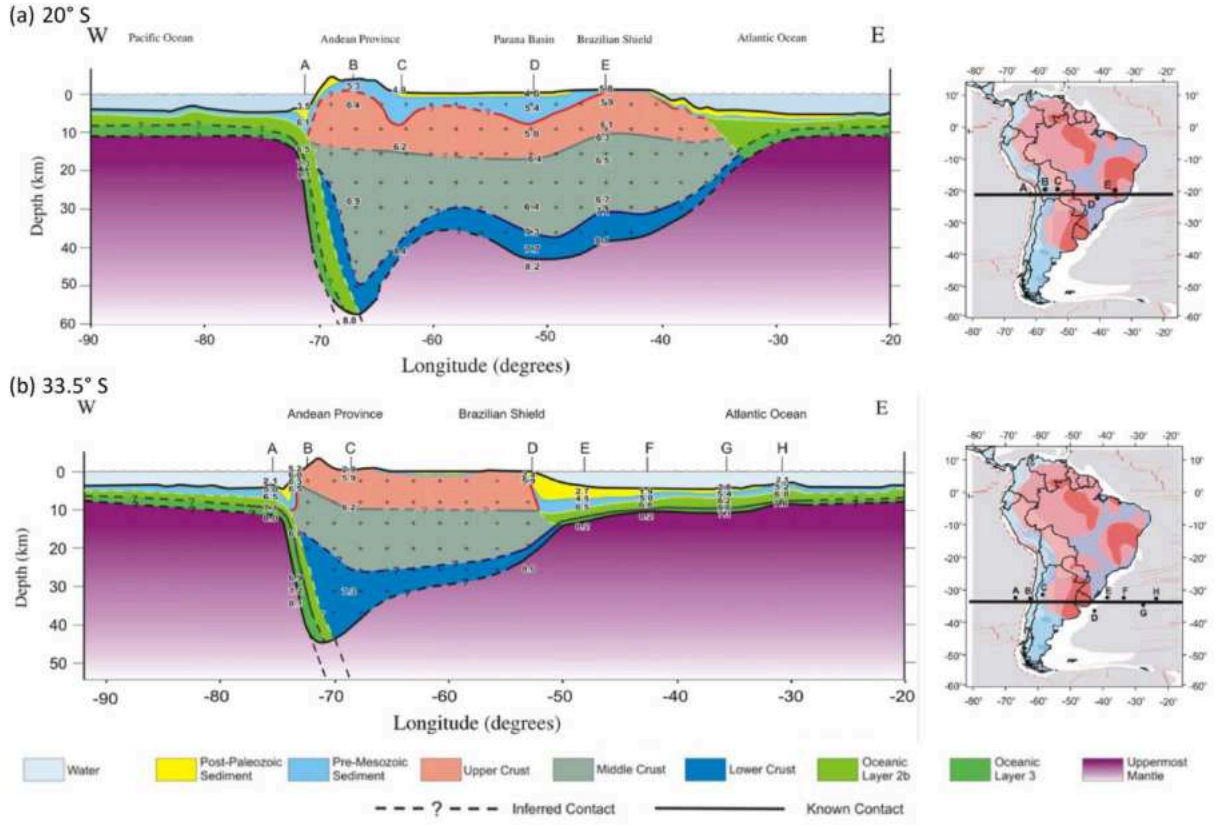


Fig. 2. Lithospheric structural model of the South American continent at (a) 20° S latitude (vertical exaggeration is 110), and (b) 33.5° S latitude (vertical exaggeration is 130), calculated from seismic P-wave velocities, which are indicated by the black bold numbers on the cross-section. Modified from Chulick *et al.* (2013).

The Moho depth varies depending on the regional geological context. In the westernmost parts of central and southern South America (Chile and W-Argentina), corresponding to the Arc region of the Nazca subduction beneath South America, a crustal root records active crustal growth due to magma ascent from the lithospheric mantle. The crustal root extends to a depth of 60 km in the Central Andes and streches up to several hundred kilometres to the east (Wigger *et al.*, 1994; Fig. 2). However, in the Southern Andes, it reaches a depth of only 40 km, and its E-W extension is limited (Tassara & Echaurren, 2012; Fig. 2). This discrepancy in crustal thickness between the Central and Southern Andes is a subject of ongoing debate (e.g. Chen *et al.*, 2019). The difference in shortening, with

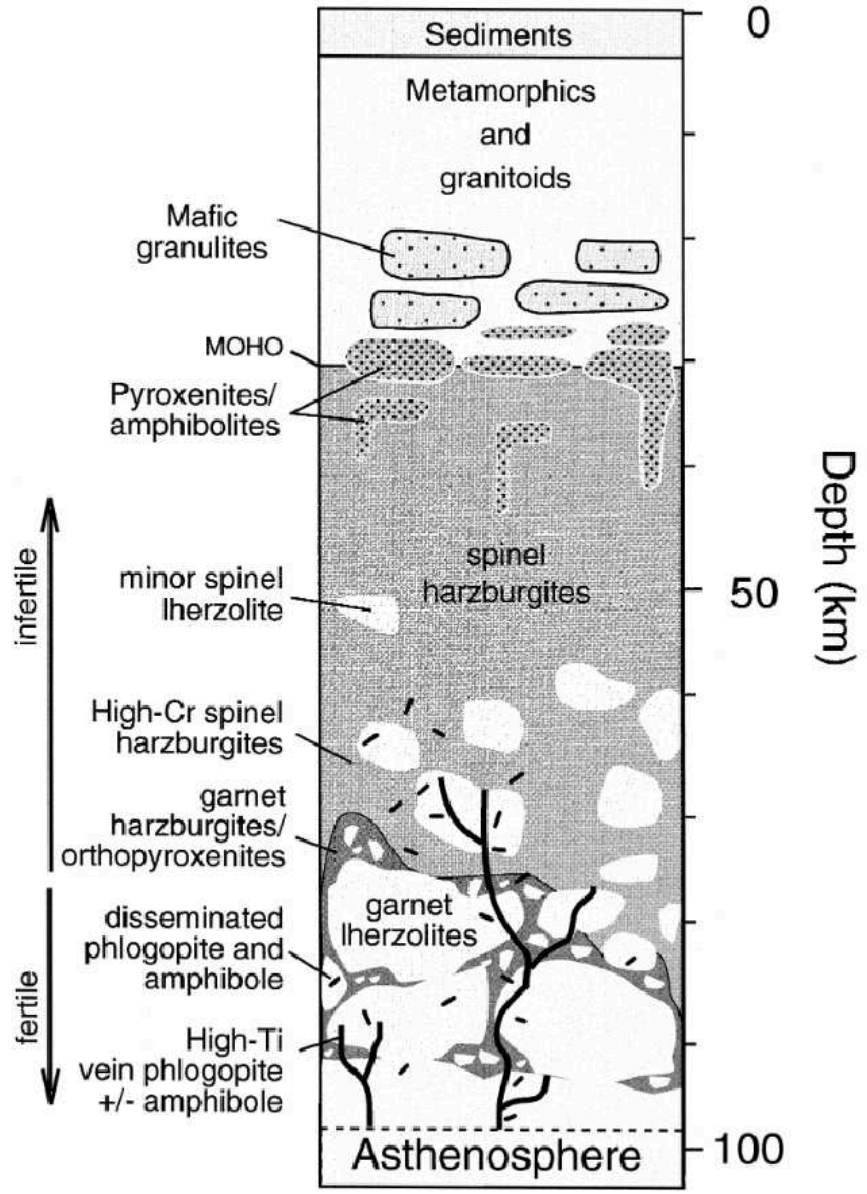


Fig. 3. Lithological section of the southernmost region of Patagonia, suggested by the P-T estimates of the Pali-Aike xenoliths (figure from Stern *et al.*, 1999). The lower crust contains mafic granulites. Depleted spinel harzburgites dominate the uppermost part of the lithospheric mantle, while the lower part is composed of fertile garnet lherzolites. The lower part of the lithosphere was affected by cryptic and modal metasomatism contemporaneous with the generation of the Pali-Aike basalts.

approximately 200 km in Central Andes and about 20 km in Southern Andes (Echaurren *et al.*, 2022), might be a key factor in explaining this variation in crustal thickness.

In the back-arc region of the Pacific-South America convergence system located in NW Argentina, the Moho is relatively deep (40 km) and stable since the Devonian period, corresponding to the end of Early Paleozoic Pampian and Famatinian orogenic events

(Heredia *et al.*, 2016). During the Cretaceous period, a thermal heating event occurred, forming intracontinental rift basins and leaving a lasting imprint on the region (Lucassen *et al.*, 2005). In contrast, Patagonia experienced intense magmatic activity from the Devonian to recent times (e.g. Kay *et al.*, 2004; Foley *et al.*, 2023; Oriolo *et al.*, 2023). This thermal anomaly results in a thin lithosphere, approximately 100 km thick, across Patagonia (Stern *et al.*, 1999; Bjerg *et al.*, 2009; Fig. 3). However, the Moho depth is heterogeneous, as it is shallower beneath Mesozoic basins (e.g. Gómez Dacal *et al.*, 2017) and thicker in undeformed regions such as the North Patagonian Massif (NPM; Fig. 4). Overall, the diversity of central and southern South American geology involves heterogeneous lower crust and uppermost mantle heritage, magmatic activity and thermal state which comprehension is still ongoing. Moreover, the deformation type and repartition occurring in the lower crust and the SCLM, and thus, in relation with the Moho, in various regions of the continent, is poorly constrained.

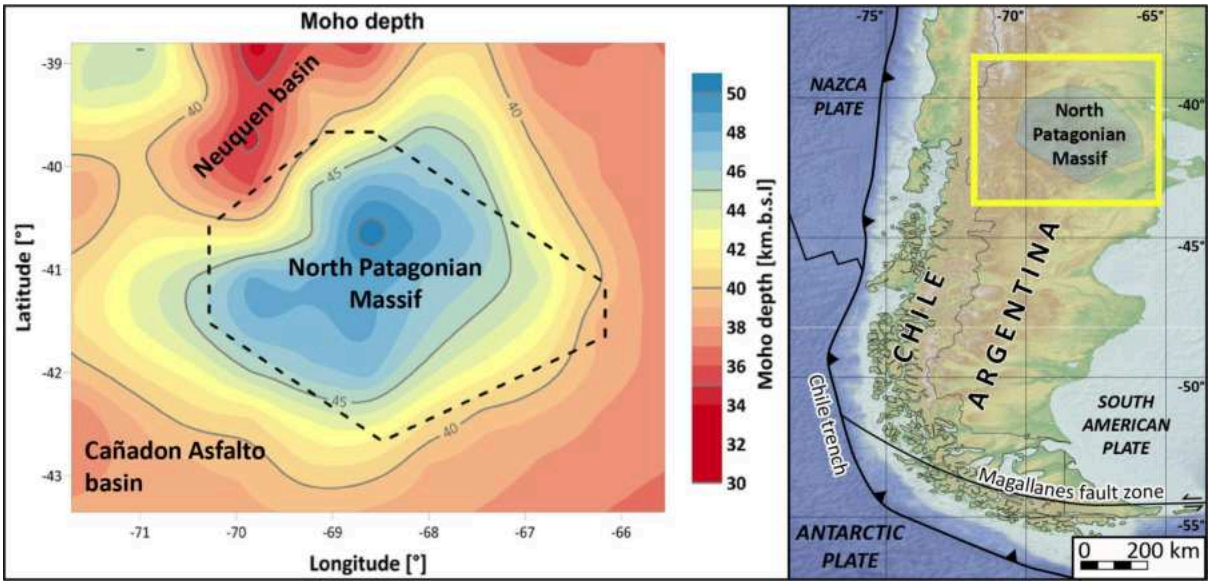


Fig. 4. Moho depth map in Northern Patagonia (modified after Gómez Dacal *et al.*, 2021). Yellow square indicates emplacement of the map in Southern South America.

5 AIMS AND PLAN OF THIS STUDY

This manuscript presents microstructural (EBSD), petrological and geochemical analysis (whole rock and mineral major and trace elements, and zircon U-Pb dating) of lower crustal and mantle xenoliths from three distinct regions from central and southern South America: the Las Conchas Valley in the Cretaceous Salta rift basins (26° S, Argentina), the NPM (41-43° S, Argentina) and the Calbuco volcano in the North Patagonian Andes (41° S, Chile).

Using both new and existing data, models have been developed for each region. These models consider deformation, thermal state, thickness, nature, origin and evolution of the lower crust. Upper mantle xenoliths from the NPM and the Salta rift have enabled the extension of these models to the SCLM and, consequently, the Petrological Moho of these two regions. By comparing the petrological and petrophysical state of the Moho between the three regions, this study aims to provide insights into their common history on a large scale, considering the Pacific-South America convergence occurring over the past 500 Ma, as well as their contrasting heritage and finer-scale geological contexts.

Chapter I summarises the geological history of central and southern South America and sets the three investigated zones studied in this thesis within this broader context. It also presents the current knowledge about their lithospheric structure and composition.

Chapter II relates to a lower crustal xenolith suite from the North Patagonian Massif in Argentina (41-43° S), sampled by Oligo-Miocene and Pleitocene lavas. Therefore it presents a model of the deformation, thermal state, thickness, nature, origin and evolution of the recent lower crust in a back-arc context. This model is based on microstructural analysis as well as whole rocks and minerals major and trace elements compositions of mafic granulites and websterites xenoliths.

Chapter III presents the study of a xenolith suite sampled on the Calbuco volcano in the southern volcanic zone (41°S), which were brought recently to the surface. The microstructural and petrological analysis of these mylonitic and igneous-textured xenoliths enables us to characterise plastic deformation and their link with contemporary magmatic events in a magmatic transform zone.

Chapter IV focuses on the thermal state and the deformation of the lower crust beneath Salta intracontinental rift basins during the Cretaceous. The proposed model uses new microstructural analysis of felsic and mafic granulite xenoliths as well as zircon U-Pb dating and trace element analysis from a felsic granulite.

Chapter V focuses on microstructural features of the mantle xenoliths from both the NPM and Salta intracontinental rift zones. These new data are combined with existing petrological and geochemical data, and results are compared to lower crust models from the precedent chapters in order to propose a deformational, thermic and evolutional model of the Petrological Moho beneath the NPM and the Salta rift.

CHAPTER I: Geological setting

ABSTRACT

The present PhD manuscript focuses on the lower crust and the petrological Moho from three localities of central and southern South America, in the Andean cordillera arc (Chile) and in the South American continental lithosphere (Argentina). The two first localities are the North Patagonian Massif (NPM) in Argentina (41-43°S) and the Calbuco volcano in Chile (41°S). The first one corresponds to a Cenozoic volcanic province emplaced into a Mesoproterozoic massif of South America continent positioned in the back-arc area, while the second is an active volcano from the arc-cordillera formed above the oceanic Nazca plate subducted below South America. The third area corresponds to the Salta basin rift at 23° S latitude, in the Andes Oriental Cordillera. If the two first localities display xenoliths brought up by recent magmatism (actual for Calbuco, Oligo-Miocene to Pleistocene for the NPM; Melchiorre *et al.*, 2020), Salta xenoliths have been brought up by Campanian magmatism (78-76 Ma; Marquillas *et al.*, 2005). This chapter aims to review 1) the main geological events at the origin of the actual configuration of the central and southern South American lithosphere; 2) the previous mantle and crustal xenolith studies focusing on the South American localities occurring between 20° and 50° S latitude are reviewed, and what significant constraints they provide regarding the petrological and petrophysical characteristics of the South American lithosphere; and 3) the geological settings of the three investigated localities, at 23° and 41° S latitude, with the significant features and parameters characterising the lithosphere. A detailed geological context for each locality could be found in the following chapters: II.2 (NPM); III.2 (Calbuco); and IV.2 (Salta).

RÉSUMÉ

Le présent Chapitre s'intéresse au contexte géologique de l'Amérique du Sud centrale et méridionale, et plus spécifiquement sur les trois zones d'études de cette thèse, à savoir le Massif Nord Patagonien (41-43° S), le volcan Calbuco (41° S) et le rift intracontinental de Salta (26°S). Les caractéristiques de la lithosphère de ces trois zones est décrite, tandis

qu'une synthèse des occurrences de xénolithes dans cette partie du continent Sud-américain est proposée.

La première partie de ce Chapitre se penche sur l'évolution post-Mésoprotérozoique de l'Amérique du Sud centrale et méridionale, en se concentrant sur la géodynamique globale, les événements tectoniques et les processus magmatiques. L'Amérique du Sud se compose d'une part de blocs cratoniques Archéens à Paléoprotérozoiques séparés entre eux par des ceintures orogéniques Néoprotérozoiques et formant le Gondwana occidental, d'autres part de "terranes" constitué d'un socle crustal Mésoprotérozoique, accrétés contre la marge occidentale gondwanienne au cours du Paléozoique, et constituant le socle actuel de l'Amérique du Sud occidentale. La fin du Paléozoique et le Trias sont associés à une extension intense sur la marge active Chilienne et dans le Nord de la Patagonie, liée à des détachements ou des retraits des slabs subductés engendrant des remontées de matériel asthénosphérique. L'anomalie thermique associée à généré une province magmatique exceptionnelle au niveau des zones concernées. Au Jurassique, le retrait des slabs des plaques du Protopacifique en subduction, associée aux panache mantellique du Karoo marquant l'ouverture de l'Océan Atlantique Sud, a généré des provinces magmatiques encore conséquentes en Patagonie, laissant une lithosphère et une croûte marquées par le magmatisme dans cette région. Le Crétacé voit les premières phases compressives du cycle andin en Amérique du Sud occidentale et une série de rifts intracontinentaux en Argentine occidentale. L'ère Cénozoïque est marquée par un important raccourcissement de la croûte au niveau de la marge active Pacifique-Amérique du Sud, établissant le relief actuel des Andes, accompagné par un magmatisme intraplaque généralisé en Patagonie.

La deuxième partie du Chapitre synthétise l'occurrence de xénolithes en Amérique du Sud centrale et méridionale, divisés en trois groupes principaux. Le premier regroupe les xénolithes issus du volcanisme alcalin des systèmes de rifts intracontinentaux du Crétacé dans le centre-ouest et le nord-ouest de l'Argentine. Le deuxième groupe rassemble des xénolithes issus du volcanisme alcalin de plusieurs provinces volcaniques cénozoïques de Patagonie. Enfin, le troisième groupe rassemble des xénolithes provenant de volcans Pliocène à actuels situés tout au long de l'arc andin. Il est évident qu'il existe un lien entre type de volcanisme et l'occurrence et la lithologie des xénolithes. Les xénolithes connus liés au rift Crétacé et les collections de xénolithes cénozoïques de Patagonie contiennent surtout des péridotites du manteau, ainsi que de rares pyroxénites et, encore moins fréquemment, des granulites de la croûte inférieure. Ces xénolithes sont généralement échantillonnés par des

magmas basaltiques alcalins dans un contexte continental d'arrière-arc. D'autre part, les magmas andésitiques liés à l'arc actuel peuvent transporter des xénolithes crustaux - généralement des roches magmatiques - de la croûte moyenne à supérieure et plus rarement des témoins granulitiques de la croûte inférieure.

La 3e partie du Chapitre s'attarde sur la structure et la composition de la lithosphère des régions de l'Amérique du Sud centrale et méridionale étudiées au cours de cette thèse, à savoir le Massif Nord-Patagonien, la région autour du volcan Calbuco au Chili et la province de Salta en Argentine. Les données géophysiques et les analyses pétrologiques révèlent des variations significatives de l'épaisseur et de la composition de la lithosphère dans ces régions. Dans le massif nord-patagonien, la lithosphère est remarquablement mince (<100 km). Cet amincissement est attribué à une activité magmatique intense du Permian au Miocène, qui a entraîné un appauvrissement important suivi de processus de refertilisation du manteau lithosphérique. La croûte a une épaisseur estimée entre 30 et 50 km et consiste en un socle Mésoprotérozoïque remanié pendant le Phanérozoïque et recouvert de roches magmatiques du Permien et du Jurassique. À Calbuco, la lithosphère est également mince (50-70 km) en raison de la subduction adjacente de la plaque Nazca qui génère un coin mantellique hydraté et un gradient thermique chaud. La profondeur de la croûte est de 20 à 30 km, le socle crustal étant composé de métasédiments du Dévonien au Carbonifère et de diverses roches magmatiques, ainsi que par des batholites jurassiques et miocènes dans les Andes nord-patagoniennes. À Salta, au Crétacé, la formation de bassins intracontinentaux et le magmatisme alcalin associé sont liés à une anomalie thermique dans la lithosphère. La transition lithosphère-asthénosphère est estimée se situer à 70 km de profondeur, et le manteau lithosphérique est appauvri mais a également enregistré un métasomatisme cryptique. La profondeur du Moho pétrologique est d'environ 35 km, tandis que la croûte inférieure est ultra-dominée par des granulites felsiques, correspondant aux métasédiments anciennement déposés sur la marge passive Gondwanienne pendant le cycle Pampien.

I. 1 CENTRAL AND SOUTHERN SOUTH AMERICA

The South American lithosphere is composed of several continental blocks with Mesoproterozoic crustal basement ages, distributed between thick, large and rigid cratonic blocks and thinner and smaller ones, described as "terranes" (Alkmim *et al.*, 2001; Ramos,

2009, 2010; Fig. I.1a). The cratonic blocks are separated from each other by Neoproterozoic belts, altogether forming the Brazilian shield which is considered as the western part of the Gondwana supercontinent (Fig. I.1b). The three main cratons are the Amazonia, the São Francisco and the Rio de la Plata cratons for which basement age is between the Paleoproterozoic and the Archean (references and details in section I.1.1). In contrast, the terranes were continuously amalgamated against the West-Gondwana margin during the Paleozoic (Fig. I.1b-e). Thus, the Western margin of South America is considered to be active since the Early Paleozoic (Hérédia *et al.*, 2016). The terranes are, from North to South, the Arequipa and Antofalla terranes which are closely linked together and thus can be referred as the MARA block (e.g. Casquet *et al.*, 2018); the Pampia whose existence as a terrane is still debated (Casquet *et al.*, 2018); the Cuyana and the Chilenia (or PreCordillera) terranes; the Patagonia terrane which encompasses the North Patagonian Massif and the Deseado Massif (Fig. I.1.1). The origin and evolution of each crustal block remain elusive during Precambrian times, but they are better constrained and accurate for Pan-African orogeny (ca. 630-550 Ma; Rino *et al.*, 2008; Stern, 2008) and Phanerozoic times.

I. 1.1 Cratons and Terranes formation

The crustal continental basement of Amazonia, São Francisco and Rio de la Plata cratons is composed mainly of Paleoproterozoic granite-gneissic terrains (2.2-2.1 Ga; U–Pb in zircon) which are thought to be the result of the recycling of an older crust (2.7-2.2 Ga Sm-Nd and Hf model ages, positive to slightly negative $\varepsilon Nd_{(t)}$ values; Rapela *et al.*, 2007; Oyhantçabal *et al.*, 2018). In parallel, much of the West Gondwana continental crust has been produced during the Mesoproterozoic Greenvilian orogeny (1.2-1.0 Ga), resulting from the collision of Gondwana with Laurentia that created the Rodinia supercontinent (Alkmim *et al.*, 2001). The basement of the Arequipa terrane is dated at 1.9-1.8 Ga from inherited zircon U/Pb ages recovered from the metamorphic basement and igneous rocks (Ramos, 2009). The Arequipa basement, the Antofalla and Pampia terranes recorded Greenvilian metamorphism (Ramos, 2010). The Cuyania terrane basement is composed of Greenville rocks but is interpreted to represent the southern extension of the Ouachita embayment (Appalachian system, NE-United States) from the Laurentian block, by their paleomagnetic data, stratigraphy successions and fauna similarities (Thomas & Astini, 1996; Rapalini & Astini, 1998; Ramos, 2010), conferring an exotic origin to the Cuyania terrane. The Chilenia terrane is also suggested to have an exotic Laurentia origin although less well-constrained (Ramos, 2010).

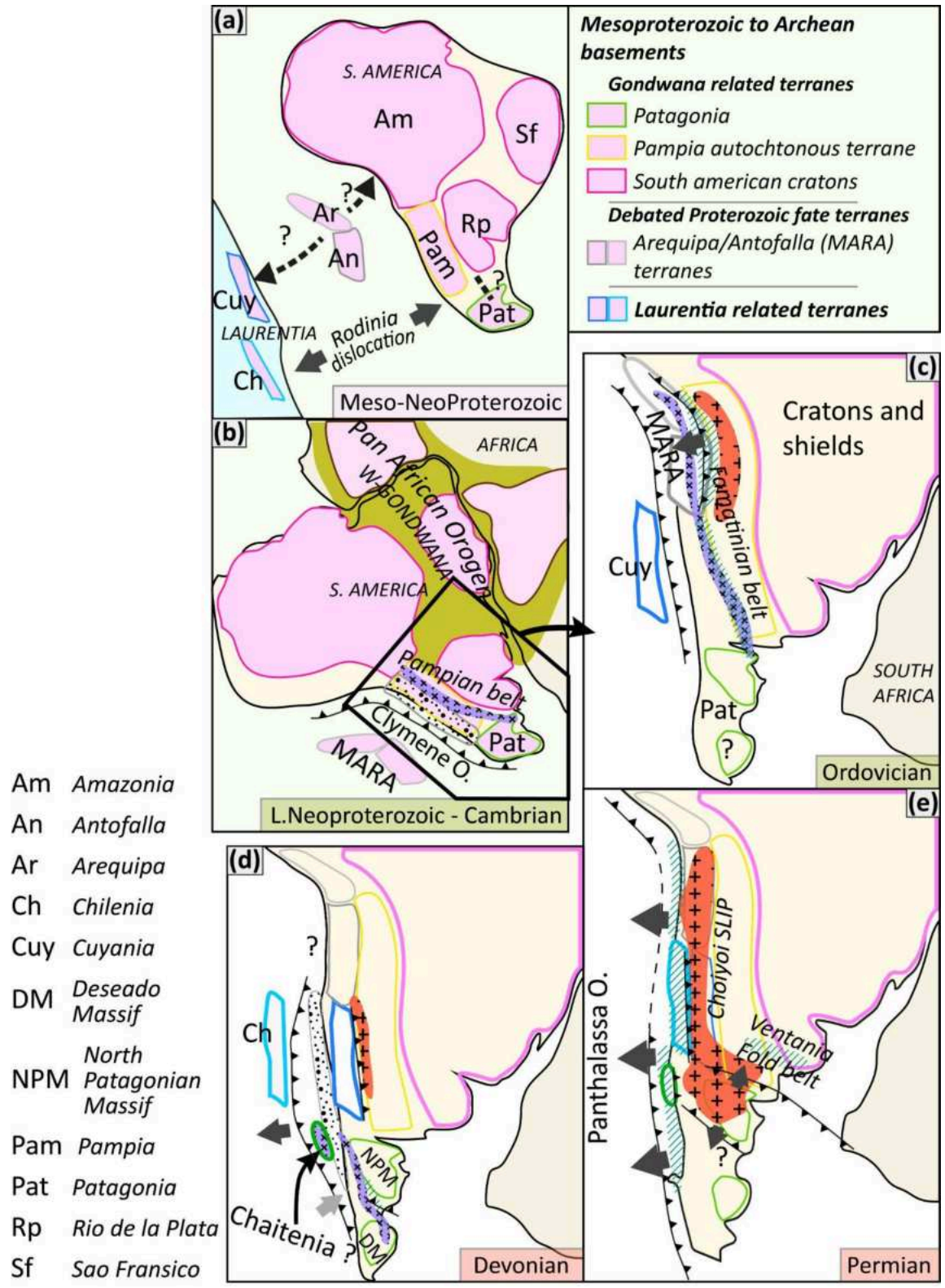


Fig. I.1: Schematic structural maps displaying major geodynamical events in central and southern South America from the Mesoproterozoic to the Permian. (a) Early Neoproterozoic map. (b) Late Neoproterozoic/Cambrian map. (c) Ordovician map. (d) Devonian map. (e) Permian map. Legend of magmatic, metamorphic, sedimentary and tectonic events is in figure I.2.

Concerning the NPM, early Paleozoic rocks provide bulk crustal average ages between late Paleoproterozoic (Nd ages of 2.1-1.6 Ga T_{DM}; Martínez Dopico *et al.*, 2011) and Mesoproterozoic (Nd and Hf model ages of 1.1-2.0 Ga; Pankhurst *et al.*, 2014). Some detrital zircons from North-East NPM display Mesoproterozoic Greenvilian ages and similarities with detrital zircons and crustal rocks from terranes located more to the North (MARA block and Pampia; Uriz *et al.*, 2011; Rapalini *et al.*, 2013). The NPM is thus considered to have been formed during the Greenvilian orogen (Pankhurst *et al.*, 2014).

I. 1.2 Rodinia dislocation

The Greenville orogeny was followed by the Rodinia supercontinent dislocation at ca. 750 Ma (Rino *et al.*, 2008; Fig. I.1a), which separated all the above-cited crustal blocks from each other. This rifting event initiated the Pan-African orogenic cycle which led to a major collision between South American cratons and African cratons, forming Neoproterozoic orogenic belts between the cratons (ca. 550 Ma; Rapela *et al.*, 2007; Rino *et al.*, 2008; Fig. I.1b). South American cratons and South American Neoproterozoic belts form the Brasilian shield, which is considered to have a thick and cold cratonic lithosphere (e.g. McKenzie *et al.*, 2015; Pearson *et al.*, 2021).

There are still some debates about the journey of the MARA block after the Rodinia dislocation, considered either para-autochtonous (Ramos, 2010) or to be derived from the Laurentian side (Rapela *et al.*, 2016; Casquet *et al.*, 2018; Fig. I.1b). It is on the other hand accepted that the Pampia terrane remained attached to the West-Gondwana block. Casquet *et al.*, (2018) consider this terrane as the West-Gondwana hyper-extended continental margin. Moreover, Cuyania and Chilenia terranes are considered to be derived from the Laurentian side (Fig. I.1b). Finally, some authors proposed that entire Patagonia was separated from the West Gondwana before the Late Paleozoic, and, thus, allochthonous (e.g. Pankhurst *et al.*, 2006; Ramos, 2008; Von Gosen, 2009); however, there seems to be some consensus that Northern Patagonia was autochthonous (e.g. Rapalini *et al.*, 2013; Ramos *et al.*, 2020; Rapela and Pankhurst, 2020; Oriolo *et al.*, 2023). Southern Patagonia could be attached to the Antarctic Peninsula during the Neoproterozoic and Early Paleozoic but this sector is less constrained (Ramos, 2008; Ramos *et al.*, 2020).

I. 1.3 Early Paleozoic sutures

During the Late Neoproterozoic to Early Cambrian, the Pampia block formed the hyper-extended margin between the West-Gondwana continent and the Clymene Ocean (Casquet *et al.*, 2018; Fig. I.1b). The Punscoviscana Formation first group deposited on the hyper-extended margin and is composed of detritus from a felsic basement lacking mafic rocks (Weinberg *et al.*, 2018). During the Early Cambrian, the beginning of the subduction and closing of the Clymene Ocean below West Gondwana initiated the Pampean orogeny. The latter is associated with the production of cordilleran I-type magmatism (537-528 Ma) and is traceable in the Puncoviscana Formation second group (Casquet *et al.*, 2018). The final closure of the Clymene Ocean and the collision between the MARA block and the West Gondwana led to strong deformation and metamorphism at 530-520 Ma, as well as peraluminous S-type magmatism (Casquet *et al.*, 2018; Fig. I.1c). The beginning of the Famatinian orogeny corresponds to a slab rollback below the West-Gondwana margin consequently to the MARA docking during Late Cambrian (Weinberg *et al.*, 2018). This led to widespread crustal anatexis and overprint on the Pampian arc. A new oceanic subduction configuration resulted from the slab roll-back, i.e. the Proto-Pacific subduction, and generated a Famatinian magmatic arc far from the extinct Pampian arc during the Ordovician. The latter became the back arc of the Famatinian system. The docking of the Cuyania terrane corresponds to the end of this Famatinian phase (Rapela *et al.*, 2018; Weinberg *et al.*, 2018; Fig. I.1d).

In North-East of the NPM, detrital zircon populations and petrological and structural studies of Cambrian and Ordovician granites highlighted the continuity of the Pampean and the Famatinian belts from NW Argentina to NE Patagonia (Valcheta area; Rapalini *et al.*, 2013; Pankhurst *et al.*, 2014; Rapela & Pankhurst, 2020), which suggests the presence of a stretched N-S Gondwana active margin during the Early Paleozoic, spanning over 2000 km (Fig. I.1c).

I. 1.4 Middle to Late Paleozoic active margin

During Devonian times, docking of the Chilenia terrane occurred along the South America active margin at Central Andes latitudes (Willner *et al.*, 2011; Fig. I.1d), while a long magmatic arc has been recognised for Northern Patagonia (Rapela *et al.*, 2021; Serra-Varela *et al.*, 2021) including the Deseado Massif (Ballivián Justiniano *et al.*, 2023). At the North Patagonian latitudes, some authors propose that a Devonian roll-back stage generated an

oceanic arc, i.e. the Chaitenia arc, which was accreted to the Patagonian margin during Late Devonian-Carboniferous times (Hervé *et al.*, 2016; Rapela *et al.*, 2021; Fig. I.1d). However, alternative models proposed that the shallowing of the subducting slab is sufficient to explain the crustal thickening, without oceanic arc accretion (Oriolo *et al.*, 2019, 2023). To the South, the Devonian metamorphic ages of the Patagonian western belt might be related to the convergence of the Deseado Massif to the NPM (Martínez Dopico *et al.*, 2011). Finally, in Central and Northern Chile, Carboniferous metasedimentary complexes occurring near the actual coastline are mostly related to a subduction-accretion system, which highlights the beginning of arc-related rocks until the earliest Jurassic (Pankhurst *et al.*, 2016).

I. 1.5 Late Paleozoic-Early Mesozoic Choiyoi magmatic province

Devonian-Carboniferous times led to the formation of the Northern magmatic arc in the North Patagonian Massif, producing early I-type granites (Pankhurst *et al.*, 2006; Martínez Dopico *et al.*, 2017). In parallel, the Ventania Fold-Belt developed between the NPM and Rio de la Plata craton (Ramos *et al.*, 2014; Fig. I.1e). Magmatism occurrence and fold-belt formation are related to the convergence between Patagonia and Southern Gondwana. The more recent models draw a consensus around a non-collisional convergence between those two blocks, and explain the compression with a flattening of the west-dipping oceanic slab (Ramos *et al.*, 2020; Rapela & Pankhurst, 2020; Oriolo *et al.*, 2023). In the NPM, I-type magmatism was followed by the emplacement of voluminous Permo-Trias S-type granites and rhyolites, which had slab-derived fluids and crustal reworking signatures. Similar magma signatures occur on the N-S magmatic belt in Northern and Central Chile, which form with NPM magmas a huge area of 909.250 km² (Gianni & Navarrete, 2022; Fig. I.1e), known as the Choiyoi silicic large igneous province (SLIP), which persisted during 40 million years (from 286 to 247 Ma). Magma signatures and seismic tomography argue that slab retreat and break-off or delamination processes affected the area, related to the Pangea formation, which generated asthenospheric upwelling, crustal anatexis and, thus, voluminous magmatism (Pankhurst *et al.*, 2006; Falco *et al.*, 2022; Gianni & Navarrete, 2022.

I. 1.6 Mesozoic arcs and rifting events

During the Mesozoic, Central and Southern South America were trapped between Pacific subduction to the West and progressive Pangea break-up and Atlantic Ocean opening to the East (Lovecchio *et al.*, 2020; Fig. I.2a, b).

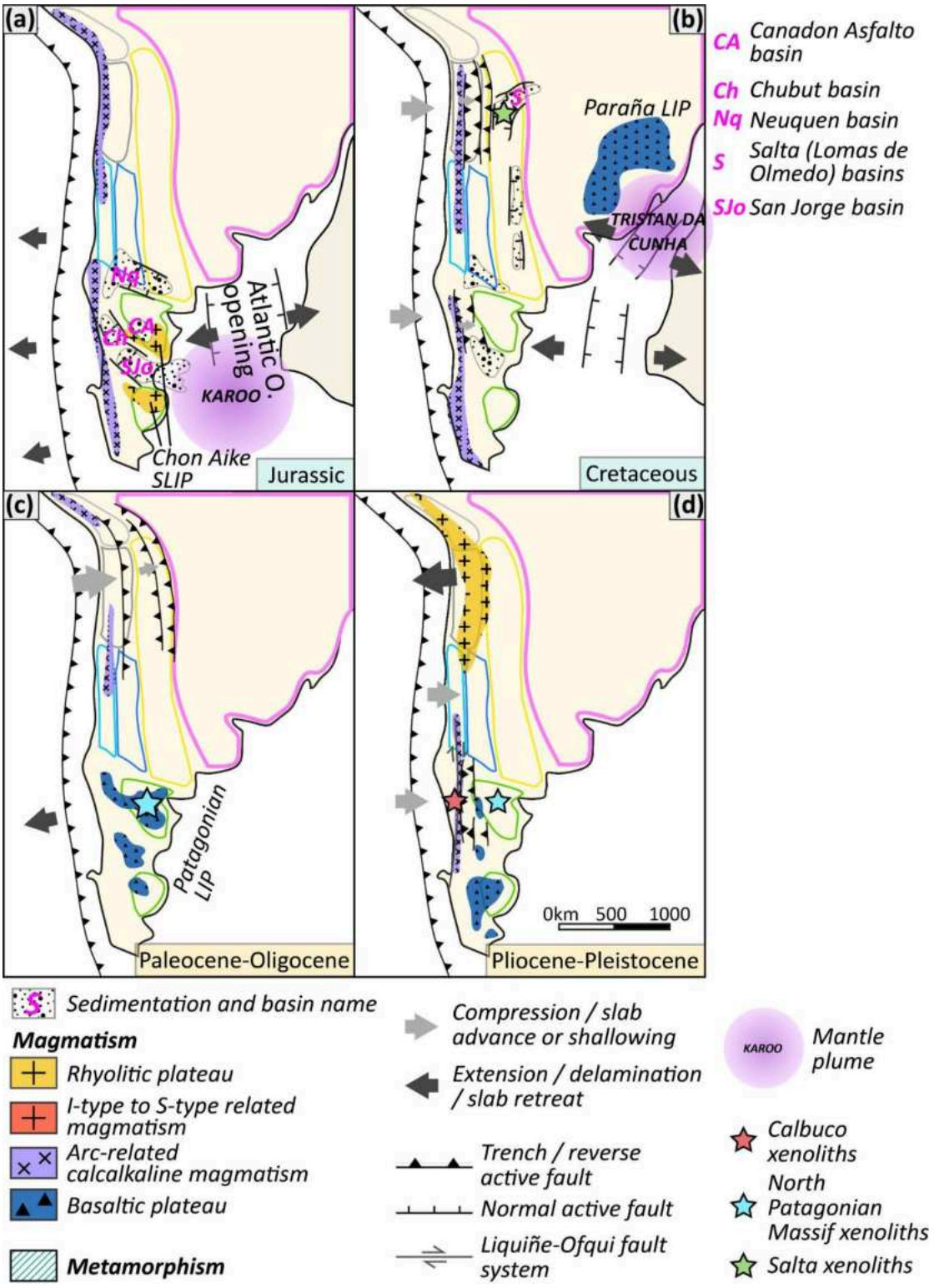


Fig. I.2: Schematic structural maps displaying major geodynamical events in central and southern South America during Mesozoic and Cenozoic. (a) Jurassic map. (b) Cretaceous map. (c) Paleocene-Oligocene map. (d) Pliocene-Pleistocene map. The color code of terranes contour is the same than in figure I.1.

The South Atlantic Ocean opening in the Early Jurassic was contemporaneous with the rollback of the subducting oceanic plates of the Panthalassa Ocean and the Phoenix Ocean and the rise of the Karoo mantle plume between the Patagonia, South Africa and East-Antarctica thresholds (Echaurren *et al.*, 2016; Navarrete *et al.*, 2019; Lovecchio *et al.*, 2020; Genge *et al.*, 2021; Fig. I.2a). Slab rollback and potential break-off associated with the Karoo Mantle plume rise caused asthenospheric upwelling and created a thermal anomaly beneath Patagonia, at the origin of a new voluminous bimodal magmatic province, pervasive through Patagonia and known as the Chon Aike province (188-145 Ma; Pankhurst *et al.*, 1998; Lovecchio *et al.*, 2020). Chon Aike volcanic rocks observed at the surface involve a crustal anatexis source (Pankhurst & Rapela, 1995; Pankhurst *et al.*, 1998, 2000a). However, crustal melts have been triggered by heating from underplating melts in the lower crust, that took their source either in the lithospheric mantle and/or the upwelling asthenosphere upwelling melts (Navarrete *et al.*, 2019). The NPM, having experienced Choiyoi and Chon Aike SLIP events, was characterised by a very thin lithosphere (Schilling *et al.*, 2017; Navarrete *et al.*, 2019) and a refractory lower crust (Pankhurst & Rapela, 1995; Foley *et al.*, 2023). Additionally, the combination of slab retreat and thermal heating led to extension in Patagonia, resulting in the formation of numerous Mesozoic sedimentary basins around the NPM (Fig. I.2a). To the South, these basins include the Cañadon Asfalto, the Chubut and the San Jorge basins, while to the North, the Neuquen basin remained active from Trias to Cretaceous times (Poupon, 2017). Finally, Jurassic and Cretaceous times are characterised by arc-related magmatism in Western Patagonia, along the active margin, including the North Patagonian Batholith (Rapela *et al.*, 2005; Echaurren *et al.*, 2016, 2017; Fig. I.2a, b).

In Central and Northern Chile (19-28 ° S), the magmatism related to the Phoenix plate subduction produced the Jurassic and Cretaceous coastal batholiths (Stern *et al.*, 2007; Fig. I.2a, b). The propagating Atlantic Ocean opened at these latitudes during Early Cretaceous times which was contemporaneous with the Tristan da Cunha mantle plume rise, at the origin of the Paraña large igneous province (LIP) in S-E Brasil (ca. 136-132 Ma; Ernst & Bell, 2010; Gomes & Vasconcelos, 2021; Fig. I.2b). Between the Phoenix subduction to the West and Atlantic ocean opening to the East, Central and N-W Argentina recorded a series of N-S oriented intracontinental rift basins associated with alkaline magmatism, including the Salta Group basins that were filled until the Paleogene (Viramonte *et al.*, 1999; Marquillas *et al.*, 2005).

I. 1.7 Cretaceous-Paleogene inversion

In Northern Patagonia, the onset of Cretaceous inversion of rift basins is interpreted to result from the Phoenix slab shallowing and a possible oceanic ridge subduction (Echaurren *et al.*, 2016; Genge *et al.*, 2021; Fig. I.2b). This led to an Eastward quiescence of the magmatic arc, the exhumation of the Paleozoic Basement near the coastline and the deformation from the arc to the back-arc basins (i.e. the broken foreland; Echaurren *et al.*, 2016). Shortening events since the Cretaceous did not deform the rigid North Patagonian Massif Crust (Aragón *et al.*, 2011).

In Northern Chile and Argentina, the intracontinental rift stage continued during Upper Cretaceous as the Proto-Pacific slab advanced and initiated the first arc crustal wedge formation, until the Paleocene (Martinod *et al.*, 2020; Fig. I.2b).

I. 1.8 Cenozoic crustal shortening and Patagonian magmatism

In N-Chile and N-Argentina, the thickening of the crust occurred during Late Eocene Oligocene result by crustal shortening increasing towards the East leading to the formation of the Sierras Pampeanas in Argentina (Fig. I.2c). Arc-magmatism quiescence is associated with that episode, thus interpreted as a flat-slab subduction episode (e.g. Ramos, 2009; Martinod *et al.*, 2020). This is followed by the formation of the Altiplano-Puna plateau defined by an average elevation of 3700 m, and is associated with the production of a massive rhyolitic plateau from Miocene to Pliocene (Kay & Coira, 2009; Wörner *et al.*, 2018; Fig. I.2d). This magmatism is interpreted to be linked to the retreat of the flat slab and associated heating by mantle upwelling, along with possible delamination of the Altiplano-Puna lower crust. Thus, massive lithosphere heating produced uplift and crustal thickening as well as the Altiplano-Puna magma body (Chmielowski *et al.*, 1999; Zandt *et al.*, 2003; Prezzi *et al.*, 2009). Today, magmatism is a typical andesite-arc type. The amount of shortening linked to the Pacific-South America convergence is estimated to be about 300 km at the Altiplano-Puña latitudes (Echaurren *et al.*, 2022; Giambiagi *et al.*, 2022).

In Patagonia, the retroarc recorded intense intraplate Cenozoic magmatism, mainly expressed through mantle-derived alkaline to tholeiitic basaltic plateaus, lacking or showing minor crustal contamination (Kay *et al.*, 2007; Fig. I.2c, d). A first Paleocene-Eocene intraplate magmatism event has been linked to a slab window opening and asthenosphere upwelling consequently from the Phoenix(Aluk)/Farallon ridge collision/subduction below the South American plate (Fernández Paz *et al.*, 2018; Navarrete *et al.*, 2020; Fig. I.2c). This

episode is followed by a back-arc extensive setting linked to the Farallon slab retreat. It led to a second magmatic pulse in Northern Patagonia from the Oligocene to the Early Miocene. It is expressed by i) arc-related andesites on the Pacific coast; ii) the Maiten Belt, composed of andesites and occurring near the actual arc, but emplaced in a retro-arc context; iii) a LIP located far in the retro-arc, on the North Patagonian Massif, that produced several basaltic plateau, the larger one being the Meseta de Somuncura. This LIP had an asthenospheric source, colder than those of OIB magmas and that may contain slab-derived components, but its origin is still a matter of debate (Kay *et al.*, 2007; Navarrete *et al.*, 2020; Asiain *et al.*, 2022). Finally, Late Miocene to Quaternary times recorded a second compressional regime between Nazca and the South American plates (Fig. I.2d). It is evidenced by a trench advance, which is associated with Miocene plutonism in the actual arc, and an increase of convergence rates (Echaurren *et al.*, 2016, 2022a). The associated deformation affected the arc and propagated to the Mesozoic sedimentary retro-arc basins (broken foreland). Because of the oblique convergence between Nazca and South American plates, a margin-parallel transverse fault system (i.e., the Liquiñe-Ofqui fault system, LOFS) accommodated the convergence rate differential, greater to the South (Sielfeld *et al.*, 2019). It is still today associated with arc-magmatism that started in this area of weakness (Hickey-Vargas *et al.*, 2016; Fig. I.2d). The amount of shortening reached from the Pacific-South America convergence is about only 30 km at the North Patagonia latitudes (Echaurren *et al.*, 2022).

I. 2 XENOLITH OCCURRENCES IN CENTRAL AND SOUTHERN SOUTH AMERICA

Even if Central and Southern South America carry a complex heritage and many magmatism episodes, xenolith outcrops can somehow be divided into three main geological setting groups. The first one regroups xenoliths brought up by alkaline volcanism from Mesozoic Cretaceous intracontinental rift systems in Central and North-Western Argentina (Fig. I.3). The second group gathers xenoliths brought up by alkaline volcanism from several Cenozoic volcanic fields in Patagonia (Fig. I.3). Finally, the third group gathers xenoliths brought up by Pliocene to actual arc-related volcanoes all along the Andes arc. Obviously, there is a link between volcanism style and xenolith occurrence and lithology. Known Mesozoic rift-related xenoliths and Cenozoic Patagonian xenoliths suites contain especially mantle peridotites, as

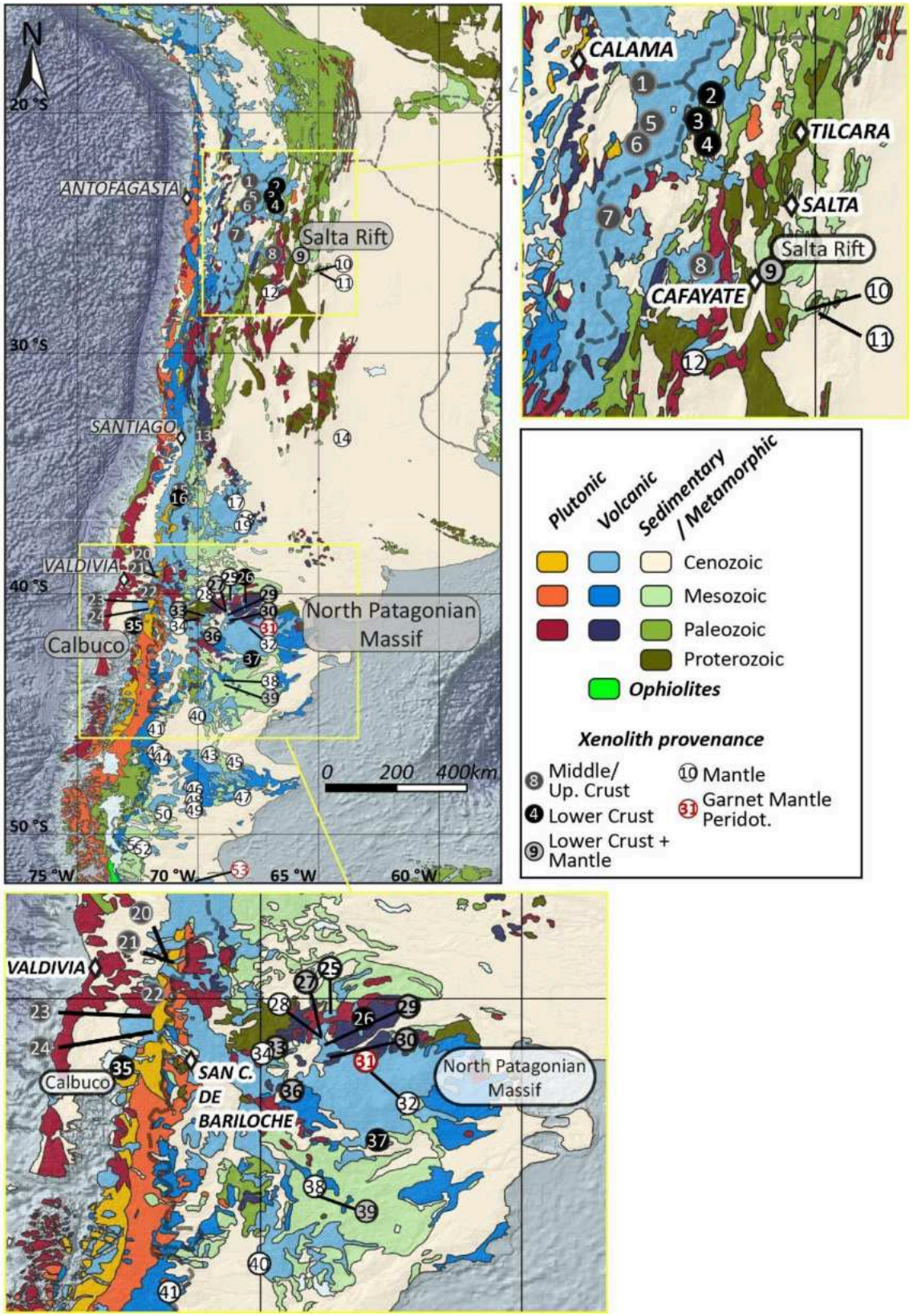


Fig. I.3. Simplified geological map of Central and Southern South America, highlighting xenolith occurrences. Locality numbers refer to Table I.1. A zoom-in view of the Salta and North Patagonian regions is provided; for further details, readers are directed to maps in Chapters II, III and IV.

well as rare pyroxenites and even less frequent lower crustal granulites. They are commonly brought up by alkaline basalt-type volcanic magmas occurring in a continental back-arc setting. Arc-related andesitic magmas could carry crustal xenoliths, commonly magmatic rocks from the middle to the upper crust and more rarely witnesses of the lower crust, granulites.

I. 2.1 Mesozoic-Cretaceous rift-related xenoliths, including Salta xenoliths

Most Cretaceous xenolith-bearing basaltic outcrops have been reported to carry small peridotite xenoliths. The latter have been studied, as well as volcanic suites, in order to assess the nature and evolution of the Cretaceous lithospheric mantle (Table I.1, N°9-12, 14; Lucassen *et al.*, 2007). As a whole, these studies brought evidence that the subcontinental mantle below NW Argentina was young and depleted, related to long-lived oceanic subduction from the Pacific side since the Early Paleozoic, associated with several magmatic events and associated mantle modifications linked to interaction with subducting plate or asthenospheric upwellings including mantle plumes.

The most interesting cretaceous xenolith suite is certainly the Las Conchas Valley xenolith suite, from the Salta Rift Basin (Lucassen *et al.*, 1999b, 2005). This suite consists of numerous peridotites, pyroxenites and granulites, which were used, based on thermobarometry and major and trace elements analyses, to define the Cretaceous Lithosphere Asthenosphere Boundary (LAB) at 70 km depth. The results evidence the depleted nature of the lithospheric mantle with rare occurrence of a Late Mesozoic metasomatism. Moreover, Sr, Nd and Pb isotopes study demonstrated the young reworked nature of the mantle with few evidence of Proterozoic inheritance (Lucassen *et al.*, 2005).

The petrological and isotopic features of felsic and mafic granulite xenoliths from Las Conchas Valley (Table I.1, N°9) are in agreement with a thermally hot Cretaceous lithosphere (lower crust at ca. 900 °C; 10 kbar by thermobarometry calculation; Lucassen *et al.*, 1999b). Finally, the felsic granulites are related to the NeoProterozoic-Cambian metasediments outcropping in the region (Lucassen *et al.*, 1999b).

I. 2.2 Cenozoic Patagonian xenoliths, including North Patagonian Massif xenoliths

Most of the studies on Cenozoic Patagonian xenolith suites targeted petrological, geochemical and isotopic analyses of mantle peridotites xenoliths (Stern *et al.*, 1999; Mallmann, 2004; Schilling *et al.*, 2005; Dantas, 2007; Bjerg *et al.*, 2009; Oppezzo, 2016;

Rubiano Lorenzoni, 2016 and references therein). The studies of mantle xenoliths from Northern Patagonia (39-45° S latitude) have evidence that the underlying lithospheric mantle is highly depleted with melt extraction up to 30% (Melchiorre *et al.*, 2020). Mantle xenoliths age models by Re-Os dating argue for a large age ranging from Phanerozoic to Mesoproterozoic depletion ages (0-1.3 Ga; Schilling *et al.*, 2008, 2017; Mundl *et al.*, 2016) with rare older refractory Paleoroterozoic samples (1.7 Ga). Schilling *et al.* (2017) proposed that Phanerozoic depletion ages could be attributed to Late Paleozoic convergence events involving the Rio de la Plata craton, North Patagonia and South Patagonia. During this period, delamination of the North Patagonian lithosphere and asthenospheric upwelling might have led to significant lithospheric mantle melting and depletion. In this area, after depletion, the upper mantle record a late refertilisation event (e.g. Rivalenti *et al.*, 2004; Bjerg *et al.*, 2005) during the Cenozoic LIP that implies a deep melt source and the percolation of melts within the lithospheric mantle (Mundl *et al.*, 2016; Schilling *et al.*, 2017).

In Central and Southern Patagonia (South of 45° S latitude), lithospheric mantle xenoliths display melt extraction rates from 0 to 30 % and show overall lower depletion rates than in Northern Patagonia (Bjerg *et al.*, 2005; Ntaflos *et al.*, 2007; Melchiorre *et al.*, 2020). As in Northern Patagonia, the upper mantle recorded metasomatism (Rivalenti *et al.*, 2004), involving subduction-related fluids percolation for localities near the Nazca or Antarctica subduction trenches (Faccini *et al.*, 2013; Melchiorre *et al.*, 2015; Jalowitzki *et al.*, 2017; Novais-Rodrigues *et al.*, 2021). Model age calculations have been carried out for the mantle xenoliths from the Deseado Massif (from 0.5 to 2.1 Ga, with an average of 1.5 Ga; Mundl *et al.*, 2015; Schilling *et al.*, 2017), which support the stabilization of the Deseado cratonic lithospheric mantle during Proterozoic times as contemporaneous to those of the NPM cratonic lithosphere remnants (Schilling *et al.*, 2017). Finally, Plio-Pleistocene mantle peridotite xenolith suites located further North than Patagonia (36-37° S latitude; Table I.1 N° 17-19) lack or only display weak major and trace elements depletion (Bertotto, 2003; Bertotto *et al.*, 2013, 2022).

Peridotite textures are globally variable and of various types in all Patagonia mantle xenolith localities. Only one study targeted in detail peridotite microstructures, from Gobernador Gregores and Pali Aike mantle xenolith suites, Southern Patagonia (Table I.1, N°48, 53; Zaffarana *et al.*, 2014; Fig. I.3). The majority of their samples are coarse-grained and display low intracrystalline deformation, which they interpret as extensive annealing fabrics, recording multiple percolating-melt events. Some websterite xenoliths from

Patagonia have textures interpreted as magmatic cumulative textures (Dantas, 2007; Dantas *et al.*, 2009; Faccini *et al.*, 2013).

Lower crustal xenolith studies are scarce and restricted to a region located between Northern and Central Patagonia, i.e. at the Sierra de les Chacays and Pasos dos Indios (42-44 ° S latitude; Table I.1, N° 37, 39; Fig. I.3). Those studies focused on mafic granulite xenoliths which are interpreted to be lower crustal residues from Jurassic melt extraction (Pankhurst & Rapela, 1995; Castro *et al.*, 2011). Hornblendite cumulates have been sampled in Quepuniyeu basanites (Table I.1, N°26; Fig. I.3; Cordenons *et al.*, 2020) but have not been studied yet.

I. 2.3 Recent arc crustal xenoliths, including Calbuco xenoliths: Crustal contamination magmas and related xenoliths

Cordillera of the Andes crustal xenoliths are brought up by recent arc-related magmas, and are found either in Andesitic stratovolcanoes or in monogenetic basaltic cones (Table I.1; McGee *et al.*, 2017; Ureta *et al.*, 2020, 2021 and references therein). Most of these xenoliths are middle- to upper-crustal granitoïds xenoliths and have been investigated in order to quantify the level of crustal assimilation of the ascendant magma (Thorpe *et al.*, 1984; Hildreth & Moorbath, 1988; McMillan *et al.*, 1989; Richards & Villeneuve, 2002; Jicha *et al.*, 2007; Figueroa *et al.*, 2009). Some exceptions should be noted such as the pyroxenites from the Puña middle crust (P-T equilibrations at 8 kbar, 969-1246 °C; Maro et al., 2016; Table I.1, N° 2-4; Fig. I.3) or the mafic xenoliths from the Holocene to pre-Quaternary plutons uplifted by the Tatara San Pedro volcano (Costa Rodriguez, 2000; Costa *et al.*, 2002; Table I.1, N° 16). Finally, the Calbuco volcano could be also considered as an exception as it provides lower crustal xenoliths (Table I.1, N° 35; Fig. I.3). Hickey-Vargas *et al.* (1995) studied the petrologic and geochemical features of those lower crustal xenoliths and discriminated two populations: the first consists of gabbronorites considered as cognates of the Calbuco andesites and the second corresponds to mafic granulites interpreted as oceanic-derived metabasalts (Hickey-Vargas *et al.*, 1995).

Table II.1: Xenolith occurrences in South America, South to 21 ° S latitude, with the nature, the morphology and the age of the host rock. Reported harzburgites and lherzolites marked with an (*) may carry garnet. References are listed, except for Melchiorre *et al.* (2020) who present a large dataset for localities N° 25, 27-31, 33-36, 38-53.

N°	Name	Latitude (°S)	Longitude (°W)	Granitoids	Mafic Cumulates	*Granulites*	*Pyroxenites*	*Dunite/Wehrlite*	*Harzburgites*	*Lherzolites*	Host lava	Host rock morphology	Host lava age (Ma)	References
1	Licancabur	22°50'	67°52'		x						Andesite/dacite	Lava flows	12 ka	Figueroa et al. (2009)
2	Rio el Toro	23°04'	66°44'				x							
3	Cerro el Chileno	23°28'	66°55'				x				Basaltic andesite	Monogenetic cones	3-23	Maro et al. (2016)
4	Salar de Cauchari	23°51'	66°48'				x							
5	Cerro Overo	23°31'	67°39'	x							Basaltic andesite	Pyroclastic deposits	<1,8	Ureta et al. (2021)
6	Cerro Tujle	23°31'	67°39'	x							Andesite	Pyroclastic deposits	<1,8	Ureta et al. (2020)
7	Cerro Escorial	25°04'	68°22'	x							Andesite	Lavas, tuffs	8	Richards and Villeneuve
8	Cerro Galan	25°55'	66°52'	x			x				Basaltic andesite	Monogenetic cones	<1,8	Thorpe et al. (1984)
9	**Las Conchas**	25°55'	65°43'			x	x	x	x	x	basanite	Breccias	78-76	Lucassen et al. (1999, 2005)
10	Dique Cadillal	26°37	65°11'							x	Trachyte, basanite	Dykes	100-130	Viramonte et al. (1999); Lucassen et al. (2007)
11	Finca del Rodeo	26°39'	64°57'							x	Basanite	Dykes	95-98	Viramonte et al. (1999); Lucassen et al. (2007)
12	Belen	27°33'	67'00'							x	Basanite	Pyroclastic flows	~130	Lucassen et al. (2007)
13	Tupungatito	33°25'	69°47'	x							Dacite	Lavas/pyrocalstic flows	<1,8	Hildreth and Moorbath (1988)
14	Chajan	33°40'	64°00'							x	Basanite	Lavas/pyrocalstic flows	~67	Lucassen et al. (2007)
15	Cerro Azul	35°39'	70°45'	x							Andesite	Lavas/pyrocalstic flows	<1,8	Hildreth and Moorbath (1988)
16	Tatara San Pedro	36°00'	71°51'		x						Dacite	Lava flows	12 ka	Costa Rodriguez (2000); Costa et al. (2003)
17	De la Laguna	36°13'	68°26'				x	x	x	x	Basanite	Lavas/pyrocalstic flows	<1,8	Bertotto (2003)
18	Agua Poca	37°01'	68°07'				x		x	x	Trachybasalt	Lavas/pyrocalstic flows	0,6	Bertotto (2003); Bertotto et al. (2013)
19	Huanul	37°17'	68°32'							x	Basanite	Lava flows	0,84	Betotto et al. (2022)

N°	Name	Latitude (°S)	Longitude (°W)	Granitoïds	Mafic Cumulates	*Granulites*	*Pyroxenites*	*Dunite/Wehrlite*	*Harzburgites*	*Lherzolites*	Host lava	Host rock morphology	Host lava age (Ma)	References
20	La Barda	39°13'	71°46'	x							Basalt	Tephras	12 ka	McGee et al. (2017)
21	San Jorge	39°18'	71°39'	x							Basalt	Tephras	12 ka	McGee et al. (2017)
22	Mocho Choshuenco	39°54'	72°02'	x							Basaltic andesite	Lava flows	<1,8	McMillan et al. (1989)
23	Mirador	40°21'	72°03'	x							Basalt	Bombs, lava flows	1979 A.D.	samples I collected in 2022
24	Puyehue	40°35'	72°07'	x							Pumice	Pumices	1 ka	Jicha et al. (2007)
25	**Laguna Fria**	40°21'	68°38'						x	x	Alkaline basalt or basanite	Lava flows	1-5	Bjerg et al. (2005)
26	Quepuniyeu	40°30'	68°02'		x						Basanite	-	21-19	Cordenons et al. (2020)
27	**Cerro Chenque**	40°29'	68°44'			x	x	x	x		Trachybasalt	Basaltic necks	23-25	Mundle et al. (2016)
28	Puesto diaz	40°30'	68°44'								Trachybasalt	Basaltic necks	23-25	Mundle et al. (2016)
29	**Estancia Alvarez**	40°46'	68°45'	x		x		x	x	x	Alkaline basalt	Lava flows	20-29	Mallmann (2004); Rivalenti et al. (2004)
30	**Cerro Aznares**	40°48'	68°41'			x	x		x		Alkaline basalt	Dykes	20-29	Dantas (2007)
31	**Prahuanyieu**	41°20'	67°54'				x	x	x*	x*	Alkaline basalt	Nephenilites, tuffs	21-22	Bjerg et al. (2009); Rubiano Lorenzoni (2016)
32	Cerro Medina	41°28'	67°59'	x					x	x	Alkaline basalt	Pyroclastic deposits	3,2	Oppezzo (2016)
33	**Comallo**	40°55'	69°52'	x			x	x	x	x	Trachybasalt	Lava flows	0,9-1,7	Mundl et al. (2016)
34	Cerro Mojon	41°06'	70°13'				x	x	x	x	Basalt	Lava flows	2-5	Mundl et al. (2016)
35	**Calbuco**	41°16'	72°32'	x	x	x					Andesite or dacite	Lava flows	< 12 ka	Hickey Vargas et al. (1995)
36	**Cerro Traful**	41°38'	69°18'			x				x	Alkaline basalt	Basaltic necks	23-25	Bjerg et al. (2005)
37	Sierra de los Chacays	42°41'	67°48'			x	x				Latite	Latite plugs	19	Pankhurst & Rapela (1995)
38	Chubut	43°38'	68°58'				x	x	x	x	Basanite	Lava flows/ dykes	49-52	Dantas (2007)
39	Pasos dos Indios	43°45'	68°57'			x	x		x	x	Basalts	Dykes/ lava flows	49-52	Bertotto et al. (2021); Castro et al. (2011)
40	Cerro de los Chenques	44°52'	70°04'				x			x	alkaline basalts	Pyroclastic deposits	20-25	Dantas et al. (2009)

N°	Name	Latitude (°S)	Longitude (°W)	Granitoïds	Mafic Cumulates	*Granulites*	*Pyroxenites*	*Dunite/Wehrlite*	*Harzburgites*	*Lherzolites*	Host lava	Host rock morphology	Host lava age (Ma)	References
41	Coyhaique	45°46'	71°47'							x	alkaline basalts	Flood basalts	54-59	Jalowitzki et al. (2017); Schilling et al. (2017); Novais-Rodrigues et al. (2021)
42	Chile Chico	46°34'	71°46'							x	alkaline basalts	Volcanic necks	40,7	Schilling et al. (2017)
43	Cerro Clark	46°43'	69°30'				x			x	Basanite	Lava flows/ dykes	11-12	Schilling et al. (2017)
44	Estancia Sol de Mayo	46°49'	71°25'					x	x	x	Basaltic trachyandesite	Scories, flows, pyroclastic deposits	7-2	Melchiorre et al. (2015)
45	Don Camilo	46°59'	68°32'						x	x	Alkaline basalt or basanite	Lava flows or pyroclastics deposits	<5	Mundle et al. (2015)
46	Cerro Cuadrado	48°07'	70°08'						x	x	-	-	-	Rivalenti et al. (2004)
47	Auvernia	48°27'	68°10'						x	x	-	-	<1	Schilling et al. (2017)
48	Gob Gregores	48°34'	70°10'					x	x	x	Alkaline basalt and hawaiite	Pyroclastic deposits	3-4	Rivalenti et al. (2004); Zaffarana et al. (2014)
49	Cerro Redondo	48°59'	70°10'						x	x	Alkaline basalt	-	-	Schilling et al. (2005)
50	Tres Lagos	49°11'	71°20'				x	x	x	x	-	Pyroclastic deposits, bombs	4-7	Rivalenti et al. (2004); Schilling et al. (2017)
51	Cerro Fraile	50°33'	72°38'	x			x		x	x	Basalt	Lava flows	1-2	Rivalenti et al. (2004); Faccini et al. (2013)
52	Las Cumbres	50°42'	72°20'					x	x	x	Basalt	Lava flows	-	Rivalenti et al. (2004)
53	Pali Aike Volcanic Field	52°01'	72°20'				x	x	x*	x*	Alkaline and olivine basalt, basanite	Tuffs, lava flows	<3,8	Dantas (2007); Zaffarana et al. (2014); Mundle et al. (2015)

I. 3 STRUCTURE AND COMPOSITION OF THE LITHOSPHERE FROM THE STUDIED ZONES

I. 3.1 North Patagonian Massif

The North Patagonian Massif (NPM) lithosphere is thin as suggested by geophysical constraints placing the Lithosphere Asthenosphere Boundary (LAB) at a depth ranging between 60 and 100 km (Afonso *et al.*, 2019), and thermobarometry estimates from garnet peridotite xenoliths which also highlighted a hot geotherm below the massif (e.g. Bjerg *et al.*, 2009; Fig. I.4a). The thinning of the NPM lithosphere is thought to be a consequence of thermal erosion involved by the intense magmatic activity that occurred in an extensive context that affected the NPM since the Permian - including Choiyoi (Permo-Trias) and Chon Aike (Jurassic) silicic LIP followed by Cenozoic LIP (e.g. Kay *et al.*, 2007; Massaferro *et al.*, 2014; Navarrete *et al.*, 2019; Gianni and Navarrete, 2022). However, recent geophysical model from Gómez Dacal *et al.* (2021) set the NPM LAB much deeper, between 100 km to the SE and 200 km to the NW (Fig. I.4b). The NPM lithospheric mantle is strongly depleted (melting rate estimates reach 30%; Melchiorre *et al.*, 2020; Fig. I.5a). The depletion event has been dated between 0 and 1.3 Ga from Re-Os isotopy (Schilling *et al.*, 2008; Mundl *et al.*, 2016). However, Schilling *et al.* (2008, 2017) propose that Late Paleozoic asthenosphere upwelling after delamination in North Patagonia led to significant melting and depletion of the SCLM. Preserved old Paleoproterozoic mantle remnants have been recognised in Prahuaniyeu xenoliths (1.7 Ga by Re-Os dating; Schilling *et al.*, 2008; Mundl *et al.*, 2016). Finally, hydrated phases (amphibole, phlogopite) and Sr and Nd isotopic compositions of Comallo peridotites xenoliths (W-NPM) have been linked to modal metasomatism related to the dehydration of the Pacific-slabs subduction (Mundl *et al.*, 2016).

The depth of the Crust Mantle Boundary (CMB) is estimated to range between 30 and 50 kilometres by the interpretations of gravity anomalies and seismic tomography models, deeper than that of the surrounding sedimentary basins (Assumpção *et al.*, 2013; Chulick *et al.*, 2013; van der Meijde *et al.*, 2013; Gómez Dacal *et al.*, 2017; Fig. I.5a). Paleo- to Meso-proterozoic metamorphic basement (Martínez Dopico *et al.*, 2011; Pankhurst *et al.*, 2014) has been reworked by crustal anatexis and juvenile mantle-derived magmas during Permian and Jurassic SLIP, the latter being highlighted to have left a residual lower crust (Pankhurst & Rapela, 1995; Kay *et al.*, 2007; Foley *et al.*, 2023; Fig. I.5a). This Phanerozoic

crustal reworking has been suggested to be pervasive within the Proterozoic basement (Oriolo *et al.*, 2023). Devonian I-type granitoïds related to the ancient West arc as well as Carboniferous to Permian I- to S-type granitoïds both compose the intrusive part of the NPM and are associated with Permian Choiyoi rhyolites (Pankhurst *et al.*, 2006; Fig. I.5a). The top of the NPM crust is made of Jurassic rhyolites intruded by Oligo-Miocene basalts (Pankhurst *et al.*, 1998; Cordenons *et al.*, 2020; Fig. I.5a).

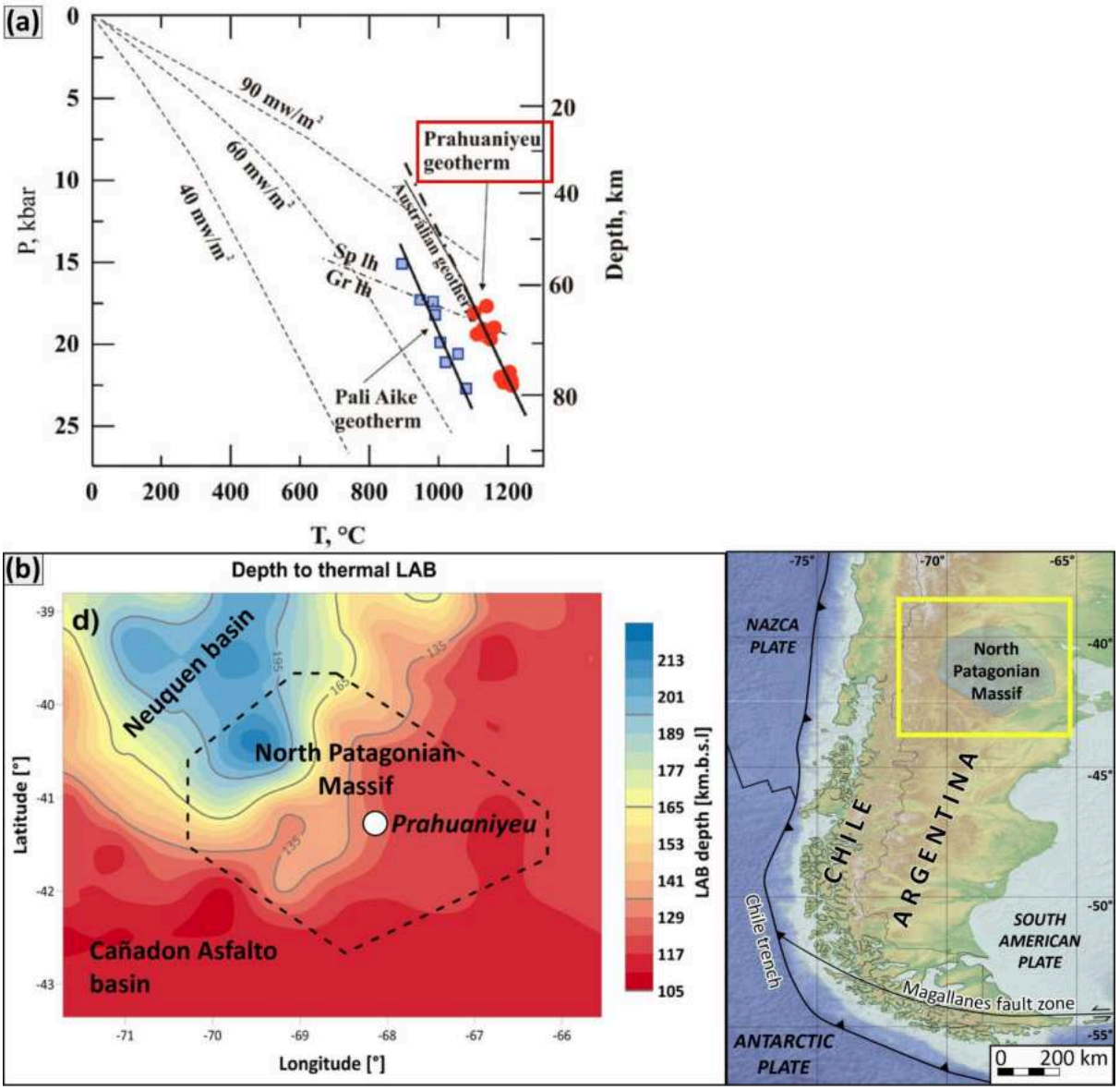


Fig. I.4. (a) Prahunaiyeu geotherm suggested by spinel- and garnet- peridotite xenoliths (modified from Bjerg *et al.*, 200. The Lithosphere-Asthenosphere Boundary (LAB) associated is ca. 90 km deep. (b) LAB depth of North Patagonian Massif region (modified after Gómez Dacal *et al.*, 2021). Prahuaniyeu emplacement is precised for comparison with (a). Yellow square indicates emplacement of the map in Southern South America.

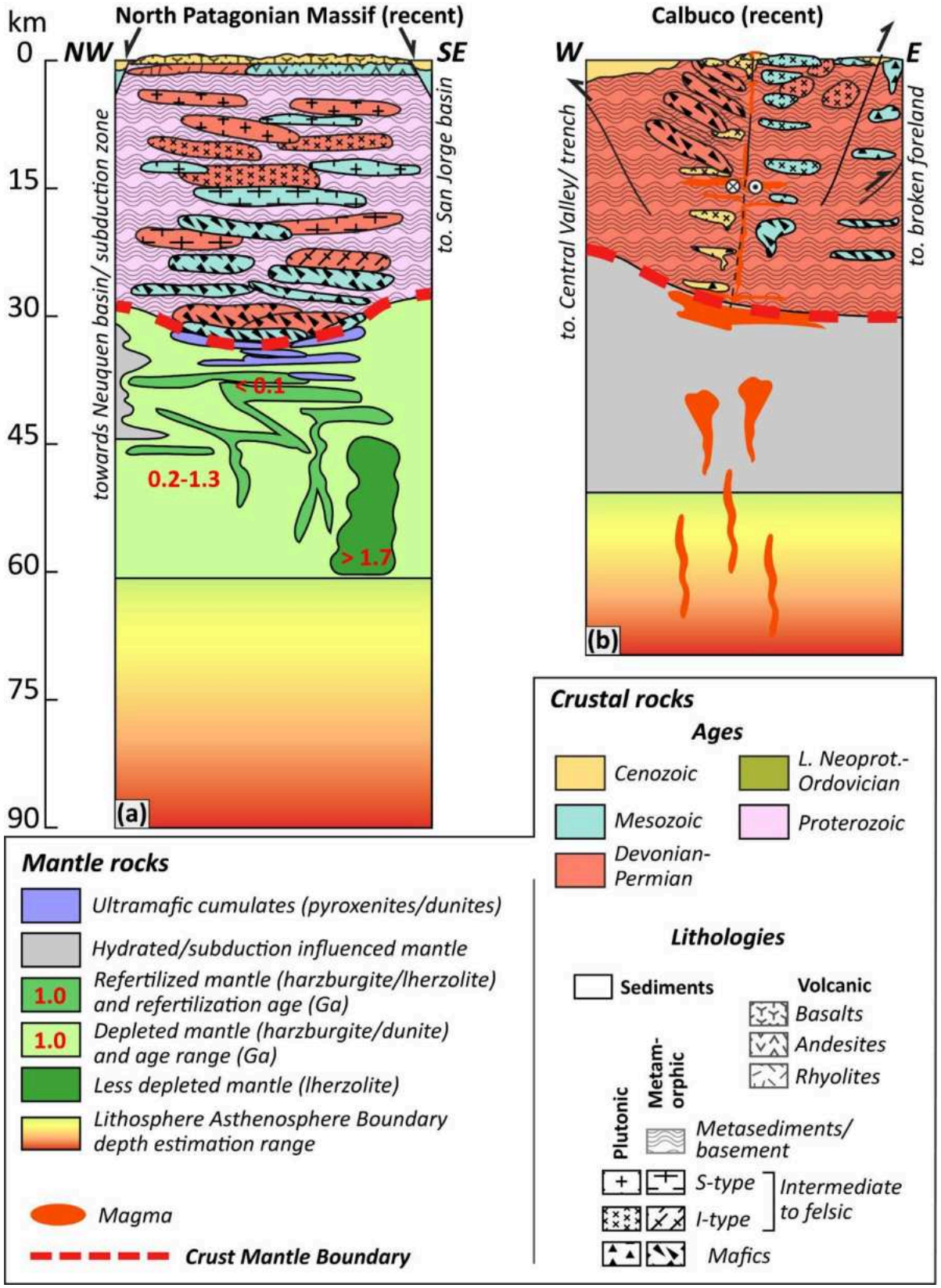


Fig. I.5. Schematic lithospheric sections of the three studied localities. (a) North Patagonian Massif (40-42 ° S latitude), (b) Calbuco volcano (40 ° S), (c) Salta Rift Basin (22 ° S). References within the text.

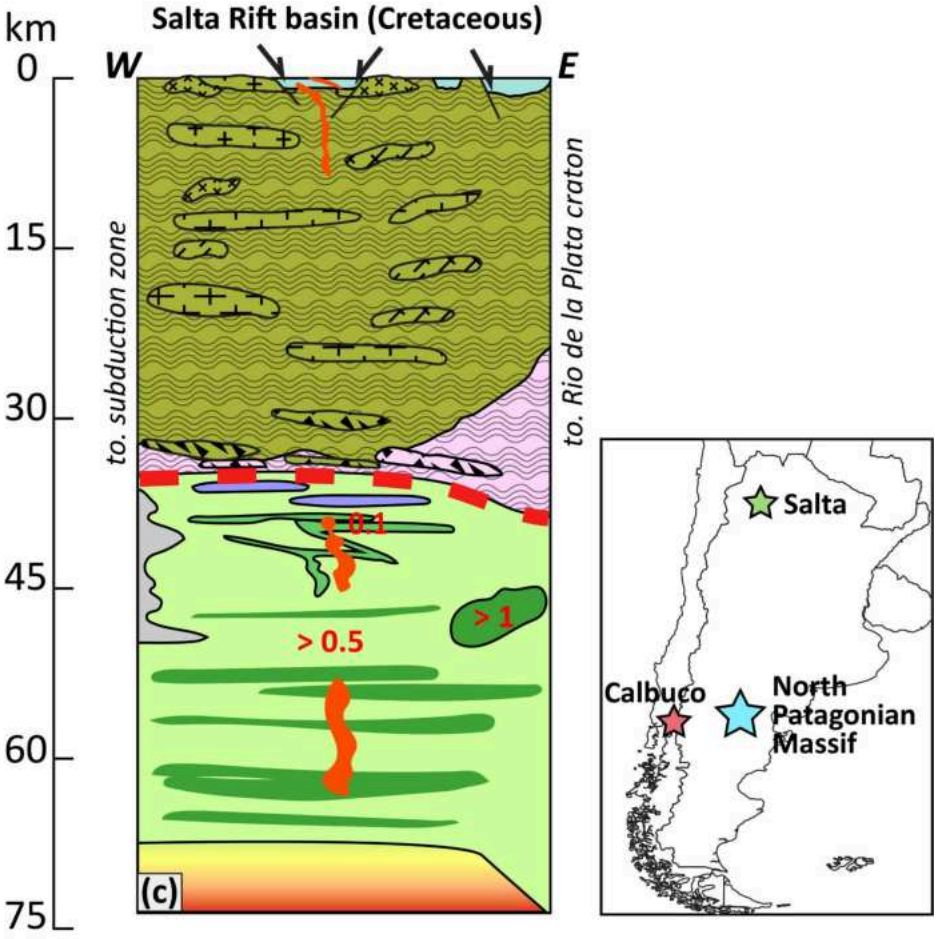


Fig. I.5. (continued).

I. 3.2 Calbuco

Near the North Patagonian Andes and Calbuco volcano, the South American lithosphere is considered to be relatively thin from geophysical models (LAB at ca. 50-70 km deep; Echaurren *et al.*, 2016, 2022; Afonso *et al.*, 2019; Fig. I.5b). Below the South American lithospheric mantle, the subducting Nazca plate, located at a depth ca. 80-100km (Tassara & Echaurren, 2012) releases fluids (melts) by slab-dehydration reactions, which results in a hydrated mantle wedge composition and a hot thermal gradient.

The depth of the CMB near the Patagonian Andes is 20-30 km (Echaurren *et al.*, 2016, 2022; Fig. I.5b). The crustal basement consists of Devonian to Carboniferous metasediments, I-type magmatic felsic rocks as well as metabasic rocks from the accreted Chaitenia oceanic arc (Hervé *et al.*, 2016; Oriolo *et al.*, 2019; Rapela *et al.*, 2021; Fig. I.5b). The basement is intruded by numerous arc-type magmatic products, including the mafic Jurassic Subcordilleran batholith and the North Patagonian batholith, formed during the

Jurassic-Cretaceous and that are associated with andesites and a Miocene batholith (Pankhurst *et al.*, 1999; Echaurren *et al.*, 2016; Fig. I.5b). Arc-related magmatism occurring today in the Patagonian Andes is concentrated along the LOFS, which constitutes a weak zone where andesite magmas may find their way up to the surface. However, Vander Auwera *et al.*, (2021) proposed that magma resided at the ductile-brittle transition zone at 15 km deep or near the Moho, forming pyroxenite cumulates.

I. 3.3 Salta

During Cretaceous times, Salta intracontinenetal rift basins formation was associated with alkaline magmatism (Viramonte *et al.*, 1999; Marquillas *et al.*, 2005) that resulted from an upwelling of the asthenosphere, which set the LAB at 70 km deep after P-T estimates on peridotite xenoliths from Lucassen *et al.*, (2005; Fig. I.5c). The surrounding lithospheric mantle is essentially depleted as evidenced by peridotite xenolith major element compositions (Lucassen *et al.*, 2005). Moreover, in those samples, mineralogical assemblages lack of hydrous phases but enrichment in light to medium rare earth elements and radiogenic isotope composition changes have involved Cretaceous cryptic metasomatism within the lithospheric mantle. Finally, isotopes reflect the influence do not contain any metasomatic hydrated phases nor evidence of a subduction-modified mantle. Nevertheless, Lucassen *et al.* (2005, 2007) proposed that the lithospheric mantle was modified by “material influx” during subduction events from the West since at least the early Paleozoic, based on Sr-Nd-Pb isotopes-ratios in Cretaceous xenoliths and alkaline mafic volcanic rocks. compositions. Those authors also described clinopyroxenite xenoliths that they interpreted as magmatic cumulates and only suggested that they could have been emplaced in the lithospheric mantle (Lucassen *et al.*, 2005; Fig. I.5c).

The Petrological Moho depth has been estimated at ca. 35 km during Cretaceous times by P-T estimations of mafic granulites (Lucassen *et al.*, 1999b; Fig. I.5c). The xenolith study by the same authors revealed that felsic lithologies were dominant within the lower crust, supporting the model of Weinberg *et al.*, (2018), who proposed that the metasedimentary crust is inherited from the thinned Proterozoic Rio de la Plata passive margin (Fig. I.5c). Sedimentary Puncoviscanan formation deposited above it during late Neoproterozoic to Cambrian, and then has been metamorphosed during Cambrian Pampian and Ordovician Famatinian cycles, and associated to I-type and S-type magmatism (Casquet *et al.*, 2018; Rapela *et al.*, 2018; Weinberg *et al.*, 2018).

CHAPTER II: Petrology and microstructures of deep crustal rocks from the North Patagonian Massif, given by meta-igneous granulite xenoliths.

Draft accepted with major modifications to Journal of Petrology

Noé Muckensturm[1]*, Mary-Alix Kaczmarek[1], Michel Gregoire[1], Theodoros Ntaflos[2], Ernesto A. Bjerg[3] and Fréderic Mouthereau[1]

[1]Géosciences Environnement Toulouse, UPS OMP-CNRS-IRD, 14 Avenue E. Belin, 31400 Toulouse, France

[2]University of Vienna, Department of Lithospheric Research, Josef-Holaubek-Platz 2, 1090 Wien, Austria

[3]Instituto Geológico del Sur (INGEOSUR, UNS-CONICET), Departamento de Geología, Universidad Nacional del Sur, San Juan 670, 8000, Bahía Blanca, Buenos Aires, Argentina

* Corresponding author. Telephone : (+33) 638680157. E-mail: noe.muckensturm@outlook.com

ABSTRACT

The continental lower crust constitutes a key zone for understanding the mantle-crust magmatic and mechanical transfers, but the scarcity of lower crust samples makes its study complicated. Here, we characterise the petrological, geochemical and petrophysical processes structuring the lower crust of the North Patagonian Massif (NPM; Argentina) with a suite of representative mafic granulite and websterite xenoliths. Those xenoliths were brought up by alkaline lavas from 5 volcanic centres that erupted between the Oligocene and Pleistocene. Electron microprobe and laser ablation Inductively Coupled Plasma Mass Spectrometer

(LA-ICPMS) have been used to obtain in-situ geochemical data on minerals, while microstructural data have been acquired through Electron Backscatter Diffraction (EBSD). Both granulites and websterites display a granoblastic texture and sometimes a weak inherited magmatic layering. Mafic granulite xenoliths show an assemblage of plagioclase + clinopyroxene ± orthopyroxene commonly associated with spinel or titanomagnetite. Websterites xenoliths show an association of clinopyroxene + orthopyroxene + spinel, along with accessory plagioclase. Mafic granulites and websterites have a SiO_2 content ranging from 44 to 53 wt % while their Mg# varies from 39 to 67. Clinopyroxenes are characterised by weak upward convex chondrite-normalised Rare Earth Elements - REE patterns (Low-REE </<< Mid-REE > High-REE) which are similar to clinopyroxene phenocrysts and megacrysts from intra-plate basalts. Calculated liquid in equilibrium with clinopyroxene have similar REE patterns to those found in Permian, Jurassic and Cenozoic volcanic rocks from the NPM, which suggests that the xenolith suite represents witnesses of underplating processes associated with the intense magmatic activity occurring in the NPM since the Permo-Trias. Mafic granulites and websterites display a weak mineral shape preferred orientation and an associated weak crystal preferred orientation (CPO) related to the magmatic layering. Recorded plastic deformation goes along with the activation of both (100)[001] and (001)[100] slip systems in clinopyroxene, (100)[001] in orthopyroxene and (010)[001] in plagioclase. Nevertheless, slip systems activation is not correlated with observed CPO, suggesting that the lower crust underwent sub-solidus equilibration and low plastic deformation in an inactive tectonic context, in order to preserve an inherited magmatic layering. Two-pyroxene (Fe-Mg) thermometers and pseudosection calculation define P-T conditions of the main paragenesis at 760-1120°C and 7.2-10.3 kbar, which allows to define the Cenozoic geotherm of the NPM crust at 30°C/km and reconsider the Petrologic Moho depth at ca. 40 km.

Keywords: Xenoliths, mafic granulites, microstructure, thermobarometry, trace elements, Patagonia.

RÉSUMÉ

La croûte inférieure continentale constitue une zone clé pour étudier les transferts magmatiques et mécaniques entre le manteau et la croûte, mais la rareté des échantillons accessibles de la croûte inférieure complique son étude. Nous caractérisons ici les processus

pétrologiques, géochimiques et pétrophysiques qui structurent la croûte inférieure du massif nord-patagonien (MNP ; province de Rio Negro, Argentine) à l'aide d'une série de xénolithes de granulite mafiques et de websterites représentatifs. Ces xénolithes ont été remontés à la surface par des laves alcalines provenant de cinq centres éruptifs datés de l'Oligocène au Pléistocène. Des analyses par microsonde électronique et par Ablation laser Spectrométrie de masse à plasma à couplage inductif (LA-ICPMS) ont été réalisées pour obtenir des données géochimiques in situ sur les minéraux, tandis que les données microstructurales ont été obtenues par Electron Backscattered Diffranction (EBSD). Les granulites mafiques et les websterites présentent toutes une texture granoblastique et certaines un faible litage magmatique hérité. Les granulites mafiques présentent une paragénèse de type plagioclase + clinopyroxène ± orthopyroxène généralement associée à du spinelle ou de la titanomagnétite. Les websterites ont une paragénèse de type clinopyroxène + orthopyroxène + spinelle, accompagnée du plagioclase accessoire. Les granulites mafiques et les websterites ont une teneur en SiO_2 allant de 44 à 53 wt.%, tandis que leur Mg# varie entre 39 et 67. Les clinopyroxènes sont caractérisés par des profils de terres rares normalisés aux chondrites, légèrement convexes (terres rares légères </<< terres rares médianes > terres rares lourdes), qui sont similaires à ceux des phénocristaux et mégacristaux de clinopyroxène provenant de basaltes de contexte intraplaques. Les liquides calculés en équilibre avec le clinopyroxène ont des profils de terre rare similaires à ceux des roches volcaniques permiennes, jurassiques et cénozoïques du MNP, ce qui suggère que la suite de xénolithes représente des témoins des processus de sous-plaquage lié à l'intense activité magmatique qui s'est produite dans le MNP depuis le Permo-Trias. Les granulites mafiques et les websterites présentent une faible orientation préférentielle de forme et une faible orientation préférentielle des cristaux (CPO) reliées à l'ancien litage magmatique. L'étude des axes de désorientation aux sous-joints de grain ou aux joints de grains de faible angle suggère que la déformation plastique enregistrée va de pair avec l'activation des systèmes de glissement (100)[001] et (001)[100] dans le clinopyroxène, (100)[001] dans l'orthopyroxène et (010)[001] dans le plagioclase. Néanmoins, l'activation des systèmes de glissement n'est pas corrélée avec la CPO observée, ce qui suggère que la croûte inférieure a subi un équilibrage sub-solidus et une déformation plastique faible dans un contexte tectonique inactif, afin de préserver le litage magmatique observé. Les thermomètres d'échange Fe-Mg entre clinopyroxène et orthopyroxène et le calcul de pseudosections définissent les conditions pression-température de la paragenèse principale à 760-1120°C et 7,2-10,3 kbar, ce qui permet de définir le géotherme Cénozoïque

de la croûte du MNP à 30°C/km et de reconsidérer la profondeur du Moho pétrologique à environ 40 km.

Mots-clés: Xénolithes, granulites mafiques, microstructure, thermobarométrie, éléments traces, Patagonie.

II. 1. INTRODUCTION

The debate surrounding the constitution and the structuration of the continental lower crust, and its transition to the mantle, is ongoing. The lower crust constitutes an important zone for understanding the complex processes of crust-mantle transfers. Those transfers may be magmatic in nature (e.g. magma underplating, associated magma fractionation and assimilation, or lithospheric delamination; Cawood *et al.*, 2013, 2022; Gianni & Navarrete, 2022) and mechanical, with the transfer of plate tectonic strain into the crust via decoupling processes at the crust-mantle boundary (Coltice *et al.*, 2019; Mouthereau *et al.*, 2021). However, understanding the impacts of these transfers on the structure of the continental lower crust is challenging for two main reasons: the lower crust is rarely exposed on the Earth surface, and existing knowledge has primarily been derived from xenoliths studies which does not provide spatial resolution (Mengel & Kern, 1992; Rudnick & Fountain, 1995; O'Reilly & Griffin, 2013; Hacker *et al.*, 2015).

The North Patagonian Massif (NPM; Rio Negro Province, Argentina) lacks mid-to-lower crustal rock outcrops (e.g. Rapela & Pankhurst, 2020), hence, the nature of its lower crust remains controversial. While the oldest exposed rocks in the massif are igneous and metasedimentary Early Paleozoic (Early Cambrian to Silurian), the age of the basement has been indirectly inferred as Mesoproterozoic (1200-1000 Ma) from U-Pb ages in detrital zircons (Pankhurst *et al.*, 2006; Rapalini *et al.*, 2013), from U-Pb ages and Hf model ages of inherited metamorphic and magmatic zircon cores (Rapalini *et al.*, 2013; Pankhurst *et al.*, 2014; Rapela and Pankhurst, 2020), and from whole-rock Nd model ages of igneous Paleozoic rocks (Martínez Dopico *et al.*, 2011; Pankhurst *et al.*, 2014). The NPM Mesoproterozoic lower crust has a refractory character based on the geochemical study of xenoliths from Sierra de los Chacays (Southern NPM, Pankhurst & Rapela, 1995). It recorded crustal anatexis, magmatic remobilization between the Devonian (Late Paleozoic) and the Jurassic (Pankhurst & Rapela, 1995; Pankhurst *et al.*, 1998; Pankhurst *et al.*, 2006; Luppo *et*

al., 2018; Zaffarana *et al.*, 2020; Falco *et al.*, 2022; Gianni & Navarrete, 2022, Oriolo *et al.*, 2023). Studies on the NPM lower crust have established the occurrence of successive melts and magmatic events responsible for its compositional heterogeneities, and structure.

The thickness and the geotherm of the NPM lower crust are constrained mainly by interpretations of gravity anomalies and seismic tomography models. The Moho depth is estimated at ca. 30-40 km (Assumpção *et al.*, 2013; Chulick *et al.*, 2013; Van der Meijde *et al.*, 2013), while high surface heat flow (ca. 65-135 mW/m²; Idárraga-García & Vargas, 2018; Christiansen *et al.*, 2022) and the thin lithosphere (<100 km; e.g. Afonso *et al.*, 2019) indicate the likelihood of high temperatures and geothermal gradient in the lower crust. However, a recent geophysical model, combining large types of data (tomography models, rock densities, rock thermal conductivity and heat flow data), proposed a deeper Moho at 40-50 km, a crustal geotherm of 25°C/km for the 30 first kilometres and a lithosphere thickness ranging between 115 and 200 km which suggest a colder thermal regime than the one previously proposed (Gómez-Dacal *et al.*, 2017, 2021). Despite the lack of knowledge of the structure of the lower crust, the petrology and the geochemistry of the NPM lower crust have only been scarcely characterised (Pankhurst & Rapela, 1995), and its petrophysical characteristics remain unknown.

A detailed petrological, geochemical and microstructural characterisation of the NPM lower crust, will better constrain the magmatic and rheological relationships at the mantle-crust transition. In this study, the rheology and the magmatic processes recorded by the NPM lower crust has been investigated in detail by analysing the microstructure of granulites and websterites, as well as the chemical composition of minerals (major and trace elements). The combination of these new data allows us to present a model of the deformation, the thermal regime, the thickness, the origin and the evolution of the recent lower crust of the North Patagonian Massif. To build this model we use a collection of xenoliths of mafic granulites and websterites from Oligo-Miocene to Pleistocene volcanics occurring in five different localities within the massif.

II. 2. GEOLOGICAL SETTING

The North Patagonian Massif (NPM) is a plateau extended to 100 000 km² located in Río Negro and Chubut provinces, Argentina (39-43° S; Fig. II.1). The NPM is bordered to the North by Neuquén and Colorado basins, and to the South by the Cañadón Asfalto and the San

Jorge basins. It is settled East to the mountain range and magmatic arc Cordillera of the Andes, resulting from the East dipping long-lived ocean-continent subduction (e.g. Aragón *et al.*, 2011). The NPM, together with the Deseado Massif to the South, is known to be one of the two massifs exposing basement rocks of the Patagonia geological province (Ramos, 2008). Basement outcrops display scarce Early to Late Paleozoic magmatic and metamorphic rocks (Cambro-Ordivician in the North East, Devonian to Carboniferous in the West; Pankhurst *et al.*, 2006; Martínez Dopico *et al.*, 2011) and abundant Permo-Triassic magmatic rocks, the latter including granitoids, andesites and rhyolites (Pankhurst *et al.*, 2006). This exposed basement is overlayed by Jurassic andesites, rhyolites and rare granitoids (Zaffarana *et al.*, 2020). Late Paleozoic to Jurassic magmatic rocks involve the Devonian to Permian I- to S- type magmatism (Oriolo *et al.* 2023) and the formation of Choiyoi (Permian-Lower Trias; 295-248 Ma) and Chon Aike (Early Jurassic; 200-175 Ma) silicic large igneous provinces (SLIP; Pankhurst & Rapela, 1995; Pankhurst *et al.*, 1998; Luppo *et al.*, 2018; Zaffarana *et al.*, 2020; Falco *et al.*, 2022; Gianni & Navarrete, 2022), and significantly evidence the lower crustal growth and the rework of the NPM basement. Moreover, mafic crustal xenoliths found in the Paso de Indios Paleogene basalts (Cañadón Asfalto Basin, South to the NPM) have been dated at 175.9 Ma by U Pb/zircon (Castro *et al.*, 2011), and thus have been attributed to the formation of a residual crust during the Chon Aike SLIP. The lithosphere of the NPM is considered to have been thinned and reworked which is directly linked with thermal erosion involved by the intense magmatic activity during both Choiyoi and Chon Aike SLIP (Navarrete *et al.*, 2019; Gianni and Navarrete, 2022), which is supported by Re-Os systematics applied on peridotite xenoliths from Pleistocene volcanics which yielded Mesoproterozoic to Phanerozoic T_{RD} ages (1.3-0 Ga; Schilling *et al.*, 2008, 2017; Mundl *et al.*, 2016).

Finally, Cenozoic volcanic rocks, mainly Oligo-Miocene flood basalts (Cordenons *et al.*, 2020) form the upper part of the sequence. They belong to a Cenozoic intraplate large igneous province (LIP) with an asthenospheric mantle source that occurred in Patagonia (Kay *et al.*, 2007; Navarrete *et al.*, 2020) and which might include slight lower crust fractionation of the mantle source melts (Kay *et al.*, 2007; Cordenons *et al.*, 2020). The origin of the asthenospheric melting is not well constrained, contrary to the magmatic evolution of the LIP (Kay *et al.*, 2007; Cordenons *et al.*, 2020). Early to Middle Oligocene first magmatic phases are mainly alkaline. Late Oligocene to Early Miocene phases are dominated by tholeiitic flood basalts production, and are followed by Middle to Late Miocene alkaline phases

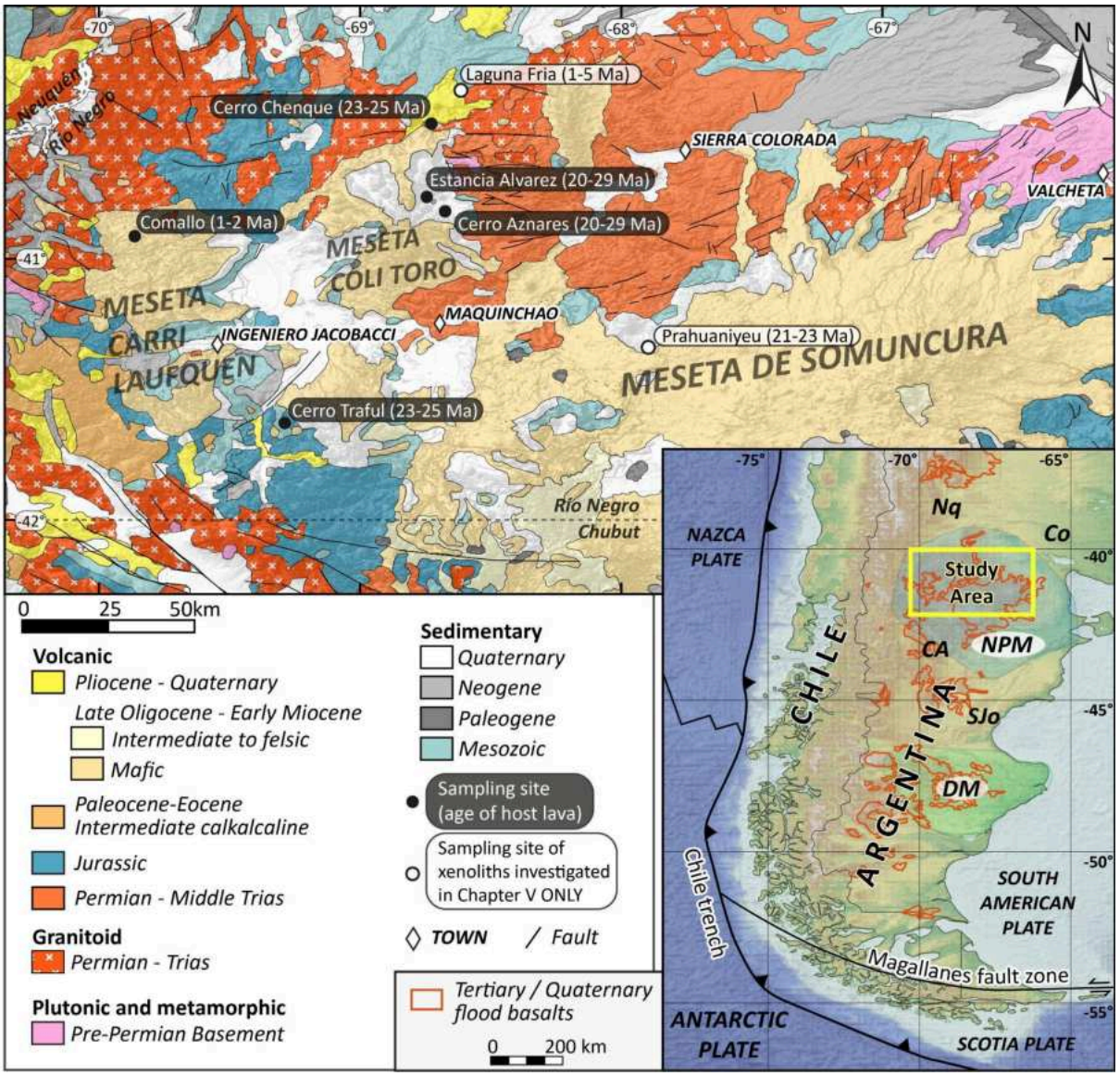


Fig. II.1. Simplified geological map of the North Patagonian Massif, with its setting in Patagonia. After Pankhurst *et al.* (2014), Cordenons *et al.* (2020), Zaffarana *et al.* (2020) and Falco *et al.* (2022), based on SegemAR maps. Nq: Neuquen basin, Co: Colorado basin, NPM: North Patagonian Massif, CA: Cañadon Asfalto basin, SJo: San Jorge basin, DM: Deseado Massif.

synonym of the extinction of the LIP. The associated lower crust has not been characterised, however, extensive Cenozoic tectonics did not affect the NPM besides minor faulting and uplift when it affected all the surrounding basins (Aragón *et al.*, 2011). Hence, the basement is compared to a cratonic bloc.

North Patagonian Massif xenoliths occur in Oligocene to Pleistocene volcanic rocks and display spinel and rare garnet peridotites, spinel pyroxenites, and granulites. Mantle peridotite xenoliths have been previously studied and discussed from petrological and geochemical points of view (e.g. Bjerg *et al.*, 2005, 2009; Mundl *et al.*, 2016; Schilling *et al.*,

2017; Melchiorre *et al.*, 2020). However, the study of granulite xenoliths has not yet been undertaken in the NPM despite their importance to characterise the lower crust.

II. 3. SAMPLE COLLECTION AND ANALYTICAL METHODS

II. 3.1. Samples collection

Xenoliths were sampled within lava flows, basaltic necks or basaltic dykes from 5 different localities from North Patagonia: Comallo, Cerro Traful, Cerro Aznares, Estancia Alvarez and Cerro Chenque (Fig. II.1). Host rocks are Late Oligocene to Early Miocene alkaline trachybasalts and basalts with Cerro Chenque and Cerro Traful dated from 23 to 25 Ma and Cerro Aznares and Estancia Alvarez from 20 to 29 Ma (Mallmann, 2004; Bjerg *et al.*, 2005; Dantas, 2007; Mundl *et al.*, 2016; Melchiorre *et al.*, 2020), except Comallo where the host-lava flow has been dated Early Pleistocene from 0.9 to 1.4 Ma (Mundl *et al.*, 2016). Xenoliths have an average diameter of 8 to 12 cm. A series of 20 mafic granulites and 3 websterites collected by T. Ntaflos and E. Bjerg in 2001, and a xenolith collection from C. Dantas (2007) consisting of 7 websterites and 1 mafic granulite from Cerro Aznares were used for this study. Among these two collections, 9 granulites and 1 websterite were selected for major and trace elements bulk-rock analysis, 7 granulites and 2 websterites for major element analysis on minerals, 5 granulites and 2 websterites for trace element analysis on minerals, 6 granulites and 2 websterites for detailed microstructural analyses (Table II.1).

Table 1: Host rock age, coordinates, modal proportions and results of the Wells (1977) thermometry of the investigated xenoliths. Modal proportions are estimated with EBSD data (with an *) or estimated (with a range of ±3%) with the optical microscope. MG: metagabbro; MGn: metagabbronorite; TiMag: titanomagnetite; Sp: spinel; W: websterite; Pl: plagioclase; Cpx: clinopyroxene; Opx: orthopyroxene; Ol: olivine; Ilm: ilmenite.

Sample	CO10A1*	CXTRA1*	CXTRA2	CXTRA4*	CXALV1*	CXCHE1	CXCHE2*	CXCHE3	CXCHE4*	CXAZN1*	CXAZN2	PM6C8*	PM6C10	PM6Cx
Outcrop	Comallo	Cerro Traful			Est. Alvarez	Cerro Chenque				Cerro Aznares				
Host Rock Age (Ma)	1-2	23-25			20-29	23-25						20-29		
Latitude (°S)	40°55'	41°38'			40°46'	40°29'						40°49'		
Longitude (°O)	69°52'	69°18'			68°45'	68°44'						68°41'		
Rock type	Sp-W	Sp-MGn	TiMag-MG	Sp-MGn	Sp-MG	Sp-W	MG	TiMag-MG	Sp-MGn	TiMag-MGn	Sp-MGn	Sp-W	Sp-MGn	
Modal prop. (%)														Sp-Websterite suite from Dantas (2007)
Pl	0.1	14.2	60-66	55.1	63	1-7	63.7	49-55	48.3	72	33-39	1.6	2-8	
Cpx	74.8	25.8	17-23	31.2	31.5	51-57	30.3	38-44	35.1	11.7	38-44	56	79-85	
Opx	9.45	51.5	6-12	11.2	0.8	26-32	4		12.3	12.4	11-17	29.9	2-8	
Ol	5.9	1.7	1-7	2.2			2		0.6	3.1				
Sp	9.9	7		0.3	4.7	10-16			3.7		3-9	12.5	5-11	
Ti-Mag			1-7					4-10		<0,5				
Ilm										<0,5				
T [Wells] ±70°C	920	816		836	917		1070			820	815	762		762-829

II. 3.2. Bulk-rock analyses

Bulk rock preparation has been done using the following protocol. All samples were crushed in an agate-crusher and subsequently reduced to powder using an agate disk mill. Bulk rock major and the trace elements Ba, Co, Cr, Ga, Ni, Rb, Sc, Sr, V, Zn and Zr were analysed with the sequential X-ray spectrometer Philips PW 2400, equipped with an Rh-excitation source (University of Vienna, Department of Lithospheric Research). Fused beads were produced at 950°C from a mixture of the specimen and $Li_2B_4O_7$ flux, diluted 1:5 to gain accurate and precise results. The trace elements were measured on powder pellets. Standard used for the callibration were international geostandards BCR-1, BHVO-1, BIR-1, DR-N, SGD-1a, MO-1, GSR-2, GSR3-3 (Gonvindaraju, 1989). Replicate analyses of geo-standard GSR-3 gave an overall procedural error better than 2% for major elements and 5% (Cu=8.5%) for trace elements.

For small-size samples a bulk rock chemical analysis was not possible and their compositions have been calculated combining their mineral modal compositions obtained by Electron Backscatter Diffraction maps and mineral major elements composition obtained by microprobe analyses (Table II.2). Bulk Fe_2O_3 was calculated based on the ratio Fe_2O_3/FeOt in two-pyroxenes and spinel or titanomagnetite.

II. 3.3. Backscatter images and minerals major elements compositions

Polished thick sections were covered with a 20 nm carbon deposit using a carbon evaporator Leica EM ACE600 for secondary Electron Microscope (SEM) observations and microprobe measurements. SEM qualitative chemical analyses were carried out at the Géosciences Environnement Toulouse (GET) laboratory (CNRS-CNES-IRD-University Paul Sabatier, Toulouse), Observatoire Midi Pyrénées (Toulouse, France), using a Tescan Vega 4 equipped with an EDS Bruker Quantax 30mm². The analysis conditions were performed with an acceleration voltage of 20 kV, a probe current of 3 nA and a working distance of 15 mm.

Minerals major element analyses were carried out using a Cameca SX Five electron microprobe from the micro-characterisation centre Raimond Castaing (University Paul Sabatier, Toulouse). Measurements were made with an acceleration voltage of 15 kV and a probe current of 20 nA. Acquisition times were 10 s on peak and 5 s on either side of the peak for the continuous background. The standards used are natural or synthetic minerals as well as pure metals. The data summary and detection limits are available in Supplementary Table S1.

II. 3.4. Clinopyroxene trace elements

Trace element contents in clinopyroxene was measured using the ELEMENT XR High Resolution ICP-MS (Thermo Scientific) coupled to the New Wave Research NWR213 Nd YAG 213 nm laser ablation unit from the GET laboratory (Observatoire Midi Pyrénées, Toulouse, France). Ablations were performed in a pure He atmosphere (500-600 xl/min) using a 50 or 30 μm spot size with a fluence of 1.5-2 J/cm^2, an energy of 20-30 % and 10 Hz repetition (pulse) rate. Counting time for one analysis was 210 s (60 s on gas blank to establish background, then 120 s for data acquisition followed by 30 s washout). The reference materials NIST SRM 610 and NIST SRM 612 were used as external standards (Jochum *et al.*, 2011), bracketing at most 12 unknowns. CaO values (wt%) determined with the electron microprobe served as internal standard. The relative precision and accuracy for laser analysis range from 1 to 10% for most of the elements, and is at 15% for Nb and Ta. The theoretical detection limits range from 10 to 60 ppb and for Sc and V is 100 ppb, for Ti is 2 ppm and for Ni and Cr is 0.7 ppm. Data reduction and processing were performed using the Glitter software (Van Achterbergh, 2001; Griffin *et al.*, 2008).

II. 3.5. Thermobarometry

Calculations were made in the Na_2O-CaO-K_2O-FeO-MgO-TiO_2-Al_2O_3-SiO_2-O_2 system, using the software Perple_X 6.9.1 and the internally consistent thermodynamic dataset (hp622ver) of Holland & Powell (2011). Solution models used were those from Fuhrman & Lindsley (1988) for plagioclase (Pl), Green *et al.* (2016) for clinopyroxene (Cpx) and melt, White *et al.* (2014) for orthopyroxene (Opx) and garnet (Grt), White *et al.* (2002) for spinel (Sp) and Holland & Powell (1998) for olivine (Ol). To avoid interferences from the host lava with the xenolith bulk composition, calculated bulk rock compositions based on mineralogical proportions and microprobe analyses were preferred for pseudosection calculation. O_2 bulk was calculated using the formula $O_{2\ mol} = 0.5*Fe_2O_{3\ mol}$. The TiO_2 from pyroxenes was not taken into the bulk rock incrementation into Perple_X, as used solution models from minerals without titanium. Four samples were selected for isochemical phase diagram calculations, as they are well preserved xenoliths from lava interaction.

II. 3.6. Crystallographic orientations of minerals

A mechanic-chemical polishing using a Vibromet (Buehler) was applied on 8 thick sections for 1h15 with a colloidal silica suspension (pH 10) to remove mechanically induced surface

damage. Electron Backscatter Diffraction (EBSD) data acquisition was performed with a JEOL 7100 Secondary Electron microscope at the centre of micro-characterization Raimond Castaing (University Paul Sabatier, Toulouse), equipped with an EBSD camera CMOS Symmetry S2 (Oxford Instruments). The analyses were performed with an acceleration voltage of 20 kV, a probe current of 16 nA and a working distance of 15 or 17 mm with a stage tilt of 70°. Automatic indexing was performed using AZTec software (version 6.0 Oxford Instruments). For mapping the step size used varies between 15 and 20 µm depending on the grain size. The EBSD data were then processed in MATLAB (version R2020b) using the MTex toolbox (version 5.7.0; Bachmann *et al.,* 2010, 2011). A value of 10° as the cut-off angle for the determination of the grains has been used, and low-angle boundaries are ≥ 2° and < 10°. Pole figures were plotted on a lower-hemisphere, equal-area stereographic projection. To avoid oversampling of large clinopyroxene and orthopyroxene crystals, pole figures were plotted with one point per grain, while plagioclase pole figures represent all the available measurements because twins increase the number of detected grains. The strength of the crystallographic preferred orientation was estimated using both the J- and M-indices (Bunge, 1982; Skemer *et al.*, 2005). In addition, the misorientation of each pixel was calculated relative to the mean orientation of its corresponding grain and then combined as maps of misorientation relative to mean grain orientation. In parallel, for each sample, pixel proportions relative to their misorientation angle were plotted in normalised histograms.

II. 4. RESULTS

II. 4.1. Sample description and petrography

II. 4.1.1. Mafic granulites

Mafic granulite xenoliths are metagabbros and metagabbronorites composed of plagioclase (14-72 vol.%; Table II.1), clinopyroxene (12-85 vol.%) ± orthopyroxene (0-52 vol.%), along with either spinel (samples CXTRA1, CXTRA4, CXALV1, CXCHE4 and CXAZN2; Fig. II.2a), titanomagnetite (sample CXAZN1, CXCHE3 and CXTRA2; Fig. II.2b, c) or with no oxide in sample CXCHE2 from Cerro Chenque (Fig. II.2f). Sample CXALV1, from Estancia Alvarez, is characterised by two types of spinel, Ferrian-pleonaste and Al-magnetite, that can form a symplectite with a single-crystal-shape-like (Fig. II.2d). Accessory olivine was found only in the sample CXAZN1 (Fig. II.2c). Traces of ilmenite also appear in this sample.

Mafic granulites display a granoblastic texture with clinopyroxene- or plagioclase-rich layers where crystals are flattened and slightly elongated (aspect ratio up to 2:1; Fig. II.2b, c, e). The grain size distribution is rather unimodal with clinopyroxene, plagioclase and orthopyroxene ranging from 300 μm to 5 mm (Fig. II.2). Many samples display linear grain boundaries (samples CXALV1, CXAZN2, CXCHE3, CXTRA1, CXTRA4) with numerous 120° triple junctions (Fig. II.2a, b, e) and some samples present slightly curved grain boundaries (CXAZN1, CXCHE4; Fig. II.2c). Metagabbro CXCHE2 has

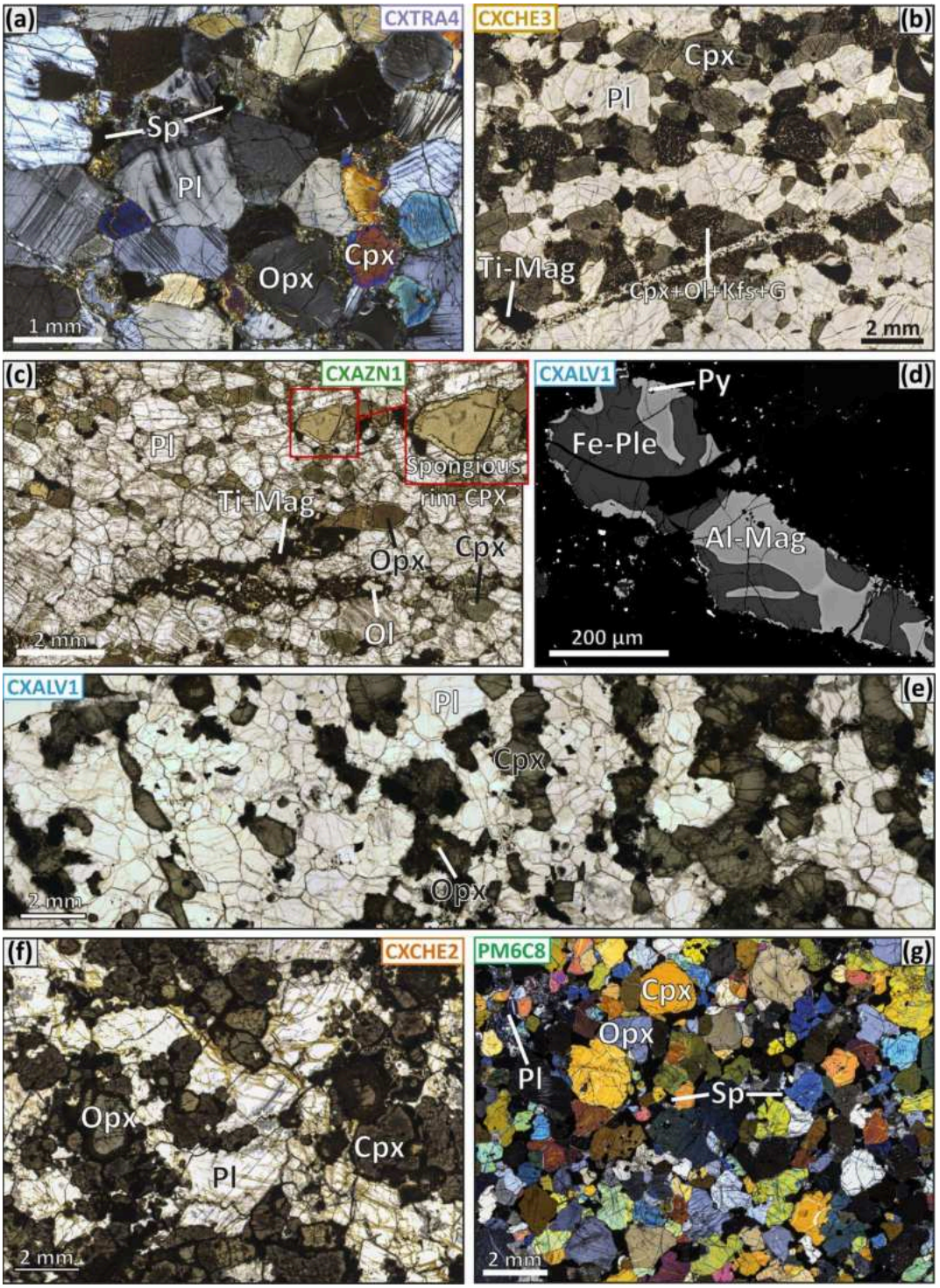


Fig. II.2. Photomicrographs of north Patagonian lower crustal xenoliths. (a) Spinel metagabbronorite (sample CXTRA4) under cross-polarized light; note conical albite twinning in plagioclase crystals. (b) Titanomagnetite metagabbro (sample CXCHE3) under plane-polarized light. (c) Titanomagnetite and olivine metagabbronorite (sample CXAZN1) under plane-polarized light. Note Clinopyroxene spongious rim highlights by red boxes. (d) Ferrian-pleonaste and Al-magnetite relations in metagabbro CXALV1, under backscattered electrons. (e) Compositional layering in metagabbro CXALV1, under plane-polarized light. (f) CXCHE2 metagabbro under plane-polarized light. (g) Spinel websterite (sample PM6C8) under cross-polarized light.

a texture that stands out from the suite by displaying fine (ca. 300 µm) to very-coarse plagioclase grains (up to 1 cm) together with curved grains boundaries and rare 120° triple junctions (Fig. II.2f). Albite twinning is observed in all samples, as it can be tapered (Fig. II.2a). Partial melting during xenolith transport by the host lava produces at the expense of orthopyroxene subhedral olivine II grains that can reach 100 µm in size, rims of orthopyroxene II (<50 µm) on orthopyroxene I grains and interstitial glass and potassic feldspar (Supplementary Fig. S1). These reactions are almost absent (e.g. CXTRA4) to omnipresent, and sometimes form pockets (e.g. CXCHE3; Fig. II.2b). Spongy rims of clinopyroxene II also might be observed in clinopyroxenes from reaction during host lava transport, and are generally large of a few micrometres except in sample CXAZN1 where they are 50 µm long (Fig. II.2c). Finally, clinopyroxene in some samples displays Fe-Ti exsolution lamellae too thin to be analysed with the microprobe.

II. 4.1.2. Websterites

Spinel-websterites from Comallo, Cerro Aznares and Cerro Chenque (samples CO10A1, PM6C8 and CXCHE1) display a granoblastic texture. They are composed of clinopyroxene and orthopyroxene with a grain size varying from 500 µm to 3 mm, spinel (grain size from 100 µm to 1.5 mm), and a low proportion of plagioclase (100 µm - 1 mm; Fig. II.2g; Table II.1). No shape-preferred orientation is observed and almost no deformation markers. Grain boundaries between phases are slightly curved and 120° triple junctions are common.

Reactions with host lava can also be observed, similar to those occurring in granulites, with the crystallisation of secondary olivine, clinopyroxene, K feldspar and glass.

II. 4.2. Bulk-rock chemistry

II. 4.2.1. Major elements

All xenoliths have a SiO_2 content ranging from 44 to 53 wt% while Mg# (100 x Mg/(Mg+Fet)) varying from 39 to 67 (Fig. II.3; Table II.2). The Mg# is high in websterite (samples CO10A1 and PM6C8) and in a metagabbronorite from Cerro Traful (CXTRA1). These samples plot in both the mafic 2 and the primitive basalt fields from Kempton & Harmon (1992; Fig. II.3). The SiO_2/Al_2O_3 content varies from 2.16 to 3.95 where the higher ratio is the websterite from Comallo and the lower content is the metagabbro from Estancia Alvarez. Some samples have lower SiO_2/Al_2O_3 ratios (CXTRA4, CXALV1, CXAZN2, CXCHE4) that can be attributed to the accumulation of Al-rich mineral phases such as

plagioclase or spinel (Fig. II.3). The Na_2O content covers a large range from 0.54 to 3.88 wt% (Table II.2). The Al_2O_3, Na_2O, Sr and Ba contents positively correlate with the volume proportion of plagioclase and negatively with MgO, Ni, Co and Cr contents.

Table 2: Analysed and calculated (with an *) major elements bulk rock compositions. Rock abbreviations are the same as for Table 1.

Sample	*CO10A1**	CXTRA1	CXTRA2	CXTRA4	CXALV1	CXCHE1	CXCHE2	CXCHE3	CXCHE4	CXAZN1	CXAZN2	*PM6C8**
Outcrop	Comallo	Cerro Traful			Est. Alvarez	Cerro Chenque				Cerro Aznares		
Rock type	*Sp-W*	*Sp-MGn*	*TiMag-MG*	*Sp-MGn*	*Sp-MG*	*Sp-W*	*MG*	*TiMag-MG*	*Sp-MGn*	*TiMag-MGn*	*SP-MGn*	*SP-W*
wt%												
SiO2	*45,06*	46,04	49,48	47,74	47,05	44,20	51,49	46,42	46,79	52,61	44,71	*45,24*
TiO2	*0,64*	0,27	0,73	0,33	0,57	0,19	0,78	1,38	0,32	0,80	0,19	*0,16*
Al2O3	*11,41*	14,44	17,78	20,83	21,73	13,45	13,91	16,76	20,48	18,30	19,36	*13,27*
Fe2O3	*3,76*											*1,94*
FeO	*6,11*	11,39	7,79	4,86	7,21	9,21	7,82	11,46	7,48	7,72	6,99	*7,11*
MnO	*0,14*	0,17	0,13	0,08	0,09	0,14	0,14	0,14	0,11	0,13	0,10	*0,14*
MgO	*15,29*	18,03	7,88	7,80	6,10	19,04	11,12	7,47	10,01	5,80	11,22	*18,52*
CaO	*16,93*	7,23	11,44	15,37	12,22	11,73	10,11	11,77	11,05	8,36	14,72	*13,09*
Na2O	*0,66*	0,90	2,41	1,76	2,93	0,54	2,67	2,50	1,97	3,88	0,86	*0,53*
K2O	*0,01*	0,50	1,02	0,51	0,42	0,15	0,77	0,68	0,45	1,01	0,24	*0,01*
P2O5		0,05	0,03	0,03	0,04	0,02	0,10	0,06	0,04	0,19	0,02	
Total	*100,00*	100,28	99,55	99,85	99,16	99,69	99,78	99,91	99,53	99,66	99,19	*100,00*
Mg#	*61,70*	61,30	50,30	61,61	45,83	67,41	58,71	39,47	57,24	42,89	61,60	*67,66*
ppm												
Nb		1,8	28,6	2,6	4,3	2	7,6	5,7	2,4	4,8	2,4	
Zr		15,5	141,3	26,7	31,2	8,5	40	38,3	25,9	46,1	15,7	
Y		3	16,8	7,4	6,4	3,7	8,8	9,2	3,8	13,4	4,5	
Sr		677,6	996,3	1073,9	1290,6	334,3	396,6	1016,1	1176	901,3	713	
Rb		10,7	37,4	16	11,5	3,6	12,1	14,7	13	10,8	6,7	
Pb		<5	5,8	<5	16,4	<5	<5	9,4	15,7	7,3	<5	
Ga		13,8	19,3	16,9	25,1	11,8	14,9	21	21,8	20,1	14,1	
Zn		96,1	77,9	64	69,6	58,4	78,6	83,2	72,3	90,7	54,7	
Cu		24,4	29,4	44,1	26	110,9	48,8	145,9	31,4	9	75,1	
Ni		241,9	50,3	42,4	23,7	198,6	194,1	65,4	121,9	52	114,7	
Co		75,2	29,2	32,3	28,9	72,3	43	44,4	43,7	32,4	44,2	
Cr		213,8	51,7	138,3	54,5	418,1	450,4	152,8	295,7	94,3	444,8	
Sc		19,9	16,6	31,9	20,1	36,4	31,3	41,9	20,9	20,6	36	
V		61,1	123,5	156,1	198,8	84,3	158,3	349,7	76,4	160	70,8	
Ce		<10	73	<10	<10	38,5	<10	<10	<10	38	<10	
Ba		375,8	694,7	631,8	246,5	1,7	112,6	500,4	374,5	524,6	52,3	
La		<10	26,5	<10	<10	<10	<10	<10	<10	16,7	<10	

The bulk rock compositions of the investigated xenoliths plot within the mafic 2, mafic 3 or intermediate fields of the granulite classification proposed by Kempton & Harmon (1992; Fig. II.3). When plotted within this figure the north Patagonian Cenozoic lavas (Kay *et al.*, 2004, 2007; Jacques *et al.*, 2014; Massaferro *et al.*, 2014, Asiain *et al.*, 2022) draw a field following the alkaline differentiation trend with a decrease of Mg# for a constant SiO_2/Al_2O_3 content (Fig. II.3). Titanomagnetite-bearing granulites show higher abundances of TiO_2 (0.73-1.38 wt%) than other granulites (0.19-0.57 wt%). Granulite xenoliths from Pankhurst & Rapela (1995; Sierra de los Chacays, southern NPM) and Castro et al. (2011; Pasos de Indios, Cañadon Asfalto basin) display for most of them similar Mg# and SiO_2/Al_2O_3 ratios and plot in the mafic 2 and mafic 3 fields (Fig. II.3).

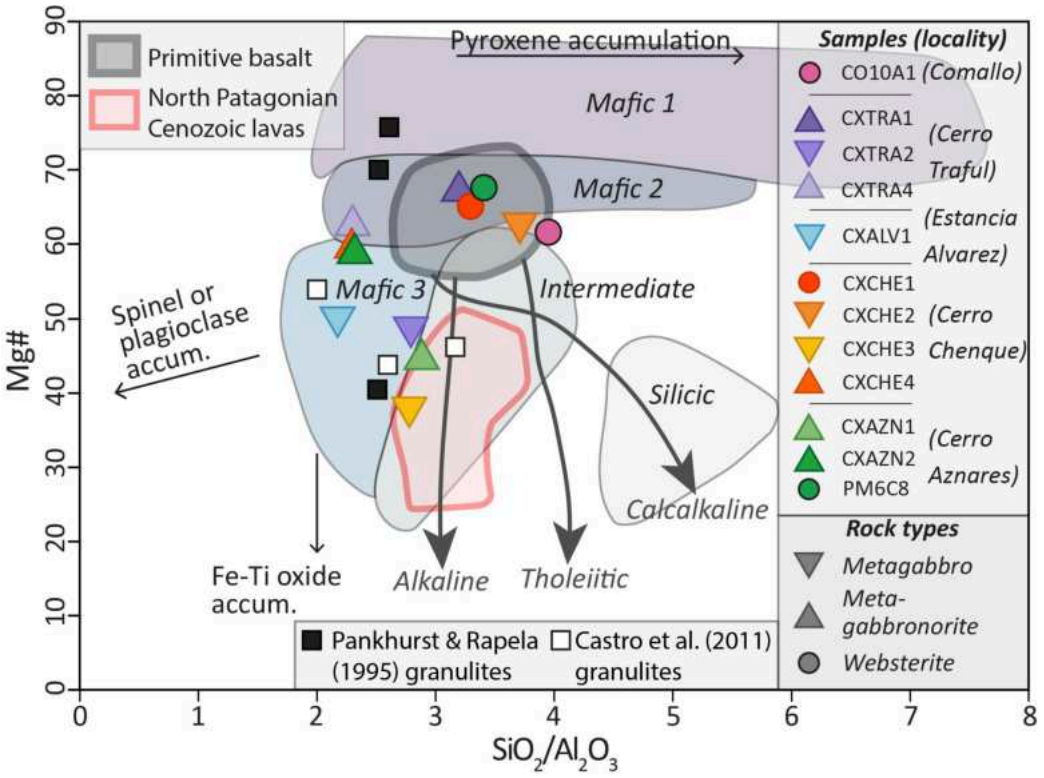


Fig. II.3. Bulk rock Mg# vs. SiO_2/Al_2O_3 plotted in the granulite classification of Kempton and Harmon (1992). Primitive basalt field and differentiation trends are from the same authors. North Patagonian Cenozoic lavas field is from Kay *et al.* (2004, 2007), Jacques *et al.* (2014), Massaferro *et al.* (2014) and Asiain *et al.* (2022). Granulite compositions from Pankhurst & Rapela (1995; Sierra de los Chacays, southern NPM) and Castro *et al.* (2011; Pasos de Indios, Cañadon Asfalto basin) are added for comparison.

II. 4.2.2. Trace elements

The xenolith suite, excluding CXTRA2, displays homogeneous and low concentrations of incompatible elements such as Nb, Zr, Y and Rb, with Nb ranging from 2 to 8 ppm, Zr from 8 to 46 ppm, Y from 3 to 17 ppm and Rb from 7 to 15 ppm (Table II.2). The factor of variation ranges between 2 and 6 across samples. In contrast, sample CXTRA2 displays high concentrations of Nb (29 ppm), Zr (141 ppm), and Rb (37 ppm). Some compatible elements, like Ni (ranging from 24 to 242 ppm) and Co (ranging from 29 to 75 ppm), show heterogeneous concentrations within the suite (Table II.2). Sr and Cr display higher abundances compared to the aforementioned elements (334-1291 ppm and 52-450 ppm respectively), while Ba, which is compatible with plagioclase, displays highly variable concentrations ranging from 2 to 695 ppm, representing a 400-fold variation.

Titanomagnetite-bearing granulites show higher abundances of Y (9-17 ppm) than other granulites (3-7 ppm), as observed for TiO_2. There are no significant differences in major and trace element abundances between metagabbro, metagrabbronorite, and websterites, and the whole xenolith suite displays a continuous compositional range.

II. 4.3. Minerals major elements composition

II. 4.3.1. Clinopyroxene

Clinopyroxene is usually Al-diopside (Al_2O_3 > 4 wt%), even if diopside sensu stricto occurs in the titanomagnetite and olivine-bearing metagabbronorite CXAZN1 from Cerro Aznares, and Al-Augite in sample CXCHE2 and some websterites of the suite from Dantas (2007; PM6Cx Cerro Aznares; Fig. II.4a, c; Supplementary Table S1). Clinopyroxene crystals of all the investigated samples have a distribution of Al between IV and VI sites that follows a ratio near 1:1 (Fig. II.4b), and they plot within the granulite field from the classification of Aoki & Kushiro (1968; Fig. II.4b). The Al_2O_3 content varies between 5.7-9.4 wt% but for the metagabbronorite CXAZN1 and PM6Cx showing values ranging from 2.5 to 4 wt% and from 3.1 to 4.1 wt% respectively (Fig. II.4c). Mg# ranges from 66 to 79 except for both websterites PM6C8 and PM6Cx from Cerro Aznares which have high Mg# values (83-90). The investigated suite is characterised by a negative correlation between Al_2O_3 content and Mg# (Fig. II.4c). Samples from Cerro Aznares (CXAZN1, CXAZN2, PM6C8, PM6Cx) have low TiO_2 content (0.25-0.48 wt%) while those from Comallo, Cerro Traful and Estancia Alvarez display a higher TiO_2 content (0.6-1.12 wt%) (Fig. II.4d). Finally, the Cerro Chenque xenoliths have high TiO_2 content (0.84-1.72 wt%). The calculated Fe_2O_3 content (by stoichiometry) is homogeneous between samples (1.5-3.5 wt%), whereas FeO content may vary between samples (7.7-8.3 wt% in samples CXCHE2 and CXAZN1 respectively and 3.5-5.8 wt% for the others; Supplementary Table S1). Na_2O content is always lower than 1 wt%. Compositions of the clinopyroxene spongy rims are the same as cores, except for TiO_2 contents which may decrease by <0.2 wt%. Clinopyroxene II and spongy clinopyroxene rims (Supplementary Fig. S1) measured in samples CXAZN1, CXCHE2 and CXCHE3 has Al_2O_3 contents lower than 1 wt% and has Mg# values bracketed between 75 and 79. Otherwise, it displays similar compositions to clinopyroxene I.

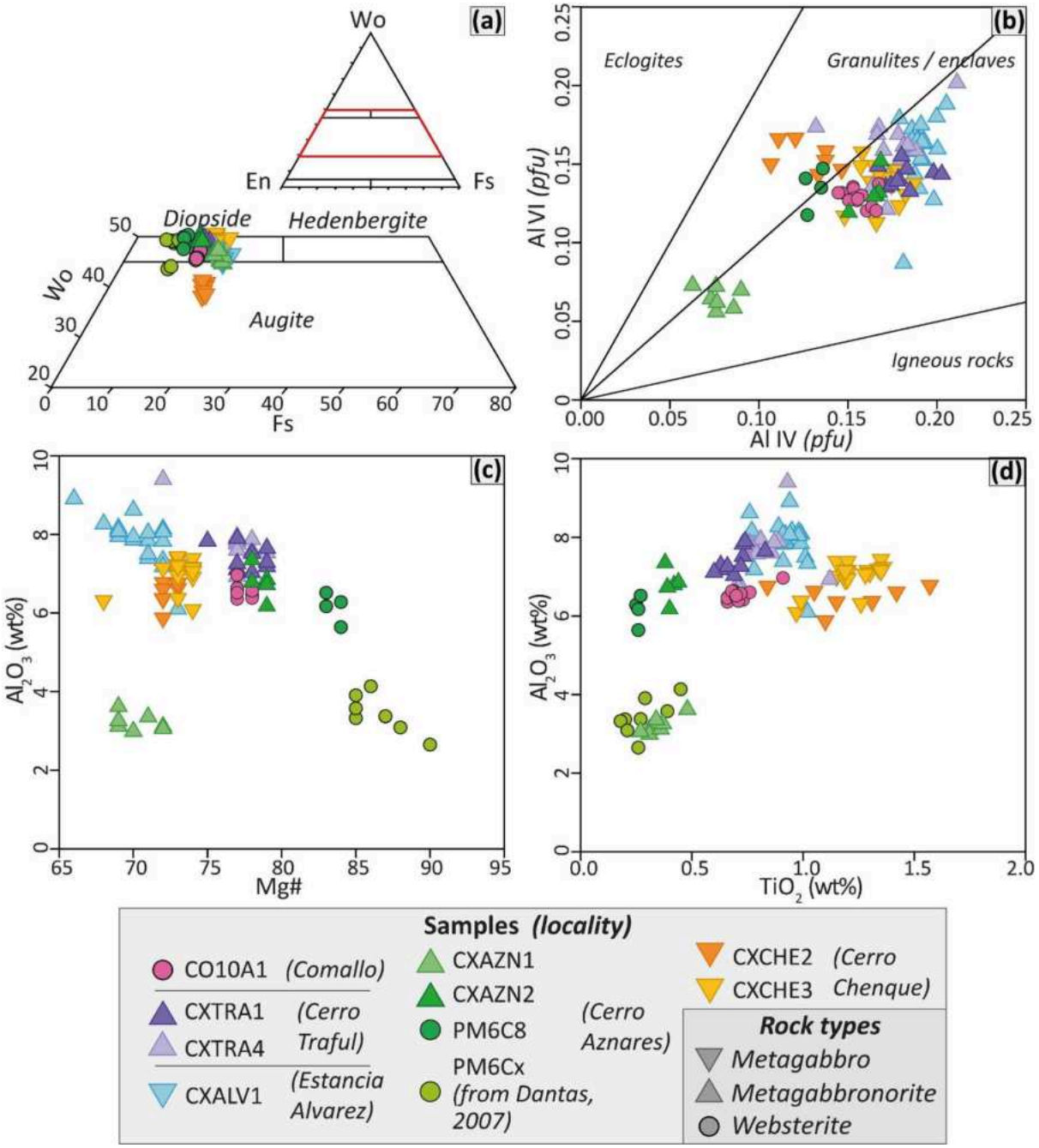


Fig. II.4. Major element diagrams of clinopyroxene. (a) Ternary wollastonite-enstatite-hedenbergite plot of pyroxenes. (b) Plot of Al_{VI} *vs.* Al_{IV}. Compositional fields are from Aoki & Kushiro (1968). Al_{IV} = 2-(Si+Ti), molar; $Al_{VI} = Al_{tot}-Al_{IV}$, molar. (c) Plot of Al_2O_3 vs Mg#. (d) Plot of Al_2O_3 vs TiO_2. Mg # = 100 x Mg/(Mg+Fet), molar.

II. 4.3.2. Orthopyroxene

Orthopyroxene from metagabbros and metagabbronorite is Al-enstatite (Al_2O_3 content between 4 and 6.5 wt%) and displays a Mg# varying from 71 to 77 (Fig. II.5a, c; Supplementary Table S1). The Mg# and Al_2O_3 diagram displays an anti-correlation trend as

already observed for clinopyroxene (Fig. II.4). As for clinopyroxene, the orthopyroxene from sample CXAZN1 (Cerro Aznares) has significantly lower Mg# (61-62), and Al_2O_3 content (2 wt%) than other granulites (Fig. II.5b). Orthopyroxene from websterites CO10A1 (Comallo) and PM6C8 (Cerro Aznares) have slightly higher Mg# (77-81) and similar Al_2O_3 content (4.9-5.4 wt%) than other granulites. Cerro Aznares websterites from Dantas (2007; samples PM6Cx) have high Mg# (80-86) and Cr_2O_3 content (up to 0.37) but display low Al_2O_3 content (1.2-3.2 wt%), similar to those from CXAZN1. Orthopyroxene II measured in samples CXTRA4, CXAZN1, CXAZN2, and CXCHE2 has the same composition as orthopyroxene I except for Al_2O_3 content that is lower (< 2wt%) and the Mg# in the sample CXAZN1 which is higher (68).

II. 4.3.3. Plagioclase

Plagioclase varies from bytownite to andesine (An_{88-40}) with orthoclase contents always <5 %mol (Fig. II.5d; Supplementary Table S1). Plagioclase from metagabbronorite granulites CXAZN2, CXTRA1 and CXTRA4 is the most calcic plagioclase of the whole suite with a bytownite (An_{88-65}) composition. Websterites CO10A1 and PM6C8 have accessory plagioclase that varies between bytownite and labradorite (An_{66} and An_{63-72} respectively). Plagioclase from CXALV1 and CXCHE3 is essentially labradorite (An_{65-46}) while that of the samples CXCHE2 and CXAZN1 is essentially andesine (An_{50-40}). Also, the albite content of plagioclase is positively correlated with bulk rock Na2O content but also with Zr content (Table II.2; Supplementary Table S1). Bédard (2006) evidenced that the increase of Na2O content in plagioclase increases the compatibility of Zr for this mineral.

II. 4.3.4. Spinel-group

In spinel-websterites and granulites, spinel is usually pleonaste (samples CXTRA1, CXTRA4, CXAZN2, CO10A1, PM6C8; Supplementary Table S1; Supplementary Fig. S2). TiO_2 and Cr_2O_3 contents are low (<0.56 wt% and <1.61 wt%, respectively) and Fe_2O_3 content increases up to 13 wt% when the Al_2O_3 content decreases from 62 to 52 wt% (Supplementary Table S1). Websterite PM6C8 is characterised by a spinel with a higher Mg# (67-69) than one of the other samples (56-61). Metagabbro CXALV1 (Estancia Alvarez) hosts two different types of spinel: ferrian-pleonaste and Al-magnetite (Supplementary Fig. S1). They have low Cr_2O_3 <0.2 wt% and MnO and 0.17-0.32 wt% contents. Ferrian-pleonaste has a Mg# of 41-47, a content of Al_2O_3 of 41-43 wt%, a high Fe_2O_3 (20-23 wt%) and a low TiO_2 (1.5-2

wt%). Al-magnetite has a lower Mg# (20-24), lower content of Al_2O_3 (15-19 wt%), higher Fe_2O_3 (36-39 wt%) and TiO_2 (6-8 wt%) than other spinels.

Titanomagnetite occurring in samples CXAZN1 and CXCHE3 is characterised by low MgO (2.1-3.6 wt%) and Al_2O_3 contents (2.1-5.1 wt%). Titanomagnetite in sample CXCHE3 has TiO_2 contents of 13.7-15.1 wt% and FeO_t contents of 68.3-73.2 wt%. CXAZN1 has greater TiO_2 contents (21.6-22.6 wt%) but lower FeO_t contents (65.7-67.6 wt%).

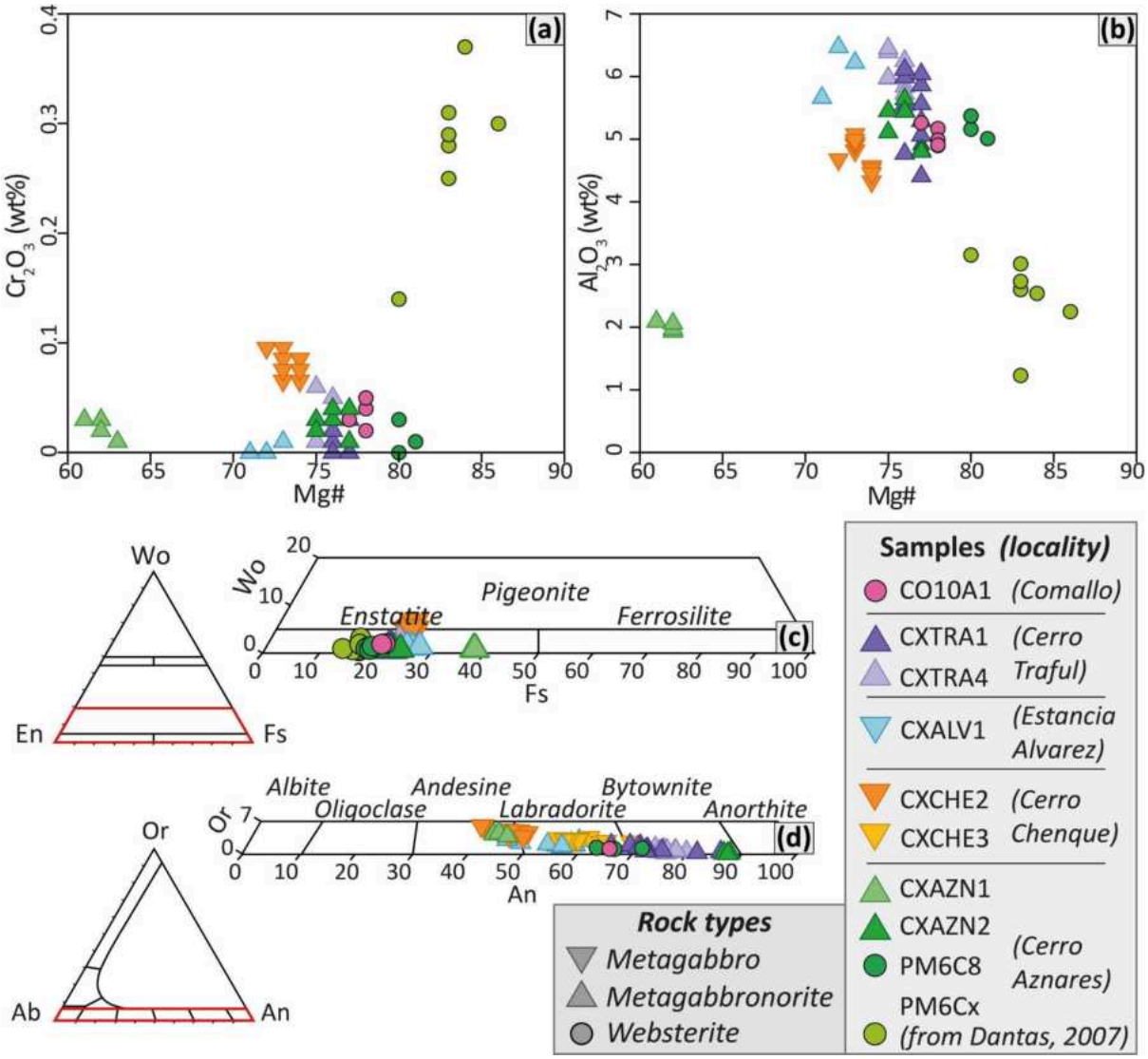


Fig. II.5. Major element diagrams of orthopyroxene and plagioclase. (a) Plot of Cr_2O_3 vs Mg# of orthopyroxene. (b) Plot of Al_2O_3 vs Mg# of orthopyroxene. (c) Detailed wollastonite-enstatite-hedenbergite ternary plot of pyroxene. (d) Detailed orthoclase-albite-anorthite ternary plot of feldspar.

II. 4.3.5. Accessory minerals (olivine, ilmenite)

Metaggabronorite CXAZN1 displays accessory olivine with a Mg# of 61 (Table II.7) and traces of ilmenite.

II. 4.4. Clinopyroxene trace elements

II. 4.4.1. Rare Earth Elements

All the investigated samples are characterised by smoothly convex chondrite-normalised rare earth elements (REE) patterns related to enrichment in medium rare earth elements (MREE; Sm to Ho) over light rare earth elements (LREE; La to Nd) and heavy rare earth elements (HREE; Er to Lu; $0.1<La_n/Sm_n<0.9$; $0.3<Yb_n/Sm_n<0.4$; Fig. II.6a; Table II.3). The metagabbronorites from Cerro Aznares display a higher REE concentration than the other samples, especially metagabbronorites CXAZN1 and PM6C10, the former displaying a negative Eu anomaly and HREE enrichment. The two metagabbros (CXALV1 and CXCHE2) have similar MREE and HREE concentrations but sample CXALV1 displays lower LREE contents that widely vary between clinopyroxene grains (see Supplementary Fig. S3) and a slight positive Eu anomaly. Websterite CO10A1 from Comallo displays a similar pattern to that of websterite PM6C8 but at a higher level of concentration (Fig. II.6a). Websterite suite PM6Cx from Dantas (2007) displays similar patterns and REE concentrations bracketed between both investigated websterites CO10A1 and PM6C8, except in LREE values that can reach lower concentrations than websterite PM6C8.

II. 4.4.2. Trace Elements

The investigated clinopyroxene grains are characterised by Ti anomaly that can be strongly negative (sample CXAZN1), slightly negative (samples CO10A1, CXTRA4, CXALV1, PM6C8, PM6C10), or slightly positive (sample CXCHE2; Fig. II.6b). All samples display a Zr-Hf negative anomaly, deeper for sample CXALV1. Except for sample CXALV1, all the investigated granulites have a negative Sr anomaly, which is even stronger for the two metagabbronorites CXAZN1 and PM6C10 (Fig. II.6). The clinopyroxene from the two websterites display a positive Sr anomaly, deep for sample PM6C8 and slight for sample CO10A1.

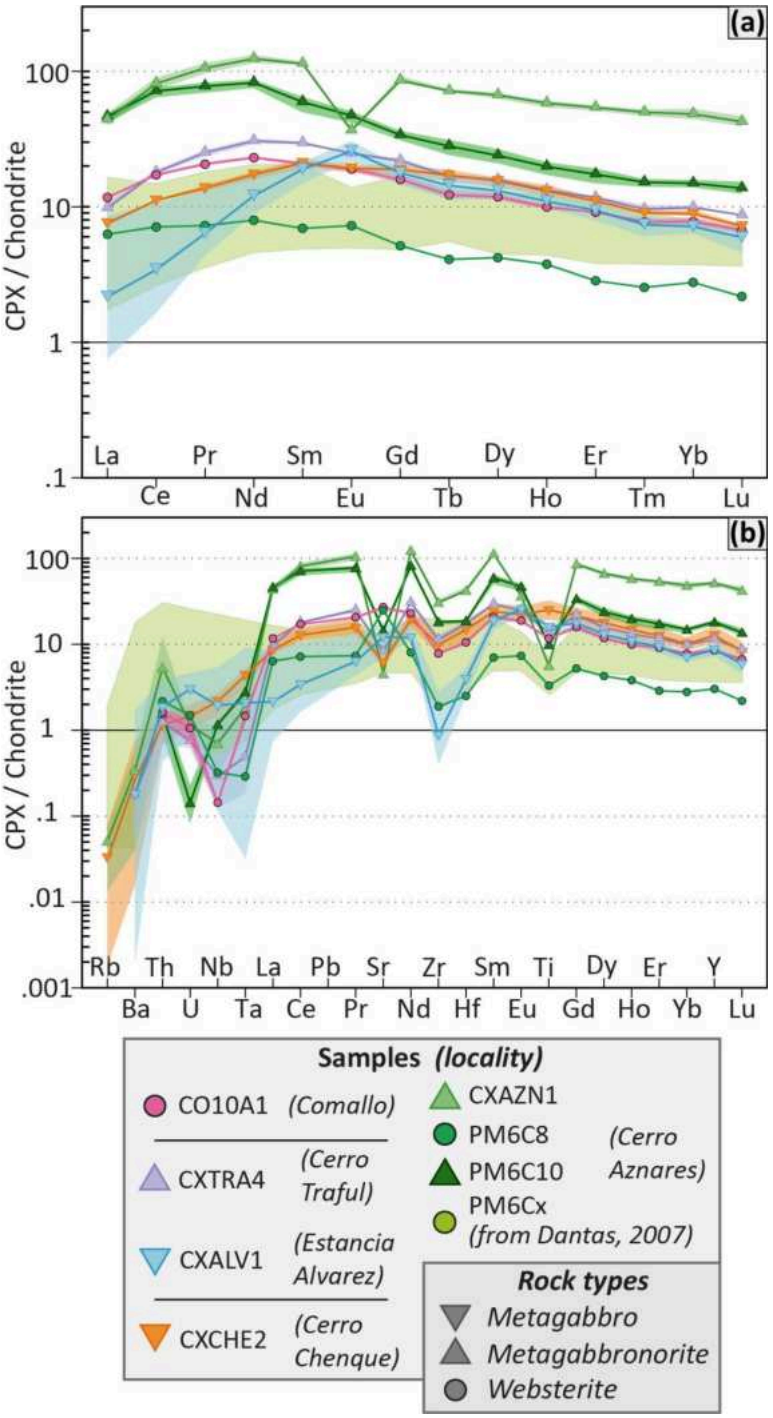


Fig. II.6. Rare earth and trace elements patterns of clinopyroxene normalized to chondrite. (a) REE patterns of north Patagonian granulite xenoliths. (b) Trace elements patterns. Chondrite values are from McDonough & Sun (1995). Symbols and full lines represent analysis means while faded surfaces represent ranges of all analysis (see Table 3 for number of analyses).

Table II.3: Clinopyroxene trace element compositions. n indicates the number of analyses for each sample.

Standard	CO10A1	CXTRA4	CXALV1	CXCHE2	CXAZN1	PM6C8	PM6C10
n	3	3	13	3	3	1	3
ppm							
Sc	65.7	91.0	74.4	52.6	133.9	37.1	70.8
Ti	5152	6016	7072	9673	2488	1443	4361
V	249	288	351	382	407	74	198
Co	41.3	31.3	28.8	61.9	46.2	22.8	41.8
Rb	bdl	0.01	0.31	0.07	0.12	bdl	bdl
Sr	197	60	89	39	33	1	105
Y	13	18	14	18	82	5	28
Zr	30	43	3	33	117	7	70
Nb	0.03	0.07	0.47	0.46	0.17	0.08	0.28
Ba	bdl	0.43	0.44	0.63	0.82	bdl	bdl
La	2.78	2.32	0.51	1.79	10.40	1.49	11.00
Ce	10.54	11.02	2.11	6.83	49.78	4.36	43.85
Pr	1.92	2.33	0.59	1.27	9.80	0.68	7.19
Nd	10.54	14.00	5.51	7.92	56.56	3.64	37.65
Sm	3.09	4.37	2.80	3.12	16.82	1.03	8.78
Eu	1.07	1.40	1.45	1.09	2.06	0.41	2.65
Gd	3.17	4.35	3.53	3.75	17.05	1.03	6.73
Tb	0.44	0.61	0.52	0.62	2.58	0.15	1.01
Dy	2.91	3.89	3.23	3.83	16.43	1.04	5.87
Ho	0.54	0.73	0.60	0.71	3.18	0.21	1.08
Er	1.46	1.87	1.51	1.77	8.64	0.46	2.78
Tm	0.19	0.24	0.18	0.22	1.23	0.06	0.38
Yb	1.25	1.59	1.15	1.43	7.78	0.45	2.40
Lu	0.16	0.21	0.15	0.18	1.04	0.05	0.34
Hf	1.09	1.81	0.41	1.35	4.36	0.26	1.93
Ta	0.02	0.01	0.03	0.05	0.02	0.00	0.04
Th	0.05	0.04	0.05	0.03	0.15	0.06	0.05
U	0.01	0.01	0.02	0.01	0.01	0.01	0.00
Eu/Eu*	1.0	1.0	1.4	1.0	0.4	1.2	1.1
(La/Yb)n	1.5	1.0	0.3	0.9	0.9	2.3	3.1
(La/Sm)n	0.6	0.3	0.1	0.4	0.4	0.9	0.8
(Yb/Sm)n	0.4	0.3	0.4	0.4	0.4	0.4	0.3

II. 4.5. Thermobarometry

Fe-Mg exchange two-pyroxene thermometer from Wells (1977) has been applied to all the investigated samples containing both pyroxenes (4 metagabbronorites, 2 metagabbros, 2 websterites; Table II.1) and on the PM6Cx websterite suite from Dantas (2007). It yields a temperature range of 762-1070°C ±70°C as mafic granulites and websterites display similar temperature ranges.

Pseudosection calculation has been applied on 2 metagabbronorites (CXTRA1, CXTRA4) and 2 websterites (CO10A1, PM6C8). Among those samples, sample CXTRA4

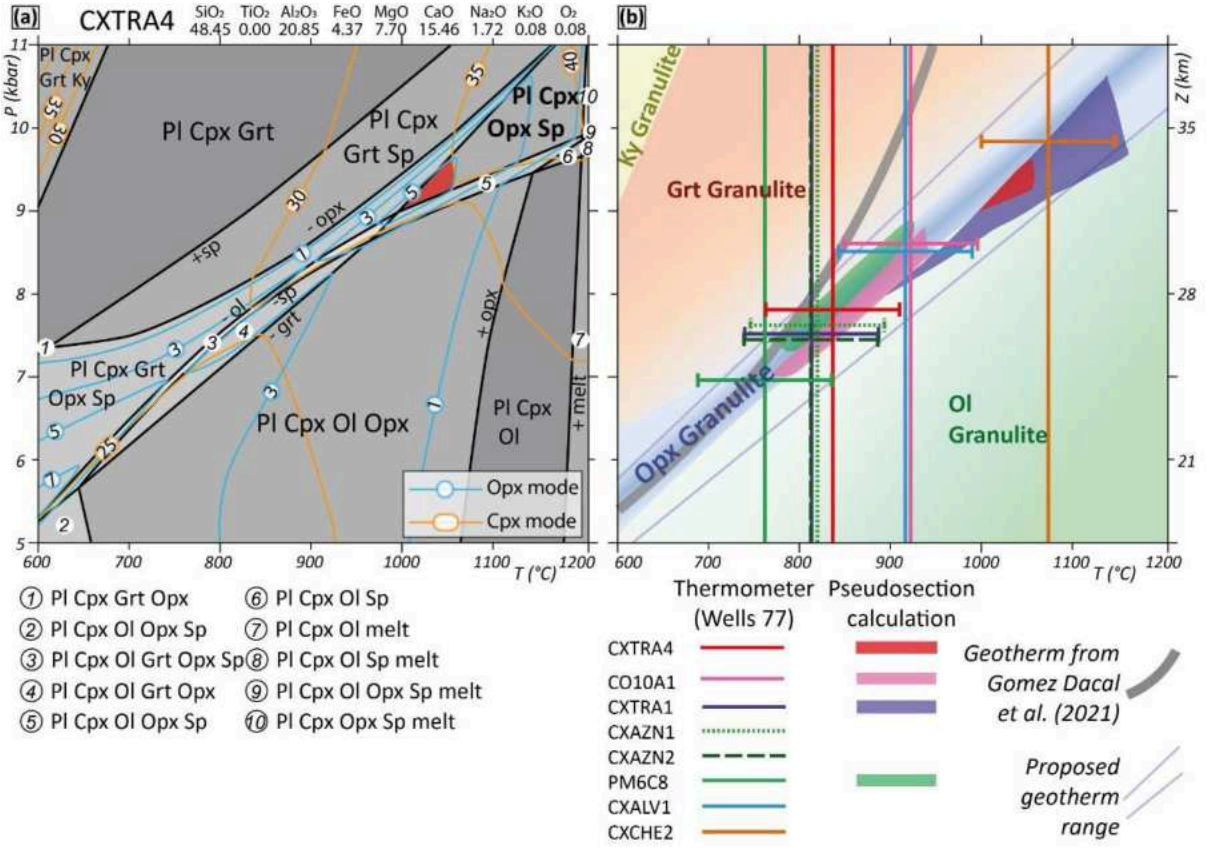


Fig. II.7. Estimated temperature and pressure of granulite xenoliths. (a) Calculated P-T pseudosection for sample CXTRA4, with contoured modal proportions for orthopyroxene and clinopyroxene. Because they did not provide more precision to the P-T stability field determination, the plagioclase and spinel modal were not contoured to make the figure readable. (b) P-T diagram compiling all thermometer and pseudosection calculations results. Drawn granulite stability fields correspond to a mean of stability fields of all the concerned samples.

from Cerro Traful is the most representative of the whole xenolith suite (metagabbronorite with modal proportions of plagioclase > clinopyroxene > orthopyroxene > spinel; Table II.1), thus results from this sample are presented in detail (Fig. II.7a). Pseudosection calculations applied to other samples are available in Supplementary Fig. S4. The metagabbronorite CXTRA4 contains 55 vol.% plagioclase, 31 vol.% clinopyroxene, 11 vol.% orthopyroxene, spinel as an accessory mineral and 2 vol.% interstitial olivine (olivine II) which does not belong to the main paragenesis (Table II.1). The comparison of pseudosection topology and petrological observations (main plagioclase-clinopyroxene-orthopyroxene-spinel assemblage and corresponding stability field) as well as the comparison between calculated and observed modal proportions (53-58 vol.% plagioclase, 30-35 vol.% clinopyroxene, >5 vol.%

orthopyroxene) define P-T conditions at 9-9.8 kbar and 1000-1050°C (red area in Fig. II.7a). In figure II.7b, all pseudosection calculations are reported and yield pressure conditions between 7 and 11.8 kbar and temperature between 760 and 1150°C within the orthopyroxene-granulite stability field (Fig. II.7b; Supplementary Fig. S4). This estimation brackets both the Pleistocene xenolith (sample CO10A1, 7-8.8 kbar, 770-930 °C; Fig. II.7b) and Oligo-Miocene xenoliths (all the other samples). In conclusion, the pseudosection calculations with petrological observations allow to define a geotherm between 28°C/km and 31.5°C/km (Fig. II.7b).

II. 4.6. Microstructures

II. 4.6.1. Crystallographic Preferential Orientation (CPO)

Clinopyroxene. Most of the mafic granulite samples (i.e. metagabbros and metagabbronorites) from all localities display weak CPO patterns (J-index 1.49-2.8; M-index 0.007-0.036) with a point concentration on [100] axes parallel to X that could represent a lineation, and a more scattered distribution on [010] and [001] axes (Fig. II.8). The metagabbro from Cerro Traful, CXTRA1, display strong clusters on [010] axes parallel to Z, perpendicular to the layering and [001] axes forming a weak girdle in the XY plane with concentration points within the layering. [100] axes in that sample weakly cluster near [001] axes concentration points. The metagabbronorite CXCHE4 displays a second point concentration on [100] near Z, and [010] axes cluster parallel to Y. The titanomagnetite-metagabbronorite sample CXAZN1 from Cerro Aznares displays a CPO similar to sample CXTRA1 from Cerro Traful, with a point concentration of [010] axes parallel to Z and [001] axes that girdle within the XY plane forming the layering. [100] axes display a point concentration at 40° to X (Fig. II.8). Websterite samples CO10A1 and PM6C8 display the maximum clustering on [001] axes sub-parallel to X, [010] axes are perpendicular to the layering and [100] axes are randomly distributed.

Orthopyroxene. Mafic granulites and websterites have weak orthopyroxene CPO patterns (J-index 1.50-2.18; M-index 0.015-0.025, Fig. II.8), as for clinopyroxene. Sample CXTRA1, CXCHE4 and CXAZN1 [001] axes form a point concentration parallel to X, and a possible girdle in the XY plane (well present in sample CXTRA1), and [010] axes display a weak point concentration parallel to Z (Fig. II.8). The spinel-metagrabbronorite CXTRA4 displays a point concentration of [100] axes sub-parallel to X, and few orthopyroxene grains from samples CXALV1 display similar orientations (Fig. II.8). Websterite PM6C8 displays [001]

axes sub-parallel to X, and parallel to clinopyroxene [001] axes. CO10A1 doesn't have a readable CPO as the number of indexed grains is too low.

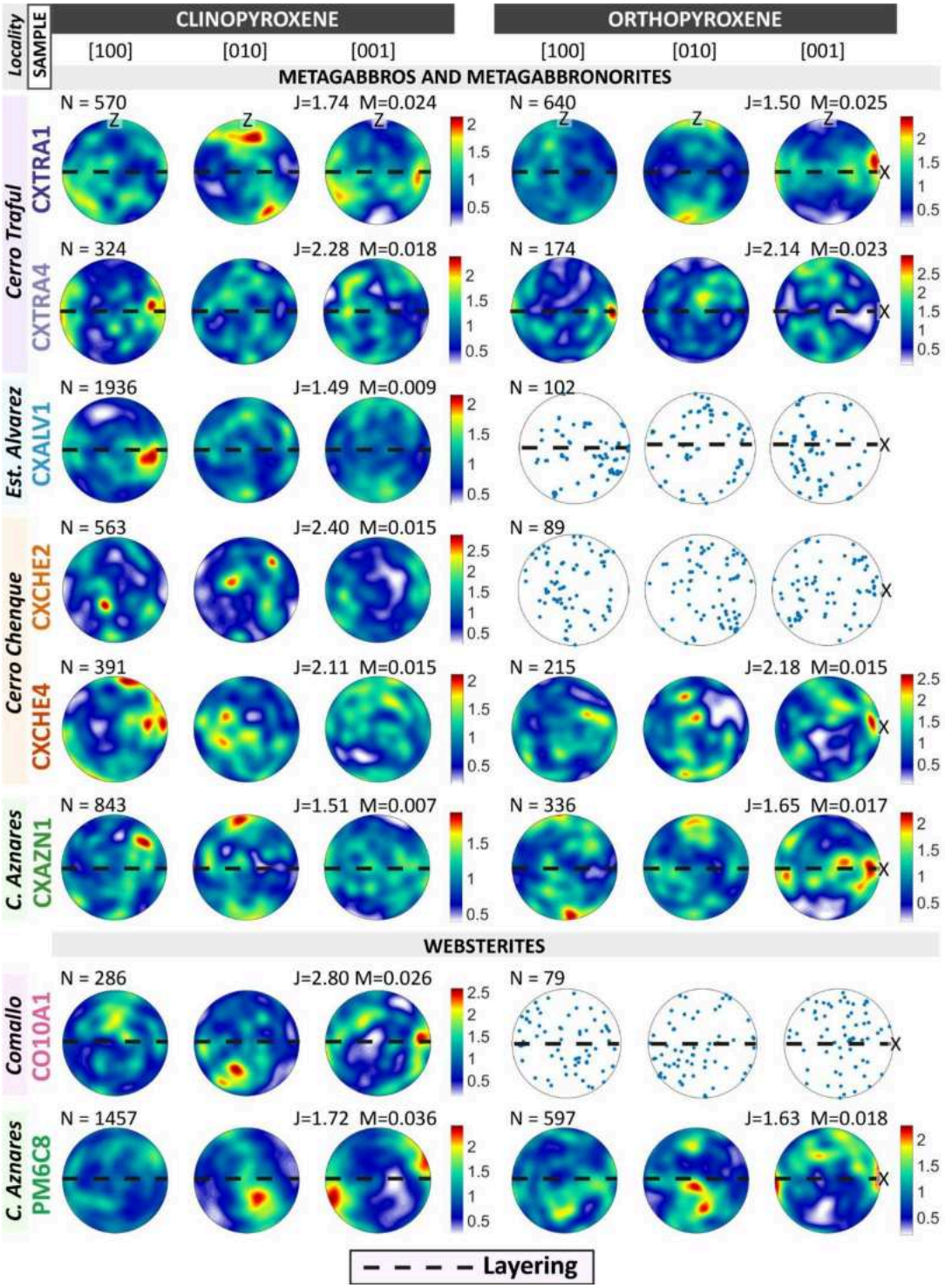


Fig. II.8. Crystallographic preferred orientation of clinopyroxene and orthopyroxene of analysed metagabbros, metagabbronorites and websterites. When detected, compositional layering is tagged and pole figures are rotated as the layering normal to Z. N is the number of grains and the strength is represented by J-index and M-index. The rainbow scale represents the mud (multiply uniform density).

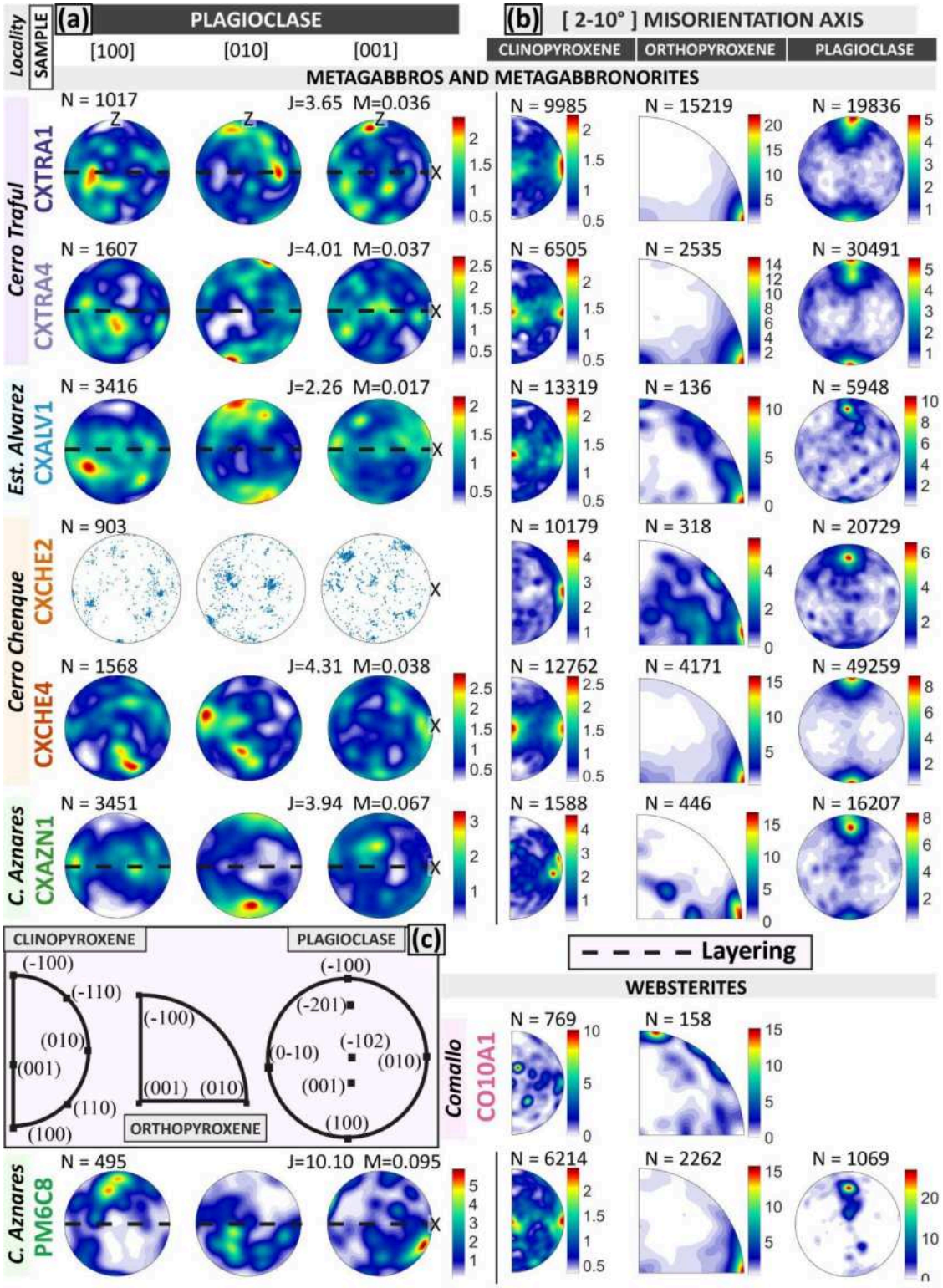


Fig. II.9. (a) Crystallographic preferred orientation of plagioclase. N is the number of grains, the strength is represented by J-index and M- index. Sample CXCHE2 was not contoured because the CPO pattern is saturated by multiplied very coarse grains. It was plotted with one point per grain in order to lighten the pole figure. (b) Rotation axes accommodating low angle (2-10°) misorientations in clinopyroxene, orthopyroxene and plagioclase grains. Data is represented in inverse pole figures where the legend can be found in (c). N is the number of pixels plotted.

Plagioclase. Mafic granulites display weak CPO patterns, as indicated by the J-index (2.26-4.31) and M-index (0.017-0.038), except for the sample CXAZN1 (M-index 0.067; Fig. II.9a). Most of the mafic granulites display [010] plagioclase axes parallel or at a low angle to Z, [100] axes within the XY plane, and scattered [001] orientations. In sample CXAZN1, [100] axes display a weak point concentration parallel to X. Sample CXTRA1 has a maximum [001] point concentration parallel to Z (Fig. II.9a). Websterite PM6C8 displays [001] axes at low angle to X and to the pyroxenes [001] orientations. [100] axes cluster parallel to Z, as [010] axes weakly cluster near Y. J-index and M-index are extremely high (10.10) but it may be related to the low proportion of indexed plagioclase in this sample (495 grains and <1.6 vol%; Fig. II.9).

II. 4.6.2. Intragranular deformation

Clinopyroxene. Intragranular deformation in clinopyroxene is well developed in metagabbronorites CXCHE4, CXCHE2, CXTRA1 and CXTRA4, regarding the whole suite (Fig. II.10a). In those samples, the distribution of deformation reaches all grain sizes, even if it is more heterogeneous within the sample CXCHE2 where intragranular deformation spares some grains and highly penetrates the others. Clinopyroxene from the metagabbro CXALV1, as observed in sample CXCHE2, displays, for similar grain size, both deformed and undeformed grains (Fig. II.10a). However, in sample CXALV1 clinopyroxene grains with high internal deformation can have polygonal grain boundaries and undeformed grains display linear grain boundaries and seem to penetrate deformed grains. In these samples clinopyroxene subgrain boundaries are either perpendicular to the long axes of the grains or form a conic shape with a high degree of misorientation at the tip of the grains (Fig. II.10a).

The distribution and repartition of the misorientation axes within the grains indicate that more than the half of misorientation are bracketed between > 1 and 3° for both clinopyroxene and orthopyroxene (Fig. II.10c). Among the studied samples, the websterites (PM6C8 and CO10A1) display weak internal deformation (29 and 18 % of the clinopyroxene surface, respectively) and rare subgrain boundaries (Fig. II.10a, c).

Clinopyroxene misorientation axes at low angle boundaries or subgrain boundaries are distributed around both [001] and [010] axes in the samples CXTRA1, CXTRA4, CXALV1, CXCHE4 and PM6C8, and only around [010] axis in CXCHE2 and CXAZN1 samples (Fig. II.9b, c).

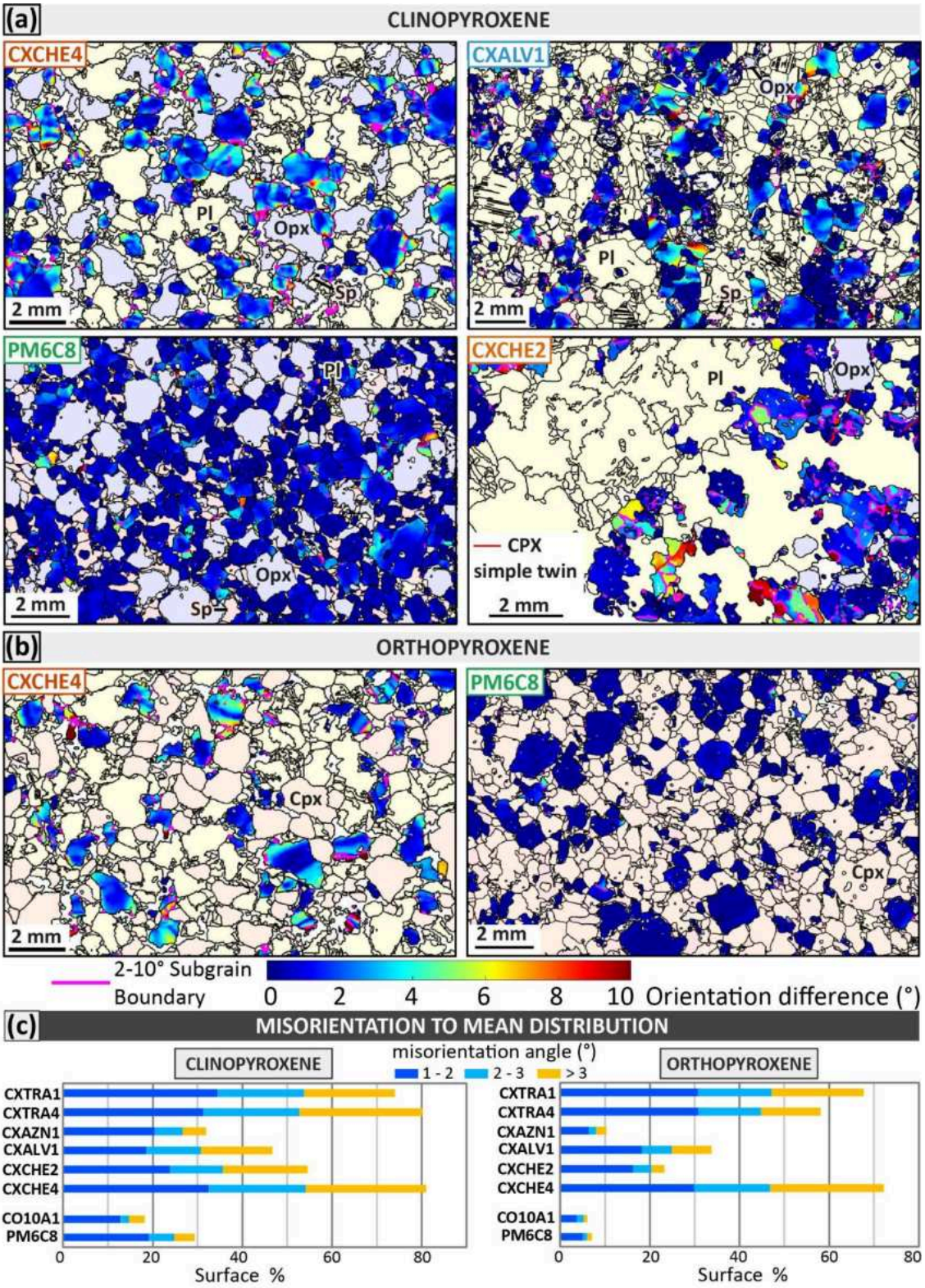


Fig. II.10. Maps of intragranular deformation relative to the mean orientation of the grains for (a) clinopyroxene and (b) orthopyroxene. Deep blue grains are undeformed while the intragranular deformation is strong in green to red areas. Light blue grains are orthopyroxene, light orange is for clinopyroxene, light yellow is for plagioclase and light pink is for spinel. (c) Normalized histograms representing clinopyroxene and orthopyroxene surface proportions vs. misorientation angles (>1°) relative to mean grain orientations.

Orthopyroxene. Samples CXTRA1, CXTRA4, CXCHE2 and CXCHE4, display the stronger orthopyroxene intragranular deformation (58-72 % of the orthopyroxene surface; Fig. II.10b, c) as it occurs homogeneously within the samples. Subgrain boundaries are more frequently perpendicular to the long axes of the grains than in clinopyroxenes, even if conic shape subgrain boundaries are also present at the grain tips. In other metagabbros, metagabbronorites and websterites, orthopyroxene grains display weak internal deformation (7-33 % of the orthopyroxene surface; Fig. II.10 b, c) and are composed mostly of low misorientation angles (< 3°) compared to the deformed sample group (Fig. II.10c).

Misorientation axes at subgrain boundaries of all samples are preferentially arranged around the [010] axis, except CO10A1 which shows an arrangement around the [100] axis (Fig. II.9b). However, this result must be taken with caution as the subgrain boundaries dataset for this sample is small.

Plagioclase. In samples CXTRA1, CXTRA4, CXCHE2 and CXCHE4, a large surface ofthe plagioclase is affected by intragranular deformation (at least 84% with misorientation > 1°), as observed in associated pyroxenes (Figs. II.11a and II.10). Plagioclase subgrain boundaries are more frequently angular to the grain tips than perpendicular to the long axis of the grains. In sample CXCHE2, plagioclase displays many long (up to 2 mm) and non-linear grain-cross-cutting subgrain boundaries. In sample CXAZN1, the intragranular deformation is homogeneous and affects a larger surface in plagioclase (62% with misorientation > 1°) than in pyroxene, where it reaches 31% for clinopyroxene and 10% for orthopyroxene, respectively (Fig. II.11a, c). Sample CXALV1 displays less intragranular deformation (17% of the plagioclase surface) than other mafic granulites (62-89% of the plagioclase surface; Fig. II.11a, b). Also, it shows a bimodal distribution between large and deformed plagioclase grains, and undeformed smaller grains. Large grains display curved grain boundaries and are surrounded by numerous small undeformed grains with linear boundaries. Albite twinning occurs in both large deformed grains and small undeformed grains (Fig. II.11a).

Misorientation axes at subgrain boundaries cluster around the [100] axis and less frequently around the [20-1] axis in the spinel granulites CXTRA1, CXTRA4 and CXCHE4 (Fig. II.9b). In the other samples, they cluster around the [30-1] axis.

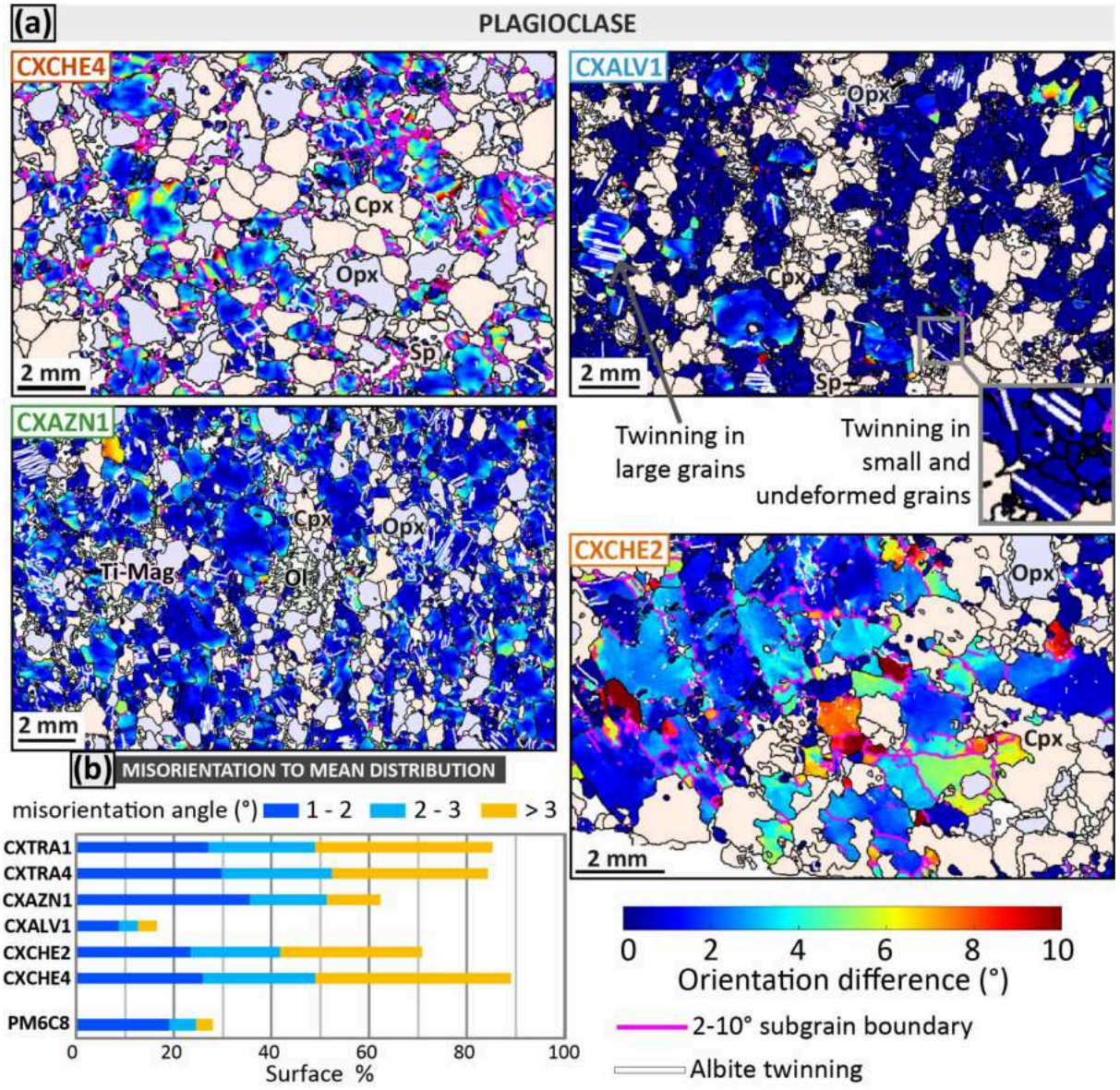


Fig. II.11. (a) Plagioclase maps of intragranular deformation relative to the mean orientation of the grains. Deep blue grains are undeformed while the intragranular deformation is strong in green to red areas. Light blue grains are orthopyroxene, light orange is for clinopyroxene, light pink is for spinel and light green is for olivine. (b) Normalized histograms representing plagioclase surface proportion vs. misorientation angles (>1°) relative to mean grain orientations.

II. 5. DISCUSSION

II. 5.1. Protolith of mafic granulite and websterite xenoliths

The mafic granulites, except the samples CXTRA2 and CXCHE2, display a well-defined pyroxene and plagioclase (or spinel)-rich layering (Fig. II.2). The presence of this layering is in agreement with a magmatic protolith. All the studied samples plot within the Mafic 2 field

(Mg# = 0.6 to 0.7; Fig. II.3) or Mafic 3 field (Mg# <0.6) defined by Kempton & Harmon (1992). They suggested that the Mafic 2 field may correspond to granulites from cumulates *sensu stricto* derived from slightly evolved melts (Mg# of 0.4 to 0.5), although this is unlikely because they generally have high incompatible trace element contents, or to solidified evolved melts that have accumulated a large proportion of phenocrysts phase. Additionally, they proposed that the Mafic 3 field does not correspond to cumulates because they display a low SiO_2/Al_2O_3 ratio compared to basalts and their differentiates (Fig. II.3). Therefore, they are either solidified intermediate melts formed after fractional crystallisation, where feldspar dominates the assemblage, or residues from metasediments or intermediate igneous rocks after partial melting. Moreover, the calculated pressures and temperatures of the investigated samples (Table II.1; Fig. II.7b) are homogeneous despite variations in the mineralogy and the bulk rock and mineral compositions (e.g. plagioclase variation from bytownite to andesine; Supplementary Table S1; Fig. II.5d). The positive correlation between plagioclase Na_2O content and bulk rock Na_2O composition suggests that plagioclase composition is primarily controlled by bulk rock Na_2O budget (Supplementary Table S1). This indicates that these multiple variations are not only governed by pressure and temperature conditions but also reflect the record of parent magma compositions and evolution.

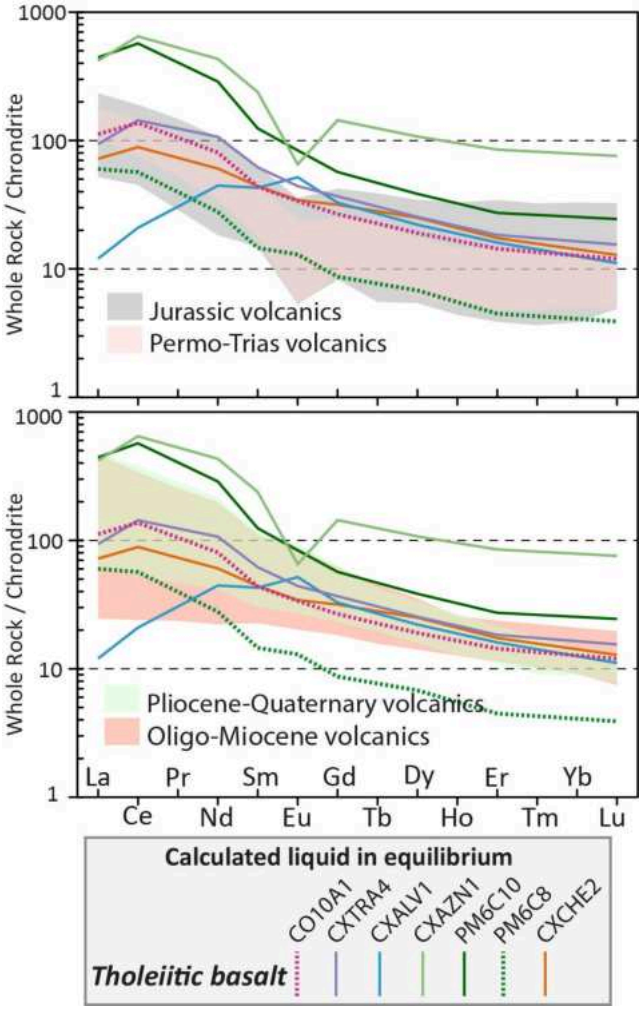


Fig. II.12. Calculated normalised tholeiitic and alkaline basalts in equilibrium with clinopyroxene. Jurassic, Permo-Trias, Oligo-Miocene and Quaternary REE volcanic compositions near the studied xenoliths are plotted (from Stern *et al.*, 1990; López de Luchi *et al.*, 2002; Kay *et al.*, 2004, 2007; Jacques *et al.*, 2014; Massaferro *et al.*, 2014; Martínez Dopico *et al.*, 2019; Zaffarana *et al.*, 2019, 2020; Asiain *et al.*, 2022).

The cpx upward convex REE chondrite normalised patterns of mafic granulites and websterites are similar to those of cpx phenocrysts (Beccaluva *et al.*, 2009; McCoy-West *et al.*, 2010; Desta *et al.*, 2014; Natali *et al.*, 2016; Lee *et al.*, 2021) or megacrysts (Sun *et al.*, 2022) from LIP basalts (Fig. II.6; and see comparison in Supplementary Fig. S5). Websterite xenoliths from Cerro Aznares studied by Dantas (2007; samples PM6Cx) display similar patterns and are interpreted as cumulates crystallised from a basalt (Fig. II.6). Moreover, LIP basalts are typically formed from mantle sources with no or only minor crustal mixing or contamination (e.g. Bryan & Ferrari, 2013). This suggests that a fraction of a basaltic liquid in a LIP context may have been stored in the crust and formed granulite protoliths and that the rest of the fraction may have formed surface basalt without contamination. Kay *et al.* (2007) proposed that the tholeiitic magmatic phase of the Cenozoic (Oligo-Miocene) basaltic LIP in the North Patagonian region (the Somucura LIP) produced slightly differentiated volcanic products linked to magmatic underplating processes at the crust-mantle boundary and minor crustal contamination. Both mantle and crustal sources are proposed for the Permo-Trias and the Jurassic SLIP (Pankhurst *et al.*, 2006; Kay *et al.*, 2007; Zaffarana *et al.*, 2020). Pankhurst *et al.* (1998) even suggest that primary basalts are rare through the Jurassic Chon Aike province and that most mantle-derived magmas underwent a mixing process with crustal-derived magmas. Volcanic rocks produced during the two Choiyoi and Chon Aike SLIP - mainly dacites and rhyolites and andesites, respectively - are more differentiated than the investigated xenoliths suite. However, it is accepted that SLIP also produced mafic cumulates within the lower crust and crust-mantle boundary (e.g. Bryan & Ferrari, 2013). To assess the affinity between the investigated xenoliths and the different SLIP of the region, the REE composition of melts in equilibrium with the cpx has been calculated, using partition coefficients between the cpx and a tholeiitic basalt from Fujimaki *et al.* (1984; Fig. II.12). The calculated melt REE patterns have been compared with REE patterns from Jurassic volcanics (mainly andesites; López De Luchi & Rapalini, 2002; Zaffarana *et al.*, 2019, 2020), Permo-Trias volcanics (mainly dacite or rhyolite; Martínez Dopico *et al.*, 2019), as well as Oligo-Miocene and Quaternary basalts (Stern *et al.*, 1990; Kay *et al.*, 2004, 2007; Jacques *et al.*, 2014; Massaferro *et al.*, 2014; Asiain *et al.*, 2022). In Figure II.12, the obtained calculated REE patterns are consistent with those of the volcanics of the three main LIPs that affected the NPM). Many samples (CO10A1, CXTRA4, CXCHE2, and MREE and HREE of CXALV1) match the Cenozoic volcanic patterns, which are slightly more enriched in LREE and MREE than Permo-Trias and Jurassic volcanics. Nevertheless, no clear distinction can be

made. These results suggest that the metagabbro, metagabbronorite and websterite investigated suite was initially formed by basaltic cumulates from a long-lived magmatic activity, since Permo-Trias times, that contributed to the crustal growth of the NPM (Fig. II.13). This is in line with conclusions by Oriolo *et al.* (2023) who suggested that the North Patagonian basement had recorded significant crustal growth and remobilization during the Late Paleozoic.

II. 5.2. Magmatic and deformation processes recorded by the xenolith suite

II. 5.2.1. Mafic Granulites

The metagabbro CXCHE2 from Cerro Chenque displays very coarse grains (porphyritic-like texture) and augite twinning known as a magmatic characteristic (Griffin *et al.*, 2022; Fig. II.10a). The clinopyroxene CPO in this sample is weak, lacking clear concentration axes and dominant slip systems (Fig. II.8), suggesting the magmatic texture. Nevertheless, at crystal scale, some large grains display intense dislocation creep, expressed by strong intragranular deformation, numerous subgrain boundaries (grains with misorientations > 4° and < 10° in Figs. II.10, II.11), and well-concentrated misorientation axes concentrated along [010] axes, indicative of dislocation creep with the activation of (100)[001] slip system (Fig. II.9; Griffin *et al.* 2022). It is associated with curved grain boundaries which are known to be related to high-temperature recrystallisation mechanisms (Passchier & Trouw, 2005). Sample CXCHE2 has preserved microstructural evidence of its magmatic protolith although this texture has been partially overprinted by high-temperature deformation. While the other xenoliths display more 120° triple junctions compared to sample CXCHE2 and no magmatic features listed above (Fig. II.2), sample CXCHE2 likely represents the protolith formed more recently than other samples before their ascent as xenoliths.

All other mafic granulites are characterised by the presence of intragranular misorientation and subgrain boundaries in pyroxenes and plagioclase, as well as conical albite twinning. These features are indicative of plastic deformation and dislocation creep (Figs. II.10, II.11). However, the intensity of deformation varies across the mafic granulites. The most deformed rocks include CXTRA1, CXTRA4 from Cerro Traful, CXCHE4 and CXCHE2 (the latter discussed above) from Cerro Chenque (Figs. II.10, II.11). These two localities represent the northern and southern ends of the studied area, suggesting only weak deformation in the entire region (Fig. II.1). Sample CXAZN1 from Cerro Aznares displays less intragranular deformation, particularly in orthopyroxene (Figs. II.10c, II.11).

The entire mafic granulite suite is characterised by relatively weak clinopyroxene CPO patterns (J-index up to 2.4; Figs. II.8, II.9), even in samples displaying important intragranular deformation (CXTRA1, CXTRA4, CXCHE2, CXCHE4; Fig. II.10). In samples CXTRA1 and CXAZN1, the clinopyroxene CPO patterns show concentration of [001] axes parallel to X and [010] axes parallel to Z, indicating the possible activation of (010)[001] slip system (Fig. II.8). While this system is known, and it has been observed in the lower crust (van der Werf *et al.*, 2017) it's less common for clinopyroxene (SL-type, Helmstaedt *et al.*, 1972, Zhang *et al.*, 2006; van der Werf *et al.*, 2017) because it is difficult to activate (Amiguet, 2009) yet. In samples CXTRA4 and CXCHE4, the clinopyroxene [100] axes are parallel to X, and two other axes are more scattered. The alignment of clinopyroxene [100] axes parallel to X is quite unusual, but the [100](001) slip system is described and is considered to play a minor role in clinopyroxene strain accommodation (Amiguet, 2009). In the deformed samples CXTRA1, CXTRA4 and CXAZN1, the orientation of orthopyroxene axes is similar to clinopyroxene axes (Fig. II.8), suggesting similar formation or deformation conditions. The alignment of both clinopyroxene and orthopyroxene [100] axes parallel to the lineation is uncommon in terrestrial rocks. However, in the sub-continental mantle, Kourim *et al.* (2015) report a weak alignment of both clinopyroxene and orthopyroxene [100] axes with the lineation and weak CPO, proposing a post-deformation-recrystallisation event. Moreover, a concentration of clinopyroxene [100] axes representing the lineation has been observed in clinopyroxene-rich meteorites and interpreted as a cumulate texture (e.g. Daly *et al.*, 2019). These results suggest that the clinopyroxene and orthopyroxene CPO with [100] axes parallel to X could testify for primary magmatic crystallization and early weak deformation.

In these four samples (CXTRA1, CXTRA4, CHCHE4, CXAZN1), plagioclase displays internal deformation (Fig. II.11), and similar to pyroxenes, the CPO is weak. The plagioclase CPO consistently displays a concentration of [010] axes pattern parallel to Z and a concentration point of [100] axes within the foliation plane (Fig. II.9). The presence of plagioclase [100] axes parallel to the lineation is a common observation. Interpreting the plagioclase fabric in the studied samples is challenging, but the slight angle between the plagioclase [100] axis and pyroxenes [100] or [001] axes suggests changing constraints. The fabric related to magma crystallisation might be represented by a [100](010) fabric in plagioclase and either a [001](010) or [100](001) fabric in pyroxenes; with both clinopyroxene and orthopyroxene developing the same fabric within a sample.

The deformed samples display intragranular deformation, sub-grain boundaries and slightly curved grain boundaries (Figs. II.2, II.10, II.11) suggesting plastic deformation. To assess the plastic deformation recorded by minerals through dislocation creep and identify the slip system, misorientation axes serve as useful indicators (Fig. II.9). Samples with significant internal deformation show clinopyroxene low-angle misorientation axes aligned either with [010] and [001] axes or [010] axis (Fig. II.9). Although these paired axes rotations have been linked to mechanical twinning (Frets *et al.*, 2012; Soret *et al.*, 2019; Taufner *et al.*, 2021), which has not been observed in the suite, Griffin *et al.* (2022) correlate such low-angle misorientations with the activation of paired dominant [001](100) and minor [100](001) slip systems. They argue that this combination is common in "most Earth-relevant extrinsic conditions". Thus, the presence of [010] misorientations may indicate activation of the clinopyroxene [001](100) slip system which has been described as the dominant slip system at 800-1000°C (Raterron *et al.*, 1994; Amiguet, 2009; Wang *et al.*, 2012). These interpretations suggest that plastic deformation in our samples is supported in clinopyroxene by the [001](100) slip system and confirm that clinopyroxene CPO with [100] parallel to X (Fig. II.8) represent a magmatic event. Orthopyroxene displays [010] low-angle misorientation in all samples, correlated with the activation of the [001](100) slip system, which is by far the most commonly activated to accommodate deformation (e.g. Wang *et al.*, 2012; Bernard *et al.*, 2021). Moreover, plagioclase low-angle misorientation axes align with the [100] axis, attributed to the [001](010) slip system (van der Werf *et al.*, 2017; Allard *et al.*, 2021).

To summarise, slip systems suggested by low-angle misorientation analysis would have systematically been [001](100) in clinopyroxene, sometimes paired with minor [100](001); [001](100) in orthopyroxene and [001](010) in the plagioclase. However, the dislocation creep mechanism may have been too low to erase the pre-existing CPO and would only have reduced the magmatic fabric strength and the associated shape preferred orientation.

The metagabbro CXALV1, characterised by large deformed clinopyroxene and plagioclase grains surrounded by numerous small and undeformed grains with linear grain boundaries, displays a unique texture distinct from other samples. It displays similar clinopyroxene and plagioclase CPO to that observed in other mafic granulites (Figs. II.8-11). The texture and shape of undeformed grains have only been observed in this sample, suggesting late-stage crystallisation (Figs. II.10, II.11). Moreover, the high proportion of newly formed crystals in this sample shows slightly different chemical composition

compared to both neighbouring large grains, with low CaO and Mg# in clinopyroxene (Fig. II.4), and other granulites, with low LREE content in clinopyroxene, orthopyroxene and plagioclase as well as overall bulk rock LREE compositions (Supplementary Tables S1, S2; Supplementary Fig. S3). These results suggest that this sample may have recorded a low degree of partial melting. The circulation of a melt could have enhanced diffusion creep, leading to the crystallisation of equilibrated grains at the expense of porphyroclasts.

II. 5.2.2. Websterites

Websterite samples CO10A1 and PM6C8 display weak or absent intragranular misorientation, very rare subgrain boundaries and linear grain boundaries (Figs. II.10, II.11). The clinopyroxene CPO patterns in both websterites CO10A1 and PM6C8 are also weak, displaying concentration of [001] axes parallel to X and [010] parallel to Z, as observed in two mafic granulites (CXTRA1, CXAZN1) suggesting the activation of (010)[001] slip system (Fig. II.8) (SL-type, Helmstaedt *et al.*, 1972, Zhang *et al.*, 2006). In the websterite PM6C8, the [001](010) plagioclase fabric correlates with the pyroxenes fabric, with [001] axes parallel in the three phases. The orthopyroxene and clinopyroxene CPO fabrics are similar, with [001] axes parallel to X and [010] parallel to Z suggesting similar crystallisation conditions.

In websterite PM6C8, clinopyroxene low-angle misorientations axes are aligned with both [010] and [001] axes (Fig. II.9), which can be related to the activation of the [001](010) slip system (Griffin *et al.*, 2022). Orthopyroxene occurrence of [010] low-angle misorientation can be correlated to the activation of the [001](100) slip system, while plagioclase occurrence of [100] low-angle misorientation can be attributed to the [001](010) slip system (van der Werf *et al.*, 2017; Allard *et al.*, 2021). Thus, slip systems activating low-angle misorientations are the same as those developing the CPO, which suggests that CPO and rare misorientations development are contemporaneous, reflecting a cumulate texture. It would have been followed by only diffusion creep to equilibrate grains and erase the cumulative texture. The differences in deformation intensity recorded between mafic granulites and websterites could be attributed to the age of their protolith formation. It is possible that websterites protolith is younger than mafic granulite protoliths, which might have recorded deformational events before their ascent. In this scenario, websterites formation could be almost contemporaneous with their ascent in the host lava, dated at 20-29 Ma and 1-2 Ma for Cerro Aznares and Comallo, respectively (Fig. II.1). However, these

differences could also be explained by mineralogy. Experiments and modelling indicate that at 1000°C, the clinopyroxene is stronger than plagioclase for a stress between 1 and 100 MPa, and a strain rate < 10-7s-1 (Tullis et al. 1991). Indeed, mafic granulites, containing a larger proportion of plagioclase compared to websterites, could preferentially accommodate strain recorded in the NPM crust, acting as a weaker phase compared to clinopyroxene under similar P-T conditions.

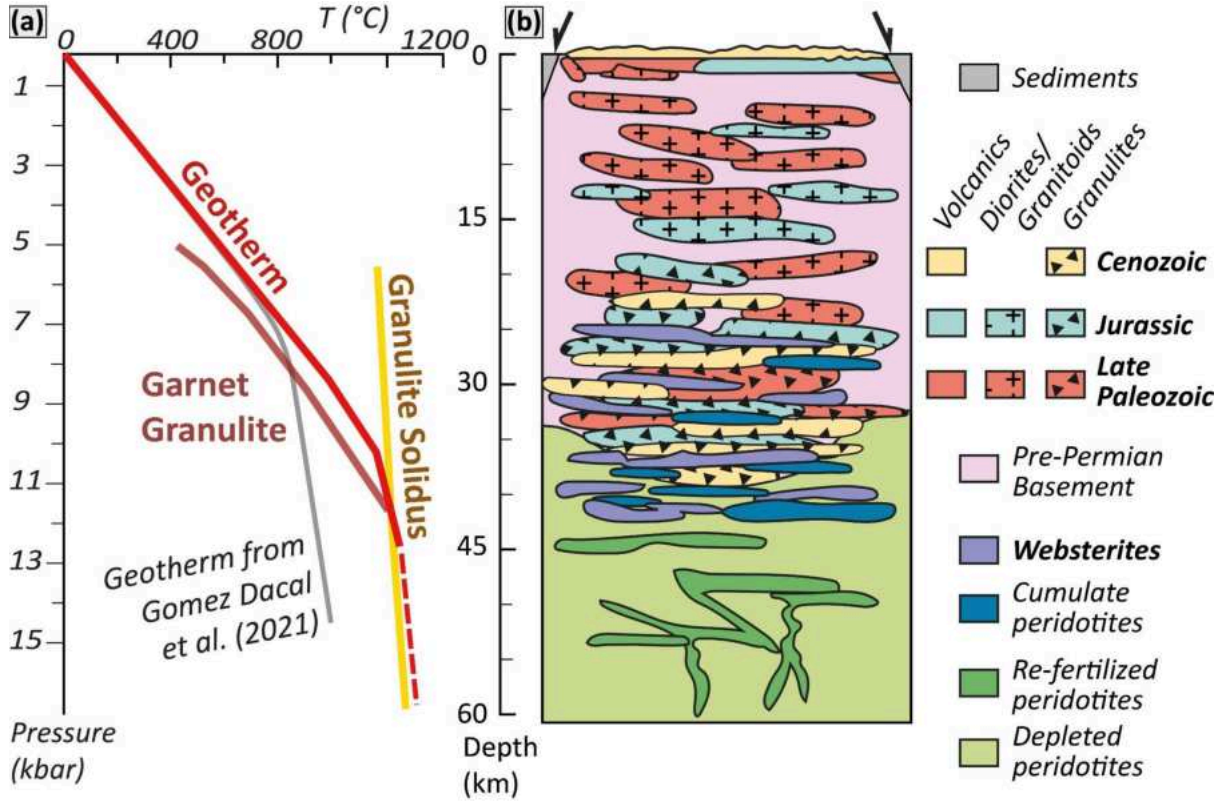


Fig. II.13. (a) Estimated Cenozoic- to Quaternary-geotherm of the North Patagonian Massif and the associated lithologic section of the lithosphere between 0 and 60 km. (b) Simplified lithospheric section until 60 km in depth. The Moho is located around 32 km deep and displays an accumulation of all ages granulite lenses and websterite. The occurrence of depleted and re-fertilized peridotites and peridotite cumulates is from Mundle *et al.* (2016).

II. 5.3. Pressure, temperature conditions and stability of the lower crust

The investigated xenolith collection contains metagabbros, metagabbronorites and websterites which paragenesis equilibrated in the orthopyroxene-bearing granulite metamorphic field (Fig. II.7). More precisely, orthopyroxene-clinopyroxene thermometry and pseudosection calculation applied on both orthopyroxene-bearing mafic granulites and websterites yield paragenesis stabilisation conditions ranging from 760-820°C at 7.2-7.9 kbar to 1000-1150°C at 9-10.8 kbar (Fig. II.7). Hence, the maximal depth recorded by these

samples is estimated between 32 and 37 km, as it sets the origin of the xenoliths from the NPM lower crust (Fig. II.13).

The orthopyroxene granulite stability field is bracketed by a thermal gradient ranging between 28 and 31.5°C/km (Fig. II.7b). Currently, evidence for lower crustal melting in the NPM, such as the observation of a low-velocity zone at lower crust depth (ref) or the presence of leucosomes associated with low-Al content in pyroxenes in granulite samples, are lacking (high-Al pyroxenes; Figs. II.2, II.4). Therefore, the solidus temperature of mafic granulites represents the maximum temperature reached by the NPM lower crust. At high pressures, the solidus temperature calculated in the pseudosection is ca. 1180°C (Fig. II.7a; Supplementary Fig. S4), consistent with the known dry solidus temperature of mafic granulites (Bucher & Grapes, 2011). Based on our petrological estimated geotherm, this temperature is reached at a depth of 37.5-42 km (Fig. II.7). The inferred depth for the emplacement of mafic granulite is interpreted as the depth of the petrological Moho. It is in agreement with the estimated Moho depth of the NPM between 30 and 40 km, from recent gravity, seismic and tomographic studies (Van der Meijde *et al.*, 2013; Chulick *et al.*, 2013; Assumpção *et al.*, 2013). However, the study of Gomez Dacal *et al.* (2021) estimated in the NPM a deeper Moho located between 45 and 50 km, and a lower crust geotherm decreasing from 29°C/km to less than 8°C/km. They evidence that in the NPM the thermal anomaly and the global heating of the lithosphere occurred between 40 and 20 Ma, and the cooling phase since is slow enough to maintain until today a similar gradient in the lithosphere. The studied xenoliths have been transported to the surface by 20 and 30 Ma lavas (Fig. II.1), an age range comprising the global heating in the NPM. Furthermore, the unique Pleistocene xenolith (the websterite CO10A1 from Comallo) matches the P-T estimation (7-8.8 kbar, 770-930°C; Fig. II.7b) range of all the other older xenoliths (i.e. Oligo-Miocene). Hence, the proposed NPM crustal geotherm has been constant since the Oligo-Miocene, and we cannot exclude that this geotherm may be stable beyond Oligocene times. In the same way, if the proposed maximum depth of origin of the investigated granulites - which is based almost exclusively on Oligo-Miocene xenoliths - is comparable with today's geophysical Moho models (Van der Meijde *et al.*, 2013; Chulick *et al.*, 2013; Assumpção *et al.*, 2013), then the NPM crustal structure might have remained unchanged since Oligo-Miocene times and the last LIP event.

II. 5.4. New constraints on the lower crust and the petrological Moho below the NPM

From the studied xenoliths, the NPM lower crust P-T conditions range from 760-820°C at 7.2-7.9 kbar to 1000-1150°C at 9-10.8 kbar (Fig. II.7). Thus, the observed dislocation creep mechanisms and associated slip systems inferred from misorientation axes occurred within this P-T range. Slip systems were consistent between samples, developing [001](100) with minor [100](001) in clinopyroxene (e.g. Raterron *et al.*, 1994), [001](100) in orthopyroxene (e.g. Jung *et al.*, 2010) and [001](010) in plagioclase (e.g. Kruse *et al.*, 2001; Figs. II.8, II.9). The weak plastic deformation recorded by the xenoliths has been recorded under the orthopyroxene granulite facies P-T conditions (Fig. II.7).

The major compressive tectonics affecting the NPM was during the Late Paleozoic (e.g. Von Gosen, 2009), which correspond to the mafic granulites and websterites protolith crystallization. Since this period, the NPM lower crustal xenoliths did not record much plastic deformation which allow the preservation of protolith magmatic fabrics. However, Patagonian Trias and Jurassic extension generated basins surrounding the NPM but preserved the latter from massive faulting (e.g. Renda *et al.*, 2019). Lately, Aragón *et al.* (2011) proposed that the NPM has remained undeformed by Cenozoic tectonics besides faulting and massive uplift and designated the NPM as a rigid lithospheric block. The present microstructural analysis supports the view that the NPM lower crust remained underformed throughout the Cenozoic and, to the maximum extent, since the end of Late Paleozoic tectonic events.

The Petrologic Moho below the NPM can be seen as a significantly magmatic-influenced Moho, as the lower crust is mainly composed of mafic granulites with mixed protoliths from the Late Paleozoic to the Cenozoic (Fig. II.13). Moreover, the lower crust did not record significant deformational events and both its composition and rheology appear homogeneous between 32 and 37 km deep. Lately, the recorded magmatism still impacts today the relatively hot geotherm (ca. 30°C/km; Fig. II.13).

II. 6. CONCLUSIONS

- The North Patagonian Massif (NPM) lower crust displays a main plagioclase-clinopyroxene-orthopyroxene assemblage.
- Petrology, geochemistry and microstructures suggest that mafic granulite and websterite have a magmatic protolith, related to one of the magmatic events that

occurred in the North Patagonian Massif since the Permo-Trias, namely, the Permo-Trias Choiyoi silicic LIP, the Jurassic Chon Aike silicic LIP and the Oligo-Miocene LIP. The websterites, which are almost undeformed compared to the mafic granulite, may be younger than the latter (no deformation) or are contemporaneous to the formation of the granulites, but the high proportion of clinopyroxene makes them mechanically stronger and they are preserved of deformation.

- The P-T conditions of xenoliths have been established between 760-820°C at 7.2-7.9 kbar and 1000-1150°C at 9-10.8 kbar, defining an Oligocene to Pleistocene geotherm in the NPM crust of 28-31.5°C/km and a Petrological Moho located at a depth of 37.5-42 km.
- The low-angle misorientation analysis reveals that dislocation creep developed through [001](100)/[100](001) slip system in the clinopyroxene, [001](100) in the orthopyroxene and [001](100) in the plagioclase. However, the dislocation creep mechanisms did not erase inherited magmatic CPO, which produced in both clinopyroxene and orthopyroxene a [001](010) or [100](001) fabric, and a [100](010) fabric in the plagioclase.
- The preservation of the magmatic fabrics in the xenolith suite suggests that the NPM lower crust has been preserved from tectonics since the crystallisation of xenolith. It has already been suggested that the NPM was free of tectonics during the Cenozoic (Aragón *et al.*, 2011), however, this free-strain preservation period could be extended, with caution, to the end of Choiyoi magmatism during the Trias.

FUNDING

This study has been partially supported through the French ministry of Higher Education, Research and Innovation PhD scholarship of N. Muckensturm, the grant EUR TESS N°ANR-18-EURE-0018 in the framework of the Programme des Investissements d'Avenir and ISIFOR CaMaMiCu project.

ACKNOWLEDGEMENTS

We are grateful to Fabienne de Parseval for high-quality thin sections, Françoise Maubé for assistance with SEM, Philippe De Parserval for assistance with Electron microprobe, Aurélie Marquet for assistance with LA-ICPMS, and Arnaud Proietti for assistance with SEM-EBSD.

DATA AVAILABILITY STATEMENT

The data underlying this article will be shared on reasonable request to the corresponding author.

REFERENCES

Afonso, J. C., Salajegheh, F., Szwillus, W., Ebbing, J. & Gaina, C. (2019). A global reference model of the lithosphere and upper mantle from joint inversion and analysis of multiple data sets. *Geophysical Journal International* **217**, 1602–1628.

Amiguet, E. (2009). Déformation expérimentale de diopside dans les conditions de pression et température du manteau supérieur. Université des Sciences et Technologies de Lille, p.145.

Allard, M., Ildefonse, B., Oliot, É. & Barou, F. (2021). Plastic Deformation of Plagioclase in Oceanic Gabbro Accreted at a Slow‐Spreading Ridge (Hole U1473A, Atlantis Bank, Southwest Indian Ridge). *Journal of Geophysical Research: Solid Earth* **126**.

Aoki, K.I. & Kushiro, I. (1968). Some clinopyroxenes from ultramafic inclusions in Dreiser Weiher, Eifel. *Contributions to Mineralogy and Petrology* **18**, 326–337.

Aragón, E. *et al.* (2011). Tectono-magmatic response to major convergence changes in the North Patagonian suprasubduction system; the Paleogene subduction–transcurrent plate margin transition. *Tectonophysics* **509**, 218–237.

Asiain, L., Florencia Gargiulo, M., Ferracutti, G., Hauser, N. & Bjerg, E. A. (2022). Evolution of the volcanism in the northwestern part of meseta de Somuncurá, Patagonia, Argentina. *Journal of South American Earth Sciences* **113**, 103653.

Assumpção, M., Feng, M., Tassara, A. & Julià, J. (2013). Models of crustal thickness for South America from seismic refraction, receiver functions and surface wave tomography. *Tectonophysics* **609**, 82–96.

Avé Lallemant, H. G. (1978). Experimental deformation of diopside and websterite.

Tectonophysics **48**, 1–27.

Bachmann, F., Hielscher, R. & Schaeben, H. (2010). Texture Analysis with MTEX – Free and Open Source Software Toolbox. *Solid State Phenomena* **160**, 63–68.

Bachmann, F., Hielscher, R. & Schaeben, H. (2011). Grain detection from 2d and 3d EBSD data—Specification of the MTEX algorithm. *Ultramicroscopy* **111**, 1720–1733.

Beccaluva, L., Bianchini, G., Natali, C. & Siena, F. (2009). Continental Flood Basalts and Mantle Plumes: a Case Study of the Northern Ethiopian Plateau. *Journal of Petrology* **50**, 1377–1403.

Bédard, J. H. (2006). Trace element partitioning in plagioclase feldspar. *Geochimica et Cosmochimica Acta* **70**, 3717–3742.

Bernard, R. E., Schulte-Pelkum, V. & Behr, W. M. (2021). The competing effects of olivine and orthopyroxene CPO on seismic anisotropy. *Tectonophysics* **814**, 228954.

Bjerg, E. A., Ntaflos, T., Kurat, G., Dobosi, G. & Labudía, C. H. (2005). The upper mantle beneath Patagonia, Argentina, documented by xenoliths from alkali basalts. *Journal of South American Earth Sciences* **18**, 125–145.

Bjerg, E. A., Ntaflos, T., Thoni, M., Aliani, P. & Labudia, C. H. (2009). Heterogeneous Lithospheric Mantle beneath Northern Patagonia: Evidence from Prahuaniyeu Garnet- and Spinel-Peridotites. *Journal of Petrology* **50**, 1267–1298.

Bryan, S. E. & Ferrari, L. (2013). Large igneous provinces and silicic large igneous provinces: Progress in our understanding over the last 25 years. *Geological Society of America Bulletin* **125**, 1053–1078.

Bucher, K. & Grapes, R. (2011). *Petrogenesis of Metamorphic Rocks*. Berlin, Heidelberg: Springer Berlin Heidelberg.

Bunge, H.J., 1982. Texture Analysis in Materials Science. Butterworth-Heinemann, London, 599 pp.

Castro, A., Aragón, E., Díaz-Alvarado, J., Blanco, I., García-Casco, A., Vogt, K. & Liu, D.-Y. (2011). Age and composition of granulite xenoliths from Paso de Indios, Chubut province, Argentina. *Journal of South American Earth Sciences* **32**, 567–574.

Cawood, P. A., Hawkesworth, C. J. & Dhuime, B. (2013). The continental record and the generation of continental crust. *Geological Society of America Bulletin* **125**, 14–32.

Cawood, P. A., Chowdhury, P., Mulder, J. A., Hawkesworth, C. J., Capitanio, F. A., Gunawardana, P. M. & Nebel, O. (2022). Secular Evolution of Continents and the Earth System. *Reviews of Geophysics* **60**.

Christiansen, R. O., Gianni, G. M., Ballivián Justiniano, C. A., García, H. P. A. & Wohnlich, S. (2022). The role of geotectonic setting on the heat flow distribution of southern South America. *Geophysical Journal International* **230**, 1911–1927.

Chulick, G. S., Detweiler, S. & Mooney, W. D. (2013). Seismic structure of the crust and uppermost mantle of South America and surrounding oceanic basins. *Journal of South American Earth Sciences* **42**, 260–276.

Coltice, N., Husson, L., Faccenna, C. & Arnould, M. (2019). What drives tectonic plates? *Science Advances* **5**, eaax4295.

Cordenons, P. D., Remesal, M. B., Salani, F. M. & Cerredo, M. E. (2020). Temporal and spatial evolution of the Somún Curá Magmatic Province, Northern Extra-Andean Patagonia, Argentina. *Journal of South American Earth Sciences* **104**, 102881.

Daly, L. *et al.* (2019). Understanding the emplacement of Martian volcanic rocks using petrofabrics of the nakhlite meteorites. *Earth and Planetary Science Letters* **520**, 220–230.

Dantas, C. (2007). Caractérisation du manteau supérieur patagonien: les enclaves ultramafiques et mafiques dans les laves alcalines. Université de Toulouse III, p. 336.

Desta, M. T., Ayalew, D., Ishiwatari, A., Arai, S. & Tamura, A. (2014). Ferropicrite from the Lalibela area in the Ethiopian large igneous province. *Journal of Mineralogical and Petrological Sciences* **109**, 191–207.

Falco, J. I., Hauser, N., Scivetti, N., Reimold, W. U., Schmitt, R. T. & Folguera, A. (2022). Upper Triassic to Middle Jurassic magmatic evolution of northern Patagonia: Insights from the tectonic and crustal evolution of the Los Menucos area, North Patagonian Massif, Argentina. *Journal of South American Earth Sciences* **113**, 103631.

Ferracutti, G. R., Gargiulo, M. F., Ganuza, M. L., Bjerg, E. A. & Castro, S. M. (2015). Determination of the spinel group end-members based on electron microprobe analyses. Mineralogy and Petrology 109, 153–160.

Frets, E., Tommasi, A., Garrido, C. J., Padrón-Navarta, J. A., Amri, I. & Targuisti, K. (2012). Deformation processes and rheology of pyroxenites under lithospheric mantle conditions. *Journal of Structural Geology* **39**, 138–157.

Fuhrman, M. L. & Lindsley, D. H. (1988). Ternary-feldspar modeling and thermometry. *American Mineralogist* **73**, 201–215.

Fujimaki, H., Tatsumoto, M. and Aoki, K.-i. (1984). Partition coefficients of Hf, Zr, and REE between phenocrysts and groundmasses. *Journal of Geophysical Research* **89**, 662-672.

Gianni, G. M. & Navarrete, C. R. (2022). Catastrophic slab loss in southwestern Pangea preserved in the mantle and igneous record. *Nature Communications* **13**, 698.

Gómez Dacal, M. L., Scheck-Wenderoth, M., Aragón, E., Bott, J., Cacace, M. & Tocho, C. (2021). Unravelling the lithospheric-scale thermal field of the North Patagonian Massif plateau (Argentina) and its relations to the topographic evolution of the area. *International Journal of Earth Sciences* **110**, 2315–2331.

Gómez Dacal, M. L., Tocho, C., Aragón, E., Sippel, J., Scheck-Wenderoth, M. & Ponce, A.

(2017). Lithospheric 3D gravity modelling using upper-mantle density constraints: Towards a characterization of the crustal configuration in the North Patagonian Massif area, Argentina. *Tectonophysics* **700–701**, 150–161.

Govindaraju, K. (1989). 1989 COMPILATION OF WORKING VALUES AND SAMPLE DESCRIPTION FOR 272 GEOSTANDARDS. *Geostandards Newsletter* **13**, 1–113.

Green, E. C. R., White, R. W., Diener, J. F. A., Powell, R., Holland, T. J. B. & Palin, R. M. (2016). Activity-composition relations for the calculation of partial melting equilibria in metabasic rocks. *Journal of Metamorphic Geology* **34**, 845–869.

Griffin, S. *et al.* (2022). Can the Magmatic Conditions of the Martian Nakhlites be Discerned via Investigation of Clinopyroxene and Olivine Intracrystalline Misorientations? *Journal of Geophysical Research: Planets* **127**.

Griffin, W., Powell, W., Pearson, N. J. & O'Reilly, S. (2008). GLITTER: data reduction software for laser ablation ICP-MS. *Short Course Series* **40**, 308–311.

Hacker, B. R., Kelemen, P. B. & Behn, M. D. (2015). Continental Lower Crust. *Annual Review of Earth and Planetary Sciences* **43**, 167–205.

Helmstaedt, H., Anderson, O. L., & Gavasci, A. T. (1972). Petrofabric studies of eclogite, spinel‐Websterite, and spinel‐lherzolite Xenoliths from kimberlite‐bearing breccia pipes in southeastern Utah and northeastern Arizona. *Journal of Geophysical Research* **77**(23), 4350-4365.

Holland, T. J. B. & Powell, R. (2004). An internally consistent thermodynamic data set for phases of petrological interest: AN INTERNALLY CONSISTENT THERMODYNAMIC DATA SET. *Journal of Metamorphic Geology* **16**, 309–343.

Holland, T. J. B. & Powell, R. (2011). An improved and extended internally consistent thermodynamic dataset for phases of petrological interest, involving a new equation of state for solids: THERMODYNAMIC DATASET FOR PHASES OF PETROLOGICAL INTEREST. *Journal of Metamorphic Geology* **29**, 333–383.

Idárraga-García, J. & Vargas, C. A. (2018). Depth to the bottom of magnetic layer in South America and its relationship to Curie isotherm, Moho depth and seismicity behavior. *Geodesy and Geodynamics* **9**, 93–107.

Jacques, G., Hoernle, K., Gill, J., Wehrmann, H., Bindeman, I. & Lara, L. E. (2014). Geochemical variations in the Central Southern Volcanic Zone, Chile (38–43°S): The role of fluids in generating arc magmas. *Chemical Geology* **371**, 27–45.

Jochum, K. P. *et al.* (2011). Determination of Reference Values for NIST SRM 610-617 Glasses Following ISO Guidelines. *Geostandards and Geoanalytical Research* **35**, 397–429.

Jung, H., Park, M., Jung, S., & Lee, J. (2010). Lattice preferred orientation, water content, and seismic anisotropy of orthopyroxene. *Journal of Earth Science*, ***21***(5), 555-568.

Kay, S. M., Gorring, M. & Ramos, V. A. (2004). Magmatic sources, setting and causes of Eocene to Recent Patagonian plateau magmatism (36°S to 52°S latitude). *Revista de la Asociación Geológica Argentina* **59** (4), 556-568.

Kay, S. M., Ardolino, A. A., Gorring, M. L. & Ramos, V. A. (2007). The Somuncura Large Igneous Province in Patagonia: Interaction of a Transient Mantle Thermal Anomaly with a Subducting Slab. *Journal of Petrology* **48**, 43–77.

Kempton, P. D. & Harmon, R. S. (1992). Oxygen isotope evidence for large-scale hybridization of the lower crust during magmatic underplating. *Geochimica et Cosmochimica Acta* **56**, 971–986.

Kourim, F., Vauchez, A., Bodinier, J.-L., Alard, O. & Bendaoud, A. (2015). Subcontinental lithosphere reactivation beneath the Hoggar swell (Algeria): Localized deformation, melt channeling and heat advection. *Tectonophysics* **650**, 18–33.

Kruse, R., Stünitz, H., & Kunze, K. (2001). Dynamic recrystallization processes in plagioclase porphyroclasts. *Journal of Structural Geology*, ***23***(11), 1781-1802.

Lee, W., Lee, H., Kim, D., Kim, J., Oh, J., Song, J.-H., Kim, C. H., Park, C. H. & Stuart, F. M. (2021). Trace element and helium isotope geochemistry of the Cenozoic intraplate volcanism in the East Sea (Sea of Japan): Implications for lithosphere-asthenosphere interaction. *Lithos* **388–389**, 106075.

López De Luchi, M. G. & Rapalini, A. E. (2002). Middle Jurassic dyke swarms in the North Patagonian Massif: the Lonco Trapial Formation in the Sierra de Mamil Choique, Río Negro province, Argentina. *Journal of South American Earth Sciences* **15**, 625–641.

Luppo, T., López de Luchi, M. G., Rapalini, A. E., Martínez Dopico, C. I. & Fanning, C. M. (2018). Geochronologic evidence of a large magmatic province in northern Patagonia encompassing the Permian-Triassic boundary. *Journal of South American Earth Sciences* **82**, 346–355.

Mallmann, G. (2004). Processos e Componentes Mantélicos no Norte da Patagônia (Argentina) e Relações com a Subducção Andina: Evidências Petrográficas, Geoquímicas e Isotópicas em Xenólitos Ultramáficos Mantélicos. Universidade Federal do Rio Grande do Sul Instituto de Geociências, p.102.

Martínez Dopico, C. I., López de Luchi, M. G., Rapalini, A. E. & Kleinhanns, I. C. (2011). Crustal segments in the North Patagonian Massif, Patagonia: An integrated perspective based on Sm–Nd isotope systematics. *Journal of South American Earth Sciences* **31**, 324–341.

Martínez Dopico, C. I., López De Luchi, M. G., Rapalini, A. E., Fanning, C. M. & Antonio, P. Y. J. (2019). Geochemistry and geochronology of the shallow-level La Esperanza magmatic system (Permian-Triassic), Northern Patagonia. *Journal of South American Earth Sciences* **96**, 102347.

Massaferro, G. I., Haller, M. J., Dostal, J., Pécskay, Z., Prez, H., Meister, C. & Alric, V. (2014). Possible sources for monogenetic Pliocene–Quaternary basaltic volcanism in northern Patagonia. *Journal of South American Earth Sciences* **55**, 29–42.

McCoy-West, A. J., Baker, J. A., Faure, K. & Wysoczanski, R. (2010). Petrogenesis and

Origins of Mid-Cretaceous Continental Intraplate Volcanism in Marlborough, New Zealand: Implications for the Long-lived HIMU Magmatic Mega-province of the SW Pacific. *Journal of Petrology* **51**, 2003–2045.

McDonough, W. F. & Sun, S. -s. (1995). The composition of the Earth. *Chemical Geology* **120**, 223–253.

Melchiorre, M., Faccini, B., Grégoire, M., Benoit, M., Casetta, F. & Coltorti, M. (2020). Melting and metasomatism/refertilisation processes in the Patagonian sub-continental lithospheric mantle: A review. *Lithos* **354–355**, 105324.

Mengel, K. & Kern, H. (1992). Evolution of the petrological and seismic Moho-implications for the continental crust-mantle boundary. *Terra Nova* **4**, 109–116.

Mouthereau, F. *et al.* (2021). Cenozoic mountain building and topographic evolution in Western Europe: impact of billions of years of lithosphere evolution and plate kinematics. *BSGF - Earth Sciences Bulletin* **192**, 56.

Mundl, A., Ntaflos, T., Ackerman, L., Bizimis, M., Bjerg, E. A., Wegner, W. & Hauzenberger, C. A. (2016). Geochemical and Os–Hf–Nd–Sr Isotopic Characterization of North Patagonian Mantle Xenoliths: Implications for Extensive Melt Extraction and Percolation Processes. *Journal of Petrology* **57**, 685–715.

Navarrete, C., Gianni, G., Encinas, A., Márquez, M., Kamerbeek, Y., Valle, M. & Folguera, A. (2019). Triassic to Middle Jurassic geodynamic evolution of southwestern Gondwana: From a large flat-slab to mantle plume suction in a rollback subduction setting. *Earth-Science Reviews* **194**, 125–159.

Navarrete, C., Gianni, G., Massaferro, G. & Butler, K. (2020). The fate of the Farallon slab beneath Patagonia and its links to Cenozoic intraplate magmatism, marine transgressions and topographic uplift. *Earth-Science Reviews* **210**, 103379.

Natali, C., Beccaluva, L., Bianchini, G., Ellam, R. M., Savo, A., Siena, F. & Stuart, F. M.

(2016). High-MgO lavas associated to CFB as indicators of plume-related thermochemical effects: The case of ultra-titaniferous picrite–basalt from the Northern Ethiopian–Yemeni Plateau. *Gondwana Research* **34**, 29–48.

O'Reilly, S. Y. & Griffin, W. L. (2013). Moho vs crust–mantle boundary: Evolution of an idea. *Tectonophysics* **609**, 535–546.

Oriolo, S. *et al.* (2023). Linking accretionary orogens with continental crustal growth and stabilization: Lessons from Patagonia. *Gondwana Research* **121**, 368–382.

Pankhurst, R. J. & Rapela, C. R. (1995). Production of Jurassic rhyolite by anatexis of the lower crust of Patagonia. *Earth and Planetary Science Letters* **134**, 23–36.

Pankhurst, R. J., Leat, P. T., Sruoga, P., Rapela, C. W., Márquez, M., Storey, B. C. & Riley, T. R. (1998). The Chon Aike province of Patagonia and related rocks in West Antarctica: A silicic large igneous province. *Journal of Volcanology and Geothermal Research* **81**, 113–136.

Pankhurst, R. J., Rapela, C. W., Fanning, C. M. & Márquez, M. (2006). Gondwanide continental collision and the origin of Patagonia. *Earth-Science Reviews* **76**, 235–257.

Pankhurst, R. J., Rapela, C. W., López De Luchi, M. G., Rapalini, A. E., Fanning, C. M. & Galindo, C. (2014). The Gondwana connections of northern Patagonia. *Journal of the Geological Society* **171**, 313–328.

Passchier, C. W. & Trouw, R. A. J. (2005). Microtectonics (pp. 1–366). Berlin Heidelberg: Springer. Retrieved from https://link.springer.com/book/10.1007/3-540-29359-0

Ramos, V. A. (2008). Patagonia: A paleozoic continent adrift? *Journal of South American Earth Sciences* **26**, 235–251.

Rapalini, A. E., De Luchi, M. L., Tohver, E. & Cawood, P. A. (2013). The South American ancestry of the North Patagonian Massif: geochronological evidence for an autochthonous origin? *Terra Nova* **25**, 337–342.

Rapela, C. W. & Pankhurst, R. J. (2020). The Continental Crust of Northeastern Patagonia. *Ameghiniana* **57**.

Raterron, P., Doukhan, N., Jaoul, O. & Doukhan, J. C. (1994). High temperature deformation of diopside IV: predominance of {110} glide above 1000°C. *Physics of the Earth and Planetary Interiors* **82**, 209–222.

Renda, E. M., Alvarez, D., Prezzi, C., Oriolo, S. & Vizán, H. (2019). Inherited basement structures and their influence in foreland evolution: A case study in Central Patagonia, Argentina. *Tectonophysics* **772**, 228232.

Rudnick, R. L. & Fountain, D. M. (1995). Nature and composition of the continental crust: A lower crustal perspective. *Reviews of Geophysics* **33**, 267.

Satsukawa, T., Ildefonse, B., Mainprice, D., Morales, L. F. G., Michibayashi, K. & Barou, F. (2013). A database of plagioclase crystal preferred orientations (CPO) and microstructures – implications for CPO origin, strength, symmetry and seismic anisotropy in gabbroic rocks. *Solid Earth* **4**, 511–542.

Schilling, M. E., Carlson, R. W., Conceição, R. V., Dantas, C., Bertotto, G. W. & Koester, E. (2008). Re–Os isotope constraints on subcontinental lithospheric mantle evolution of southern South America. *Earth and Planetary Science Letters* **268**, 89–101.

Schilling, M. E., Carlson R.W., Tassara A., Conceição R.V., Bertotto G.W., Vásquez M., Muñoz D., Jalowitzki T., Gervasoni F., Morata D. (2017). The origin of Patagonia revealed by Re-Os systematics of mantle xenoliths. *Precambrian Research* **294**, 15–32.

Soret, M., Agard, P., Ildefonse, B., Dubacq, B., Prigent, C. & Rosenberg, C. (2019). Deformation mechanisms in mafic amphibolites and granulites: record from the Semail metamorphic sole during subduction infancy. *Solid Earth* **10**, 1733–1755.

Stern, C. R., Frey, F. A., Futa, K., Zartman, R. E., Peng, Z. & Kurtis Kyser, T. (1990).

Trace-element and Sr, Nd, Pb, and O isotopic composition of Pliocene and Quaternary alkali basalts of the Patagonian Plateau lavas of southernmost South America. *Contributions to Mineralogy and Petrology* **104**, 294–308.

Sun, P., Niu, Y., Guo, P., Duan, M., Wang, X. & Gong, H. (2022). Sublithosphere Mantle Crystallization and Immiscible Sulfide Melt Segregation in Continental Basalt Magmatism: Evidence from Clinopyroxene Megacrysts in the Cenozoic Basalts of Eastern China. *Journal of Petrology* **63**, egac001.

Skemer, P., Katayama, I., Jiang, Z. & Karato, S. (2005). The misorientation index: Development of a new method for calculating the strength of lattice-preferred orientation. *Tectonophysics* **411**, 157–167.

Taufner, R., Viegas, G., Faleiros, F. M., Castellan, P. & Silva, R. (2021). Deformation mechanisms of granulite-facies mafic shear zones from hole U1473A, Atlantis Bank, Southwest Indian Ridge (IODP Expedition 360). *Journal of Structural Geology* **149**, 104380.

Tullis, T. E., Horowitz, F. G. & Tullis, J. (1991). Flow laws of polyphase aggregates from end‐member flow laws. *Journal of Geophysical Research: Solid Earth* **96**, 8081–8096.

Ulrich, S. & Mainprice, D. (2005). Does cation ordering in omphacite influence development of lattice-preferred orientation? *Journal of Structural Geology* **27**, 419–431.

van der Meijde, M., Julià, J. & Assumpção, M. (2013). Gravity derived Moho for South America. *Tectonophysics* **609**, 456–467.

van der Werf, T., Chatzaras, V., Kriegsman, L. M., Kronenberg, A., Tikoff, B. & Drury, M. R. (2017). Constraints on the rheology of the lower crust in a strike-slip plate boundary: evidence from the San Quintín xenoliths, Baja California, Mexico. *Solid Earth* **8**, 1211–1239.

van Achterbergh, E. (2001). Data reduction software for LA-ICP-MS : appendix. *Laser Ablation-ICP-Mass Spectrometry in the Earth Sciences : Principles and Applications,* 239-243.

Von Gosen, W. (2009). Stages of Late Palaeozoic deformation and intrusive activity in the western part of the North Patagonian Massif (southern Argentina) and their geotectonic implications. *Geological Magazine* **146**, 48–71.

Wang, Y. F., Zhang, J. F., Jin, Z. M. & Green, H. W. (2012). Mafic granulite rheology: Implications for a weak continental lower crust. *Earth and Planetary Science Letters* **353–354**, 99–107.

Wells, P. R. A. (1977). Pyroxene thermometry in simple and complex systems. *Contributions to Mineralogy and Petrology* **62**, 129–139.

White, R. W., Powell, R. & Clarke, G. L. (2002). The interpretation of reaction textures in Fe-rich metapelitic granulites of the Musgrave Block, central Australia: constraints from mineral equilibria calculations in the system K2O-FeO-MgO-Al2O3-SiO2-H2O-TiO2-Fe2O3: REACTION TEXTURES, MUSGRAVE BLOCK GRANULITES. *Journal of Metamorphic Geology* **20**, 41–55.

White, R. W., Powell, R., Holland, T. J. B., Johnson, T. E. & Green, E. C. R. (2014). New mineral activity-composition relations for thermodynamic calculations in metapelitic systems. *Journal of Metamorphic Geology* **32**, 261–286.

Zack, T., Brumm, R. (1998). Ilmenite/liquid partition coefficients of 26 trace elements determined through ilmenite/clinopyroxene partitioning in garnet pyroxenites (1998). *International Kimberlite Conference Extended Abstracts: 1998*. paper presented at the International Kimberlite Conference. University of Alberta. 986-988.

Zaffarana, C. *et al.* (2019). First geochemical and geochronological characterization of Late Cretaceous mesosilicic magmatism in Gastre, Northern Patagonia, and its tectonic relation to other coeval volcanic rocks in the region. *Geological Magazine* **156**, 1285–1294.

Zaffarana, C. B. *et al.* (2020). Petrogenetic study of the Lonco Trapial volcanism and its comparison with the Early-Middle Jurassic magmatic units from northern Patagonia. *Journal of South American Earth Sciences* **101**, 102624.

Zhang, J., Green II, H. W., & Bozhilov, K. N. (2006). Rheology of omphacite at high temperature and pressure and significance of its lattice preferred orientations. *Earth and Planetary Science Letters*, ***246***(3-4), 432-443.

CHAPTER III: The deformation of the deep crust from the southern Cordillera of the Andes: Calbuco xenoliths

In collaboration with Mary-Alix Kaczmarek, Michel Grégoire and Alexandre Corgne.

ABSTRACT

The Southern Volcanic Zone in the Andes Cordillera presents a remarkable combination of the activity of an active strikeslip fault (the LOFZ) and volcanic eruptions along this fault. However, the relationship between accommodated deformation in this zone and magmatic activity in the lower crust has never been directly observed. We present here a microstructural study using Electron Backscattered Diffraction (EBSD) coupled with microprobe chemical analyses of minerals major elements, focusing on a series of xenoliths with either ultra-mylonitic and mylonitic or magmatic porphyric textures, sampled from the products of a recent eruption of the active Calbuco volcano (41°20' S, Chile). The mylonites display a paragenesis of plagioclase ± clinopyroxene ± orthopyroxene + Fe-Ti oxides ± ilmenite and a very fine-grained texture, often <100 μm, with a well-marked foliation. In contrast, the magmatic rocks display a plagioclase + orthopyroxene + olivine + amphibole + clinopyroxene + Fe-Ti oxides assemblage and a preserved cumulative texture. Pseudosection calculations indicate that mylonites have equilibrium temperatures and pressures that vary greatly from sample to sample, ranging from those of greenschist facies to those of granulite facies. Additionally, the pressures and temperatures calculated with pseudosections and thermometers can vary by more than 400°C and more than 5 kbar for the same mylonite sample. The increase in temperature is positively correlated with the Mg# and Al_2O_3 content of clinopyroxenes, and high-temperature mylonites have chemical compositions and equilibration temperatures similar to those of igneous rocks (Mg# clinopyroxene >70, Al_2O_3 clinopyroxene > 1.5 wt%, 900-1000°C). Although intragranular deformation is absent in mylonites, their crystallographic preferential orientation (CPO) is well-marked, particularly in pyroxenes, which display a CPO that corresponds to activation of the [001](100) slip

system, common to orthopyroxene and active in clinopyroxene at temperatures of 800-900°C. Additionally, the lineation and strength of the fabric seems to become more pronounced with increasing temperature, as suggested by thermobarometry. Finally, a hybrid sample displays a late crystallised igneous part against an early mylonitic part, confirming the coexistence of magmas crystallising in the middle to lower crust and the active ductile deformation affecting this part of the crust.

RÉSUMÉ

La zone volcanique Sud-Andine présente une combinaison remarquable entre l'activité d'une faille active décrochante (la Zone de Faille Liquiñe-Ofqui) et les éruptions volcaniques le long de cette cette faille. Cependant, la relation entre la déformation accommodée dans cette zone et l'activité magmatique dans la croûte inférieure n'a jamais pu être observée directement. Nous présentons ici une étude microstructurale par *Electron Backscattered Diffraction* (EBSD) couplée à des analyses chimiques des éléments majeurs des minéraux par microsonde, d'une série de xénolithes avec des textures soit ultra-mylonitiques et mylonitiques soit magmatiques porphyriques, échantillonnée au niveau des produits d'une éruption récente du volcan actif Calbuco (41°20' S, Chili). Les mylonites présentent une paragénèse de type plagioclase ± clinopyroxène ± orthopyroxène + oxydes fe-ti ± ilménite et une texture à grains très fins, souvent <100 μm et une foliation très fortement marquée. Les roches ignées, quant à elles, présentent un assemblage plagioclase + orthopyroxène + olivine + amphibole + clinopyroxène + oxydes ferro-titanés et ont une texture cumulative préservée. Les calculs de pseudosection indiquent que les mylonites ont des températures et pression d'équilibres qui varient beaucoup d'un échantillon à l'autre, s'étalant depuis celles du faciès schiste vert jusqu'à celles du faciès granulite. En outre, les pressions et températures calculées avec des pseudosections et thermomètres peuvent varier jusqu'à plus de 400°C et plus de 5 kbar pour un même échantillon de mylonite. L'augmentation de température est corrélée positivement avec le Mg# et la teneur en Al_2O_3 des clinopyroxènes, et les mylonites de haute température ont des compositions chimiques et des températures d'équilibration semblables à celles des roches ignées (Mg# clinopyroxene >70, Al_2O_3 clinopyroxène > 1.5 wt%, 900-1000°C). Si la déformation intragranulaire est absente dans les mylonites, leur orientation préférentielle cristallographique (CPO) est très bien marquée, notamment dans les pyroxènes, qui ont un CPO allant de pair avec l'activation du système de glissement

[001](100), commune pour l'orthopyroxène et actif dans le clinopyroxène à des températures de 800-900°C. De plus, la linéation et la force de la fabrique semble se marquer davantage avec l'augmentation de température suggérée par la thermobarométrie. Enfin, un échantillon hybride présente une partie ignée cristallisée plus tardivement contre une partie mylonitique plus précoce. Cet échantillon confirme la coexistence entre des magmas cristallisant dans la croûte moyenne à inférieure et la déformation ductile active affectant cette partie de la croûte.

III. 1 INTRODUCTION

The Northwestern Patagonian crust, in Southern South America, is settled on an active margin setting regarding the Pacific subduction since the Paleozoic and thus has been affected by contrasted growing and deformation events, which are not fully understood (Hervé *et al.*, 2007; Oliveros *et al.*, 2020; Fig. III.1). Its basement consists of Devonian to Carboniferous metasediments and metabasites, accreted during a Late Devonian-Carboniferous compressive episode affecting the active margin located between the Protopacific oceanic plates subducting below the South American lithosphere (Hervé *et al.*, 2007; Martínez *et al.*, 2012; Hervé *et al.*, 2018; Oriolo *et al.*, 2019; Rapela *et al.*, 2021). During Mesozoic and Cenozoic times, the arc-related magmatism, dependent on the varying angle of the subducting slab, was especially active during the Jurassic and the Miocene, producing many intrusive magmatic complexes contributing to crustal growth in the actual North Patagonian Andes (Rapela *et al.*, 2005; Echaurren *et al.*, 2016, 2017; Genge *et al.*, 2021). Since recent times, the arc magmatism and associated crustal growth are still active, as illustrated by active volcanoes (Stern *et al.*, 2007). The latter are moreover located on or near the Liquiñe-Ofqui fault zone (LOFZ), a N-S dextral transpressional triple-slip fault which accommodates the oblique convergence between Nazca and South American plates (Arancibia *et al.*, 1999; Sielfeld *et al.*, 2019; Fig. III.1). The LOFZ is the main active deformation zone occurring in the North Patagonian upper crust. Its activity is expressed by seismicity, active crustal faulting, and Miocene to Pliocene ductile deformation structures that have been exhumed (Arancibia *et al.*, 1999). However, the actual deformation of the ductile

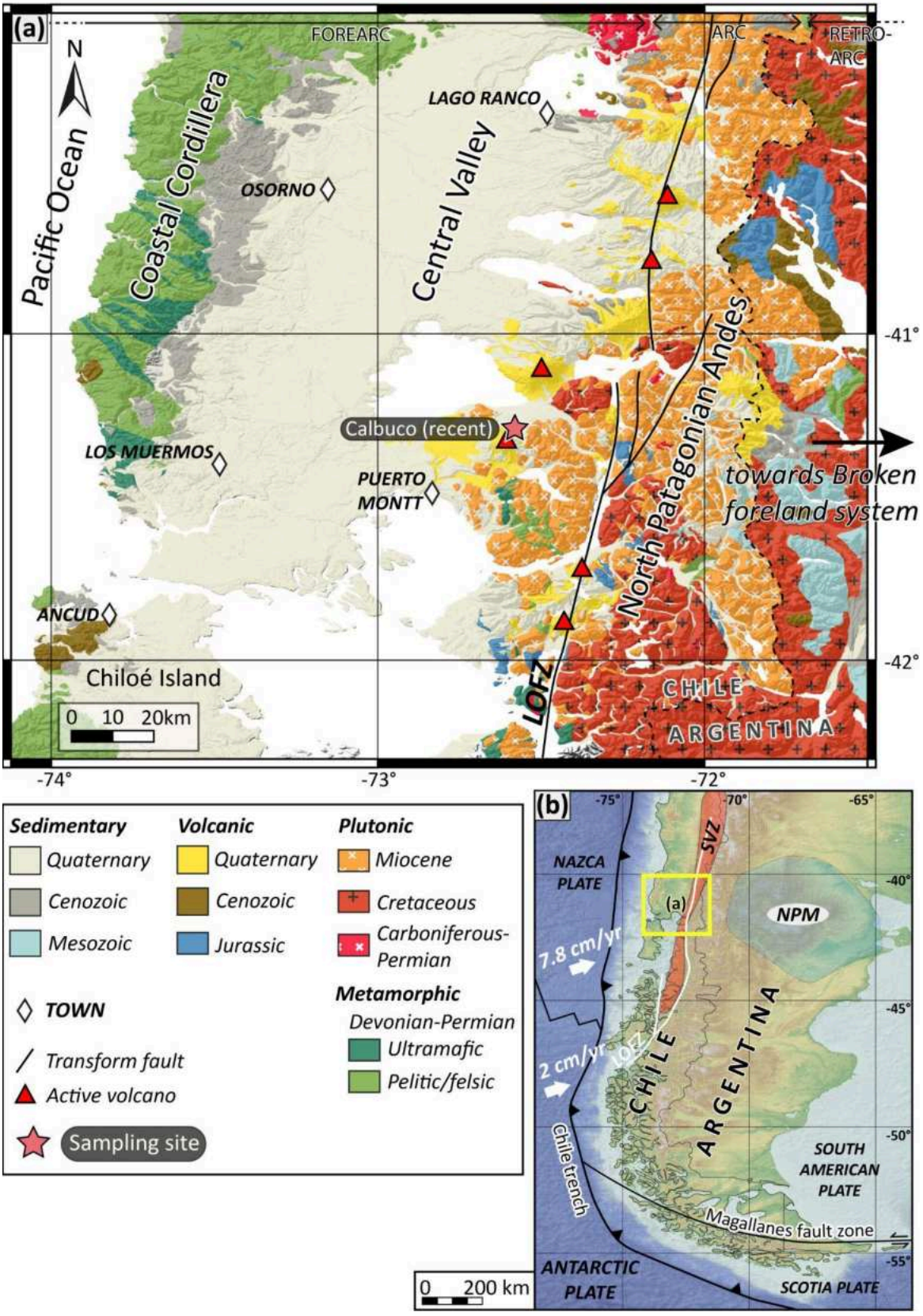


Fig. III.1. (a) Geological setting near the Calbuco xenoliths and (b) in Southern South America. After Echaurren *et al.* (2016, 2022), based on IDE Chile and SegemAR maps. LOFZ: Liquiñe-Ofqui fault zone, NPM: North Patagonian Massif, SVZ: Southern Volcanic Zone.

lower crust remains mysterious. Finally, if a control of the deformation upon magma ascent and storage does exist (Chaussard & Amelung, 2014), it remains elusive.

Regarding the Calbuco volcano (41°20’ S), located 20 kilometres to the West of the LOFZ, the occurrence of crustal xenoliths allowed to access the middle to lower crust Paleozoic mafic metamorphic basement as well as cumulates related to Calbuco magmas (Hickey-Vargas *et al.*, 1995). In this chapter, the rheology and the magmatic processes recorded in the lower crust beneath the Calbuco volcano have been investigated by analysing the microstructure and the mineral chemical composition (major elements) of mylonite and igneous xenoliths brought up to the surface by recent Calbuco lavas. The combination of these new datasets allows presenting a model of the deformation along with the magmatism occurring in the lower crust beneath the Calbuco volcano, linked to the LOFZ activity.

III. 2 GEOLOGICAL SETTING

Calbuco volcano is a stratovolcano that occurs in the Central Southern Volcanic Zone (CSVZ; Fig. III.1), at the westernmost part of the North Patagonian Andes, the latter corresponding to the Arc region characterised by the Nazca subduction below the South American plate. North Patagonian Andes displays a few Devonian to Carboniferous metamorphic rocks and I-type granitoids, voluminous Jurassic and Miocene plutons, and recent andesitic volcanic rocks (Fig. III.1). West to the Arc, the forearc region comprises, from West to East, the subduction accretionary prism, composed of Mesozoic to actual sediments, the coastal cordillera which displays Devonian to Carboniferous basement metamorphic rocks, and the Central depression, composed of Mesozoic to actual sediments (Fig. III.1; Echaurren *et al.*, 2016, 2022). East to the Arc, the retro-arc comprises the “broken foreland system” fold-thrust belt which mainly displays Mesozoic and Cenozoic sedimentary and volcanic rocks. This region accommodated most of the shortening (ca. 30 km) during the compressive episodes of the Pacific-South American convergence, especially during the Cretaceous and Miocene periods (Echaurren *et al.*, 2022). East to the broken foreland system, the retro-arc comprises the North Patagonian Massif, which is known to be a rigid and undeformed crustal block (Aragón *et al.*, 2011). The basement of the fore-arc, the arc and the broken foreland system from the retro-arc is considered to be Devonian to Carboniferous metamorphic rocks, i.e. corresponding to those outcropping in the Coastal Cordillera and in the North Patagonian Andes (Hervé *et al.*, 2007). Seismic models (Dzierma *et al.*, 2012;

Tassara & Echaurren, 2012) and derived tectonic models (Echaurren *et al.*, 2016, 2022) set the depth of the geophysical crust-mantle boundary (CMB) at 20-25 km beneath the Central Valley which increases to 40 km beneath the North Patagonian Andes. Hence, the CMB depth beneath Calbuco volcano, at the threshold between these two regions, can be seen as an in-between.

Southern Volcanic Zone magmatism involves hydrous magmas derived from the dehydration melting of the South American lithospheric mantle from fluids released by the Nazca subducting oceanic plate (e.g. Stern *et al.*, 2007; Hickey-Vargas *et al.*, 2016; Vander Auwera *et al.*, 2019, 2021). In the Calbuco volcano, no primary magma reached the surface; lower crust reservoirs, near the Moho, are involved in the crystallization of pyroxenite cumulates and the differentiation of the magmas (Vander Auwera *et al.*, 2021). Nevertheless, shallower reservoirs (2.1-4.6 kbar; ca. 10-18 km) are responsible for most of the differentiation that is reflected by the composition of erupted lavas which range from basalts to dacites (Morgado *et al.*, 2019; Vander Auwera *et al.*, 2021).

Xenoliths occur in Calbuco andesites and consist of mafic mylonites and ultra-mylonites, igneous rocks and hornblendites. A previous petrological and geochemical study has been made on these xenoliths (Hickey-Vargas *et al.*, 1995) but they have not yet been studied from a microstructural point of view.

III. 3 SAMPLE COLLECTION AND ANALYTICAL METHODS

III. 3.1 Sample collection

Xenoliths were sampled directly within Calbuco andesites, that were either “in place” andesites from the 1961 eruption, or fresh andesites in the Rio Blanco stream supplied by Calbuco clasts (41°16’24” S, 72°32’30” W) from undated but recent eruptions (maximum 100 ka; Mixon *et al.*, 2021; Fig. III.1). Mafic magmatic porphyric xenoliths are the most common lithology found in host andesites with a size that can reach 20 cm in diameter. Hornblendite xenoliths and highly foliated mafic xenoliths are less common and can reach 30 and 10 cm in diameter, respectively. More than 50 xenoliths have been collected. Among this collection, three magmatic porphyric and four mylonite xenoliths (including one sample from the 1961 eruption xenoliths collection from J. Vander Auwera) were selected for major element analysis. Two magmatic porphyric and three mylonite xenoliths were selected for detailed microstructural analysis (Table III.1).

III. 3.2 Minerals major and minor elements compositions

Polished thick sections were covered with a 20nm carbon deposit using a carbon evaporator Leica EM ACE600 for secondary Electron Microscope (SEM**)** observations and microprobe measurements. SEM qualitative chemical analyses were carried out at the Géosciences Environnement Toulouse (GET) laboratory (CNRS-CNES-IRD-University Paul Sabatier, Toulouse), Observatoire Midi Pyrénées (Toulouse, France), using a Tescan Vega 4 equipped with an EDS Bruker Quantax 30mm². The analysis conditions were performed with an acceleration voltage of 20 kV, a probe current of 3 nA and a working distance of 15 mm.

Minerals major element analyses were carried out using a Cameca SX Five electron microprobe from the microcharacterisation centre Raimond Castaing (CNRS-University Paul Sabatier, Toulouse). Measurements were made with an acceleration voltage of 15 kV and a probe current of 20 nA. Acquisition times were 10 s on peak and 5 s on either side of the peak for the continuous background. The standards used are natural or synthetic minerals as well as pure metals. The data summary is in Tables III.2-5 and detection limits are available in *Supplementary Material Table SIII.1*.

III. 3.3 Phase equilibrium modelling

Calculations were applied on three samples using the Na_2O-CaO-K_2O-FeO-MgO-Al_2O_3-SiO_2-TiO_2-O_2 system, with the software Perple_X 7.0.0 and the internally consistent thermodynamic dataset (hp622ver) of Holland & Powell (2011). Solution models used were those from Fuhrman & Lindsley (1988) for plagioclase (Pl), Green *et al.* (2016) for clinopyroxene (Cpx), amphibole (Am) and melt, White *et al.* (2014) for orthopyroxene (Opx), garnet (Grt) and ilmenite (Ilm), White *et al.* (2002) for spinel (Sp) and Holland & Powell (1998) for olivine (Ol). Bulk-rock composition of the investigated samples was calculated using mineralogical modal proportions, microprobe analyses and mineral densities. Details on selected densities are available in *Supplementary Material*. Bulk Fe_2O_3 was calculated based on the ratio Fe_2O_3/FeOt in two-pyroxenes and Fe-Ti phases. O_2 bulk was calculated using the formula $O_{2\ mol} = 0.5*Fe_2O_{3\ mol}$. H_2O was incremented supposing that the amphibole contains 0.5 wt% H_2O. TiO_2 from pyroxenes was not taken into the bulk rock incrementation into Perple_X, as solution models from those minerals does not include titanium. Three samples were selected for isochemical phase diagram calculation.

III. 3.4 Crystallographic orientations of minerals

A mechanic-chemical polishing using a Vibromet (Buehler) was applied on five thick sections for 2h with a colloidal silica suspension (pH 10) to remove mechanically induced surface damage. Electron Backscatter Diffraction (EBSD) data acquisition was performed with a JEOL 7100 microscope at the centre of microcharacterisation Raimond Castaing (University Paul Sabatier, Toulouse), equipped with an EBSD camera CMOS Symmetry S2 (Oxford Instruments). The analysis conditions were performed with an acceleration voltage of 20 kV, a probe current of 16 nA and a working distance of 17 mm with a stage tilt of 70°. Automatic indexing was performed using AZTec software (version 6.0 Oxford Instruments). For mapping the step size used varies between 15 and 20 µm depending on the grain size. The resulting EBSD data were then processed in MATLAB (version R2020b) using the MTex toolbox (version 5.7.0; Bachmann *et al.* 2010, 2011). A value of 10° as the cut-off angle for the determination of the grains has been used. Pole figures were plotted on a lower-hemisphere, equal-area stereographic projection. To avoid oversampling of large crystals, pole figures were plotted with one point per grain, except for plagioclase, where pole figures represent all the available measurements due to the presence of twins, which increases the number of detected grains. For clarity, pole figures were rotated as the inferred foliation was the XY plan and lineation parallel to X. These interpretations take into account the trace of the foliation in xenoliths, the correlation of Crystallographic preferred orientation (CPO) concentration point between minerals. An example of a rotated pole figure procedure is given in *Supplementary Fig. SV.1*. The strength of the crystallographic preferred orientation was estimated using both the J- and M-indices (Bunge 1982; Skemer *et al.* 2005). In addition, the misorientation of each pixel was calculated relative to the mean orientation of its corresponding grain and then combined as maps of misorientation relative to mean grain orientation. In parallel, for each sample, pixel proportions relative to their misorientation angle were plotted in normalised histograms.

III. 4 RESULTS

III. 4.1 Sample description and petrography

All the investigated Calbuco xenoliths display mineralogy consisting of plagioclase ± orthopyroxene ± olivine ± clinopyroxene ± amphibole assemblages (Table III.1). The

xenolith collection has been subdivided in two groups based on textures: the mylonite group and the magmatic porphyric group.

Table III.1: Modal proportions of the investigated xenoliths. Modal proportions are estimated with EBSD data (with an *) or estimated (some are with a range of ±5%) with the optical microscope. MN: metanorite; Gbn: gabbronorite; MGbbn: metagabbronorite; MGb: metagabbro; N: norite; Hbd: hornblendite; An: anorthosite; Pl: plagioclase; Opx: orthopyroxene; Cpx: clinopyroxene; Ol: olivine; Amph: amphibole; Bt: biotite; Ti-Mag: titanomagnetite; Ilm: ilmenite; Sp: spinel; Titn: titanite; Ap: apatite.

Group	Mylonites							Igneous rocks					
Sample	**CAL9**	**CAL28A***	**CAL28B***	**CAL29A***	**CAL29B***	**CAL50A***	**CAL50B***	**CL61**	**CAL1**	**CAL5**	**CAL8***	**CAL33**	**CAL41***
Rock type	Bt-MN	MN	Gbn	MN	MGbn	MGbn	MGb	MN	N	N	Ol-N	Hbd	An
Modal prop. (%)													
Pl	> 65	59,4	54,5	73,3	56,5	52,3	48,0	> 75	> 80	> 80	69,1	< 10	89,6
Opx	5 - 20	39,6	20,1	3,6	15,3	12,6		10 - 20	5 - 15	5 - 15	24,2		3,9
Cpx		0,2	20,1	21,8	26,9	34	49,6	< 0,5	< 5		< 0,1		2,6
Ol			0,3							< 5	6,2		2,9
Amph		0,2	4							< 5	0,4	> 90	0,1
Bt	< 10												
Ti-Mag	< 5	0,6	0,9	0,9	1	0,3	2,2	< 3	< 2	< 1	< 0,1		0,9
Ilm			< 0,2	0,4	0,2	0,8	0,2	< 1					
Sp	< 2												
Titn							< 0,2						
Ap								< 0,5					

III. 4.1.1 Mylonites and ultra-mylonites

The mylonite xenoliths group mostly consists of ultra-mylonite textured rocks composed of plagioclase, orthopyroxene and variable proportions of clinopyroxene. The suite is composed of metagabbro (samples CAL29A, CAL50B; Fig. III.2a, b, d, f), metagabbronorite (samples CAL29B and CAL50A; Fig. III.2c, e) or metanorite (samples CAL28, CL61; Fig. III.3a, b). Thus, two different assemblages may be observed in a single sample, as in one hand samples CAL29 and CAL50, divided into a metagabbronorite part (respectively named CAL29B and CAL50A; Fig. III.2e) and a metagabbro part (respectively named CAL29A and CAL50B; Fig. III.2f). On the other hand, the sample CAL28 is divided into a metanorite (named CAL28A; Fig. III.3b) and a gabbronorite part (named CAL28B; Fig. III.3c). The sample CAL9 differs from other xenoliths by a plagioclase-orthopyroxene-phlogopite assemblage (Fig. III.3d, e). Main minerals are associated with accessory (<2 vol.%) titanomagnetite (all the samples) and ilmenite (samples CAL28B, CAL29, CAL50A-B, CL61). More rarely, accessory titanite (sample CAL50B; Fig. III.2g), spinel (sample CAL9; Fig. III.3e), apatite (sample CL61) or quartz (sample CAL50A) occurs.

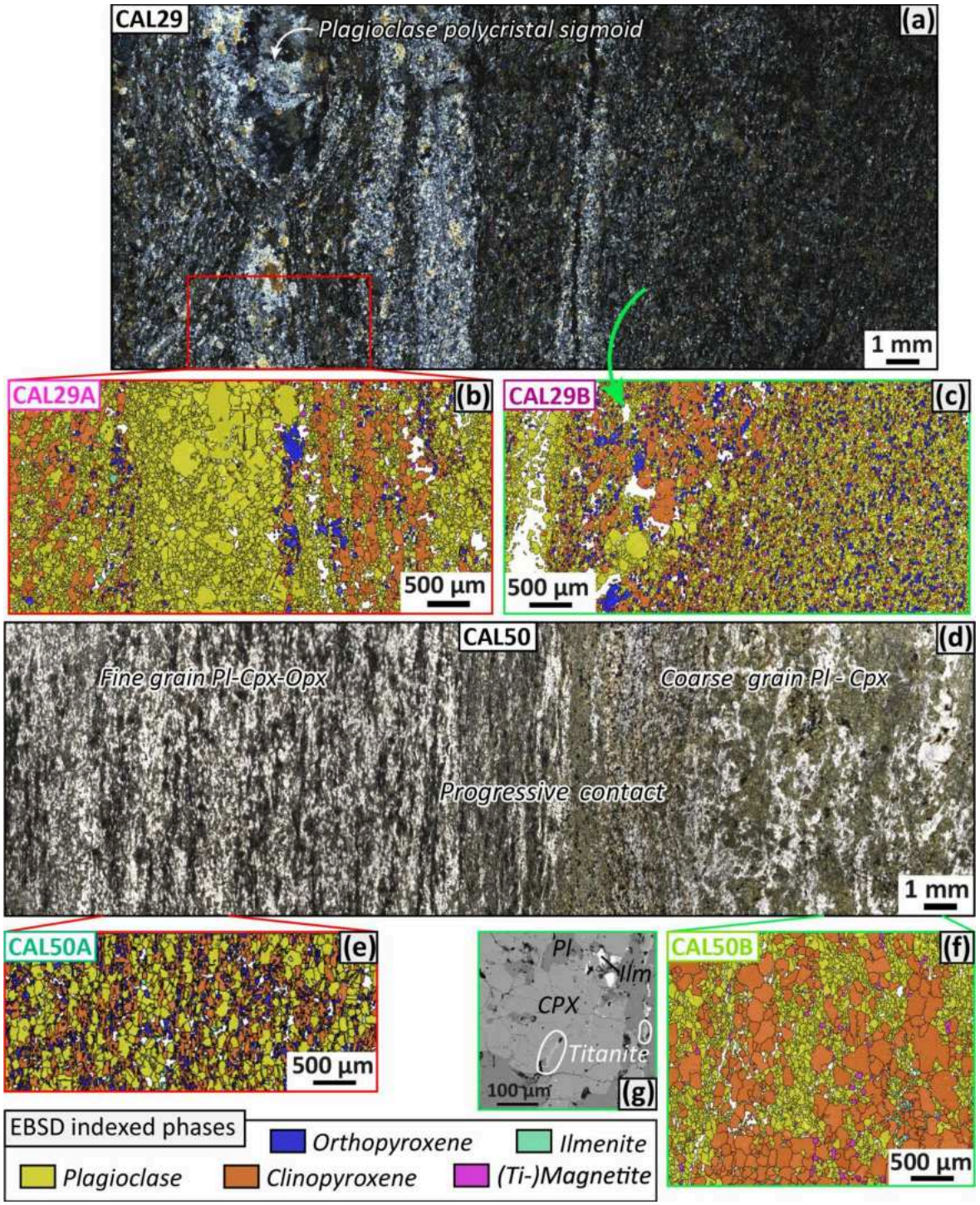


Fig. III.2. Photomicrographs and EBSD phase maps of ultra-mylonitic samples CAL29 and CAL50 from Calbuco. (a) Mylonite CAL29 under cross-polarised light; note the alternance of plagioclase-rich layers with plagioclase + two-pyroxenes layers to the left and the homogeneous assemblage to the right. (b, c) EBSD phase maps of the two textural zones (CAL29A, -B) of sample CAL29. (d) Ultra-mylonite CAL50 under plane-polarised light; note the progressive contact (at a microscopic scale) between the metagabbronorite zone to the left and the metagabbro zone to the right. (e) Phase map of the metagabbronorite zone (CAL50A). (f) Phase map and (g) backscattered electron image of the metagabbro zone (CAL50B).

Most of the samples display rather unimodal grain size for plagioclase, clinopyroxene, orthopyroxene and accessory phases, ranging from 20 to 300 μm and are ultra-mylonites except CAL50B, which is mylonitic and CAL28B which display a magmatic porphyric texture. All mylonites and ultramylonites display a foliation and a lineation. Pyroxenes display aspect ratios that can reach 7:1, whereas plagioclase typically has smaller aspect ratios, reaching 4:1.

The variation of textures among samples and even inside the same sample is significant and goes along with mineralogical assemblage variations. Sample CAL29 displays two distinct textural zones: (i) CAL29A, characterised by plagioclase-rich layers with polycrystals sigmoids (Fig. III.2a, b), where plagioclase grains can be larger (100 μm - 1 mm) than the matrix grains (30 - 300 μm); (ii) CAL29B, which displays a homogeneous assemblage (grain size 30 - 100 μm) with occasional bigger plagioclase or pyroxene grains (100 μm - 1 mm). In the sample CAL50, the plagioclase-two-pyroxenes zone (CAL50A) displays smaller grain size (20 - 100 μm) and more elongated grains (aspect ratio up to 7:1) than in the plagioclase-clinopyroxene zone (CAL50B; grain size 300 - 700 μm; aspect ratio up to 4:1). In CAL50A zone, the orthopyroxene grains are eithers at the clinopyroxene grain boundaries, or are included in clinopyroxene grains with an elongated shape (Fig. III.10). Moreover, the contact between the two textural zones is 7 mm thick (Fig. III.2d). Finally, the sample CAL28 displays two distinct textural zones: (i) a plagioclase-orthopyroxene ultra-mylonitic zone (CAL28A) with a layering and a few orthopyroxene polycrystals sigmoids (Fig. III.3a, b); (ii) a plagioclase-orthopyroxene-clinopyroxene zone without foliation (CAL28B) with very fine-grained matrix (<700 μm) associated with automorphic and zoned medium-grained plagioclase (1 - 3 mm; Fig. III.3c). The contact between the two textural zones is sharp and discordant, as the foliation of the ultra-mylonite is intersected by the fined-grained magmatic porphyric textural zone. In this sample, the amphibole poikiloblasts occur in the two zones.

III. 4.1.2 Magmatic porphyric rocks

Magmatic textured xenoliths group consists of olivine-norite (sample CAL8; Fig. III.4a), anorthosite (sample CAL41; Fig. III.4b) or norite (samples CAL1 and CAL5; Fig. III.4c). When they are not essential minerals, accessory minerals are orthopyroxene (sample CAL41), olivine (samples CAL5 and CAL41), clinopyroxene (samples CAL1, CAL8 and CAL41), amphibole (samples CAL5, CAL8 and CAL41) and titanomagnetite (all the

samples). The sample CAL33 differs from other xenoliths by consisting of one amphibole poikiloblast measuring the size of a thin section and which contains numerous oriented plagioclase inclusions (Fig. III.4d).

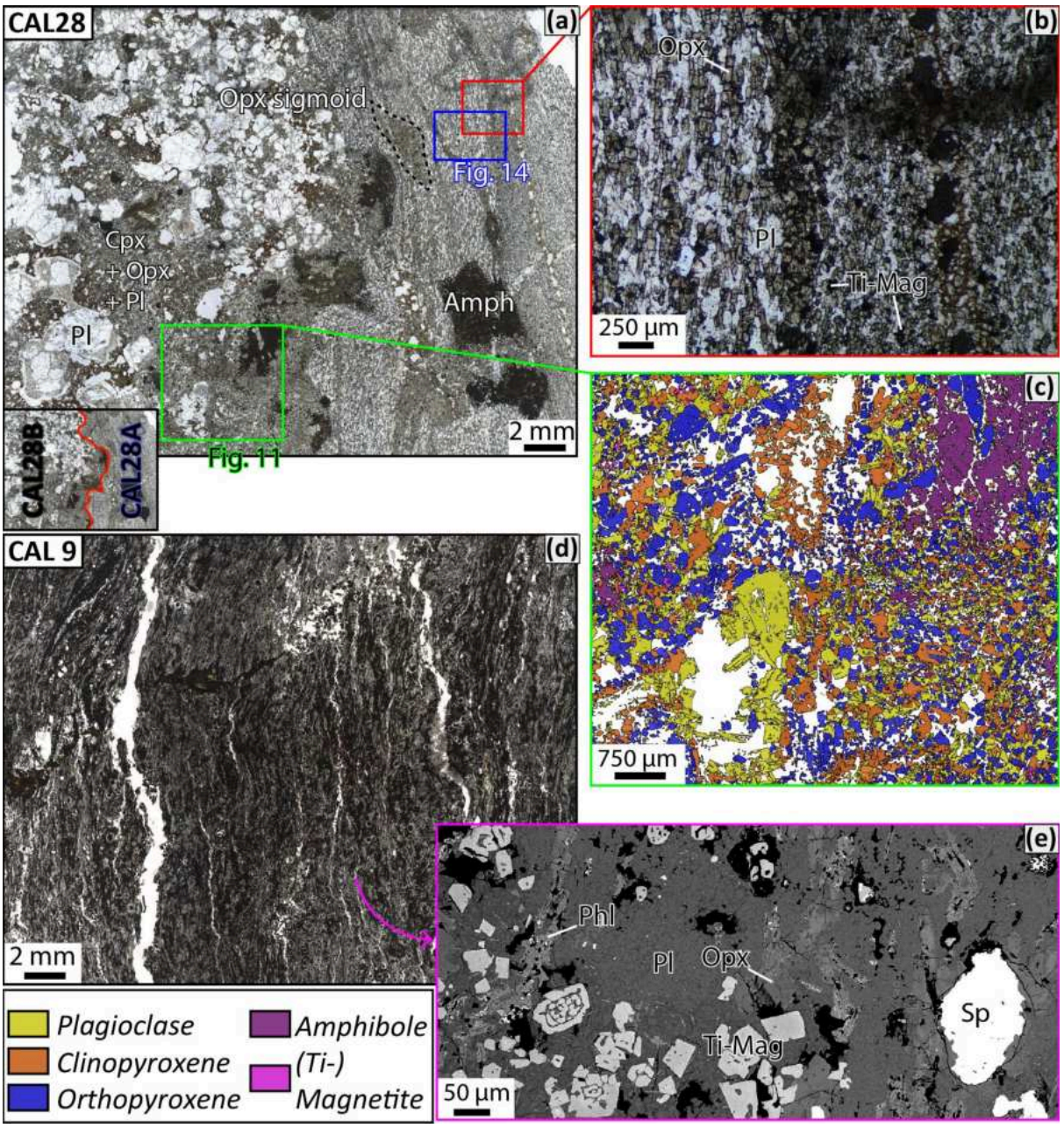


Fig. III.3. Photomicrographs of xenolith samples CAL28 and CAL9 from Calbuco. (a) Mylonite CAL28 under plane-polarised light; note the discordant contact between the gabbronorite zone CAL28B to the left and the metanorite zone CAL28A to the right. The black dashed line underlined an orthopyroxene polycrystal sigmoid. The small insert displays with the red line, the discordant limit between the two textures. (b) Metanorite CAL28A under plane-polarised light. (c) EBSD phase map of the gabbronorite zone CAL28B. (d) Phlogopite-norite ultra-mylonite CAL9 under plane-polarised light and (g) under backscattered electrons.

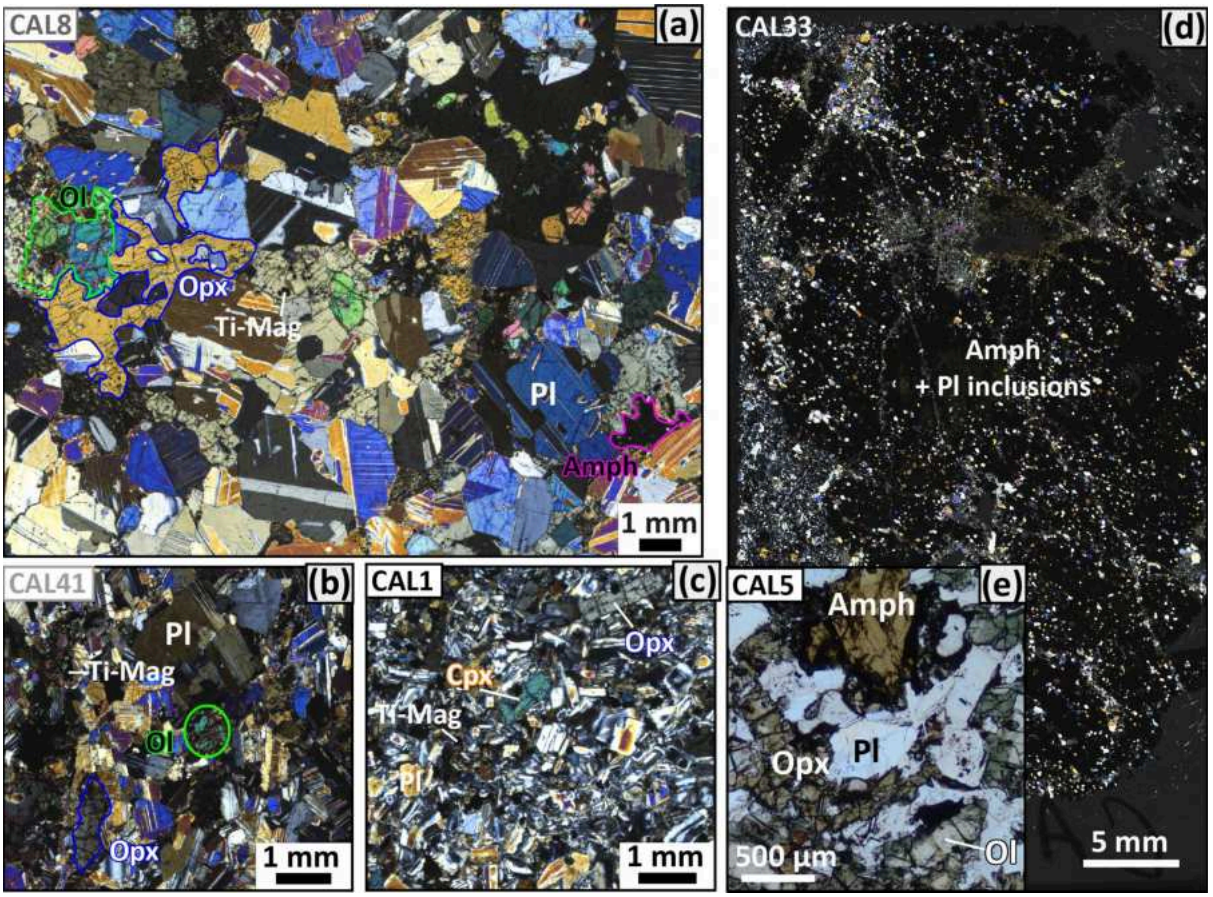


Fig. III.4. Photomicrographs of magmatic porphyric xenoliths from Calbuco. (a) Olivine-Norite CAL8 under cross-polarised light. (b) Anorthosite CAL41 under cross-polarised light. (c) Norite CAL1 under cross-polarised light. (d) Hornblendite CAL33 under cross-polarised light. (e) Norite CAL5 under plane-polarised light. Note the "black-type" breakdown reaction on the amphibole rims. Sections have a thickness of 50 µm and plagioclase may display second-order colours under cross-polarised light.

Grain size in the sample CAL8 is rather unimodal, with medium to coarse-grained (>1 mm) plagioclase (up to 5 mm) and orthopyroxene (up to 1 cm), medium-grained olivine and amphibole (1 - 3 mm), and fine-grained clinopyroxene and titanomagnetite (ca. 200 µm). Samples CAL41, CAL1 and CAL5 display fine- to medium-grained plagioclase, orthopyroxene, clinopyroxene and olivine, with a grain size ranging from 200 microns to 3 mm, and fine-grained (<1 mm) titanomagnetite and amphibole. In all the samples, plagioclase appears as automorph grains which display zonations and numerous twins. Orthopyroxene is sub-automorphic to automorphic and moreover appears as oikocryst in the sample CAL8, several millimetres in size and occurring between plagioclase grain boundaries. Olivine,

clinopyroxene and amphibole are sub-euhedral; however, olivine and amphibole develop at the expense of orthopyroxene. Plagioclase grain boundaries are highly linear and those of the other minerals are mostly curved, except for orthopyroxene in sample CAL8, which displays linear contact with plagioclase grains.

Table III.2: Average clinopyroxene major element compositions. Cations on the basis of 6 oxygens.

Group	Mylonites							Igneous rocks	
Sample	**CAL28 B**	**CAL29 A**	**CAL29 B**	**CAL50 A**	**CAL50 trans**	**CAL50 B**	**CL61**	**CAL8**	**CAL41**
Rock type	Gbn	MN	MGbn	MGbn	MGbn	MGb	MN	Ol-N	An
n	7	11	5	7	7	3	1	3	3
wt%									
SiO2	51.23	51.67	51.68	50.84	51.71	51.31	51.96	51.12	50.62
TiO2	0.65	0.27	0.48	0.75	0.18	0.09	0.40	0.44	0.58
Al2O3	2.17	1.34	1.74	2.52	1.59	1.00	1.79	2.78	2.73
Cr2O3	0.05	0.03	0.02	0.03	0.02	0.08	0.02	0.01	0.03
Fe2O3	2.66	2.18	2.17	2.83	2.74	3.32	1.77	3.53	3.22
FeO	6.23	8.94	7.29	6.74	7.01	8.62	7.67	5.26	5.80
MnO	0.25	0.32	0.29	0.31	0.32	0.34	0.28	0.19	0.25
NiO	0.03	0.03	0.04	0.01	0.03	0.02	0.02	0.01	0.01
MgO	15.08	13.47	14.49	14.81	13.34	11.47	14.22	15.07	14.93
CaO	21.01	21.32	21.32	20.41	22.70	23.67	21.38	21.52	21.03
Na2O	0.32	0.29	0.30	0.39	0.38	0.35	0.36	0.34	0.31
K2O	0.01	0.01	0.00	0.01	0.00	0.01	0.03	0.00	0.00
Total	99.68	99.86	99.84	99.65	100.02	100.27	99.90	100.28	99.51
Wo	43.1	43.9	43.8	42.3	46.7	48.6	44.2	43.8	43.3
En	43.1	38.6	41.4	42.7	38.1	32.8	40.9	42.7	42.7
Ferr	13.8	17.5	14.8	15.0	15.2	18.6	14.9	13.4	14.0
Al IV	0.074	0.050	0.058	0.081	0.060	0.057	0.050	0.097	0.094
Al VI	0.022	0.010	0.019	0.030	0.010	-0.013	0.028	0.024	0.026
Mg#	75.7	68.8	73.6	74.0	71.5	63.8	73.2	76.1	75.4
σ									
SiO2	*0.837*	*0.312*	*0.113*	*0.574*	*0.377*	*0.291*		*0.993*	*0.454*
TiO2	*0.239*	*0.146*	*0.034*	*0.147*	*0.081*	*0.070*		*0.145*	*0.092*
Al2O3	*0.847*	*0.406*	*0.115*	*0.488*	*0.534*	*0.222*		*0.660*	*0.171*
Cr2O3	*0.047*	*0.027*	*0.016*	*0.023*	*0.012*	*0.091*		*0.006*	*0.010*
Fe2O3	*0.668*	*0.484*	*0.396*	*0.586*	*0.378*	*0.702*		*0.588*	*0.625*
FeO	*0.970*	*1.202*	*0.418*	*0.504*	*0.416*	*0.379*		*0.438*	*0.577*
MnO	*0.059*	*0.090*	*0.046*	*0.046*	*0.032*	*0.030*		*0.023*	*0.064*
NiO	*0.015*	*0.021*	*0.019*	*0.015*	*0.020*	*0.025*		*0.010*	*0.006*
MgO	*0.300*	*0.821*	*0.201*	*0.254*	*0.885*	*0.021*		*0.420*	*0.127*
CaO	*0.437*	*0.633*	*0.231*	*0.462*	*1.062*	*0.061*		*0.122*	*0.284*
Na2O	*0.064*	*0.052*	*0.030*	*0.050*	*0.064*	*0.026*		*0.012*	*0.032*
K2O	*0.008*	*0.015*	*0.009*	*0.008*	*0.000*	*0.010*		*0.006*	*0.000*
Total	*0.179*	*0.226*	*0.362*	*0.362*	*0.381*	*0.351*		*0.637*	*0.242*
Wo	*0.973*	*1.282*	*0.526*	*0.637*	*2.148*	*0.279*		*0.566*	*0.578*
En	*0.679*	*2.272*	*0.573*	*0.491*	*2.434*	*0.172*		*0.846*	*0.370*
Ferr	*0.617*	*1.841*	*0.817*	*0.907*	*1.062*	*0.422*		*0.280*	*0.212*
Al IV	*0.025*	*0.013*	*0.005*	*0.014*	*0.015*	*0.014*		*0.022*	*0.011*
Al VI	*0.014*	*0.009*	*0.006*	*0.015*	*0.010*	*0.004*		*0.009*	*0.005*
Mg#	*0.847*	*3.364*	*1.284*	*1.346*	*2.326*	*0.634*		*0.737*	*0.131*

III. 4.2 Minerals major elements chemistry

III. 4.2.1 Clinopyroxene

Clinopyroxenes are usually augites but in the sample CAL50B and the transition zone between CAL50A and CAL50B whose display diopside (Fig. III.5a; Table III.2). Regarding the distribution of Al between IV and VI sites, clinopyroxenes in all the samples either plot within the granulite field or the igneous rocks field according to the classification by Aoki & Kushiro (1968; Fig. III.5b). Notably, only the mylonite CAL50 shows a trend: clinopyroxene in the metagabbronorite zone CAL50A tends to plot within the granulite field (5 out of 7 points), while those in the metagabbro zone CAL50B plots within the igneous rocks field (Fig. III.5b). The Al_2O_3 content varies between 0.5 and 3.44 wt% and is positively correlated with Mg# (100 x Mg/(Mg+FeOt)) which range from 63 and 77 (Fig. III.5c; Table III.2). Mylonites CAL50A and CAL28B, as well as magmatic porphyric xenoliths CAL8 and CAL41 display higher Al_2O_3 and Mg# (1.93-3.44 wt% and 72-77, respectively) than mylonites CAL50B (Al_2O_3 0.76-1.2 wt%; Mg# 63-64), CAL29A (Al_2O_3 0.68-1.84 wt%; Mg# 63-74) and CAL29B (Al_2O_3 1.61-1.88 wt%; Mg# 72-75). However, a clinopyroxene inclusion in plagioclase from the gabbronorite zone CAL28B displays low Al_2O_3 content (0.5 wt%) but a high Mg# (75). It is worth noting that the metagabbronorite zone CAL50A of the mylonite CAL50 displays higher Al_2O_3 contents and Mg# than the metagabbro zone CAL50B, while the transition zone displays intermediate and continuous Al_2O_3 content (0.95-2.33 wt%) and Mg# (67-74) between CAL50A and B (Fig. III.5c; Table III.2). Moreover, clinopyroxene from the CAL29A zone displays lower Al_2O_3 contents and Mg# than the CAL29B zone. TiO_2 contents are positively correlated with Al_2O_3 contents, and samples CAL28B, CAL41 and CAL50A display higher TiO_2 contents (0.5-0.96 wt%) than samples CAL8, CAL29, CL61, CAL50B and the CAL50 transition zone (0.06-0.53 wt%; Fig. III.5d; Table III.2). Na_2O content is always low (< 0.5 wt%) and rather homogeneous between samples (Fig. III.5e).

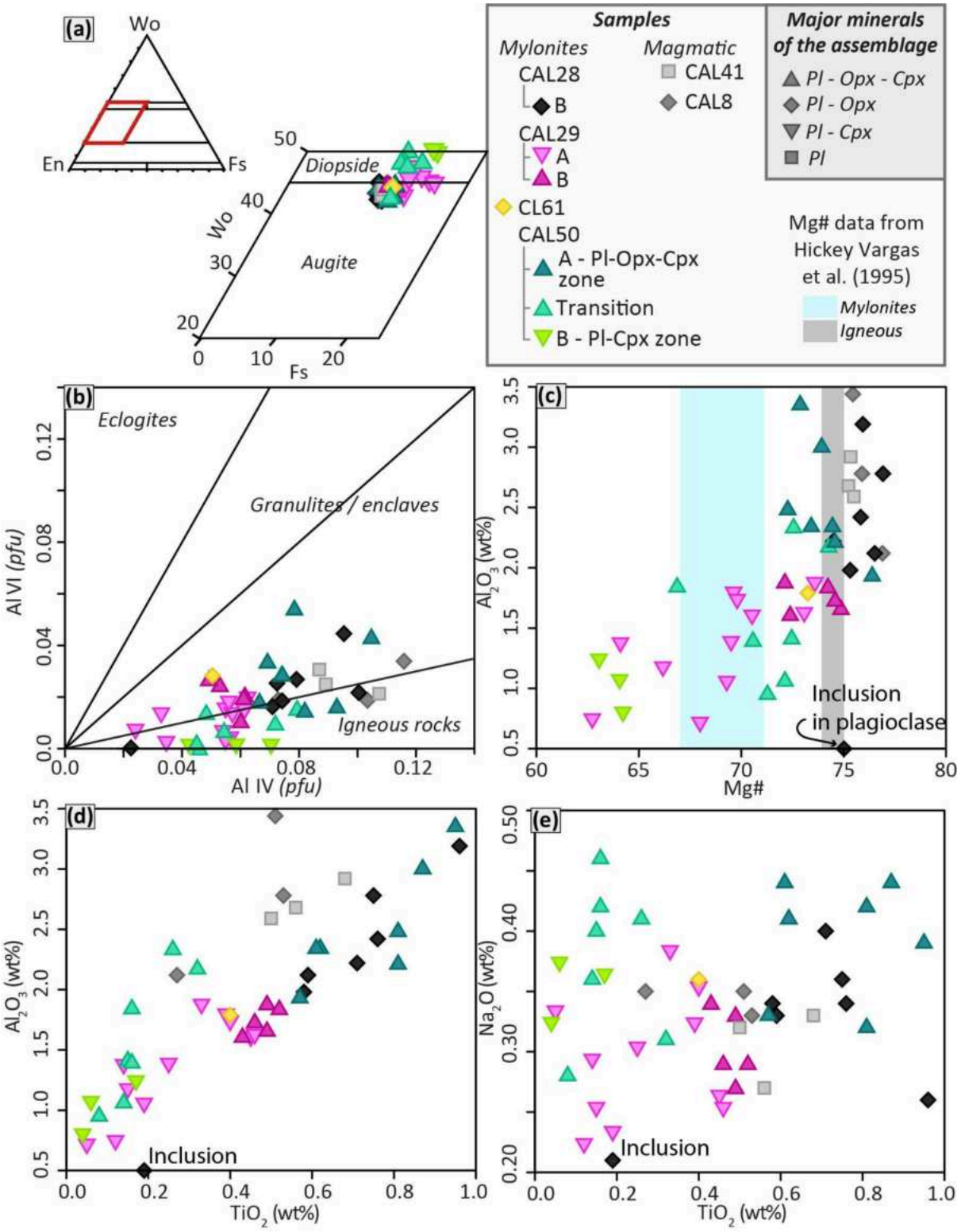


Fig. III.5. Major element diagrams of clinopyroxene. (a) Ternary wollastonite-enstatite-hedenbergite plot of pyroxenes. (b) Plot of Al_{VI} *vs.* Al_{IV}. Compositional fields are from Aoki & Kushiro (1968). Al_{IV} = 2-(Si+Ti), molar; $Al_{VI} = Al_{tot}$-Al_{IV}, molar. (c) Plot of Al_2O_3 vs Mg#. (d) Plot of Al_2O_3 vs TiO_2. (e) Plot of Na_2O vs TiO_2. Mg # = 100 x Mg/(Mg+FeOt).

Table III.3: Average orthopyroxene major element compositions. Cations on the basis of 6 oxygens.

Group	Mylonites					Igneous rocks			
Sample	**CAL28 A**	**CAL28 B**	**CAL29 A**	**CAL29 B**	**CAL50 A**	**CL61**	**CAL5**	**CAL8**	**CAL41**
Rock type	MN	Gbn	MN	MGbn	MGbn	MN	N	Ol-N	An
n	9	8	3	4	3	6	4	7	5
wt%									
SiO2	53.22	52.95	53.21	52.21	52.48	53.27	51.06	53.10	52.87
TiO2	0.22	0.14	0.17	0.29	0.35	0.13	0.16	0.14	0.25
Al2O3	1.09	1.26	0.74	1.36	1.47	0.73	3.99	2.30	1.59
Cr2O3	0.02	0.04	0.01	0.04	0.02	0.01	0.01	0.00	0.01
Fe2O3	1.19	1.63	0.29	1.32	0.55	0.88	2.66	2.11	1.75
FeO	17.54	17.88	21.11	19.17	19.27	18.62	15.88	14.19	16.27
MnO	0.56	0.59	0.52	0.50	0.50	0.70	0.47	0.34	0.43
NiO	0.04	0.03	0.01	0.04	0.01	0.01	0.02	0.01	0.02
MgO	24.48	24.47	22.65	22.70	23.07	24.22	24.48	26.71	25.15
CaO	1.47	0.94	1.21	1.70	1.59	0.95	0.87	1.06	1.42
Na2O	0.03	0.02	0.04	0.06	0.02	0.01	0.01	0.02	0.01
K2O	0.00	0.01	0.00	0.00	0.00	0.01	0.01	0.00	0.01
Total	99.85	99.95	99.96	99.38	99.34	99.54	99.60	99.99	99.76
Wo	2.9	1.9	2.5	3.5	3.2	1.9	1.8	2.1	2.8
En	68.0	68.0	63.8	64.2	65.3	67.7	69.2	73.2	69.5
Ferr	29.0	30.1	33.8	32.3	31.4	30.4	29.0	24.7	27.7
Mg#	70.1	69.3	65.4	66.5	67.5	69.0	70.5	74.7	71.5
σ									
SiO2	*0.270*	*0.490*	*0.145*	*0.592*	*0.450*	*0.502*	*0.549*	*0.890*	*0.317*
TiO2	*0.045*	*0.019*	*0.006*	*0.095*	*0.045*	*0.060*	*0.033*	*0.040*	*0.030*
Al2O3	*0.313*	*0.503*	*0.015*	*0.184*	*0.197*	*0.317*	*0.715*	*1.111*	*0.147*
Cr2O3	*0.013*	*0.041*	*0.006*	*0.014*	*0.017*	*0.008*	*0.006*	*0.005*	*0.008*
Fe2O3	*0.520*	*0.624*	*0.195*	*0.621*	*0.496*	*0.469*	*0.524*	*0.449*	*0.410*
FeO	*1.095*	*0.449*	*2.464*	*1.941*	*1.168*	*0.357*	*0.599*	*0.597*	*0.532*
MnO	*0.049*	*0.018*	*0.068*	*0.072*	*0.053*	*0.198*	*0.055*	*0.031*	*0.023*
NiO	*0.037*	*0.021*	*0.023*	*0.031*	*0.010*	*0.012*	*0.024*	*0.024*	*0.036*
MgO	*0.494*	*0.332*	*1.452*	*1.314*	*0.786*	*0.325*	*0.535*	*0.664*	*0.301*
CaO	*0.825*	*0.123*	*0.165*	*0.211*	*0.070*	*0.310*	*0.169*	*0.123*	*0.220*
Na2O	*0.028*	*0.013*	*0.025*	*0.015*	*0.015*	*0.010*	*0.014*	*0.020*	*0.011*
K2O	*0.000*	*0.008*	*0.006*	*0.000*	*0.006*	*0.005*	*0.006*	*0.008*	*0.009*
Total	*0.322*	*0.405*	*0.632*	*0.427*	*0.405*	*0.459*	*0.266*	*0.316*	*0.278*
Wo	*1.632*	*0.232*	*0.316*	*0.413*	*0.142*	*0.625*	*0.329*	*0.226*	*0.443*
En	*1.105*	*0.482*	*3.593*	*3.044*	*1.815*	*0.586*	*0.680*	*1.193*	*0.622*
Ferr	*1.346*	*0.632*	*3.909*	*3.151*	*1.818*	*0.729*	*0.964*	*1.162*	*0.370*
Mg#	*1.070*	*0.592*	*3.890*	*3.218*	*1.877*	*0.632*	*0.890*	*1.192*	*0.422*

III. 4.2.2 Orthopyroxene

Orthoyproxene is enstatite, except for one orthopyroxene of the gabbronorite zone CAL28B which is a pigeonite (Fig. III.6a; Table III.3). All the samples except norite CAL8 and gabbronorite CAL5 display homogeneous Al_2O_3 contents bracketed between 0.27 and 2.26 wt%. CAL8 displays more scattered Al_2O_3 content (0.81-3.45 wt%) while CAL5 has high Al_2O_3 contents (3.22-4.94 wt%; Fig. III.6b; Table III.3). Orthopyroxene from magmatic porphyric rocks rather has higher Mg# (69-76) than mylonites (62-71), as already observed by Hickey-Vargas *et al.* (1995). Cr_2O_3 content is low (< 0.07 wt%) but one orthopyroxene of

the metanorite zone CAL28A displays higher Cr_2O_3 contents (0.13 wt%; Fig. III.6c; Table III.3).

III. 4.2.3 Plagioclase

Plagioclase varies from anorthite to andesine (An_{94-41}) with orthose contents always <2 %mol (Fig. III.6d; Table III.4). Magmatic porphyric xenoliths CAL5, CAL8 and CAL41 and mylonite xenoliths CAL28A and CAL50B display the most calcic plagioclase of the whole suite (An_{94-82}). Plagioclase from ultra-mylonites CAL29B, CAL50A and CL61 varies between labradorite and andesine (An_{61-45}). Zoned plagioclase from the gabbronorite zone CAL28B (sample CAL28) displays scattered anorthite values that vary between An_{93} and An_{41}, as well as plagioclase grains forming a sigmoid in the metagabbro zone CAL29A (An_{86-59}; Fig. III.2a, d; Fig. III.6d; Table III.4).

Table III.4: Average plagioclase major element compositions. Cations on the basis of 8 oxygens.

Group	Mylonites							Igneous rocks			
Sample	**CAL28 A**	**CAL28 B**	**CAL29A**	**CAL29 B**	**CAL50 A**	**CAL50 trans**	**CAL50 B**	**CL61**	**CAL5**	**CAL8**	**CAL41**
Rock type	MN	Gbn	MN	MGbn	MGbn	MGbn	MGb	MN	N	Ol-N	An
n	4	15	6	2	3	2	3	4	10	6	6
wt%											
SiO2	46.68	48.89	48.69	52.57	54.29	52.57	45.56	55.42	45.51	44.84	44.85
TiO2	0.01	0.02	0.01	0.02	0.05	0.02	0.01	0.01	0.01	0.00	0.00
Al2O3	32.88	31.25	31.39	29.10	27.82	29.10	33.58	26.98	33.30	34.08	33.65
Cr2O3	0.01	0.00	0.01	0.00	0.00	0.00	0.00	0.01	0.00	0.01	0.00
FeO	0.64	0.54	0.52	0.64	0.71	0.64	0.54	0.55	0.54	0.45	0.42
MnO	0.02	0.02	0.03	0.03	0.03	0.03	0.01	0.01	0.00	0.02	0.03
MgO	0.02	0.04	0.03	0.02	0.06	0.02	0.02	0.05	0.05	0.03	0.03
CaO	17.03	15.43	15.63	12.56	11.28	12.56	18.34	10.09	18.06	18.65	18.41
Na2O	1.93	2.80	2.74	4.46	4.88	4.46	1.33	5.58	1.44	1.10	1.21
K2O	0.02	0.06	0.07	0.14	0.21	0.14	0.02	0.24	0.02	0.01	0.02
BaO	0.01	0.01	0.01	0.01	0.02	0.01	0.02	0.01	0.01	0.03	0.01
Total	99.23	99.05	99.11	99.53	99.36	99.53	99.42	98.93	98.93	99.19	98.63
An	82.9	75.0	75.7	60.4	55.4	63.0	88.3	49.3	87.3	90.3	89.3
Ab	17.0	24.7	23.9	38.8	43.3	36.3	11.6	49.3	12.6	9.6	10.6
Or	0.1	0.3	0.4	0.8	1.3	0.7	0.1	1.4	0.1	0.0	0.1
σ											
SiO2	*0.313*	*4.433*	*2.805*	*0.304*	*0.536*	*0.304*	*0.520*	*1.451*	*0.795*	*1.041*	*0.725*
TiO2	*0.006*	*0.032*	*0.008*	*0.007*	*0.058*	*0.007*	*0.017*	*0.020*	*0.008*	*0.000*	*0.004*
Al2O3	*0.397*	*2.976*	*1.938*	*0.269*	*0.207*	*0.269*	*0.405*	*0.565*	*0.513*	*0.852*	*0.566*
Cr2O3	*0.015*	*0.006*	*0.010*	*0.000*	*0.000*	*0.000*	*0.006*	*0.010*	*0.005*	*0.010*	*0.004*
FeO	*0.123*	*0.133*	*0.132*	*0.064*	*0.115*	*0.064*	*0.070*	*0.160*	*0.115*	*0.142*	*0.042*
MnO	*0.019*	*0.021*	*0.020*	*0.042*	*0.010*	*0.042*	*0.015*	*0.010*	*0.000*	*0.016*	*0.022*
MgO	*0.010*	*0.023*	*0.019*	*0.014*	*0.025*	*0.014*	*0.000*	*0.026*	*0.028*	*0.025*	*0.015*
CaO	*0.392*	*3.434*	*2.109*	*0.354*	*0.396*	*0.354*	*0.326*	*0.979*	*0.682*	*0.921*	*0.528*
Na2O	*0.172*	*1.803*	*1.216*	*0.170*	*0.435*	*0.170*	*0.190*	*0.726*	*0.388*	*0.455*	*0.275*
K2O	*0.014*	*0.066*	*0.056*	*0.007*	*0.095*	*0.007*	*0.012*	*0.078*	*0.027*	*0.013*	*0.012*
BaO	*0.010*	*0.016*	*0.010*	*0.014*	*0.026*	*0.014*	*0.020*	*0.010*	*0.013*	*0.043*	*0.016*
Total	*0.417*	*0.329*	*0.291*	*0.028*	*0.398*	*0.028*	*0.318*	*0.441*	*0.224*	*0.680*	*0.399*
An	*1.619*	*16.478*	*10.744*	*1.590*	*2.717*	*3.617*	*1.593*	*5.482*	*3.444*	*4.011*	*2.399*
Ab	*1.576*	*16.126*	*10.464*	*1.548*	*3.251*	*3.535*	*1.650*	*5.838*	*3.355*	*4.039*	*2.430*
Or	*0.082*	*0.389*	*0.321*	*0.042*	*0.573*	*0.082*	*0.066*	*0.471*	*0.151*	*0.076*	*0.070*

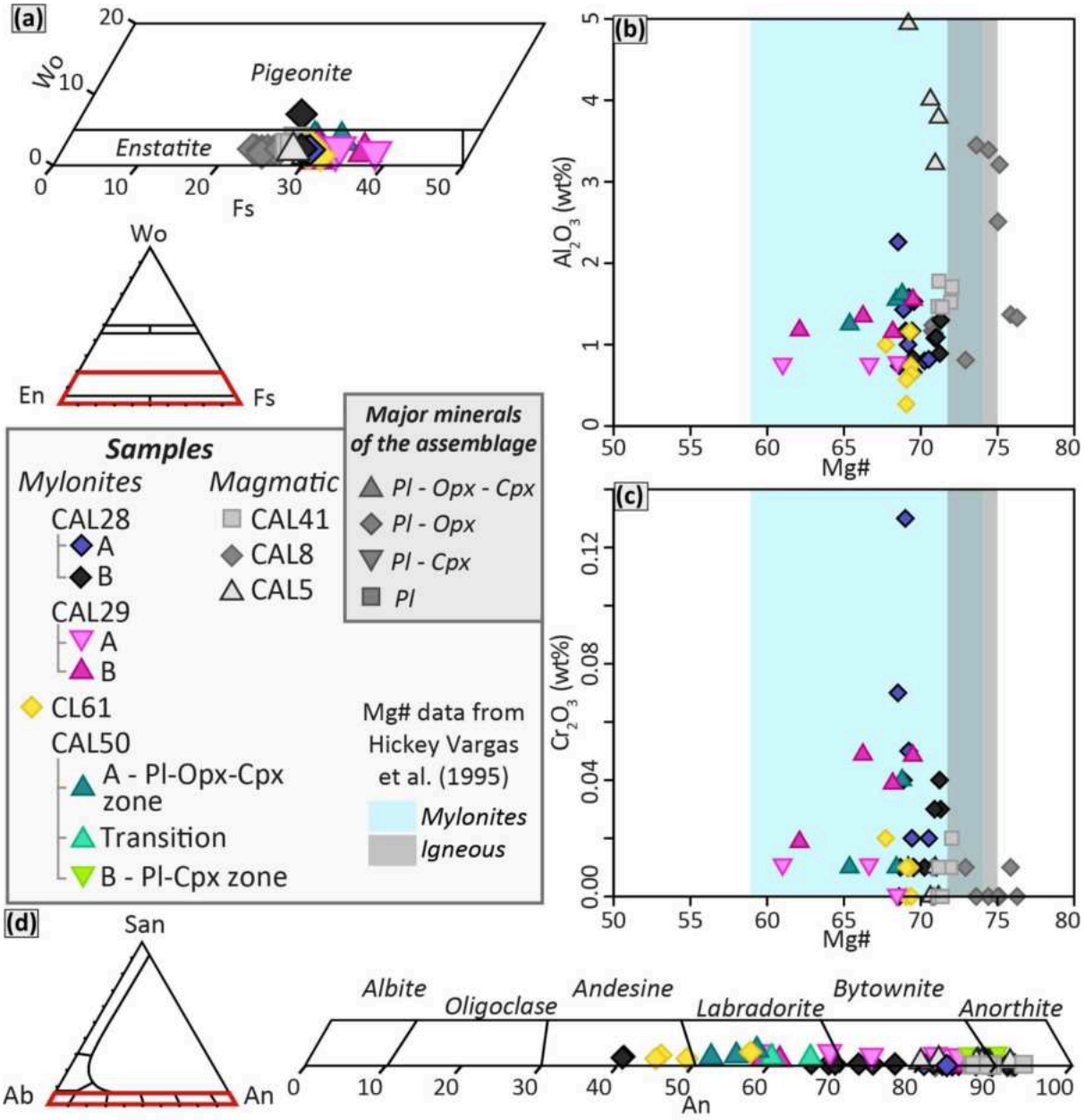


Fig. III.6. Major element diagrams of orthopyroxene and plagioclase. (a) Detailed wollastonite-enstatite-hedenbergite ternary plot of pyroxene. (b) Plot of Al_2O_3 vs Mg# of orthopyroxene. (c) Plot of Cr_2O_3 vs Mg# of orthopyroxene. (d) Detailed orthose-albite-anorthite ternary plot of feldspath.

III. 4.2.4 Amphibole

Amphibole in the magmatic porphyric xenoliths CAL5, CAL8 and CAL41 and the ultra-mylonite CAL28A is pargasite, except two amphibole grains in CAL28 that display edenite compositions (Fig. III.7). Pargasite displays a homogeneous Mg# through the

xenolith suite (66-69; Fig. III.7; Table III.5). Ti is always low in the magmatic porphyric xenolith CAL8 (0.13-0.18 p.f.u.) but can be higher in other samples (0.21-0.33 p.f.u.).

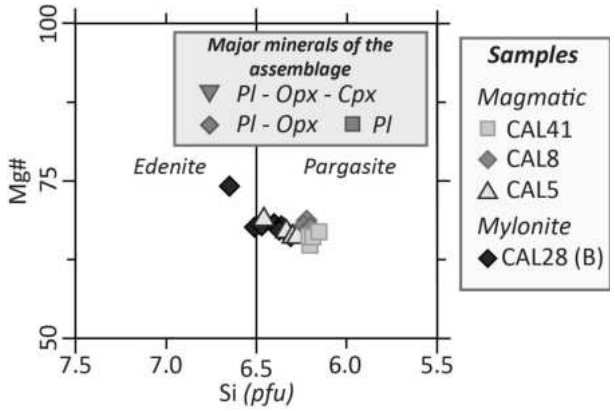


Fig. III.7. Chemical composition (Si vs Mg#) of amphibole in magmatic porphyric and mylonitic samples.

III. 4.2.5 Olivine

Olivine in the norite CAL5 and the Olivine-norite CAL8 have forsterite values ranging from Fo_{76} to Fo_{71} (Table III.5). Olivine is more ferrous in the anorthosite CAL41 (Fo_{67}).

III. 4.2.6 Titanomagnetite

Titanomagnetite is characterised by low MgO contents in mylonites CAL28, CAL29, CAL50, CL61 and in the magmatic porphyric xenolith CAL5 (0.59-2.7 wt%), which are slightly higher in magmatic porphyric xenoliths CAL8 and CAL41 (3.05-4.5 wt%). Al_2O_3 contents are low in mylonites CL61 and CAL50 (1.83-2.86 wt%) and slightly higher in other samples (3.26-6.19 wt%). Across investigated samples, TiO_2 contents range from 5.94 to 17.83 wt% and FeOt ranges from 71.97 to 80.7 wt%.

Table III.5: Average amphibole and olivine major element compositions. Cations on the basis of 23 (for amhibole) and 4 (for olivine) oxygens.

Amphibole					**Olivine**			
Group	Mylonite	Igneous rocks			Group	Igneous rocks		
Sample	**CAL28**	**CAL5**	**CAL8**	**CAL41**	**Sample**	**CAL5**	**CAL8**	**CAL41**
Rock type	MN	N	Ol-N	An	Rock type	N	Ol-N	An
n	7	4	4	4	n	9	6	1
wt%					wt%			
SiO2	43.66	43.09	41.77	41.40	SiO2	37.78	37.53	36.45
TiO2	2.27	2.13	1.42	2.57	TiO2	0.00	0.00	0.00
Al2O3	10.28	11.64	12.56	11.94	Al2O3	0.02	0.02	0.00
Cr2O3	0.08	0.01	0.01	0.01	Cr2O3	0.01	0.01	0.00
FeO	11.80	12.23	11.97	12.30	FeO	24.36	25.48	29.32
MnO	0.21	0.18	0.11	0.20	MnO	0.39	0.36	0.42
MgO	14.56	14.32	14.46	13.66	MgO	37.27	36.80	33.23
CaO	11.42	10.89	11.13	11.31	CaO	0.11	0.07	0.08
Na2O	2.40	2.46	2.59	2.64	Na2O	0.00	0.01	0.02
K2O	0.21	0.21	0.30	0.35	K2O	0.00	0.01	0.00
NiO	0.05	0.02	0.05	0.03	NiO	0.05	0.02	0.06
F	0.33	0.07	0.24	0.39				
Cl	0.03	0.02	0.03	0.26				
BaO	0.01	0.02	0.00	0.02				
Total	97.31	97.28	96.64	97.05	Total	100.01	100.30	99.58
Mg#	68.7	67.6	68.3	66.4	Fo	73.2	72.0	66.9
Si	6.46	6.36	6.23	6.20	Fa	26.8	28.0	33.1
Ti	0.25	0.24	0.16	0.29				
σ					*σ*			
SiO2	*1.007*	*0.625*	*0.199*	*0.130*	*SiO2*	*0.245*	*0.476*	
TiO2	*0.487*	*0.183*	*0.173*	*0.357*	*TiO2*	*0.007*	*0.000*	
Al2O3	*0.794*	*0.491*	*0.212*	*0.424*	*Al2O3*	*0.015*	*0.014*	
Cr2O3	*0.017*	*0.010*	*0.015*	*0.014*	*Cr2O3*	*0.008*	*0.005*	
FeO	*0.750*	*0.450*	*0.150*	*0.269*	*FeO*	*1.418*	*0.738*	
MnO	*0.049*	*0.066*	*0.024*	*0.059*	*MnO*	*0.027*	*0.035*	
MgO	*0.767*	*0.285*	*0.172*	*0.313*	*MgO*	*1.120*	*0.544*	
CaO	*0.512*	*0.176*	*0.248*	*0.050*	*CaO*	*0.033*	*0.056*	
Na2O	*0.277*	*0.215*	*0.138*	*0.109*	*Na2O*	*0.009*	*0.018*	
K2O	*0.031*	*0.097*	*0.070*	*0.031*	*K2O*	*0.004*	*0.008*	
NiO	*0.039*	*0.021*	*0.044*	*0.030*	*NiO*	*0.035*	*0.028*	
F	*0.196*	*0.078*	*0.119*	*0.176*				
Cl	*0.011*	*0.005*	*0.019*	*0.037*				
BaO	*0.017*	*0.034*	*0.000*	*0.030*				
Total	*0.392*	*0.454*	*0.344*	*0.166*	*Total*	*0.327*	*0.348*	
Mg#	*2.418*	*1.238*	*0.515*	*0.823*	*Fo*	*1.716*	*0.878*	
Si	*0.115*	*0.083*	*0.019*	*0.025*	*Fa*	*1.716*	*0.878*	
Ti	*0.055*	*0.019*	*0.019*	*0.041*				

III. 4.3 Thermometry and phase equilibrium modelling

III. 4.3.1 Thermometry

Fe-Mg exchange two-pyroxene thermometer from Wells (1977) has been applied to all the investigated samples containing both pyroxenes (3 metagabbronorites, 2 metanorites, 1 norite, 1 olivine-norite and 1 anorthosite; Table III.6). It yields a temperature range of 791-1006 °C ±70°C as mylonites and magmatic porphyric xenoliths display similar temperature ranges. The temperatures in metagabbro zone CAL29A were calculated with three clinopyroxene-orthopyroxene couples instead of mean compositions (T= 791, 901, 979 ±70°C; Table III.6). This approach was chosen due to significant variation in compositions observed in the minerals (Figs. III.5, 6), which would not have been accurately represented by a mean composition.

Moreover, the enstatite-in-clinopyroxene thermometer from Nimis & Taylor (2000) has been applied to the same samples and to the metagabbro zone CAL50B from the mylonite CAL50. It yields a temperature range of 944-1019 °C ±60 °C for the two-pyroxene samples also tested with Wells (1977) thermometer. The difference in calculated temperature between the two thermometers is included in their 2σ confidence indices as those differences range between 5 and 28 °C with a mean difference of 11 °C. The Nimis & Taylor (2000) thermometer yields a significantly lower temperature for the metagabbro zone CAL50B (448 °C ±60 °C) than other samples.

Table III.6: Results of Wells (1977) two-pyroxene and Nimis & Taylor (2000) clinopyroxene thermometers.

Group	Mylonites					Igneous rocks			
Sample	**CAL28 B**	**CAL29 A**	**CAL29 B**	**CAL50 A**	**CAL50 B**	**CL61**	**CAL5**	**CAL8**	**CAL41**
Rock type	MGn	MN	MGbn	MGbn	MGb	MN	N	Ol-N	An
T [Wells] ±70°C	980	791; 901; 979 (n=3)	960	1006		937	1003	972	988
T [NTcpx] ±60°C	987	944	965	1019	448	947	1014	977	999

III. 4.3.2 Phase equilibrium modelling

Phase equilibrium modelling has been applied to the two metagabbronorite ultramylonite zones CAL29B (in the sample CAL29) and CAL50A (in the sample CAL50), as the plagioclase-clinopyroxene-orthopyroxene main assemblage they display is the most representative of the mylonite xenoliths. It also has been applied to the metagabbro zone CAL50B in contact with CAL50A, in order to compare the P-T conditions differences

between the two zones with temperature differences yielded by conventional thermometry (Table III.6).

CAL29B. The metagabbronorite zone CAL29B contains 56.5 vol.% plagioclase which has a composition of An_{62-59}; 27 vol.% clinopyroxene which has a Mg# bracketed between 72 and 75 and an Al content of 0.07-0.08 p.f.u. Moreover, the sample contains 15 vol.% orthopyroxene which has a Mg# varying from 62 to 69 and an Al content of 0.05-0.07 p.f.u.

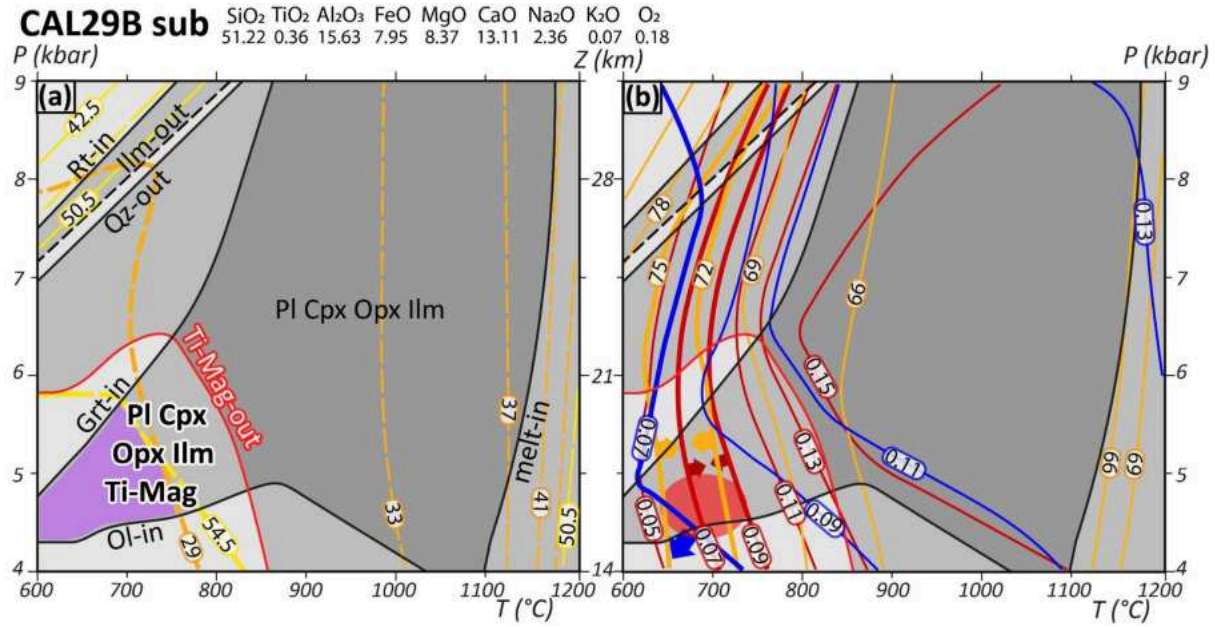


Fig. III.8. Isochemical phase diagrams computed for bulk-composition estimation of Calbuco mylonite xenoliths. (a) Stable assemblages and contoured modal proportions of clinopyroxene and plagioclase and (b) compositional isopleths of the metagabbronorite zone CAL29 B from the mylonite CAL29. (c) Stable assemblages and contoured modal proportions of clinopyroxene and orthopyroxene and (b) compositional isopleths of the metagabbronorite zone CAL50 A from the mylonite CAL50. (d) Stable assemblages and contoured modal proportions of clinopyroxene and orthopyroxene and (b) compositional isopleths of the metagabbro zone CAL50 B from the mylonite CAL50. Modal proportions are used with a range of ± 2 vol.% to constrain the P-T conditions while compositional isopleths take all the compositional variation of a phase within a sample. In each sample, some phase proportions and chemical composition are not contoured because they do not provide more precision to the P-T stability field determination, to make the figure more readable. Arrows helps to visualise the P-T domain constrained by compositional isopleths.

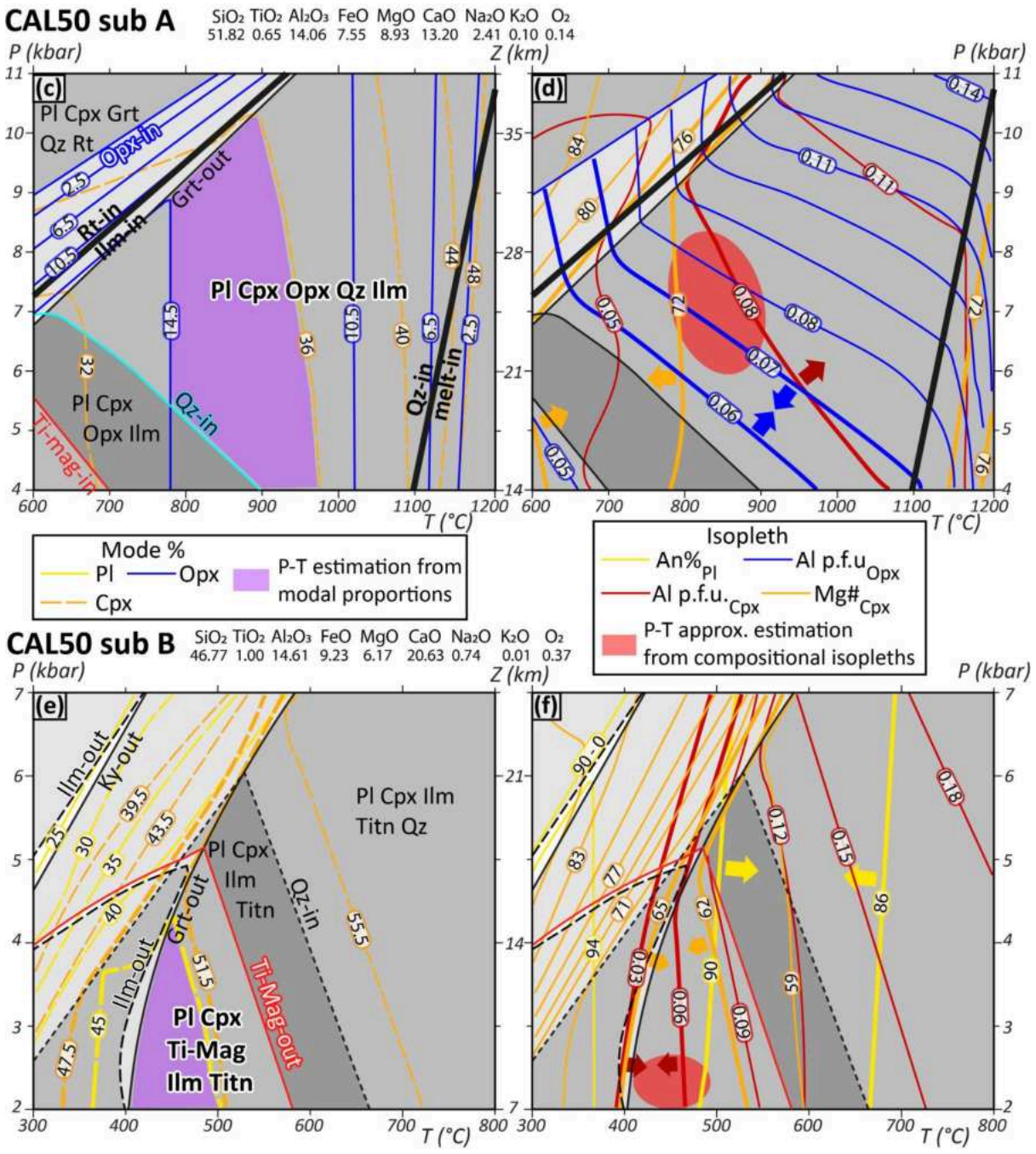


Fig. III.8. (continued).

The sample also hosts 1 vol.% titanomagnetite and trace ilmenite. The results of pseudosection modelling suggest that the plagioclase-clinopyroxene-orthopyroxene-ilmenite-titanomagnetite assemblage is stable at temperatures of 600-850 °C with pressures at 4.5-6 kbar (Fig. III.8a), however, plagioclase and clinopyroxene modal proportions (54.5-58.5 vol.% and 25-26 vol%, respectively) constrain the P-T conditions at 600-750 °C, 4.5-5.5 kbar. Modal proportions of the other

phases do not bring more constraints on the estimation of the P-T conditions. Moreover, representative isopleths of the clinopyroxene composition (Mg# 72-75; Al 0.07-0.09 p.f.u.) intersect at 670-720°C while the representative isopleth Al content in the orthopyroxene (0.05-0.07 p.f.u) suggesting pressures below 4.5 kbar (Fig. III.8b). The anorthite content in plagioclase and Mg# ratio in orthopyroxene do not bring more constraint on the estimation of the P-T conditions. Thus, the best fitting between compositional isopleths and the calculated stability field of the main assemblage define P-T conditions at 650-720 °C, 4.5-5 kbar (Fig. III.8b). Pseudosection was also calculated with the bulk-rock from the metagabbro zone CAL29A which yielded similar P-T ranges than metagabbronorite zone CAL29B.

CAL50A. The metagabbronorite zone CAL50A contains 52 vol.% plagioclase which has a composition of An_{58-53}; 34 vol.% clinopyroxene which has a Mg# bracketed between 72 and 76 and an Al content of 0.08-0.15 p.f.u. Moreover, the sample contains 12.5 vol.% orthopyroxene which has a Mg# varying from 65 to 69 and an Al content of 0.06-0.07 p.f.u. The sample also hosts 1 vol.% ilmenite, trace titanomagnetite and quartz. Pseudosection modelling indicates that quartz and titanomagnetite cannot coexist in the same stable assemblage (Fig. III.8c). Nevertheless, modal proportions of clinopyroxene (32-36 vol.%) and orthopyroxene (10.5-14.5 vol.%) suggest pressures and temperatures consistent with the plagioclase-clinopyroxene-orthopyroxene-ilmenite-quartz stable assemblage, at 4-10 kbar and 780-970 °C (Fig. III.8c). Plagioclase, ilmenite and quartz modal proportions do not bring better constraints on the estimation of the P-T conditions. Moreover, the representative isopleths of the clinopyroxene (Mg#: 72-76; Al: 0.08-0.15 p.f.u.) and orthopyroxene composition (Al: 0.06-0.07) are near to intersect at pressures of 6-8 kbar and temperatures of 800-920 °C (Fig. III.8d). The anorthite content in plagioclase and Mg# ratio in orthopyroxene does not bring better constraints on the estimation of the P-T conditions.

CAL50B. The metagabbro zone CAL50B contains 48 vol.% plagioclase which has a composition of An_{90-87}; 49.5 vol.% clinopyroxene which has a Mg# of 63-64 and an Al content of 0.03-0.05 p.f.u. The sample also hosts 2 vol.% titanomagnetite, trace ilmenite and titanite. Results of pseudosection modelling indicate that the plagioclase-clinopyroxene-titanomagnetite-ilmenite-titanite assemblage is stable at temperatures of 400-580 °C with pressures <5 kbar (Fig. III.8e); however, plagioclase and clinopyroxene modal proportions (45-50 vol.% and 47.5-51.5 vol%, respectively) constrain the P-T conditions at 400-500 °C, <4 kbar. Moreover, the representative isopleths of the clinopyroxene (Mg#: 62-65; Al: 0.03-0.05 p.f.u.) and plagioclase composition (Al: 0.06-0.07)

are near to intersect at temperatures of 420-550 °C and pressures <2.5 kbar (Fig. III.8f). Thus, the best fitting between compositional isopleths and the calculated stability field of the main assemblage suggest low-pressure conditions below 2.5 kbar and temperatures of 420-500 °C (Fig. III.8f).

III. 4.4 Microstructures

III. 4.4.1 Mylonite crystal preferred orientation (CPO)

Pyroxenes. The mylonites CAL29A and B, CAL28A and CAL50A display medium to strong clinopyroxene and orthopyroxene CPO patterns, as indicated by clinopyroxene J-index (2.61-6.63) and M-index (0.074-0.193), as well as orthopyroxene J-index (3.01-6.28) and M-index (0.153-0.285; Fig. III.9). However, the metagabbroic zone CAL50B, clinopyroxene display a weak CPO pattern (J-index 1.20; M-index 0.005). In the metagabbro zone CAL29A and the metagabbronorite zone CAL29B, both clinopyroxene and orthopyroxene display a concentration point on [100] axes parallel to Z, and [001] axes form maximum concentration point parallel to X (Fig. III.9). [010] axes display a weak concentration point parallel to Y. In the metanorite zone CAL28A and the metagabbronorite zone CAL50A, both clinopyroxene and orthopyroxene display a concentration point on [001] axes parallel to X, while both [100] and [010] axes form a girdle in the XZ plane (Fig. III.9). Orthopyroxene in CAL50A zone are small grains located either at the contact with clinopyroxene and are often included in the clinopyroxene and display an elongated shape (Fig. III.10). A comparison of the CPO for three clinopyroxene-orthopyroxene couples reveals that the variation of orientation within a couple is about less than 1° on [100] and [010] axes and around 5° on the [001] axis (Fig. III.10b). Finally, clinopyroxene from the metagabbro zone CAL50B displays a weak concentration point on [001] axes parallel to X (Fig. III.9). [100] axes form a weak girdle in the YZ plane and [010] axes are randomly distributed.

Pyroxenes from the gabbronorite zone CAL28B, showing a magmatic texture, display in the mean orientation maps different patches of the same colour (same orientation), which correspond to large crystals of pyroxenes (Fig. III.11). This is also observed in the mean orientation map of amphiboles. The apparent small grain sizes is not related to a mylonitic texture, but to a magmatic, probably reactional texture. he comparison of the CPO in four amphibole-two-pyroxenes assemblage reveals that the variation in orientation between minerals is about 1° on the [100] and [010] axes and around 10° on the [001] axis between

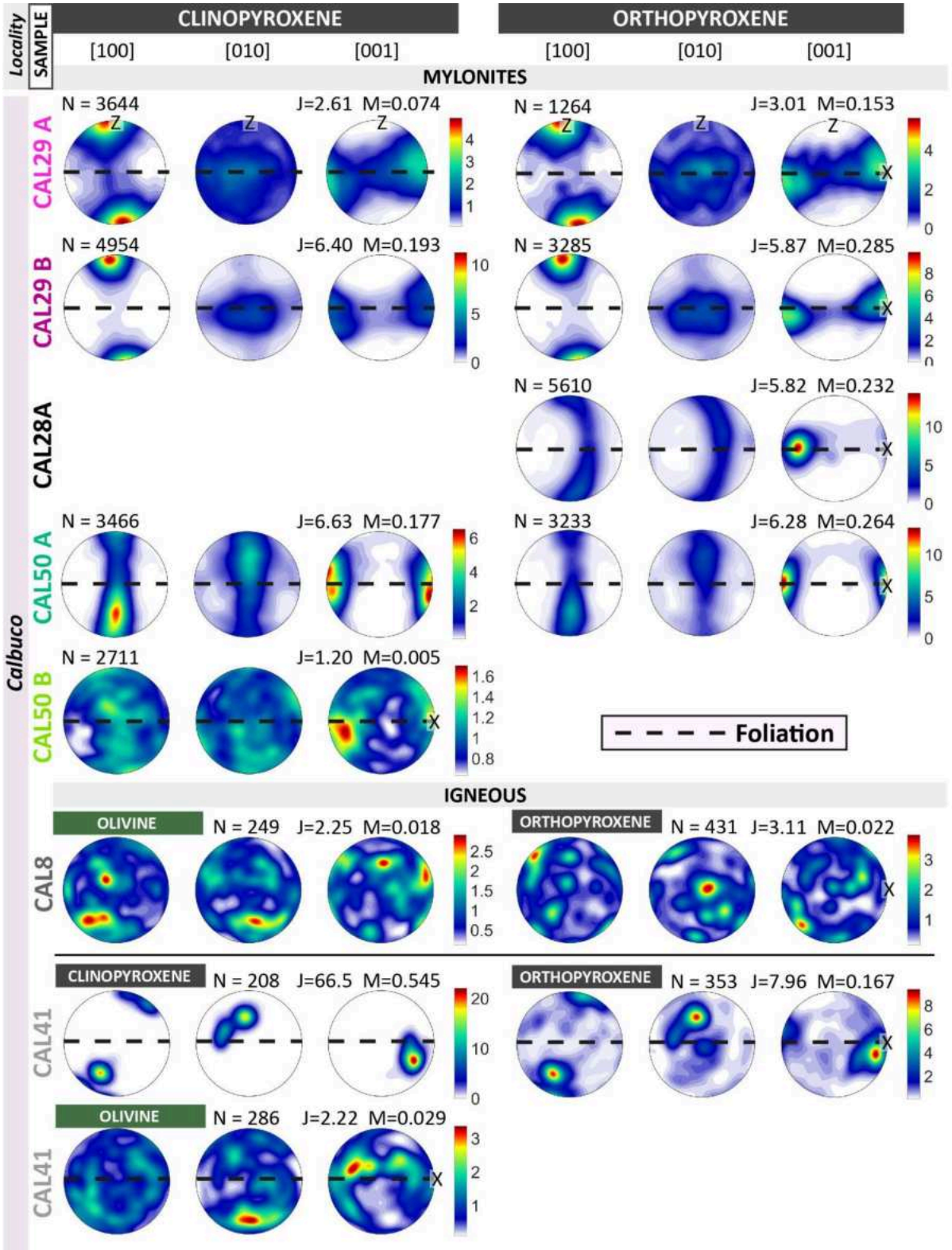


Fig. III.9. Crystallographic preferred orientation of clinopyroxene, orthopyroxene and olivine of analysed mylonites and igneous xenoliths. When detected, compositional layering is tagged and pole figures are rotated as the layering parallel to the XY plane. N is the number of grains and the strength is represented by J-index and M-index. The rainbow scale represents the mud (multiply uniform density).

the amphibole and the clinopyroxene, while the orthopyroxene displays a mean orientation between the two others phases (Fig. III.11b).

Plagioclase. All the investigated mylonites display weak plagioclase CPO patterns (J-index: 1.37-2.00; M-index: 0.018-0.047; Fig. III.12a). In both metagabbro zone CAL29A and metagabbronorite zone CAL29B, plagioclase has random orientations (Fig. III.12a). In the metanorite zone CAL28A and metagabbronorite zone CAL50A, [001] axes of the plagioclase form a girdle in the XZ plane with a maximum concentration point sub-parallel to Z (Fig. III.12a). Moreover, [100] axes in CAL28A zone display a weak girdle in the XY plane. Finally, plagioclase from the metagabbro zone CAL50B displays [100] axes that form a girdle in the YZ plane and random orientations on both [010] and [001] axes (Fig. III.12a).

III. 4.4.2 Igneous rocks CPO

The two investigated igneous xenoliths CAL8 and CAL41 display distinct CPO (Figs. III.9). The olivine-norite CAL8 displays random CPO patterns on the orthopyroxene (J-index 3.11; M-index 0.022), the olivine (J-index 2.25; M-index 0.018) and the plagioclase (J-index 3.81; M-index 0.011; Figs. III.9, 12a). No shape-preferred orientation has been detected in this sample and no clear correlation can be made between the CPO of the minerals. The mean orientation maps reveal that the sample contains only a few large orthopyroxene grains which are cartographically separated on small grains and correspond to a poecilitic grains (Fig. III.13a).

In contrast, the anorthosite CAL41 displays strong CPO patterns on the clinopyroxene (J-index 66.5; M-index 0.545), orthopyroxene (J-index 7.96; M-index 0.167) and weak CPO patterns on olivine (J-index 2.22; M-index 0.029) and plagioclase (J-index 2.05; M-index 0.052; Figs. III.9, 12a). In this sample, clinopyroxene corresponds to large grains which are texturally dispatched in the texture as poikilitic grains (Fig. III.13.e) and show only three point concentrations (three grains) in the CPO with remarkably similar orientations (Fig. III.9). The three grains have their [001] axes sub-parallel to X, and [100] axes sub-parallel to Z (Fig. III.9). It is worth noting that this texture is similar to the texture observed for orthopyroxene in the olivine-norite CAL 8 (Fig. III.13e). In this sample, the orthopyroxene grains located near the clinopyroxene and forming aggregates, display weaker but similar CPO to clinopyroxene. The olivine displays a concentration point on [010] axes parallel to Z, and a point concentration on [001] axes sub-parallel to X (Fig. III.9). The crystallographic orientations of olivine and pyroxene are mostly discordant. Finally, the plagioclase displays a

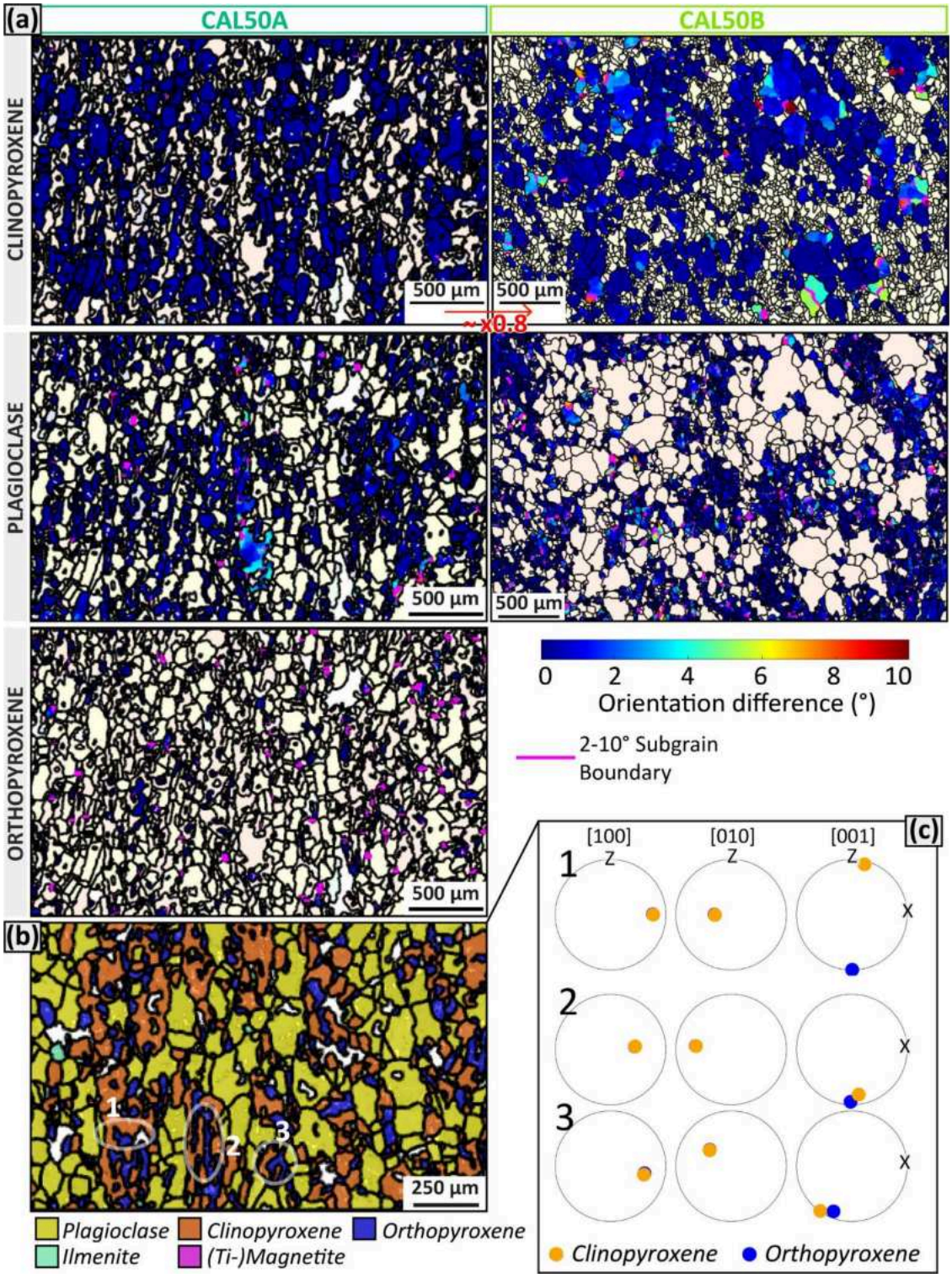


Fig. III.10. (a) Maps of intragranular deformation relative to the mean orientation of clinopyroxene, plagioclase and orthopyroxene grains of the metagabbronorite zone CAL50 A and the metagabbro zone CAL50 B from the mylonite CAL50. Light blue grains are orthopyroxene, light orange is for clinopyroxene and light yellow is for plagioclase. (b) Phase map of the zone CAL50 A. (c) CPO of clinopyroxene and orthopyroxene in the three encircled areas in (b). For each area, one grain of the two phases has been plotted.

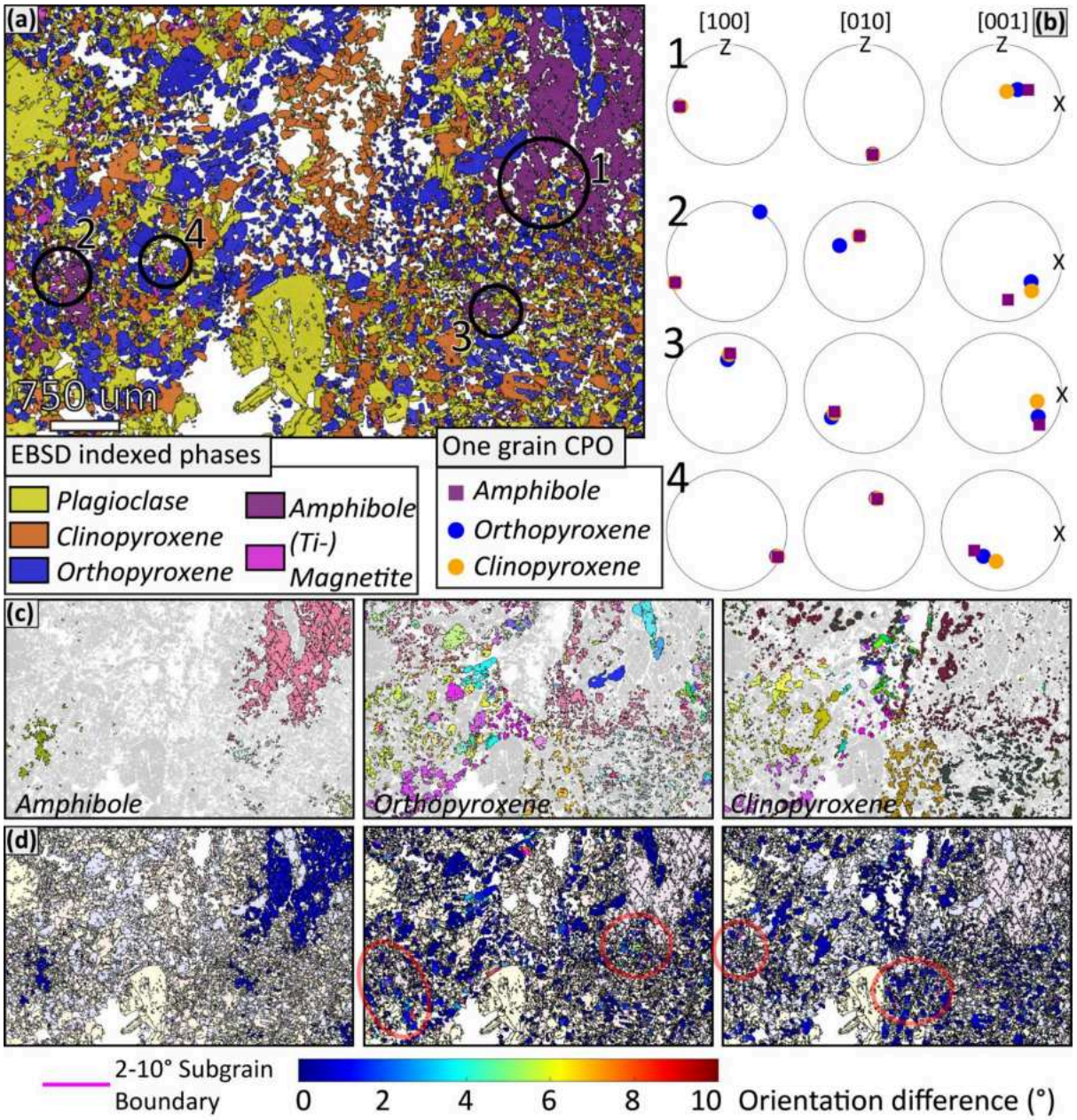


Fig. III.11. CPO relationships of growing amphibole regarding clinopyroxene and orthopyroxene in the sample CAL28B. (a) Phase map. (b) CPO of amphibole, clinopyroxene and orthopyroxene in the four selected areas. For each area, one grain of the three phases has been plotted. (c) Phases mean orientation. Colour suggests how close is the orientation of two different grains of the same phase. Nevertheless, it has no significance between different phases and has no referential. (d) Maps of intragranular deformation relative to the mean orientation of the grains. Red circles highlight zones where pyroxenes oikocrysts display intragranular deformation.

concentration point on [010] axes parallel to Z, as [100] axes form a girdle in the XZ plane and [001] axes have random orientations (Fig. III.12a).

III. 4.4.3 Intragranular deformation

Intragranular deformation maps. In all the mylonites, intragranular deformation of clinopyroxene, orthopyroxene, plagioclase and olivine is rather weak, as it affects the surface of those phases from 3 to 35 % (Figs. III.10, 13-15). The amphibole occurring in both zones of the mylonite CAL28As well as in the olivine-norite CAL8 does not display any intragranular deformation (Fig. III.11). For all the phases, subgrain boundaries are rare in both mylonites and igneous rock. In the igneous xenoliths, plagioclase displays numerous albite and Carlsbad twin grain boundaries (Fig. III.13c).

Clinopyroxene in the metagabbro zone CAL50B from sample CAL50 displays higher intragranular deformation than in the metagabbronorite zone CAL50A and displays grain-cross-cutting subgrain boundaries (Figs. III.10a, 14c). In the same way, plagioclase intragranular deformation looks slightly more intense in the CAL50B zone than in the CAL50A zone. The clinopyroxene in the anorthosite CAL41 with an igneous texture displays higher intragranular deformation than the rest of the suite (56 % of the clinopyroxene surface is affected by misorientations >1°; Fig. III.14b), and displays many conic subgrain boundaries that form on the grain tips (Fig. III.13f). Finally, in the mylonite CAL29, plagioclase intragranular deformation is stronger in the plagioclase enriched layer from the polycrystal sigmoids (35% of plagioclase surface affected by misorientations >1° in the CAL29A zone) than in the rest of the sample (5% of plagioclase surface in the CAL29B zone; Figs. III.14b, 15).

Misorientation axes at low angle boundaries or subgrain boundaries. Clinopyroxene misorientation axes at low angle boundaries are weakly distributed around [010], [100] and [-100] axes in the metagabbro zone CAL29A from the ultra-mylonite CAL29A and only around the [010] axis in the metagabbronorite zone CAL29B (Fig. III.12b). In the metagabbronorite zone CAL50A from the sample CAL50, clinopyroxene misorientation axes at low angle boundaries are distributed around [001], [010] and [100] axes whereas their distribution is scarce in the metagabbro zone CAL50B from the same sample. In the anorthosite CAL41, they are distributed around both [010] and [001] axes (Fig. III.12b).

Orthopyroxene misorientation axes at low angle boundaries are distributed around the [010] axis and weakly around the [001] axis in the ultra-mylonites CAL29A and CAL50A and weakly around the [010] axis in the anorthosite CAL41 (Fig. III.12b). In contrast, misorientation axes are distributed around the [100] axis in the metanorite zone CAL28A and around the [001] axis in the olivine-norite CAL8.

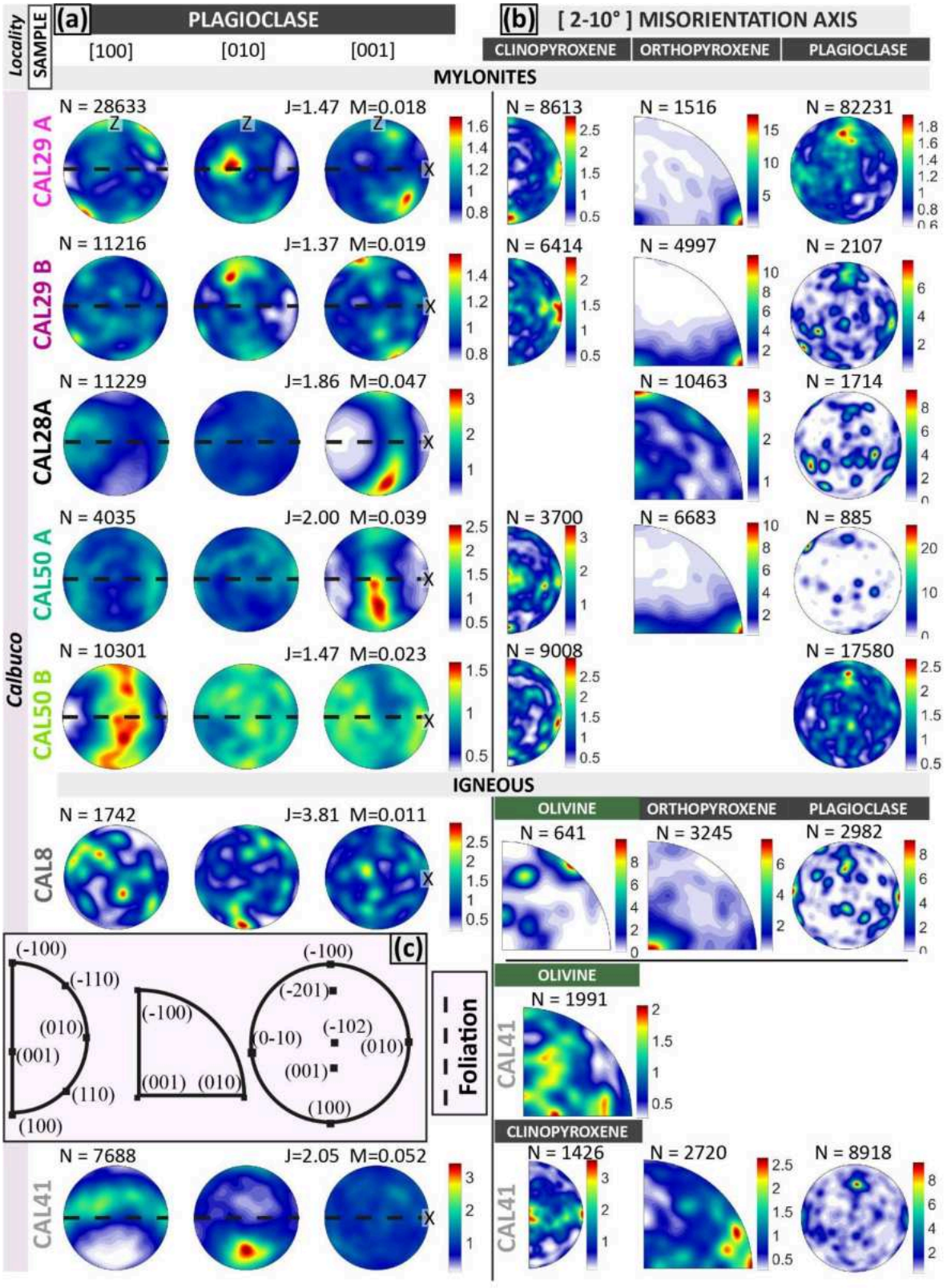


Fig. III.12. (a) Crystallographic preferred orientation of plagioclase. N is the number of grains, the strength is represented by J-index and M-index. (b) Rotation axes accommodating low angle (2-10°) misorientations in clinopyroxene, orthopyroxene, plagioclase and olivine grains. Data is represented in inverse pole figures where the legend can be found in (c). N is the number of pixels plotted.

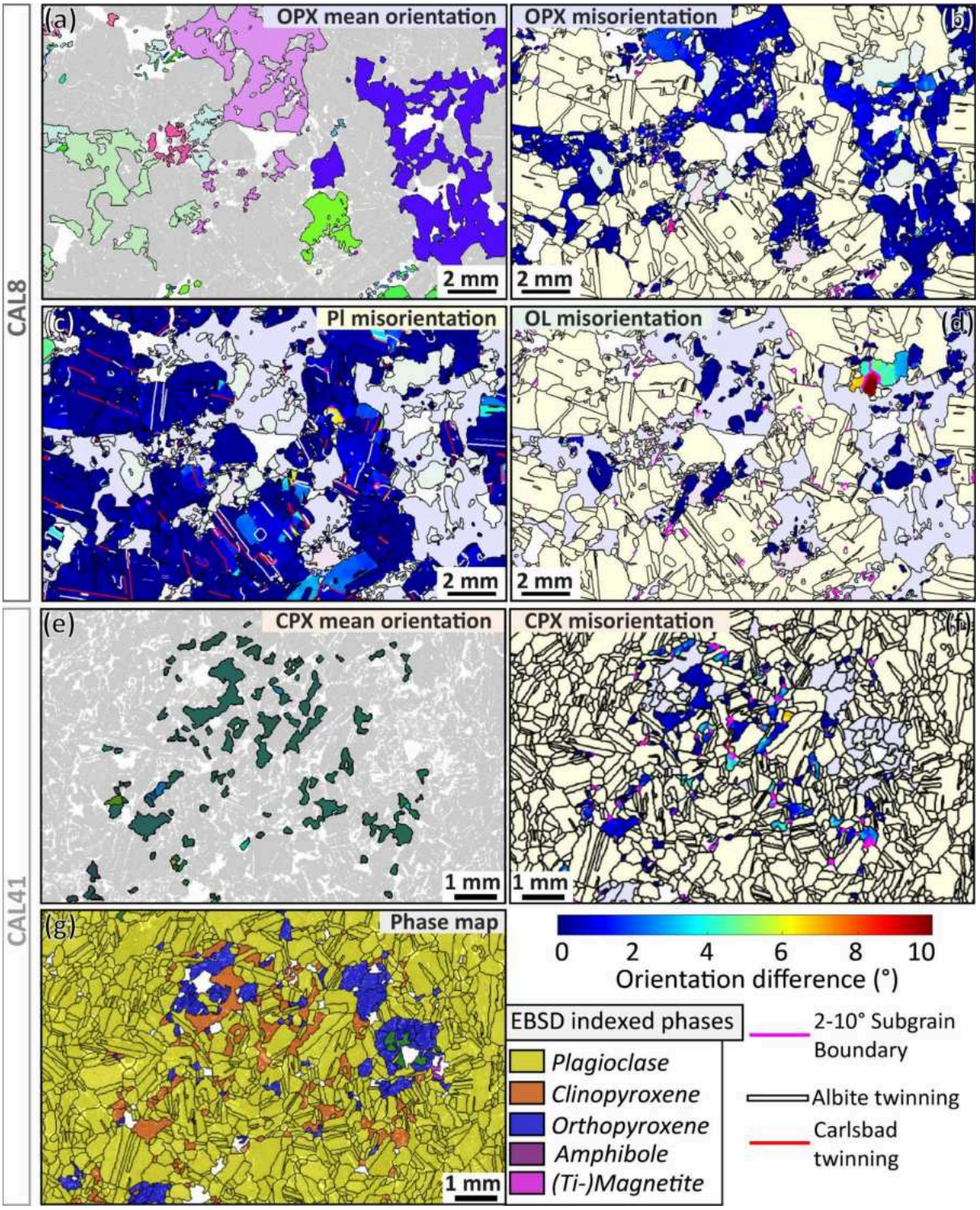


Fig. III.13. Magmatic porphyric xenolith maps (a) Orthopyroxene mean orientation in the sample CAL8. Colour suggests how close is the orientation of two different grains of the same phase. Nevertheless, it has no significance between different phases and has no referential. (b, c, d) Intragranular deformation relative to the mean orientation of orthopyroxene, plagioclase and olivine grains of sample CAL8. Light blue grains are orthopyroxene, light green is for olivine and light yellow is for plagioclase. (e, f) Clinopyroxene mean orientation and intragranular deformation in the sample CAL41. (g) Phase map of the sample CAL41.

Plagioclase misorientation axes at low angle boundaries or subgrain boundaries display a scarce distribution in all the investigated samples, with a weak maximum distribution around the [-201] axis (m.u.d. <2) in the metagabbro zone CAL29A, and distribution around [-201], [010] and [1-10] axes in the metagabbronorite zone CAL29B (Fig. III.12b). The crystallographic planes (100) and (-201) are crystallographically very close and could be considered as similar orientations. As a consequence, both corresponding misorientation axes will be discussed as [100] (e.g. Allard *et al.*, 2021). In the metagabbronorite CAL50A, rare misorientation axes (n= 885) are distributed around the [-1-10] axis, whereas they are distributed around the [-201] axis in the metagabbro zone CAL50B. In the magmatic porphyric xenoliths CAL8 and CAL41, they are distributed around [-201], [0-10] and [010] axes (Fig. III.12b). In the metagabbronorite CAL28A, plagioclase misorientation axes display a random distribution.

III. 5 DISCUSSION

III. 5.1 Pressure-temperature estimations

Both conventional thermometry and pseudosection calculations indicated a wide pressure and temperature range throughout the xenolith suite, ranging from 420 °C and <2.5 kbar to 1019 °C and 8 kbar. Similar variability (540 and 1020 °C) was observed by Hickey Vargas *et al.* (1995) in their Calbuco xenolith suite, which contained mylonites (referred to as granulites in their article) and gabbros. They calculated equilibrium temperature between 540 and 1020 °C. Equilibrium pressures of 6-8 kbar were determined using amphibole barometers; thus, these were not applied to amphibole-free samples.

Thermometers and pseudosection calculation provided similar equilibrium temperatures for the metagabbro zone CAL50B (420-500°C). However, there were discrepancies between thermometry and pseudosection calculation for the metagabbronorite zone CAL50A (1006-1019 °C vs. 800-920 °C, respectively) and CAL29B (960-965 °C vs. 670-720 °C, respectively; Fig. III.8; Table III.6). This discrepancy complicates the interpretation of the P-T calculations. While compositional isopleths might be less reliable when using pseudosection for P-T estimations, calculated stable assemblages and phase modal proportions are generally more robust. For instance, the presence of titanomagnetite (1 vol.%) in the metagabbronorite zone CAL29B is stable for the given bulk-rock composition only below 6 kbar and 850 °C. These conditions fall outside the confidence range of Wells

(1977) and Nimis & Taylor (2000) thermometers. It is plausible that these results reflect different metamorphic events. For instance, during a temperature decrease, Fe-Mg exchange between pyroxenes could become fixed due to reduced diffusion efficiency in pyroxenes.

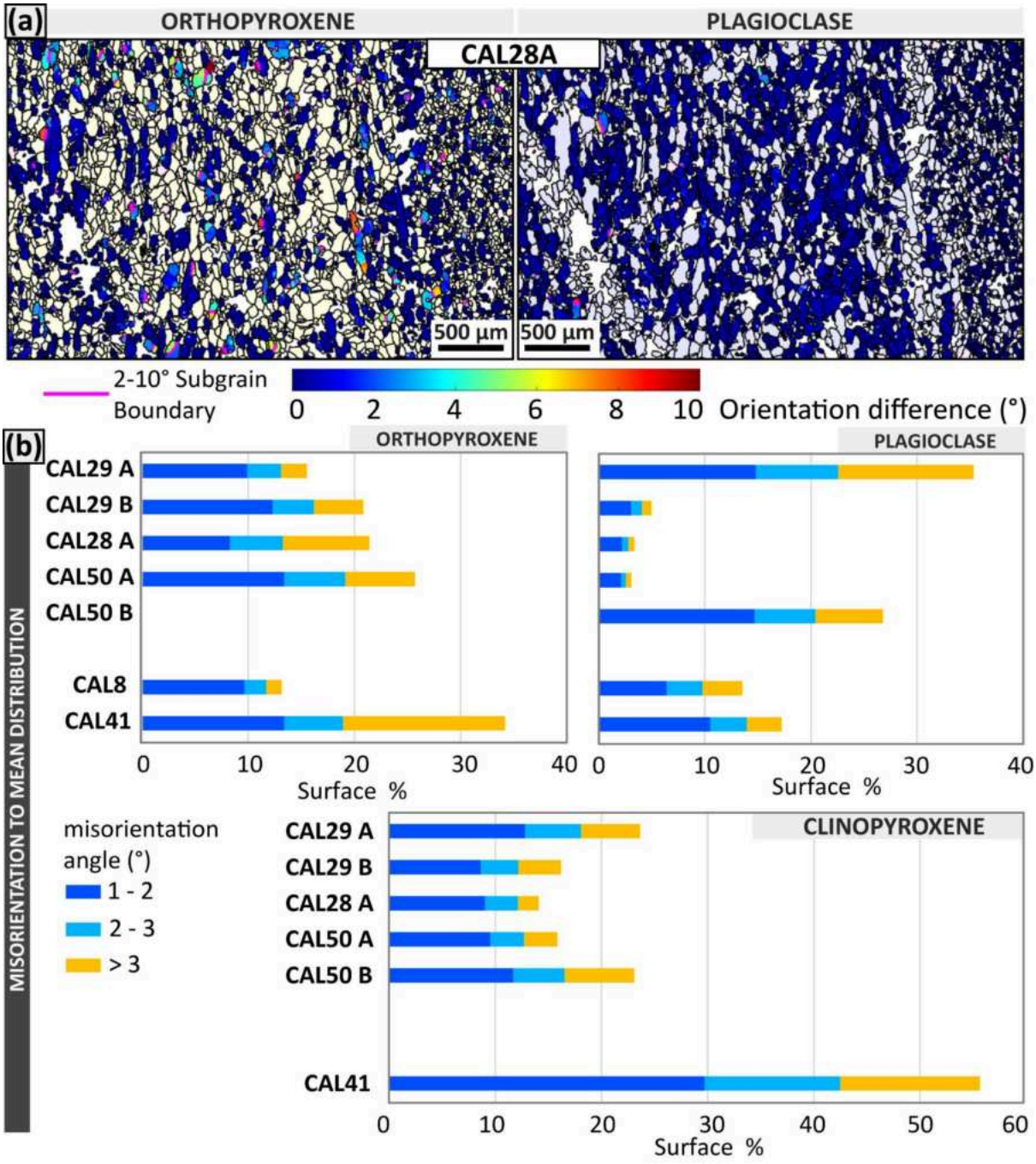


Fig. III.14. (a) Maps of intragranular deformation relative to the mean orientation of orthopyroxene and plagioclase grains of the ultra-mylonite zone CAL28A from sample CAL28. Light blue grains are orthopyroxene and light yellow is for plagioclase. (b) Normalized histograms representing orthopyroxene, plagioclase and clinopyroxene surface proportions of Calbuco xenoliths vs. misorientation angles (>1°) relative to mean grain orientations.

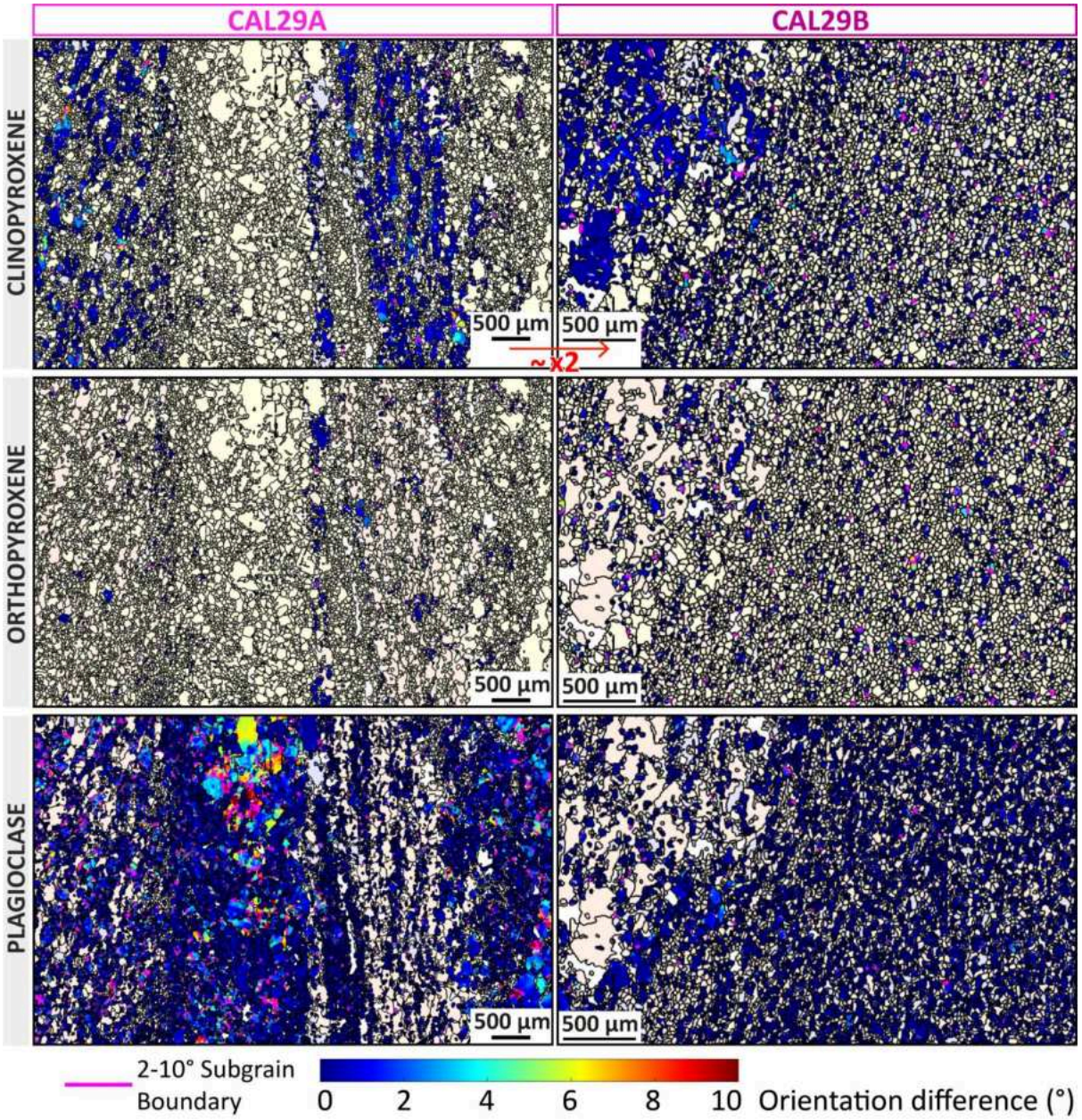


Fig. III.15. Maps of intragranular deformation relative to the mean orientation of clinopyroxene, orthopyroxene and plagioclase grains of the metagabbro zone CAL29 A and the metagabbronorite zone CAL29 B from the ultra-mylonite CAL29. Light blue grains are orthopyroxene, light orange is for clinopyroxene and light yellow is for plagioclase.

Simultaneously, certain metamorphic reactions and lower-temperature assemblages may develop.

Surprisingly, pseudosection calculations revealed significant temperature differences between the metagabbro zone CAL50B and the metagabbronorite zone CAL50A within the same thin section (Fig. III.2d-f). The calculated P-T conditions for CAL50B were 420-500 °C and <2.5 kbar, whereas for CAL50A, they were 800-920 °C and 6-8 kbar (Fig. III.8). The

Nimis & Taylor (2000) thermometer corroborates this trend, yielding temperatures of 448 °C for CAL50B and 1019 °C for CAL50A. Although the Nimis & Taylor (2000) thermometer was initially developed for garnet-peridotites, Purtika (2008) tested it on magmatic rocks and validated its applicability. Moreover, the temperature differences obtained from both the Wells (1977) and Nimis & Taylor (2000) thermometers are minimal (mean difference of 11 °C; Table III.6) and well within their confidence intervals (60-70 °C), reinforcing the reliability of the temperatures inferred from Nimis & Taylor (2000) thermometer. Thus, the jump in temperatures (~ 400°C) and pressure (~ 5 Kbar) recorded in the mylonite CAL50, at the scale of the centimetre, can be considered robust and will be discussed later.

III. 5.2 Crystallisation sequence

The gabbronorite zone CAL28B displays patches of clinopyroxene-orthopyroxene-amphibole with precisely the same orientations of both [100] and [010] axes, and slight orientation differences (<10°) on the [001] axis (Fig. III.11). This characteristic is also observed in the metagabbronorite zone CAL50A, where long inclusions of orthopyroxene within clinopyroxene grains share identical CPO (Fig. III.10), suggesting intergrowth of these phases. The orientation difference on the [001] axis reflects the symmetry variations between clinopyroxene, orthopyroxene and amphibole in CAL28B zone. In the crystallisation sequence of arc-type magmas, clinopyroxene is one of the first phases to crystallise, whereas orthopyroxene forms later (i.e. at lower temperatures), regardless of the pressure and the H_2O content of the melt (Pichavant *et al.*, 2002; Blatter *et al.*, 2013). We propose that in both zones CAL50A and CAL28B, orthopyroxene grows at the expense of clinopyroxene, indicating a temperature decrease.

In the hybrid xenolith CAL28 formed by a mylonitic texture (CAL28A) is cross-cuted by an magmatic porphyric texture (CAL28B), millimetric-grained amphibole is associated with micrometric grains of plagioclase and pyroxenes and occurs in both mylonite and magmatic porphyric zones, sometimes crossing both zones (Figs. III.3a, c, 11). Consequently, its crystallisation can reasonably be interpreted as late poikiloblasts. In the gabbronorite zone CAL28B, the growth of amphibole, subsequent to orthopyroxene growth, can be explained by the passage of a hydrated melt in the rock. However, studies by Pichavant *et al.* (2002) and Blatter *et al.* (2013) indicate that amphibole can crystallise during magma cooling after orthopyroxene without changing the magma composition (for H_2O=2 wt% from Blatter *et al.*, 2013; H_2O=5-6 wt% from Pichavant *et al.*, 2002). Hence, the texture of orthopyroxene and

amphibole assemblage in the hybrid xenolith CAL28 could correspond to a temperature decrease after the percolation of a hydrated magma. The crystallisation of both phases may not be necessary for two different magma percolation stages. Finally, the tardive black breakdown rims of the amphibole observed in most amphibole-bearing samples are related to the amphibole dehydration melting reaction during the ascent of the xenolith within the magma (Hickey-Vargas *et al.*, 1995; Horst, 2007; Fig. III.4e).

In the olivine-norite CAL8, orthopyroxene, which occurs as centimetric grains interconnected between plagioclase and olivine, corresponds to oikocrysts that seem to have crystallised lately in a highly porous plagioclase-olivine assemblage because orthopyroxene oikocrysts extend over 20 vol.% (Figs. III.4a, 13). Olivine replacement by orthopyroxene is typical during the crystallisation sequences of arc-basalts (Blatter *et al.*, 2013). Similarly, clinopyroxene in the anorthosite CAL41 displays the same texture as orthopyroxene from sample CAL8, even if it occurs in low proportions (2.6 vol.%; Fig. III.13).

III. 5.3 Deformation recorded by the lower crust

III. 5.3.1 Mylonites and ultramylonites

High temperature deformation. In the ultra-mylonite CAL29A, plagioclase sigmoids display significant intragranular deformation and subgrain boundaries compared to plagioclase in other mylonites and from CAL29B, suggesting their origin as porphyroclasts within a zone undergoing strong deformation (Figs. III.2a, b, 15). In this sample, the plagioclase CPO are almost random and the weak point concentrations are discordant to the lineation (J-index 1.47; Fig. III.12a). To assess the plastic deformation recorded by minerals through dislocation creep and to identify the activated slip systems, misorientation axes are useful indicators and must be compared to CPO. In this sample, low angle misorientation axes of plagioclase display a weak point concentration on [100] axes, suggesting the activation of the [001](010) slip system (Kruse *et al.* 2001; van der Werf *et al.*, 2017; Allard *et al.*, 2021; Fig. III.12b). This difference between CPO and misorientation axes could suggest that the plagioclase CPO is the remnant of primary crystallisation and the deformation is recorded by the misorientations. Additionally, orthopyroxenes from the ultra-mylonite CAL29 display a [001](100) pattern (known as AC-type; Jung *et al.*, 2010) and clinopyroxene also has a [001](100) CPO pattern. The misorientation axes of orthopyroxene indicate the activation of [001](100) slip-system (Figs. III.12) which is coherent with the CPO. However, the strength of the fabric in CAL29A is weaker than in

CAL29B and at the opposite, the point concentration of the misorientation axes and the internal deformation of orthopyroxene is stronger in CAL29A than in CAL29B (Figs. III.9, 12, 15). This suggests that the internal deformation partially erased the CPO patterns. Theorthopyroxene [001](010) slip system inferred from the misorientation axes is the most common slip system observed in both naturally and experimentally deformed orthopyroxene (e.g. Ross & Nielsen, 1978; Sawaguchi & Ishii, 2003; Manthilake *et al.*, 2013; Bernard *et al.*, 2021). The activation of the clinopyroxene [001](010) slip system has been described as the dominant slip system at 800-1000°C (Raterron *et al.*, 1994; Amiguet, 2009; Wang *et al.*, 2012). Both clinopyroxene and orthopyroxene indicate deformation under high-temperature, high strain conditions.

In the metanorite ultra-mylonitic zone CAL28A, the orthopyroxene displays a [001]-fiber CPO (known as ABC-type; Jung *et al.*, 2010; Fig. III.9), which suggests the predominance of the [001] glide. Jung *et al.* (2010) reported this CPO in mantle xenoliths with a porphyroclastic texture containing a large proportion of orthopyroxene (17 %), and they suggest the combined activation of both (100)[001] and (010)[001] slip systems. The orthopyroxene misorientations at low-angle boundaries or subgrain boundaries in this sample (CAL28A), are parallel to the [100] axis, suggesting the prevalence of [001](010) slip system (BC-type; Fig. III.12b). This slip system is suggested to be activated in the ABC-type, and is less common in naturally and experimentally deformed orthopyroxene (Toy *et al.*, 2010; Manthilake *et al.*, 2013; Bernard *et al.*, 2021). The occurrence of [001](010) slip system in natural and experimentally specimen have been related to potentially important strain rates (Mercier & Nicolas, 1975; Ross & Nielsen, 1978; Nicolas & Christensen, 1987; Soustelle *et al.*, 2010; Frets *et al.*, 2012) and moderate water content (Manthilake *et al.*, 2013). Therefore, the orthopyroxene CPO may be related to both expression [001](010) slip system and the classically observed (100)[001] slip-system, indicative of high strain conditions and high temperature conditions.

The metagabbronorite ultra-mylonitic zone CAL50A displays both clinopyroxene and orthopyroxene similar CPO patterns which correspond to a [001]-fibre CPO (similar to orthopyroxene in sample CAL28A). Contrary to the sample CAL28A, the orthopyroxene misorientation axes plot around [010] suggesting the activation of the [001](100) slip system (Figs. III.9, 12), as it has been reported in sample CAL29 and the strength of the concentration point is similar to CAL29B, as the orthopyroxene is weakly or undeformed

(Figs. III.9, 10, 12). This sample CAL50A records a similar clinopyroxene and orthopyroxene deformation history than CAL29A at similar temperatures (Table III.6).

High to low temperature deformation. In the metagabbro zone CAL50B, with an estimated temperature at 420-500°C, clinopyroxene and plagioclase display close-to-random CPO patterns (J-index 1.20 and 2.00, respectively Figs. III.9, 12a). Nevertheless, intragranular deformation in clinopyroxene is well pronounced compared to other mylonites and strength of point concentration of misorientation axes is similar to samples CAL29A with a point concentration on [010] axes suggesting the activation of (100)[001] slip system (Fig. III.10a, 14). Moreover, plagioclase displays misorientations along the [100] axis that can be interpreted as the activation of the [001](010) slip system (van der Werf et al., 2017; Allard *et al.*, 2021), as observed in plagioclase sigmoids from the metagabbro zone CAL29A (Fig. III.12b). Although the grain size of this sample is within the range typical of matrix ultra-mylonite grain size (300 - 700 µm), it remains larger than in other ultra-mylonite samples, which have a matrix grain size ranging between 20 and 300 µm (Figs. III.2, 3), this could represent a late growth and/or partial re-equilibration of the clinopyroxene. Both clinopyroxene and plagioclase CPO are weaker than in other ultra-mylonite, with a strong girdle on [100] axes of the plagiolcase. Overall, the metagabbro zone CAL50B recorded significantly different deformation conditions recorded at lower temperature (clear different clinopyroxene compositions between CAL50A and B, see next section) compared to other mylonite samples, including the metagabbronorite zone CAL50A, in direct contact with the CAL50B zone.

III. 5.3.2 Magmatic porphyric xenolith fabrics

In the magmatic porphyric xenoliths, plagioclase grains are automorphic and display numerous albite and Carlsbad twinning, along with pyroxene oikocrysts (Fig. III.13). These features reflect the cumulative environment of these samples and have not undergone re-equilibration by dislocation creep mechanisms, such as grain boundary migration or the formation of 120° triple junctions. The CPO in the olivine-norite CAL8 is rather random. In contrast, the anorthosite CAL41 displays a plagioclase (010)-fibre CPO, defining the foliation plane. Similar patterns have been reported in plagioclase-bearing cumulates (e.g. Satsukawa *et al.*, 2013; Figs. III.9, 12a). Additionally, two-pyroxenes in this sample display a [001]-fibre CPO which may define their crystallisation direction.

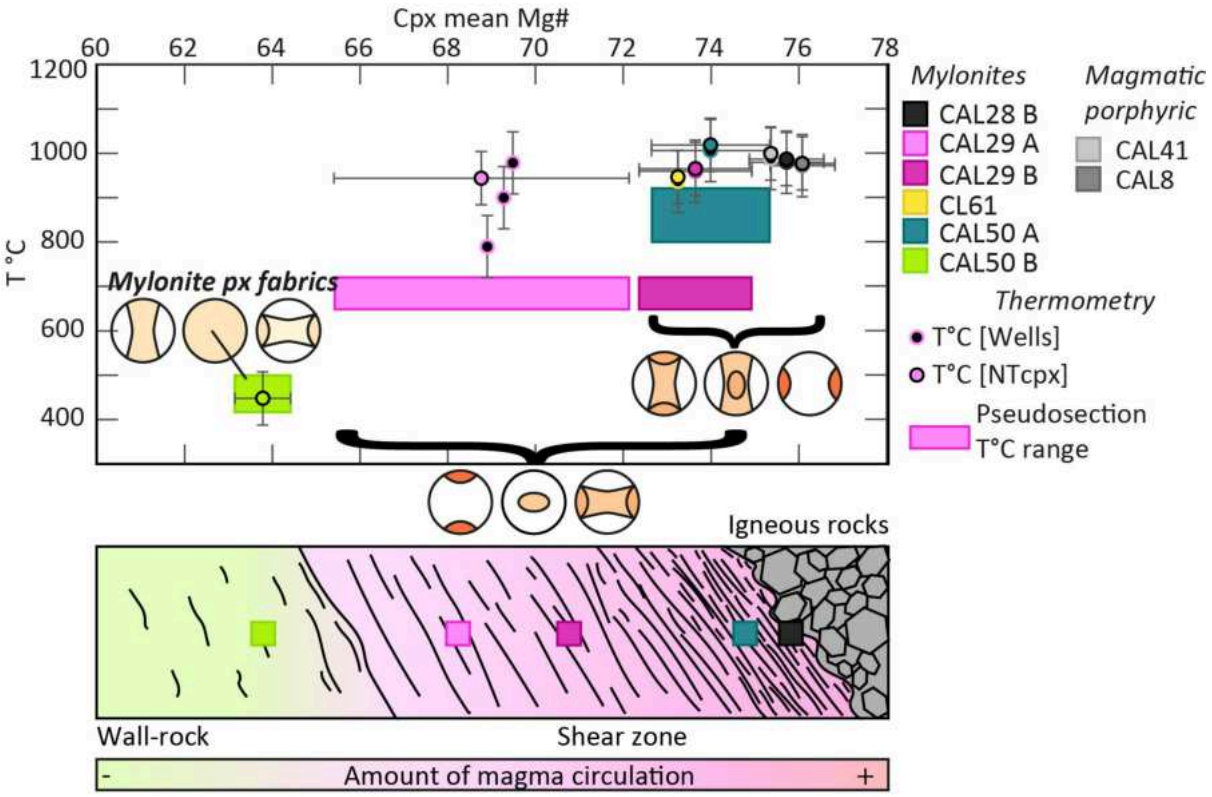


Fig. III.16. Summary of observations from Calbuco xenoliths. Diagram of calculated equilibrium temperatures vs. clinopyroxene Mg#. Error bars are uncertainties of thermometers and standard deviations of mean Mg#, respectively. In the middle, mylonite clinopyroxene fabrics are represented following the Mg# trend. At the bottom, conceptual drawing of different contact between wall-rock, deformation zone and crystallising magma below the Calbuco volcano.

III. 5.4 A temporal model of crystallisation and deformation of Calbuco xenoliths

This Chapter described the chemical, microstructures and P-T estimation heterogeneities recorded throughout the mylonite xenoliths suite. The Mg#, Al_2O_3 and TiO_2 contents in clinopyroxene are positively correlated overall (Fig. III.5). The metagabbronorite zone CAL50A, record the highest equilibration temperature (up to 1019°C, Table III.6), displays the highest clinopyroxene Mg# (73-77), Al_2O_3 (2.0-3.3 wt%) and TiO_2 contents (0.6-1.0 wt%), closely resembling the composition of clinopyroxene in the magmatic porphyric xenoliths (Mg# 75-77; Al_2O_3 2.0-3.4 wt%; TiO_2 >0.3 wt%). To a lesser extent, this result is shared with orthopyroxene compositions (Fig. III.6a-c). In fact, this mineral compositional diversity seems to be correlated with mylonite fabrics and P-T estimations - especially those from pseudosection calculation - as illustrated in figure III.16. Moreover, the 400°C P-T conditions changed across on 1 cm between CAL50B and CAL50A zones (Fig. III.8; Table

III.6), followed by a significant fabric change and mineralogical major element compositions (Figs. III.9, 10,12), is also accompanied by a change of bulk-rock composition. Indeed, the CAL50A zone has 5 wt% more SiO_2 and 2 wt% more Na_2O than the CAL50B zone, but it displays 7 wt% less CaO (Fig. III.8). We propose that the metanorite (CAL28A) and metagabbronorite (CAL29 and CAL50A) ultra-mylonites correspond to infiltrated shear zones within the Calbuco magmatic system and that CAL50B likely represents a slightly modified wall-rock (Fig. III.16). The mineralogical proportions changes, as well as fabric and P-T estimations, may be dependent on the location within the shear zone. For instance, sample CAL29 kept plagioclase porphyroclast along with a random CPO, while pyroxenes developed a [010]-fibre CPO and pseudosection yielded amphibolite facies P-T conditions. On the contrary, CAL50A and CAL28A zone pyroxenes developed a [001]-fibre CPO, along with a (010)-fibre plagioclase CPO, granulite facies P-T conditions. The former may correspond to a zone less affected than melt percolation and deformation, while the latter may correspond to the highest-deformed shear zone area (Fig. III.16). The significant interconnection of melt percolation and deformation is evident in the hybrid xenolith CAL28, where a discordant contact between the magmatic porphyric gabbronorite zone CAL28B and the mylonitic metanorite zone CAL28A suggests magma input into the circulation-deformation system. This process led to crystallisation without stress, resulting in an magmatic porphyric texture of CAL28B zone (Fig. III.3a-c).

Additionally, orthopyroxene and amphibole exsolution can be seen as markers of a temperature decrease after a significant event of deformation and melt percolation in the shear zone. Thus, the crystallisation of the magmatic porphyric part in contact with the mylonite part in sample CAL28 has been made without strain, crystallising undeformed automorphic crystal and amphibole poikiloblast (Figs. III.3a-c, 11). Hence, this model implies that millimetric-scale plagioclase grains have crystallised from a magma fast enough to not let the mylonite part CAL28A reequilibrate. Moreover, it implies that melt percolation, associated heating, deformation and orthopyroxene-exsolution occurred in the CAL50A zone without significantly affecting the CAL50B zone yet on direct contact (Fig. III.2d-f).

While the coexistence of magmatism and deformation has been documented in the LOFZ in the Southern Volcanic Zone of the Andes (Chaussard & Amelung, 2014), this is the first description of the contact and the relationship between these magmatic and deformational systems. The depth of this system is however difficult to establish, as the pressure calculated corresponds to depth from ca. 10 to 30 km in the middle to the lower crust

levels (Fig. III.8). If the CAL50B zone corresponds to the wall-rock, calculated pressures below 2.5 kbar for this sample may correspond to the depth of the described system, i.e. at middle crustal depth (<14 km; Fig. III.8). Finally, we relate the occurrence of AC, ABC and BC slip system in clinopyroxene and orthopyroxene to the strike-slip deformation of the LOFZ, reaching middle to lower crustal levels in ductile-deformation conditions, with a slight transpressional component (Arancibia *et al.*, 1999).

III. 6 CONCLUSION

- Mafic ultra-mylonites xenoliths occur along with mafic magmatic porphyric xenoliths in Calbuco lavas
- Mylonites equilbration temperatures range from 450 to 1000°C as pressure range from <2.5 kbar to 8 kbar
- Plastic deformation goes along with clinopyroxene and orthopyroxene [001](100) or [001]-fibre CPO and weak plagioclase CPO patterns
- P-T conditions seem positively correlated to pyroxenes Mg#, Al_2O_3 and TiO_2 contents and lineation development in pyroxenes CPO
- Ultra-mylonites represent a shear zone below Calbuco volcano, associated with melt passage and crystallisation of cumulates.

CHAPTER IV: The lower crust beneath Salta intracontinental rift: zircon petrochronology and microstructural analysis of granulite xenoliths

In collaboration with Mary-Alix Kaczmarek, Michel Grégoire, Friedrich Lucassen, Caliméria Passos Do Carmo, Oscar Laurent and Frédéric Mouthereau.

ABSTRACT

Punctual thermal events in the lithosphere can result to the formation of intracontinental rift basins at the surface, often associated with alkaline magmatism. However, in tha case that rifts do not reach advanced maturation stage, the metamorphic and deformational modifications in deeper sections of the crust remain poorly described. We present here a petrochronological study combining zircon (U-Pb dating coupled with in situ trace element analyses) and microstructural (by Electron Backscattered Diffraction, EBSD) of a series of felsic and mafic granulite xenoliths from the Salta intracontinental rift (NW-Argentina). These xenoliths were brought to the surface by alkaline lavas dated to the Upper Cretaceous. Analysis of zircons in a felsic granulite, characterised by a plagioclase-quartz-garnet-rutile paragenesis, reveals the presence of two distinct populations: zoned and heterogeneous zircons, and homogeneous, non-zoned zircons. Zoned zircons have U-Pb ages ranging from Ordovician to Lower Cretaceous (452-100 Ma), and trace element compositions similar to magmatic rock zircons. This suggests detrital origin and confirms the sedimentary protolith of felsic granulites, likely deposited in the Neoproterozoic or Cambrian Pampian margin of Gondwana. Homogeneous zircons yield a concordant Lower Cretaceous age of 114 Ma and display trace element compositions of ultra-high temperature (UHT) metamorphic zircons. Pseudosection calculations suggest that the observed pargenesis of felsic granulites is in equilibrium at temperature above 800°C for pressures above 10 kbar, conditions conducive to partial melting of such assemblages. These pressures redefine the depth of the petrological Moho in the region at 40-45 km. Ti-in-zircon thermometry indicates equilibrium

temperatures ranging between 830 and 850°C. We propose that these felsic granulites experienced significant heating during the first phase of rifting, resulting in ca. 2 vol.% partial melting and the crystallisation of metamorphic zircons. The liquid phase from the partial melting did not remain in the rock, rendering the felsic granulites anhydrous. Microstructural analyses of both felsic and mafic granulites reveal minimal traces of internal deformation but show a crystallographic preferential orientation (CPO) defining a clear lineation. Clinopyroxene in mafic granulites display a [001](010)-type crystallographic preferential orientation (CPO), suggesting activation of the {110}[001], {110}½ slip system observed in clinopyroxene at high temperatures. We propose that the initial rifting phase induced extensional processes in the lower crust, leading to the formation of a dislocation creep lineation under UHT conditions. The close timing between this event and the ascent of xenoliths allowed the granulites to equilibrate, causing intragranular deformation to almost vash. These findings offer insights into the metamorphism affecting the lower crust during the formation of intracontinental rifts and establish a connection between surface deformation and deeper section of the continental lithosphere.

RÉSUMÉ

Des événements thermiques ponctuels dans la lithosphère peuvent engendrer la formation de bassins de rift intracontinental en surface associés avec du magmatisme alcalin. Cependant, dans le cas où ces rifts n'atteignent pas un stade de maturation avancée, les modifications métamorphiques ou déformationelles dans des sections plus profondes de la croûte sont mal décrites. Nous présentons ici une étude pétrochronologique sur zircon (datation U-Pb couplée à analyses des éléments traces in situ) et microstructurale (par *Electron Backscattered Diffraction*, EBSD) d'une série de xénolithes de granulites felsiques et mafiques provenant du rift intracontinental de Salta (NO-Argentine), et remontés à la surface par des laves alcalines datées du Crétacé Supérieur. L'analyse des zircons d'une granulite felsique, qui présente une paragénèse plagioclase-quartz-grenat-rutile, indique qu'elle contient une population de zircons zonés et hétérogènes et une autre de zircons homogènes et non zonés. Les zircons zonés présentent des âges U-Pb étalés entre l'Ordovicien et le Crétacé Inférieur (452-100 Ma), des compositions en éléments traces similaire aux zircons des roches magmatiques, ce qui suggère que ces zircons sont détritiques et confirme le protolithe sédimentaire des granulites felsiques, certainement déposés au Néoprotérozoique ou au

Cambrien sur la marge Pampienne du Gondwana. Les zircons homogènes ont un âge concordant Crétacé Inférieur de 114 Ma et une composition en élément traces de zircons métamorphiques de ultra-haute température (UHT). En parallèle, les calculs de pseudosections suggèrent que la pargénèse des granulites felsiques observées est à l'équilibre dans des conditions de température supérieures à 800°C pour des pressions supérieures à 10 kbar, des conditions permettant la fusion partielle d'un tel assemblage. De telles pressions redéfinissent la profondeur du Moho pétrologique de la région à 40-45 km. La thermométrie Ti-dans-zircon indique des températures d'équilibre situées entre 830 et 850°C. Ainsi, nous proposons que ces granulites felsiques ont enregistré un réchauffement significatif lors de la première phase de rifting, générant de la fusion partielle à hauteur de ~2 vol.% et à l'origine de la cristallisation de zircons métamorphiques. Le liquide issu de la fusion partielle ne serait pas resté dans la roche et aurait ainsi laissé les granulites felsiques anhydres. En parallèle, les analyses microstructurales des granulites felsiques et mafiques indiquent que ces roches n'ont conservé que de très rares traces de déformation interne, mais montrent une orientation préférentielle cristallographique (CPO) qui définit très nettement une linéation. De plus, les clinopyroxènes des granulites mafiques ont une orientation préférentielle cristallographique (CPO) de type [001](010), qui pourrait suggérer l'activation du système de glissement {110}[001], {110}½<110> qui est observé à haute température. Nous proposons que la phase initiale de rifting a généré des processus d'extension dans la croûte inférieure, entraînant la formation d'une linéation par *dislocation creep* dans des conditions UHT. Le timing serré séparant cet événement de la remontée des xénolithes aurait permis la rééquilibration des granulites et la disparition de la déformation intragranulaire. Ces données fournissent des indications sur le métamorphisme affectant la croûte inférieure pendant la formation des rifts intracontinentaux et permettent de relier la déformation observée à la surface à celle affectant des sections plus profondes de la lithosphère continentale.

IV. 1 INTRODUCTION

Studying crustal xenoliths helps in understanding the nature and evolution of the lower crust, especially in areas lacking exposed lower crustal sections (Mengel & Kern, 1992; Rudnick & Fountain, 1995; O'Reilly & Griffin, 2013; Hacker *et al.*, 2015). This is the case in the Central Andes, where the most recent accessible lower crustal rocks are the Don Javier crustal xenoliths (NW Argentina; Lucassen *et al.*, 1999b), sampled by the Las Conchas alkaline

basanites, brought up during a Cretaceous intracontinental rifting process (Marquillas *et al.*, 2005). In contrast, granulites or eclogites outcrops in this region are rare, are Permian in age for the younger (Limon Verde granulites, N-Chile; Lucassen *et al.*, 1999a; Soto Verdugo, 2013) and do not represent stable lower crustal sections but rather subducted rocks that were fastly exhumed, without recording lower crust granulite metamorphic conditions. For this study, only xenoliths recording the granulite facies are targeted.

It is accepted that the NW Argentina basement corresponds to pieces of the Late Neoproterozoic Gondwana West-passive margin, above which were deposited a massive sediment sequence, namely, the Puncoviscana formation, which was metamorphosed during Pampian and Famatinian cycles, from Late Neoproterozoic to Ordovician (Casquet *et al.*, 2018; Rapela *et al.*, 2018; Weinberg *et al.*, 2018). Crustal xenoliths from Don Javier clarified the nature of the NW Argentina lower crust at Cretaceous times. As a matter of fact, Lucassen *et al.*, (1999b) reported granulitic assemblage in both mafic and felsic xenoliths. Using thermobarometry on mafic granulites, they estimated the Cretaceous Moho depth at ca. 35 km. They proposed a similar origin between both felsic and mafic granulites, and the Early Paleozoic metamorphic basement and amphibolites outcropping in Central Andes, based on Sm-Nd and Rb-Sr isotopic signatures. Finally, they proposed that the lower crust of NW Argentina was mainly felsic as it was the dominant lithology in the crustal xenolith collection. This hypothesis was supported by Weinberg *et al.* (2018), who linked this observation with the inferred felsic nature of the lower crust inferred from seismic profiles (Wigger *et al.*, 1994).

It is worth noting that the thermobarometry constraints only came from the study of the mafic granulite xenoliths and that it has been only proposed that felsic granulites come from the same crustal section (Lucassen *et al.*, 1999b). Moreover, the evolution of the conditions of the metamorphism of the lower crust, especially during the Cretaceous Salta rifting, and the possibly associated deformation have never been characterised. Hence, the structure and the evolution of the NW Argentina basement are still elusive.

In this study, we bring new constraints on the origin, the metamorphic conditions and the deformation of the NW Argentina lower crust during the Cretaceous, using a crustal xenolith suite from Las Conchas. Those constraints integrate the characterisation of the felsic granulites zircon population using U-Pb datation and trace element analyses, phase equilibrium modelling on felsic granulites and microstructural analysis on both felsic and mafic xenoliths.

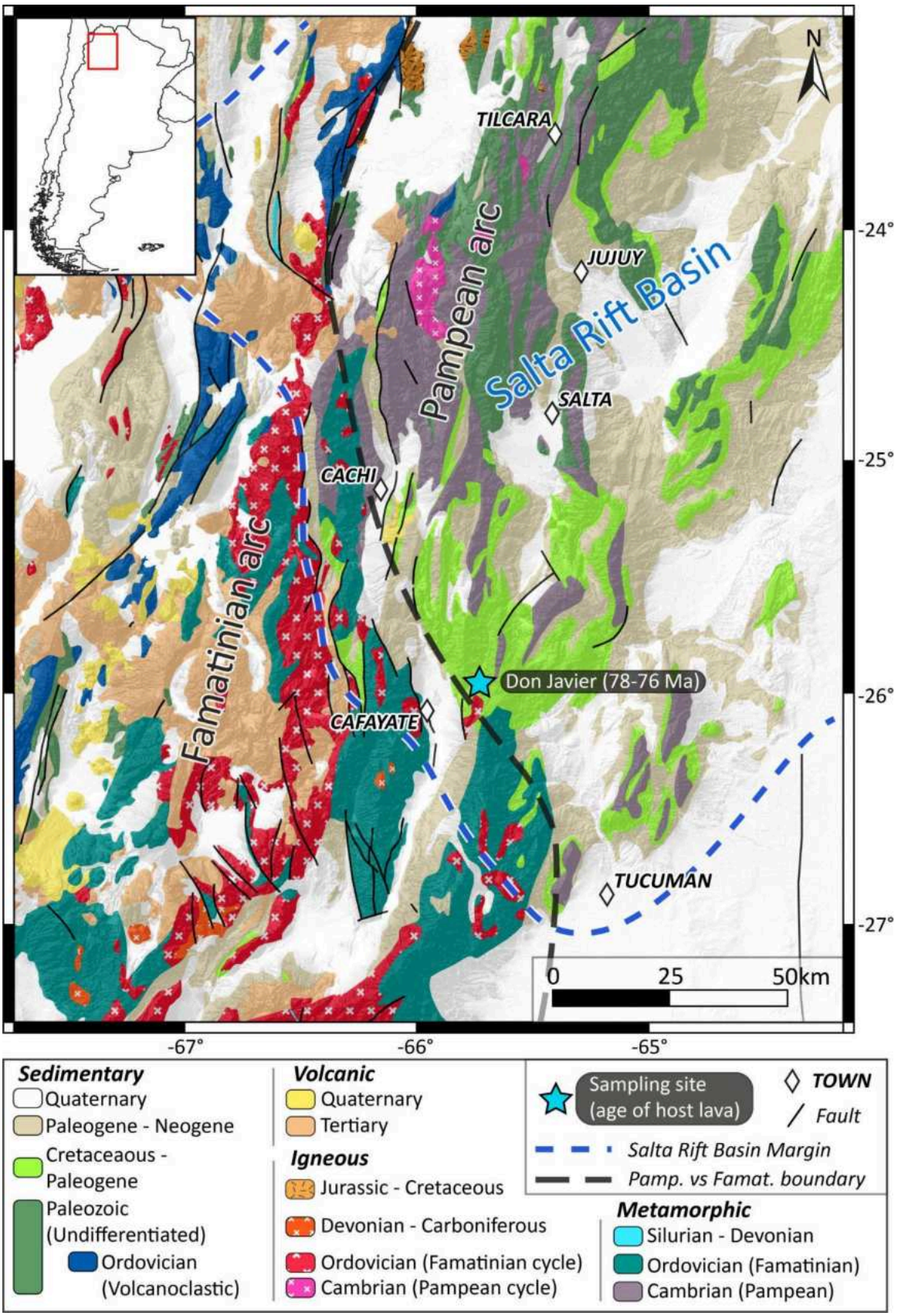


Fig. IV.1. Geological setting near the Don Javier xenoliths, after Marquillas *et al.* (2005), Rapela *et al.* (2018), Weinberg *et al.* (2018), based on SegemAR maps.

IV. 2 GEOLOGICAL SETTING

Cretaceous rift-related sediments deposited on top of the Puncoviscanian Formation, which is composed of sediments and metasediments (Fig. IV.1). The protolith of the Puncoviscanian Formation deposited on a non-volcanic-hyper-extended passive margin, primarily consisting of felsic rocks and lacking mafic rocks (Wigger *et al.*, 1994; Weinberg et al., 2018). The oldest sources are believed to be from the cratonic parts of the Gondwana to the East, ranging from Greenvilian-Mesoproterozoic to Archean sources; (Casquet *et al.*, 2006; Rapela *et al.*, 2016; Weinberg *et al.*, 2018). The age of deposition is bracketed between >600 and 520 Ma (Late Neoproterozoic to Cambrian). Around 550 Ma, the Puncoviscanian Formation recorded a change from a passive to an active margin setting. This transition was indicated by intrusive Late Neoproterozoic to Early Cambrian I-type magmatic rocks (Fig. IV.1) and associated detrital zircons found in the Cambrian upper parts of the Puncoviscanian Formation, as well as the medium to high-grade Cambrian metamorphism of the latter (Weinberg *et al.*, 2018). To the West, the Pampian cycle ended with the collision of the MARA block (named after three of its alleged outcrops: Sierra de Maz, ARequipa (Peru) and Rio Apa (southern Brazil); Casquet *et al.*, 2012) with the West-Gondwana margin, during which the Puncoviscanian Formation recorded metamorphism, accompanied by the intrusion of Cambrian to Ordovician I- to S-types igneous rocks (e.g. Rapela *et al.*, 2016; Weinberg *et al.*, 2018). Extensive post-collision setting marked the onset of the Famatinian cycle at the Cambrian-Ordovician transition (ca. 485 Ma), during which High-Temperature metamorphism persisted and overprinted Pampian metamorphism, along with paired I-type and S-type magmatism. Famatinian magmatism and metamorphism persisted until Devonian times, culminating in the docking of the Cuyania/Precordillera terrane with the West-Gondwana margin (Ramos, 2008; Rapela *et al.*, 2018; Weinberg *et al.*, 2018).

Postdating the Paleozoic rocks are Cretaceous to Paleogene sediments deposited in the Salta basins (also named Lomas de Olmedo basins; Fig. IV.1; Lovecchio *et al.*, 2020), located in both NW Argentina and Bolivia (20-27 °S latitude) and which developed during an episode of Cretaceous crustal extension (Marquillas *et al.*, 2005). The latter affected the W-Argentina over a distance of 2000 km from the Salta basins to the Macachín basins (Lovecchio *et al.*, 2020) and occurred in an intracontinental rift setting, influenced by both its back-arc position regarding the Nazca subduction below South America, and the Atlantic Ocean opening East of South America (Viramonte et al., 1999). The associated deposits have

a thickness that reaches 5000 m (Marquillas *et al.*, 2005). They are accompanied by several magmatic phases, corresponding to i) a pre-rift stage (130-120 Ma) which is characterised by anorogenic plutonism, ii) a syn-rift stage which is characterised by two volcanic episodes at 110-100 Ma and 80-75 Ma respectively, both producing alkaline basaltic volcanics and iii) a last volcanic episode (65-60 Ma) characterised by K rich lavas (Viramonte *et al.*, 1999).

Peridotites, pyroxenites and granulite xenoliths are found in the syn-rift Las Conchas basaltic volcanism (78-76 Ma; Marquillas *et al.*, 2005), which outcrops in the Las Conchas valley. The emplacement of Las Conchas basalts occurred in the centre of the Alemanía subbasin, SW of the Salta rift, during the rift climax (Marquillas *et al.*, 2005). This basin remained in the Pampean ranges, West of the Sub Andean ranges, East of the Altiplano-Puña plateau (Marquillas *et al.*, 2005; Armijo *et al.*, 2015; Heredia *et al.*, 2016) and near the boundary between Paleozoic Pampean and Famatinian arcs.

IV. 3 SAMPLE COLLECTION AND ANALYTICAL METHODS

IV. 3.1 Sample collection

Xenoliths occur within Quebrada de Don Javier breccias (25°57’ S; 65°44’ W; Fig. IV.1). Host rocks are breccias filling volcanic vents (Lucassen *et al.*, 1999; Viramonte *et al.*, 1999), intruded by Campanian basanite dykes which belong to the Las Conchas Basalt formation (78-76 Ma; Marquillas *et al.*, 2005). A collection of more than 40 xenoliths was provided by F. Lucassen. The collection is made of felsic and mafic granulite xenoliths (which compose 95 and 5 % of the collection, respectively). The sizes of the samples are <30 cm in diameter for the felsic xenoliths and <10 cm in diameter for the mafic xenoliths (Lucassen *et al.*, 1999). Among this collection, 2 felsic and 2 mafic granulites representative of the suite were selected for detailed microstructural analysis. One felsic granulite was selected for major element analysis and phase equilibrium modelling, and another one for zircon in-situ U-Pb datation.

IV. 3.2 Phase equilibrium modelling

Calculations were applied on the sample 4-304-1 using the Na_2O-CaO-K_2O-FeO-MnO-MgO-TiO_2-Al_2O_3-SiO_2-H_2O-O_2 system, with the software Perple_X 7.0.0 and the internally consistent thermodynamic dataset (hp622ver) of Holland & Powell (2011). Solution models used were those from Fuhrman & Lindsley (1988) for

plagioclase (Pl), Green *et al.* (2016) for clinopyroxene (Cpx) and melt, White *et al.* (2014) for orthopyroxene (Opx), garnet (Grt) and ilmenite (Ilm), White *et al.* (2002) for spinel (Sp) and Holland & Powell (1998) for olivine (Ol). To avoid interferences from the host lava with the xenolith bulk composition, calculated bulk rock compositions based on mineralogical proportions, microprobe analyses and mineral densities were used for pseudosection calculation. Bulk Fe_2O_3 was calculated based on the ratio Fe_2O_3/FeOt in two-pyroxenes and spinel. Moreover, Perple_X calculates Fe_2O_3 contents based on the formula $O_{2\ mol} = 0.5*Fe_2O_{3\ mol}$. Details on chosen densities are available in *Supplementary Table SIV.1*. Since garnet high-kelyphitisation skewed the garnet proportions from the granulite stable assemblage, corrections were made on the EBSD garnet proportion estimations, measuring non-indexed garnet contours that correspond to kelyphitisation. We estimated that 97% of the garnet surface has been kelyphitised. Several pseudosections have been calculated to test various ratios of garnet kelyphitisation, and the variation of this ratio does not affect the calculated chemical compositions of the phases.

IV. 3.3 Backscatter images and minerals major elements compositions

Polished thick sections were covered with a 20 nm carbon deposit using a carbon evaporator Leica EM ACE600 for secondary Electron Microscope (SEM) observations. SEM qualitative chemical analyses were carried out at the Géosciences Environnement Toulouse (GET) laboratory (CNRS-CNES-IRD-University Paul Sabatier, Toulouse), Observatoire Midi Pyrénées (Toulouse, France), using a Tescan Vega 4 equipped with an EDS Bruker Quantax 30mm². The analysis conditions were performed with an acceleration voltage of 20 kV, a probe current of 3 nA and a working distance of 15 mm. Cathodoluminescence imaging was coupled with SEM analyses, using a “hot-cathode” Lumic HC6-LM.

IV. 3.4 Zircon U-Pb datation and trace elements analyses

Simultaneous zircon U-Pb dating and trace element analyses were carried out at ETH Zürich (Switzerland) by laser ablation - inductively coupled plasma - mass spectrometry (LA-ICP-MS) using a RESOlution S-155 (ASI) 193 nm (ArF) excimer laser system coupled to an Element XR (Thermo Scientific) sector-field ICP-MS. Measurements were performed with a laser spot diameter of 19 μm, repetition rate of 4 Hz and energy density of ca. 2.5 J/cm². Ablations were performed in the built-in, dual-volume, fast-washout ablation cell (<1 cm^3 effective volume) flushed with He carrier gas (ca. 0.25 L/min) to which was admixed Ar

(ca. 1 L/min) and N_2 (ca. 2 mL/min) make-up gas downstream of the ablation cell before introduction in the plasma. Counting time for one analysis was 60 s (30 s on gas blank to establish the background, then 25 s for data acquisition followed by 5 s washout). The primary reference material GJ-1 (Jackson *et al.*, 2004) was used for U-Pb dating, as used secondary (validation) reference materials were 91500 (Wiedenbeck *et al.*, 2004), Plešovice (Sláma *et al.*, 2008), AUSZ7-1 (Kennedy *et al.*, 2014) and NIST SRM 610 (Jochum *et al.*, 2011). NIST SRM 612 (Jochum *et al.*, 2011) was used as primary reference material for trace element quantification. Stoechiometric SiO_2 content of zircon (15.2 wt%) served as internal standard. The relative precision and accuracy for laser analysis range from 1 to 10% for most of the elements, and is at 15% for La and Pr. The theoretical detection limits range from 10 to 60 ppb and for Nd, Y, Gd and 238U is 100 ppb, for Ti is 1 ppm, for 178Hf is 1.5 ppm, for Al and Zr is 4 ppm, for P is 30 ppm and for Si is 300 ppm. The data reduction was performed using Iolite 4.0 (Paton *et al.*, 2010, 2011; Petrus & Kamber, 2012).

IV. 3.5 Crystallographic orientations of minerals

A mechanic-chemical polishing using a Vibromet (Buehler) was applied on four thick sections for 2h30 with a colloidal silica suspension (pH 10) to remove mechanically induced surface damage. Electron Backscatter Diffraction (EBSD) data acquisition was performed with a JEOL 7100 microscope at the centre Raimond Castaing (CNRS-University Paul Sabatier, Toulouse), equipped with an EBSD camera CMOS Symmetry S2 (Oxford Instruments). The analysis conditions were performed with an acceleration voltage of 20 kV, a probe current of 16 nA and a working distance of 17 mm with a stage tilt of 70°. Automatic indexing was performed using AZTec software (version 6.0 Oxford Instruments). For mapping the step size used varies between 15 and 20 µm depending on the grain size. The EBSD data were then processed in MATLAB (version R2020b) using the MTex toolbox (Bachmann *et al.* 2010, 2011). A value of 10° as the cut-off angle for the determination of the grains has been used.

For clinopyroxene and plagioclase, pole figures were plotted on a lower-hemisphere, equal-area stereographic projection. To avoid the oversampling of large clinopyroxene crystals, pole figures were plotted with one point per grain. In contrast, plagioclase pole figures represent all the available measurements as twinning is relatively common. For clarity, pole figures were rotated as the inferred foliation was the XY plan and lineation parallel to X. These interpretations take into account the trace of the foliation in xenoliths, the

correlation of Crystallographic preferred orientation (CPO) concentration points between minerals. An example of a rotated pole figure procedure is given in *Supplementary Fig. SV.1*. The strength of the crystallographic preferred orientation was estimated using the J- and M-indices (Bunge 1982; Skemer *et al.*, 2005). In addition, the misorientation of each pixel was calculated relative to the mean orientation of its corresponding grain (mis2mean) and then combined as maps of misorientation relative to mean grain orientation.

In our analysis, quartz-quartz boundary misorientations show a high proportion of rotation of 60° around the [0001] axis (c-axis). However, observations in optical microscopy do not match these data thus hinting. This means that our quartz is likely misindexed as it was already observed (Wenk *et al.*, 2011), which affected the quartz grain reconstruction. Thus, in order to observe the internal misorientation of the quartz grains, we used the Kernel average distribution (KAM; misorientation of a pixel relative to the mean of the 8 surrounding pixels) which is not grain-boundary dependant, instead of the mis2mean distribution. As the misindexation is a rotation around the quartz c-axis, orientation data for the c-axis is not affected by this analytical issue and can be discussed.

IV. 4 RESULTS

IV. 4.1 Sample description and petrography

Felsic granulite xenoliths (samples 4-302, 4-302b and 4-304-1) mostly consist of plagioclase, quartz, garnet, with accessory (<1 vol.%) rutile, zircon and sometimes spinel (Fig. IV.2a, b). Sample A-112b differs from other felsic xenoliths by displaying accessory apatite (2 vol.%) and spinel but lacking quartz (Fig. IV.2c). Mafic granulite xenoliths (sample 4-301b and A62) consist of plagioclase, clinopyroxene and garnet (Fig. IV.2d).

Xenoliths display a granoblastic texture, a rather unimodal grain size for plagioclase, quartz, clinopyroxene and most of the garnet, ranging from 200 µm to 5mm. The latter are mostly round-shaped but sometimes automorph to sub-automorph. When occurring, the rutile is coarse and may have an elongated-like shape up to 4 mm long (Fig. IV.2a). Grain boundaries are linear with 120° triple junctions. However, in felsic granulites, the quartz-plagioclase assemblage displays loboid grain boundaries, abundant albite twinning within the plagioclase and rare undulose extinction within quartz grains (Fig. IV.2a). Mafic granulites may display clinopyroxene+garnet- or plagioclase-rich layers where crystals are flattened and slightly elongated, underlining a layering (aspect ratio up to 3:1; Fig. IV.2d).

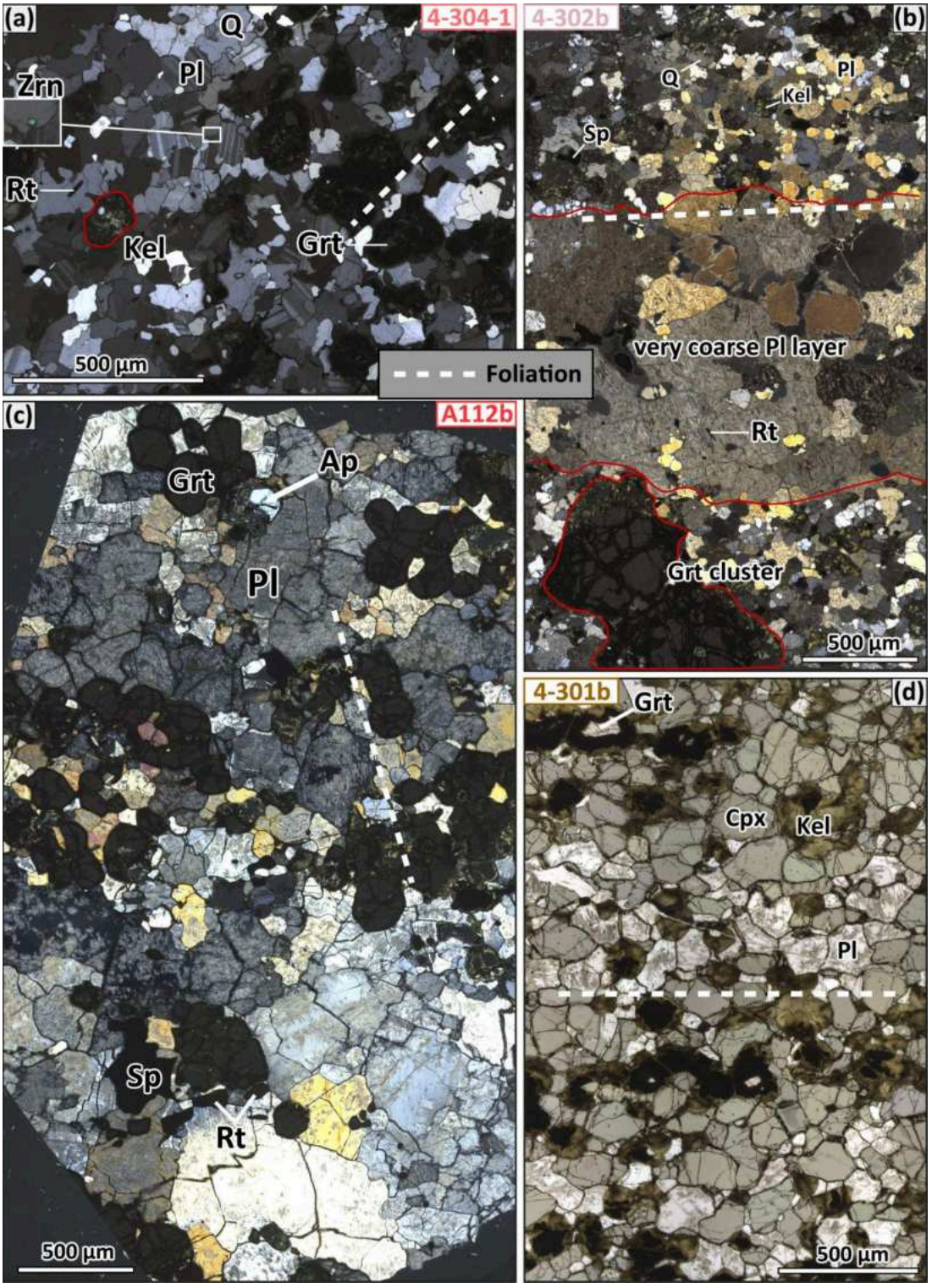


Fig. IV.2. Photomicrographs of Quebrada de Don Javier lower crustal xenoliths. (a) Felsic granulite (sample 4-304-1) under cross-polarised light. (b) Felsic granulite (sample 4-302b) under cross-polarised light, displaying a very coarse plagioclase grain layer and very coarse garnet clusters. (c) Plagioclase-garnet granulite (sample A-112b) under cross-polarised light. (d) Mafic granulite (sample 4-301b) under plane-polarised light. The white dashed-line represents the layering.

Felsic granulites may display layers (up to 1 cm large) of very-coarse plagioclase grains (up to 1 cm) and clusters of very-coarse garnet grains (up to 8 mm; Fig. IV.2b). The sample A-112b stands out from the suite since its entire assemblage consists of very-coarse plagioclase and garnet grains (both up to 1 cm), the latter forming clusters that seem to mark a weak foliation, while apatite is coarse-grained (up to 2 mm; Fig. IV.2c). Minerals are unzoned except some clinopyroxenes from mafic granulites, which display thin corona (30 μm) attributed to reactions with host-lava (Lucassen *et al.*, 1999).

Garnet occurs as a highly kelyphitised form in some samples (e.g. 4-304-1 and 4-301b; Fig. IV.2a, d). In that way, if EBSD-indexing indicates a low garnet proportion in some samples (<2 vol.%), microscope observation suggests that proportions are higher (16 vol.% and 34 vol.% in samples 4-301b and 4-304-1, respectively). Lucassen *et al.* (1999) argue that kelyphitisation is related to alteration processes during host basalt intrusion within sediments. In the mafic granulites, alteration can be pervasive within the plagioclase. Reaction with host lava produces fine interstitial veins or patches of glass but doesn't change major element phase composition (see more details in Lucassen *et al.*, 1999).

IV. 4.2 Zircon dating and trace element compositions

In the felsic granulite 4-302, zircon occurs as transparent, yellowish to colourless crystals with a size ranging from 20 to 250 μm. Zircon shapes are generally rounded, with the exception of a few elongated grains (Fig. IV.3a). Two zircon domains are identified based on CL images (Fig. IV.3a). The first corresponds to entire grains or cores showing well-developed oscillatory zoning. The second domain corresponds to entire grains or rims mantling the cores, showing dark and homogeneous luminescence and absence or weak zoning. The cores have characteristics of resorbed zircon with internal zoning truncated by irregular and sharp boundaries (Fig. IV.3a). If the homogeneous rims and grains are visible, rare sector or radial zoning textures can be observed. The volume ratio between homogeneous rims/grains and zoned cores/grains varies from one grain to another but, at the scale of the sample, homogeneous rims/grains dominate.

Zircon displays clear differences between zoned core/grains and homogeneous rims/grains, in terms of U-Pb dates and trace element compositions. Most of the zoned cores/grains analyses (9 out of 13) show a spread of (sub-) concordant U-Pb dates (Fig. IV.3b), ranging from Ordovician to Lower Cretaceous (452 ± 14 to 131 ± 4 Ma), as the other analyses show younger and consistent dates (100-102 ± 3 Ma). In contrast, homogeneous

rims/grains display more clustered Albian dates between 111 and 104 Ma but two analyses stand out at 144 ± 5 and 188 ± 7 Ma (Fig. IV.3b). The Concordia date calculated from this population is 113.57 ± 2.67 Ma (2 S.D.; n=11; MSWD =0.53).

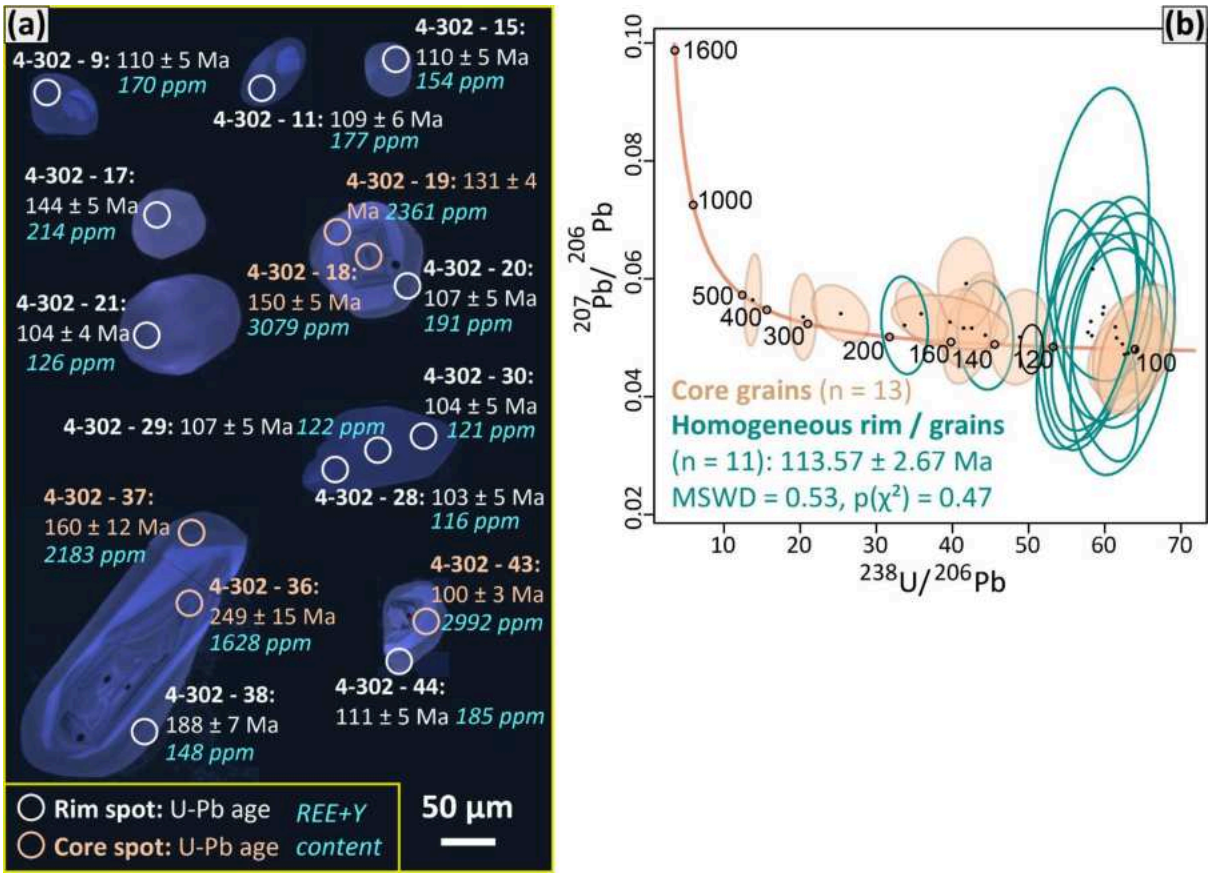


Fig. IV.3. (a) Representative cathodoluminescence images of zircon grains from the Don Javier felsic granulite 4-302. The circles represent the position of the laser spots for U–Pb dating/trace element, with corresponding spot name, $^{238}U/^{206}Pb$ date ±2σ uncertainty (in Ma) and REE+Y content (in blue). (b) Results of zircon U-Pb analyses shown as Tera–Wasserburg diagrams ($^{238}U/^{206}Pb$ vs. $^{207}Pb/^{206}Pb$) with error ellipses quoted at the 95% confidence level.

Zoned cores/grains show higher abundances of Yb (171-958 ppm; Fig. IV.4a), rare earth elements (REE) + Y (1263-6371 ppm; Fig. IV.4b) and Nb (0.8-7 ppm; Fig. IV.4c) than homogeneous rims/grains (Yb 4-33 ppm, REE+Y 116-295 ppm, Nb 0.2-0.4 ppm). However, zoned core/grains show lower GdN/YbN (0.02-0.09) and Eu_N/Eu^* ratios (0.04-0.21) than homogeneous rims/grains (0.4-2.1 and 0.22-0.33, respectively), as well as comparable U abundances (336-1467 ppm for zoned core/grains and 57-696 ppm for homogeneous rims/grains). Zoned core/grains plot within the composition fields of magmatic zircons as compiled by Laurent *et al.* (2023; Fig. IV.4a, b, c), especially within the fields of zircons with I-type and S-type affinities. Thus, they have a composition comparable with zircons from

more evolved melts from the Ivrea Mafic Complex (Fig. IV.4a, b). In contrast, homogeneous rims/grains plot within the field of zircon from ultra-(U)HT migmatites & granulites (Fig. IV.4a, b, c), with the only exception of the Eu_N/Eu^* ratio from homogeneous rims/grains that is slightly higher than those of the (U)HT migmatites and granulites field.

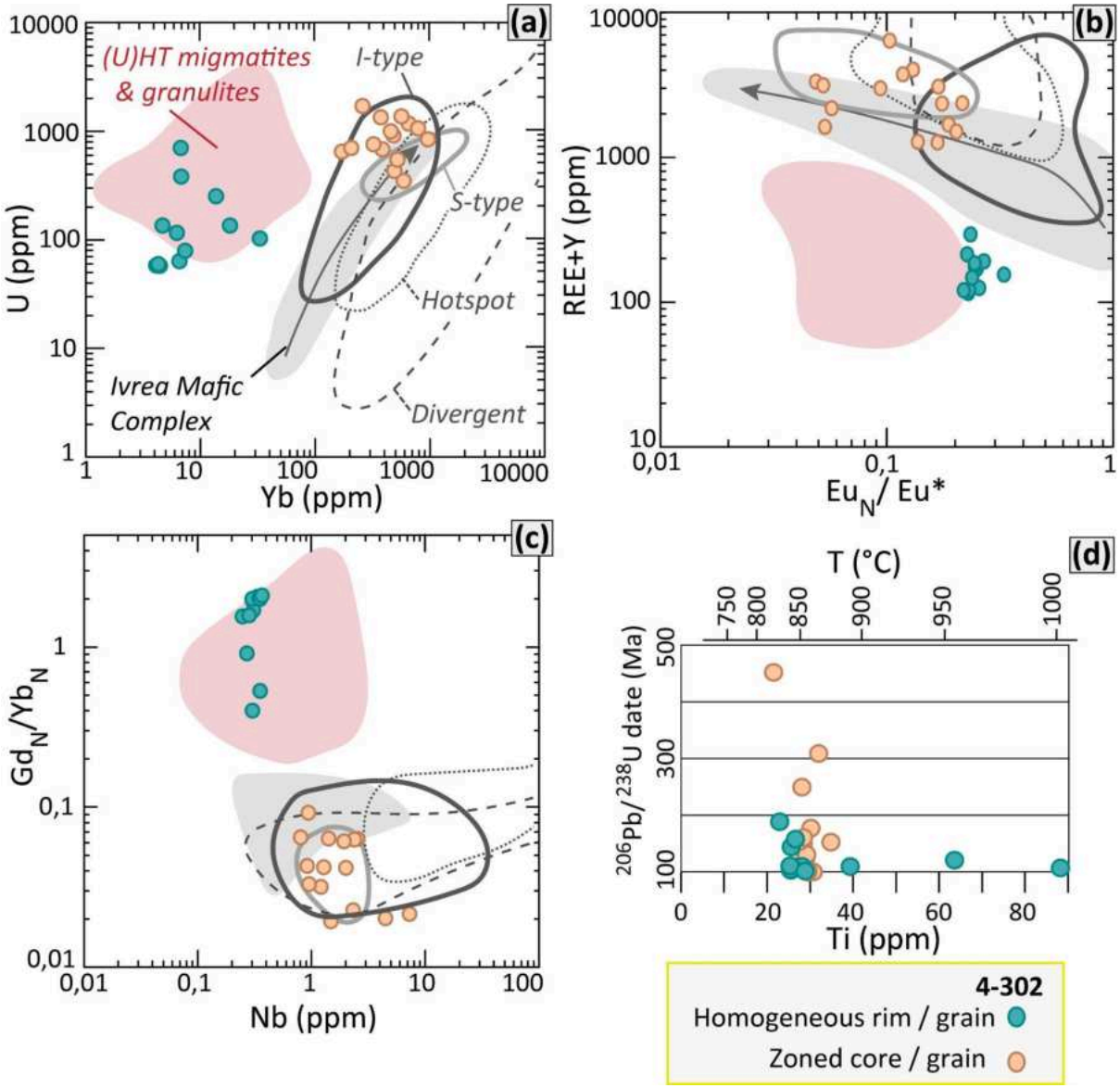


Fig. IV.4. (a, b, c) Selected trace element plots comparing the compositions of zircons from the Don Javier felsic granulite 4-302 to those of zircon from various parental magmas and geodynamic environments, (U)HT migmatites and granulites and the Ivrea Mafic Complex (modified after Laurent *et al.*, 2023). For the latter, the arrows depict the igneous evolution from the most mafic to the most evolved magmas. (d) Plot of zircon Ti contents vs. $^{238}U/^{206}Pb$ date of sample 4-302, and the associated Ti-in-zircon temperatures using the calibration of Ferry and Watson (2007) with $a(TiO_2) = a(SiO_2) = 1$.

IV. 4.3 Phase equilibrium modelling and thermometry

The felsic granulite 4-304-1 contains 35 vol.% plagioclase which varies in composition from oligoclase to andesine (An_{26-31}, Ab_{51-66}, San_{7-8}), 34 vol.% of garnet (Alm_{49-51}, $Spss_{<1}$, Pyr_{42-46}, Grs_{2-7}), 30.4 vol.% of quartz and 0.6 vol.% of rutile (*Supplementary Fig. SIV.1; Tables SIV.1,2*). The results of pseudosection modelling suggest that the dry (amphibole- and biotite-free) assemblage of the sample 4-304-1 is stable at temperatures >800 °C (Fig. IV.5), as the presence of rutile, together with the absence of kyanite, constrain pressures between 10 and 13 kbar (considering temperature <1000 °C). Phase equilibrium modelling was also performed on the felsic granulite 4-304-1 considering a dry system (H_2O= 0 wt%), as for the mafic granulite 4-301b which results and discussion can be found in *Supplementary Fig. IV.S2*.

Ti-in-zircon thermometer from Ferry & Watson (2007) has been applied on sample 4-304-1 and yields a temperature range of 823-1002 °C (Fig. IV.4d). However, all zoned cores/grains are bracketed between 823 and 870 °C, while most of the homogeneous rims/grains analyses (10 out of 13) are bracketed between 830 and 853 °C.

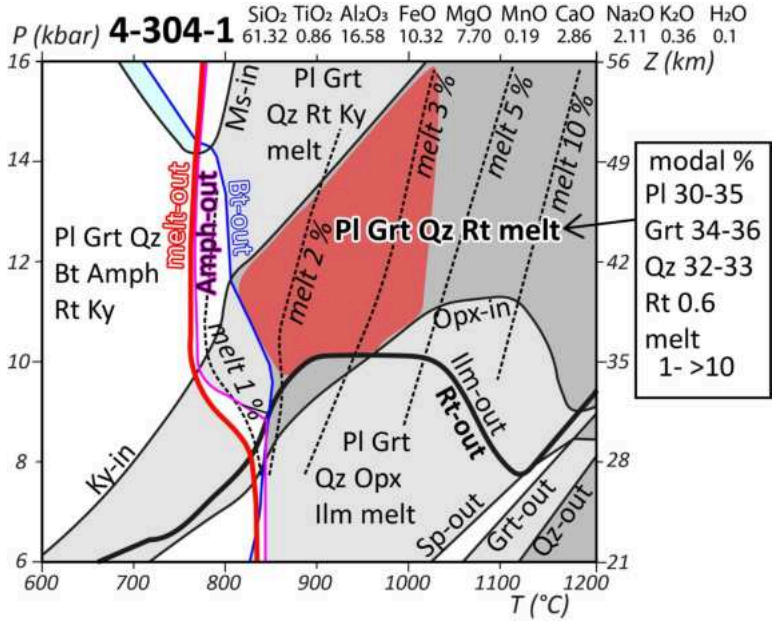


Fig. IV.5. Isochemical phase diagrams computed with bulk-composition estimation of the sample 4-304-1. Modal compositions of the phases from the highlighted stability domain are indicated in the white box.

IV. 4.4 Microstructures

IV. 4.4.1 Crystallographic Preferential Orientation (CPO)

Mafic granulites. Clinopyroxenes of the two mafic granulites display weak to medium CPO patterns (J-index 2.14-3.34; M-index 0.025-0.035; Fig. IV.6). They display a point

concentration on [001] axes parallel to X of the pole figure, a slightly more scattered point concentration on [010] axes parallel to Z and [100] axes that are randomly distributed.

Plagioclase CPO patterns are weak following the M-index values, varying between 0.018 and 0.032 (Fig. IV.6a). However, the J-index is somewhat high (5.31-11.82) but it may be related to plagioclase indexation problems (see *Supplementary Table SIV.1)* and low plagioclase grain population for sample 4-301b (n= 552). Sample A62 displays a concentration point on [100] axes parallel to both X and the clinopyroxene [001] concentration point, and displays [010] and [001] axes that are randomly distributed. Sample 4-301b has a maximum concentration point on the [100] axis parallel to Z and concentration points on [010] and [001] axes at low angle to X. However, those concentration points seem to reflect an over-sampling of one larger grain (*Supplementary Fig. SIV.3)*.

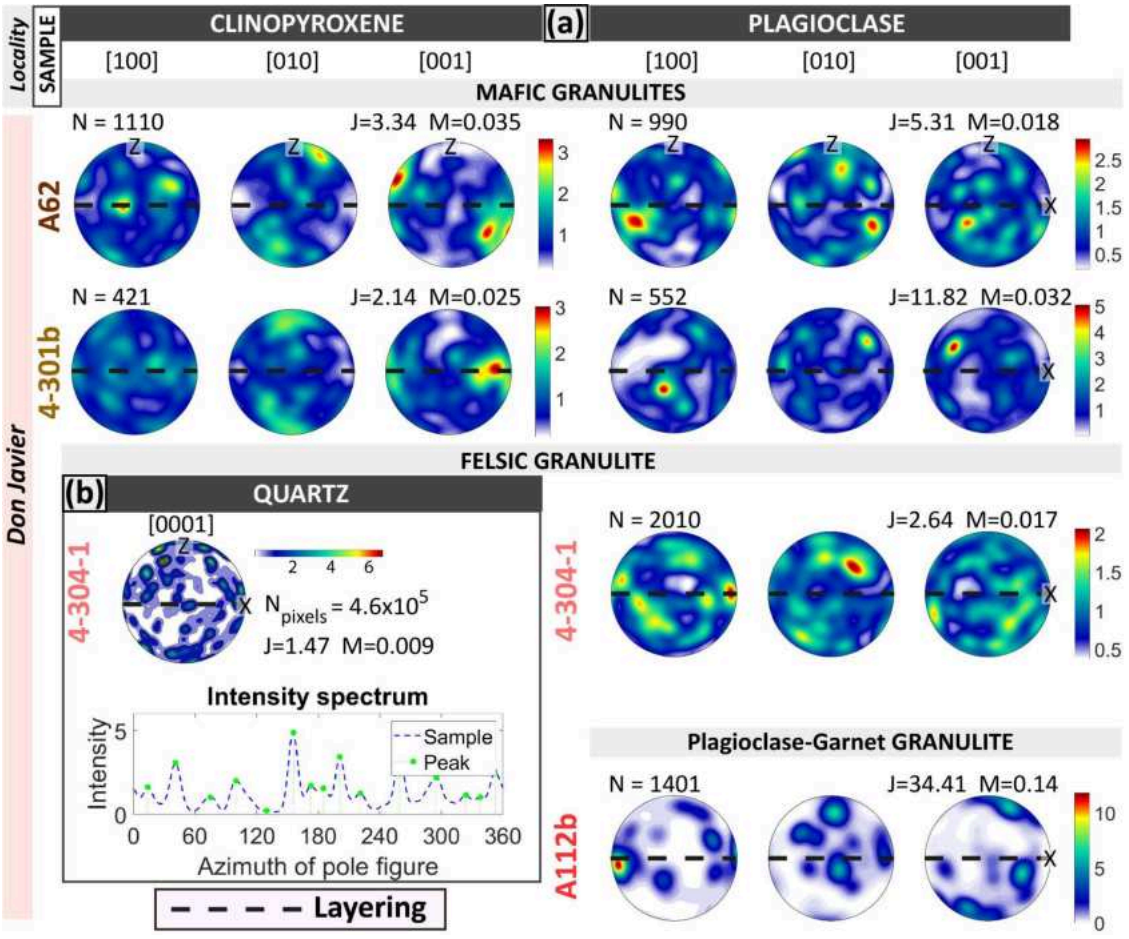


Fig. IV.6. (a) Crystallographic preferred orientation of clinopyroxene, plagioclase of analysed felsic and mafic granulites. Pole figures are rotated as the layering is parallel to X. N is the number of grains and the strength is represented by J-index and M-index. The rainbow scale represents the mud (multiply uniform density). (b) Pole figure of the orientation distribution function of the quartz [0001] axis and associated 1-360° intensity spectrum, from the method of Hunter et al. (2018), with 10 plunge lines analysed.

Felsic granulite. Sample 4-304-1 displays weak plagioclase CPO patterns (J-index 2.64; M-index 0.17), characterised by weak concentration points on the [100] axis parallel to X and on the [010] axis at a low angle to Z, and [001] axes that are randomly distributed (Fig. IV.6a). Quartz CPO patterns are weak (J-index 1.47; M-index 0.009) and orientations are random, as indicated by the absence of [0001] particular pattern and the absence of a significant peak on the intensity spectrum (Fig. IV.6b).

Plagioclase garnet granulite. Sample A-112b has plagioclase strong CPO (J-index 34.41; M-index 0.14; Fig. IV.6a) and displays a patched pattern that illustrates the little variability of plagioclase orientations within this sample. However, the CPO displays a strong concentration point on the [100] axis parallel to X, and concentration points on [010] and [001] axes parallel to Y and sub-parallel to Z, respectively.

IV. 4.4.2 Intragranular deformation

Mafic granulites. Clinopyroxene and plagioclase from samples 4-301b and A62 display weak internal deformation of clinopyroxene and plagioclase which affects only a few grains (Fig. IV.7a). Clinopyroxene misorientations axes at low angle boundaries or subgrain boundaries seem to be distributed around both [110] and [-110] axes, while those of the plagioclase seem to be distributed around both [-201] and [001] axes. However, the dataset of low-angle misorientations is small and this observation must be taken with caution (Fig. IV.7b).

Felsic granulite. Plagioclase and quartz intragranular deformation are low to absent in sample 4-304-1 (Fig. IV.7b, c). Plagioclase displays few conic subgrain boundaries at the tip of the grains and albite twinning boundaries which are not conical. Plagioclase misorientations at low-angle boundaries or subgrain boundaries are distributed around the [100] axis but the dataset is quite small and must be taken with caution (Fig. IV.7b).

Plagioclase garnet granulite. Intragranular deformation is developed in plagioclase from sample A-112b as it affects all grain sizes (Fig. IV.7b). Subgrain boundaries are rare and cross-cutting grains without preferred direction. Misorientation axes at low-angle boundaries are clustered near the [100] axis and the [110] axis, along with a third weaker cluster on the [001] axis.

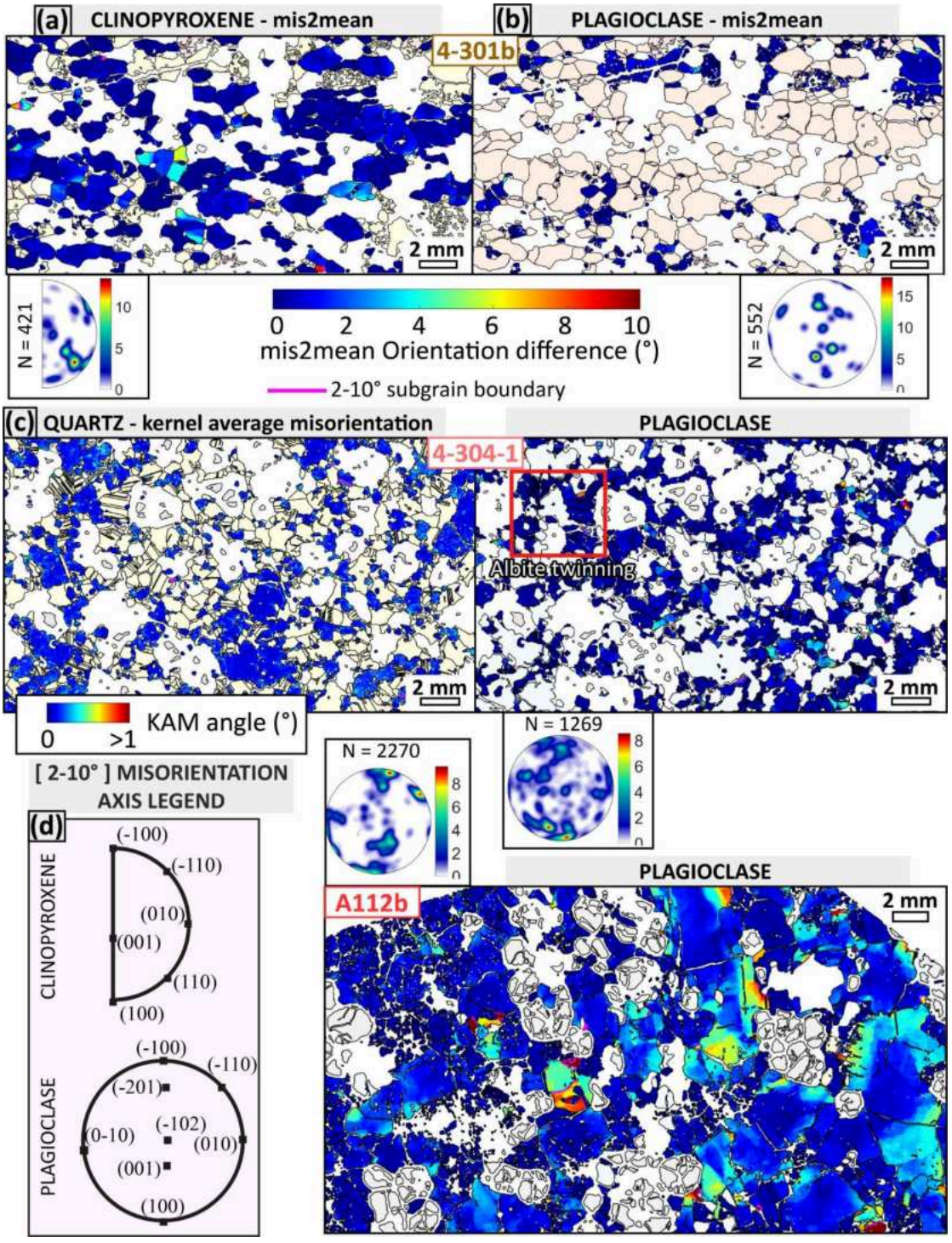


Fig. IV.7. Maps of intragranular deformation relative to the mean orientation of the grains for (a) clinopyroxene and (b) plagioclase, and associated rotation axes accommodating low angle (2-10°) misorientations. Data is represented in inverse pole figures. N is the number of pixels plotted. Light orange grains are clinopyroxene, light yellow is for plagioclase, white is for quartz and light grey is for garnet. (c) Map of 0-1° kernel average misorientation (misorientation of a pixel relative to the mean orientation of the 8 surrounding pixels) for quartz in the felsic granulite 4-304-1. (d) Legend of the clinopyroxene and plagioclase inverse pole figures.

IV. 5 DISCUSSION

IV. 5.1 Petrochronology of the zircon from the Salta granulites

The observed dichotomy between core and rim grains is typical of zircon from (U)HT felsic granulites and indicates a blend of protolith inheritance and metamorphic growth (Laurent *et al.*, 2023; Fig. IV.3, 4), confirming the sedimentary protolith of the felsic granulites as suggested by Lucassen *et al.* (1999b). Trace element compositions and U-Pb ages of the zircon cores align with an inherited detrital zircon population. The maximum age found, 452 Ma (Fig. IV.3b), corresponds to the end of crustal anatexis during the Famatinian orogen in NW Argentina (Weinberg *et al.*, 2018). Continuous ages between 290 Ma and 100 Ma might represent either true concordant ages or Early Paleozoic ages with Pb loss during the Cretaceous (U)HT event. Considering the absence of reported magmatic activity in the Late Paleozoic and Early Mesozoic periods in the region and the possibility that this population represents detrital zircons, the latter hypothesis appears more plausible. In this scenario, the inherited zircons could originate from Late Famatinian magmatic I- to S-type granitoids.

However, the investigated zircon population is limited. An anomalous zircon analysis provided a Mesoproterozoic age (1.9 Ga; *Supplementary Table SIV.2*). As metasediments from the Pampian and Famatinian orogenies in the region display distinct sources and zircon populations, notably Mesoproterozoic (1200-1000 Ma) and Late Neoproterozoic to Early Paleozoic zircons (Casquet *et al.*, 2018; Rapela *et al.*, 2018; Weinberg *et al.*, 2018), additional zircon dating within the Don Javier felsic granulites is necessary, as an adequate dataset may help identify the source of the sedimentary protolith.

On the other hand, the crystallisation of homogeneous rims/grains during Cretaceous metamorphism is supported by their consistent and concordant U-Pb dates, averaging 114 ± 4 Ma (Fig. IV.3b), as well as their trace element signature, aligning with metamorphic zircon from (U)HT granulites (Laurent *et al.*, 2023; Fig. IV.4a, b, c). The homogeneous zircon grains/rims display trace element compositions within the field of the (U)HT migmatites and granulites, suggesting growth under supra-solidus, potentially UHT conditions (Laurent *et al.*, 2023). The lower Nb contents of homogeneous rims/grains compared to heterogeneous grains/rims may result from rutile presence throughout zircon crystallisation, controlling most of the Nb budget of the rocks (Laurent *et al.*, 2023; Fig. IV.4c). The low Eu anomaly in homogeneous rims/grains (Eu_N/Eu^* 0.22-0.33; Fig. IV.4b) may indicate zircon crystallisation in the presence of a slightly peraluminous melt, reducing the incompatibility of europium in

comparison with more peraluminous melt (Trail *et al.*, 2012). Felsic granulite 4-302, which has a rather high CaO content of 2.19 wt% (Lucassen *et al.,* 1999b), suggests the potential production of a slightly peraluminous melt (almost metaluminous) after partial melting of this sample. Furthermore, the high Gd_N/Yb_N ratio and low Y–HREE contents suggest zircon crystallisation in the presence of garnet (Laurent *et al.*, 2023; Fig. IV.4b, c). While it's proposed that zircons in (U)HT metamorphic rocks could grow either at the onset of partial melting during the prograde path (Rubatto *et al.*, 2013) or during the retrograde path (Laurent *et al.*, 2023), textural indications and age precision are lacking to support either case.

Finally, Pankhurst *et al.* (2000b) proposed that Don Javier felsic xenoliths might represent residues of the partially melted source of TTG and I-type Famatinian (i.e. Early Ordovician 495-470 Ma) granites in the region. However, the metamorphic zircon population does not corroborate this age, leaving the possibility of inherited metamorphic zircons undergoing dissolution-reprecipitation processes during the Cretaceous UHT event. If this hypothesis may be convoluted, only an extensive zircon petrochronology study on Don Javier xenoliths will confirm if felsic granulites recorded partial melting associated with Famatinian metamorphism.

IV. 5.2 P-T conditions of the felsic granulites

Zircon metamorphic growth in sample 4-302 argues for the record of a partial melting event by the Don Javier felsic granulites. Hence, potassic feldspar reported in some felsic granulites by Lucassen *et al.* (1999b) could come from biotite dehydration melting reactions (Rubatto *et al.,* 2013; Laurent *et al.*, 2023). Moreover, P-T conditions of sample 4-304-1 suggest that this sample has recorded partial melting from amphibole- and biotite-dehydration reaction until temperatures >800 °C (Fig. IV.5). However, White & Powell (2002) suggest that the preservation of the peak granulite assemblage in aluminous metapelites is possible only if nearly all of the melt at temperatures above the biotite breakdown is lost. Thus, the felsic granulites may have lost all the melt to display the dry-granulite assemblage observed in optical microscopy (Fig. IV.2a-c).

In sample 4-302, rutile remained stable from the homogeneous zircon rims/grains formation to the loss of melt and the timing of the stabilisation of the dry assemblage, suggesting pressures exceeding 10 kbar during the P-T peak and the retrograde path (Fig. IV.5). Kyanite has been reported in some felsic granulites (Lucassen *et al.*, 1999) which suggests that the dry assemblage was stabilised in the kyanite stability field (Fig. IV.8).

Results of the Ti-in-zircon thermometry from Ferry & Watson (2007) give temperatures of 830-853 °C for most of the sample 4-302 homogeneous zircon rims/grains, consistent with a maximum melt volume of 2 % (Figs. IV.4d, 5). Three analyses give higher equilibrium temperatures (893-1002 °C), which suggest a melt production of 3 to 5 vol.%. However, since crustal melting has never been reported during the Salta rift basin formation, we suggest that partial melting produced minor volumes of melt, consistent with the maximum temperatures reached by felsic granulites of 830-853 °C and pressures of 10-13 kbar (Fig. IV.8).

IV. 5.3 Deformation events recorded by the xenolith suite

The mafic granulites A62 and 4-301b display well-equilibrated textures, as they lack intragranular misorientation and subgrain boundaries and display linear grain boundaries (Figs. IV.2, 7). However, clinopyroxene displays a clear [001](010) fabric (Fig. IV.6a). Activation of [001](010) slip system is uncommon in clinopyroxene (Amiguet, 2009). However, Bascou *et al.* (2001) reported the development of a [001](010) fabric with the {110}[001], {110}½<110> slip system in natural omphacite and numerical models. Additionally, the few clinopyroxene misorientations at low-angle boundaries align with (-110) and (110) axes (Fig. IV.7a), indicative of the activation of {110}[001], {110}½<110> slip system (Griffin *et al.*, 2022), commonly associated with high-temperature deformation (>1000°C; Amiguet, 2009). Previous studies proposed (U)HT metamorphism conditions for Don Javier mafic granulites at 830-970 °C, 9.5-10.2 kbar (Lucassen *et al.*, 1999b). We propose that slight plastic deformation occurred in these mafic granulites under (U)HT conditions, activating the {110}[001], {110}½<110> slip system in clinopyroxene, although no specific fabric is preserved in plagioclase. Despite the intragranular deformation being erased by static recrystallisation, the preserved CPO and shape preferred orientation (SPO) suggest that the strain responsible for these features was still present during grain recovery. This suggests that this deformation event occurred just before the xenolith sampling from host lava, possibly during the early rift stages during the Early Cretaceous, within an extensive setting.

Felsic granulite 4-304-1 displays an equilibrated texture with no intragranular misorientation or fabric observed in plagioclase and quartz, and only a slight SPO (Figs. IV.2a, 7). Plagioclase and quartz weak CPO do not reveal any specific system that can be inferred from (Fig. IV.6); however, amoeboid quartz grain boundaries are related to grain

boundary migration recrystallisation under the high-temperature regime (Passchier & Trouw, 2005). We suggest that (U)HT metamorphic and sub-solidus conditions favoured recrystallisation through dislocation creep mechanisms (grain boundary migration), erasing a potential inherited deformation in felsic granulite 4-304-1.

Sample A-112b textures stand out of the suite due to intragranular deformation observed in plagioclase porphyroclasts and the presence of subgrain boundaries, indicating activation of dislocation creep mechanisms in plagioclase (Fig. IV.7b). Misorientations at low-angle boundaries or subgrain boundaries along the [100], [-110] and [001] axes suggest the activation of multiple slip systems. Although the strong [100]-fibre fabric observed in plagioclase (Fig. IV.6a), other phases such as garnet, apatite and rutile lack intragranular deformation and display random fabrics. The SPO is very weak, and we therefore propose that the deformation recorded in this sample was not intense as it affected only the plagioclase which is softer than the other phases. Thus, it did not develop a strong SPO but only a [100]-fibre fabric in plagioclase. Lucassen *et al.* (1999b) suggested metasomatism during Cretaceous rifting, based on whole-rock and apatite trace element analysis as well as whole-rock Sm/Nd, Rb/Sr and Pb isotopy for this sample. Hence, deformation under (U)HT metamorphism conditions occurred in sample A-112b, similar to the mafic granulites, producing the [100]-fibre fabric in plagioclase without affecting other phases. Subsequently, metasomatism may have occurred alongside a local deformation event, as evidenced by the activation of minor dislocation creep mechanisms and multiple slip systems in plagioclase. Apatite, rutile and garnet could also be tardive phases equilibrated during the metasomatism event.

IV. 5.4 Structure of the lower crust during the Salta rift event

The age of the metamorphic growth of felsic granulite zircons is 113 ± 4 Ma, which is bracketed between the Salta pre-rift stage (130-120 Ma), characterised by an anorogenic plutonism, and the first syn-rift volcanic episode (110-100 Ma; Viramonte *et al.*, 1999). Overall, the (U)HT metamorphism of the Salta lower crust corresponds to the early phases of the rift, as late volcanic stages are recorded at 60 Ma (Viramonte *et al.*, 1999). However, depending on the uncertainties and because we do not know if this age corresponds to the prograde or the retrograde path of the associated (U)HT metamorphism, we can not precisely relate the Salta lower crust metamorphism to one of the listed rift stages.

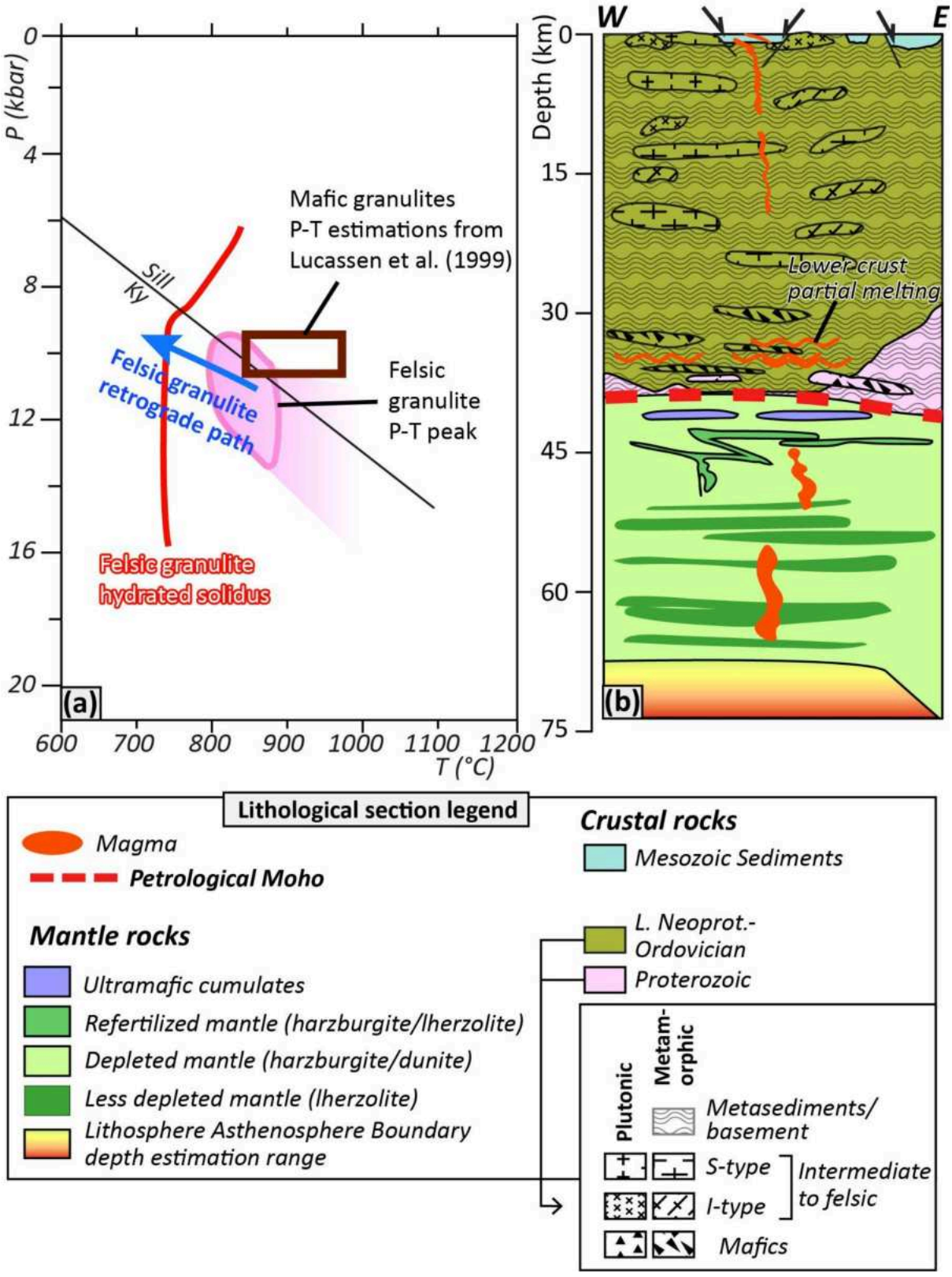


Fig. IV.8. (a) Estimated P-T domains of the Las Conchas granulites. (b) Simplified lithosphere section until 75 km in depth near Las Conchas Valley during the Late Cretaceous. The Moho is located around 40 km deep and the felsic lower crust records partial melting.

The described metamorphism and partial melting in felsic granulites go along with extensive deformation fabrics at (U)HT temperatures associated with late grain boundary migration and re-equilibrated textures in both mafic and felsic granulites. The metasomatism reported in some mafic and felsic granulites and in the sample A-112b by isotopic data of Lucassen *et al.* (1999b) could be a tardive process that took place between a partial melting event and xenolith sampling by basaltic magmas at 78-76 Ma (Marquillas *et al.*, 2005).

P-T conditions of felsic granulites of 10-12 kbar and 800-860 °C are comparable to those of the mafic granulites proposed by Lucassen *et al.* (1999b) at 9.5-10.5 kbar, 830-970 °C (Fig. IV.8a). Uncertainties of thermobarometry do not allow yet to distinguish P-T conditions between the two granulite groups. Nevertheless, pressure estimation of felsic xenolith extends the Moho depth at 40-45 km (Fig. IV.8b). Finally, Ti-in zircon calculated temperatures in the felsic granulite 4-302 that reach 1000 °C, HT clinopyroxene fabrics in mafic granulites, as well as supplementary pseudosection calculation (*Supplementary Fig. SIV.2*), constitute a base for further investigations to understand if Don Javier granulites recorded temperatures greater than 1000°C during the Cretaceous rift-related metamorphism.

IV. 6 CONCLUSIONS

- Las Conchas felsic granulites display both inherited magmatic and metamorphic zircon populations
- Zircon petrochronology confirms the metasedimentary nature of felsic granulites and highlights a UHT metamorphism event dated at 114 Ma, related to the first Salta rifting stage
- Thermobarometry yielded T >800 °C and P >10 kbar for the UHT metamorphism event and redefined the Moho depth at 40-45 km
- Mafic granulites recorded HT deformation - possibly contemporaneous to UHT metamorphism in felsic granulites - overprinted by re-equilibration.

CHAPTER V: The microstructural state of the lithospheric mantle near the Moho in the North Patagonian Massif and Salta rift

In collaboration with Mary-Alix Kaczmarek, Michel Grégoire, Theodoros Ntaflos, Ernesto Bjerg, Friedrich Lucassen, Hadrien Henry and Frédéric Mouthereau.

ABSTRACT

The Petrological Moho is a complex zone between the sub-continental lithospheric mantle and the mafic and/or felsic lower crust, where magmatic and mechanical processes interact. Its complexity and inaccessibility mean that the chemical and physical transfers between the crust and the mantle are, in many cases, still poorly understood. In this chapter, we present new major and trace mineral composition and microstructural data on mantle xenoliths from both the Oligo-Miocene and Pleistocene lavas of the North Patagonian Massif (NPM; 41-43° S, Argentina), and the Upper Cretaceous lavas of the Salta intracontinental rift (26° S). These two localities are located in the back-arc domain in relation to the Nazca/South America convergence zone. The peridotites of the MNP display significant variations in terms of mineralogy, chemistry and texture, whereas the Salta peridotites are more homogeneous. In the western NPM, spinel harzburgites, depleted in major and trace elements, display a [100]-fibre fabric in olivine, attributed to extensional plastic deformation processes. A spinel harzburgite and a garnet lherzolite from Prahuaniyeu in eastern NPM display A-type and (010)-fibre fabric, respectively, and are both slightly depleted compared to harzburgites from the western NPM. Additionally, a dunite and a wehrlite from the western NPM correspond to ultramafic cumulates or percolation rocks intensely influenced by magma circulations. They display (010)-fibre fabric in olivine interpreted as resulting from a cumulative environment, and equilibration temperatures of 800-900°C, suggesting emplacement close to the petrological Moho. Finally, a spinel lherzolite shows a deformation identical to that of the mafic granulites in the region, and its low equilibration temperatures (700°C) suggest emplacement from lower crust depths. At Salta, the peridotites display an olivine fabric

intermediate between (010)-fibre and A-type, interpreted as plastic deformation in extension with a slight shear component. Almost all samples from both regions show a very high concentration of misorientations at low angle boundaries in olivine parallel to the (010) axis, associated with activation of the [001](100) and [100](001) slip systems. For both regions, this feature is associated with cooling after the deformation events that generated the peridotite fabrics. This late event is associated with less intense deformation, which did not erase the fabric inherited from the rocks. This study, combining microstructure, petrology and geochemistry, demonstrates the diversity of rocks present at or near the Moho influenced by magmatic processes below the NPM, as well as the deformation between western and eastern NPM, which contrasts with the Moho region below Salta, appearing much more homogeneous. These two regions, which also show similarities in the deformation regime of the upper mantle, provide insights into the deformation of the upper mantle in the back-arc domain.

RÉSUMÉ

Le Moho Pétrologique est une zone complexe entre le manteau lithosphérique sous continental et la croûte inférieure mafique et/ou felsique, où des processus magmatiques et mécaniques sont mis en jeu et interagissent. Sa complexité et son inaccessibilité font que les transferts chimiques et physiques entre la croûte et le manteau sont dans de nombreux cas encore peu compris. Dans ce chapitre, nous présentons des nouvelles données de composition majeurs et traces des minéraux et de nouvelles données microstructurales sur des xénolithes mantelliques provenant à la fois des laves oligo-miocènes et pléistocènes du Massif Nord Patagonien (MNP; 41-43° S, Argentine), et des laves du Crétacé Supérieur du rift intracontinental de Salta (26° S). Ces deux localités se situent en domaine arrière arc par rapport à la zone de convergence Nazca/Amérique du Sud. Les péridotites du MNP ont une minéralogie, une chimie et des textures très variées tandis que les péridotites de Salta sont très homogènes. Dans l'Ouest du MNP, les harzburgites à spinelles, appauvries en éléments majeurs et traces, ont une fabrique de l'olivine de type fibre-[100] qui peuvent être reliées à des processus de déformation plastique en extension. Une harzburgite à spinelle et une lherzolite à grenat, provenant de Prahuaniyeu dans l'Est du MNP, présentent une fabrique de type-A et de type fibre-(010) respectivement, et sont toutes deux peu appauvries par rapport aux harzburgites de l'ouest du MNP. De plus, une dunite et une wehrlite de l'ouest du MNP

correspondent à des cumulats ultramafiques ou à des roches réactionnelles intensément circulées par des magmas. Elles ont des fabriques de type fibre-(010) dans l'olivine interprétées comme issues d'un environnement cumulatif et ont des températures d'équilibration de 800-900°C suggérant qu'elles ont été mises en place à proximité du Moho pétrologique. Enfin, une lherzolite à spinelle présente une déformation identique à celle des granulites mafiques de la région, et de par ses faibles températures d'équilibration (700°C), est interprétée comme potentiellement issue de la croûte inférieure. A Salta, les péridotites ont une fabrique de l'olivine intermédiaire entre le type fibre-(010) et le type-A, interprétées comme de la déformation plastique en extension avec une légère composante cisaillante. Enfin, la quasi-totalité des échantillons des deux régions présentent une très forte concentration des désorientations aux sous-joints de grains dans l'olivine parallèles à l'axe (010), allant de pair avec l'activation des systèmes de glissement [001](100) et [100](001). Cette caractéristique est associée pour les deux régions à un refroidissement postérieur aux événements de déformation ayant généré les fabriques des péridotites. Cet événement tardif est donc associé à une déformation moins intense, qui n'a pas effacé la fabrique héritée des roches. Cette étude combinant microstructure, pétrologie et géochimie démontre ainsi la diversité de roches présentes au niveau ou proches du Moho influencé par des processus magmatiques à l'aplomb du MNP, mais aussi de la déformation entre l'Ouest et l'Est du MNP, ce qui contraste avec la région du Moho à l'aplomb de Salta qui semble beaucoup plus homogène. Ces deux régions qui présentent par ailleurs des similarités dans le régime de déformation du manteau supérieur, ouvrent des portes à une meilleure compréhension de la déformation du manteau supérieur en domaine arrière-arc.

V. 1 INTRODUCTION

The Petrological Moho is a very complex boundary, between the ultramafic subcontinental lithospheric mantle (SCLM) and the mafic to felsic continental lower crust (Griffin & O'Reilly, 1987; Mengel & Kern, 1992; O'Reilly & Griffin, 2013). At this very complex boundary there is an interplay of magmatic and mechanical processes. The SCLM and the lower crust are commonly sampled by xenoliths brought up by alkaline and high alkaline volcanic rocks (O'Reilly & Griffin, 2013). In central and southern South America, mantle and lower crust xenoliths occur in the back-arc region of the Nazca/Antarctica subduction beneath South America. The uplift of xenoliths dates back from Pleistocene to maximum Oligocene

period South of 36°S latitude, while they primarily occur within Cretaceous volcanic rocks in central South America.

Over the past three decades, extensive petrological and geochemical studies have characterised the composition, evolution and chemical heterogeneities of the South American back-arc SCLM. The Cretaceous back-arc SCLM between 22 and 34°S latitude appears relatively homogeneous and depleted in terms of mineralogical assemblages and major element compositions. However, variations in trace elements and radiogenic isotopes compositions (Sr, Nd, Pb) indicate that subduction-related processes (i.e. fluid-percolation, asthenosphere upwelling during slab retreat or mechanical erosion during slab shallowing) affected this SCLM since at least Early Paleozoic times. In contrast, the SCLM beneath the Patagonia back-arc contains cratonic remnants as suggested by Re-Os datation (rhenium depletion ages, T_{RD}) that yield Phanerozoic to Paleoproterozoic ages (up to 2.5 Ga; Mundl *et al.*, 2015, 2016; Schilling *et al.*, 2017), but also shows evidence of significant and heterogeneous melt extraction, ranging from 1 to 30 % (Melchiorre *et al.*, 2020). This extraction is supported by xenolith major and trace element compositions and may be linked to intense magmatic activity during Paleozoic and Mesozoic times (Mundl *et al.*, 2016; Schilling *et al.*, 2017). Lately, the Patagonian SCLM has undergone re-fertilization through metasomatism, both modal with crystallisation of hydrous minerals, in localities near the Nazca or Antarctica subduction trenches (Faccini *et al.*, 2013; Melchiorre *et al.*, 2015; Jalowitzki *et al.*, 2017; Novais-Rodrigues *et al.*, 2021) and cryptic (e.g. Mallmann, 2004; Bjerg *et al.*, 2009). Some authors linked metasomatism to Cenozoic intraplate magmatism in Patagonia (e.g. Stern *et al.*, 1999; Melchiorre *et al.*, 2020). Despite these detailed petrological and geochemical characterisations, the petrophysical state of the South American back-arc SCLM remains poorly constrained. Only one study has indeed focused on Southern Patagonia xenolith microstructures, which revealed extensive annealing fabrics and multiple percolating melt events in coarse-grained and texturally equilibrated peridotites (Zaffarana *et al.*, 2014). In addition, the petrophysical state of the SCLM to the North of Southern Patagonia has never been characterised.

Above the Petrological Moho, the petrological, geochemical and petrophysical features of the lower crust have been studied in both the North Patagonian Massif (NPM; 40-42°S latitude; chapter III) and central South America Cretaceous back-arc (from Las Conchas Valley xenoliths, 26°S latitude; chapter IV; Lucassen *et al.*, 1999). In the NPM, the lower crust displays homogeneous low plastic deformation as it shows mafic granulite mineral assemblages, and major and trace element compositions that reflect the intense

magmatic activity that led to lower crustal growth and reworking since the Late Paleozoic. In contrast, the Cretaceous xenoliths from Las Conchas Valley in the Salta intracontinental rift show HT annealed fabrics and evidence of UHT metamorphism (chapter IV). These features are linked to the Cretaceous intracontinental rift and indicate a Late Proterozoic to Ordovician metasedimentary origin for the Salta lower crust (Chapter IV; Lucassen *et al.*, 1999).

In this chapter, I studied the rheology and associated magmatic processes recorded by the SCLM in central and southern South America by investigating the microstructure of peridotites and clinopyroxenites xenoliths, and their relationship with the chemical composition of the minerals. A collection of Oligo-Miocene to Pleistocene peridotite xenoliths from five different localities in the NPM, as well as Cretaceous peridotite and clinopyroxenite xenoliths from the Las Conchas Valley has been used. The new obtained data, combined with existing petrological, geochemical and rheological data, allow to propose a model for the deformation, thermal state, and evolution of the Petrological Moho beneath two distinct regions of the central and southern South America back-arc, namely, the actual NPM (41-43°S) and the Cretaceous Salta intracontinental rift (26°S).

V. 2 GEOLOGICAL SETTING

The central and southern South American lithosphere consists of continental blocks with primarily Mesoproterozoic crustal basement ages. Its western margin has been considered to be active since the Early Paleozoic, significantly influencing lithospheric evolution. The NPM (41-43°S; Fig. V.1), located in the back-arc area regarding the Nazca subduction, is surrounded by several Mesozoic basins reworked during the Cenozoic (Fig. V.1). In contrast, the NPM displays only minor faults and is regarded as a rigid lithospheric block (Aragón *et al.*, 2011). In the field, the NPM displays Cambrian to Ordovician magmatic and metasedimentary rocks to the NE and Devonian to Carboniferous ones to the West (Pankhurst *et al.*, 2006; Martínez Dopico *et al.*, 2011). Those Paleozoic rocks are overlain by Permo-Trias granitoids and rhyolites, Jurassic andesites and rhyolites and abundant Cenozoic (especially Oligo-Miocene) alkaline basalts plateaus (see Figure II.1 in Chapter II). Although the crustal basement is considered to be Mesoproterozoic in age (Martínez Dopico *et al.*, 2011; Uriz *et al.*, 2011; Rapalini *et al.*, 2013; Pankhurst *et al.*, 2014; see Chapter I and II), studies have shown significant remobilisation and growth of the lower crust from the

Devonian to the Cenozoic (Oriolo *et al.*, 2023; Chapter II). Our granulite xenolith study revealed that the NPM lower crust has homogeneous chemical and petrophysical properties, characterised by low plastic deformation and composed of orthopyroxene-bearing mafic granulites and websterites with a magmatic protolith (Chapter II; Muckensturm *et al.*, Submitted). The associated geotherm is approximately 30°C/km and the Petrological Moho is estimated to be at a depth of 40 km. Beneath the NPM lower crust, the SCLM is highly depleted, with xenoliths primarily consisting of harzburgites except at Prahuaniyeu, East-NPM, where both fertile lherzolite and harzburgite occur (Mundl *et al.*, 2016). Re-depletion model ages (T_{RD}) determined from Re-Os isotopic analysis on mantle xenoliths from most NPM localities range from 0.03 to 1.3 Ga, while Paleoproterozoic T_{RD} (1.7 Ga) from Prahuaniyeu are related to a much older SCLM remnant of the NPM (Schilling *et al.*, 2008, 2017; Mundl *et al.*, 2016). Modal metasomatism has been recognised at Comallo, Cerro del Mojón and Prahuaniyeu (Bjerg *et al.*, 2005; Schilling *et al.*, 2008), with the presence of amphibole or phlogopite in peridotite assemblages. However, it is rather cryptic in xenoliths from other NPM localities, as indicated by clinopyroxene light rare earth elements (LREE) enrichment, rare earth element (REE)-V shape patterns, Hf, Nd and Sr isotopic compositions, and platinum group element abundances (PGE; Mundl *et al.*, 2016).

In contrast, the Salta rift basins (ca. 26°S; Fig. V.1) are N-S oriented Cretaceous to Paleogene basins formed in the back-arc area regarding the subduction of Protopacific oceanic plates. These basins developed during an intracontinental rift associated with alkaline magmatism (Viramonte *et al.*, 1999; Marquillas *et al.*, 2005). They occur on a basement composed of Cambrian to Ordovician metasediments, with protoliths dated between >600 and 520 Ma (i.e. the Late Neoproterozoic to Cambrian Puncoviscanian Formation; Casquet *et al.*, 2006; Rapela *et al.*, 2016; Weinberg *et al.*, 2018) and intruded by numerous Cambrian to Devonian granitoids (see figure IV.1 from Chapter IV). The lower crust in this region is mainly felsic, as suggested by xenolith sampling and seismic models (Wigger *et al.*, 1994; Lucassen *et al.*, 1999). It recorded low deformation and reequilibrated fabrics associated with ultra-high temperature (UHT) metamorphism and partial melting during the early Cretaceous, as indicated by zircon U-Pb dating (113± 4 Ma Ma; Chapter IV). The Cretaceous geotherm of the lower crust is estimated at ca. 23°C/km, with a Petrological Moho located at a depth of 40-45 km. The SCLM near Salta consists of both lherzolites and harzburgites, ranging from depleted peridotites to rather primitive ones based on major and trace element compositions (Lucassen *et al.*, 2005). Cryptic metasomatism is present in the SCLM but has been detected

only through slight variations in trace element and radiogenic isotope compositions (Sr, Nd, Pb; Lucassen *et al.*, 2005).

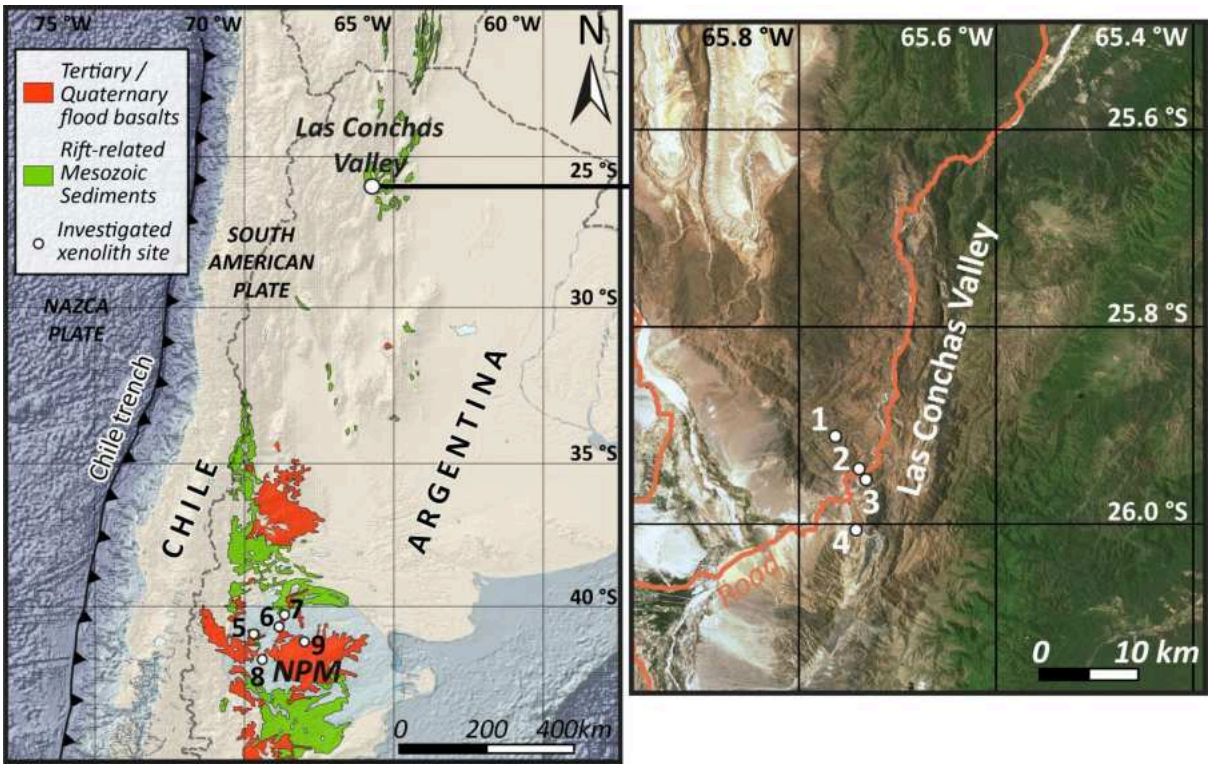


Fig. V.1. Localities of investigated xenoliths on a simplified geological map of South America (20-45° S latitude) and a satellite view (from BDOrtho IGN) of Las Conchas Valley (Salta province, Argentina). 1: Quedebrada Los Nacimientos; 2: El Sapo; 3: Quedebrada Don Javier; 4: Cerro Amarillo; 5: Comallo; 6: Laguna Fría; 7: Cerro Chenque; 8: Cerro Traful; 9: Prahuaniyeu; NPM: North Patagonian Massif. For details of North Patagonian Massif geology and xenolith localities, refer to Figure II.1 from Chapter II.

Xenoliths from the NPM are found in Oligocene to Pleistocene volcanic rocks and comprise spinel and rare garnet peridotites, spinel pyroxenites, and granulites. Host rocks are alkaline trachybasalts and basalts dated from the Late Oligocene to Early Miocene for Cerro Chenque and Cerro Traful (23-25 Ma; Mundl *et al.*, 2016), Early Miocene for Prahuaniyeu (21-23 Ma; Mundl *et al.*, 2016), Pliocene-Pleistocene for Laguna Fría (1-5 Ma; Bjerg *et al.*, 2005) and Early Pleistocene for Comallo (0.9-1.4 Ma; Mundl *et al.*, 2016).

Salta rift xenoliths are located in the Las Conchas valley (Fig. V.1). Host rocks are breccias filling volcanic vents (Lucassen *et al.*, 1999, 2005; Viramonte *et al.*, 1999), intruded by Campanian basanite dykes which belong to the Las Conchas Basalt formation (78-76 Ma; Marquillas *et al.*, 2005).

V. 3 SAMPLE COLLECTION AND ANALYTICAL METHODS

V. 3.1 Sample collection

Norht Patagonian Massif xenoliths were sampled by T. Ntaflos and E. Bjerg within lava flows, basaltic necks and basaltic dykes from five different localities: Comallo, Cerro Traful, Laguna Fría, Cerro Chenque and Prahuaniyeu (Fig. V.1 and Table V.1). Xenoliths from Laguna Fría, and Prahuaniyeu volcanoes are spinel harzburgite (Table V.1). Comallo contains both spinel harzburgite and websterite, and Cerro Chenque, both spinel harzburgite and dunite. Volcano Prahuaniyeu also contains garnet lherzolite and Cerro Traful spinel lherzolite. Xenoliths have an average diameter of 8 to 12 cm but reach 30 cm in diameter at Traful and Laguna Fría (Bjerg *et al.*, 2005). Eight investigated mantle peridotite xenoliths from the NPM were studied.

In the Las Conchas Valley, among the xenolith sites, Quedebrada Los Nacimientos contains mantle peridotites and clinopyroxenites, Cerro Amarillo contains mantle peridotites, El Sapo contains mantle clinopyroxenites and Quedebrada Don Javier contains felsic and mafic granulites, mantle clinopyroxenites and carbonatized peridotites (i.e. replaced by carbonates, nomenclature from Lucassen *et al.*, 2005 and for peridotites and clinopyroxenites occurrences). Six ultramafic xenoliths (2 peridotites from Los Nacimientos and 2 from Cerro Amarillo, 2 clinopyroxenites from El Sapo), representative of the suite's texture, were selected for in-depth microstructural analysis from a xenolith collection provided by F. Lucassen.

V. 3.2 Crystallographic orientations of minerals

A mechanic-chemical polishing using a Vibromet (Buehler) was applied on 14 thin sections for 1h15 with a colloidal silica suspension (pH 10) to remove mechanically induced surface damage. Electron Backscatter Diffraction (EBSD) data acquisition was performed with a JEOL 7100 Secondary Electron microscope at the centre of microcharacterization Raimond Castaing (University Paul Sabatier, Toulouse), equipped with an EBSD camera CMOS Symmetry S2 (Oxford Instruments). The analyses were performed with an acceleration voltage of 20 kV, a probe current of 16 nA and a working distance of 15, 17 or 25 mm with a stage tilt of 70°. Automatic indexing was performed using AZTec software (version 6.0 Oxford Instruments). For mapping the step size used varies between 15 and 20 µm depending on the grain size. The EBSD data were then processed in MATLAB (version R2020b) using

Table V.1: Summary of host rock age, coordinates, modal compositions and olivine textural parameters of the investigated xenoliths. Modal proportions are estimated with EBSD data. BA and BC indexes are textural indexes from Mainrpice *et al.* (2015). *BKN* and *Wells* thermometers are those of Brey & Köhler (1990) and Wells (1977), respectively. [1]: from Mundl *et al.* (2016); [2]: from Bjerg *et al.* (2005); [3]: from Bjerg *et al.* (2009); [4]: from Viramonte *et al.* (1999). Ol: olivine; Opx: orthopyroxene; Cpx: clinopyroxene; Sp: spinel; Grt: garnet; Amph: amphibole; Wh: wehrlite; Lh: lherzolite; Hz: harzburgite; D: dunite; Cpxite: clinopyroxenite.

Locality	Sample	Host Rock Age (Ma)	Latitude (°S)	Longitude (°O)	*Rock type*	Modal prop. (%)						BA index	BC index	T°C	
North Patagonian Massif						Ol	Opx	Cpx	Sp	Grt	Amph	Ol	Ol	BKN	Wells
Comallo	**COM206**	1-2[1]	40°55'	69°52'	*Sp-Hz*	83.2	12.3	3.8	0.7			0.61	0.49		
C. Chenque	**CH42**	23-25[1]	40°29'	68°44'	*Sp-Hz*	86.3	12.2	1.3	<0,1			0.56	0.46	989	999
Laguna Fría	**LaFr8**	1-5[2]	40°21'	68°38'	*Sp-Hz*	82,2	15.9	1.8	<0,1			0.86	0.64	1190	1146
Prahuaniyeu	**PRA1**	21-22[1]	41°20'	67°54'	*Sp-Hz*	76	20.7	3.1	0.2			0.35	0.39	1061[3]	
	PRA33				*Grt-Lh*	65.7	22.7	9.6		2		0.16	0.20	1215[3]	
Cerro Traful	**TR45**	23-25[1]	41°38'	69°18'	*Sp-Lh*	60.4	13	20.3	6.2			0.63	0.50	744	798
Comallo	**COM138**	1-2[1]	40°55'	69°52'	*Wh*	79	2.7	16.1	2.1		0.1	0.06	0.06	893	920
C. Chenque	**CH48**	23-25[1]	40°29'	68°44'	*D*	93.8	1.8	2.3	2.1			0.13	0.11	854	881
Las Conchas Valley															
Los Nacimientos	**7-168a**	76-78[4]	25°55'42"	65°43'48"	*Sp-Hz*	60.4	34.8	4.4	0.3			0.24	0.26		
	6-181				*Sp-Lh*	73.1	19.9	6.3	0.7			0.27	0.25	1131	1025
Cerro Amarillo	**A-106**	76-78[4]	26°00'19"	65°44'34"	*Sp-Hz*	77.2	17.5	4.7	0.6			0.22	0.36	1014	1000
	4-147g				*Sp-Lh*	60.5	22	11.2	0.3		6	0.11	0.13	930	921
El Sapo	**4-235**	76-78[4]	25°56'34"	65°44'21"	*Cpxite*	92.3			7.7						
	4-242				*Cpxite*	99.1			0.9						

the MTex toolbox (version 5.7.0; Bachmann *et al.*, 2010, 2011). A value of 10° as the cut-off angle for the determination of the grains has been used. Pole figures were plotted on a lower-hemisphere, equal-area stereographic projection. To avoid oversampling of large olivine, orthopyroxene and clinopyroxene crystals, pole figures were plotted with one point per grain. For clarity, pole figures were rotated as the inferred foliation was the XY plan and lineation parallel to X. These interpretations take into account the trace of the foliation in xenoliths, the correlation of Crystallographic preferred orientation (CPO) concentration point between minerals. An example of a rotated pole figure procedure is given in *Supplementary Fig. SV.1*. The strength of the crystallographic preferred orientation was estimated using both the J- and M-indices (Bunge, 1982; Skemer *et al.*, 2005). BA-index was also calculated for olivine, and is defined by 1/2[2 − {P010/(G010 + P010)} − {G100/(G100 + P100)}] (Mainprice *et al.*, 2015). In the case of olivine, the values varies between 0 and 1, where BA values <0.35 represent a [010]-axial fabric, BA values between 0.35 and 0.65 an orthorhombic fabric and BA >0.65 corresponds to a [100]-axial fabric. In addition, the misorientation of each pixel was calculated relative to the mean orientation of its corresponding grain and then combined as maps of misorientation relative to mean grain orientation. In parallel, for each sample, pixel proportions relative to their misorientation angle were plotted in normalised histograms.

V. 4 RESULTS

V. 4.1 Sample description and petrography

V. 4.1.1 North Patagonian Massif peridotite xenoliths

North Patagonian Massif peridotite xenolith suite comprises spinel harzburgites ($Ol_{76\text{-}86\%}$ $Opx_{12\text{-}20\%}$ $Cpx_{1\text{-}4\%}$; samples COM206, CH42, LaFr8, PRA1), a garnet lherzolite ($Ol_{66\%}$ $Opx_{23\%}$ $Cpx_{10\%}$; sample PRA33), a spinel lherzolite ($Ol_{60\%}$ $Opx_{13\%}$ $Cpx_{20\%}$; sample TR45), a wehrlite ($Ol_{79\%}$ $Opx_{3\%}$ $Cpx_{16\%}$; sample COM138) and a dunite ($Ol_{94\%}$ $Opx_{2\%}$ $Cpx_{2\%}$; sample CH48; Table V.1; Figs. V.2, 3). Spinel modal proportion is always low in spinel-harzburgite (<0.7 vol.%) but somewhat relatively high in both the wehrlite and the dunite (2.1 vol.%) and even higher in the spinel-lherzolite (6.2 vol.%; Table V.1). The garnet-lherzolite PRA33 from Prahuaniyeu displays garnet modal proportions of 2 vol.%, as wehrlite COM138 from Comallo displays trace of pargasite.

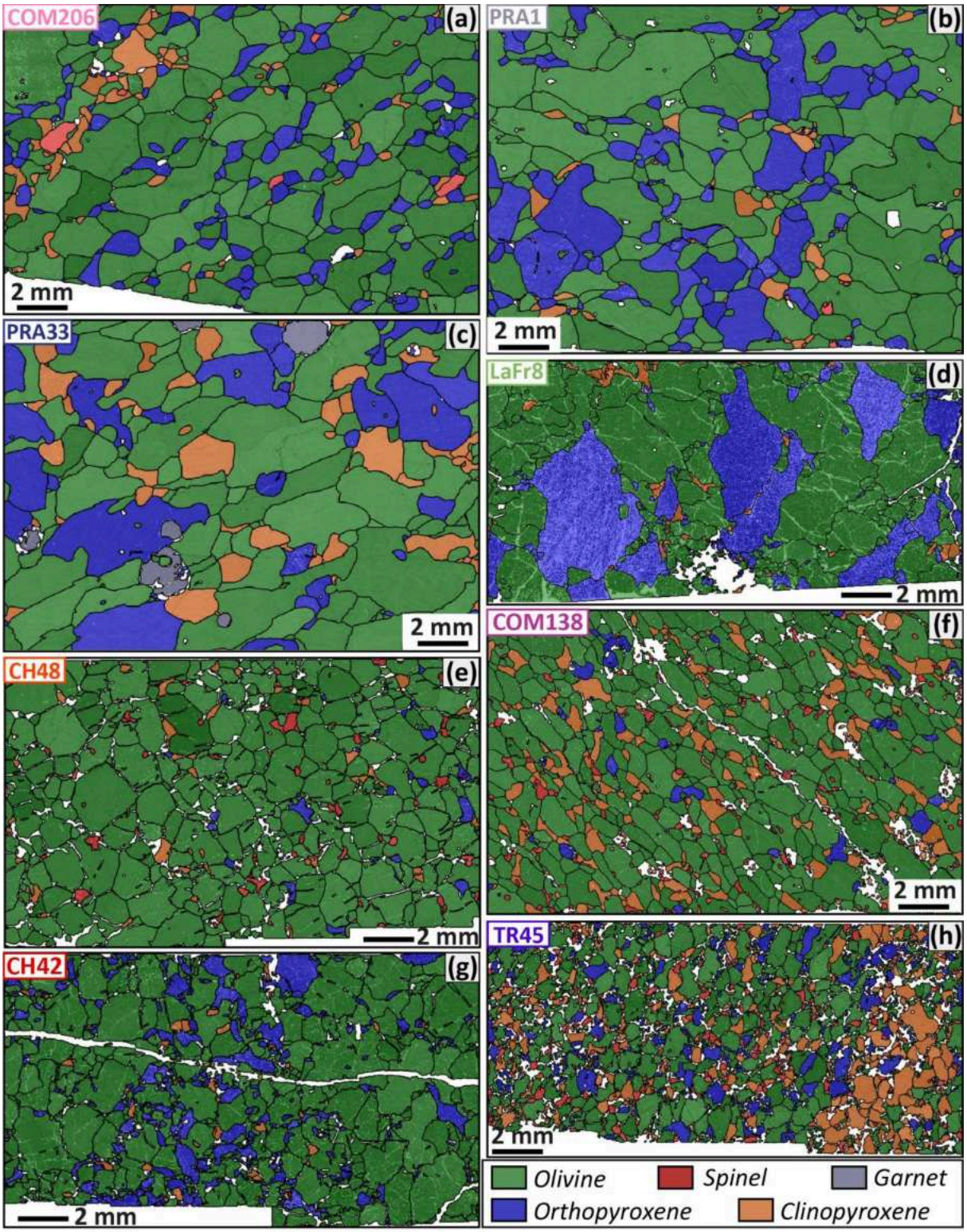


Fig. V.2. EBSD phase maps of North Patagonian Massif (NPM) peridotite xenoliths. (a, b, d, g) Spinel-harzburgites COM206, PRA1, LaFr8 and CH42. (c) Garnet-lherzolite PRA33. (e) Dunite CH48. (f) Wehrlite COM138. (h) Spinel-lherzolite TR45.

Spinel harzburgites COM206, PRA1, LaFR8 and the garnet lherzolite PRA33 display either medium- or coarse-grained texture with a grain size varying between 1 and 7 mm (Figs.

V.2a-d, 3a-c). The spinel harzburgite, CH42, the wehrlite COM138 and dunite CH48 display a medium grain size (1-3 mm; Figs. V.2e-g, 3d, e) and the spinel lherzolite TR45 display a fine-grained texture (300 μm to 2 mm; Figs. V.2h, 3f). Shape preferred orientation (SPO) is well-developed in samples COM206, PRA1, PRA33 and COM138 (olivine aspect ratio up to 4:1; Fig. V.2). It is less clear in samples TR45 and CH48 (aspect ratio up to 2:1) and weak to undetectable in spinel-lherzolites CH42 and LaFr8. Many samples display linear grain boundaries, tabular olivine grains and numerous 120° triple junctions (samples COM206, PRA1, PRA33, COM138 and CH48; Figs. V.2, 3). The spinel-lherzolite TR45 displays linear to slightly curved grain boundaries and numerous 120° triple junctions (Figs. V.2h, 3f). Finally, spinel-harzburgites CH42 and LaFr8 display highly polygonal grain boundaries and rare 120° triple junctions (Fig. V.3c, e).

Sample LaFr8 display the larger orthopyroxene grains (up to 8mm) from the xenolith suite (Figs. V.2d, 3c). In other xenoliths, Orthopyroxene grain size is bimodal in samples PRA1, PRA33 and Ch42, as large grains reach the size of olivine grains and small grains (<1 mm) occur at olivine triple junctions (Fig. V.2b, c, g). In samples COM206, CH48, and COM138, the orthopyroxene grain size is unimodal, with a grain size similar to smaller grains in other xenoliths. These grains occur at olivine triple junctions suggesting interstitial orthopyroxene grains (Fig. V.2a, e, f). Finally, in the spinel-lherzolite TR45, the orthopyroxene and clinopyroxene grain size is the same as the olivine grains (i.e. 300 μm to 2 mm; Figs. V.2h, 3f).

Clinopyroxene may form discontinuous layers, 1 mm thick in sample COM206 and 2-3 mm thick in sample TR45, with grain size up to 1 mm (Fig. 2a, h). In most samples, from all lithologies, small clinopyroxenes grains are located at olivine triple junctions, with lobate shape, suggesting interstitial grains. In the garnet-lherzolite PRA33 and the wehrlite COM138, the clinopyroxene appears also as medium grains (1-3 mm; Fig. V.2c, f). Spinel is always fine-grained (<1 mm) and occurs most of the time at triple junctions of olivine or pyroxene grains. The garnet is round-shaped and medium-grained (up to 2 mm) in the garnet-lherzolite PRA33 (Figs. V.2c, 3b).

V. 4.1.2 Las Conchas Valley ultramafic xenoliths

Peridotites. Las Conchas Valley investigated peridotite xenoliths comprises clinopyroxene-rich spinel-harzburgites ($Ol_{60\text{-}77\%}$ $Opx_{16\text{-}35\%}$ $Cpx_{4.4\text{-}4.7\%}$; samples 7-168a and A-106) and spinel-lherzolites ($Ol_{61\text{-}73\%}$ $Opx_{20\text{-}22\%}$ $Cpx_{6\text{-}11\%}$; sample 6-181 and 4-147g; Table V.1; Fig. V.4). Spinel modal proportions are always low (<0.7 vol.%). The spinel-lherzolite

from Cerro Amarillo 4-147g contains pargasite (6 vol.%) which often appears as clusters surrounding spinel grains (Fig. V.4d, e).

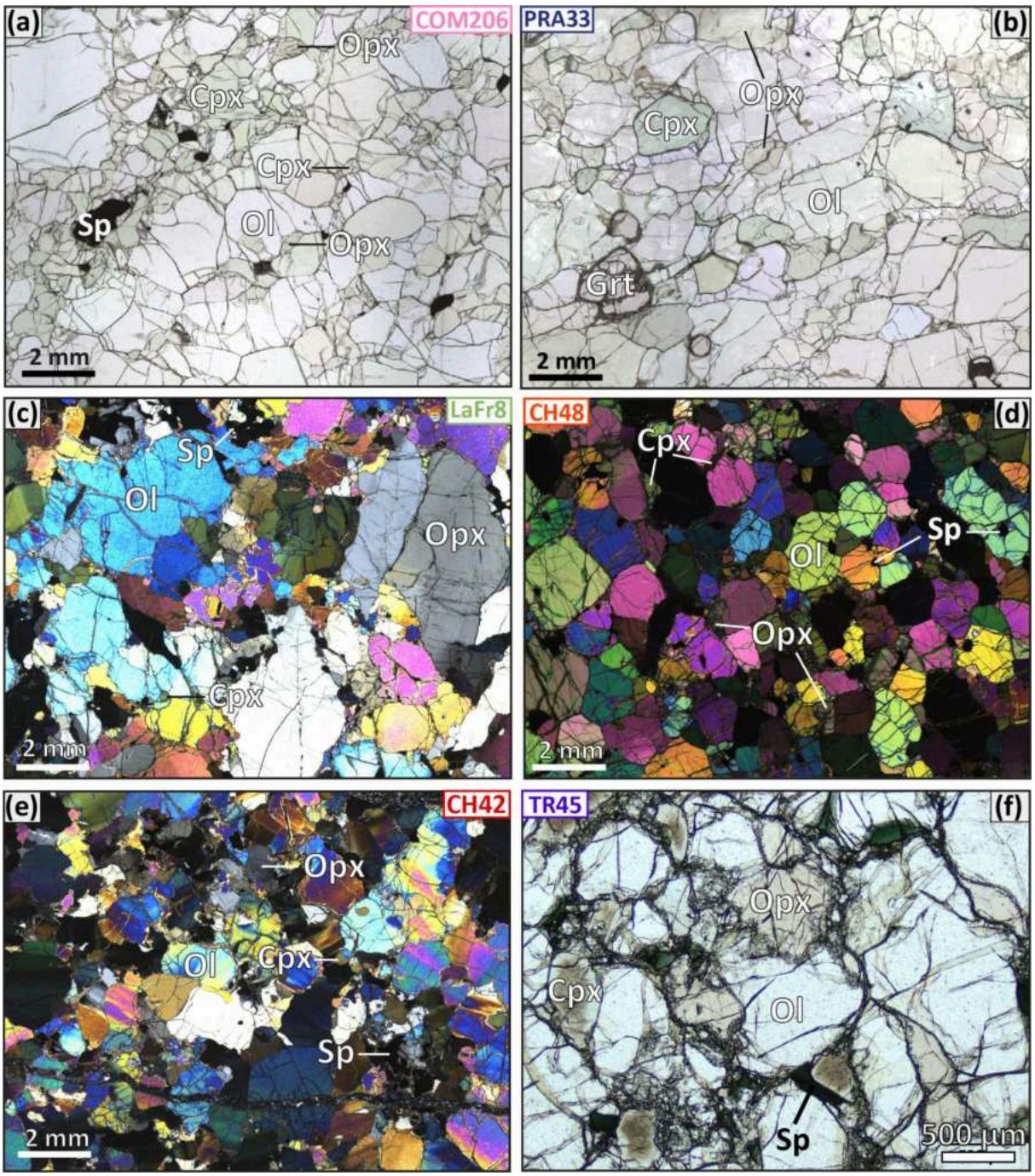


Fig. V.3. Photomicrographs of North Patagonian Massif (NPM) peridotite xenoliths. (a) Spine-harzburgite COM206 under plane-polarised light. (b) Garnet-lherzolite PRA33 under plane-polarised light. (c, e) Spinel-harzburgites LaFr8 and CH42 under cross-polarised light. (d) Dunite CH48 under cross-polarised light. (f) Spinel-lherzolite TR45 under plane-polarised light.

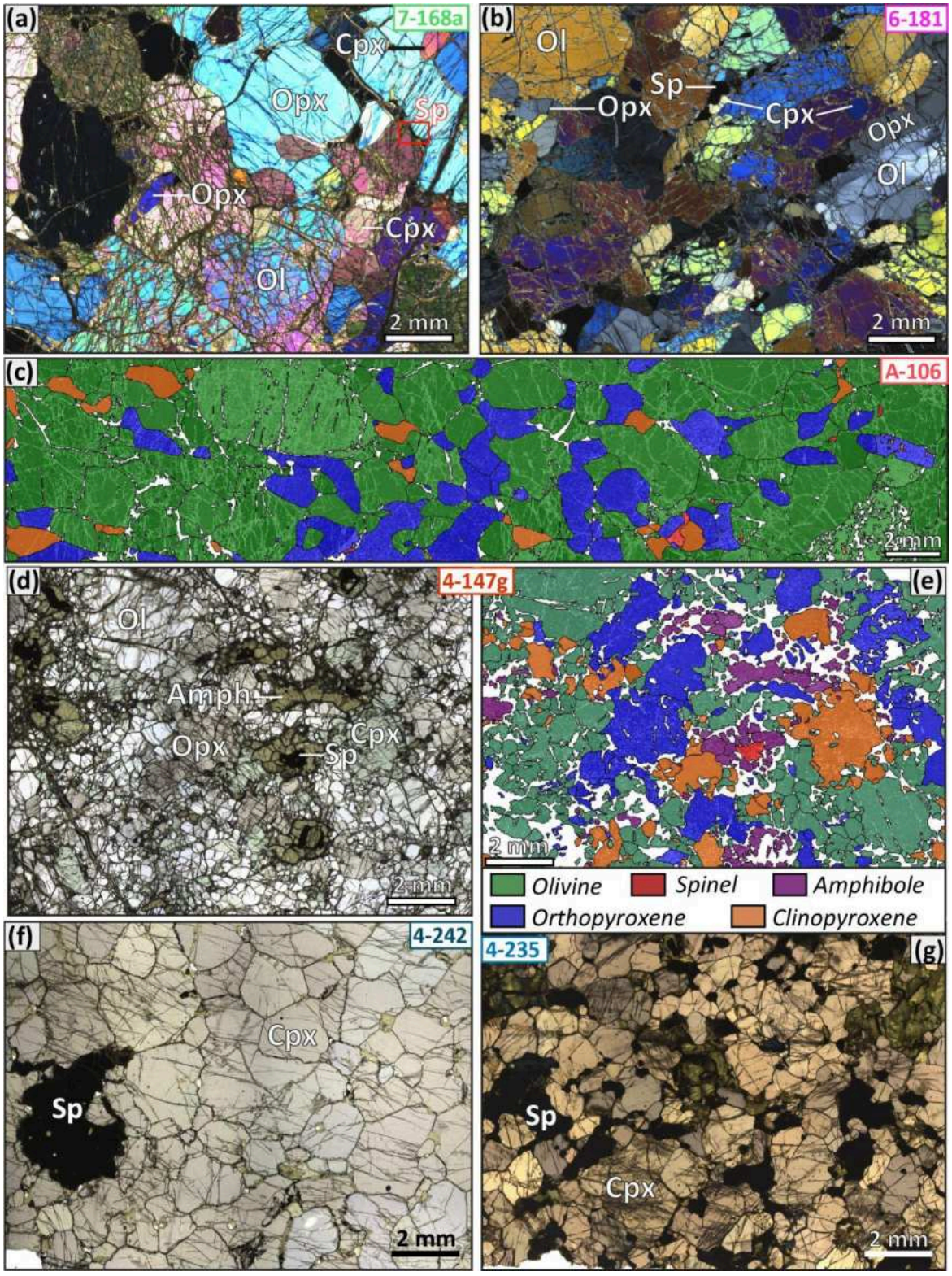


Fig. V.4. Photomicrographs and EBSD phase maps of Las Conchas Valley ultramafic xenoliths. (a) Spinel-harzburgite (sample 7-168a) with no shape preferred orientation (SPO), under cross-polarised light. (b) Spinel-lherzolite (sample 6-181) with a clear SPO, under cross-polarised light. (c) EBSD phase map of spinel-lherzolite A-106 with a clear SPO. (d) Plane-polarised light view and (e) EBSD phase map of porphyroclastic spinel-harzburgite (samples 4-147g). (f, g) Spinel-clinopyroxenites (samples 4-242 and 4-235) under plane-polarised light.

Spinel harzburgites 7-168a and 6-181 and the spinel lherzolite A-106 display fine- to coarse-grained texture with a grain size varying between 500 μm and 7 mm (Fig. V.4a-c). SPO is absent in the spinel-harzburgite 7-168a and well-developed in samples A-106 and 6-181, as it affects olivine, orthopyroxene and clinopyroxene (aspect ratio up to 4:1; Fig. V.4a-c). Grain boundary shape varies from rather curved (samples 7-168a and 6-181) to rather linear (A-106) - 120° triple junctions are not common. Amphibole-bearing spinel-lherzolite 4-147g displays a porphyroclastic texture, with either large and elongated grains (>1 mm), which define the sample SPO (aspect ratio up to 4:1) and display curved to highly polygonal grain boundaries, or small and round-shaped grains (<1 mm) which display linear grain boundaries. 120° triple junctions occur only between small grains.

In spinel-harzburgites 7-168a and A-106 and in the spinel-lherzolite 6-181, grain size is unimodal for the same phase, as olivine is coarse-grained and reaches 7 mm in peridotites (Fig. V.4a-c). Orthopyroxene displays a similar grain size distribution to olivine in sample 7-168a but is rather smaller than olivine in samples A-106 and 6-181 (500 μm to 5 mm). Clinopyroxene is always smaller than olivine (500 μm to 2 mm). Grain size distribution range of amphibole-bearing spinel-lherzolite 4-147g is wide, as it ranges from 100 μm to 7 mm for olivine and orthopyroxene and from 100 μm to 4 mm for clinopyroxene and amphibole (Fig. V.4d, e).

Clinopyroxenites. Samples 4-235 and 4-242 are clinopyroxenites which contain accessory spinel that occurs homogeneously in sample 4-235 (7.7 vol.%) but only as a single patch (0.9 vol.%) of 1 cm long (Fig. V.4f, g). The grain size is unimodal, ranging from 500 μm to 4 mm. Grain boundaries are linear and 120° triple junctions are numerous in sample 4-242, however, grain boundaries are much more curved in sample 4-235 and 120° triple junctions are less frequent (Fig. V.4f, g). The clinopyroxenite xenolith group contains samples with clinopyroxene grains that reach several centimetres but EBSD has not been carried out on those samples as only very little microstructural information can be extracted from large grains (Lucassen *et al.*, 2005).

V. 4.2 Minerals major and trace element compositions

V. 4.2.1 Chemical compositions of minerals from the North Patagonian Massif

NPM ultramafic xenolith clinopyroxene are either diopside or augite (Fig. V.5; *Supplementary Table. SV.1*). Clinopyroxene from all peridotite xenoliths, except lherzolite TR45 from Cerro Traful, has high Mg# (89-95). Moreover, its Al_2O_3 content varies between 2 and 8 wt% and is negatively correlated with Mg#. Clinopyroxene from TR45, as well as those

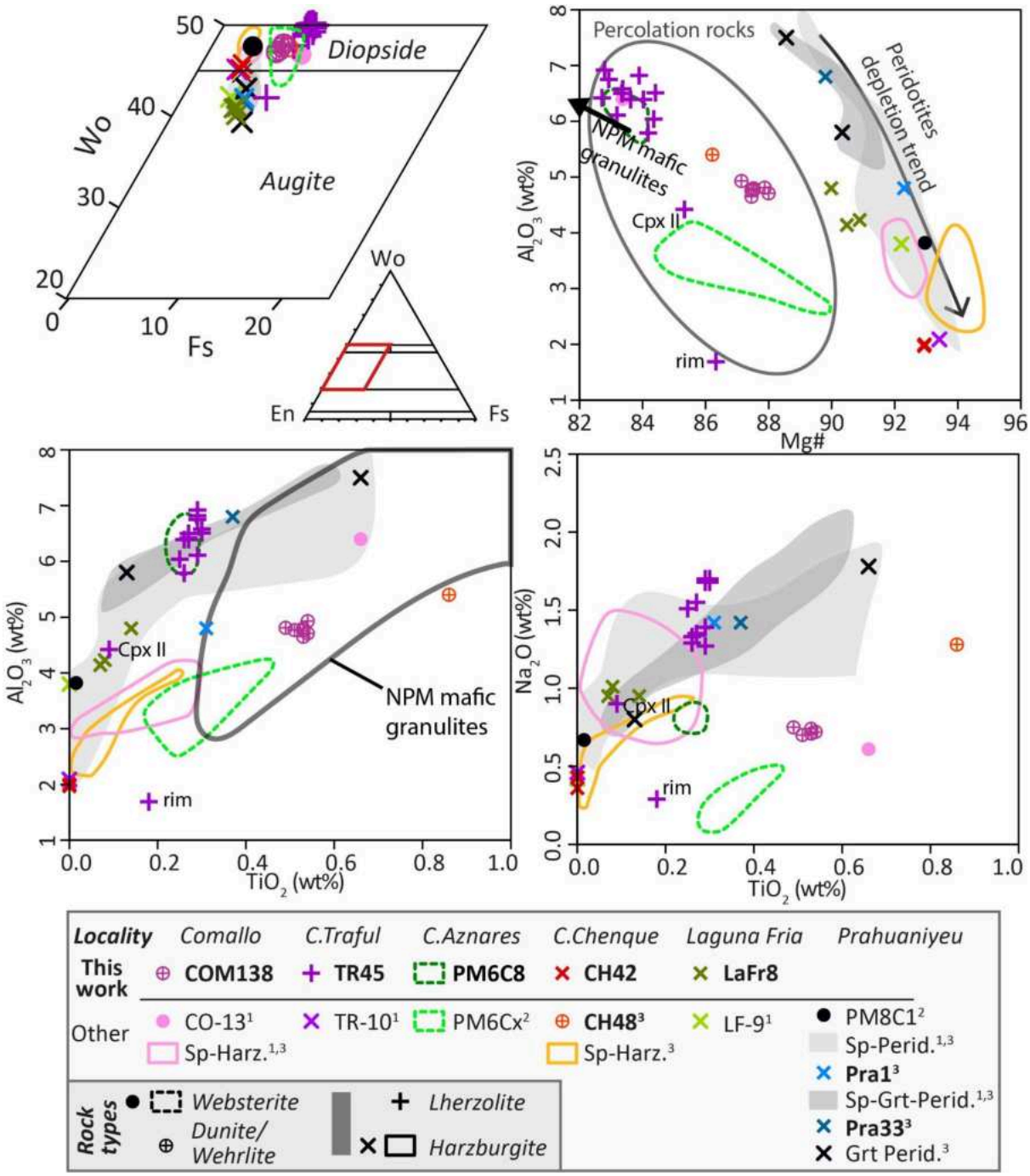


Fig. V.5. North Patagonian Massif (NPM) peridotites clinopyroxene major element compositional diagrams. Annotated data are from 1: Bjerg *et al.* (2005); 2: Dantas (2007); 3: Bjerg *et al.* (2009). PM6C8 and NPM mafic granulites are from Chapter II. When the NPM mafic granulite field is out of the diagram, its approximative position is indicated with an arrow.

from websterites, wehrlite COM138 from Comallo and dunite CH48 from Cerro Chenque does not plot on this trend and display lower Mg# (82.5-90; Fig. V.5). Some of these less magnesian clinopyroxenes, including those of spinel lherzolite TR45, display compositions close to those of some NPM mafic granulites for which Mg# ranges between 66 and 80

(Chapter II). Al_2O_3 and TiO_2 clinopyroxene contents of peridotite xenoliths are positively correlated and seem to follow a trend, as well as Na_2O and TiO_2 contents. However, websterites from Cerro Aznares and Comallo, wehrlite COM138 and dunite CH48 does not follow this trend (Fig. V.5).

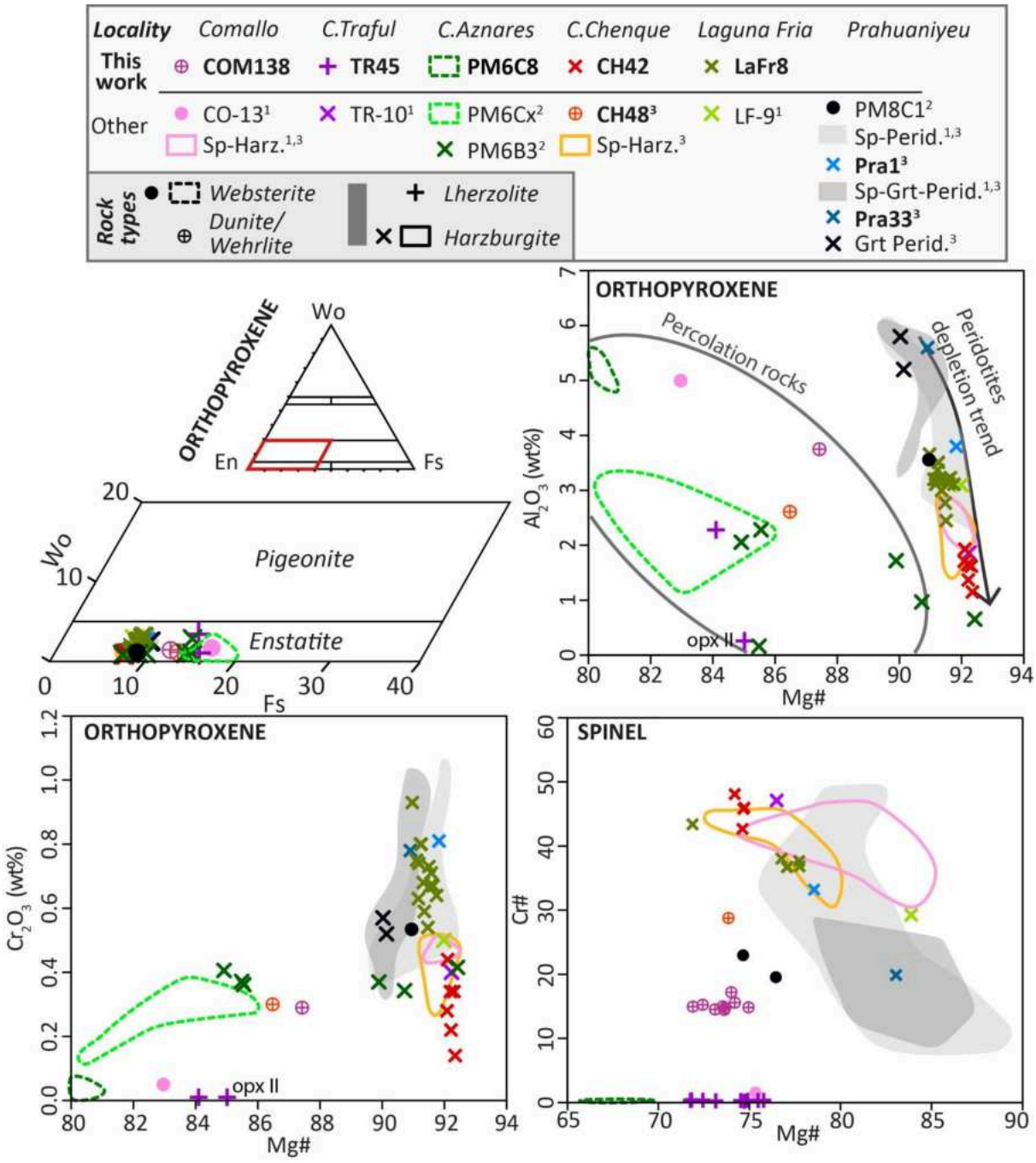


Fig. V.6. NPM peridotites orthopyroxene and spinel major element compositional diagrams. Annotated data are from 1: Bjerg *et al.* (2005); 2: Dantas (2007); 3: Bjerg *et al.* (2009). PM6C8 and NPM mafic granulites are from Chapter II. NPM mafic granulite compositions plot out the diagrams and their approximative position is indicated with an arrow.

Orthopyroxene is enstatite in composition and displays a Mg# higher than 90 for all ultramafic xenoliths except websterites from Cerro Aznares and Comallo, spinel lherzolite TR45, wehrlite COM138, dunite CH48 and spinel harzburgite PM6B3 (Fig. V.6). Spinel from the latter samples are also less magnesian (Mg# 65-76) than those from other ultramafic xenoliths (Mg# 73-90; Fig. V.6). Amphibole I in wehrlite COM138 is pargasite (*Supplementary Table. SV.2).*

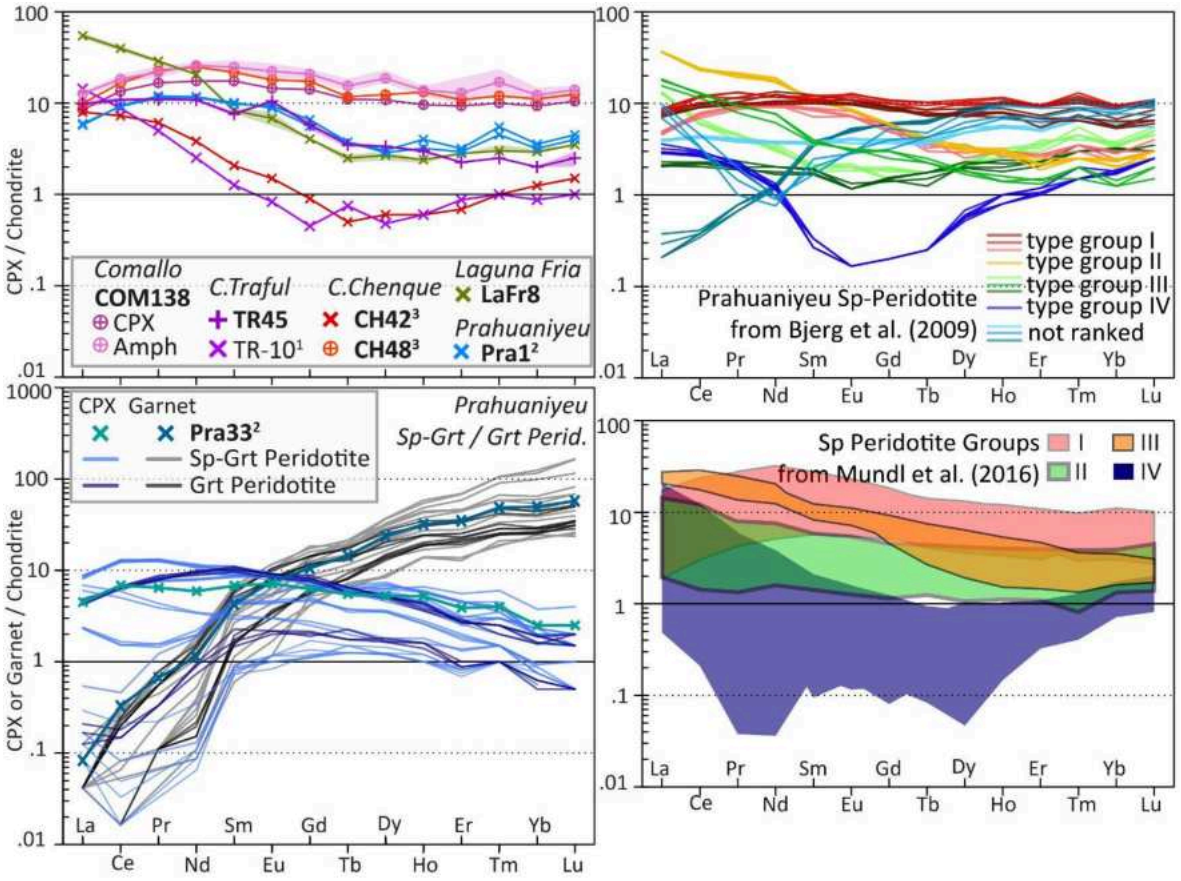


Fig. V.7. Normalised clinopyroxene, amphibole and garnet rare earth element patterns (REE) from North Patagonian Massif peridotites xenoliths. The legend for the rock type is the same as in figures V.5 and 6. Prahuaniyeu sp-peridotite data from Bjerg *et al.* (2009) have been classified following NPM sp-peridotite classification from Mundl *et al.* (2016) as follows: Group I: light REE (LREE) < medium REE (MREE) > heavy REE (HREE); Group II: LREE > MREE = HREE; Group III: LREE > MREE > HREE; Group IV: LREE > MREE < HREE. Annotated data are from 1: Bjerg *et al.* (2005); 2: Bjerg *et al.* (2009). Chondrite values are from McDonough & Sun (1995).

New investigated samples display various clinopyroxene chondrite-normalised rare earth elements (REE) patterns. Wehrlite COM138 and dunite CH48 display flat/smoothly convex patterns, related to enrichment in medium rare earth elements (MREE; Sm to Ho) over light rare earth elements (LREE; La to Nd) and heavy rare earth elements (HREE; Er to Lu; Fig. V.7; *Supplementary Table SV.3*), similar to patterns of NPM mafic granulites and

Cerro Aznares websterites (Chapter II), and to group I peridotites from the NPM, following the classification of Mundl *et al.* (2016). Spinel lherzolite displays a similar pattern but has lower MREE and HREE contents, as already observed for the spinel harzburgite PRA1 from Prahuaniyeu (Bjerg *et al.*, 2009). Spinel harzburgite LaFr8 from Laguna Fría displays a LREE enrichment over MREE and HREE, similar to group II peridotites. Moreover, clinopyroxene of the spinel harzburgite CH42 from Cerro Chenque displays a V-shape pattern (LREE > MREE < HREE) similar to group IV peridotites and spinel harzburgite TR-10 from Cerro Traful. Finally, clinopyroxene and garnet from garnet lherzolite PRA33 have REE patterns among the less depleted in LREE (Bjerg *et al.*, 2009).

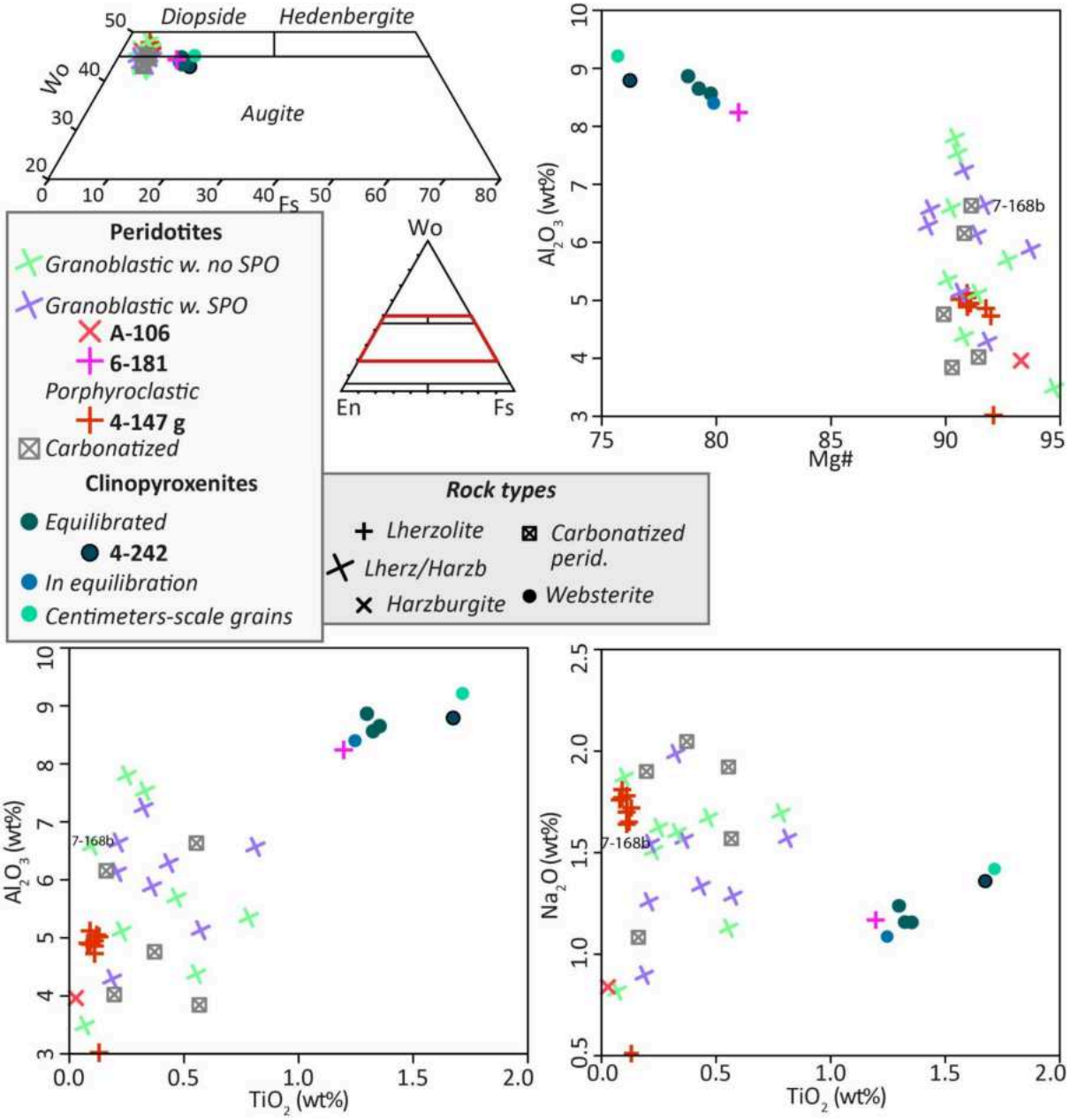


Fig. V.8. Salta peridotites and pyroxenites clinopyroxene major element compositional diagrams. All values except for sample 4-147g are from Lucassen *et al.* (2005).

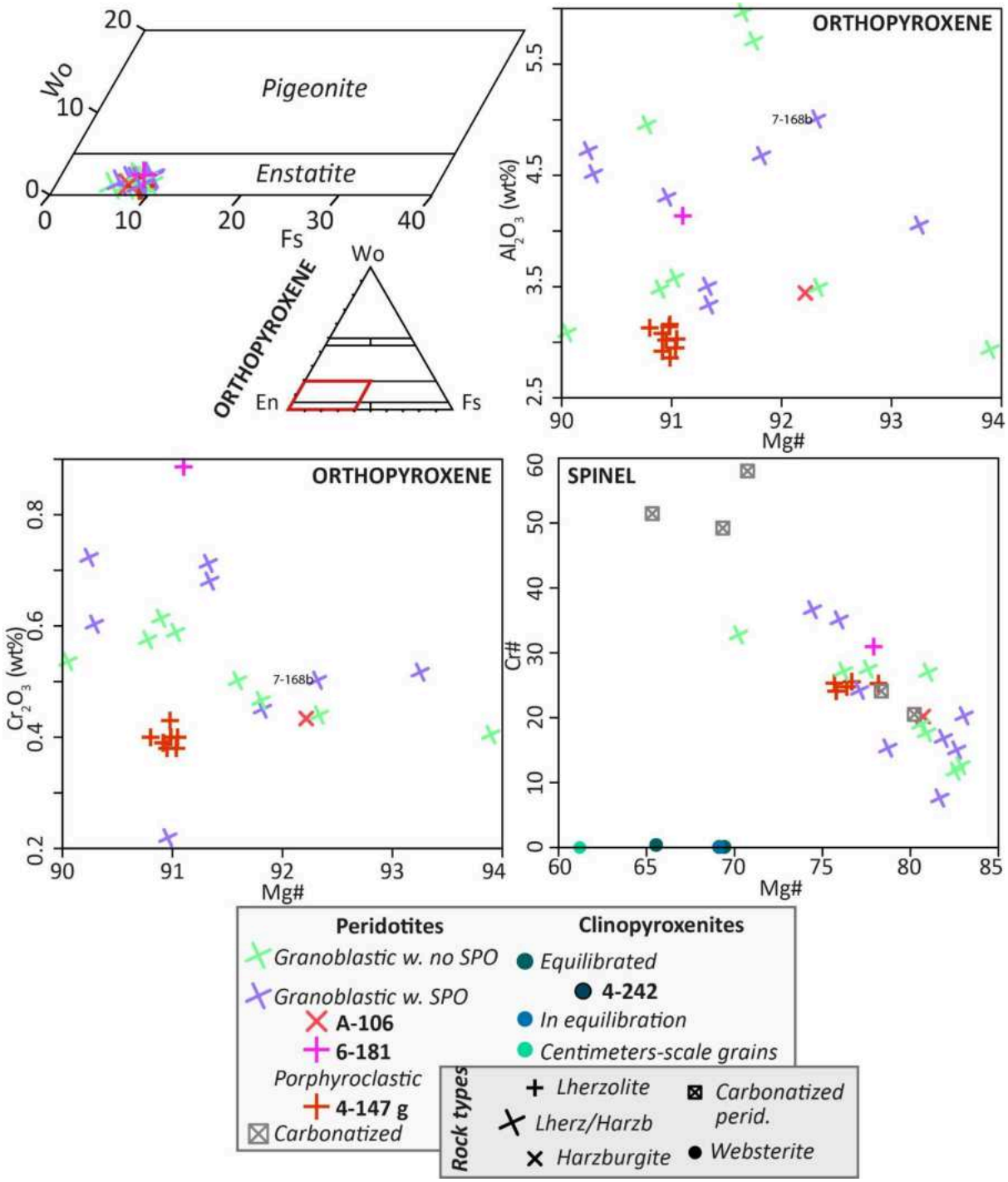


Fig. V.9. Salta peridotites and pyroxenites orthopyroxene and spinel major element compositional diagrams. All values except for sample 4-147g are from Lucassen *et al.* (2005).

V. 4.2.2 Chemical compositions of minerals from Las Conchas Valley

Clinopyroxene of peridotite xenoliths from Las Conchas Valley, including spinel lherzolite 4-147g, has a high Mg# ranging from 89 and 95, various Al_2O_3 contents, ranging from 3 and 8 wt%, and low TiO_2 contents (<0.9 wt%; Fig. V.8). Clinopyroxene from clinopyroxenites have lower Mg# (76-80), but higher Al_2O_3 (8.2-9.2 wt%) and TiO_2 contents (>1.2 wt%).

Spinel-lherzolite 6-181 displays clinopyroxene compositions close to those of clinopyroxenite. Original data are from Lucassen *et al.* (2005) and are reported here but will not be included in the discussion (new analyses are required). Orthopyroxene from Las Conchas peridotites relatively homogeneous in composition, with Mg# varying between 90 and 94, Al_2O_3 contents between 2.7 and 6.0 wt% (Fig. V.9). Cr_2O_3 content is low (<0.9 wt%). Spinel from peridotites has a Mg# bracketed between 70 and 83, while it is lower in clinopyroxenites (61-69; Fig. V.9). Amphibole from spinel lherzolite 4-147g is pargasite (*Supplementary Table. SV.2)*.

V. 4.3 Thermometry

Among the three NPM spinel-harzburgites, samples CH42 and LaFr8 display a wide range of equilibrium temperatures, ranging from 980 to 1190°C (Table V.1). Wehrlite COM138 and dunite CH48 display lower equilibrium temperatures which range between 855 and 920°C, while the spinel lherzolite displays even lower temperatures (745-800°C).

Temperatures estimated for the three peridotites from Las Conchas Valley are variable ranging between 920 and 1130°C (Table V.1). Spinel lherzolite 4-147g provides slightly lower temperatures than spinel harzburgite A-106 and spinel lherzolite 6-181.

V. 4.4 Microstructures

V. 4.4.1 North Patagonian Massif peridotites

Crystal Preferred Orientation (CPO). The studied peridotites display strong olivine CPO patterns (J-index 3.79-8.86; M-index 0.11-0.27; Fig. V.10) except for samples COM206, CH42 and TR45 which display weak olivine CPO patterns (J-index 1.73-2.44; M-index 0.06-0.11). Olivine from spinel harzburgite COM206, CH42 and LaFr8 displays a concentration point on [100] axes parallel to X, as [010] and [001] axes form a girdle in the YZ plane (Fig. V.10). CPO of samples COM206 and LaFr8 thus show a [100]-fibre (BA-index 0.64-0.86; Table V.1) while the CPO-type from sample CH42 is rather orthorombic-[100]{0kl} as suggested by its BA index of 0.56. The spinel harzburgite PRA1 from Prahuaniyeu and spinel lherzolite TR45 from Cerro Traful display a concentration point on [010] axes parallel or at a low angle to Z, a concentration point on [100] axes parallel/at a low angle to X and a concentration point on [001] axes parallel to Y. Finally, the garnet lherzolite PRA33, and the dunite COM138 and wehrlite CH48 display a concentration point on [010] axes normal to the XY plane and [100] and [001] axes form girdles in the XY plane.

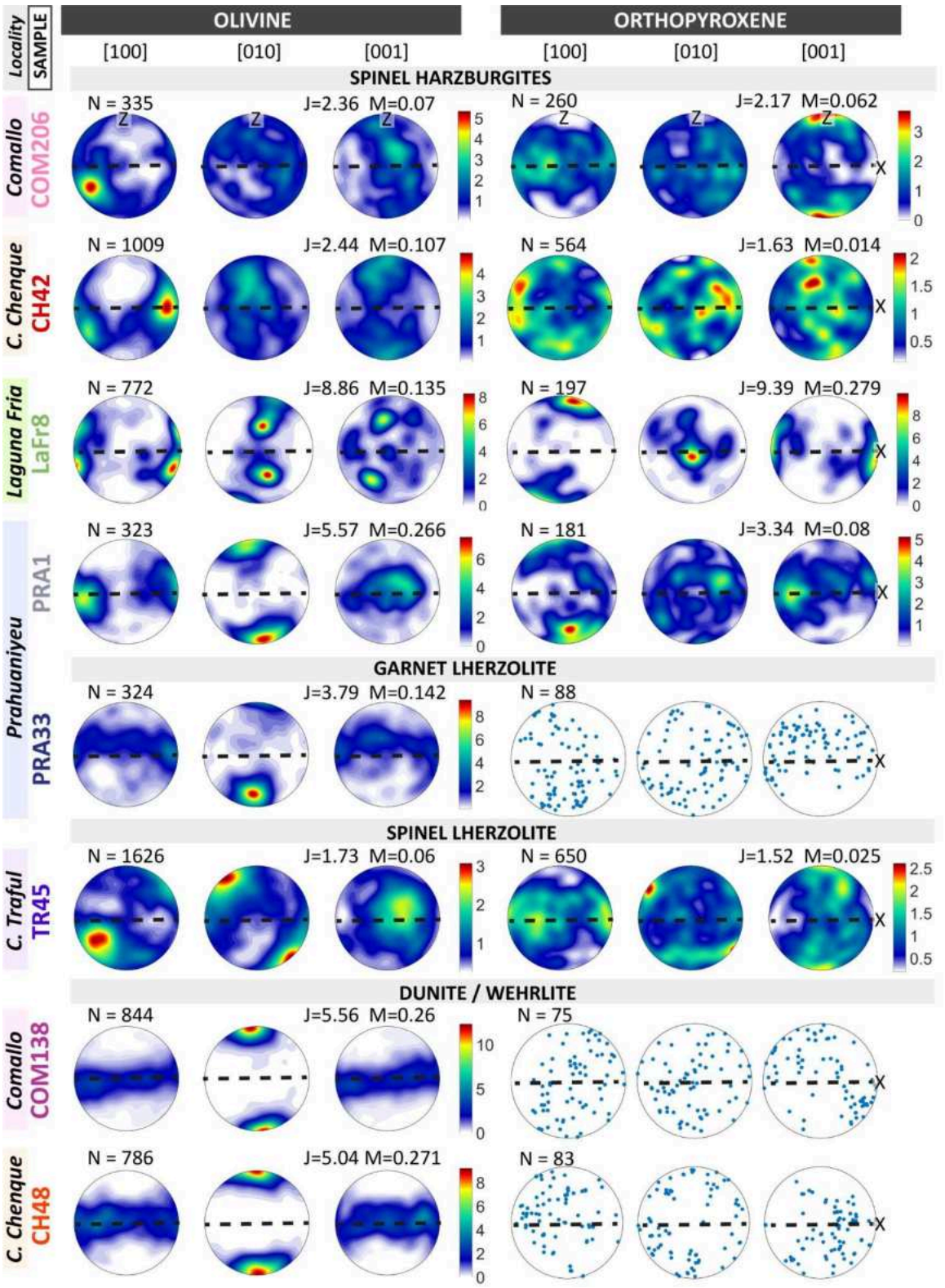


Fig. V.10. Olivine and orthopyroxene crystallographic preferred orientation of NPM peridotite xenoliths. Pole figures are rotated as the lineation parallel to X and the foliation plane normal to Z. Determination of the lineation direction and the foliation plane are explained in *Supplementary Fig.SV.1*. N is the number of grains and the strength is represented by J-index and M-index. The rainbow scale represents the multiply uniform density (mud).

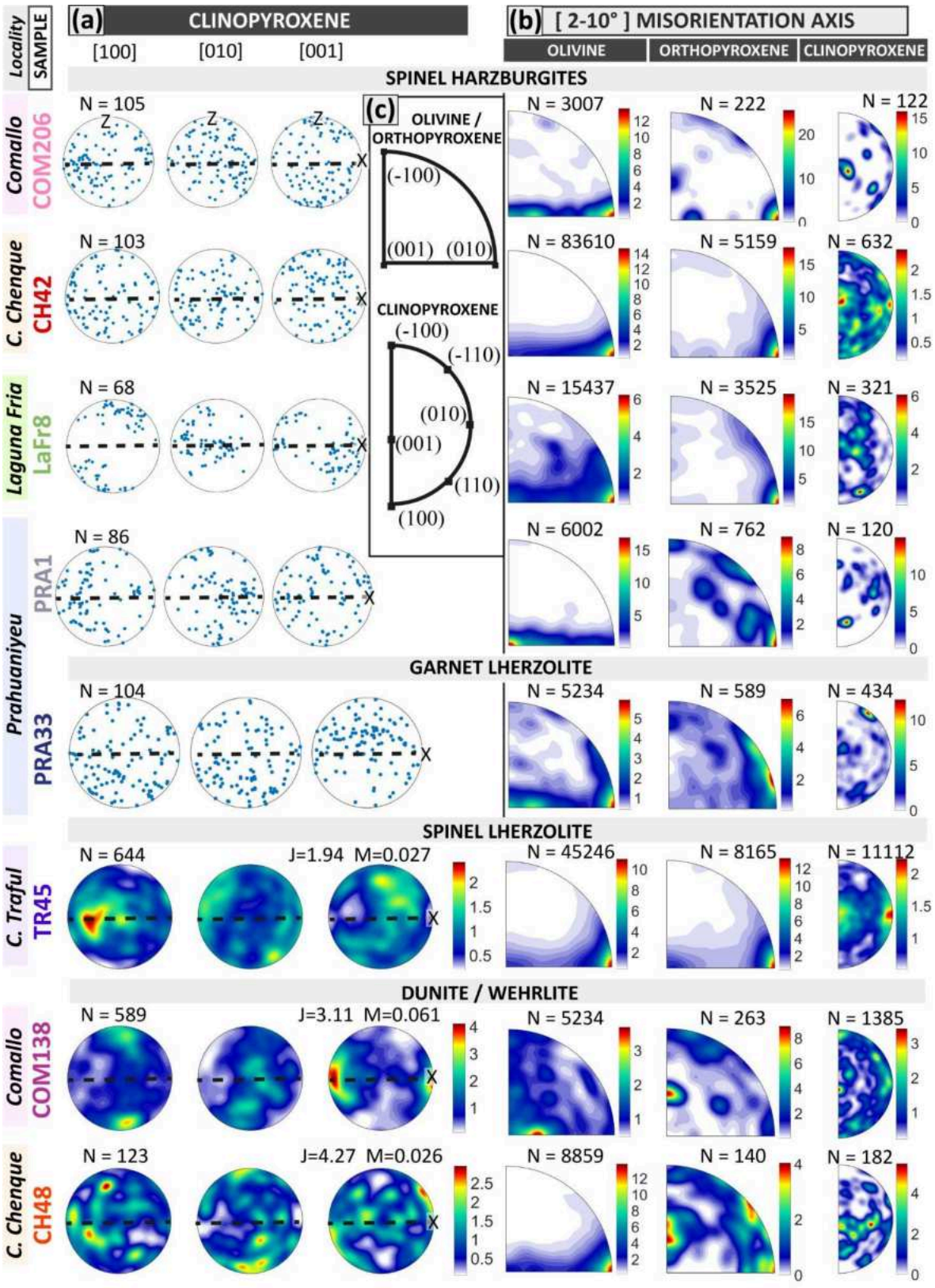


Fig. V.11. (a) Clinopyroxene crystallographic preferred orientation of NPM peridotite xenoliths. N is the number of grains, the strength is represented by J-index and M- index. (b) Rotation axes accommodating low angle (2-10°) misorientations in olivine, orthopyroxene and clinopyroxene grains. Data is represented in inverse pole figures where the legend can be found in (c). N is the number of pixels plotted.

The olivine CPO from these samples show a (010)-fibre as suggested by the BA index which ranges from 0.06 to 0.16 (Table V.1).

Orthopyroxene of NPM peridotites have weak CPO patterns (J-index 1.52-3.34; M-index 0.01-0.08; Fig. V.10) except for the spinel harzburgite LaFr8 from Laguna Fría which displays a strong CPO pattern (J-index 9.39; M-index 0.28). Orthopyroxene from spinel harzburgite COM206 displays a concentration point on [001] axes parallel to Z and to the concentration point of the olivine-[100] axes, while [100] axes form a girdle in the XY plane and [010] axes have a scattered distribution (Fig. V.10). The spinel lherzolite TR45 from Cerro Traful has orthopyroxene with pattern of spinel-harzburgites COM206 and CH42 with [001] axes showing a weak point concentration parallel to Z, and [100] axes parallel to X (Fig. V.10). The two harzburgites LaFr8 and PRA1 display a concentration point on [100] axes parallel to Z and to the concentration points of the olivine [010] axes of the sample PRA1. Furthermore, they display a concentration point on [001] axes parallel to X and to olivine-[100] axes, and a weaker concentration point on [010] axes parallel to Y. Clinopyroxene of the spinel harzburgite LaFr8 from Laguna Fría displays [001] axes that cluster near X and [100] axes that cluster near Z (Fig. V.11a). Clinopyroxene from the spinel-lherzolite TR45 have weak CPO patterns (J-index 1.94; M-index 0.03) and displays a concentration point on [100] axis sub-parallel to X, [001] axes that form a weak girdle in the YZ plane and [010] axes that are randomly distributed (Fig. V.11a). Clinopyroxene from the wehrlite COM138 and the dunite CH48 displays medium CPO patterns (J-index 3.11-4.27; M-index 0.03-0.06). The wehrlite COM138 displays a concentration point on [001] axes parallel to X and [100] and [010] axes that form girdles in the YZ plane., The dunite CH48 displays a weak concentration point on [001] sub-parallel to X and [010] and [100] axes are randomly distributed.

Intragranular deformation. Intragranular deformation in olivine is weak in spinel harzburgites COM206, PRA1, and the garnet lherzolite PRA33 showing a medium- or coarse-grained texture(Fig. V.12) and misorientation angles >1° affecting the olivine surface in these samples varies from 12 to 41 % (Fig. V.13). In these samples the deformed grains display low angle boundaries perpendicular to the grain elongation and they display lobate and mostly concave grain boundaries. The undeformed grains, which display more linear grain boundaries, seem to penetrate deformed grains (Fig. V.12). Contrary to other samples with a coarse-grained texture, the spinel harzburgite LaFR8 from Laguna Fría, display a strong olivine internal deformation, with the grains affected by deformation up to 80% of

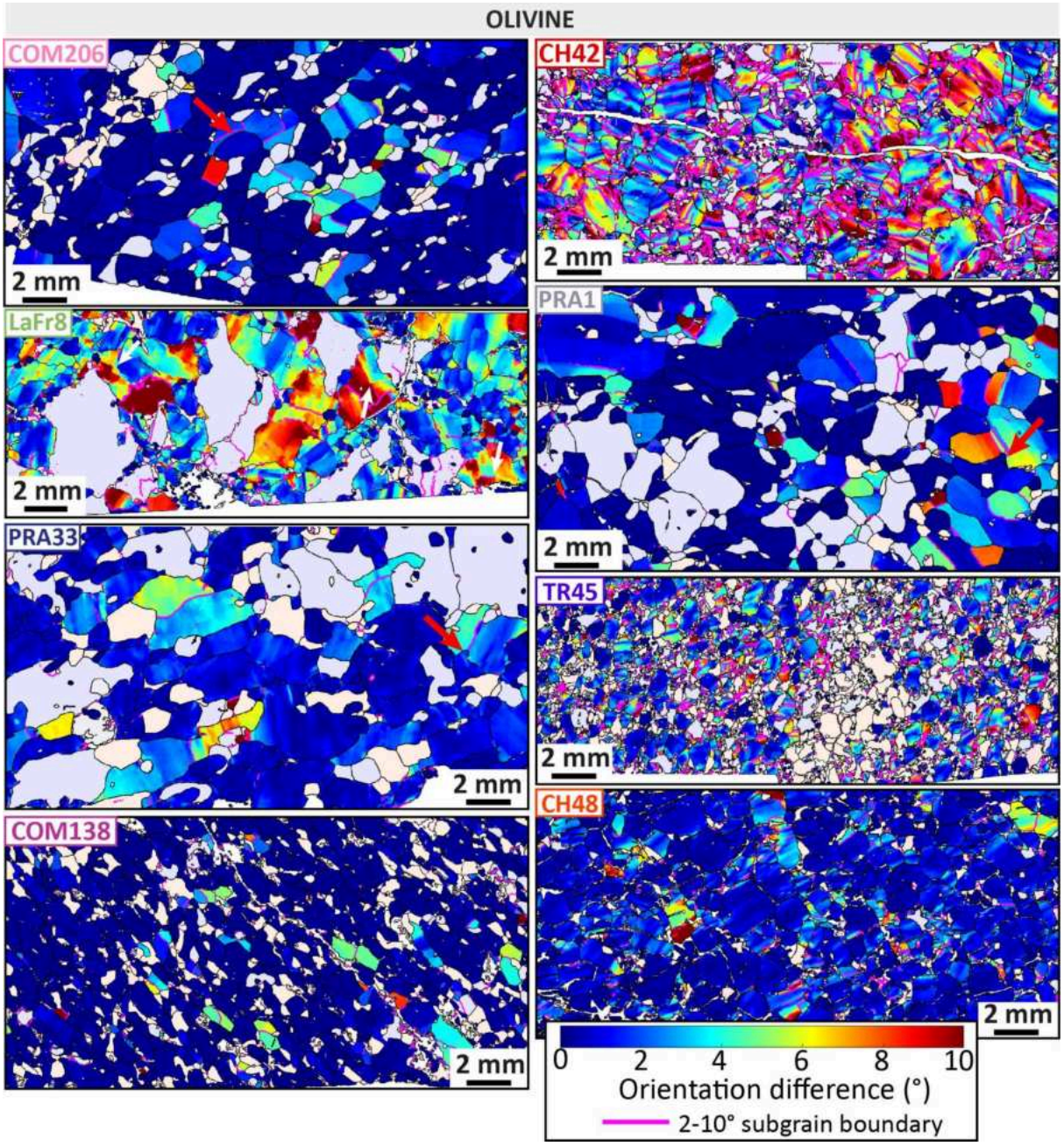


Fig. V.12. NPM peridotite xenoliths maps of intragranular deformation relative to the mean orientation of olivine grains. Light blue grains are orthopyroxene, light orange is for clinopyroxene, light pink is for spinel and light grey is for garnet. Red arrows on COM206, PRA1 and PRA33 maps highlight undeformed grains that seem to penetrate deformed grains. White arrows on the LaFr8 map highlight low-angle boundaries perpendicular between them. Pyroxene subgrain boundaries are also represented in all samples except sample TR45.

their surface and misorientation angles >4° more than 40 % of the olivine surface (Figs V.12 and V.13). The olivine crystals display numerous low angle boundaries, mostly perpendicular to the elongation of the crystals and several grains display two families of low angle boundaries perpendicular between them (Fig. V.12). In samples with a medium grain size, the

internal deformation of olivine a very weak or nonexistent in the wehrlite COM138 (12% of the olivine surface is deformed); intermediate in the dunite CH48 with numerous low angle boundaries perpendicular to the long axis of the olivine, but the internal deformation is most of the time below 3°; and the sample CH42 display a strong internal deformation of the olivine grains (up to 80% of the surface) as in sample LaFr8 (Figs. V.12, V.13). Olivine in the garnet lherzolite TR45 with a fine-grained texture, display an intermediate state of internal deformation with 75% of the olivine surface deformed (Fig. V.13). In this sample subgrain boundaries are frequently linear and perpendicular to the long axes of the grains and conic shape subgrain boundaries are also present at the grain tips.

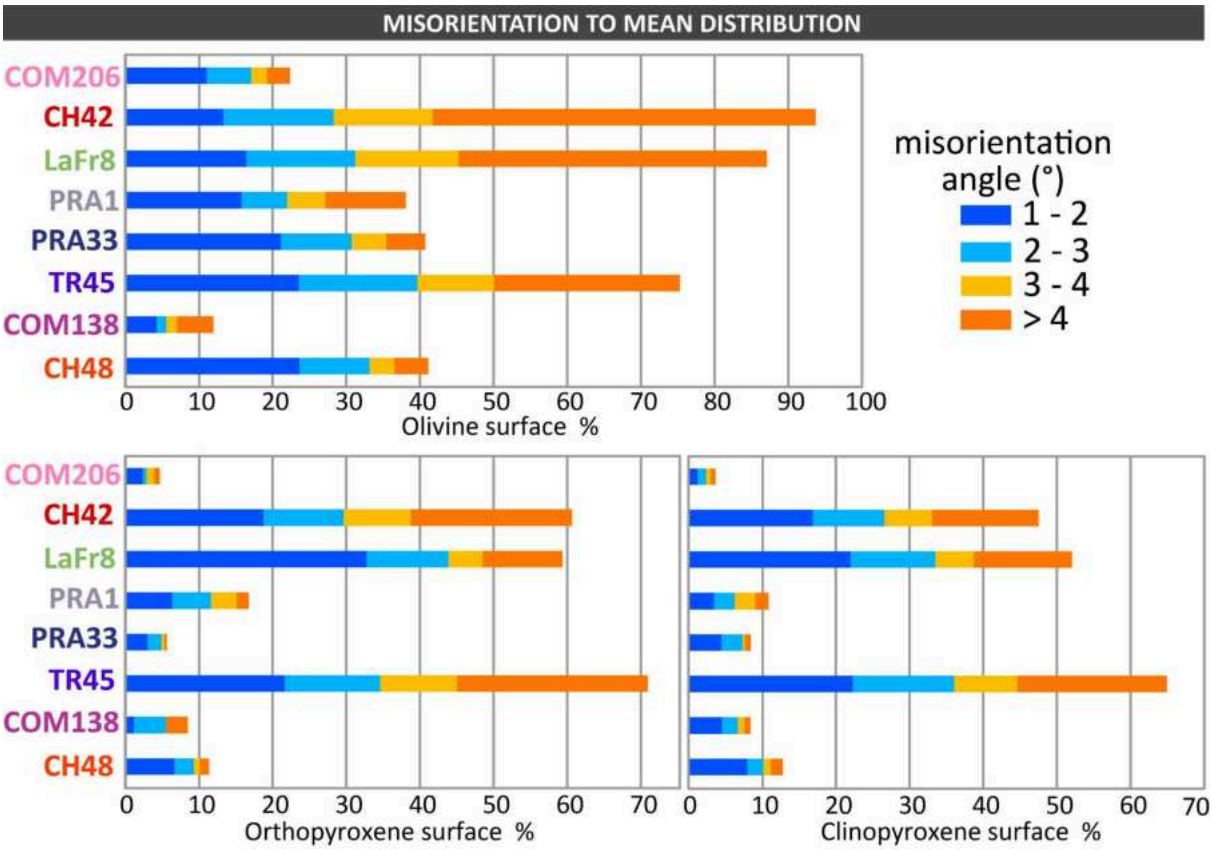


Fig. V.13. Normalized histograms representing olivine, clinopyroxene and orthopyroxene surface proportions of NPM xenoliths vs. misorientation angles (>1°) relative to mean grain orientations.

Orthopyroxene and clinopyroxene intragranular deformation is weak to almost absent in samples COM206, PRA1, PRA33 with a coarse-grained texture, in samples COM138 and CH48 with a medium grain size, as misorientation angles >1° affect 5 to 18 % and 4 to 13 % of orthopyroxene and clinopyroxene grains surface, respectively (Fig. V.13). Pyroxenes intragranular deformation is strong in spinel harzburgite LaFr8 with a coarse-grained texture containing large orthopyroxene crystals. The large orthopyroxene are less deformed than

smaller orthopyroxene grains displaying numerous low angle boundaries. The pyroxene

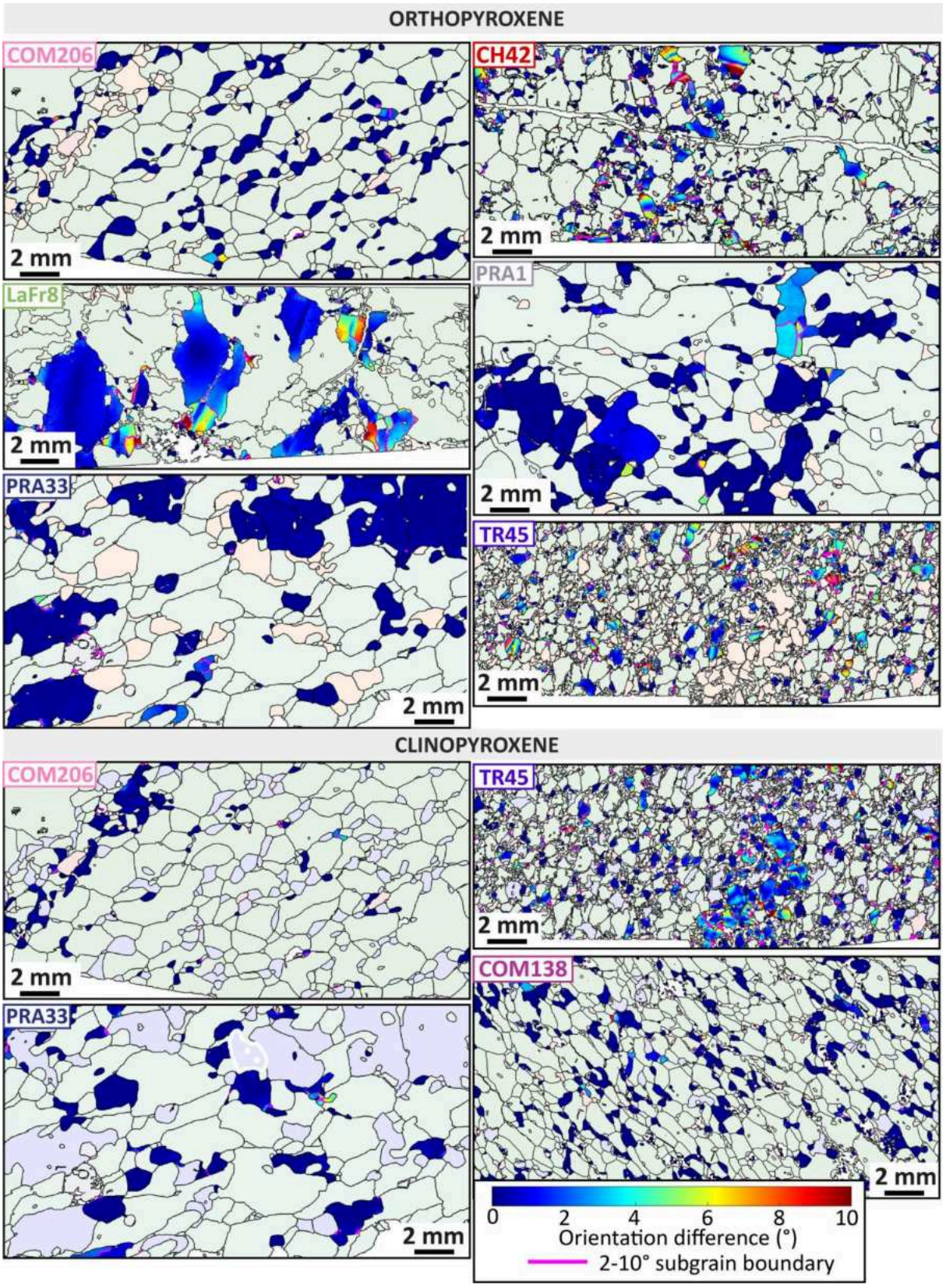


Fig. V.14. NPM peridotite xenoliths maps of intragranular deformation relative to the mean orientation of orthopyroxene and clinopyroxene grains. Light green grains are olivine, light blue is for orthopyroxene, light orange is for clinopyroxene, light pink is for spinel and light grey is for garnet.

intragranular deformation is also strong in the spinel harzburgite CH42 with an intermediate grain-size texture and the spinel lherzolite TR45 with a fine-grained texture (Figs. V.13-14). The distribution of the deformation is homogeneous in sample TR45 and heterogeneous in samples CH42 where large grains are more deformed. In all samples except sample TR45, intragranular deformation in pyroxenes is weaker than in olivine, with pyroxenes displaying 29 % to 86 % less deformed surface than olivine (Fig. V.13). In the spinel lherzolite TR45, the intragranular deformation is similar in all three phases, as orthopyroxene and clinopyroxene display 13 and 5 % less deformed surface, respectively, compared to olivine (Fig. V.13). In the clinopyroxene, conic-shaped subgrain boundaries present at the grain tips are more frequent than linear subgrain boundaries.

Olivine misorientation axes at low angle boundaries or subgrain boundaries are preferentially arranged around the [010] axis in all the samples except PRA1 where the misorientation axes are around [001] axis and in COM138 where the misorientation axes are distributed between [001] and [010] axes (Fig. V.11b). Some samples display a weaker second cluster between [001] and [010] axes (sample COM206 and PRA33) as observed in the wehrlite COM 138 (Fig. V.11b). Orthopyroxene misorientation axes at low angle boundaries or subgrain boundaries are preferentially arranged around the [010] axis except in the wehrlite COM138 and dunite CH48 which display clusters around [101] axis and both [101], [010] and [110] axes, respectively (Fig. V.11b). However, this result must be taken with caution as the subgrain boundaries dataset for these samples is small. The dataset of clinopyroxene misorientation axes at low angle boundaries or subgrain boundaries is small for most of the NPM peridotites except for garnet lherzolite TR45 (n=11112) and the wehrlite COM138 (n=1385; Fig. V.11b). Sample TR45 displays clusters between both [001] and [010] axes, while sample COM138 displays scattered clinopyroxene misorientation axes at low angle boundary distribution.

V. 4.4.2 Las Conchas Valley peridotites

Crystallographic preferred orientation. The olivine of the four Las Conchas peridotites display strong CPO patterns (J-index 5.52-7.69; M-index 0.19-0.33; Fig. V.15) which is rather uniform in spinel lherzolite and spinel harzburgite. The CPO display a concentration point on [010] axes normal parallel to Z, while both [010] and [001] axes form a girdle in the XY plane, with a maximum concentration point parallel to X and Y, respectively (Fig. V.15). Moreover, the BA index which ranges from 0.11 to 0.27 suggests that the olivine CPO from those samples have a [010]-fibre (Table V.1).

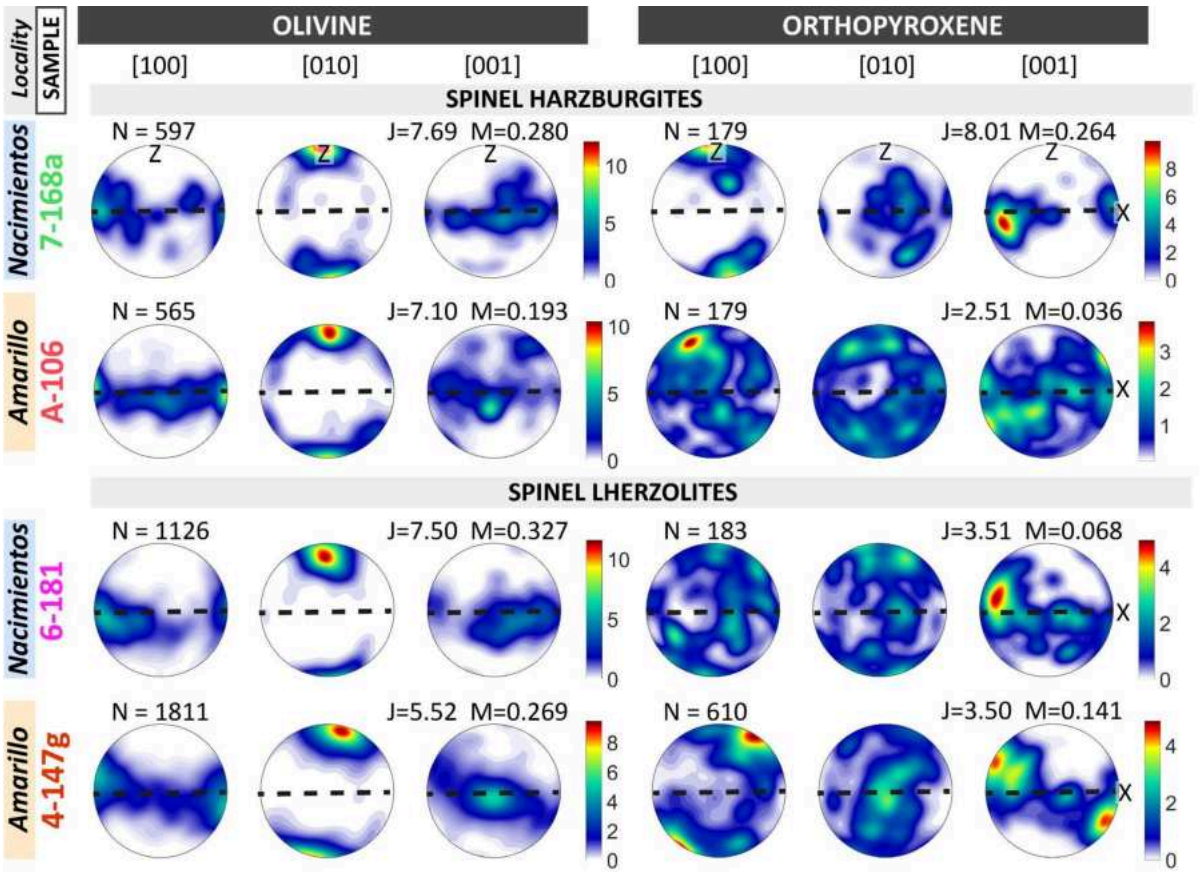


Fig. V.15. Crystallographic preferred orientation of olivine and orthopyroxene of Las Conchas Valley peridotite xenoliths. Pole figures are rotated as the lineation parallel to X and the foliation plane normal to Z. N is the number of grains and the strength is represented by J-index and M-index. The rainbow scale represents the multiply uniform density (mud).

Orthopyroxene has a strong CPO in the spinel harzburgite 7-168a (J-index 8.01; M-index 0.26), and a weak/medium CPO in the spinel harzburgite A-106, and spinel lherzolites 6-181 and 4-147g (J-index 2.51-3.51; M-index: 0.04-0.14; Fig. V.15). Orthoyproxene in the four peridotites has [001] axes that form a girdle in the XY plane with a maximum concentration point parallel to X and to olivine-[100] axes (Fig. V.15). In samples 7-168a, A-106 and 4-147g, orthopyroxene displays a concentration point on [100] axes at low angle to Z and parallel to olivine-[010] axes.

Clinopyroxene has strong CPO in spinel harzburgite A-106 and spinel lherzolite 6-181 (J-index 6.69-8.79, M-index 0.04-0.10; Fig. V.16a) and weak in spinel lherzolite 4-147g (J-index 3.14, M-index 0.05). Clinopyroxene from samples A-106 and 6-181 displays a concentration point on [001] axes at low angle to X and parallel to orthopyroxene-[001] axes. The clinopyroxene CPO of these samples display a concentration point on [010] axes parallel to Z and to olivine-[010] axes (Fig. V.16a). Clinopyroxene CPO pattern from sample 4-147g

is weaker but similar to samples A-106 and 6-181. Sample 7-168a displays few clinopyroxene grains which display a cluster on [100] axes sub-parallel to Z (Fig. V.16a).

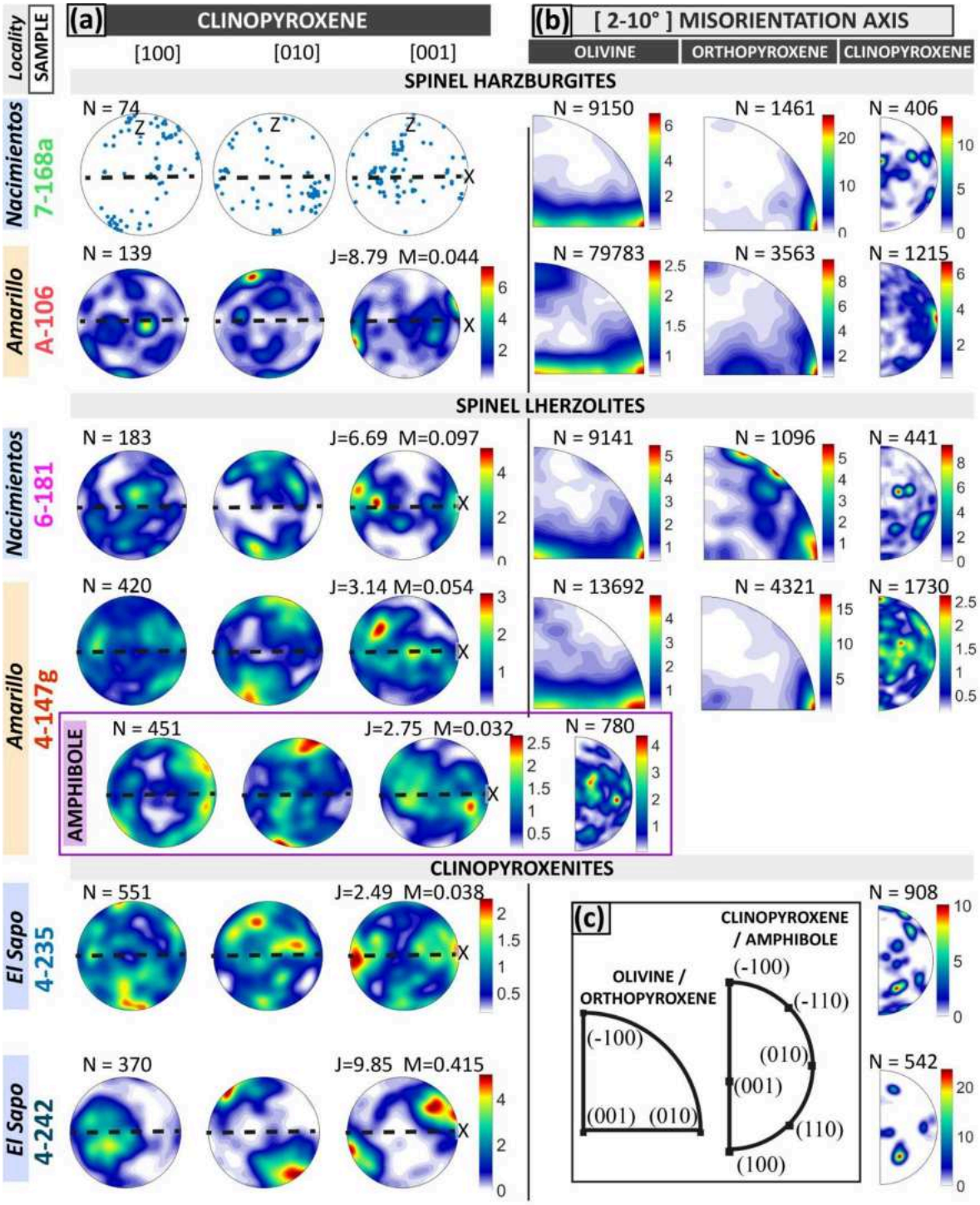


Fig. V.16. (a) Clinopyroxene crystallographic preferred orientation of Las Conchas Valley peridotite and pyroxenite xenoliths. N is the number of grains, the strength is represented by J-index and M-index. (b) Rotation axes accommodating low angle (2-10°) misorientations in olivine, orthopyroxene and clinopyroxene grains. Data is represented in inverse pole figures where the legend can be found in (c). N is the number of pixels plotted.

Amphibole in sample 4-147g has a weak CPO (J-index 2.75, M-index 0.03; Fig. V.16a) and displays [010] axes that form a girdle on the YZ plane with a maximum concentration point sub-parallel to Z, [001] axes that form a girdle sub-parallel to the XY plane and a concentration point on [100] between X and Z directions. This CPO is very similar to the clinopyroxene CPO.

Intragranular deformation. The olivine intragranular deformation is moderate in samples 7-168a, A-106 and 6-181, as it appears stronger than in the weakly deformed NPM peridotites but weaker than in the strongly deformed NPM peridotites (i.e. samples CH42 and LaFr8; Figs. V.12, 17a). It affects the olivine surface from 64 to 71 % and occurs homogeneously in samples 7-168a, A-106 and 6-181. Subgrain boundaries are frequent in olivine and they could occur in large and /or small grains (Figs. V.17, 18). In this suite of peridotite xenoliths, the olivine is more deformed than pyroxenes. Orthopyroxene and clinopyroxene intragranular deformation is weak in samples 7-168a, A-106 and 6-181 and affects 17-39 % of orthopyroxene grains surface and 23-34 % of clinopyroxene grain surface (Figs. V.17, 18). In those samples, few grains concentrate the deformation with low angle boundaries. Sample 4-147g displays a more intragranular deformation in orthopyroxene (58 % of the orthopyroxene surface) than other peridotites (Fig. V.17). In this sample, olivine and two-pyroxenes intragranular deformation occurs only in large and curved grains while it is absent in small and round-shaped grains. Intragranular deformation in sample 4-147g is associated with subgrain boundaries which are large, linear, grain cross-cutting, are oriented most of the time perpendicular to the long axis of the grains and seem to occur with the same frequency in olivine, orthopyroxene and clinopyroxene grains.

Olivine misorientation axes at low angle boundaries or subgrain boundaries are distributed around both [010] and [001] axes in all the peridotites (Fig. V.16b). Orthopyroxene misorientation axes at low angle boundaries are preferentially arranged around the [010] axis in all samples, but 6-181 shows supplementary clusters between [100] and [010] axes (Fig. V.16b). Clinopyroxene misorientation axes are preferentially arranged around the [010] axis in the spinel harzburgite A-106 while they cluster between [001] and [010] axes and around the [-100] axis in sample 4-147g (Fig. V.16b). Samples 7-168a and 6-181 display few clinopyroxene misorientation axes at low angle boundaries or subgrain boundaries which have a scattered distribution. Finally, amphibole misorientation axes are distributed between [001] and [010] axes in sample 4-147g (Fig. V.16b).

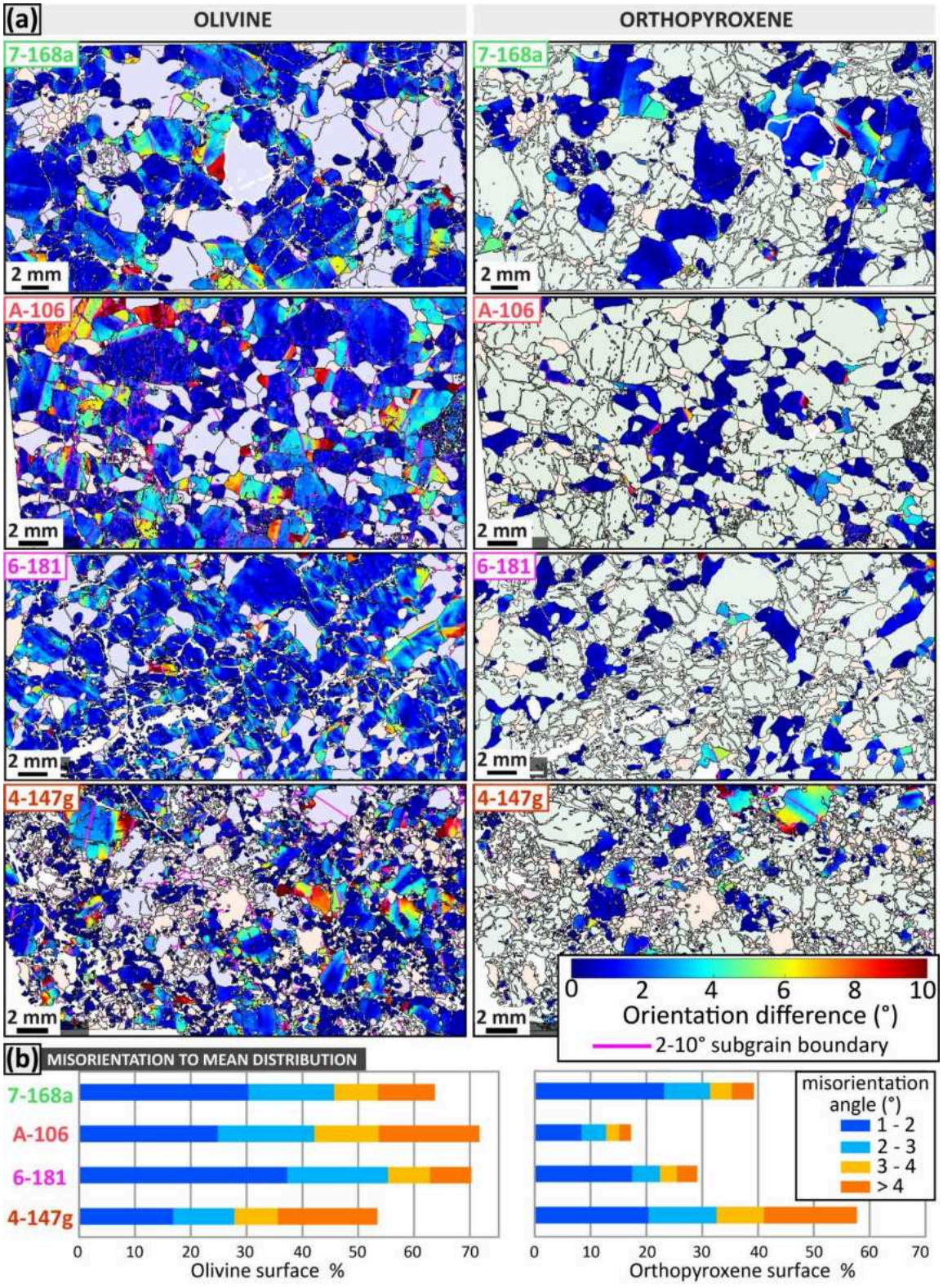


Fig. V.17. (a) Las Conchas Valley peridotite xenoliths maps of intragranular deformation relative to the mean orientation of olivine and orthopyroxene grains. Light green grains are olivine, light blue is for orthopyroxene, light orange is for clinopyroxene, light purple is for amphibole and light pink is for spinel. Pyroxene subgrain boundaries are represented on intragranular deformation maps in all samples. (b) Normalised histograms representing olivine and orthopyroxene surface proportions vs. misorientation angles (>1°) relative to mean grain orientations.

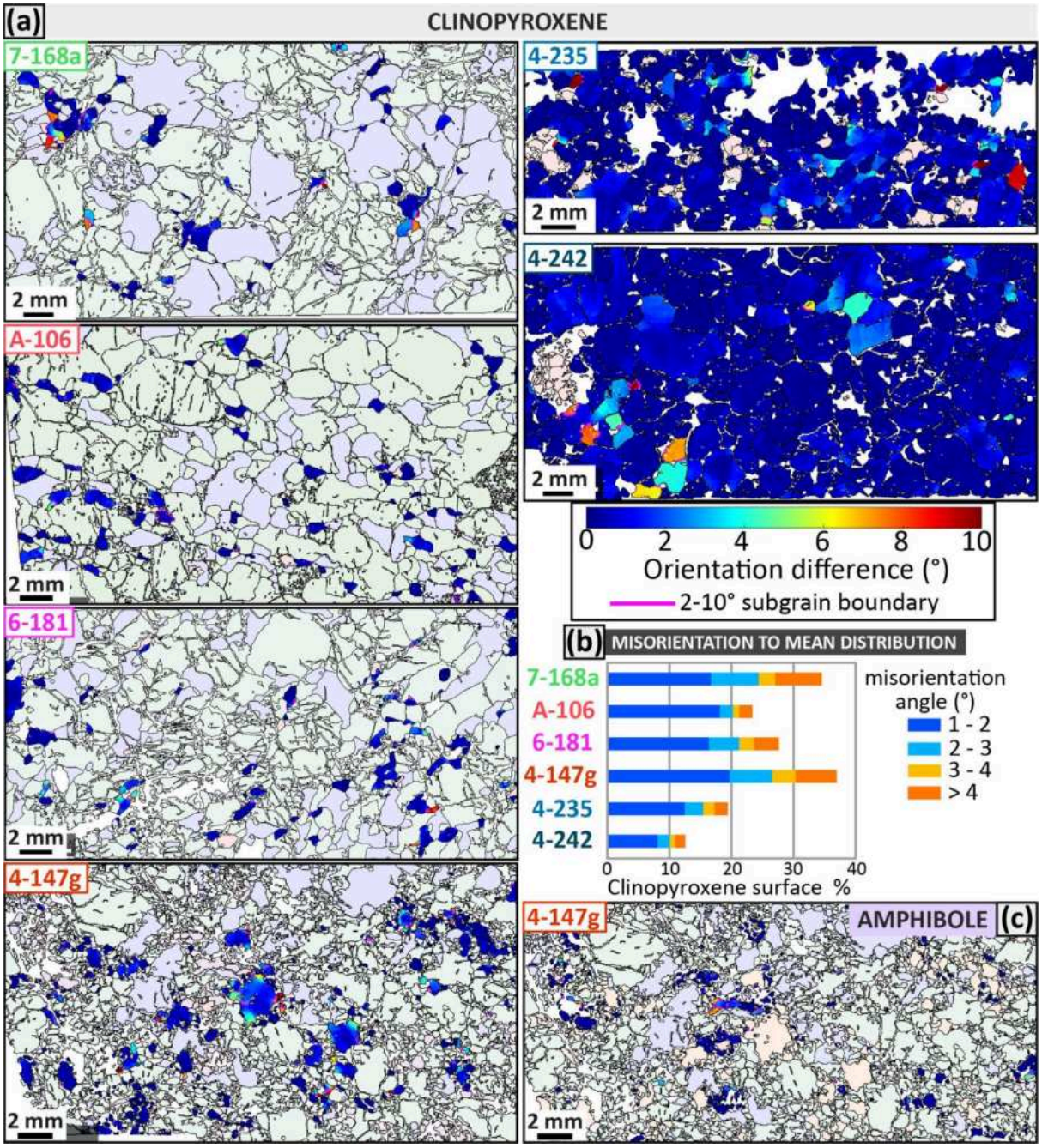


Fig. V.18. (a) Las Conchas Valley peridotite and pyroxenite xenoliths maps of intragranular deformation relative to the mean orientation of clinopyroxene grains. Light green grains are olivine, light blue is for orthopyroxene, light purple is for amphibole and light pink is for spinel. (b) Normalised histograms representing clinopyroxene surface proportions vs. misorientation angles (>1°) relative to mean grain orientations. (c) 4-147g map of intragranular deformation relative to the mean orientation of amphibole grains.

V. 4.4.3 Las Conchas Valley clinopyroxenites

Crystallographic preferred orientations. Clinopyroxene has a weak CPO in sample 4-235 (J-index 2.49, M-index 0.04; Fig. V.16a), as it displays a concentration point on [001] axes parallel to X, a weak concentration point on [100] axes parallel to Z and [010] axes that

are scattered. In contrast, clinopyroxene has a strong CPO in sample 4-242 (J-index 9.85, M-index 0.42; Fig. V.16a) as it displays a concentration point on [001] axes sub-parallel to Z, a concentration point on [010] axes sub-parallel to Y and one on [100] axes sub-parallel to Z.

Intragranular deformation. Clinopyroxene intragranular deformation is weak in both investigated samples, as most of the grains display no intragranular deformation (Fig. V.18) and subgrain boundaries are rare. Moreover, the samples display few clinopyroxene misorientation axes at low angle boundaries or subgrain boundaries which rather cluster around both [-110] and [110] axes in sample 4-235 and show a scattered distribution in sample 4-242 (Fig. V.16b).

V. 5 DISCUSSION

V. 5.1 Plastic deformation recorded by North Patagonian Massif xenoliths

V. 5.1.1 Plastic deformation

Olivine CPO of the NPM xenoliths can be sorted into three groups: i) pure/orthorhombic [100]-fibre group, characterised by a lineation strongly marked by the [100] axis and rather weakly marked foliation planes, which includes spinel harzburgites COM206 from Comallo, CH42 from Cerro Chenque and LaFr8 from Laguna Fría; ii) the A-type [100](010) CPO group, characterised by a lineation marked by the [100] axis while the (010) plane marks the foliation plane, which includes the spinel harzburgite PRA1 from Prahuaniyeu and the spinel lherzolite TR45 from Cerro Traful; iii) the (010)-fibre group, characterised by a strong foliation on the (010) plane and an absence of (or a weak) lineation, which includes the garnet lherzolite PRA33 from Prahuaniyeu, the wehrlite from COM138 from Comallo and the dunite CH48 from Cerro Chenque (Fig. V.10; Table V.1).

Misorientation axes at low angle boundaries or subgrain boundaries are the expression of the internal deformation, and as a consequence the activation of slip systems due to plastic deformation. In many xenoliths from the NPM, the olivine misorientation axes are concentrated on [010] suggesting the activation of C/E (001)[100] and (100)[001] slip systems. In the spinel harzburgite PRA1, the misorientation axes are concentrated on [001] suggesting the activation of A-type (010)[100] slip system. The garnet lherzolite PRA33 and the spinel harzburgite COM206 also display this point concentration, suggesting the activation of the A-type slip system (Fig. V.11b).

The results highlight that slip-systems that could be inferred from CPO are generally different from those inferred from misorientation axes. Only the spinel harzburgite PRA1 display similar suggested activated slip systems with CPO and misorientation axes: the A-type [100](010). A-type CPO is the most commonly reported olivine slip system in the upper mantle (e.g. Karato *et al.*, 2008; Henry, 2018), resulting from low strain conditions at high temperatures (>1000°C; Nicolas & Christensen, 1987; Ismaïl & Mainprice, 1998). This is coherent with the weakly deformed texture of this sample, and the equilibrium temperature at 1061°C calculated by Bjerg *et al.*, (2009). Moreover, the orthopyroxene also display a weak internal deformation and [001] axes are parallel to olivine [100] axes suggesting concordant deformation (Fig. V.10).

In other samples, the CPO pattern suggest three different slip systems: D-type [100]-fibre, A-type [100](010), and [010]-fibre, while misorientation axes, clear indicators of plastic deformation suggests C-type (001)[100] and E-type (100)[001] slip systems in almost all samples (Fig. V.10, V.11). E-type are common in nature and may form in several conditions: (1) plastic flow under low stress and intermediate water content (Katayama *et al.*, 2004); (2) high stress, moderate temperatures conditions ~900°C in hydrated domains (Michibayashi & Oohara, 2013); (3) high-temperature deformation with a Si-undersaturated melt (Suhr, 1993; Tommasi *et al.*, 2006) and (4) at low temperature during the mechanical weakening of a pre-existing anisotropy (Michibayashi, 2004). C-type slip system are relatively rare in natural example and may form (1) at low temperature and high strain rate (Carter & Avé Lallemant, 1970); (2) at high water content (i.e. >800 ppm H/Si; Jung & Karato, 2001), (3) during high pressure flow where the water solubility is enough to keep [001](100) slip active (Couvy *et al.*, 2004; Raterron *et al.*, 2007) and (4) at high temperature (Skemer *et al.*, 2006). This short review shows that E-type is more common in nature than C-type and that these slip systems could be activated in many environments.

Among the studied xenoliths, samples LaFr8, CH42 and Tr45, are the more deformed samples with high internal deformation (Figs. V.12, 13) showing C- and E-type slip systems activated and the estimated temperatures are from 1190°C to 744°C (Table V.1). These observations suggest strong deformation recorded by the mantle in three localities, Laguna Fría, Cerro Chenque and Traful, which are located North and South of the studied area (Fig. V.1). However, sample TR45 shows very weak olivine, orthopyroxene and clinopyroxene CPO fabrics (J-index 1.52-1.94), no clear correlation between pyroxenes and olivine fabrics and a strong internal deformation of olivine and pyroxenes (Figs. V.10-14). This supports the hypothesis that CPO fabrics are the remnant of a primary deformation event that has not been

completely erased by strong deformation. In the two other strongly deformed samples, CPO patterns suggest [100]-fibre for both LaFr8, CH42, which could be also the relic of primary deformation event. [100]-fibre symmetry, or D-type [100]{0kl} CPO, develops via the activation of the [100] glide on multiple planes (Liptai, 2018). D-type CPO has been observed to develop either at high temperatures (Zhang & Karato, 1995; Bystricky *et al.*, 2000; Hansen *et al.*, 2014) or low temperatures (ca. 750°C; Park & Jung, 2017) under intense simple shear such as lithospheric shear zones or under transtensional deformation regime (Tommasi *et al.*, 1999), or at low/moderate stress and temperatures (ca. 900°C; Michibayashi & Oohara, 2013).

The garnet lherzolite PRA33, wherlite COM138, and dunite CH48 display similar concentration of misorientation axes but CPO indicate [010]-fibre symmetry. These samples recorded high temperature 1215°C for the garnet peridotite and moderate temperature (854-920°C) for the wehrlite and the dunite. Previous studies indicate that for high temperature conditions, this fabric may develop under axial shortening or transpression mechanisms (Tommasi *et al.,* 1999). Moreover, the (010)-fibre may also result from the transition between the A-type [100](010) and B-type [001](010) fabrics when slip direction changes from [100] to [001], which may involve deformation with interstitial melt and change of pressure (Holtzman *et al.*, 2003; Mainprice *et al.*, 2005; Vauchez *et al.*, 2005).

V. 5.1.2 Thermal and magmatic state of the mantle in the NPM

The depleted Lithospheric mantle. Spinel harzburgites CH42, LaFr8 and PRA1, as well as the garnet lherzolite PRA33 display mineral major element composition similar to those from other regular peridotites from the NPM (Figs. V.5, 6; Bjerg *et al.*, 2005, 2009; Mundl *et al.*, 2016). The decrease of Al_2O_3 contents with increase of Mg# in both clinopyroxene and orthopyroxene in peridotites may go along with melt extraction (e.g. Melchiorre *et al.*, 2020). Hence, NPM peridotites experienced various melt extraction rates based on pyroxene major element compositions, varying from 1 to 30% (Melchiorre *et al.*, 2020). Following this trend, samples CH42, LaFr8, PRA1 and PRA33 range from slightly-depleted samples (PRA33; Figs V.5, 6) to the most depleted samples among the NPM peridotites (CH42), and represent the variability of primary SCLM peridotites in the NPM. Additionally, equilibrium temperatures of those four peridotites display a wide range, from 989 to 1215°C (Table V.1), and equilibirum pressures of the garnet peridotite PRA33 of 22.3 kbar (Bjerg *et al.*, 2009) suggest that the SCLM rock column represented by those peridotites is large and is not only restricted to depths close to the Petrological Moho. Therefore, we

suggest that the NPM SCLM, represented by spinel-harzburgite CH42, LaFr8 and PRA1 as well as the garnet-lherzolite PRA1 recorded plastic deformation along with a glide on olivine [100] axis direction, developing either in a possible strong deformation regime through D-type [100]-fibre CPO, or softer deformation regime through A-type [100](010) CPO or [010]-fibre CPO (Fig. V.10). If we do not have yet mineral chemical composition of spinel harzburgite COM206, the resemblance of its CPO with those of other spinel harzburgite is mandatory that it is a regular SCLM peridotite. The D-type CPO is developed in west localities (Comallo, Cerro Chenque and Laguna Fría; see Fig. II.1 in Capter II) while A-type and [010]-fibre CPO on the East-NPM (Prahuaniyeu), which could highlight two structural SCLM domains in the NPM as already proposed by Mundl *et al.* (2016) and Schilling *et al.* (2017), based on Re-Os dating. However, our dataset remains quite low to discuss structural domains.

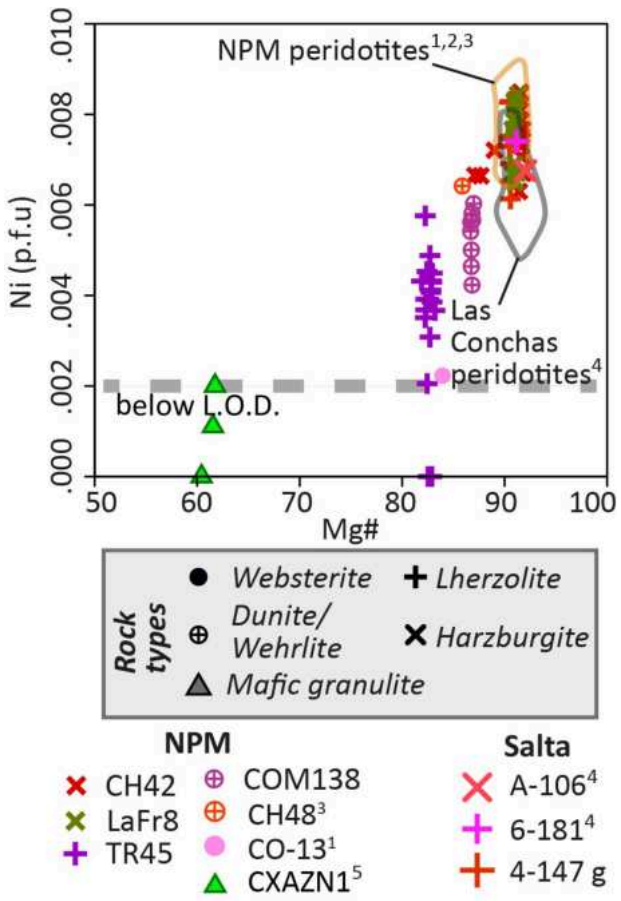


Fig. V.19. Olivine Ni vs. Mg# composition from NPM and Las Conchas xenoliths, including peridotites, olivine-bearing pyroxenite and olivine-bearing mafic granulite. 1: Bjerg *et al.* (2005); 2: Bjerg *et al.* (2009); 3: Mundl *et al.* (2016); 4: Lucassen *et al.* (2005); 5: Chapter II.

Highly-percolated peridotites and cumulates. Wehrlite COM138 and dunite CH48 display mineral major element compositions that deviate significantly from regular NPM peridotite compositions. Notably, they display lower clinopyroxene and orthopyroxene Mg# (86-88 for both; Figs V.5, 6) compared to regular NPM peridotites (89-95 for clinopyroxene, 89-93 for orthopyroxene). Moreover, their olivine compositions reveal lower Mg# (86-87) and Ni_{molar} values (0.004-0.0065 p.f.u) in contrast to regular NPM peridotites (Mg# 88-92; Ni 0.0065-0.009 p.f.u; Fig. V. 19). Clinopyroxene and amphibole in COM138 display REE normalised-patterns patterns with upward convex shapes, reminiscent of patterns found in NPM websterites interpreted to have magmatic protoliths (Chapter III; Dantas, 2007).

Chemical analyses suggest that these rocks have recorded significant percolation or are ultramafic cumulates. Reactions such as Opx + melt → Ol (indictive of dunitisation) or Cpx + melt → Ol + Cpx (indicative of wehrlitisation) may have occurred, depending of the melt composition (e.g. Dantas, 2007). The presence of pargasite in wehrlite COM138 implies that its wherlitisation is associated with a hydrous melt, aligning with modal metasomatism observed in several Comallo peridotites (Mundl *et al.*, 2016).

Notably, both samples olivine display a (010)-fibre CPO, which has been extensively observed in Trinity ultramafic cumulates and interpreted to result from magmatic processes such as crystal settling (Henry *et al.*, 2021). These observations, coupled with low equilibration temperatures ranging from 854 to 920°C (Table V.1), indicate that wehrlite COM138 and dunite CH48 likely represent rocks of magmatic origin, equilibrating at depths near the Moho and developing an olivine [010]-fibre texture.

Ultramafic crustal rock. The spinel lherzolite TR45 from Cerro Traful displays remarkably low equilibration temperatures (744-798°C; Table V.1). While such low temperatures have been sporadically calculated in NPM peridotites (Mundl *et al.*, 2016), NPM mafic granulite and websterite xenoliths display an equilibration temperature range of 760-1150°C (Chapter II). Thus, TR45 stands out among thecoldest NPM lower crust xenolith samples.

Furthermore, TR45 displays very low Mg# values in clinopyroxene (82.5-84.5), orthopyroxene (84-85), olivine (82-83) and spinel with no Cr (Cr# <1; Figs. V.5, 6). These mineral major element compositions deviate from the the general compositions of NPM SCLM peridotites but align with magmatic and metamagmatic rocks of the NPM, such as websterites, mafic granulites, the wehrlite COM138 and the dunite CH48 (Figs. V.5, 6).

Notably, TR45 overall texture, characterised by a fine to medium grain size homogeneous between phases and conic-shaped subgrain boundaries occurring at the grain tips, closely resembles that described in mafic granulites (Fig. V.3f; Chapter II). Strikingly, these textures are unique to the spinel lherzolite TR45 and are absent in other investigated NPM peridotites (Figs. V.2, 3). We propose that TR45 may represent a peridotite crystallised from an ultramafic melt in depths akin to those of mafic granulites. Subsequently, it recorded metamorphism under granulite facies and lower crustal low-deformation conditions, leading to the observed weak CPO patterns (Figs. V.10, 11a). This observation highlights that the mantle and crust from the NPM have recorded distinct ancient deformation events. Crustal rocks typically display weak CPO patterns, indicative of mild plastic deformation (Chapter II), while mantle rocks display clear fabrics indicative of significant plastic deformation (Fig. V.10).

V. 5.1.3 Deformation and chemistry relationships

The decorrelation between slip systems associated with CPO and those related to misorientation has been observed in orthopyroxene, clinopyroxene and plagioclase of NPM mafic granulites (Chapter II; Muckensturm *et al.*, submitted). Consequently, the shift in deformation patterns may be linked to a processes affecting both the NPM SCLM and the lower crust, potentially involving ultramafic cumulates such as the dunite CH48.

In spinel-harzburgites CH42 and LaFr8, intragranular deformation occured under the C/E [001](100), [100](001) slip system (Figs. V.10, 12-14). Clinopyroxene REE V-shaped patterns, commonly associated with refertilisation processes in initially depleted peridotite (e.g. Mundl *et al.*, 2016), are observed in these samples (Fig. V.7). In the spinel harzburgite LaFr8, both orthopyroxene and clinopyroxene have a strong CPO (orthopyroxene J-index is 9.39; Fig. V.10) with a [001](100) pattern, and a lineation parallel to the olivine [100] axis. This suggests that pyroxenes recorded the ancient same plastic deformation as olivine. In contrary, pyroxenes CPO in spinel harzburgite CH42 are weak (orthopyroxene J-index is 1.63) and not ccorrelated with olivine CPO, implying that they did not record an ancient deformation event. They could have been crystallised lately through metasomatism and deformed under a new regime, along with olivine. Lastly, spinel harzburgite COM206 displays underformed droplet-shapes pyroxene grains at olivine grain tips (Fig. V.2). The pyroxene CPO has a maximum concentration point on the [001] axis parallel to Z, which is perpendicular to the lineation of the olivine on the [100] axis (Fig. V.10). This suggests that

pyroxene likely crystallised lately and would not have undergone ancient deformation as seen in CH42.

V. 5.1.4 Timing of deformational processes

Chemical and/or microstructural analyses provide evidence that spinel harzburgites CH42, LaFr8 and COM206 recorded refertilisation/cryptic metasomatism processes, extensively documented in the NPM (e.g. Rivalenti *et al.*, 2004; Bjerg *et al.*, 2005, 2009; Mundl *et al.*, 2016). These processes have been associated with Cenozoic Large Igneous Province (LIP)-related alkaline magmatism (Melchiorre *et al.*, 2020). In spinel harzburgite CH42 and LaFr8, sampled from lavas dated at 25-23 and 5-1 Ma, respectively (Table V.1), plastic deformation related to olivine C/E slip system activation occurred subsequent to this metasomatism. This suggests the possibility of extending this slip system activity and the associated deformation into the Cenozoic.

E-type slip system have been widely reported in East-African rifting peridotites, associated with A-type and C-type slip system (Kaczmarek & Reddy, 2013). It is possible that the Cenozoic LIP may have induced slight extension in the SCLM. Consequently, the [100]-fiber, A-type, and [010]-fibre olivine CPO patterns observed in spinel harzbrugites and the garnet lherzolite may have been inherited from a pre-Cenozoic deformation event.

Zaffarana *et al.* (2014) reported plastic deformation leading to [100]-fiber olivine CPO in olivine from Plio-Pleistocene peridotite xenoliths from Gobernador Gregores and Pali Aike alkaline lavas in Southern Patagonia. Similar to our xenoliths, they noted that deformation was evident only in CPO but had been annealed under static conditions. Therefore, considering an extension of pre-Cenozoic deformation in the SCLM as a common event between Northern and Southern Patagonia could provide insights into the geodynamic processes underlying the observed deformation. For instance, overall Patagonia recorded significant extension in a back-arc setting during the Jurassic, associated with extensive magmatism in both lower and mantle (Chon Aike silicous LIP, 188-145 Ma; Pankhurst & Rapela, 1995; Pankhurst *et al.*, 1998, 2000a; Navarette *et al.*, 2019; Lovecchio *et al.*, 2020), and could constitute a potential candidate to the inherited deformation of NPM (and possibly Southern Patagonia) SCLM.

V. 5.2 Plastic deformation recorded by Salta rift xenoliths

V. 5.2.1 Plastic deformation

The olivine CPO in the four investigated peridotites from Las Conchas Valley displays a mix of (010)-fibre and A-type [100](010) patterns (Fig. V.15). Olivine [100] axis is rather parallel to orthopyroxene and clinopyroxene [001] axes and suggest that three phases shared a common plastic deformation. Olivine displays a mix between [010]-fibre and A-type slip system, similar to the observations in peridotites PRA1 and PRA33 (Fig. V.10), and conditions associated with those slip systems have been reported in section V.5.1.1. Orthopyroxene displays a [001](100) CPO (Fig. V.15), indicative of activation of the [001](100) slip system, largely reported in mantle rocks (e.g. Bernard *et al.*, 2021). Clinopyroxene displays a [001](010) CPO (Fig. V.16a). Activation of [001](010) slip system is uncommon in clinopyroxene (Amiguet, 2009), however, Bascou *et al.* (2001) reported the development of a [001](010) fabric with the {110}[001], {110}½<110> slip system in natural omphacite and numerical models. {110}[001], {110}½<110> slip system is commonly associated with high-temperature deformation (>1000°C; Amiguet, 2009).

Olivine misorientation at low-angle boundaries and subgrain boundaries mainly occur along the [010] axis, suggesting activation of C-type [100](001) and/or E-type [001](100). Misorientations occur less frequently along the [001] axis and between [001] and [010] axes [0kl] (Fig. V.16b), suggesting the activation of A-type [100](010) and D-type [100]-fibre slip system, respectively.

The results indicate a decoupling between plastic deformation inferred from [010] low-angle misorientation and the [010]-fibre CPO, the latter being correlated with the few [001] misorientations. Similar to observations in NPM peridotites, olivine and pyroxene CPO may have been inherited from a previous deformational event, while misorientations signify a shift in the deformation regime, likely preserving the inherited CPO.

Clinopyroxenites 4-265 and 4-242 display a distinct [001](010) CPO, along with clear requilibrated textures (Figs V.4, 16, 18). These samples could have developed this CPO from plastic deformation activating {110}[001], {110}½<110> slip system at high temperature regime (>1000°C; Bascou et al., 2001; Amiguet, 2009). However, the cumulative origin proposed by Lucassen *et al.* (2005) based on major and trace element compositions implies that the CPO could also have originated during a magmatic rock crystallisation. The origin of these CPO patterns, whether from plastic deformation of crystallisation, remains undetermined.

V. 5.2.2 Deformation and chemistry relationships

The investigated peridotites samples from Las Conchas display homogeneous clinopyroxene, orthopyroxene, spinel and olivine major element composition that fit the range of composition of the SCLM below Salta intracontinental rift previously reported by Lucassen *et al.* (2005; Figs. V.8, 9, 19). Combined with whole-rock and mineral trace element compositions, Las Conchas mineral major element compositions analysed by Lucassen *et al.* (2005) suggested only minor depletion or refertilisation events.

An exception is noted in spinel lherzolite 4-147g, which contains a significant amount of pargasite (6 vol.%; Table V.1; Fig. V.4d, e). Pargasite displays a [001](010) CPO pattern (Fig. V.16a), and shows similar intragranular deformation amounts than olivine and pyroxenes (Figs. V.17, 18). Although [001](010) slip system is not the most commonly reported slip system in mantle amphiboles (e.g. Ko and Jung 2015; Díaz Aspiroz *et al.*, 2007; Puelles *et al.*, 2009; Getsinger *et al.*, 2013), it is known to be easily activated (Hacker & Christie, 1990). The microstructural position of amphibole grains, clustering around spinels, suggests their formation through hydrous-liquid percolation. Furthermore, the consistent deformation observed in olivine, pyroxenes and amphibole implies that the recorded deformation in this sample occurred after amphibole crystallisation, which would have recorded [001](010) slip system. Calculated temperatures for this sample yielded medium mantle temperatures (921-930 °C; Table V.1), which are among the lower temperatures calculated in the Salta peridotites presented here (921-1131 °C) and those reported by Lucassen *et al.* (2005; 900-1190 °C). These temperatures are even close to the lower crust temperatures documented in both mafic and felsic granulites (800-980 °C; Chapter IV; Lucassen *et al.*, 1999b). This suggests that the percolation event recorded by spinel lherzolite 4-147g likely occurred at the uppermost level of the SCLM.

V. 6 CONCLUSION

This Chapter highlights the contrasting petrological and petrophysical characteristics between the Cenozoic-to-recent North Patagonian Massif SCLM and the Cretaceous Salta SCLM. The formed displays significant depletion and recorded many magmatic events, including extensive metasomatism/refertilisation processes coupled with localised deformation. It also contains numerous cumulative/highly percolated rocks near the Moho, and magmatic activity heritage is prevalent even up to lower crust depths. In contrast, the Salta SCLM is

comparatively less depleted, displaying more subtil metasomatism. Cumulative rocks appear to be less common, and the lower crust maintains a metasedimentary nature.

However, the decoupling observed between the CPO and the slip systems inferred from low-angle misorientation axes suggests that both the NPM and Las Conchas peridotites recorded a multi-stage deformation history. We suggest that they initially experienced a plastic deformation event within the stability field of D-type slip in the NPM, along with a mix of A-type/ [010]-fiber slip system. This event is responsible of observed CPO in most of peridotites. Subsequent deformation, indicated by the presence of subgrains boundaries, suggests a shift in deformation condition with the activation of C/E slips both localities.

Thus, despite these two SCLM portions displaying distinct magmatic activities, they display a common deformational behavior. This shared characteristic can be linked to their similar back-arc position regarding the Pacific subduction, implying that they may have recorded analogous geodynamic events.

CONCLUSIONS & PERSPECTIVES

This study aimed to characterise the Moho in orogenic domain by investigating two East-West transects in South America at 23° S and 40-43° S. Detailed petrological, geochemical and microstructural observations were combined to highlight the variability of the processes in both the lower crust and the subcontinental lithospheric mantle (SCLM) in central and southern Argentina. These findings allowed to propose a model detailing the historical and current state of the Moho in these diverse regions.

Southern transect: North Patagonian Massif - Calbuco

In the North Patagonian Massif (NPM), the lower crust has been significantly affected by magmatic events since the Devonian. However, its petrophysical and petrological state remains uniform across the massif, and little or no deformation occurred during the Cenozoic in the lower crust. The magmatic impact extends to the petrological Moho at ca. 40 km deep and continues into the SCLM. Here, ultramafic cumulates and depleted peridotites display occurence of modal and cryptic metasomatism.

At Calbuco volcano, located in the arc domain at similar latitudes to the back-arc NPM, xenoliths revealed a close relationship between crustal growth and active deformation within the lower crust. Mylonites and cumulates formed simultaneously, indicating that deformation resulting from the stress induced by the Nazca/South America convergence is geographically limited in recent times, primarily occurring in the region of the active transverse Liquiñe-Ofqui fault zone (LOFZ), and does not extend into the back-arc domain. However, the MNP peridotites indicate that deformation at depth can be observed in a back-arc context, although this deformation is likely linked to older geodynamic events distinct from those recent. Nevertheless, the SCLM preserved witnesses of ancient deformation, whereas the MNP crustal basement is considered cratonic, dating back at least 65 Ma.

Northern transect: Cretaceous intracontinental Salta rift

The petrological Moho near Salta intracontinental rift is sharper than in the North Patagonian Massif, located at a depth of 40-45 km. The lower crust above the Moho is homogeneous and primarily of metasedimentary origin. It recorded a partial melting event dated at 114 Ma by

U-Pb on zircon, concurrent with the initial phases of Cretaceous rifting in the region. Salta mafic granulites display remnants of ancient high-temperature deformation erased by reequilibration during the ultra-high-temperature metamorphism linked to rifting. Below the Moho, the SCLM is chemically and microstructurally consistent and displays evidence of a first deformational event that shifted into a milder deformation regime, still active in the Upper Cretaceous.

Comparison between North and South transects

Comparative petrological, geochemical and petrophysical observations of the lower crust and the SCLM from Salta and MNP highlight differences between the two regions. Deformation at the mantle-crust transition (MCT) in Salta is homogeneous, affecting both the lower crust and the SCLM. In contrast, deformation in the MNP is localised in the mantle. The MCT in the North Patagonian Massif also recorded numerous magmatic events, significantly altering the lower crust and resulting in traces of percolation, as well as cryptic and modal metasomatism in the mantle. The presence of magmatic liquid in the SCLM, coupled with high-temperature events, may have localised deformation in the mantle, decoupling crust and mantle in the MNP. Similarly, the absence of substantial percolation in Salta lithosphere, concurrent with lower-temperature geodynamic events, may have imparted a more 'rigid' behaviour, coupling deformation in the lower crust and mantle. These observations are noteworthy because the rheological properties of Salta felsic crust greatly differ from those of mantle peridotites. This distinction could lead to a decoupling between the two layers, whereas the mafic granulites of the MNP lower crust have properties more akin to peridotites.

However, the evolution of deformation in the mantle of both regions is broadly identical. Peridotites acquired a crystallographic preferred orientation in association with high-temperature, low-stress deformation, followed by refertilisation (more significant in the MNP, minimal in Salta) and a subsequent change in the plastic deformation regime, evident in misorientations at subgrain boundaries, possibly due to a temperature decrease.

Similar deformation events have been documented in the southernmost region of Patagonia (Zaffarana *et al.*, 2014). Therefore, although the age of this deformation differs between Patagonia and Salta, their similarities can be attributed to their comparable Mesozoic and Cenozoic geodynamic contexts. Both regions are located in a back-arc context regarding the Pacific-South American convergence. Thus, this study highlights the significance of structural and chemical heritage, local tectonic and magmatic events in mantle-crust

interactions, crustal growth and deformation. It also highlights how larger-scale geodynamic events can impart a first-order deformation common to different region lithospheric mantles.

Perspectives

While this study represents one of the first explorations of mantle-crust interactions in these regions, its objective was to illustrate the diversity of deformation and chemical processes occurring in each locality. Given the heterogeneous nature of these processes and the limited number of investigated samples, attributing them to a dominant process in the study area is challenging. Extensive analysis and scaling up of the data sets will be necessary to identify the primary chemical and microstructural processes and comprehensively quantify their effects. Additionally, anisotropy calculations based on xenolith microstructures will be crucial to establish seismic wave velocities in the lower crust and mantle, essential for calibrating models based on seismic data.

On a local scale, conducting geochemical studies of mantle xenoliths and surface magmatic rocks in the MNP has established a robust chronology of magmatic events in the region and their impact on the lithosphere. Extending the chronology of these events to the lower crust by searching for zircon in mafic granulites would be valuable. By dating and analysing their trace element composition, even a few zircons could provide critical information about the metasedimentary origin of granulites. Other phases, such as apatites, could be dated to ascertain metasomatic events in the lower crust.

Mineral trace element analyses in Calbuco could highlight material exchange between the lower crust and the magmas, providing new constraints on the origin of the mylonites.

Similarly, analysing garnet and rutile trace elements in Salta felsic granulites would refine the petrochronological study of the zircons, especially confirming the presence of liquid during the crystallisation of metamorphic zircons. Notably, the existence of a Cretaceous partial melting event in the lower crust has not been reported in the region. Furthermore, substantiating the zircon population in felsic granulites is crucial to establishing a robust dataset characterising detrital zircon populations. The garnet-feldspar-rutile-apatite-zircon A-112b granulite could provide valuable insights into understanding metasomatism or partial melting recorded in the lower crust at Salta.

Trace element analysis of clinopyroxene and garnet in the mafic granulites of the Las Conchas Valley would help to better constrain their protolith nature.

Lastly, in-situ analysis of trace elements in minerals from the Las Conchas Valley peridotites could refine the link between microstructural analysis and metasomatism.

BIBLIOGRAPHY

Abbott, D. H., Mooney, W. D. & VanTongeren, J. A. (2013). The character of the Moho and lower crust within Archean cratons and the tectonic implications. *Tectonophysics* **609**, 690–705.

Afonso, J. C., Salajegheh, F., Szwillus, W., Ebbing, J. & Gaina, C. (2019). A global reference model of the lithosphere and upper mantle from joint inversion and analysis of multiple data sets. *Geophysical Journal International* **217**, 1602–1628.

Alkmim, F. F., Marshak, S. & Fonseca, M. A. (2001). Assembling West Gondwana in the Neoproterozoic: Clues from the São Francisco craton region, Brazil. *Geology* **29**, 319.

Almqvist, B. S. G. & Mainprice, D. (2017). Seismic properties and anisotropy of the continental crust: Predictions based on mineral texture and rock microstructure. *Reviews of Geophysics* **55**, 367–433.

Allard, M., Ildefonse, B., Oliot, É. & Barou, F. (2021). Plastic Deformation of Plagioclase in Oceanic Gabbro Accreted at a Slow‐Spreading Ridge (Hole U1473A, Atlantis Bank, Southwest Indian Ridge). *Journal of Geophysical Research: Solid Earth* **126**.

Amiguet, E. (2009). Déformation expérimentale de diopside dans les conditions de pression et température du manteau supérieur. Université des Sciences et Technologies de Lille, p.145.

Aoki, K.I. & Kushiro, I. (1968). Some clinopyroxenes from ultramafic inclusions in Dreiser Weiher, Eifel. *Contributions to Mineralogy and Petrology* **18**, 326–337.

Aragón, E. *et al.* (2011). Tectono-magmatic response to major convergence changes in the North Patagonian suprasubduction system; the Paleogene subduction–transcurrent plate margin transition. *Tectonophysics* **509**, 218–237.

Arancibia, G., Cembrano, J. & Lavenu, A. (1999). Transpresión dextral y partición de la deformación en la Zona de Falla Liquiñe-Ofqui, Aisén, Chile (44-45°S). *Revista geológica de Chile* **26**, 3–22.

Armijo, R., Lacassin, R., Coudurier-Curveur, A. & Carrizo, D. (2015). Coupled tectonic evolution of Andean orogeny and global climate. *Earth-Science Reviews* **143**, 1–35.

Asiain, L., Florencia Gargiulo, M., Ferracutti, G., Hauser, N. & Bjerg, E. A. (2022). Evolution of the volcanism in the northwestern part of meseta de Somuncurá, Patagonia, Argentina. *Journal of South American Earth Sciences* **113**, 103653.

Assumpção, M., Feng, M., Tassara, A. & Julià, J. (2013). Models of crustal thickness for South America from seismic refraction, receiver functions and surface wave tomography. *Tectonophysics* **609**, 82–96.

Austrheim, H. (2013). Fluid and deformation induced metamorphic processes around Moho beneath continent collision zones: Examples from the exposed root zone of the Caledonian mountain belt, W-Norway. *Tectonophysics* **609**, 620–635.

Avé Lallemant, H. G. (1978). Experimental deformation of diopside and websterite. *Tectonophysics* **48**, 1–27.

Bachmann, F., Hielscher, R. & Schaeben, H. (2010). Texture Analysis with MTEX – Free and Open Source Software Toolbox. *Solid State Phenomena* **160**, 63–68.

Bachmann, F., Hielscher, R. & Schaeben, H. (2011). Grain detection from 2d and 3d EBSD data—Specification of the MTEX algorithm. *Ultramicroscopy* **111**, 1720–1733.

Ballivián Justiniano, C. A., Oriolo, S. & Basei, M. A. S. (2023). Coupled U–Pb and Lu–Hf zircon data of Late Devonian magmatism from Bajo de La Leona (Deseado Massif, Argentina): Tracking the southernmost exposure of the Devonian magmatic arc of Patagonia. *Journal of South American Earth Sciences* **128**, 104455.

Baptiste, V., Tommasi, A., Vauchez, A., Demouchy, S. & Rudnick, R. L. (2015). Deformation, hydration, and anisotropy of the lithospheric mantle in an active rift: Constraints from mantle xenoliths from the North Tanzanian Divergence of the East African Rift. *Tectonophysics* **639**, 34–55.

Bascou, J., Barruol, G., Vauchez, A., Mainprice, D. & Egydio-Silva, M. (2001). EBSD-measured lattice-preferred orientations and seismic properties of eclogites. *Tectonophysics* **342**, 61–80.

Beccaluva, L., Bianchini, G., Natali, C. & Siena, F. (2009). Continental Flood Basalts and Mantle Plumes: a Case Study of the Northern Ethiopian Plateau. *Journal of Petrology* **50**, 1377–1403.

Bédard, J. H. (2006). Trace element partitioning in plagioclase feldspar. *Geochimica et Cosmochimica Acta* **70**, 3717–3742.

Bernard, R. E. & Behr, W. M. (2017). Fabric heterogeneity in the Mojave lower crust and lithospheric mantle in Southern California: HETEROGENEITY IN THE MOJAVE LITHOSPHERE. *Journal of Geophysical Research: Solid Earth* **122**, 5000–5025.

Bernard, R. E., Schulte-Pelkum, V. & Behr, W. M. (2021). The competing effects of olivine and orthopyroxene CPO on seismic anisotropy. *Tectonophysics* **814**, 228954.

Bertotto, G. W. (2003). Evolución geológica y petrológica de los conos basálticos cenozoicos portadores de xenolitos ultramáficos del margen oriental de la provincia basáltica andino cuyana, provincias de La Pampa y Mendoza. Doctor en Ciencias Naturales, Universidad Nacional de La Plata.

Bertotto, G. W., Mazzucchelli, M., Zanetti, A. & Vannucci, R. (2013). Petrology and

geochemistry of the back-arc lithospheric mantle beneath eastern Payunia (La Pampa, Argentina): Evidence from Agua Poca peridotite xenoliths. *GEOCHEMICAL JOURNAL* **47**, 219–234.

Bertotto, G. W. *et al.* (2022). Mantle Xenoliths from Huanul Volcano (Central-West Argentina): A Poorly Depleted Mantle Source under Southern Payenia. *Geosciences* **12**, 157.

Beslier, M.-O., Ask, M. & Boillot, G. (1993). Ocean-continent boundary in the Iberia Abyssal Plain from multichannel seismic data. *Tectonophysics* **218**, 383–393.

Bianchini, G., Braga, R. & Langone, A. (2013). Crustal xenoliths from Tallante (Betic Cordillera, Spain): insights into the crust–mantle boundary. *Geological Magazine* **150**, 952–958.

Bickert, M., Kaczmarek, M.-A., Brunelli, D., Maia, M., Campos, T. F. C. & Sichel, S. E. (2023). Fluid-assisted grain size reduction leads to strain localization in oceanic transform faults. *Nature Communications* **14**, 4087.

Bjerg, E. A., Ntaflos, T., Kurat, G., Dobosi, G. & Labudía, C. H. (2005). The upper mantle beneath Patagonia, Argentina, documented by xenoliths from alkali basalts. *Journal of South American Earth Sciences* **18**, 125–145.

Bjerg, E. A., Ntaflos, T., Thoni, M., Aliani, P. & Labudia, C. H. (2009). Heterogeneous Lithospheric Mantle beneath Northern Patagonia: Evidence from Prahuaniyeu Garnet- and Spinel-Peridotites. *Journal of Petrology* **50**, 1267–1298.

Blatter, D. L., Sisson, T. W. & Hankins, W. B. (2013). Crystallization of oxidized, moderately hydrous arc basalt at mid- to lower-crustal pressures: implications for andesite genesis. *Contributions to Mineralogy and Petrology* **166**, 861–886.

Boillot, G., Girardeau, J., Kornprobst, J. (1988). Rifting of the galicia margin : crustal thinning and emplacement of mantle rocks on the seafloor. *Proceedings of the Ocean Drilling Program, Scientific Results* **103**, 741-756.

Brey, G. P. & Köhler, T. (1990). Geothermobarometry in Four-phase Lherzolites II. New Thermobarometers, and Practical Assessment of Existing Thermobarometers. *Journal of Petrology* **31**, 1353–1378.

Bryan, S. E. & Ferrari, L. (2013). Large igneous provinces and silicic large igneous provinces: Progress in our understanding over the last 25 years. *Geological Society of America Bulletin* **125**, 1053–1078.

Bryant, J. A., Yogodzinski, G. M. & Churikova, T. G. (2007). Melt-mantle interactions beneath the Kamchatka arc: Evidence from ultramafic xenoliths from Shiveluch volcano: SUB-ARC MELT-MANTLE INTERACTIONS. *Geochemistry, Geophysics, Geosystems* **8**.

Bunge, H.J., 1982. Texture Analysis in Materials Science. Butterworth-Heinemann, London, 599 pp.

Burns, D. H., de Silva, S. L., Tepley, F. J. & Schmitt, A. K. (2020). Chasing the mantle: Deciphering cryptic mantle signals through Earth's thickest continental magmatic arc. *Earth and Planetary Science Letters* **531**, 115985.

Bystricky, M., Kunze, K., Burlini, L. & Burg, J.-P. (2000). High Shear Strain of Olivine Aggregates: Rheological and Seismic Consequences. *Science* **290**, 1564–1567.

Carter, N. L. & Avé Lallemant, H. G. (1970). High Temperature Flow of Dunite and Peridotite. *Geological Society of America Bulletin* **81**, 2181–2202.

Casquet, C., Pankhurst, R. J., Fanning, C. M., Baldo, E., Galindo, C., Rapela, C. W., González-Casado, J. M. & Dahlquist, J. A. (2006). U–Pb SHRIMP zircon dating of Grenvillian metamorphism in Western Sierras Pampeanas (Argentina): Correlation with the Arequipa-Antofalla craton and constraints on the extent of the Precordillera Terrane. *Gondwana Research* **9**, 524–529.

Casquet, C., Rapela, C. W., Pankhurst, R. J., Baldo, E. G., Galindo, C., Fanning, C. M., & Saavedra, J. (2012). A history of Proterozoic terranes in southern South America: From Rodinia to Gondwana. *Geoscience Frontiers*, **3** (2), 137-145.

Casquet, C. *et al.* (2018). Review of the Cambrian Pampean orogeny of Argentina; a displaced orogen formerly attached to the Saldania Belt of South Africa? *Earth-Science Reviews* **177**, 209–225.

Castro, A., Aragón, E., Díaz-Alvarado, J., Blanco, I., García-Casco, A., Vogt, K. & Liu, D.-Y. (2011). Age and composition of granulite xenoliths from Paso de Indios, Chubut province, Argentina. *Journal of South American Earth Sciences* **32**, 567–574.

Cawood, P. A., Chowdhury, P., Mulder, J. A., Hawkesworth, C. J., Capitanio, F. A., Gunawardana, P. M. & Nebel, O. (2022). Secular Evolution of Continents and the Earth System. *Reviews of Geophysics* **60**.

Cawood, P. A., Hawkesworth, C. J. & Dhuime, B. (2013). The continental record and the generation of continental crust. *Geological Society of America Bulletin* **125**, 14–32.

Chaussard, E. & Amelung, F. (2014). Regional controls on magma ascent and storage in volcanic arcs. *Geochemistry, Geophysics, Geosystems* **15**, 1407–1418.

Chen, Y.-W., Wu, J. & Suppe, J. (2019). Southward propagation of Nazca subduction along the Andes. *Nature* **565**, 441–447.

Chmielowski, J., Zandt, G. & Haberland, C. (1999). The Central Andean Altiplano-Puna magma body. *Geophysical Research Letters* **26**, 783–786.

Christiansen, R. O., Gianni, G. M., Ballivián Justiniano, C. A., García, H. P. A. & Wohnlich, S. (2022). The role of geotectonic setting on the heat flow distribution of southern South America. *Geophysical Journal International* **230**, 1911–1927.

Chulick, G. S., Detweiler, S. & Mooney, W. D. (2013). Seismic structure of the crust and uppermost mantle of South America and surrounding oceanic basins. *Journal of South American Earth Sciences* **42**, 260–276.

Coltice, N., Husson, L., Faccenna, C. & Arnould, M. (2019). What drives tectonic plates? *Science Advances* **5**, eaax4295.

Contreras-Reyes, E. *et al.* (2021). Subduction zone fluids and arc magmas conducted by lithospheric deformed regions beneath the central Andes. *Scientific Reports* **11**, 23078.

Cordenons, P. D., Remesal, M. B., Salani, F. M. & Cerredo, M. E. (2020). Temporal and spatial evolution of the Somún Curá Magmatic Province, Northern Extra-Andean Patagonia, Argentina. *Journal of South American Earth Sciences* **104**, 102881.

Costa Rodriguez, F. (2000). The petrology and geochemistry of diverse crustal xenoliths, Tatara-San Pedro volcanic complex, Chilean Andes. Université de Genève.

Costa, F., Dungan, M. A. & Singer, B. S. (2002). Hornblende- and Phlogopite-Bearing Gabbroic Xenoliths from Volca´n San Pedro (36° S), Chilean Andes: Evidence for Melt and Fluid Migration and Reactions in Subduction-Related Plutons. **43**, 23.

Couvy, H., Frost, D. J., Heidelbach, F., Nyilas, K., Ungár, T., Mackwell, S. & Cordier, P. (2004). Shear deformation experiments of forsterite at 11 GPa - 1400C in the multianvil apparatus. *European Journal of Mineralogy* **16**, 877–889.

Daly, L. *et al.* (2019). Understanding the emplacement of Martian volcanic rocks using petrofabrics of the nakhlite meteorites. *Earth and Planetary Science Letters* **520**, 220–230.

Dantas, C. (2007). Caractérisation du manteau supérieur patagonien: les enclaves ultramafiques et mafiques dans les laves alcalines. Université de Toulouse III, p. 336.

Dantas, C., Grégoire, M., Koester, E., Conceição, R. V. & Rieck, N. (2009). The lherzolite–websterite xenolith suite from Northern Patagonia (Argentina): Evidence of mantle–melt reaction processes. *Lithos* **107**, 107–120.

Degli Alessandrini, G., Menegon, L., Malaspina, N., Dijkstra, A. H. & Anderson, M. W. (2017). Creep of mafic dykes infiltrated by melt in the lower continental crust (Seiland Igneous Province, Norway). *Lithos* **274–275**, 169–187.

Desta, M. T., Ayalew, D., Ishiwatari, A., Arai, S. & Tamura, A. (2014). Ferropicrite from the Lalibela area in the Ethiopian large igneous province. *Journal of Mineralogical and Petrological Sciences* **109**, 191–207.

Díaz Aspiroz, M., Lloyd, G. E. & Fernández, C. (2007). Development of lattice preferred orientation in clinoamphiboles deformed under low-pressure metamorphic conditions. A SEM/EBSD study of metabasites from the Aracena metamorphic belt (SW Spain). *Journal of Structural Geology* **29**, 629–645.

Dorfler, K. M., Caddick, M. J. & Tracy, R. J. (2015). Thermodynamic Modeling of Crustal Melting Using Xenolith Analogs from the Cortlandt Complex, New York, USA. *Journal of Petrology* **56**, 20.

Downes, H. (1993). The nature of the lower continental crust of Europe: petrological and geochemical evidence from xenoliths. *Physics of the Earth and Planetary Interiors* **79**, 195–218.

Downes, H. (2001). Formation and Modification of the Shallow Sub-continental Lithospheric Mantle: a Review of Geochemical Evidence from Ultramafic Xenolith Suites and Tectonically Emplaced Ultramafic Massifs of Western and Central Europe. *Journal of Petrology* **42**, 233–250.

Duretz, T., Petri, B., Mohn, G., Schmalholz, S. M., Schenker, F. L. & Müntener, O. (2016). The importance of structural softening for the evolution and architecture of passive margins. *Scientific Reports* **6**, 38704.

Dzierma, Y., Thorwart, M. & Rabbel, W. (2012). Moho topography and subducting oceanic slab of the Chilean continental margin in the maximum slip segment of the 1960 Mw 9.5 Valdivia (Chile) earthquake from P-receiver functions.

Echaurren, A., Folguera, A., Gianni, G., Orts, D., Tassara, A., Encinas, A., Giménez, M. & Valencia, V. (2016). Tectonic evolution of the North Patagonian Andes (41°–44° S) through recognition of syntectonic strata. *Tectonophysics* **677–678**, 99–114.

Echaurren, A., Oliveros, V., Folguera, A., Ibarra, F., Creixell, C. & Lucassen, F. (2017). Early Andean tectonomagmatic stages in north Patagonia: insights from field and geochemical data. *Journal of the Geological Society* **174**, 405–421.

Echaurren, A., Encinas, A., Sagripanti, L., Gianni, G., Zambrano, P., Duhart, P. & Folguera, A. (2022). Fore-to-retroarc crustal structure of the north Patagonian margin: How is shortening distributed in Andean-type orogens? *Global and Planetary Change* **209**, 103734.

Embey-Isztin, A., Scharbert, H. G., Dietrich, H. & Poultidis, H. (1990). Mafic granulites and clinopyroxenite xenoliths from the Transdanubian Volcanic Region (Hungary): implications for the deep structure of the Pannonian Basin. *Mineralogical Magazine* **54**, 463–483.

Ernst, R. E. & Bell, K. (2010). Large igneous provinces (LIPs) and carbonatites. *Mineralogy and Petrology* **98**, 55–76.

Faccini, B., Bonadiman, C., Coltorti, M., Grégoire, M. & Siena, F. (2013). Oceanic Material Recycled within the Sub-Patagonian Lithospheric Mantle (Cerro del Fraile, Argentina). *Journal of Petrology* **54**, 1211–1258.

Falco, J. I., Hauser, N., Scivetti, N., Reimold, W. U., Schmitt, R. T. & Folguera, A. (2022). Upper Triassic to Middle Jurassic magmatic evolution of northern Patagonia: Insights from the tectonic and crustal evolution of the Los Menucos area, North Patagonian Massif, Argentina. *Journal of South American Earth Sciences* **113**, 103631.

Fernández Paz, L., Litvak, V. D., Echaurren, A., Iannelli, S. B., Encinas, A., Folguera, A. & Valencia, V. (2018). Late Eocene volcanism in North Patagonia (42°30′–43° S): Arc resumption after a stage of within-plate magmatism. *Journal of Geodynamics* **113**, 13–31.

Fernández-Roig, M., Galán, G. & Mariani, E. (2018). Crystal preferred orientation of olivine in mantle xenoliths from Catalonia (NE Spain) Orientación cristalina preferente del olivino en xenolitos mantélicos de Cataluña (NE de España). *Trabajos de Geología* **36**, 119.

Ferracutti, G. R., Gargiulo, M. F., Ganuza, M. L., Bjerg, E. A. & Castro, S. M. (2015). Determination of the spinel group end-members based on electron microprobe analyses. Mineralogy and Petrology 109, 153–160.

Figueroa, O., Déruelle, B. & Demaiffe, D. (2009). Genesis of adakite-like lavas of Licancabur volcano (Chile—Bolivia, Central Andes). *Comptes Rendus Geoscience* **341**, 310–318.

Finlayson, D.M., Owen, A., Johnstone, D. & Wake-Dyster, K.D. (1993). Moho and petrologic crust–mantle boundary coincide under southeastern Australia. **Geology** *21*, 707–710.

Foley, M. L., Putlitz, B., Baumgartner, L. P., Bégué, F., Siron, G. & Kosmal, A. (2023). Generating large volumes of crust-derived high δ18O rhyolites in the Chon Aike Silicic Large Igneous Province, Patagonia. *Geosphere* **19**, 975–1005.

Frets, E., Tommasi, A., Garrido, C. J., Padrón-Navarta, J. A., Amri, I. & Targuisti, K. (2012). Deformation processes and rheology of pyroxenites under lithospheric mantle conditions. *Journal of Structural Geology* **39**, 138–157.

Fuhrman, M. L. & Lindsley, D. H. (1988). Ternary-feldspar modeling and thermometry. *American Mineralogist* **73**, 201–215.

Fujimaki, H., Tatsumoto, M. and Aoki, K.-i. (1984). Partition coefficients of Hf, Zr, and REE between phenocrysts and groundmasses. *Journal of Geophysical Research* **89**, 662-672.

Ganade, C., Riel, N., Manatschal, G., Tesser, L., Rubatto, D., Hermann, J., Weinberg, R., Lanari, P. & Kaus, B. (2023). *Emergence of modern-style continental subduction modulated by rifted margin-subduction feedback*. preprint. In Review.

Genge, M. C., Zattin, M., Savignano, E., Franchini, M., Gautheron, C., Ramos, V. A. & Mazzoli, S. (2021). The role of slab geometry in the exhumation of cordilleran-type orogens and their forelands: Insights from northern Patagonia. *GSA Bulletin* **133**, 2535–2548.

Getsinger, A. J., Hirth, G., Stünitz, H. & Goergen, E. T. (2013). Influence of water on rheology and strain localization in the lower continental crust: Water, Rheology, and Strain Localization. *Geochemistry, Geophysics, Geosystems* **14**, 2247–2264.

Giambiagi, L. *et al.* (2022). Crustal anatomy and evolution of a subduction-related orogenic system: Insights from the Southern Central Andes (22-35° S). *Earth-Science Reviews* **232**, 104138.

Gianni, G. M. & Navarrete, C. R. (2022). Catastrophic slab loss in southwestern Pangea preserved in the mantle and igneous record. *Nature Communications* **13**, 698.

Godard, M. *et al.* (2009). Geochemistry of a long in-situ section of intrusive slow-spread oceanic lithosphere: Results from IODP Site U1309 (Atlantis Massif, 30°N Mid-Atlantic-Ridge). *Earth and Planetary Science Letters* **279**, 110–122.

Gomes, A. S. & Vasconcelos, P. M. (2021). Geochronology of the Paraná-Etendeka large igneous province. *Earth-Science Reviews* **220**, 103716.

Gómez Dacal, M. L., Scheck-Wenderoth, M., Aragón, E., Bott, J., Cacace, M. & Tocho, C. (2021). Unravelling the lithospheric-scale thermal field of the North Patagonian Massif plateau (Argentina) and its relations to the topographic evolution of the area. *International Journal of Earth Sciences* **110**, 2315–2331.

Gómez Dacal, M. L., Tocho, C., Aragón, E., Sippel, J., Scheck-Wenderoth, M. & Ponce, A. (2017). Lithospheric 3D gravity modelling using upper-mantle density constraints: Towards a characterization of the crustal configuration in the North Patagonian Massif area, Argentina. *Tectonophysics* **700–701**, 150–161.

Green, E. C. R., White, R. W., Diener, J. F. A., Powell, R., Holland, T. J. B. & Palin, R. M. (2016). Activity-composition relations for the calculation of partial melting equilibria in metabasic rocks. *Journal of Metamorphic Geology* **34**, 845–869.

Grégoire, M., Cottin, J. Y., Giret, A., Mattielli, N. & Weis, D. (1998). The meta-igneous granulite xenoliths from Kerguelen Archipelago: evidence of a continent nucleation in an oceanic setting. *Contributions to Mineralogy and Petrology* **133**, 259–283.

Grégoire, M., Mattielli, N., Nicollet, C., Cottin, J. Y., Leyrit, H., Weis, D., Shimizu, N. & Giret, A. (1994). Oceanic mafic granulite xenoliths from the Kerguelen archipelago. *Nature* **367**, 360–363.

Grégoire, M., Jackson, I., O'Reilly, S. & Cottin, J. (2001). The lithospheric mantle beneath the Kerguelen Islands (Indian Ocean): petrological and petrophysical characteristics of

mantle mafic rock types and correlation with seismic profiles. *Contributions to Mineralogy and Petrology* **142**, 244–259.

Griffin, S. *et al.* (2022). Can the Magmatic Conditions of the Martian Nakhlites be Discerned via Investigation of Clinopyroxene and Olivine Intracrystalline Misorientations? *Journal of Geophysical Research: Planets* **127**.

Griffin, W. L. & O'Reilly, S. Y. (1987). Is the continental Moho the crust-mantle boundary? *Geology* **15**, 241.

Griffin, W., Powell, W., Pearson, N. J. & O'Reilly, S. (2008). GLITTER: data reduction software for laser ablation ICP-MS. *Short Course Series* **40**, 308–311.

Gutscher, M., Spakman, W., Bijwaard, H. & Engdahl, E. R. (2000). Geodynamics of flat subduction: Seismicity and tomographic constraints from the Andean margin. *Tectonics* **19**, 814–833.

Hacker, B. R. & Christie, J. M. (1990). Brittle/ductile and plastic/cataclastic transitions in experimentally deformed and metamorphosed amphibolite. In: Duba, A. G., Durham, W. B., Handin, J. W. & Wang, H. F. (eds) *Geophysical Monograph Series*. Washington, D. C.: American Geophysical Union, 127–147.

Hacker, B. R., Kelemen, P. B. & Behn, M. D. (2015). Continental Lower Crust. *Annual Review of Earth and Planetary Sciences* **43**, 167–205.

Hansen, L. N., Zhao, Y.-H., Zimmerman, M. E. & Kohlstedt, D. L. (2014). Protracted fabric evolution in olivine: Implications for the relationship among strain, crystallographic fabric, and seismic anisotropy. *Earth and Planetary Science Letters* **387**, 157–168.

Heckel, C., Woodland, A. B., Linckens, J., Gibson, S. A. & Seitz, H.-M. (2022). Sheared Peridotites from Kimberley (Kaapvaal Craton, RSA): Record of Multiple Metasomatic Events Accompanied with Deformation. *Journal of Petrology* **63**, egac096.

Helmstaedt, H., Anderson, O. L., & Gavasci, A. T. (1972). Petrofabric studies of eclogite, spinel‐Websterite, and spinel‐lherzolite Xenoliths from kimberlite‐bearing breccia pipes in southeastern Utah and northeastern Arizona. *Journal of Geophysical Research* **77**(23), 4350-4365.

Henry, H., Tilhac, R., Griffin, W. L., O'Reilly, S. Y., Satsukawa, T., Kaczmarek, M.-A., Grégoire, M. & Ceuleneer, G. (2017). Deformation of mantle pyroxenites provides clues to geodynamic processes in subduction zones: Case study of the Cabo Ortegal Complex, Spain. *Earth and Planetary Science Letters* **472**, 174–185.

Heredia, N., García-Sansegundo, J., Gallastegui, G., Farias, P., Giacosa, R., Alonso, J. L., & Ramos, V. A. (2016). Late Neoproterozoic-Paleozoic geodynamic evolution of the Andes of Argentina, Chile and the Antarctic Penninsula. *Trabajos de Geología* **36**, 237–278.

Hervé, F., Faundez, V., Calderón, M., Massonne, H.-J. & Willner, A. P. (2007). Metamorphic and plutonic basement complexes. In: Moreno, T. & Gibbons, W. (eds) *The Geology of Chile*. The Geological Society of London, 5–19.

Hervé, F., Calderon, M., Fanning, C. M., Pankhurst, R. J., Fuentes, F., Rapela, C. W., Correa, J., Quezada, P. & Marambio, C. (2016). Devonian magmatism in the accretionary complex of southern Chile. *Journal of the Geological Society* **173**, 587–602.

Hervé, F., Calderón, M., Fanning, M., Pankhurst, R., Rapela, C. W. & Quezada, P. (2018). The country rocks of Devonian magmatism in the North Patagonian Massif and Chaitenia. *Andean Geology* **45**, 301.

Hickey-Vargas, R., Abdollahi, M. J., Parada, M. A. & Frey, F. A. (1995). Crustal xenoliths from Calbuco Volcano, Andean Southern Volcanic Zone: implications for crustal composition and magma-crust interaction. *Contributions to Mineralogy and Petrology* **119**, 331–344.

Hickey-Vargas, R., Holbik, S., Tormey, D., Frey, F. A. & Moreno Roa, H. (2016). Basaltic rocks from the Andean Southern Volcanic Zone: Insights from the comparison of along-strike and small-scale geochemical variations and their sources. *Lithos* **258–259**, 115–132.

Hidas, K., Garrido, C. J., Booth-Rea, G., Marchesi, C., Bodinier, J.-L., Dautria, J.-M., Louni-Hacini, A. & Azzouni-Sekkal, A. (2019). *Lithosphere tearing along STEP faults and synkinematic formation of lherzolite and wehrlite in the shallow subcontinental mantle*. preprint. Tectonic plate interactions, magma genesis, and lithosphere deformation at all scales/Structural geology and tectonics, rock physics, experimental deformation/Tectonics.

Hildreth, W. & Moorbath, S. (1988). Crustal contributions to arc magmatism in the Andes of Central Chile. *Contributions to Mineralogy and Petrology* **98**, 455–489.

Holland, T. J. B. & Powell, R. (2004). An internally consistent thermodynamic data set for phases of petrological interest: AN INTERNALLY CONSISTENT THERMODYNAMIC DATA SET. *Journal of Metamorphic Geology* **16**, 309–343.

Holland, T. J. B. & Powell, R. (2011). An improved and extended internally consistent thermodynamic dataset for phases of petrological interest, involving a new equation of state for solids: THERMODYNAMIC DATASET FOR PHASES OF PETROLOGICAL INTEREST. *Journal of Metamorphic Geology* **29**, 333–383.

Holtzman, B. K., Kohlstedt, D. L., Zimmerman, M. E., Heidelbach, F., Hiraga, T. & Hustoft, J. (2003). Melt Segregation and Strain Partitioning: Implications for Seismic Anisotropy and Mantle Flow. *Science* **301**, 1227–1230.

Horst, T. S. (2007). Determining magmatic processes from analysis of phenocrysts and gabbroic xenoliths contained in Calbuco andesites. Master of Science. Geosciences, Florida International University.

Idárraga-García, J. & Vargas, C. A. (2018). Depth to the bottom of magnetic layer in South America and its relationship to Curie isotherm, Moho depth and seismicity behavior. *Geodesy and Geodynamics* **9**, 93–107.

Ismaïl, W. B. & Mainprice, D. (1998). An olivine fabric database: an overview of upper mantle fabrics and seismic anisotropy. *Tectonophysics* **296**, 145–157.

Jackson, S. E., Pearson, N. J., Griffin, W. L. & Belousova, E. A. (2004). The application of laser ablation-inductively coupled plasma-mass spectrometry to in situ U–Pb zircon geochronology. *Chemical Geology* **211**, 47–69.

Jacques, G., Hoernle, K., Gill, J., Wehrmann, H., Bindeman, I. & Lara, L. E. (2014). Geochemical variations in the Central Southern Volcanic Zone, Chile (38–43°S): The role of fluids in generating arc magmas. *Chemical Geology* **371**, 27–45.

Jalowitzki, T. *et al.* (2017). Slab-derived components in the subcontinental lithospheric mantle beneath Chilean Patagonia: Geochemistry and Sr–Nd–Pb isotopes of mantle xenoliths and host basalt. *Lithos* **292–293**, 179–197.

Ji, S., Shao, T., Salisbury, M. H., Sun, S., Michibayashi, K., Zhao, W., Long, C., Liang, F. & Satsukawa, T. (2014). Plagioclase preferred orientation and induced seismic anisotropy in mafic igneous rocks: Plagioclase and seismic anisotropy. *Journal of Geophysical Research: Solid Earth* **119**, 8064–8088.

Jicha, B. R., Singer, B. S., Beard, B. L., Johnson, C. M., Moreno-Roa, H. & Naranjo, J. A. (2007). Rapid magma ascent and generation of 230Th excesses in the lower crust at Puyehue–Cordón Caulle, Southern Volcanic Zone, Chile. *Earth and Planetary Science Letters* **255**, 229–242.

Jochum, K. P. *et al.* (2011). Determination of Reference Values for NIST SRM 610-617 Glasses Following ISO Guidelines. *Geostandards and Geoanalytical Research* **35**, 397–429.

Jolivet, L. *et al.* (2018). Extensional crustal tectonics and crust-mantle coupling, a view from the geological record. *Earth-Science Reviews* **185**, 1187–1209.

Jolivet, L. *et al.* (2021). Transfer zones in Mediterranean back-arc regions and tear faults. *BSGF - Earth Sciences Bulletin* **192**, 11.

Jung, H. & Karato, S. (2001). Water-Induced Fabric Transitions in Olivine. *Science* **293**, 1460–1463.

Jung, H., Park, M., Jung, S., & Lee, J. (2010). Lattice preferred orientation, water content, and seismic anisotropy of orthopyroxene. *Journal of Earth Science*, ***21***(5), 555-568.

Kaczmarek, M.-A. & Tommasi, A. (2011). Anatomy of an extensional shear zone in the mantle, Lanzo massif, Italy: EXTENSIONAL SHEAR ZONE IN THE MANTLE. *Geochemistry, Geophysics, Geosystems* **12**.

Kaczmarek, M.-A. & Reddy, S. M. (2013). Mantle deformation during rifting: Constraints from quantitative microstructural analysis of olivine from the East African Rift (Marsabit, Kenya). *Tectonophysics* **608**, 1122–1137.

Kaczmarek, M.-A., Bodinier, J.-L., Bosch, D., Tommasi, A., Dautria, J.-M. & Kechid, S. A. (2016). Metasomatized Mantle Xenoliths as a Record of the Lithospheric Mantle Evolution of the Northern Edge of the Ahaggar Swell, In Teria (Algeria). *Journal of Petrology* **57**, 345–382.

Karato, S., Jung, H., Katayama, I. & Skemer, P. (2008). Geodynamic Significance of Seismic Anisotropy of the Upper Mantle: New Insights from Laboratory Studies. *Annual Review of Earth and Planetary Sciences* **36**, 59–95.

Katayama, I., Jung, H. & Karato, S. (2004). New type of olivine fabric from deformation experiments at modest water content and low stress. *Geology* **32**, 1045.

Kay, S. M., Gorring, M. & Ramos, V. A. (2004). Magmatic sources, setting and causes of Eocene to Recent Patagonian plateau magmatism (36°S to 52°S latitude). *Revista de la Asociación Geológica Argentina* **59** (4), 556-568.

Kay, S. M., Ardolino, A. A., Gorring, M. L. & Ramos, V. A. (2007). The Somuncura Large Igneous Province in Patagonia: Interaction of a Transient Mantle Thermal Anomaly with a Subducting Slab. *Journal of Petrology* **48**, 43–77.

Kay, S. M. & Coira, B. L. (2009). Shallowing and steepening subduction zones, continental lithospheric loss, magmatism, and crustal flow under the Central Andean Altiplano-Puna Plateau. *Backbone of the Americas: Shallow Subduction, Plateau Uplift, and Ridge and Terrane Collision*. Geological Society of America.

Kempton, P. D. & Harmon, R. S. (1992). Oxygen isotope evidence for large-scale hybridization of the lower crust during magmatic underplating. *Geochimica et Cosmochimica Acta* **56**, 971–986.

Kempton, P. D., Downes, H., Sharkov, E. V., Vetrin, V. R., Ionov, D. A., Carswell, D. A. & Beard, A. (1995). Petrology and geochemistry of xenoliths from the Northern Baltic shield: evidence for partial melting and metasomatism in the lower crust beneath an Archaean terrane. *Lithos* **36**, 157–184.

Kempton, P. D., Downes, H. & Embey-Isztin, A. (1997). Mafic Granulite Xenoliths in Neogene Alkali Basalts from the Western Pannonian Basin: Insights into the Lower Crust of a Collapsed Orogen. **38**, 30.

Kempton, P. D. (2001). Garnet Granulite Xenoliths from the Northern Baltic Shield--the Underplated Lower Crust of a Palaeoproterozoic Large Igneous Province? *Journal of Petrology* **42**, 731–763.

Kennedy, A. K., Wotzlaw, J.-F., Schaltegger, U., Crowley, J. L. & Schmitz, M. (2014). EOCENE ZIRCON REFERENCE MATERIAL FOR MICROANALYSIS OF U-Th-Pb ISOTOPES AND TRACE ELEMENTS. *The Canadian Mineralogist* **52**, 409–421.

Ko, B. & Jung, H. (2015). Crystal preferred orientation of an amphibole experimentally deformed by simple shear. *Nature Communications* **6**, 6586.

Kourim, F., Vauchez, A., Bodinier, J.-L., Alard, O. & Bendaoud, A. (2015). Subcontinental lithosphere reactivation beneath the Hoggar swell (Algeria): Localized deformation, melt channeling and heat advection. *Tectonophysics* **650**, 18–33.

Kourim, F. *et al.* (2022). Geochemical Characterization of the Oman Crust‐Mantle Transition Zone, OmanDP Holes CM1A and CM2B. *Journal of Geophysical Research: Solid Earth* **127**, e2021JB022694.

Kruse, R., Stünitz, H., & Kunze, K. (2001). Dynamic recrystallization processes in plagioclase porphyroclasts. *Journal of Structural Geology*, ***23***(11), 1781-1802.

Lamb, S. & Davis, P. (2003). Cenozoic climate change as a possible cause for the rise of the Andes. *Nature* **425**, 792–797.

Lambart, S., Koornneef, J. M., Millet, M.-A., Davies, G. R., Cook, M. & Lissenberg, C. J. (2019). Highly heterogeneous depleted mantle recorded in the lower oceanic crust. *Nature Geoscience* **12**, 482–486.

Laurent, O., Couzinié, S. & Doucet, L. S. (2023). Timescales of ultra-high temperature metamorphism and crustal differentiation: Zircon petrochronology from granulite xenoliths of the Variscan French Massif Central. *Earth and Planetary Science Letters* **611**, 118133.

Lee, W., Lee, H., Kim, D., Kim, J., Oh, J., Song, J.-H., Kim, C. H., Park, C. H. & Stuart, F. M. (2021). Trace element and helium isotope geochemistry of the Cenozoic intraplate volcanism in the East Sea (Sea of Japan): Implications for lithosphere-asthenosphere interaction. *Lithos* **388–389**, 106075.

Levin, V., VanTongeren, J. A. & Servali, A. (2016). How sharp is the sharp Archean Moho? Example from eastern Superior Province: How Sharp is Archean Moho? *Geophysical Research Letters* **43**, 1928–1933.

Li, X.-Y., Zheng, J.-P., Xiong, Q., Zhou, X. & Xiang, L. (2018). Triassic rejuvenation of unexposed Archean-Paleoproterozoic deep crust beneath the western Cathaysia block, South China. *Tectonophysics* **724–725**, 65–79.

Liptai, N. (2018). Geochemical and physical properties and evolution of the lithospheric mantle beneath the Nógrád-Gömör Volcanic Field (Northern Pannonian Basin, Central Europe). Eötvös Loránd Tudományegyetem. p. 176.

Liu, S., Tommasi, A., Vauchez, A. & Mazzucchelli, M. (2019). Crust-mantle coupling during

continental convergence and break-up: Constraints from peridotite xenoliths from the Borborema Province, northeast Brazil. *Tectonophysics* **766**, 249–269.

López De Luchi, M. G. & Rapalini, A. E. (2002). Middle Jurassic dyke swarms in the North Patagonian Massif: the Lonco Trapial Formation in the Sierra de Mamil Choique, Río Negro province, Argentina. *Journal of South American Earth Sciences* **15**, 625–641.

López De Luchi, M. G., Siegesmund, S., Wemmer, K. & Nolte, N. (2017). Petrogenesis of the postcollisional Middle Devonian monzonitic to granitic magmatism of the Sierra de San Luis, Argentina. *Lithos* **288–289**, 191–213.

Lovecchio, J. P., Rohais, S., Joseph, P., Bolatti, N. D. & Ramos, V. A. (2020). Mesozoic rifting evolution of SW Gondwana: A poly-phased, subduction-related, extensional history responsible for basin formation along the Argentinean Atlantic margin. *Earth-Science Reviews* **203**, 103138.

Lucassen, F., Franz, G. & Laber, A. (1999a). Permian high pressure rocks-the basement of the Sierra de Limón Verde in Northern Chile. *Journal of South American Earth Sciences* **12**, 183–199.

Lucassen, F., Lewerenz, S., Franz, G., Viramonte, J. & Mezger, K. (1999b). Metamorphism, isotopic ages and composition of lower crustal granulite xenoliths from the Cretaceous Salta Rift, Argentina. *Contributions to Mineralogy and Petrology* **134**, 325–341.

Lucassen, F., Franz, G., Viramonte, J., Romer, R. L., Dulski, P. & Lang, A. (2005). The late Cretaceous lithospheric mantle beneath the Central Andes: Evidence from phase equilibria and composition of mantle xenoliths. *Lithos* **82**, 379–406.

Lucassen, F., Franz, G., Romer, R. L., Schultz, F., Dulski, P. & Wemmer, K. (2007). Pre-Cenozoic intra-plate magmatism along the Central Andes (17–34° S): Composition of the mantle at an active margin. *Lithos* **99**, 312–338.

Luppo, T., López de Luchi, M. G., Rapalini, A. E., Martínez Dopico, C. I. & Fanning, C. M. (2018). Geochronologic evidence of a large magmatic province in northern Patagonia encompassing the Permian-Triassic boundary. *Journal of South American Earth Sciences* **82**, 346–355.

Mainprice, D., Tommasi, A., Couvy, H., Cordier, P. & Frost, D. J. (2005). Pressure sensitivity of olivine slip systems and seismic anisotropy of Earth's upper mantle. *Nature* **433**, 731–733.

Mainprice, D., Bachmann, F., Hielscher, R. & Schaeben, H. (2015). Descriptive tools for the analysis of texture projects with large datasets using MTEX : strength, symmetry and components. *Geological Society, London, Special Publications* **409**, 251–271.

Mallmann, G. (2004). Processos e Componentes Mantélicos no Norte da Patagônia (Argentina) e Relações com a Subducção Andina: Evidências Petrográficas, Geoquímicas e

Isotópicas em Xenólitos Ultramáficos Mantélicos. Universidade Federal do Rio Grande do Sul Instituto de Geociências, p.102.

Manatschal, G. (2004). New models for evolution of magma-poor rifted margins based on a review of data and concepts from West Iberia and the Alps. *International Journal of Earth Sciences* **93**.

Manatschal, G. & Müntener, O. (2009). A type sequence across an ancient magma-poor ocean–continent transition: the example of the western Alpine Tethys ophiolites. *Tectonophysics* **473**, 4–19.

Mange, M. A. & Morton, A. C. (2007). Chapter 13 Geochemistry of Heavy Minerals. *Developments in Sedimentology*. Elsevier, 345–391.

Manthilake, M. A. G. M., Miyajima, N., Heidelbach, F., Soustelle, V. & Frost, D. J. (2013). The effect of aluminum and water on the development of deformation fabrics of orthopyroxene. *Contributions to Mineralogy and Petrology* **165**, 495–505.

Markwick, A. J. W. & Downes, H. (2000). Lower crustal granulite xenoliths from the Arkhangelsk kimberlite pipes: petrological, geochemical and geophysical results. *Lithos* **51**, 135–151.

Markwick, A. J. W., Downes, H. & Veretennikov, N. (2001). The lower crust of SE Belarus: petrological, geophysical and geochemical constraints from xenoliths. *Tectonophysics* **339**, 215–237.

Marquillas, R. A., Del Papa, C. & Sabino, I. F. (2005). Sedimentary aspects and paleoenvironmental evolution of a rift basin: Salta Group (Cretaceous–Paleogene), northwestern Argentina. *International Journal of Earth Sciences* **94**, 94–113.

Martínez Dopico, C. I., López de Luchi, M. G., Rapalini, A. E. & Kleinhanns, I. C. (2011). Crustal segments in the North Patagonian Massif, Patagonia: An integrated perspective based on Sm–Nd isotope systematics. *Journal of South American Earth Sciences* **31**, 324–341.

Martínez Dopico, C. I., López De Luchi, M. G., Rapalini, A. E., Wemmer, K., Fanning, C. M. & Basei, M. A. S. (2017). Emplacement and temporal constraints of the Gondwanan intrusive complexes of northern Patagonia: La Esperanza plutono-volcanic case. *Tectonophysics* **712–713**, 249–269.

Martínez Dopico, C. I., López De Luchi, M. G., Rapalini, A. E., Fanning, C. M. & Antonio, P. Y. J. (2019). Geochemistry and geochronology of the shallow-level La Esperanza magmatic system (Permian-Triassic), Northern Patagonia. *Journal of South American Earth Sciences* **96**, 102347.

Martínez, J. C., Dristas, J. A. & Massonne, H.-J. (2012). Palaeozoic accretion of the

microcontinent Chilenia, North Patagonian Andes: high-pressure metamorphism and subsequent thermal relaxation. *International Geology Review* **54**, 472–490.

Martinod, J., Gérault, M., Husson, L. & Regard, V. (2020). Widening of the Andes: An interplay between subduction dynamics and crustal wedge tectonics. *Earth-Science Reviews* **204**, 103170.

Massaferro, G. I., Haller, M. J., Dostal, J., Pécskay, Z., Prez, H., Meister, C. & Alric, V. (2014). Possible sources for monogenetic Pliocene–Quaternary basaltic volcanism in northern Patagonia. *Journal of South American Earth Sciences* **55**, 29–42.

McCoy-West, A. J., Baker, J. A., Faure, K. & Wysoczanski, R. (2010). Petrogenesis and Origins of Mid-Cretaceous Continental Intraplate Volcanism in Marlborough, New Zealand: Implications for the Long-lived HIMU Magmatic Mega-province of the SW Pacific. *Journal of Petrology* **51**, 2003–2045.

McDonough, W. F. & Sun, S. -s. (1995). The composition of the Earth. *Chemical Geology* **120**, 223–253.

McGee, L. E. *et al.* (2017). A geochemical approach to distinguishing competing tectono-magmatic processes preserved in small eruptive centres. *Contributions to Mineralogy and Petrology* **172**, 44.

McKenzie, D., Daly, M. C. & Priestley, K. (2015). The lithospheric structure of Pangea. *Geology* **43**, 783–786.

McMillan, N. J., Harmon, R. S., Moorbath, S., Lopez-Escobar, L. & Strong, D. F. (1989). Crustal sources involved in continental arc magmatism: A case study of volcan Mocho-Choshuenco, southern Chile. *Geology* **17**, 1152.

Melchiorre, M., Coltorti, M., Gregoire, M. & Benoit, M. (2015). Refertilization process in the Patagonian subcontinental lithospheric mantle of Estancia Sol de Mayo (Argentina). *Tectonophysics* **650**, 124-143.

Melchiorre, M., Faccini, B., Grégoire, M., Benoit, M., Casetta, F. & Coltorti, M. (2020). Melting and metasomatism/refertilisation processes in the Patagonian sub-continental lithospheric mantle: A review. *Lithos* **354–355**, 105324.

Mengel, K. & Kern, H. (1992). Evolution of the petrological and seismic Moho-implications for the continental crust-mantle boundary. *Terra Nova* **4**, 109–116.

Mercier, J.-C. C. & Nicolas, A. (1975). Textures and Fabrics of Upper-Mantle Peridotites as Illustrated by Xenoliths from Basalts. *Journal of Petrology* **16**, 454–487.

Michibayashi, K. (2004). The Role of Pre-existing Mechanical Anisotropy on Shear Zone Development within Oceanic Mantle Lithosphere: an Example from the Oman Ophiolite. *Journal of Petrology* **45**, 405–414.

Michibayashi, K. & Oohara, T. (2013). Olivine fabric evolution in a hydrated ductile shear zone at the Moho Transition Zone, Oman Ophiolite. *Earth and Planetary Science Letters* **377–378**, 299–310.

Mixon, E. E., Singer, B. S., Jicha, B. R. & Ramirez, A. (2021). Calbuco, a monotonous andesitic high-flux volcano in the Southern Andes, Chile. *Journal of Volcanology and Geothermal Research* **416**, 107279.

Mohorovičić, A. (1910). Earthquake of 8 October 1909 (translation). **Geofizika** 9, 3–55 .

Morgado, E., Morgan, D. J., Harvey, J., Parada, M.-Á., Castruccio, A., Brahm, R., Gutiérrez, F., Georgiev, B. & Hammond, S. J. (2019). Localised heating and intensive magmatic conditions prior to the 22–23 April 2015 Calbuco volcano eruption (Southern Chile). *Bulletin of Volcanology* **81**, 24.

Mouthereau, F., Watts, A. B. & Burov, E. (2013). Structure of orogenic belts controlled by lithosphere age. *Nature Geoscience* **6**, 785–789.

Mouthereau, F. *et al.* (2021). Cenozoic mountain building and topographic evolution in Western Europe: impact of billions of years of lithosphere evolution and plate kinematics. *BSGF - Earth Sciences Bulletin* **192**, 56.

Mundl, A., Ntaflos, T., Ackerman, L., Bizimis, M., Bjerg, E. A. & Hauzenberger, C. A. (2015). Mesoproterozoic and Paleoproterozoic subcontinental lithospheric mantle domains beneath southern Patagonia: Isotopic evidence for its connection to Africa and Antarctica. *Geology* **43**, 39–42.

Mundl, A., Ntaflos, T., Ackerman, L., Bizimis, M., Bjerg, E. A., Wegner, W. & Hauzenberger, C. A. (2016). Geochemical and Os–Hf–Nd–Sr Isotopic Characterization of North Patagonian Mantle Xenoliths: Implications for Extensive Melt Extraction and Percolation Processes. *Journal of Petrology* **57**, 685–715.

Natali, C., Beccaluva, L., Bianchini, G., Ellam, R. M., Savo, A., Siena, F. & Stuart, F. M. (2016). High-MgO lavas associated to CFB as indicators of plume-related thermochemical effects: The case of ultra-titaniferous picrite–basalt from the Northern Ethiopian–Yemeni Plateau. *Gondwana Research* **34**, 29–48.

Navarrete, C., Gianni, G., Encinas, A., Márquez, M., Kamerbeek, Y., Valle, M. & Folguera, A. (2019). Triassic to Middle Jurassic geodynamic evolution of southwestern Gondwana: From a large flat-slab to mantle plume suction in a rollback subduction setting. *Earth-Science Reviews* **194**, 125–159.

Navarrete, C., Gianni, G., Massaferro, G. & Butler, K. (2020). The fate of the Farallon slab beneath Patagonia and its links to Cenozoic intraplate magmatism, marine transgressions and topographic uplift. *Earth-Science Reviews* **210**, 103379.

Nicolas, A., Boudier, F. & Boullier, A. M. (1973). Mechanisms of flow in naturally and experimentally deformed peridotites. *American Journal of Science* **273**, 853–876.

Nicolas, A. & Christensen, N. I. (1987). Formation of anisotropy in upper mantle peridotites: A review. In: Fuchs, K. & Froidevaux, C. (eds) *Geodynamics Series*. Washington, D. C.: American Geophysical Union, 111–123.

Novais-Rodrigues, E. *et al.* (2021). Partial melting and subduction-related metasomatism recorded by geochemical and isotope (He-Ne-Ar-Sr-Nd) compositions of spinel lherzolite xenoliths from Coyhaique, Chilean Patagonia. *Gondwana Research* **98**, 257–276.

Ntaflos, T., Bjerg, E. A., Labudia, C. H. & Kurat, G. (2007). Depleted lithosphere from the mantle wedge beneath Tres Lagos, southern Patagonia, Argentina. *Lithos* **94**, 46–65.

O'Reilly, S. Y. & Griffin, W. L. (1985). A xenolith-derived geotherm for southeastern australia and its geophysical implications. *Tectonophysics* **111**, 41–63.

O'Reilly, S. Y. & Griffin, W. L. (2013). Moho vs crust–mantle boundary: Evolution of an idea. *Tectonophysics* **609**, 535–546.

Oliveros, V. *et al.* (2020). Lithospheric evolution of the Pre- and Early Andean convergent margin, Chile. *Gondwana Research* **80**, 202–227.

Oncken, O. *et al.* (2003). Seismic imaging of a convergent continental margin and plateau in the central Andes (Andean Continental Research Project 1996 (ANCORP'96)): SEISMIC IMAGING OF CENTRAL ANDES. *Journal of Geophysical Research: Solid Earth* **108**.

Oppezzo, C. P. (2016). Petrografía de los xenolitos ultramáficos y de la roca portadora del Cerro Medina, Meseta de Somuncurá, Río Negro. Universidad Nacional de la Pampa.

Oriolo, S., Schulz, B., González, P. D., Bechis, F., Olaizola, E., Krause, J., Renda, E. M. & Vizán, H. (2019). The Late Paleozoic Tectonometamorphic Evolution of Patagonia Revisited: Insights From the Pressure‐Temperature‐Deformation‐Time (P‐T‐D‐t) Path of the Gondwanide Basement of the North Patagonian Cordillera (Argentina). *Tectonics* **38**, 2378–2400.

Oriolo, S. *et al.* (2023). Linking accretionary orogens with continental crustal growth and stabilization: Lessons from Patagonia. *Gondwana Research* **121**, 368–382.

Oyhantçabal, P., Cingolani, C. A., Wemmer, K. & Siegesmund, S. (2018). The Río de la Plata Craton of Argentina and Uruguay. In: Siegesmund, S., Basei, M. A. S., Oyhantçabal, P. & Oriolo, S. (eds) *Geology of Southwest Gondwana*. Cham: Springer International Publishing, 89–105.

Pankhurst, R. J. & Rapela, C. R. (1995). Production of Jurassic rhyolite by anatexis of the lower crust of Patagonia. *Earth and Planetary Science Letters* **134**, 23–36.

Pankhurst, R. J., Leat, P. T., Sruoga, P., Rapela, C. W., Márquez, M., Storey, B. C. & Riley, T. R. (1998). The Chon Aike province of Patagonia and related rocks in West Antarctica: A silicic large igneous province. *Journal of Volcanology and Geothermal Research* **81**, 113–136.

Pankhurst, R. J., Weaver, S. D., Hervé, F. & Larrondo, P. (1999). Mesozoic-Cenozoic evolution of the North Patagonian Batholith in Aysen, southern Chile. *Journal of the Geological Society* **156**, 673–694.

Pankhurst, R. J., Riley, T. R., Fanning, C. M. & Kelley, S. P. (2000a). Episodic Silicic Volcanism in Patagonia and the Antarctic Peninsula: Chronology of Magmatism Associated with the Break-up of Gondwana. *Journal of Petrology* **41**, 605–625.

Pankhurst, R. J., Rapela, C. W. & Fanning, C. M. (2000b). Age and origin of coeval TTG, I- and S-type granites in the Famatinian belt of NW Argentina. *Earth and Environmental Science Transactions of the Royal Society of Edinburgh* **91**, 151–168.

Pankhurst, R. J., Rapela, C. W., Fanning, C. M. & Márquez, M. (2006). Gondwanide continental collision and the origin of Patagonia. *Earth-Science Reviews* **76**, 235–257.

Pankhurst, R. J., Rapela, C. W., López De Luchi, M. G., Rapalini, A. E., Fanning, C. M. & Galindo, C. (2014). The Gondwana connections of northern Patagonia. *Journal of the Geological Society* **171**, 313–328.

Pankhurst, R. J., Hervé, F., Fanning, C. M., Calderón, M., Niemeyer, H., Griem-Klee, S. & Soto, F. (2016). The pre-Mesozoic rocks of northern Chile: U–Pb ages, and Hf and O isotopes. *Earth-Science Reviews* **152**, 88-105.

Park, M. & Jung, H. (2017). Microstructural evolution of the Yugu peridotites in the Gyeonggi Massif, Korea: Implications for olivine fabric transition in mantle shear zones. *Tectonophysics* **709**, 55–68.

Passchier, C. W. & Trouw, R. A. J. (2005). Microtectonics (pp. 1–366). Berlin Heidelberg: Springer. Retrieved from https://link.springer.com/book/10.1007/3-540-29359-0

Paton, C., Woodhead, J. D., Hellstrom, J. C., Hergt, J. M., Greig, A. & Maas, R. (2010). Improved laser ablation U-Pb zircon geochronology through robust downhole fractionation correction: IMPROVED LASER ABLATION U-Pb GEOCHRONOLOGY. *Geochemistry, Geophysics, Geosystems* **11**.

Paton, C., Hellstrom, J., Paul, B., Woodhead, J. & Hergt, J. (2011). Iolite: Freeware for the visualisation and processing of mass spectrometric data. *Journal of Analytical Atomic Spectrometry* **26**, 2508.

Pearson, D. G., Scott, J. M., Liu, J., Schaeffer, A., Wang, L. H., van Hunen, J., Szilas, K., Chacko, T. & Kelemen, P. B. (2021). Deep continental roots and cratons. *Nature* **596**,

199–210.

Péron-Pinvidic, G. & Manatschal, G. (2010). From microcontinents to extensional allochthons: witnesses of how continents rift and break apart? *Petroleum Geoscience* **16**, 189–197.

Peron-Pinvidic, G. (2022). The seismic reflection Moho across the mid-Norwegian continental rifted margin. *Communications Earth & Environment* **3**, 133.

Petrus, J. A. & Kamber, B. S. (2012). VizualAge: A Novel Approach to Laser Ablation ICP-MS U-Pb Geochronology Data Reduction. *Geostandards and Geoanalytical Research* **36**, 247–270.

Pichavant, M., Martel, C., Bourdier, J. & Scaillet, B. (2002). Physical conditions, structure, and dynamics of a zoned magma chamber: Mount Pelée (Martinique, Lesser Antilles Arc). *Journal of Geophysical Research: Solid Earth* **107**.

Pistone, M., Müntener, O., Ziberna, L., Hetényi, G. & Zanetti, A. (2017). Report on the ICDP workshop DIVE (Drilling the Ivrea–Verbano zonE). *Scientific Drilling* **23**, 47–56.

Poupon, Y. (2017). Évolution tectono-thermique et rôle de l'héritage dans les chaînes rétro-arc du bassin de Neuquen. Memoire, University of Toulouse III. p. 54.

Prezzi, C. B., Götze, H.-J. & Schmidt, S. (2009). 3D density model of the Central Andes. *Physics of the Earth and Planetary Interiors* **177**, 217–234.

Puelles, P., Ábalos, B. & Gil Ibarguchi, J. I. (2009). Transposed high-pressure granulite fabrics (Cabo Ortegal, NW Spain): Implications on the scales of deformation localization. *Journal of Structural Geology* **31**, 776–790.

Puziewicz, J., Matusiak-Małek, M., Ntaflos, T., Grégoire, M., Kaczmarek, M.-A., Aulbach, S., Ziobro, M. & Kukuła, A. (2020). Three major types of subcontinental lithospheric mantle beneath the Variscan orogen in Europe. *Lithos* **362–363**, 105467.

Puziewicz, J. *et al.* (2023). The origin and evolution of DMM-like lithospheric mantle beneath continents: Mantle xenoliths from the Oku Volcanic Group in the Cameroon Volcanic Line, West Africa. *Journal of Petrology* egad049.

Ramos, V. A., Escayola, M., Mutti, D. I. & Vujovich, G. I. (2000). Proterozoic-early Paleozoic ophiolites of the Andean basement of southern South America. *Ophiolites and oceanic crust: new insights from field studies and the Ocean Drilling Program*. Geological Society of America.

Ramos, V. A. (2008). Patagonia: A paleozoic continent adrift? *Journal of South American Earth Sciences* **26**, 235–251.

Ramos, V. A. (2008). The Basement of the Central Andes: The Arequipa and Related

Terranes. *Annual Review of Earth and Planetary Sciences* **36**, 289–324.

Ramos, V. A. (2009). Anatomy and global context of the Andes: Main geologic features and the Andean orogenic cycle. *Backbone of the Americas: Shallow Subduction, Plateau Uplift, and Ridge and Terrane Collision*. Geological Society of America.

Ramos, V. A. (2010). The Grenville-age basement of the Andes. *Journal of South American Earth Sciences* **29**, 77–91.

Ramos, V. A., Chemale, F., Naipauer, M. & Pazos, P. J. (2014). A provenance study of the Paleozoic Ventania System (Argentina): Transient complex sources from Western and Eastern Gondwana. *Gondwana Research* **26**, 719–740.

Ramos, V. A., Lovecchio, J. P., Naipauer, M. & Pángaro, F. (2020). The Collision of Patagonia: Geological Facts and Speculative Interpretations. *Ameghiniana* **57**.

Rapalini, A. E. & Astini, R. A. (1998). Paleomagnetic confirmation of the Laurentian origin of the Argentine Precordillera. *Earth and Planetary Science Letters* **155**, 1–14.

Rapalini, A. E., De Luchi, M. L., Tohver, E. & Cawood, P. A. (2013). The South American ancestry of the North Patagonian Massif: geochronological evidence for an autochthonous origin? *Terra Nova* **25**, 337–342.

Rapela, C. W., Pankhurst, R. J., Fanning, C. M. & Hervé, F. (2005). Pacific subduction coeval with the Karoo mantle plume: the Early Jurasssic Subcordilleran belt of northwestern Patagonia. *Geological Society, London, Special Publications* **246**, 217–239.

Rapela, C. W., Pankhurst, R. J., Casquet, C., Fanning, C. M., Baldo, E. G., González-Casado, J. M., Galindo, C. & Dahlquist, J. (2007). The Río de la Plata craton and the assembly of SW Gondwana. *Earth-Science Reviews* **83**, 49–82.

Rapela, C. W., Verdecchia, S. O., Casquet, C., Pankhurst, R. J., Baldo, E. G., Galindo, C., Murra, J. A., Dahlquist, J. A. & Fanning, C. M. (2016). Identifying Laurentian and SW Gondwana sources in the Neoproterozoic to Early Paleozoic metasedimentary rocks of the Sierras Pampeanas: Paleogeographic and tectonic implications. *Gondwana Research* **32**, 193–212.

Rapela, C. W. *et al.* (2018). A review of the Famatinian Ordovician magmatism in southern South America: evidence of lithosphere reworking and continental subduction in the early proto-Andean margin of Gondwana. *Earth-Science Reviews* **187**, 259–285.

Rapela, C. W. & Pankhurst, R. J. (2020). The Continental Crust of Northeastern Patagonia. *Ameghiniana* **57**.

Rapela, C. W., Hervé, F., Pankhurst, R. J., Calderón, M., Fanning, C. M., Quezada, P., Poblete, F., Palape, C. & Reyes, T. (2021). The Devonian accretionary orogen of the North Patagonian cordillera. *Gondwana Research* **96**, 1–21.

Raterron, P., Doukhan, N., Jaoul, O. & Doukhan, J. C. (1994). High temperature deformation of diopside IV: predominance of {110} glide above 1000°C. *Physics of the Earth and Planetary Interiors* **82**, 209–222.

Raterron, P., Chen, J., Li, L., Weidner, D. & Cordier, P. (2007). Pressure-induced slip-system transition in forsterite: Single-crystal rheological properties at mantle pressure and temperature. *American Mineralogist* **92**, 1436–1445.

Renda, E. M., Alvarez, D., Prezzi, C., Oriolo, S. & Vizán, H. (2019). Inherited basement structures and their influence in foreland evolution: A case study in Central Patagonia, Argentina. *Tectonophysics* **772**, 228232.

Richards, J. P. & Villeneuve, M. (2002). Characteristics of late Cenozoic volcanism along the Archibarca lineament from Cerro Llullaillaco to Corrida de Cori, northwest Argentina. *Journal of Volcanology and Geothermal Research* **116**, 161–200.

Rino, S., Kon, Y., Sato, W., Maruyama, S., Santosh, M. & Zhao, D. (2008). The Grenvillian and Pan-African orogens: World's largest orogenies through geologic time, and their implications on the origin of superplume. *Gondwana Research* **14**, 51–72.

Rivalenti, G., Garuti, G., Rossi, A., Siena, F. & Sinigoi, S. (1981). Existence of Different Peridotite Types and of a Layered Igneous Complex in the Ivrea Zone of the Western Alps. *Journal of Petrology* **22**, 127–153.

Rivalenti, G., Mazzucchelli, M., Laurora, A., Ciuffi, S. I. A., Zanetti, A., Vannucci, R. & Cingolani, C. A. (2004). The backarc mantle lithosphere in Patagonia, South America. *Journal of South American Earth Sciences* **17**, 121–152.

Rospabé, M., Benoit, M., Ceuleneer, G., Hodel, F. & Kaczmarek, M.-A. (2018). Extreme geochemical variability through the dunitic transition zone of the Oman ophiolite: Implications for melt/fluid-rock reactions at Moho level beneath oceanic spreading centers. *Geochimica et Cosmochimica Acta* **234**, 1–23.

Ross, J. V. & Nielsen, K. C. (1978). High-temperature flow of wet polycrystalline enstatite. *Tectonophysics* **44**, 233–261.

Rubatto, D., Chakraborty, S. & Dasgupta, S. (2013). Timescales of crustal melting in the Higher Himalayan Crystallines (Sikkim, Eastern Himalaya) inferred from trace element-constrained monazite and zircon chronology. *Contributions to Mineralogy and Petrology* **165**, 349–372.

Rubiano Lorenzoni, G. M. R. (2016). Petrografía de xenolitos del manto alojados en basaltos de la localidad de Prahuaniyeu (Río Negro). Universidad Nacional de la Pampa. p.83.

Rudnick, R. L. & Fountain, D. M. (1995). Nature and composition of the continental crust: A lower crustal perspective. *Reviews of Geophysics* **33**, 267.

Satsukawa, T., Ildefonse, B., Mainprice, D., Morales, L. F. G., Michibayashi, K. & Barou, F. (2013). A database of plagioclase crystal preferred orientations (CPO) and microstructures – implications for CPO origin, strength, symmetry and seismic anisotropy in gabbroic rocks. *Solid Earth* **4**, 511–542.

Sawaguchi, T. & Ishii, K. (2003). Three-dimensional numerical modeling of lattice- and shape-preferred orientation of orthopyroxene porphyroclasts in peridotites. *Journal of Structural Geology* **25**, 1425–1444.

Schilling, M., Conceição, R. V., Mallmann, G., Koester, E., Kawashita, K., Hervé, F., Morata, D. & Motoki, A. (2005). Spinel-facies mantle xenoliths from Cerro Redondo, Argentine Patagonia: Petrographic, geochemical, and isotopic evidence of interaction between xenoliths and host basalt. *Lithos* **82**, 485–502.

Schilling, M. E., Carlson, R. W., Conceição, R. V., Dantas, C., Bertotto, G. W. & Koester, E. (2008). Re–Os isotope constraints on subcontinental lithospheric mantle evolution of southern South America. *Earth and Planetary Science Letters* **268**, 89–101.

Schilling, M. E. *et al.* (2017). The origin of Patagonia revealed by Re-Os systematics of mantle xenoliths. *Precambrian Research* **294**, 15–32.

Serra-Varela, S., Heredia, N., Otamendi, J. & Giacosa, R. (2021). Petrology and geochronology of the San Martín de los Andes batholith: Insights into the Devonian magmatism of the North Patagonian Andes. *Journal of South American Earth Sciences* **109**, 103283.

Shatsky, V. S., Wang, Q., Skuzovatov, S. Yu. & Ragozin, A. L. (2019). The crust-mantle evolution of the Anabar tectonic province in the Siberian Craton: Coupled or decoupled? *Precambrian Research* **332**, 105388.

Siegesmund, S., Layer, P., Dunkl, I., Vollbrecht, A., Steenken, A., Wemmer, K. & Ahrendt, H. (2008). Exhumation and deformation history of the lower crustal section of the Valstrona di Omegna in the Ivrea Zone, southern Alps. *Geological Society, London, Special Publications* **298**, 45–68.

Sielfeld, G., Lange, D. & Cembrano, J. (2019). Intra‐Arc Crustal Seismicity: Seismotectonic Implications for the Southern Andes Volcanic Zone, Chile. *Tectonics* **38**, 552–578.

Skemer, P., Katayama, I., Jiang, Z. & Karato, S. (2005). The misorientation index: Development of a new method for calculating the strength of lattice-preferred orientation. *Tectonophysics* **411**, 157–167.

Skemer, P., Katayama, I. & Karato, S. (2006). Deformation fabrics of the Cima di Gagnone peridotite massif, Central Alps, Switzerland: evidence of deformation at low temperatures in the presence of water. *Contributions to Mineralogy and Petrology* **152**, 43–51.

Sláma, J. *et al.* (2008). Plešovice zircon — A new natural reference material for U–Pb and Hf isotopic microanalysis. *Chemical Geology* **249**, 1–35.

Soret, M., Agard, P., Ildefonse, B., Dubacq, B., Prigent, C. & Rosenberg, C. (2019). Deformation mechanisms in mafic amphibolites and granulites: record from the Semail metamorphic sole during subduction infancy. *Solid Earth* **10**, 1733–1755.

Soto Verdugo, M. F. (2013). Pressure-temperature-time paths of the Limón Verde metamorphic complex, Chile. Universidad de Chile.

Soustelle, V., Tommasi, A., Demouchy, S. & Ionov, D. A. (2010). Deformation and Fluid-Rock Interaction in the Supra-subduction Mantle: Microstructures and Water Contents in Peridotite Xenoliths from the Avacha Volcano, Kamchatka. *Journal of Petrology* **51**, 363–394.

Steinhart, J. S. (1967). Mohorovicic discontinuity. In: International Dictionary of Geophysics (ed. Runcorn S. K.), Pergamon Press.

Stern, C. R., Frey, F. A., Futa, K., Zartman, R. E., Peng, Z. & Kurtis Kyser, T. (1990). Trace-element and Sr, Nd, Pb, and O isotopic composition of Pliocene and Quaternary alkali basalts of the Patagonian Plateau lavas of southernmost South America. *Contributions to Mineralogy and Petrology* **104**, 294–308.

Stern, C. R., Kilian, R., Olker, B., Hauri, E. H. & Kyser, T. K. (1999). Evidence from mantle xenoliths for relatively thin (<100 km) continental lithosphere below the Phanerozoic crust of southernmost South America. *Lithos* **48**, 217-235.

Stern, C. R., Moreno, H., López-Escobar, L., Clavero, J. E., Lara, L. E., Naranjo, J. A., Parada, M. A. & Skewes, M. A. (2007). Chilean volcanoes. In: Moreno, T. & Gibbons, W. (eds) *The Geology of Chile*. The Geological Society of London, 147–178.

Stern, R. J. (2008). Neoproterozoic crustal growth: The solid Earth system during a critical episode of Earth history. *Gondwana Research* **14**, 33–50.

Stern, C. R. (2020). The role of subduction erosion in the generation of Andean and other convergent plate boundary arc magmas, the continental crust and mantle. *Gondwana Research* **88**, 220–249.

Su, B.-X., Wang, J., Liu, X., Bai, Y., Yang, Y.-H., Bao, Z.-A. & Sakyi, P. A. (2020). Mantle and crust interaction scenario at the crust-mantle transition zone: Depicted from inter-layered pyroxenite-granulite xenolith in Hannuoba area, North China Craton. *Physics of the Earth and Planetary Interiors* **309**, 106594.

Suhr, G. (1993). Evaluation of upper mantle microstructures in the Table Mountain massif (Bay of Islands ophiolite). *Journal of Structural Geology* **15**, 1273–1292.

Sun, P., Niu, Y., Guo, P., Duan, M., Wang, X. & Gong, H. (2022). Sublithosphere Mantle

Crystallization and Immiscible Sulfide Melt Segregation in Continental Basalt Magmatism: Evidence from Clinopyroxene Megacrysts in the Cenozoic Basalts of Eastern China. *Journal of Petrology* **63**, egac001.

Tassara, A. & Echaurren, A. (2012). Anatomy of the Andean subduction zone: three-dimensional density model upgraded and compared against global-scale models: Anatomy of the Andean subduction zone. *Geophysical Journal International* **189**, 161–168.

Taufner, R., Viegas, G., Faleiros, F. M., Castellan, P. & Silva, R. (2021). Deformation mechanisms of granulite-facies mafic shear zones from hole U1473A, Atlantis Bank, Southwest Indian Ridge (IODP Expedition 360). *Journal of Structural Geology* **149**, 104380.

Tedonkenfack, S. S. T., Puziewicz, J., Aulbach, S., Ntaflos, T., Kaczmarek, M.-A., Matusiak-Małek, M., Kukuła, A. & Ziobro, M. (2021). Lithospheric mantle refertilization by DMM-derived melts beneath the Cameroon Volcanic Line—a case study of the Befang xenolith suite (Oku Volcanic Group, Cameroon). *Contributions to Mineralogy and Petrology* **176**, 37.

Thomas, W. A. & Astini, R. A. (1996). The Argentine Precordillera: A Traveler from the Ouachita Embayment of North American Laurentia. *Science* **273**, 752–757.

Thorpe, R. S., Francis, P. W. & O'Gallaghan, L. (1984). Relative roles of source composition, fractional crystallization and crustal contamination in the petrogenesis of Andean volcanic rocks. *Philosophical Transactions of the Royal Society of London. Series A, Mathematical and Physical Sciences* **310**, 675–692.

Tommasi, A., Tikoff, B. & Vauchez, A. (1999). Upper mantle tectonics: three-dimensional deformation, olivine crystallographic fabrics and seismic properties. *Earth and Planetary Science Letters* **168**, 173–186.

Tommasi, A., Vauchez, A., Godard, M. & Belley, F. (2006). Deformation and melt transport in a highly depleted peridotite massif from the Canadian Cordillera: Implications to seismic anisotropy above subduction zones. *Earth and Planetary Science Letters* **252**, 245–259.

Toy, V. G., Newman, J., Lamb, W. & Tikoff, B. (2010). The Role of Pyroxenites in Formation of Shear Instabilities in the Mantle: Evidence from an Ultramafic Ultramylonite, Twin Sisters Massif, Washington. *Journal of Petrology* **51**, 55–80.

Trail, D., Bruce Watson, E. & Tailby, N. D. (2012). Ce and Eu anomalies in zircon as proxies for the oxidation state of magmas. *Geochimica et Cosmochimica Acta* **97**, 70–87.

Tubía, J. M., Cuevas, J. & Esteban, J. J. (2013). Localization of deformation and kinematic shift during the hot emplacement of the Ronda peridotites (Betic Cordilleras, southern Spain). *Journal of Structural Geology* **50**, 148–160.

Tullis, T. E., Horowitz, F. G. & Tullis, J. (1991). Flow laws of polyphase aggregates from end‐member flow laws. *Journal of Geophysical Research: Solid Earth* **96**, 8081–8096.

Ulrich, S. & Mainprice, D. (2005). Does cation ordering in omphacite influence development of lattice-preferred orientation? *Journal of Structural Geology* **27**, 419–431.

Upton, B. G. J., Downes, H., Kirstein, L. A., Bonadiman, C., Hill, P. G. & Ntaflos, T. (2011). The lithospheric mantle and lower crust–mantle relationships under Scotland: a xenolithic perspective. *Journal of the Geological Society* **168**, 873–886.

Ureta, G., Németh, K., Aguilera, F. & González, R. (2020). Features That Favor the Prediction of the Emplacement Location of Maar Volcanoes: A Case Study in the Central Andes, Northern Chile. *Geosciences* **10**, 507.

Ureta, G., Németh, K., Aguilera, F., Zimmer, M. & Menzies, A. (2021). A window on mantle-derived magmas within the Central Andes: eruption style transitions at Cerro Overo maar and La Albóndiga lava dome, northern Chile. *Bulletin of Volcanology* **83**, 19.

Uriz, N. J., Cingolani, C. A., Chemale, F., Macambira, M. B. & Armstrong, R. (2011). Isotopic studies on detrital zircons of Silurian–Devonian siliciclastic sequences from Argentinean North Patagonia and Sierra de la Ventana regions: comparative provenance. *International Journal of Earth Sciences* **100**, 571–589.

Valera, G. T. V., Payot, B. D., Arai, S., Takeuchi, M., Ishimaru, S. & Tamura, A. (2019). Petrologic nature of the active subarc crust-mantle boundary: Mixed magmatic-metasomatic processes recorded in xenoliths from Sabtang island, Luzon arc. *Journal of Volcanology and Geothermal Research* **374**, 80–99.

van Achterbergh, E. (2001). Data reduction software for LA-ICP-MS : appendix. *Laser Ablation-ICP-Mass Spectrometry in the Earth Sciences : Principles and Applications,* 239-243.

van der Meijde, M., Julià, J. & Assumpção, M. (2013). Gravity derived Moho for South America. *Tectonophysics* **609**, 456–467.

van der Werf, T., Chatzaras, V., Kriegsman, L. M., Kronenberg, A., Tikoff, B. & Drury, M. R. (2017). Constraints on the rheology of the lower crust in a strike-slip plate boundary: evidence from the San Quintín xenoliths, Baja California, Mexico. *Solid Earth* **8**, 1211–1239.

Vander Auwera, J., Namur, O., Dutrieux, A., Wilkinson, C. M., Ganerød, M., Coumont, V. & Bolle, O. (2019). Mantle Melting and Magmatic Processes Under La Picada Stratovolcano (CSVZ, Chile). *Journal of Petrology* **60**, 907–944.

Vander Auwera, J., Montalbano, S., Namur, O., Bechon, T., Schiano, P., Devidal, J.-L. & Bolle, O. (2021). The petrology of a hazardous volcano: Calbuco (Central Southern Volcanic Zone, Chile). *Contributions to Mineralogy and Petrology* **176**, 46.

Vauchez, A., Dineur, F. & Rudnick, R. (2005). Microstructure, texture and seismic anisotropy of the lithospheric mantle above a mantle plume: Insights from the Labait volcano xenoliths (Tanzania). *Earth and Planetary Science Letters* **232**, 295–314.

Vauchez, A., Tommasi, A. & Mainprice, D. (2012). Faults (shear zones) in the Earth's mantle. *Tectonophysics* **558–559**, 1–27.

Vieira Duarte, J. F., Kaczmarek, M. ‐A., Vonlanthen, P., Putlitz, B. & Müntener, O. (2020). Hydration of a Mantle Shear Zone Beyond Serpentine Stability: A Possible Link to Microseismicity Along Ultraslow Spreading Ridges? *Journal of Geophysical Research: Solid Earth* **125**, e2020JB019509.

Villaseca, C., Downes, H., Pin, C. & Barbero, L. (1999). Nature and Composition of the Lower Continental Crust in Central Spain and the Granulite-Granite Linkage: Inferences from Granulitic Xenoliths. *Journal of Petrology* **40**, 1465–1496.

Viramonte, J. G., Kay, S. M., Becchio, R., Escayola, M. & Novitski, I. (1999). Cretaceous rift related magmatism in central-western South America. *Journal of South American Earth Sciences* **12**, 109–121.

Volkova, G. D., Nosova, A. A., Voznyak, A. A., Sazonova, L. V., Yutkina, E. V., Anosova, M. O., Tikhomirova, Y. S., Kuzmenkova, O. F. & Laptsevich, A. G. (2022). Amphibole-rich xenoliths from Devonian igneous rocks of the Pripyat rift, Southeastern Belarus: a window into cratonic lower-crust–upper-mantle boundary. *Mineralogy and Petrology* **116**, 15–46.

Von Gosen, W. (2009). Stages of Late Palaeozoic deformation and intrusive activity in the western part of the North Patagonian Massif (southern Argentina) and their geotectonic implications. *Geological Magazine* **146**, 48–71.

Wang, G., Thybo, H. & Artemieva, I. M. (2021). No mafic layer in 80 km thick Tibetan crust. *Nature Communications* **12**, 1069.

Wang, Q., Bagdassarov, N. & Ji, S. (2013). The Moho as a transition zone: A revisit from seismic and electrical properties of minerals and rocks. *Tectonophysics* **609**, 395–422.

Wang, Y. F., Zhang, J. F., Jin, Z. M. & Green, H. W. (2012). Mafic granulite rheology: Implications for a weak continental lower crust. *Earth and Planetary Science Letters* **353–354**, 99–107.

Weinberg, R. F., Becchio, R., Farias, P., Suzaño, N. & Sola, A. (2018). Early Paleozoic accretionary orogenies in NW Argentina: Growth of West Gondwana. *Earth-Science Reviews* **187**, 219–247.

Wells, P. R. A. (1977). Pyroxene thermometry in simple and complex systems. *Contributions to Mineralogy and Petrology* **62**, 129–139.

Wenk, H.-R., Janssen, C., Kenkmann, T. & Dresen, G. (2011). Mechanical twinning in quartz: Shock experiments, impact, pseudotachylites and fault breccias. *Tectonophysics* **510**, 69–79.

White, R. W. & Powell, R. (2002). Melt loss and the preservation of granulite facies mineral assemblages: Melt Loss and the Preservation of Granulites. *Journal of Metamorphic Geology* **20**, 621–632.

White, R. W., Powell, R. & Clarke, G. L. (2002). The interpretation of reaction textures in Fe-rich metapelitic granulites of the Musgrave Block, central Australia: constraints from mineral equilibria calculations in the system K2O-FeO-MgO-Al2O3-SiO2-H2O-TiO2-Fe2O3: REACTION TEXTURES, MUSGRAVE BLOCK GRANULITES. *Journal of Metamorphic Geology* **20**, 41–55.

White, R. W., Powell, R., Holland, T. J. B., Johnson, T. E. & Green, E. C. R. (2014). New mineral activity-composition relations for thermodynamic calculations in metapelitic systems. *Journal of Metamorphic Geology* **32**, 261–286.

Wiedenbeck, M. *et al.* (2004). Further Characterisation of the 91500 Zircon Crystal. *Geostandards and Geoanalytical Research* **28**, 9–39.

Wigger, P. J. *et al.* (1994). Variation in the Crustal Structure of the Southern Central Andes Deduced from Seismic Refraction Investigations. In: Reutter, K.-J., Scheuber, E. & Wigger, P. J. (eds) *Tectonics of the Southern Central Andes*. Berlin, Heidelberg: Springer Berlin Heidelberg, 23–48.

Willner, A. P., Gerdes, A., Massonne, H.-J., Schmidt, A., Sudo, M., Thomson, S. N. & Vujovich, G. (2011). The geodynamics of collision of a microplate (Chilenia) in Devonian times deduced by the pressure–temperature–time evolution within part of a collisional belt (Guarguaraz Complex, W-Argentina). *Contributions to Mineralogy and Petrology* **162**, 303–327.

Wörner, G., Mamani, M. & Blum-Oeste, M. (2018). Magmatism in the Central Andes. In: Moreno, T. & Gibbons, W. (eds) *The Geology of Chile*. The Geological Society of London, 237-244.

Xu, Z., Wang, Q., Ji, S., Chen, J., Zeng, L., Yang, J., Chen, F., Liang, F. & Wenk, H.-R. (2006). Petrofabrics and seismic properties of garnet peridotite from the UHP Sulu terrane (China): Implications for olivine deformation mechanism in a cold and dry subducting continental slab. *Tectonophysics* **421**, 111–127.

Yáñez Carrizo, G. & Herrera, O. R. (2019). Crustal dense blocks in the fore-arc and arc region of Chilean ranges and their role in the magma ascent and composition: Breaking paradigms in the Andean metallogeny. *Journal of South American Earth Sciences* **93**, 51–66.

Yu, J.-H., Xu, X., O'Reilly, S. Y., Griffin, W. L. & Zhang, M. (2003). Granulite xenoliths

from Cenozoic Basalts in SE China provide geochemical fingerprints to distinguish lower crust terranes from the North and South China tectonic blocks. *Lithos* **67**, 77–102.

Zack, T., Brumm, R. (1998). Ilmenite/liquid partition coefficients of 26 trace elements determined through ilmenite/clinopyroxene partitioning in garnet pyroxenites (1998). *International Kimberlite Conference Extended Abstracts: 1998*. paper presented at the International Kimberlite Conference. University of Alberta. 986-988.

Zaffarana, C. B. *et al.* (2020). Petrogenetic study of the Lonco Trapial volcanism and its comparison with the Early-Middle Jurassic magmatic units from northern Patagonia. *Journal of South American Earth Sciences* **101**, 102624.

Zaffarana, C. *et al.* (2019). First geochemical and geochronological characterization of Late Cretaceous mesosilicic magmatism in Gastre, Northern Patagonia, and its tectonic relation to other coeval volcanic rocks in the region. *Geological Magazine* **156**, 1285–1294.

Zaffarana, C., Tommasi, A., Vauchez, A. & Grégoire, M. (2014). Microstructures and seismic properties of south Patagonian mantle xenoliths (Gobernador Gregores and Pali Aike). *Tectonophysics* **621**, 175–197.

Zandt, G., Leidig, M., Chmielowski, J., Baumont, D. & Yuan, X. (2003). Seismic Detection and Characterization of the Altiplano-Puna Magma Body, Central Andes. *Pure and Applied Geophysics* **160**, 789–807.

Zeller, M., Reid, S. B., Eberli, G. P., Weger, R. J. & Massaferro, J. L. (2015). Sequence architecture and heterogeneities of a field – Scale Vaca Muerta analog (Neuquén Basin, Argentina) – From outcrop to synthetic seismic. *Marine and Petroleum Geology* **66**, 829–847.

Zhang, J., Green II, H. W., & Bozhilov, K. N. (2006). Rheology of omphacite at high temperature and pressure and significance of its lattice preferred orientations. *Earth and Planetary Science Letters*, ***246***(3-4), 432-443.

Zhang, S. & Karato, S. (1995). Lattice preferred orientation of olivine aggregates deformed in simple shear. *Nature* **375**, 774–777.

Zingg, A., Handy, M. R., Hunziker, J. C. & Schmid, S. M. (1990). Tectonometamorphic history of the Ivrea Zone and its relationship to the crustal evolution of the Southern Alps. *Tectonophysics* **182**, 169–192.

APPENDICES

Electronic Appendix is available on the following link:

https://drive.google.com/drive/folders/1Prc-1lGAksPyfeTEoW6gcmjMP6hM4yZM?usp=sharing

It contains the list of xenolith samples investigated during this PhD with, for each sample, coordinates, mineralogy, thermometers, representative photomicrograph; all new microprobe analysis performed during this PhD; details of MTex output from Electron Bascattered Diffraction data (number of pixels, grains, grain inner boundaries segments, textural indexes…).

Supplementary Material from the Chapter II : Petrology and microstructures of deep crustal rocks from the North Patagonian Massif, given by meta-igneous granulite xenoliths.

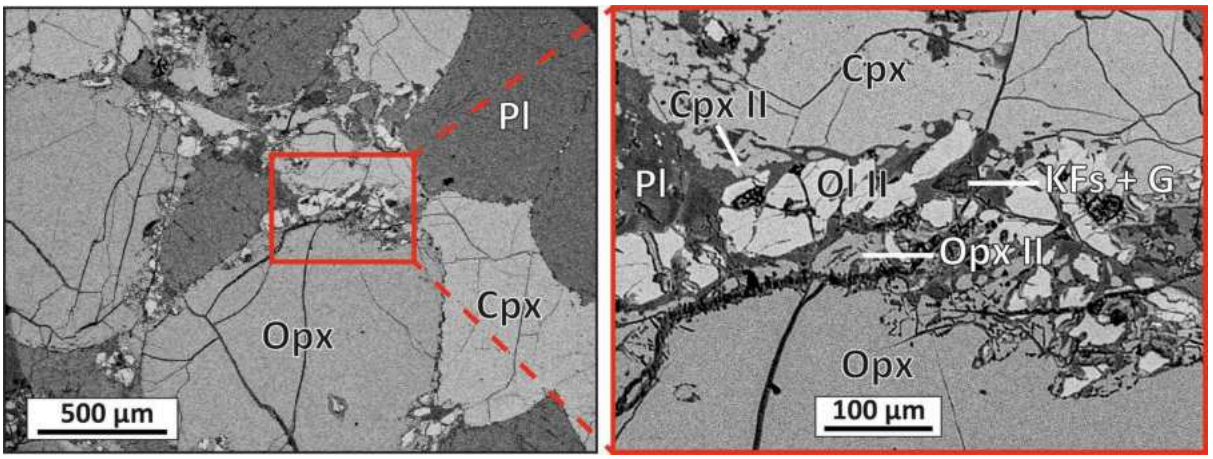


Fig. S1. Backscattered electron image of orthopyroxene reaction in the metagabbronorite CXTRA4. Partial melting during xenolith transport by the host lava produces olivine II, clinopyroxene II, orthopyroxene II, alkaline feldspar and glass, at the expense of the orthopyroxene I tip.

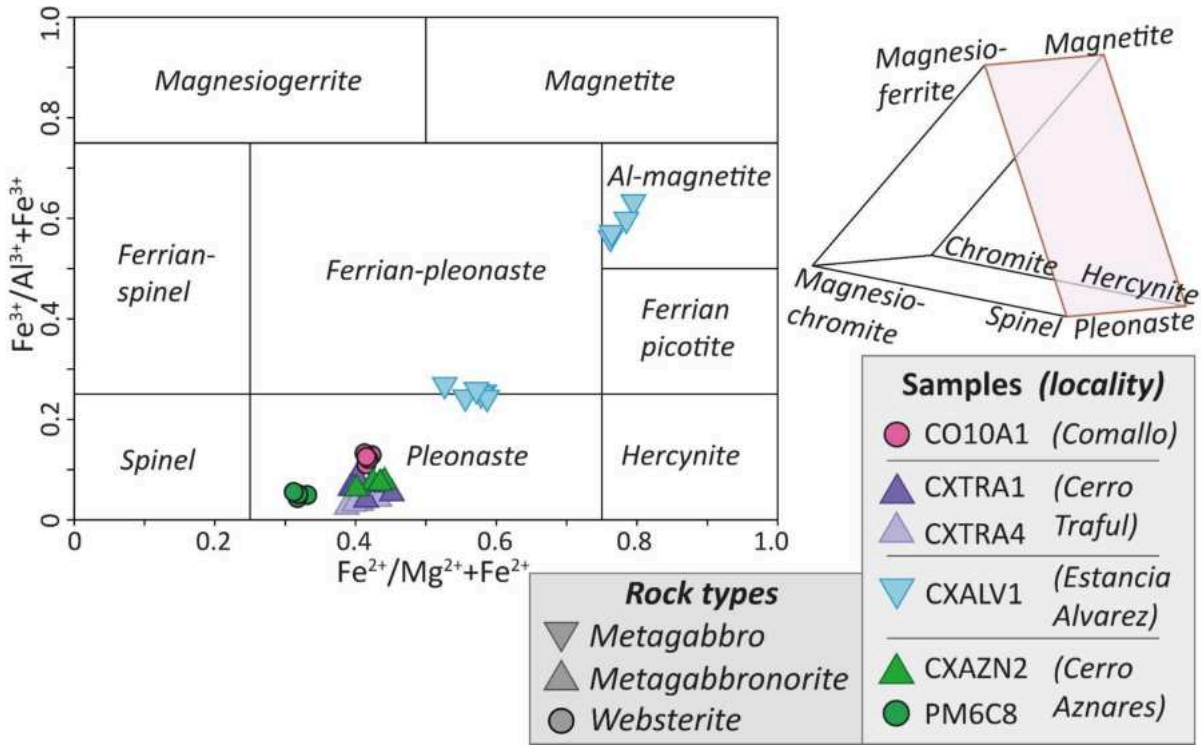


Fig. S2. Compositional diagram $Fe^{2+}/(Mg^{2+} + Fe^{2+})$ vs $Fe^{3+}/(Fe^{3+} + Al^{3+})$ of spinel, which is highlighted on the classification prism of spinel group minerals (Deer *et al.*, 1992).

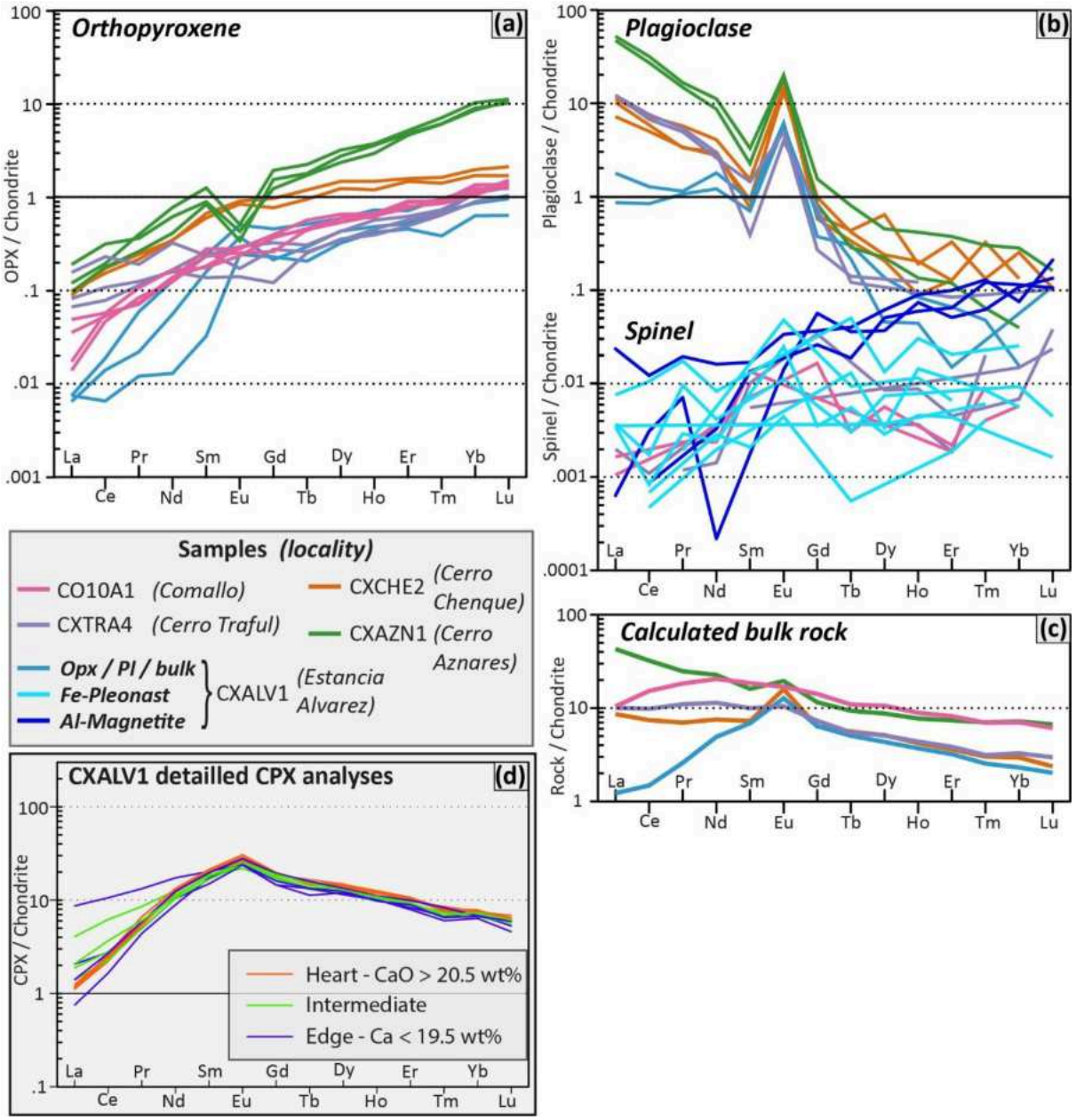


Fig. S3. Rare earth elements patterns of (a) orthopyroxene, (b) plagioclase and spinel, and (c) calculated bulk rock normalised to chondrite (values from McDonough & Sun, 1995). (d) Detailed rare earth elements normalised patterns of clinopyroxene from metagabbro CXALV1. Distinction is made between hart of large grains with high CaO contents and small grains or tips with lower CaO contents.

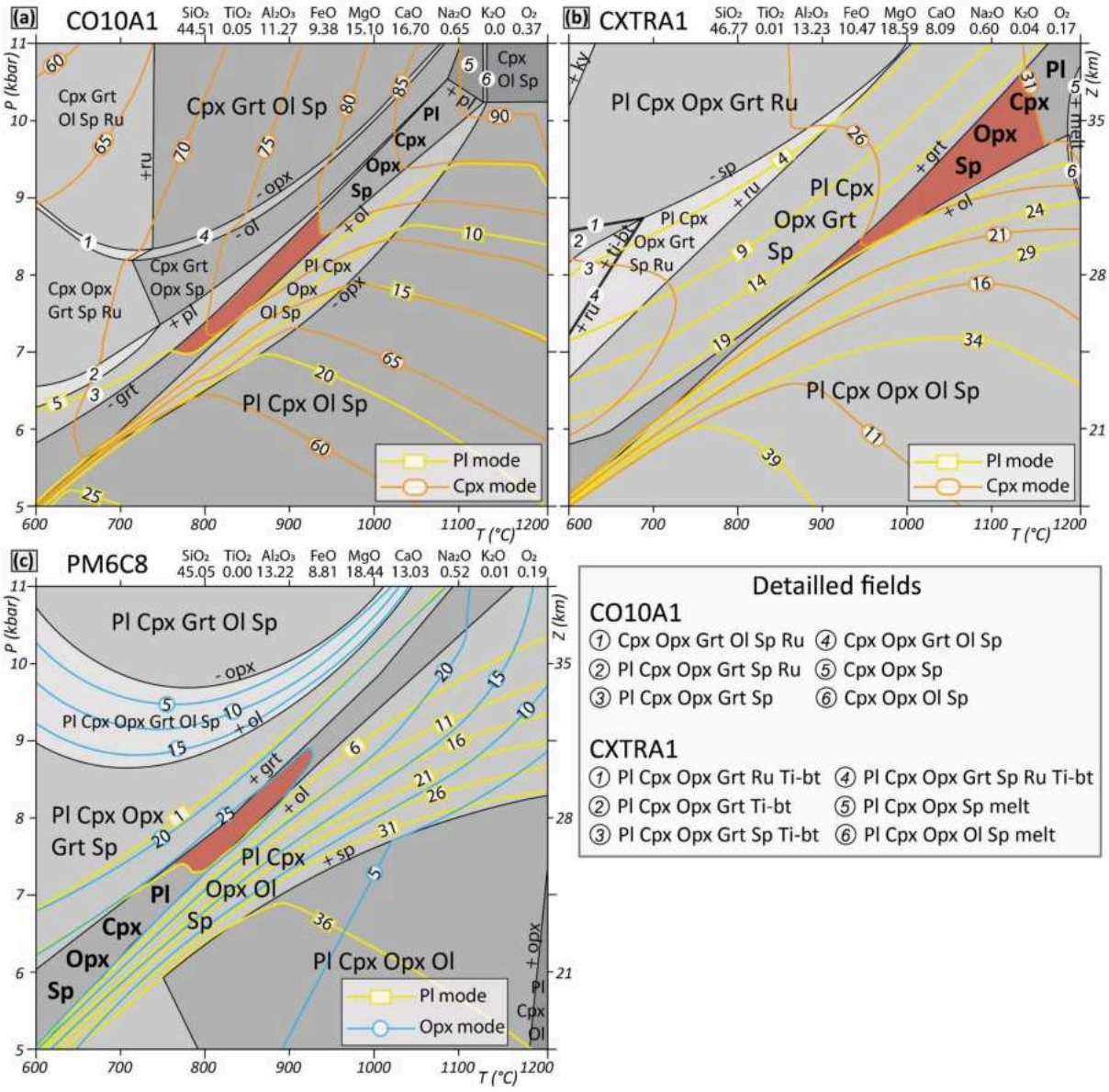


Fig. S4. Detailed pseudosection calculation used for thermobarometry constraining: a) Pyroxenite CO10A1 from Comallo. b) Metagabbronorite CXTRA1 from Cerro Traful. c) Pyroxenite PM6C8 from Cerro Aznares. Modal proportions are only represented for minerals that bring more precision to the P-T domain determination. Most of the samples have a maximum of 1 or 2 vol% olivine resulting from lava interaction, which enters the measurement standard deviation and doesn't influence the calculated bulk. However, CO10A1 has 6 vol% olivine, which significantly affects calculated bulk. Therefore, we put off olivine in the bulk calculation for pseudosection construction.

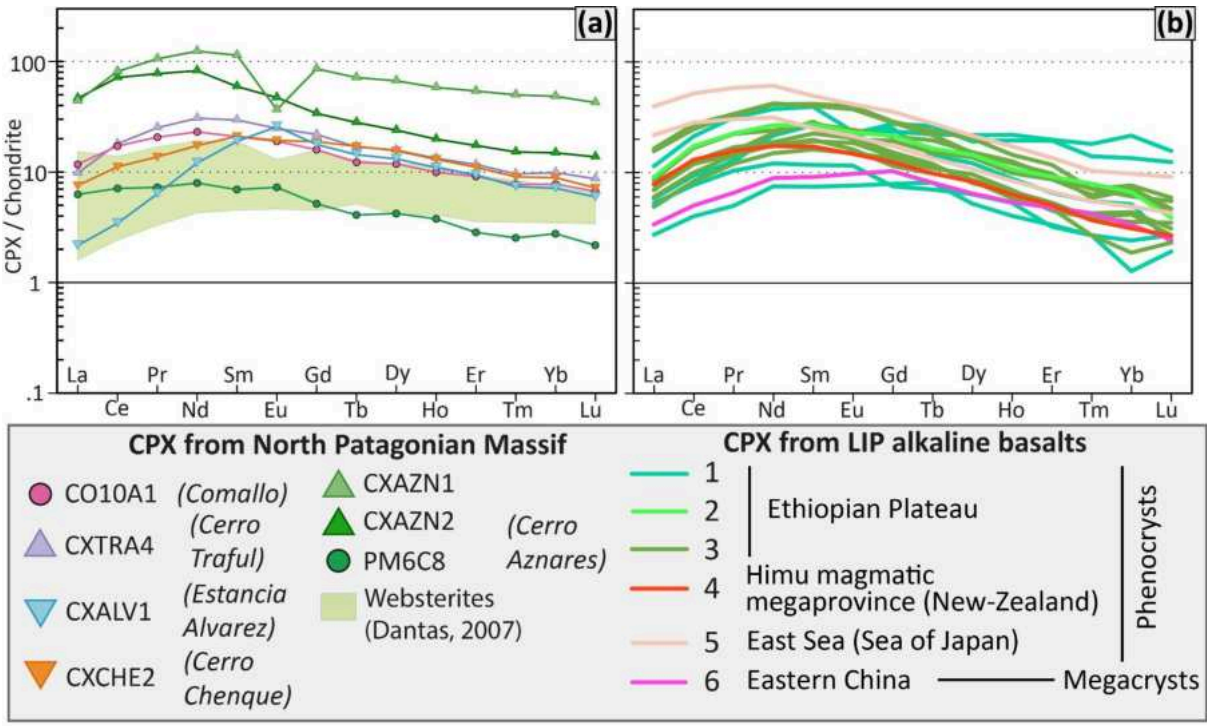


Fig. S5. Comparison between (a) the clinopyroxene REE patterns of the mafic granulites and websterites from the NPM, and (b) REE patterns of clinopyroxene phenocrysts or megacrysts from Large Igneous Province alkaline basalts. 1: Beccaluva *et al.*, 2009; 2: Desta *et al.*, 2014; 3: Natali *et al.*, 2016; 4: McCoy-West *et al.*, 2010; 5: Lee Wonhee *et al.*, 2021; 6: Sun Pu *et al.*, 2022.

Table S1: Mineral major element compositions and microprobe detection limits.

Average clinopyroxene major element compositions. bdl = below detection limits.

	CO10A1	CXTRA1	CXTRA4	CXALV1	CXCHE2	CXCHE3	CXAZN1	CXAZN2	PM6C8
Rock type	*W*	*MGn*	*MGn*	*MG*	*MG*	*MG*	*MGn*	*MGn*	*W*
n	14	10	12	21	7	18	7	5	4
wt%									
SiO2	49.39	48.41	48.40	47.69	49.26	48.10	50.94	49.27	50.69
TiO2	0.71	0.70	0.83	0.92	1.21	1.22	0.35	0.41	0.26
Al2O3	6.54	7.40	7.66	7.88	6.34	6.87	3.22	6.78	6.15
Cr2O3	0.05	0.02	0.04	bdl	0.13	0.02	0.05	0.06	0.03
Fe2O3	3.03	3.27	2.51	3.62	1.44	3.36	1.97	2.90	2.00
FeO	4.42	3.59	4.34	5.81	8.27	4.95	7.80	3.78	3.09
MnO	0.13	0.10	0.13	0.17	0.20	0.18	0.22	0.12	0.10
NiO	bdl	bdl	bdl	bdl	bdl	bdl	bdl	bdl	bdl
MgO	13.74	12.75	12.56	12.05	14.09	12.13	12.74	12.97	13.90
CaO	20.94	22.40	21.86	20.26	17.20	21.81	21.56	22.57	22.60
Na2O	0.81	0.72	0.80	0.95	0.92	0.83	0.61	0.71	0.82
K2O	bdl	bdl	bdl	bdl	bdl	bdl	bdl	bdl	bdl
Total	99.81	99.38	99.15	99.38	99.10	99.50	99.47	99.60	99.68
Cations on the basis of 6 oxygens									
Wo	45.9	49.5	49.1	45.9	38.8	48.56	46.1	49.5	49.4
En	41.9	39.2	39.3	38.0	44.3	37.59	37.9	39.6	42.3
Ferr	12.2	11.3	11.6	16.1	16.9	13.86	16.0	10.9	8.3
Al IV	0.16	0.18	0.17	0.19	0.13	0.17	0.08	0.16	0.13
Al VI	0.13	0.14	0.16	0.16	0.15	0.13	0.07	0.13	0.14
Mg#	77.4	77.7	77.2	70.3	72.4	73.06	70.0	78.0	84.0
σ									
SiO2	*0.279*	*0.365*	*0.480*	*0.256*	*0.544*	0.418	*0.253*	*0.187*	*0.243*
TiO2	*0.064*	*0.068*	*0.115*	*0.076*	*0.246*	0.112	*0.067*	*0.024*	*0.008*
Al2O3	*0.153*	*0.304*	*0.697*	*0.571*	*0.315*	0.376	*0.217*	*0.416*	*0.372*
Cr2O3	*0.010*	*0.004*	*0.011*		*0.011*	0.014	*0.010*	*0.011*	*0.006*
Fe2O3	*0.398*	*0.823*	*1.003*	*0.387*	*0.744*	0.644	*0.535*	*0.136*	*0.407*
FeO	*0.388*	*0.513*	*1.051*	*0.645*	*0.764*	0.747	*0.431*	*0.233*	*0.614*
MnO	*0.033*	*0.045*	*0.035*	*0.035*	*0.042*	0.033	*0.035*	*0.025*	*0.030*
NiO									
MgO	*0.184*	*0.253*	*0.411*	*0.472*	*0.195*	0.309	*0.181*	*0.195*	*0.352*
CaO	*0.154*	*0.318*	*0.482*	*0.763*	*0.585*	0.377	*0.470*	*0.272*	*0.586*
Na2O	*0.032*	*0.162*	*0.152*	*0.239*	*0.040*	0.179	*0.058*	*0.077*	*0.059*
K2O									
Total	*0.242*	*0.261*	*0.304*	*0.349*	*0.388*	0.468	*0.278*	*0.140*	*0.424*
Wo	*0.586*	*0.710*	*1.137*	*1.326*	*1.479*	0.748	*0.960*	*0.463*	*1.516*
En	*0.513*	*0.643*	*1.030*	*0.804*	*0.595*	0.859	*0.379*	*0.351*	*0.791*
Ferr	*0.656*	*0.835*	*1.859*	*1.335*	*1.300*	0.720	*0.748*	*0.452*	*1.068*
Al IV	*0.007*	*0.011*	*0.019*	*0.007*	*0.015*	*0.011*	*0.009*	*0.007*	*0.005*
Al VI	*0.005*	*0.007*	*0.020*	*0.022*	*0.009*	*0.012*	*0.007*	*0.012*	*0.013*
Mg#	*0.012*	*0.016*	*0.034*	*0.022*	*0.016*	0.013	*0.010*	*0.008*	*0.019*

Average orthopyroxene major element compositions.

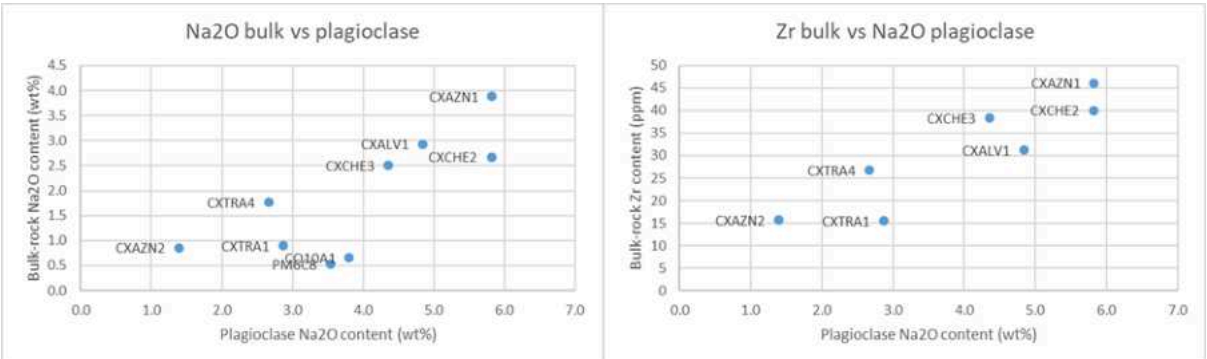
	CO10A1	CXTRA1	CXTRA4	CXALV1	CXCHE2	CXAZN1	CXAZN2	PM6C8
Rock type	*W*	*MGn*	*MGn*	*MG*	*MG*	*MGn*	*MGn*	*W*
n	5	13	8	3	10	4	5	4
wt%								
SiO2	52.40	51.95	51.41	50.85	51.75	51.81	52.10	52.98
TiO2	0.15	0.07	0.12	0.13	0.36	0.06	0.05	0.03
Al2O3	5.05	5.37	6.09	6.12	4.63	2.01	5.29	5.23
Cr2O3	0.04	0.01	0.03	0.00	0.08	0.03	0.03	0.01
Fe2O3	0.85	0.65	0.38	0.84	0.51	0.06	0.57	0.59
FeO	13.00	13.84	14.51	16.03	15.42	23.30	14.48	11.77
MnO	0.21	0.24	0.25	0.32	0.24	0.52	0.23	0.24
NiO	bdl	bdl	bdl	bdl	bdl	bdl	bdl	bdl
MgO	26.98	26.61	25.75	24.36	24.48	21.01	26.38	28.36
CaO	0.88	0.39	0.51	0.64	1.78	0.40	0.40	0.53
Na2O	0.06	bdl	0.04	0.05	0.10	bdl	bdl	bdl
K2O	bdl	bdl	bdl	bdl	bdl	bdl	bdl	bdl
Total	99.66	99.18	99.13	99.37	99.43	99.23	99.57	99.76
Cations on the basis of 6 oxygens								
Wo	1.8	0.8	1.1	1.4	3.7	0.8	0.8	1.1
En	76.4	76.1	74.8	72.0	70.6	61.1	75.2	79.6
Ferr	21.9	23.1	24.2	26.6	25.7	38.1	24.0	19.4
Mg#	77.8	76.7	75.6	73.0	73.3	61.7	76.5	80.0
σ								
SiO2	*0.225*	*0.453*	*0.201*	*0.318*	*0.390*	*0.264*	*0.723*	*0.280*
TiO2	*0.024*	*0.033*	*0.032*	*0.035*	*0.069*	*0.013*	*0.016*	*0.019*
Al2O3	*0.161*	*0.547*	*0.258*	*0.415*	*0.253*	*0.075*	*0.333*	*0.176*
Cr2O3	*0.013*	*0.011*	*0.019*	*0.006*	*0.011*	*0.005*	*0.008*	*0.014*
Fe2O3	*0.355*	*0.458*	*0.233*	*0.325*	*0.276*	*0.085*	*0.485*	*0.498*
FeO	*0.190*	*0.413*	*0.190*	*0.695*	*0.289*	*0.120*	*0.464*	*0.338*
MnO	*0.031*	*0.029*	*0.041*	*0.012*	*0.037*	*0.026*	*0.025*	*0.010*
NiO								
MgO	*0.153*	*0.256*	*0.193*	*0.402*	*0.190*	*0.116*	*0.530*	*0.061*
CaO	*0.071*	*0.174*	*0.320*	*0.055*	*0.323*	*0.049*	*0.085*	*0.123*
Na2O	*0.026*		*0.026*	*0.015*	*0.019*			
K2O								
Total	*0.454*	*0.245*	*0.168*	*0.241*	*0.382*	*0.260*	*0.730*	*0.498*
Wo	*0.147*	*0.364*	*0.670*	*0.109*	*0.654*	*0.103*	*0.184*	*0.246*
En	*0.378*	*0.610*	*0.541*	*1.151*	*0.739*	*0.168*	*0.766*	*0.572*
Ferr	*0.294*	*0.550*	*0.264*	*1.129*	*0.423*	*0.217*	*0.727*	*0.449*
Mg#	*0.314*	*0.547*	*0.205*	*1.150*	*0.454*	*0.195*	*0.738*	*0.470*

Average plagioclase major element compositions.

Plagioclase	**CO10A1**	**CXTRA1**	**CXTRA4**	**CXALV1**	**CXCHE2**	**CXCHE3**	**CXAZN1**	**CXAZN2**	**PM6C8**
Rock type	*W*	*MGn*	*MGn*	*MG*	*MG*	*MG*	*MGn*	*MGn*	*W*
n	1	11	11	13	11	14	3	3	4
wt%									
SiO2	51.22	49.12	48.58	53.50	55.65	52.52	57.03	45.73	51.08
TiO2	0.11	bdl	bdl	bdl	0.05	bdl	bdl	bdl	bdl
Al2O3	30.04	31.54	31.91	28.55	27.11	29.47	26.71	34.05	30.65
Cr2O3	bdl	bdl	bdl	bdl	bdl	bdl	bdl	bdl	bdl
FeO	1.07	0.19	0.22	0.36	0.37	0.37	0.14	0.14	0.17
MnO	bdl	bdl	bdl	bdl	bdl	bdl	bdl	bdl	bdl
MgO	bdl	0.05	0.04	0.06	0.03	0.03	0.03	0.04	0.03
CaO	13.63	14.92	15.58	11.63	9.86	12.55	9.12	17.71	13.41
Na2O	3.80	2.87	2.67	4.84	5.82	4.36	5.83	1.39	3.54
K2O	0.20	0.21	0.14	0.37	0.63	0.29	0.72	0.04	0.21
BaO	0.00	0.07	0.00	0.00	0.00	0.01	0.00	0.00	0.00
Total	100.29	99.03	99.18	99.37	99.57	99.64	99.59	99.11	99.09
Cations on the basis of 8 oxygens									
An	65.7	73.3	75.7	55.8	46.6	60.4	44.4	87.4	66.8
Ab	33.1	25.5	23.5	42.0	49.8	37.9	51.4	12.4	31.9
Or	1.1	1.2	0.8	2.1	3.5	1.7	4.2	0.2	1.2
σ									
SiO2		*1.371*	*0.682*	*1.102*	*0.855*	*0.915*	*0.235*	*1.040*	*0.148*
TiO2					*0.039*				
Al2O3		*0.934*	*0.557*	*0.638*	*0.600*	*0.468*	*0.146*	*0.087*	*0.035*
Cr2O3									
FeO		*0.058*	*0.165*	*0.192*	*0.131*	*0.122*	*0.100*	*0.050*	*0.035*
MnO									
MgO		*0.015*	*0.026*	*0.126*	*0.018*	*0.013*	*0.006*	*0.010*	*0.007*
CaO		*1.157*	*0.510*	*0.793*	*0.677*	*0.716*	*0.300*	*0.228*	*0.007*
Na2O		*0.621*	*0.281*	*0.450*	*0.272*	*0.406*	*0.119*	*0.055*	*0.042*
K2O		*0.101*	*0.061*	*0.075*	*0.122*	*0.048*	*0.055*	*0.015*	*0.021*
BaO		*0.083*	*0.000*	*0.000*	*0.006*	*0.014*	*0.000*	*0.000*	*0.000*
Total		*0.172*	*0.228*	*0.196*	*0.406*	*0.209*	*0.137*	*0.091*	*0.078*
An		*5.919*	*2.630*	*3.951*	*2.985*	*3.580*	*1.358*	*0.543*	*0.226*
Ab		*5.435*	*2.401*	*3.728*	*2.453*	*3.428*	*1.139*	*0.559*	*0.351*
Or		*0.584*	*0.346*	*0.427*	*0.700*	*0.278*	*0.304*	*0.090*	*0.125*

Bulk-rock Zr and Na2O contents and comparison with Na2O contents of plagioclase. * correspond to calculated bulk rock compositions.

Bulk-rock	***CO10A1****	**CXTRA1**	**CXTRA4**	**CXALV1**	**CXCHE2**	**CXCHE3**	**CXAZN1**	**CXAZN2**	***PM6C8****
Na2O (wt%)	*0.66*	0.90	1.76	2.93	2.67	2.50	3.88	0.86	*0.53*
Zr (ppm)		15.5	26.7	31.2	40	38.3	46.1	15.7	



Average spinel-group major element compositions. Fe_2O_3 and FeO contents were calculated with stoichiometry using EMG 8.0 software from Ferracutti *et al.* (2015), as well as cation proportions.

Pleonaste	**CO10A1**	**CXTRA1**	**CXTRA4**	**CXAZN2**	**PM6C8**	**Fe-pleonaste**	**CXALV1**	**Al-magnetite**	**CXALV1**
Rock type	*W*	*Mgn*	*MGn*	*MGn*	*W*		*MG*		*MG*
n	5	7	5	4	4		6		4
wt%									
SiO2	0.05	bdl	bdl	0.04	bdl	SiO2	0.09	SiO2	0.08
TiO2	0.50	0.15	0.09	0.04	bdl	TiO2	1.60	TiO2	6.77
Al2O3	52.78	58.53	60.43	57.49	61.74	Al2O3	42.10	Al2O3	17.30
Cr2O3	1.38	0.29	0.74	0.87	0.30	Cr2O3	0.10	Cr2O3	0.14
Fe2O3	11.64	6.82	3.84	7.54	5.06	Fe2O3	21.11	Fe2O3	37.34
FeO	18.17	18.37	18.07	18.78	14.61	FeO	23.82	FeO	31.87
MnO	0.13	0.15	0.13	0.13	0.11	MnO	0.20	MnO	0.29
NiO	0.36	0.23	0.17	0.12	0.12	NiO	0.02	NiO	0.04
MgO	14.25	14.56	14.82	14.23	17.42	MgO	10.21	MgO	5.14
Total	99.29	99.15	98.36	99.29	99.44	Total	99.28	Total	98.98
Mg#	58.3	58.5	59.4	57.5	68.0	Mg#	43.3	Mg#	22.3
Cr#	1.7	0.3	0.8	1.0	0.3	Cr#	0.2	Cr#	0.5
σ						*σ*		*σ*	
SiO2	*0.019*			*0.041*		*SiO2*	*0.032*	*SiO2*	*0.017*
TiO2	*0.036*	*0.098*	*0.064*	*0.033*		*TiO2*	*0.170*	*TiO2*	*0.643*
Al2O3	*0.643*	*1.068*	*0.729*	*0.511*	*0.386*	*Al2O3*	*0.429*	*Al2O3*	*1.798*
Cr2O3	*0.169*	*0.095*	*0.015*	*0.104*	*0.027*	*Cr2O3*	*0.039*	*Cr2O3*	*0.044*
Fe2O3	*0.778*	*1.357*	*0.541*	*0.624*	*0.510*	*Fe2O3*	*0.968*	*Fe2O3*	*1.136*
FeO	*0.197*	*0.879*	*0.554*	*0.667*	*0.396*	*FeO*	*0.892*	*FeO*	*0.791*
MnO	*0.028*	*0.034*	*0.025*	*0.034*	*0.020*	*MnO*	*0.024*	*MnO*	*0.040*
NiO	*0.050*	*0.045*	*0.051*	*0.022*	*0.043*	*NiO*	*0.013*	*NiO*	*0.042*
MgO	*0.107*	*0.637*	*0.593*	*0.524*	*0.177*	*MgO*	*0.560*	*MgO*	*0.359*
Total	*0.256*	*0.325*	*0.339*	*0.226*	*0.575*	*Total*	*0.563*	*Total*	*0.116*
Mg#	*0.408*	*2.197*	*1.713*	*1.757*	*0.798*	*Mg#*	*2.256*	*Mg#*	*1.605*
Cr#	*0.220*	*0.108*	*0.018*	*0.118*	*0.028*	*Cr#*	*0.061*	*Cr#*	*0.195*

Average olivine and ilmenite major element compositions.

Olivine	**CO10A1**	**CXTRA1**	**CXTRA4**	**CXCHE2**	**CXCHE3**	**CXAZN1**	**Ilmenite**	**CXAZN1**
Rock type	*W*	*MGn*	*MGn*	*MG*	*MG*	*MGn*		*MGn*
n	1	4	8	9	8	*3*		4
wt%								
SiO2	39.25	37.66	38.18	37.47	36.19	36.21	SiO2	0.01
TiO2	0.04	bdl	bdl	0.03	0.03	0.05	TiO2	50.91
Al2O3	bdl	bdl	bdl	bdl	bdl	bdl	Al2O3	0.21
Cr2O3	bdl	bdl	bdl	bdl	bdl	bdl	Fe2O3	5.38
FeO	19.74	25.61	22.91	25.98	33.46	32.92	FeO	37.33
MnO	0.24	0.32	0.32	0.38	0.45	0.51	MnO	0.42
MgO	40.70	35.57	37.62	35.05	28.85	29.18	MgO	4.48
CaO	0.27	0.16	0.18	0.16	0.33	0.32	CaO	0.06
Na2O	bdl	bdl	bdl	bdl	bdl	bdl		
K2O	bdl	bdl	bdl	bdl	bdl	bdl		
NiO	0.22	0.11	bdl	bdl	bdl	bdl		
Total	100.49	99.47	99.34	99.21	99.37	99.30	Total	98.78
Cations on the basis of 4 oxygens							6 oxygens	
Fo	78.61	71.22	74.53	70.62	60.51	61.24	Mg#	0.18
σ							*σ*	
SiO2		*0.120*	*0.222*	*0.234*	*0.583*	*0.257*	*SiO2*	*0.020*
TiO2				*0.023*	*0.026*	*0.052*	*TiO2*	*0.242*
Al2O3							*Al2O3*	*0.126*
Cr2O3							*Fe2O3*	*0.952*
FeO		*1.534*	*1.080*	*1.379*	*2.979*	*0.522*	*FeO*	*0.523*
MnO		*0.024*	*0.028*	*0.024*	*0.085*	*0.021*	*MnO*	*0.024*
MgO		*1.342*	*1.052*	*1.161*	*2.617*	*0.422*	*MgO*	*0.217*
CaO		*0.031*	*0.050*	*0.024*	*0.104*	*0.053*	*CaO*	*0.058*
Na2O								
K2O								
NiO		*0.050*						
Total		*0.067*	*0.354*	*0.392*	*0.338*	*0.325*	*Total*	*0.459*
Fo		*1.999*	*1.417*	*1.782*	*4.211*	*0.709*	*Mg#*	*0.009*

Microprobe detections limits

Detection Limit	Si	Ti	Al	Cr	Fe	Mn	Mg	Ca	Na	K	Ni
ppm											
Clinopyroxene	450	300	400	300	900	850	350	700	500	550	900
Orthopyroxene	450	300	400	250	950	850	400	650	550	600	900
Feldspar	450	300	400	250	850	800	300	650	550	600	900
Spinel	450	300	450	300	1050	850	400	600	700	550	1000
Titanomagnetite	450	350	450	300	1100	850	450	600	700	550	1050
Olivine	450	300	400	250	1000	850	400	650	500	550	950
Ilmenite	450	400	450	300	1100	900	450	600	700	550	1050

Supplementary Table S2: Plagioclase, orthopyroxene, spinel and calculated whole rock trace element compositions. Mineral trace element compositions were obtained by LA-ICP-MS analyses using the same conditions as for clinopyroxene trace element analysis. The calculated bulk rock was computed based on mineral modal compositions obtained by Electron backscatter diffraction data and mineral trace elements composition. n indicates the number of analyses for each sample. bdl = below detection limits.

	Plagioclase				Orthopyroxene						Spinel			Whole Rock				
	CXTRA4	CXALV1	CXCHE2	CXAZN1	CO10A1	CXTRA4	CXALV1	CXCHE2	CXAZN1	CO10A1	CXTRA4	CXALV1 Al-Mag	CXALV1 Fe-Ple	CO10A1	CXTRA4	CXALV1	CXCHE2	CXAZN1
n	2	2	3	2	3	3	3	3	3	2	3	3	7					
ppm																		
Sc	0.789	1.154	4.140	1.554	18.675	22.483	19.290	20.757	26.823	0.657	1.484	10.063	0.985	60.571	32.062	24.616	19.790	20.928
Ti	59.640	215.435	957.210	119.225	859.008	777.817	883.993	2161.173	595.350	2712.435	356.443	36858.413	6398.714	5248.886	2042.845	3276.955	3701.212	469.058
V	0.137	0.850	2.887	1.098	85.000	97.107	126.333	153.493	109.847	528.380	356.000	2735.790	888.844	343.652	104.031	200.118	126.398	64.536
Co	0.165	0.101	0.369	0.175	74.980	60.267	52.317	80.343	81.253	230.820	326.787	143.627	133.313	94.347	17.975	16.638	22.645	16.237
Rb	bdl	1.2140	3.4867	1.4955	0.0163	0.0040	bdl	bdl	0.0293	0.0392	0.0225	0.0123	0.0196	0.0102	0.0047	0.8612	2.2872	1.1387
Sr	1729.455	1885.455	1493.717	1128.045	0.314	0.252	0.194	2.041	0.285	0.0077	0.0059	0.0867	0.0239	174.629	993.602	1199.532	983.102	849.188
Y	0.08750	0.14050	0.34833	0.37300	0.91900	0.62600	0.71533	2.35333	5.23000	0.00360	0.00400	0.05313	0.00371	12.00674	5.86546	4.89056	5.73937	10.89341
Zr	bdl	bdl	0.64433	1.82000	1.95225	2.12167	0.12400	3.44667	5.23333	0.05575	0.18473	6.23000	0.09967	26.76231	14.07724	0.81786	10.75019	16.32721
Nb	0.00335	0.00375	0.20150	0.27195	0.00139	0.00128	0.02050	0.04023	0.01654	0.01410	0.00830	3.42333	0.14494	0.03382	0.02458	0.19964	0.27422	0.22638
Ba	157.385	334.180	215.117	145.195	0.029	0.040	0.007	0.071	0.009	bdl	0.003	0.020	0.011	0.003	88.812	207.903	140.025	108.884
La	2.91500	0.31650	2.28667	11.88000	0.00685	0.02407	0.00169	0.06807	0.03210	bdl	bdl	0.00288	0.00109	2.46901	2.38624	0.28984	2.04255	10.17146
Ce	4.42500	0.65500	3.74000	18.27500	0.03280	0.08507	0.00804	0.25433	0.14033	bdl	0.00067	0.00331	0.00176	9.36441	6.01941	0.90827	4.55414	19.77031
Pr	0.48450	0.10350	0.38867	1.47500	0.00780	0.01327	0.00289	0.04993	0.03163	bdl	bdl	0.00124	0.00074	1.70260	1.01886	0.24037	0.64867	2.30272
Nd	1.28500	0.69300	1.51667	4.57500	0.06408	0.09890	0.02970	0.33933	0.27467	0.00131	0.00116	0.00300	0.00180	9.36819	5.20049	2.24561	3.44842	10.34920
Sm	0.13700	0.12150	0.15933	0.41550	0.03223	0.03123	0.02123	0.15657	0.14733	0.00153	0.00077	0.00225	bdl	2.74439	1.47487	1.01721	1.07358	2.37771
Eu	0.25300	0.33450	0.85567	1.12500	0.01490	0.01140	0.02100	0.07020	0.02400	bdl	bdl	0.00135	0.00125	0.94958	0.58930	0.71775	0.89472	1.09718
Gd	0.10400	0.10100	0.14667	0.23850	0.07023	0.04787	0.05963	0.28333	0.31333	0.00330	0.00680	0.00825	0.00070	2.82005	1.45289	1.27279	1.26531	2.29493
Tb	0.00475	0.00940	0.01440	0.01980	0.01733	0.00987	0.01221	0.05400	0.06923	bdl	0.00000	0.00114	bdl	0.39409	0.19809	0.18234	0.20233	0.33788
Dy	bdl	0.02245	0.08967	0.08355	0.14605	0.09250	0.11060	0.43500	0.68100	0.00139	0.00210	0.01227	0.00152	2.60323	1.25052	1.06647	1.25918	2.15039
Ho	0.00670	0.00351	0.00887	0.01515	0.03523	0.02573	0.02970	0.09180	0.18700	bdl	bdl	0.00407	0.00084	0.48634	0.23854	0.20221	0.22944	0.42223
Er	0.01350	0.00650	0.03123	0.03975	0.13350	0.08987	0.09033	0.28233	0.77833	bdl	0.00051	0.01153	0.00134	1.31128	0.61446	0.51351	0.57826	1.18212
Tm	bdl	0.00118	0.00570	0.00455	0.02250	0.01690	0.01680	0.04267	0.15867	bdl	0.00050	0.00258	bdl	0.17214	0.07754	0.06280	0.07450	0.17379
Yb	bdl	0.00250	0.03125	0.02605	0.19300	0.16667	0.14033	0.30400	1.49667	0.00093	0.00055	0.01607	0.00217	1.13371	0.52686	0.37169	0.47485	1.16024
Lu	0.00250	0.00270	0.00260	0.00400	0.03405	0.03047	0.02353	0.04803	0.26300	bdl	bdl	0.00371	bdl	0.15013	0.07296	0.04978	0.05836	0.16412
Hf	bdl	0.00130	0.03230	0.05555	0.06785	0.10667	0.02517	0.14737	0.22400	0.00189	0.00953	0.17167	0.00491	0.97368	0.58914	0.13692	0.44410	0.60094
Ta	bdl	0.00200	0.02340	0.02100	0.00030	0.00055	0.00131	0.00351	0.00240	0.00040	0.00055	0.12170	0.00762	0.01782	0.00219	0.00682	0.03159	0.01908
Th	bdl	0.00140	0.01363	0.00684	0.00045	0.00166	0.00094	0.00222	0.00181	0.00004	0.00011	0.00055	0.00023	0.04185	0.01158	0.01271	0.01816	0.02421
U	0.00064	0.00050	0.00307	0.00255	0.00046	0.00086	0.00071	0.00073	0.00071	0.00007	0.00004	0.00267	0.00020	0.00702	0.00224	0.00673	0.00505	0.00304

APPENDICE SIII

Table SIII.1: Microprobe detection limits.

Detection Limit	Si	Ti	Al	Cr	Fe	Mn	Mg	Ca	Na	K	Ni	F	Cl	Ba
ppm														
Clinopyroxene	450	300	400	300	900	850	350	700	500	550	900			
Orthopyroxene	450	300	400	250	950	850	400	650	550	600	900			
Feldspath	450	300	400	250	850	800	300	650	550	600	900			
Amphibole	600	1300	600	400	1300	1250	550	1000	1000	900	1300	7000	350	1100
Olivine	450	300	400	250	1000	850	400	650	500	550	950			
Spinel	450	300	450	300	1050	850	400	600	700	550	1000			
Titanomagnetite	450	350	450	300	1100	850	450	600	700	550	1050			

APPENDICES SIV.

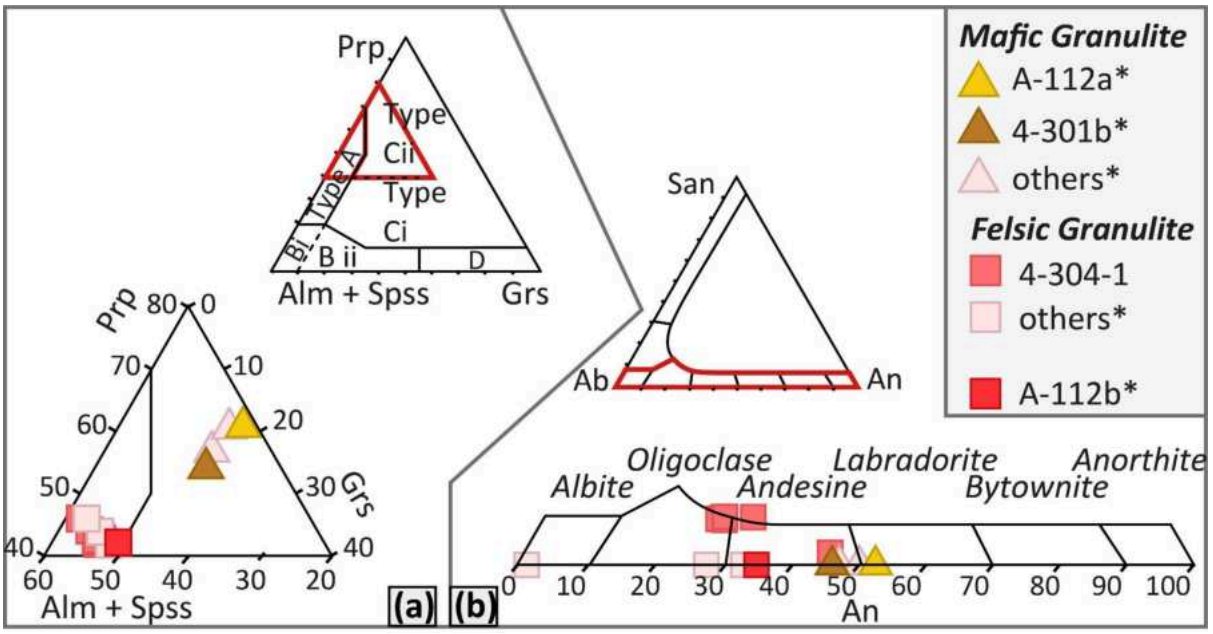


Fig. SIV.1: Major element diagrams of garnet and plagioclase. (a) Detailed pyrope-Almandin+Spessartine-Grossulaire ternary plot of garnet. (b) Detailed orthose-albite-anorthite ternary plot of feldspath. Garnet fields from Mange & Morton (2007).

Type A garnet compositional field corresponds to garnet from metasedimentary or peraluminous granite. Type Cii corresponds to garnet from magmatic mafic rocks and pyroxenites. As observed in (f), felsic granulites range in the Type A compositional fields and mafic granulites in the Type Cii. Despite it provides qualitative information about the protolith of the granulites, i.e. magmatic for the mafic granulite, rather metasedimentary for felsic ones, this classification is made for detrital garnet provenance study and is to be taken with caution.

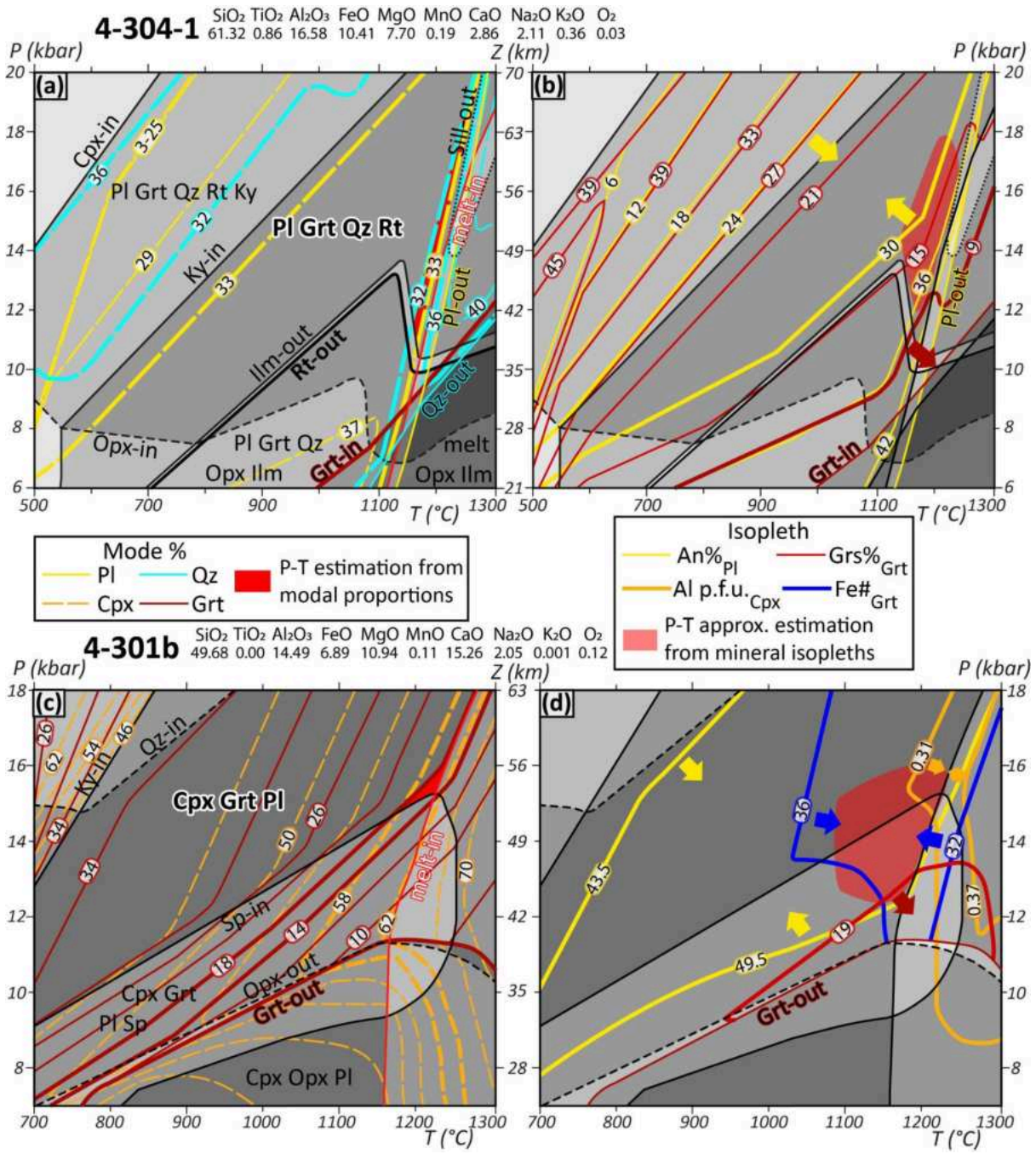


Fig. SIV.2. Isochemical phase diagrams computed from samples 4-304-1 and 4-301b compositions in dry conditions and associated pressure and temperature estimations. (a) Felsic granulite sample 4-304-1 P-T assemblage domains, modal proportions, and (b) associated isopleths. (c) Mafic granulite sample 4-301b P-T assemblage domains, modal proportions, and (d) associated isopleths. For sample 4-304-1, Garnet %modal and Fe# are not drawn, as for Plagioclase %modal and Clinopyroxene Mg# for sample 4-301b, because they do not provide more precision to P-T stability field estimations.

Both mafic and felsic granulites yield wide stable assemblage fields compatible with their observed stable assemblages. However, their modal proportions and compositional isopleths yield P-T conditions of ca. 1100-1200°C, 12-18 kbar. Those conditions are

preliminary but both lithologies display stable chemical composition close to the dry-solidus. P-T stability field estimations for the mafic granulite are the same rather pseudosection is calculated in dry or wet (H_2O=0.1 wt%) conditions, thus wet-conditions pseudosection is not represented.

Such temperatures are extremely high for lower crust conditions, especially if felsic granulite carried hydrous phases before dehydration melting. However, the possibility that felsic granulite was already dry is presented here, because metamorphic zircon growth is not direct proof of a partial melting event. Indeed, metamorphic zircon, despite their low number, were preferentially within the kelyphitised garnet rims, which may indicate that zircon grew during (U)HT event at the expense of garnet without necessarily involving liquid. Nevertheless, pressure over 12 kbar would imply a Cretaceous Moho over 42 km which is unlikely in the region. Furthermore, such conditions set felsic granulites in the sillimanite stability field which would require an anticlockwise path to be equilibrated in the kyanite stability field. Those observations are at the moment conflicting and extensive pseudosection work needs to be done on those granulites.

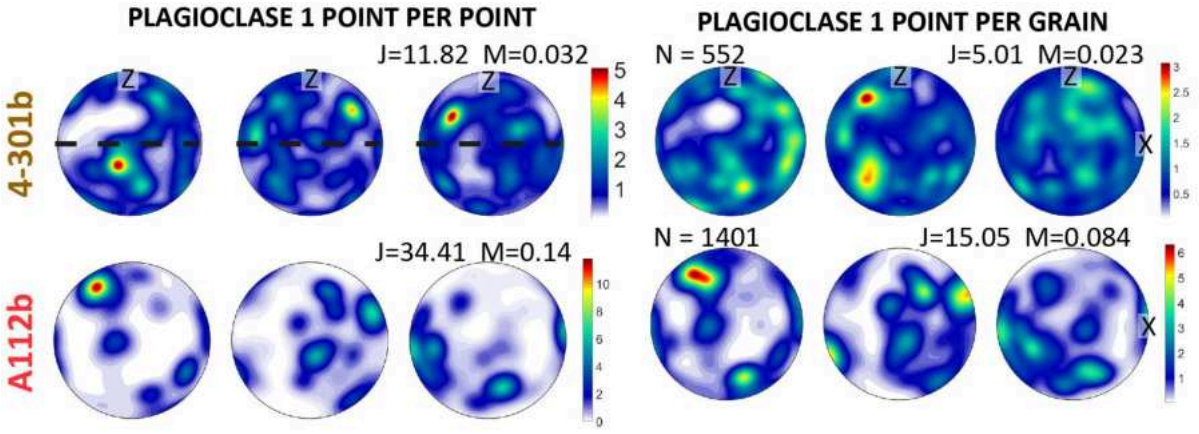


Fig. SIV.3. (a) Unrotated crystallographic preferred orientation of plagioclase from mafic granulite 4-301b and felsic granulite A112b, measured either with 1 point per point (all the available data) or with 1 point per grain. The rainbow scale represents the mud (multiply uniform density).

Both 1 point per point CPO display high textural index values (J-index and mud, to a lesser extent the M-index) which decrease using the 1 point per grain sampling method. Although the sample A-112b preserves its CPO using the 1 point per grain sampling method, the 4-301b displays a different CPO and the concentration point of the 1 point per point CPO is missing. Therefore, those strong concentration points are interpreted to come from a large plagioclase grain which has been oversampled.

Table SIV.1: Indexed (with EBSD) modal compositions of the four analysed samples and corrected modal compositions for the two samples used for equilibrium phase modelling. Q: quartz; Pl: plagioclase; Grt: garnet; Cpx: clinopyroxene; Rt: rutile.

Plagioclase in mafic granulites 4-301b and A-62 was indexed with an anorthite-indexation program using the Aztec software, although their andesine compositions (An_{50-45}). Consequently, the indexing was not accurate. The same mistake was initially made with the felsic granulite 4-304-1 (An_{31-26}), but a second EBSD analysis with the correct indexation program was performed. In the second analysis, 26.4 vol.% more plagioclase was indexed, and this value was used to correct plagioclase modal composition of mafic granulite 4-301b. Additionally, the listed corrections take into account that only 3.09 vol.% garnets were indexed, based on optical microscope and EBSD phase maps observations. The chosen densities used for bulk-rock calculations are indicated and correspond to the expected densities in the granulite facies, calculated using Perple_X 7.0.0 software and conditions specified in section V.3.2.

Group	4-304-1		A112b	4-301b		A62	
Sample	indexed	corrected	indexed	indexed	corrected	indexed	Densities
Modal prop. (%)							(kg/m3)
Q	45.6	30.4					2597
Pl	51.9	35	85.6	20.9	23.9	26.5	2640
Grt	1.5	34	12	0.6	16	0.3	3891
Cpx				76.5	60.2	72.5	3350
Rt	1	0.6	0.5				4174
Spinel			missing	2	0	0.6	3700

Table SIV.2: Sample 4-304-1 average plagioclase and garnet major element compositions. bdl = below detection limits. Cations on the basis of 8 oxygens for plagioclase and 12 oxygens for the garnet.

Polished thick sections were covered with a 20nm carbon deposit using a carbon evaporator Leica EM ACE600 for microprobe measurements. Minerals major element analyses were carried out using a Cameca SX Five electron microprobe from the microcharacterisation centre Raimond Castaing (CNRS-University Paul Sabatier, Toulouse). Measurements were made with an acceleration voltage of 15 kV and a probe current of 20 nA. Acquisition times were 10 s on peak and 5 s on either side of the peak for the continuous background. The standards used are natural or synthetic minerals as well as pure metals.

Plagioclase				**Garnet**			
	n=5	*σ*	*LOD (ppm)*		n=12	*σ*	*LOD (ppm)*
wt%							
SiO2	61.55	*0.248*	450	SiO2	39.52	*0.268*	450
TiO2	bdl		300	TiO2	0.09	*0.013*	300
Al2O3	23.46	*0.080*	400	Al2O3	21.73	*0.428*	400
Cr2O3	0.01	*0.008*	250	Cr2O3	0.04	*0.008*	250
FeO	0.25	*0.125*	850	FeO	23.68	*0.205*	950
MnO	bdl		800	MnO	0.42	*0.044*	900
MgO	bdl		300	MgO	11.31	*0.116*	350
CaO	5.49	*0.325*	650	CaO	2.32	*0.110*	650
Na2O	7.21	*0.387*	550	Na2O	0.04	*0.065*	550
K2O	1.35	*0.021*	600	K2O	bdl		550
BaO	0.01	*0.013*		NiO	0.02	*0.025*	900
Total	99.38	*0.519*		Total	99.16	*0.327*	
An	27.27	*2.002*		Alm	50.14	*0.315*	
Ab	64.77	*2.096*		Spss	0.89	*0.093*	
San	7.96	*0.221*		Pyr	42.69	*0.424*	
				Grs	6.28	*0.305*	
				Fe#	54.01	*0.371*	

Table SIV.3: LA-ICP-MS U-Pb isotopic data on zircon from the Don Javier felsic xenolith 4-302. Analyses highlighted in orange are suspicious or too short and are not used in the current study. Analyses highlighted in grey were reduced during trace element treatment to remove inclusions in zircon. However, this reduction was not applied to U-Pb data; thus, their calculated ages are considered suspicious.

	Duration (s)	Grain #	Zircon domain	207Pb / 235U	(±2σ)	206Pb / 238U	(±2σ)	Rho 75 / 68	238U / 206Pb	(±2σ)	207Pb / 206Pb	(±2σ)	Rho 86 / 76	207/235 date (Ma)	(±2σ)	206/238 date (Ma)	(±2σ)	207/206 date (Ma)	(±2σ)	208Pb / 232Th	(±2σ)	208/232 date (Ma)	(±2σ)	U/Th	% discor.
4-302																									
4-302 - 1	27,0	1	Zoned core	0,1022	0,0062	0,0156	0,0005	0,3481	64,1906	1,8506	0,0473	0,0015	0,0997	99	6	100	3	48	75	0,0050	0,0003	100	5	2,336	-1,00
4-302 - 2	12,9	2	Zoned core	0,3619	0,0238	0,0490	0,0017	0,5364	20,4289	0,6842	0,0538	0,0020	-0,0264	313	18	309	10	354	83	0,0175	0,0011	352	22	1,961	1,50
4-302 - 3	27,0	2	Zoned core	0,5646	0,0322	0,0726	0,0024	0,3097	13,8186	0,4335	0,0559	0,0015	0,5555	454	21	452	14	437	62	0,0208	0,0017	415	34	3,469	0,53
4-302 - 4	27,0	2	Hom rim	0,1725	0,0159	0,0247	0,0011	0,5491	41,0180	1,9094	0,0493	0,0028	-0,0945	161	14	157	7	140	159	0,0069	0,0007	140	14	1,730	2,28
4-302 - 5	8,6	4	Zoned core	0,2385	0,0212	0,0325	0,0016	0,8371	30,8885	1,5308	0,0537	0,0025	-0,3432	217	17	206	10	347	104	0,0115	0,0010	232	21	1,400	4,83
4-302 - 6	27,0	4	Hom rim	0,1822	0,0182	0,0189	0,0007	-0,1672	53,2639	2,0574	0,0705	0,0066	0,4036	169	16	121	5	861	230	0,0074	0,0008	148	16	0,719	28,64
4-302 - 7	27,0	5	Hom grain	0,8040	0,0523	0,0923	0,0038	0,7544	10,9355	0,4631	0,0631	0,0016	0,0847	598	29	569	22	703	54	0,0271	0,0015	539	29	0,572	4,80
4-302 - 8	9,7	6	Zoned core	0,2622	0,0321	0,0354	0,0035	0,9548	28,9967	2,6668	0,0543	0,0021	-0,3926	236	26	224	22	377	88	0,0088	0,0016	177	31	2,714	4,96
4-302 - 9	27,0	6	Hom rim	0,1250	0,0186	0,0172	0,0007	-0,0599	58,7882	2,5582	0,0534	0,0079	0,3001	118	17	110	5	195	305	0,0058	0,0005	117	11	0,212	7,27
4-302 - 10	8,1	7	Zoned core	0,1271	0,0102	0,0192	0,0007	0,4587	52,0270	1,8831	0,0484	0,0028	-0,0583	121	9	123	4	104	145	0,0063	0,0014	128	28	5,710	-1,19
4-302 - 11	19,6	7	Hom rim	0,1455	0,0280	0,0171	0,0009	-0,0952	59,2325	3,2664	0,0599	0,0111	0,4626	136	24	109	6	238	446	0,0056	0,0004	112	8	0,247	19,60
4-302 - 12	7,3	8	Zoned core	12,9227	0,7845	0,3622	0,0118	0,8287	2,7636	0,0904	0,2602	0,0050	-0,4585	2673	57	1992	56	3247	30	0,0949	0,0063	1832	115	1,127	25,47
4-302 - 13	27,0	9	Zoned core	0,1039	0,0064	0,0160	0,0005	0,1659	62,7267	1,9579	0,0473	0,0017	0,3304	100	6	102	3	45	87	0,0050	0,0003	101	7	2,114	-1,87
4-302 - 14	9,9	9	Hom rim	0,1634	0,0181	0,0185	0,0014	0,8890	54,8952	3,9245	0,0637	0,0030	-0,3106	153	16	118	9	722	106	0,0139	0,0028	278	56	9,151	22,93
4-302 - 15	10,3	10	Hom rim	0,1190	0,0239	0,0172	0,0007	0,7113	58,5320	2,5644	0,0504	0,0093	-0,6371	113	22	110	5	261	346	0,0059	0,0012	118	25	1,151	3,32
4-302 - 16	3,4	11	Hom grain	0,1223	0,0231	0,0178	0,0008	0,3744	56,1928	2,5147	0,0512	0,0086	-0,1138	117	21	114	5	202	390	0,0042	0,0005	85	9	1,660	2,64
4-302 - 17	12,0	11	Hom grain	0,1569	0,0133	0,0226	0,0008	0,4729	44,3979	1,5547	0,0505	0,0029	-0,2245	148	12	144	5	192	139	0,0082	0,0020	165	41	10,157	2,66
4-302 - 18	27,3	12	Zoned core	0,1673	0,0110	0,0235	0,0008	0,0081	42,7631	1,5208	0,0517	0,0018	0,3186	157	10	150	5	253	84	0,0076	0,0004	152	8	1,020	4,53
4-302 - 19	27,0	12	Zoned core	0,1415	0,0098	0,0205	0,0007	0,3399	49,0063	1,6238	0,0504	0,0022	0,0613	134	9	131	4	184	103	0,0076	0,0004	153	9	0,981	2,63
4-302 - 20	27,0	12	Hom rim	0,1271	0,0133	0,0167	0,0007	0,4586	60,4471	2,3874	0,0553	0,0044	-0,0522	121	12	107	5	322	203	0,0048	0,0004	96	8	1,126	11,72
4-302 - 21	27,0	13	Hom grain	0,1119	0,0143	0,0162	0,0006	0,2344	62,0479	2,4461	0,0501	0,0057	-0,0078	107	13	104	4	44	281	0,0052	0,0004	105	9	0,514	2,94
4-302 - 22	22,6	13	Hom grain	0,5599	0,1037	0,0199	0,0011	0,6944	51,0273	2,7407	0,1991	0,0306	-0,5314	435	68	127	7	2640	337	0,0095	0,0011	191	22	0,407	70,79
4-302 - 23	27,0	14	not zircon	-5,7647	11,1657	-0,0464	0,0944	0,9382	-0,3886	1,4392	0,8927	0,1136	0,1705	3501	262	-594	617	4538	136	802,509	187,804	117711	13120	-96,234	116,95
4-302 - 24	27,0	15	not zircon	1,7307	23,1893	0,0165	0,2042	0,9617	0,0599	0,8725	0,8586	0,0757	-0,1000	4190	247	-1223	1581	4732	92	-121,022	127,342	38061	5395	67,821	129,18
4-302 - 25	27,0	15	not zircon	2,6628	7,0838	0,0306	0,0687	0,9359	-1,4051	3,7401	0,9447	0,1941	-0,1733	2928	328	54	440	4345	279	-833,359	333,205	21593	5300	291,88	98,14
4-302 - 26	7,5	16	Zoned core	0,1689	0,0141	0,0248	0,0011	0,8379	40,5122	1,7568	0,0505	0,0024	-0,4620	158	12	158	7	207	111	0,0104	0,0010	210	21	3,230	0,44
4-302 - 27	22,1	16	Hom grain	0,2754	0,0181	0,0164	0,0005	0,5601	60,9795	1,9058	0,1223	0,0043	-0,2383	247	14	105	3	1980	65	0,0540	0,0052	1062	99	10,335	57,42
4-302 - 28	22,0	17	Hom grain	0,1082	0,0191	0,0160	0,0007	-0,0742	62,9214	2,8310	0,0475	0,0075	0,2725	103	17	103	5	40	351	0,0053	0,0005	107	10	0,275	0,68
4-302 - 29	23,3	17	Hom grain	0,1247	0,0164	0,0167	0,0008	-0,2489	60,4352	2,8451	0,0552	0,0073	0,4814	119	15	107	5	301	353	0,0054	0,0005	108	9	0,272	9,77
4-302 - 30	22,6	17	Hom grain	0,1164	0,0141	0,0163	0,0007	0,0806	62,0306	2,8522	0,0527	0,0061	0,2916	111	13	104	5	131	298	0,0052	0,0006	106	12	0,268	6,39
4-302 - 31	22,0	18	Zoned core	0,1717	0,0109	0,0241	0,0008	0,5686	41,6008	1,4209	0,0517	0,0017	0,0681	161	9	154	5	260	74	0,0086	0,0005	173	10	1,064	4,45
4-302 - 32	20,3	18	Zoned core	0,1952	0,0125	0,0239	0,0009	0,5473	41,9678	1,5205	0,0596	0,0021	0,2074	181	11	152	5	576	78	0,0077	0,0004	155	7	0,896	15,76
4-302 - 33	26,1	18	Zoned core	0,2076	0,0138	0,0279	0,0011	0,8236	36,1306	1,3458	0,0543	0,0013	-0,1271	191	12	177	7	377	54	0,0093	0,0005	187	10	0,702	7,42
4-302 - 34	26,7	18	Zoned core	0,1035	0,0087	0,0159	0,0005	0,1380	63,2080	1,9248	0,0477	0,0031	0,0415	100	8	101	3	17	154	0,0045	0,0005	91	11	2,026	-1,57
4-302 - 35	27,0	19	Zoned core	1,0100	0,0874	0,0546	0,0026	0,8319	18,5799	0,8847	0,1341	0,0057	-0,3764	703	43	343	16	2135	73	0,0247	0,0013	493	25	0,610	51,29
4-302 - 36	23,9	19	Zoned core	0,2943	0,0238	0,0395	0,0024	0,9067	25,9805	1,6410	0,0544	0,0016	-0,3238	261	19	249	15	376	67	0,0128	0,0020	257	40	12,283	4,46
4-302 - 37	27,0	19	Zoned core	0,1829	0,0179	0,0252	0,0020	0,9396	41,5367	2,9170	0,0529	0,0017	-0,1463	170	15	160	12	330	65	0,0094	0,0014	188	29	9,780	5,57
4-302 - 38	16,3	19	Hom rim	0,2131	0,0167	0,0297	0,0011	0,5700	33,8391	1,3202	0,0519	0,0026	-0,1225	196	14	188	7	259	113	0,0067	0,0008	135	17	1,628	3,77
4-302 - 39	27,0	20	Hom grain	417,3599	79,0679	3,5964	0,6738	0,9970	0,3645	0,0792	0,8441	0,0165	0,1073	6008	225	9480	1055	4934	32	1,8395	0,3501	19643	2598	0,163	-57,79
4-302 - 40	12,9	21	Hom grain	0,6531	0,1537	0,0231	0,0010	0,5520	43,4849	1,8895	0,2014	0,0428	-0,4487	491	95	147	6	2597	416	0,0127	0,0030	256	60	0,544	70,02
4-302 - 41	27,0	22	Hom grain	0,1141	0,0072	0,0152	0,0005	0,2628	65,9570	2,0695	0,0548	0,0020	0,1905	110	7	97	3	388	77	0,0096	0,0013	194	27	12,064	11,38
4-302 - 42	27,0	23	Zoned core	0,4517	0,0725	0,0517	0,0090	0,9783	25,1268	3,9219	0,0665	0,0040	0,4806	368	49	323	55	782	111	0,0233	0,0029	465	56	22,492	12,37
4-302 - 43	18,6	23	Zoned core	0,1032	0,0087	0,0156	0,0005	-0,1212	64,3224	2,1036	0,0486	0,0034	0,3097	100	8	100	3	67	177	0,0049	0,0008	99	15	2,637	-0,07
4-302 - 44	12,2	23	Hom rim	0,1215	0,0170	0,0173	0,0008	-0,2341	58,1768	2,8074	0,0510	0,0073	0,3318	116	15	111	5	211	434	0,0048	0,0004	98	9	0,504	4,64

Table SIV.4: LA-ICP-MS trace elements data on zircon from the Don Javier felsic xenolith 4-302.

	Grain #	Zircon domain	P (ppm)	Ti (ppm)	Y (ppm)	Nb (ppm)	La (ppm)	Ce (ppm)	Pr (ppm)	Nd (ppm)	Sm (ppm)	Eu (ppm)	Gd (ppm)	Tb (ppm)	Dy (ppm)	Ho (ppm)	Er (ppm)	Tm (ppm)	Yb (ppm)	Lu (ppm)	Hf (ppm)	232Th (ppm)	235U (ppm)	Eu$_N$/Eu*	REE+Y	GdN/YbN	Ti-in-zircon T (°C) [c]
4-302 - 1	1	Zoned core	445,75	30,74	690,28	2,00	0,06	17,06	0,12	1,59	3,27	0,42	13,34	4,29	53,19	21,82	116,95	26,12	258,26	57,19	11496,05	221,96	1701,77	0,17	1263,9	0,04	863
4-302 - 2	2	Zoned core	1856,20	31,99	3927,26	1,41	0,07	7,50	0,48	6,64	12,85	1,35	75,61	27,40	344,65	126,73	587,36	114,50	958,65	183,42	12044,11	134,53	836,47	0,10	6374,5	0,06	868
4-302 - 3	2	Zoned core	1154,01	21,48	1984,27	1,20	< LOD	2,15	0,03	0,74	2,59	0,18	23,21	10,96	159,32	62,90	315,14	64,27	589,28	116,71	11944,95	30,26	346,20	0,05	3331,8	0,03	823
4-302 - 4	2	Hom. rim	159,32	23,76	57,54	0,25	0,01	11,92	0,08	1,61	4,93	0,97	15,06	2,32	11,51	1,88	4,83	0,67	4,42	0,80	11310,68	40,57	222,28				
4-302 - 5	4	Zoned core	1342,76	37,00	2629,10	3,24	1,95	25,69	1,05	6,45	7,25	0,55	38,12	15,44	208,39	84,55	423,90	90,93	814,36	163,10	12524,59	264,10	1240,19				
4-302 - 6	4	Hom. rim	218,03	63,58	159,20	0,30	0,06	12,94	0,22	3,70	6,76	0,85	16,43	2,96	21,32	5,46	21,64	4,08	33,06	6,26	10712,30	44,86	102,34	0,23	294,9	0,40	955
4-302 - 7	5	Hom. grain	332,86	38,99	573,18	1,39	0,50	22,23	0,38	4,28	6,47	0,72	24,95	6,56	66,21	20,42	83,61	15,31	122,24	22,65	10091,70	206,53	418,69				
4-302 - 8	6	Zoned core	642,04	28,09	1136,91	1,09	< LOD	10,69	0,07	1,38	3,00	0,39	18,29	7,06	95,98	36,66	183,98	39,50	376,85	75,51	12949,73	63,02	614,21				
4-302 - 9	6	Hom. rim	191,83	26,97	81,16	0,30	< LOD	25,44	0,25	4,16	6,59	0,87	15,92	2,40	14,35	2,85	7,49	0,99	6,55	1,11	10853,04	80,93	63,62	0,25	170,1	1,97	848
4-302 - 10	7	Zoned core	517,77	28,89	809,13	0,94	< LOD	5,13	0,06	0,98	3,46	0,47	19,52	7,55	82,38	25,52	100,17	18,23	171,13	35,75	13352,44	32,19	645,78	0,14	1279,5	0,09	856
4-302 - 11	7	Hom. rim	177,99	39,34	84,41	0,31	0,08	25,39	0,31	4,42	7,45	0,88	15,51	2,55	15,60	2,97	7,65	1,11	7,36	1,22	11549,09	77,56	78,96	0,24	176,9	1,70	893
4-302 - 12	8	Zoned core	514,17	32,18	965,52	1,45	0,03	21,28	0,08	1,41	4,07	1,34	24,04	7,20	84,28	31,02	150,56	31,05	283,87	59,71	10598,86	123,88	507,15				
4-302 - 13	9	Zoned core	1352,39	29,44	2431,40	2,54	0,03	11,03	0,20	3,24	8,34	1,15	51,20	17,38	210,49	77,17	366,11	73,72	653,08	133,86	10485,97	151,12	1168,94	0,13	4038,4	0,06	858
4-302 - 14	9	Hom. rim	187,13	269,47	169,76	0,31	6,35	16,70	2,13	11,14	7,94	1,03	22,14	4,83	32,85	6,47	17,17	2,31	16,41	2,51	6193,25	14,92	472,96				
4-302 - 15	10	Hom. rim	127,88	28,20	85,75	0,25	0,03	14,84	0,07	1,40	4,41	0,83	12,02	2,09	15,24	2,91	7,22	0,86	6,24	0,86	11348,37	26,05	115,81	0,33	154,8	1,56	853
4-302 - 16	11	Hom. grain	401,79	30,76	675,17	0,66	< LOD	10,37	0,06	1,51	3,41	0,33	20,09	6,63	73,16	23,56	94,39	17,84	145,12	28,23	13239,51	65,07	385,44				
4-302 - 17	11	Hom. grain	160,22	25,60	133,57	0,33	< LOD	3,49	0,02	0,59	2,67	0,66	17,21	4,34	27,99	4,65	10,06	1,18	6,74	1,18	12921,90	17,63	696,44	0,23	214,3	2,07	842
4-302 - 18	12	Zoned core	949,69	28,36	1859,80	2,39	0,02	18,89	0,11	2,40	6,38	1,10	37,46	12,92	161,68	60,10	283,87	55,55	481,46	96,81	10144,41	235,30	915,11	0,17	3078,6	0,06	854
4-302 - 19	12	Zoned core	781,09	29,18	1401,18	1,92	< LOD	15,15	0,09	2,12	4,96	1,10	29,28	9,96	120,63	45,98	221,96	44,32	386,44	78,29	9689,24	175,96	677,18	0,22	2361,4	0,06	857
4-302 - 20	12	Hom. rim	139,12	88,25	97,28	0,27	0,13	13,70	0,29	3,77	6,13	0,90	15,51	2,75	18,05	3,62	11,24	1,77	13,69	2,37	9989,18	53,60	250,45	0,27	191,2	0,92	1002
4-302 - 21	13	Hom. grain	184,33	25,36	56,03	0,30	< LOD	24,21	0,15	2,83	5,14	0,67	11,58	1,79	10,18	1,89	5,08	0,68	4,67	0,76	12132,68	68,94	134,80	0,26	125,7	2,01	841
4-302 - 22	13	Hom. grain	274,93	29,41	155,21	0,34	0,05	26,13	0,26	4,50	8,99	0,96	21,54	4,21	28,18	5,79	15,51	2,09	13,60	2,20	11969,01	71,37	107,23				
4-302 - 23	14	not zircon	< LOD	366,96	28,45	< LOD	0,06	0,19	0,08	1,23	2,39	0,18	5,17	0,89	5,86	1,05	3,09	0,50	3,31	0,48	2,27	0,00	< LOD				
4-302 - 24	15	not zircon	71,78	384,54	36,32	< LOD	1,11	2,82	0,41	3,79	4,23	0,28	9,83	1,75	7,65	0,95	2,17	0,40	2,31	0,36	< LOD	0,11	< LOD				
4-302 - 25	15	not zircon	85,07	170,16	0,63	< LOD	0,20	0,47	0,06	0,30	0,25	< LOD	< LOD	0,05	0,20	0,04	< LOD	< LOD	< LOD	< LOD	< LOD	0,08	< LOD				
4-302 - 26	16	Zoned core	1083,43	26,60	2108,62	1,48	< LOD	4,56	0,07	0,76	2,69	0,37	18,83	9,69	145,77	64,33	351,11	81,83	786,82	160,99	13250,38	77,15	1056,15	0,12	3736,4	0,02	847
4-302 - 27	16	Hom. grain	439,09	125,52	618,32	0,42	7,80	32,18	4,62	30,84	35,01	2,65	74,23	13,89	99,58	21,67	75,02	12,76	99,05	18,31	8350,61	16,81	704,83				
4-302 - 28	17	Hom. grain	216,19	25,56	53,17	0,35	< LOD	21,90	0,13	2,51	4,35	0,52	10,32	1,55	9,72	1,79	4,75	0,63	4,11	0,66	11364,61	50,50	57,72	0,23	116,1	2,03	842
4-302 - 29	17	Hom. grain	226,05	25,73	55,79	0,35	0,02	22,80	0,14	2,72	4,82	0,57	10,98	1,70	9,86	1,94	4,78	0,66	4,43	0,71	11623,07	50,64	57,38	0,23	121,9	2,00	843
4-302 - 30	17	Hom. grain	210,14	25,40	55,32	0,37	< LOD	22,50	0,17	2,75	4,61	0,53	11,11	1,69	9,90	1,90	4,95	0,66	4,28	0,62	11129,55	53,09	59,42	0,22	121,0	2,10	842
4-302 - 31	18	Zoned core	639,97	27,55	802,26	2,31	0,04	13,95	0,14	1,80	3,17	0,45	12,79	4,32	55,74	25,43	162,70	42,42	454,89	108,00	11081,37	214,64	995,05	0,19	1688,1	0,02	851
4-302 - 32	18	Zoned core	749,25	34,81	1209,07	7,27	0,04	62,63	0,09	1,26	2,55	0,46	14,97	5,15	70,88	32,75	194,22	50,40	562,28	146,62	11227,67	360,80	1366,56	0,18	2353,4	0,02	878
4-302 - 33	18	Zoned core	565,21	30,19	750,72	4,46	0,03	41,14	0,07	1,09	2,07	0,35	9,32	3,27	45,13	20,21	126,63	33,47	373,05	99,42	11931,87	452,11	1331,47	0,20	1506,0	0,02	861
4-302 - 34	18	Zoned core	1016,54	28,87	1943,13	1,28	0,02	3,96	0,06	0,94	3,00	0,22	25,65	11,12	156,20	60,54	287,24	56,46	491,19	97,65	11745,90	48,99	428,06	0,05	3137,4	0,04	856
4-302 - 35	19	Zoned core	890,32	3658,72	1824,44	21,27	10,56	36,83	3,49	16,29	9,48	1,39	42,52	13,81	167,87	59,61	269,21	50,40	418,44	80,80	7419,37	164,10	431,46				
4-302 - 36	19	Zoned core	658,62	28,10	1072,41	0,80	< LOD	0,84	0,02	0,40	1,81	0,14	16,52	7,68	96,19	31,26	131,17	24,64	205,71	38,73	12409,70	13,44	698,72	0,05	1627,5	0,06	853
4-302 - 37	19	Zoned core	820,92	28,48	1389,17	0,91	< LOD	1,31	0,03	0,54	1,87	0,16	17,08	8,64	117,39	41,38	184,79	37,34	321,99	60,97	12534,82	18,44	754,13	0,06	2182,6	0,04	855
4-302 - 38	19	Hom. rim	167,47	22,94	81,93	0,28	< LOD	10,14	0,11	1,78	4,42	0,65	13,27	2,34	14,18	2,75	7,48	0,95	6,77	1,07	11019,56	53,26	379,64	0,24	147,8	1,59	830
4-302 - 39	20	Hom. grain	4349,50	4373,15	150,37	13,84	100,38	246,35	33,01	153,89	59,64	5,77	67,23	8,49	38,81	5,95	12,90	1,51	8,39	1,16	485,32	5,55	4,42				
4-302 - 40	21	Hom. grain	299,58	37,97	165,61	0,38	0,32	20,72	0,24	3,28	7,07	0,84	19,31	4,21	29,60	5,87	14,81	1,76	11,00	1,61	10769,28	70,79	191,40				
4-302 - 41	22	Hom. grain	5387,08	43,33	11017,64	0,87	2,45	25,88	8,55	107,57	308,44	27,10	1127,03	253,02	2031,39	398,57	1176,71	168,52	1201,43	193,15	11192,17	19,94	1057,21				
4-302 - 42	23	Zoned core	518,87	69,76	688,78	2,83	2,06	8,02	0,64	2,56	1,10	0,18	4,05	1,67	32,38	19,64	140,47	36,60	384,81	83,25	10246,81	23,65	1625,78				
4-302 - 43	23	Zoned core	923,73	29,46	1808,18	0,95	< LOD	4,33	0,04	0,87	2,96	0,33	21,23	9,76	136,96	54,17	273,51	57,87	518,85	103,00	12202,41	48,20	545,18	0,09	2992,1	0,03	858
4-302 - 44	23	Hom. rim	261,64	25,34	90,57	0,35	< LOD	21,20	0,15	3,05	5,64	0,68	11,94	1,94	12,34	3,00	11,56	2,15	18,09	3,03	11137,86	70,07	134,91	0,24	185,3	0,53	841

Table SIV.5: LA-ICP-MS trace elements standard deviation data on zircon from the Don Javier felsic xenolith 4-302.

	Grain #	Zircon domain	P (±2s)	Ti (±2s)	Y (±2s)	Nb (±2s)	La (±2s)	Ce (±2s)	Pr (±2s)	Nd (±2s)	Sm (±2s)	Eu (±2s)	Gd (±2s)	Tb (±2s)	Dy (±2s)	Ho (±2s)	Er (±2s)	Tm (±2s)	Yb (±2s)	Lu (±2s)	Hf (±2s)	232Th (±2s)	235U (±2s)
4-302 - 1	1	Zoned core	36,62	1,82	49,23	0,16	0,02	1,35	0,03	0,27	0,35	0,05	0,67	0,22	3,10	1,49	8,22	2,03	18,47	4,33	327,82	5,80	122,54
4-302 - 2	2	Zoned core	55,69	2,33	181,56	0,12	0,02	0,74	0,08	0,86	1,50	0,16	6,73	1,84	19,90	6,51	25,37	5,25	42,02	6,33	288,34	15,65	39,16
4-302 - 3	2	Zoned core	31,16	1,09	63,38	0,07	0,01	0,09	0,01	0,12	0,14	0,03	0,97	0,37	4,75	1,63	9,49	1,75	18,18	2,96	339,58	0,82	24,25
4-302 - 4	2	Hom. rim	12,64	1,54	5,01	0,04	0,01	0,50	0,02	0,16	0,29	0,09	1,09	0,20	1,07	0,18	0,48	0,07	0,51	0,11	431,87	1,08	43,35
4-302 - 5	4	Zoned core	46,91	3,03	55,43	0,18	0,98	3,58	0,53	2,30	0,86	0,08	1,67	0,48	5,72	2,21	9,51	3,43	24,98	7,79	456,25	4,81	55,67
4-302 - 6	4	Hom. rim	14,81	8,64	11,19	0,06	0,02	0,45	0,04	0,38	0,37	0,11	1,00	0,12	1,14	0,43	2,37	0,47	4,48	0,83	461,24	2,09	14,67
4-302 - 7	5	Hom. grain	15,22	2,56	25,39	0,09	0,15	0,73	0,05	0,32	0,59	0,08	1,66	0,37	3,59	0,99	3,24	0,56	4,71	0,72	301,58	8,98	31,32
4-302 - 8	6	Zoned core	54,21	2,85	169,54	0,15	0,01	1,46	0,03	0,27	0,44	0,07	1,76	0,94	12,64	4,83	24,37	4,83	49,73	8,89	464,46	4,15	82,24
4-302 - 9	6	Hom. rim	12,38	1,88	5,11	0,04	0,01	0,83	0,02	0,34	0,53	0,08	0,80	0,15	0,83	0,18	0,48	0,09	0,43	0,08	324,00	3,27	8,98
4-302 - 10	7	Zoned core	53,03	2,71	179,98	0,09	0,01	0,59	0,03	0,31	0,34	0,09	1,61	0,72	12,32	5,04	22,49	4,78	51,12	10,02	358,01	0,98	55,26
4-302 - 11	7	Hom. rim	16,03	7,23	1,61	0,05	0,05	0,69	0,04	0,27	0,49	0,07	0,67	0,09	0,57	0,13	0,41	0,10	0,52	0,08	515,92	2,47	12,46
4-302 - 12	8	Zoned core	49,05	2,87	69,56	0,16	0,02	1,15	0,02	0,29	0,26	0,13	1,64	0,63	5,92	1,64	6,83	1,35	17,65	3,44	409,24	7,25	40,86
4-302 - 13	9	Zoned core	70,38	2,16	65,59	0,13	0,02	0,71	0,03	0,18	0,42	0,08	1,79	0,59	6,67	2,47	11,05	2,12	16,21	3,77	394,87	6,15	41,84
4-302 - 14	9	Hom. rim	26,13	38,10	12,25	0,06	0,67	1,87	0,31	1,21	0,54	0,11	1,31	0,41	1,79	0,58	1,75	0,24	1,95	0,27	132,16	0,72	31,88
4-302 - 15	10	Hom. rim	15,03	1,84	2,52	0,06	0,04	0,64	0,03	0,22	0,49	0,09	1,08	0,11	0,76	0,19	0,30	0,05	0,38	0,05	321,24	1,70	18,61
4-302 - 16	11	Hom. grain	82,65	3,86	116,85	0,11	0,02	0,40	0,02	0,26	0,38	0,12	1,34	0,22	4,03	3,84	17,52	3,84	30,23	6,68	620,20	4,23	48,69
4-302 - 17	11	Hom. grain	24,86	1,96	5,91	0,06	0,01	0,32	0,01	0,10	0,37	0,06	0,94	0,19	0,80	0,30	0,75	0,10	0,86	0,11	403,27	1,00	50,37
4-302 - 18	12	Zoned core	36,17	1,73	44,85	0,12	0,01	0,56	0,01	0,19	0,28	0,09	1,31	0,40	3,35	1,28	6,40	1,21	10,81	1,92	258,13	6,31	29,19
4-302 - 19	12	Zoned core	22,97	1,53	49,30	0,14	0,01	0,37	0,02	0,16	0,22	0,08	1,31	0,29	3,01	1,24	6,13	1,22	11,91	2,27	280,42	3,62	29,77
4-302 - 20	12	Hom. rim	12,66	5,35	3,39	0,04	0,02	0,58	0,03	0,24	0,34	0,06	0,84	0,13	0,80	0,17	0,53	0,13	0,74	0,14	392,32	2,98	32,60
4-302 - 21	13	Hom. grain	13,36	1,32	1,57	0,04	0,01	0,82	0,02	0,19	0,28	0,06	0,52	0,08	0,43	0,10	0,25	0,05	0,30	0,05	408,43	2,14	12,86
4-302 - 22	13	Hom. grain	25,44	1,66	23,47	0,04	0,01	0,50	0,03	0,27	0,70	0,09	2,03	0,53	3,93	0,91	2,47	0,32	1,95	0,36	282,27	1,67	9,03
4-302 - 23	14	not zircon	17,53	15,55	2,75	0,02	0,02	0,04	0,02	0,21	0,34	0,03	0,57	0,12	0,52	0,11	0,31	0,05	0,41	0,07	1,67	0,00	0,00
4-302 - 24	15	not zircon	39,94	20,42	28,07	0,02	0,27	0,58	0,12	0,86	1,41	0,10	5,97	1,11	5,42	0,56	1,24	0,30	1,61	0,26	1,73	0,03	0,00
4-302 - 25	15	not zircon	44,54	9,14	0,46	0,02	0,08	0,14	0,03	0,15	0,20	0,02	0,25	0,03	0,14	0,02	0,07	0,00	0,03	0,01	2,60	0,04	0,00
4-302 - 26	16	Zoned core	48,27	2,09	93,17	0,20	0,01	0,40	0,03	0,18	0,31	0,07	1,17	0,43	5,46	2,72	13,55	2,94	25,53	5,23	513,93	8,68	65,91
4-302 - 27	16	Hom. grain	30,98	9,57	93,40	0,06	1,16	4,67	0,72	4,99	6,77	0,38	13,86	2,37	17,24	3,41	11,85	2,20	17,83	3,14	299,24	1,14	32,45
4-302 - 28	17	Hom. grain	11,92	1,82	1,99	0,04	0,01	0,97	0,02	0,25	0,41	0,06	0,64	0,10	0,50	0,11	0,32	0,05	0,27	0,07	472,28	1,62	6,40
4-302 - 29	17	Hom. grain	16,37	1,55	1,80	0,05	0,01	0,62	0,02	0,24	0,28	0,05	0,60	0,09	0,42	0,10	0,29	0,06	0,29	0,05	309,07	1,76	5,71
4-302 - 30	17	Hom. grain	14,90	1,39	1,22	0,04	0,01	0,61	0,02	0,22	0,34	0,04	0,44	0,09	0,36	0,09	0,25	0,05	0,28	0,05	321,93	1,29	7,13
4-302 - 31	18	Zoned core	25,15	1,97	37,58	0,17	0,02	0,87	0,03	0,23	0,25	0,05	0,59	0,18	2,26	1,14	10,31	2,72	31,16	7,78	369,67	19,25	75,95
4-302 - 32	18	Zoned core	27,73	3,49	48,77	0,35	0,02	1,19	0,02	0,20	0,25	0,07	0,92	0,23	2,50	1,05	6,14	1,45	13,42	3,11	276,80	16,33	76,28
4-302 - 33	18	Zoned core	20,89	1,56	42,39	0,16	0,02	1,84	0,02	0,13	0,24	0,04	0,83	0,25	2,81	1,06	6,98	1,97	16,26	3,84	388,00	26,00	58,61
4-302 - 34	18	Zoned core	25,94	1,37	80,70	0,09	0,01	0,16	0,01	0,12	0,28	0,03	0,91	0,38	5,31	2,19	11,34	2,57	23,48	3,97	290,84	1,68	31,88
4-302 - 35	19	Zoned core	29,63	1672,8	58,62	9,46	0,83	1,80	0,23	1,00	0,40	0,09	1,56	0,54	5,82	1,96	9,10	1,41	11,95	2,61	324,27	4,32	31,33
4-302 - 36	19	Zoned core	81,46	1,30	220,80	0,12	0,01	0,11	0,01	0,08	0,19	0,03	1,31	0,88	14,80	5,95	30,05	6,20	53,77	10,29	359,82	1,71	78,49
4-302 - 37	19	Zoned core	74,07	1,57	194,82	0,10	0,01	0,12	0,01	0,11	0,22	0,03	1,27	0,75	12,63	5,70	29,44	6,65	61,03	11,86	395,52	1,88	73,43
4-302 - 38	19	Hom. rim	16,63	1,81	6,77	0,06	0,01	0,35	0,02	0,26	0,35	0,12	1,24	0,22	1,15	0,24	0,60	0,08	0,56	0,12	356,69	1,25	47,02
4-302 - 39	20	Hom. grain	367,90	543,92	6,08	2,02	14,68	32,11	4,21	17,02	4,57	0,48	3,85	0,37	1,89	0,26	0,79	0,10	0,64	0,08	159,94	1,45	1,98
4-302 - 40	21	Hom. grain	26,04	10,73	29,13	0,07	0,18	0,45	0,05	0,35	0,85	0,09	2,35	0,60	5,24	1,03	2,57	0,36	2,27	0,25	275,67	2,22	33,75
4-302 - 41	22	Hom. grain	886,40	2,64	2026,3	0,08	0,31	2,66	1,24	14,52	49,60	3,65	195,45	43,39	383,56	77,89	213,25	25,45	165,65	22,02	530,86	0,51	69,13
4-302 - 42	23	Zoned core	33,59	13,94	38,31	0,24	0,72	2,34	0,22	0,82	0,25	0,05	0,79	0,19	1,97	1,05	8,45	2,49	29,55	6,20	176,01	4,97	242,16
4-302 - 43	23	Zoned core	23,22	1,30	56,25	0,09	0,01	0,19	0,01	0,10	0,24	0,04	0,93	0,46	4,62	1,74	7,37	1,67	16,07	2,69	314,53	2,26	30,21
4-302 - 44	23	Hom. rim	22,56	2,06	2,81	0,07	0,02	0,66	0,03	0,41	0,48	0,07	0,66	0,11	0,64	0,21	0,65	0,21	1,03	0,26	253,15	1,56	21,57

APPENDICE SV.

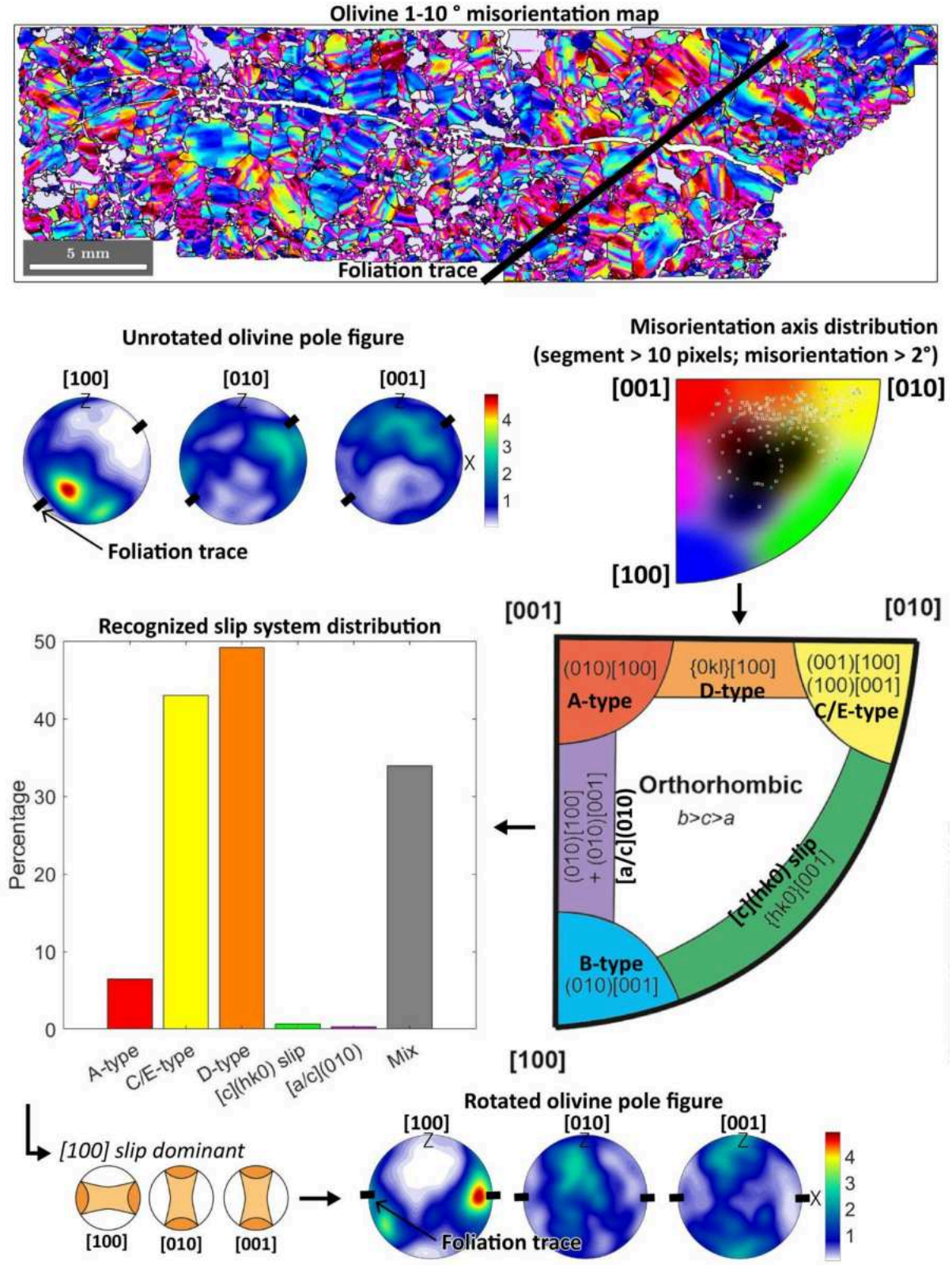


Fig. SV.1. Lineation determination method for pole figure rotation illustrated by the sample CH42 (Cerro Chenque, North Patagonian Massif). The intragranular deformation map of olivine suggests a foliation trace at ca. -45° to X. The unrotated pole figure indicates

concentration point on olivine [100], [010] and [001] axes either sub-parallel or parallel to the the foliation trace.

To identify the dominant slip direction, we used misorientation axis at low angle boundaries or subgrain boundaries statistical distribution. Only misorientation segments >10 pixels and >2 ° were considered, and we classified the axes into different domains of the inverse pole figure using a method and MTex code from N. Meunier-Mili (pers. comm.). These misorientation domains are indicative of related slip systems, as illustrated by the inverse pole figure diagram (modified from Griffin *et al.*, 2022). The sample CH42 displays misorientations related to the activation [100]{0kl} and [100](001)/[001](100) slip systems, with minor [100](010) slip system activation and only traces of other slip systems activation. The glide on the [100] direction is significantly dominant in the sample CH42. If the CPO is related to the slip systems that formed the observed misorientations at low-angle boundaries or subgrain boundaries, therefore, the sample lineation is parallel to the concentration point on olivine [100] axes, as the foliation plane would be parallel to the [100] axes that form a weak girdle. It is worth noting that the rotated pole figures show orthopyroxene concentration point on [100] axes parallel to the lineation direction and the concentration point [001] axes normal to the foliation plane (Fig. V.4), which is unusual in orthopyroxene fabric studies (Bernard *et al.*, 2021), as orthopyroxene [001] axis has been used as a lineation direction reference frame.

Sample CH42 presented a particularly complex CPO, making it a valuable reference for understanding the unrotated pole figures in the entire xenolith suite.

Table SV.1: Clinopyroxene and orthopyroxene major elements compositions microprobe analyses. Cations on the basis of 6 oxygens.

	Clinopyroxene					*Orthopyroxene*			
	North Patagonian Massif				*Las Conchas Valley*	*North Patagonian Massif*			*Las Conchas Valley*
Sample	**COM138**	**TR45**	**CH42**	**LaFr8**	**4-147g**	**TR45**	**CH42**	**LaFr8**	**4-147g**
Rock type	*Wh*	*Sp-Lh*	*Sp-Hz*	*Sp-Hz*	*Sp-Lh*	*Sp-Lh*	*Sp-Hz*	*Sp-Hz*	*Sp-Lh*
n	7	14	2	3	9	2	6	14	9
wt%									
SiO2	51,61	51,44	54,14	52,93	53,07	56,26	57,27	56,17	56,29
TiO2	0,52	0,26	0,00	0,10	0,11	0,06	0,00	0,02	0,01
Al2O3	4,78	5,95	1,99	4,39	4,73	1,27	1,57	3,15	3,03
Cr2O3	0,50	0,03	0,65	1,56	1,07	0,01	0,29	0,71	0,40
Fe2O3	0,72	1,63	0,03	0,00	0,86	0,00	0,00	0,00	0,00
FeO	3,23	3,19	2,39	3,31	1,86	9,90	5,11	5,49	5,90
MnO	0,08	0,09	0,07	0,07	0,07	0,22	0,13	0,12	0,14
NiO	0,00	0,00	0,00	0,00	0,06	0,00	0,00	0,00	0,08
MgO	15,32	13,67	17,83	17,61	15,44	30,39	33,95	32,56	33,31
CaO	22,01	21,71	22,21	18,55	20,74	1,15	0,50	1,22	0,58
Na2O	0,72	1,36	0,40	0,97	1,59	0,05	0,03	0,12	0,08
K2O	0,00	0,00	0,01	0,01	0,01	0,01	0,00	0,01	0,00
Total	99,49	99,32	99,69	99,50	99,62	99,30	98,86	99,55	99,82
Wo	47,5	49,0	45,4	40,6	46,8	2,2	1,0	2,4	1,1
En	46,0	42,8	50,7	53,7	48,5	82,7	91,3	89,2	89,9
Ferr	6,5	8,2	3,9	5,7	4,7	15,1	7,7	8,4	8,9
Mg#	87,6	83,9	92,9	90,5	91,3	84,6	92,2	91,4	91,0
σ									
SiO2	*0,173*	*0,757*	*0,028*	*0,445*	*0,295*	*0,587*	*0,212*	*0,258*	*0,163*
TiO2	*0,018*	*0,057*	*0,000*	*0,038*	*0,018*	*0,078*	*0,000*	*0,022*	*0,012*
Al2O3	*0,088*	*1,373*	*0,021*	*0,358*	*0,651*	*1,428*	*0,274*	*0,293*	*0,105*
Cr2O3	*0,027*	*0,017*	*0,021*	*0,119*	*0,078*	*0,000*	*0,105*	*0,098*	*0,015*
Fe2O3	*0,313*	*0,762*	*0,038*	*0,000*	*0,517*	*0,000*	*0,000*	*0,000*	*0,000*
FeO	*0,259*	*0,689*	*0,027*	*0,140*	*0,467*	*0,502*	*0,056*	*0,122*	*0,046*
MnO	*0,028*	*0,034*	*0,007*	*0,010*	*0,044*	*0,021*	*0,023*	*0,025*	*0,022*
NiO	*0,000*	*0,000*	*0,000*	*0,000*	*0,021*	*0,000*	*0,000*	*0,000*	*0,032*
MgO	*0,192*	*1,224*	*0,028*	*0,175*	*0,349*	*0,035*	*0,160*	*0,502*	*0,133*
CaO	*0,227*	*0,487*	*0,382*	*0,433*	*0,702*	*0,877*	*0,095*	*0,332*	*0,024*
Na2O	*0,018*	*0,379*	*0,049*	*0,035*	*0,410*	*0,014*	*0,015*	*0,025*	*0,023*
K2O	*0,008*	*0,006*	*0,007*	*0,012*	*0,017*	*0,000*	*0,005*	*0,012*	*0,004*
Total	*0,240*	*0,425*	*0,414*	*0,456*	*0,545*	*0,389*	*0,214*	*0,349*	*0,246*
Wo	*0,501*	*2,596*	*0,409*	*0,478*	*0,463*	*1,695*	*0,183*	*0,665*	*0,045*
En	*0,547*	*1,889*	*0,335*	*0,265*	*0,401*	*0,800*	*0,197*	*0,767*	*0,098*
Ferr	*0,438*	*1,007*	*0,074*	*0,307*	*0,303*	*0,895*	*0,106*	*0,189*	*0,072*
Mg#	*0,817*	*1,584*	*0,084*	*0,451*	*0,536*	*0,647*	*0,105*	*0,225*	*0,074*

Table SV.2: Olivine, spinel and amphibole major elements compositions microprobe analyses. Cations on the basis of 4 oxygens for olivine and 23 oxygens for amphibole. Cation proportions, Fe2O3 and FeO contents of spinel were calculated using EMG 8.0 software from Ferracutti et al. (2015).

	Olivine						***Spinel***						***Amphibole***		
	North Patagonian Massif				*Las Conchas Valley*		*North Patagonian Massif*				*Las Conchas Valley*		*North Patagonian Massif*		*Las Conchas Valley*
Sample	**COM138**	**TR45**	**CH42**	**LaFr8**	**4-147g**		**COM138**	**TR45**	**CH42**	**LaFr8**	**4-147g**		**COM138 I**	**COM138 II**	**4-147g**
Rock type	*Wh*	*Sp-Lh*	*Sp-Hz*	*Sp-Hz*	*Sp-Lh*		*Wh*	*Sp-Lh*	*Sp-Hz*	*Sp-Hz*	*Sp-Lh*		*Wh*	*Wh*	*Sp-lh*
n	8	19	15	12	9		9	9	4	6	5		4	6	6
wt%						wt%						wt%			
SiO2	40.52	39.75	41.35	41.30	41.03	SiO2	0.04	0.01	0.05	0.10	0.02	SiO2	41.71	43.97	43.35
TiO2	0.00	0.00	0.00	0.00	0.00	TiO2	0.32	0.04	0.00	0.20	0.04	TiO2	2.22	3.33	0.90
Al2O3	0.01	0.01	0.01	0.06	0.02	Al2O3	49.44	62.96	30.10	34.49	44.87	Al2O3	14.25	9.58	14.28
Cr2O3	0.02	0.00	0.05	0.05	0.01	Cr2O3	13.18	0.30	37.68	31.78	22.29	Cr2O3	0.88	1.21	1.72
					9.14	V2O3	0.11	0.01	0.19	0.00	0.00	FeO	5.35	3.98	3.80
					0.15	Fe2O3	5.17	3.61	3.31	4.21	2.99	MnO	0.06	0.05	0.07
FeO	12.41	15.94	8.06	8.59	48.88	FeO	11.54	11.96	10.23	9.74	10.11	NiO			0.10
MnO	0.17	0.18	0.12	0.12	0.05	MnO	0.15	0.10	0.16	0.14	0.13	MgO	16.13	11.95	17.30
NiO	0.26	0.18	0.38	0.38	0.01	NiO	0.28	0.30	0.19	0.26	0.28	CaO	11.58	22.99	10.65
MgO	45.76	42.53	49.19	48.79	0.00	MgO	17.94	18.93	16.83	17.71	18.51	Na2O	2.89	0.58	3.55
CaO	0.06	0.18	0.11	0.16	0.37	CaO	0.02	0.02	0.00	0.02	0.02	K2O	0.98	0.00	0.66
Na2O	0.00	0.01	0.01	0.02	99.66	Na2O	0.01	0.01	0.01	0.01	0.01	Total	96.31	97.85	96.37
K2O	0.00	0.01	0.01	0.00	90.5	K2O	0.01	0.00	0.01	0.01	0.01	Mg#	0.84	0.84	0.89
						ZnO	0.11	0.07	0.08	0.00	0.00	Cations on the basis of 23 oxygens			
Total	99.21	98.79	99.27	99.48		Total	98.31	98.32	98.83	98.67	99.27	Si	6.09	6.41	6.25
Fo	86.8	82.6	91.6	91.0		Mg#	73.5	73.8	74.6	76.4	76.6	Ti	0.24	0.36	0.10
						Cr#	15.2	0.3	45.6	38.2	25.0				
σ						*σ*						*σ*			
SiO2	*0.230*	*0.304*	*0.103*	*0.172*	*0.109*	*SiO2*	*0.013*	*0.010*	*0.025*	*0.013*	*0.015*	*SiO2*	*0.307*	*1.765*	*0.091*
TiO2	*0.004*	*0.010*	*0.000*	*0.000*	*0.003*	*TiO2*	*0.188*	*0.061*	*0.000*	*0.102*	*0.008*	*TiO2*	*0.078*	*0.315*	*0.061*
Al2O3	*0.009*	*0.011*	*0.011*	*0.063*	*0.016*	*Al2O3*	*1.100*	*0.833*	*1.223*	*1.980*	*0.489*	*Al2O3*	*0.107*	*2.379*	*0.158*
Cr2O3	*0.023*	*0.010*	*0.065*	*0.023*	*0.010*	*Cr2O3*	*0.580*	*0.056*	*1.876*	*1.577*	*0.442*	*Cr2O3*	*0.018*	*0.395*	*0.057*
					0.085	*V2O3*	*0.040*	*0.011*	*0.032*	*0.000*	*0.000*	*FeO*	*0.099*	*0.521*	*0.097*
					0.019	*Fe2O3*	*0.469*	*0.888*	*0.544*	*0.539*	*0.235*	*MnO*	*0.013*	*0.016*	*0.026*
FeO	*0.123*	*0.279*	*0.115*	*0.172*	*0.067*	*FeO*	*0.418*	*0.671*	*0.106*	*0.766*	*0.449*	*NiO*			*0.037*
MnO	*0.017*	*0.035*	*0.026*	*0.030*	*0.027*	*MnO*	*0.026*	*0.034*	*0.008*	*0.032*	*0.031*	*MgO*	*0.220*	*1.140*	*0.199*
NiO	*0.031*	*0.038*	*0.033*	*0.037*	*0.016*	*NiO*	*0.016*	*0.032*	*0.013*	*0.037*	*0.022*	*CaO*	*0.061*	*0.364*	*0.076*
MgO	*0.287*	*0.512*	*0.282*	*0.360*	*0.007*	*MgO*	*0.224*	*0.501*	*0.099*	*0.759*	*0.202*	*Na2O*	*0.085*	*0.142*	*0.069*
CaO	*0.030*	*0.258*	*0.042*	*0.038*	*0.037*	*CaO*	*0.036*	*0.015*	*0.000*	*0.020*	*0.029*	*K2O*	*0.029*	*0.000*	*0.062*
Na2O	*0.007*	*0.020*	*0.007*	*0.014*	*0.231*	*Na2O*	*0.015*	*0.009*	*0.010*	*0.012*	*0.008*	*Total*	*0.438*	*0.673*	*0.289*
K2O	*0.004*	*0.010*	*0.010*	*0.004*	*0.075*	*K2O*	*0.009*	*0.004*	*0.015*	*0.012*	*0.009*	*Mg#*	*0.002*	*0.029*	*0.002*
						ZnO	*0.041*	*0.076*	*0.024*	*0.000*	*0.000*	*Si*	*0.013*	*0.234*	*0.022*
Total	*0.360*	*0.612*	*0.356*	*0.348*		*Total*	*0.791*	*0.488*	*0.264*	*0.107*	*0.311*	*Ti*	*0.009*	*0.034*	*0.007*
Fo	*0.098*	*0.323*	*0.120*	*0.163*		*Mg#*	*0.912*	*1.573*	*0.243*	*2.236*	*0.993*				
						Cr#	*0.841*	*0.060*	*2.237*	*2.588*	*0.570*				

Table SV.3: Clinopyroxene trace element compositions, 2σ standard deviation and limits of detection from LA-ICP-MS measurements.

Sample	COM138	TR45		LaFr8		2σ	*COM138*	*TR45*		*LaFr8*		LOD	COM138	TR45		LaFr8	
Analysis	e5 L	E1 L	e8 L	e14 L	e18 L		*e5 L*	*E1 L*	*e8 L*	*e14 L*	*e18 L*		e5 L	E1 L	e8 L	e14 L	e18 L
ppm																	
Ca	150601	141671	128657	128144	132050		*11215*	*6215*	*6422*	*13942*	*16220*		53.0	28.3	29.9	80.5	80.3
Sc	61.17	23.46	22.12	82.31	74.00		*3.16*	*0.91*	*0.94*	*6.00*	*6.02*		0.153	0.078	0.083	0.214	0.210
V	190.26	55.97	53.50	190.73	174.15		*15.37*	*2.12*	*2.21*	*17.03*	*17.33*		0.088	0.050	0.050	0.146	0.139
Co	20.56	19.31	19.02	22.81	22.29		*1.10*	*0.67*	*0.70*	*1.55*	*1.67*		0.188	0.079	0.090	0.332	0.333
Ni	161.5	86.4	86.0	280.7	281.7		*11.2*	*5.1*	*6.0*	*77.8*	*82.8*		2.530	1.020	1.110	4.550	4.060
Rb	<0,119	0.157	0.147	<0,234	0.634		*0.046*	*0.034*	*0.038*	*0.088*	*0.096*		0.119	0.0872	0.0959	0.234	0.217
Sr	99.3	347.4	343.3	259.2	209.9		*5.5*	*11.4*	*11.8*	*19.5*	*17.6*		0.25	0.14	0.15	0.39	0.37
Y	14.03	3.66	3.23	3.47	3.69		*1.03*	*0.14*	*0.13*	*0.4*	*0.48*		0.026	0.021	0.019	0.043	0.053
Zr	41.39	4.8	4.41	34.1	33.19		*2.38*	*0.2*	*0.2*	*3.4*	*3.68*		0.021	0.018	0.012	0.029	0.034
Nb	0.096	0.199	0.202	1.98	2.01		*0.011*	*0.013*	*0.013*	*0.13*	*0.14*		0.009	0.009	0.004	0.011	0.019
Ba	0.78	0.33	0.9	0.92	<0,86		*0.18*	*0.11*	*0.14*	*0.31*	*0.34*		0.411	0.285	0.290	0.759	0.856
La	2.03	2.555	2.163	13.94	12.3		*0.13*	*0.092*	*0.083*	*1.32*	*1.32*		0.022	0.009	0.012	0.034	0.034
Ce	8.24	6.99	6.27	25.88	22.57		*0.61*	*0.33*	*0.34*	*1.68*	*1.62*		0.020	0.010	0.010	0.023	0.022
Pr	1.5	1.035	0.948	2.71	2.47		*0.12*	*0.044*	*0.044*	*0.25*	*0.26*		0.013	0.002	0.006	0.016	0.022
Nd	8.02	5.22	4.78	9.59	9.41		*0.55*	*0.27*	*0.28*	*0.92*	*1.01*		0.054	0.020	0.014	0.080	0.090
Sm	2.62	1.22	1.065	1.15	1.33		*0.24*	*0.072*	*0.068*	*0.15*	*0.18*		0.048	0.028	0.016	<0,00000	<0,00000
Eu	0.868	0.638	0.626	0.344	0.475		*0.061*	*0.03*	*0.031*	*0.049*	*0.062*		0.039	0.016	0.021	0.071	0.057
Gd	2.83	1.292	1.024	0.82	0.8		*0.24*	*0.082*	*0.076*	*0.16*	*0.17*		0.099	0.055	0.071	0.228	0.197
Tb	0.443	0.1462	0.1336	0.087	0.106		*0.038*	*0.0096*	*0.0095*	*0.019*	*0.021*		0.011	0.007	0.007	0.030	0.024
Dy	2.71	0.86	0.817	0.593	0.74		*0.2*	*0.057*	*0.058*	*0.089*	*0.11*		0.045	0.031	0.015	0.044	<0,00000
Ho	0.477	0.1505	0.1446	0.121	0.109		*0.038*	*0.0096*	*0.0096*	*0.021*	*0.021*		0.005	0.004	<0,00000	0.014	0.008
Er	1.49	0.364	0.354	0.439	0.452		*0.14*	*0.027*	*0.028*	*0.076*	*0.087*		0.014	0.011	0.011	0.033	0.049
Tm	0.197	0.047	0.0459	0.055	0.074		*0.02*	*0.0049*	*0.0051*	*0.012*	*0.015*		0.009	0.004	0.004	0.014	0.012
Yb	1.49	0.33	0.317	0.435	0.503		*0.13*	*0.029*	*0.029*	*0.079*	*0.093*		<0,00000	0.017	0.017	0.066	0.056
Lu	0.207	0.0595	0.0427	0.068	0.068		*0.021*	*0.006*	*0.0055*	*0.016*	*0.019*		0.015	0.005	0.006	0.020	0.032
Hf	1.281	0.21	0.24	0.187	0.316		*0.097*	*0.014*	*0.016*	*0.032*	*0.05*		0.014	<0,00000	<0,00000	0.030	0.036
Ta	<0,0114	<0,0045	0.0045	0.311	0.374		*0.0049*	*0.0019*	*0.0017*	*0.044*	*0.059*		0.011	0.005	0.003	0.015	0.017
Pb	0.597	0.531	0.459	0.57	0.8		*0.055*	*0.029*	*0.029*	*0.094*	*0.14*		0.048	0.025	0.027	0.066	0.062
Th	0.165	0.0302	<0,0152	0.777	1.08		*0.018*	*0.0063*	*0.006*	*0.087*	*0.14*		0.014	0.015	0.015	0.032	0.029
U	0.0527	0.0086	0.0064	0.128	0.135		*0.007*	*0.0012*	*0.001*	*0.017*	*0.019*		<0,00000	<0,00000	<0,00000	0.004	<0,00000

Table SV.4: Amphibole trace element compositions, 2σ standard deviation and limits of detection from LA-ICP-MS measurements**.**

Sample	COM138			2σ	COM138		LOD	COM138	
Analysis	E1 P	e9 P	e11 P	E1 P	e9 P	e11 P	E1 P	e9 P	e11 P
ppm									
Ca	72975.34	74707.85	76169.66	*4964.07*	*6349.79*	*6948.76*	97.6	197.6	186.55
Sc	56.02	62.26	58.75	*2.8*	*3.69*	*3.67*	0.289	0.553	0.511
V	320.26	355.36	308.12	*23.79*	*32.63*	*30.3*	0.166	0.348	0.326
Co	35.59	39.51	30.19	*1.83*	*2.47*	*2.02*	0.309	0.735	0.708
Ni	365.05	358.71	345.8	*22.2*	*30.49*	*32.28*	4.16	10	9.73
Rb	4.9	5.07	5.64	*0.3*	*0.45*	*0.46*	0.221	0.502	0.462
Sr	343.95	383.46	338.36	*17.72*	*23.73*	*22.25*	0.445	0.929	0.866
Y	22.3	22.88	23.51	*1.55*	*1.95*	*2.12*	0.0604	0.114	0.109
Zr	43.64	51.33	43.29	*2.43*	*3.39*	*3.03*	0.0558	0.102	0.115
Nb	3.51	3.2	3.61	*0.26*	*0.31*	*0.35*	0.0269	0.0625	0.0251
Ba	75.13	74.36	72.03	*4.14*	*5.07*	*5.14*	0.821	1.49	1.68
La	2.82	3.04	3.26	*0.2*	*0.28*	*0.3*	0.0355	0.0607	0.0907
Ce	10.92	12.47	10.21	*0.77*	*1.1*	*0.97*	0.034	0.0776	0.0773
Pr	1.89	2.3	1.69	*0.16*	*0.25*	*0.2*	0.0218	0.0262	0.0457
Nd	11.06	11.75	12.92	*0.87*	*1.19*	*1.32*	0.0469	0.159	0.152
Sm	3.53	4.39	3.21	*0.43*	*0.69*	*0.56*	0.131	0.26	0.144
Eu	1.26	1.13	1.62	*0.13*	*0.17*	*0.2*	0.0502	0.14	0.0935
Gd	4.08	4.74	3.65	*0.48*	*0.78*	*0.64*	0.234	0.648	0.456
Tb	0.544	0.74	0.585	*0.064*	*0.11*	*0.1*	0.0116	0.0333	0.0643
Dy	4.11	4.13	5.73	*0.39*	*0.53*	*0.69*	0.0344	0.101	0.069
Ho	0.774	0.59	0.71	*0.081*	*0.094*	*0.11*	0.0149	0.0179	0.0246
Er	1.67	1.57	2.94	*0.21*	*0.28*	*0.45*	0.0439	0.129	0.0891
Tm	0.275	0.259	0.474	*0.043*	*0.059*	*0.087*	0.0147	0.0179	0.0349
Yb	1.56	1.96	2.37	*0.22*	*0.36*	*0.41*	0.0392	<0,00000	<0,00000
Lu	0.223	0.306	0.311	*0.04*	*0.068*	*0.074*	0.019	0.0202	0.0523
Hf	1.26	1.29	1.59	*0.14*	*0.2*	*0.23*	0.0256	0.0847	0.0825
Ta	0.158	0.259	0.22	*0.027*	*0.048*	*0.047*	0.0187	0.0214	0.0361
Pb	0.692	0.75	0.86	*0.092*	*0.14*	*0.16*	0.0848	0.135	0.143
Th	0.057	<0,057	<0,069	*0.022*	*0.034*	*0.036*	0.0329	0.0572	0.0687
U	0.053	0.081	0.0134	*0.011*	*0.022*	*0.0089*	<0,00000	<0,00000	0.00779

RÉPUBLIQUE FRANÇAISE
Liberté
Égalité
Fraternité

Université de Toulouse

Titre : Etude pétrophysique, pétrologique et géochimique de l'interface croûte-manteau en Amérique du Sud centrale et méridionale

Mots clés : xénolithe, microstructure, granulite, péridotite, pétrologie

Résumé : L'interface croûte-manteau, aussi appelé Moho, est une zone clé de transfert de matière, de chaleur et mécanique pour la compréhension notamment de la croissance, de l'évolution et de la déformation de la croûte. Cependant, en domaine continental, la rareté des affleurements de cette zone de la lithosphère fait que sa compréhension reste encore limitée. Cette étude caractérise les microstructures et les processus pétrologiques en jeu en base de croûte et dans le manteau supérieur dans le domaine continental de l'Amérique du Sud centrale et méridionale. Pour ce faire, des xénolithes de granulites, de pyroxénites et de péridotites remontées par des laves de trois régions ont été sélectionnées: celles des basaltes Oligo-Miocène et Pléistocène du Massif Nord Patagonien (MNP; 41-43°S, Argentine), et celles des basaltes crétacés supérieurs de la région de Salta (26°S, Argentine), deux zones situés en domaine arrière-arc de la convergence Nazca/Amérique du Sud, ainsi que celles des andésites récentes du volcan Calbuco (41°S, Chili), situé au niveau de l'arc de cette convergence. Des analyses microstructurales par Electron Backscattered Diffraction ont été effectuées sur ces xénolithes, et couplées avec des analyses pétrologiques, géochimiques et géochronologiques. Les résultats de cette approche multidisciplinaire révèlent que la croûte inférieure du MNP est homogène, peu déformée et affectée par le magmatisme intense qui caratérise le massif depuis le Dévonien. En revanche, la croûte inférieure à Salta est d'origine métasédimentaire et présente un métamorphisme UHT et une déformation en lien avec l'événement thermique associé au rift intracontinental crétacé observé dans cette région. Le manteau lithosphérique de ces deux régions à l'héritage contrasté ont néanmoins subi des événements de déformation similaires, certainement en lien avec des phases extensives en domaine arrière-arc. Enfin, la croûte inférieure sous le volcan Calbuco présente des zones mylonitisées associées à des cumulats magmatiques, montrant le lien étroit dans cette zone entre magmatisme et déformation active. Cette étude révèle l'influence de l'héritage chimique et structural de la lithosphère et de la géodynamique sur la déformation au niveau de l'interface croûte inférieur-manteau subcontinental et des zones avoisinantes.

Title: Petrophysical, petrological and geochemical characterisation of the central and southern South America mantle-crust interface

Key words: xenolith, microstructure, granulite, peridotite, petrology

Abstract: The crust-mantle interface, also known as the Moho, is a key zone of material heat and mechanical transfer, particularly important to better understand the growth, evolution and deformation processes of the crust. However, in the continental domain, the scarcity of outcrops means that our understanding of this zone of the lithosphere remains limited. The present study characterises the microstructures and petrological processes occurring at the base of the crust and within the upper mantle from the continental domain of central and southern South America. Granulite, pyroxenite and peridotite xenoliths sampled by lavas from three regions were selected: those from the Oligo-Miocene and Pleistocene basalts from the Northern Patagonian Massif (MNP; 41-43°S, Argentina), and from the Upper Cretaceous basalts from the Salta region (26°S, Argentina), both located in the back-arc domain of the Nazca/South America convergence, as well as xenoliths from recent andesites from the Calbuco volcano (41°S, Chile), located in the arc of this convergence. Electron Backscattered Diffraction microstructural analyses were carried out on these xenoliths, coupled with petrological, geochemical and geochronological analyses. The results of this multidisciplinary approach reveal that the lower crust of the MNP is homogeneous, only slightly deformed and affected by the intense magmatism that characterises the massif since the Devonian. In contrast, the lower crust from Salta is of metasedimentary origin, showing UHT metamorphism and deformation related to the thermal event associated with the Cretaceous intracontinental rift observed in this region. The lithospheric mantle of these two regions of contrasting heritage has nevertheless undergone similar deformation events, certainly linked to extensive phases in the back-arc domain. Finally, the lower crust beneath the Calbuco volcano shows mylonitised zones associated with magmatic cumulates, demonstrating the close link in this area between magmatism and active deformation. This study reveals the influence of the petrological, chemical and structural heritage of the lithosphere and geodynamics on deformation at the lower crust-subcontinental mantle interface and in neighbouring areas.